A Mechanistic Investigation into Mn(I)-Catalysed C–H Bond Functionalisation: from Pre-Catalyst Activation to Substrate Coordination and Transformation

Lars Anders Hammarback

PhD

University of York

Chemistry

September 2019

Abstract

This thesis describes mechanistic investigations into Mn(I)-mediated C–H bond activation and functionalisation processes, with an additional focus on the factors influencing the reactivity of the manganese complexes. Initially, an investigation into Mn(I)-catalysed C–H bond alkenylation of 2-phenylpyridines was performed, utilising the distinct IR bands of the manganese carbonyl species to monitor the catalyst *in situ* (Chapter 2). The mechanistic studies allowed for a comprehensive reaction mechanism to be derived, where pre-catalyst activation was found to be substrate-dependent, leading to two distinct pathways. Furthermore, two new catalytic cycles (involving protonation by the 2-phenylpyridine and water) were discovered, in addition to the confirmation of the previously proposed cycle.

Time-Resolved InfraRed (TRIR) spectroscopy provided an opportunity to study the processes underpinning C–C bond formation in further detail, observing short-lived (0.5 ps – 1 ms) reaction intermediates and their respective kinetic behaviour (Chapter 3). Photochemical initiation led to the utilisation of a range of manganese complexes and unsaturated substrates. The uni- and bimolecular behaviour of the intermediates and their kinetics were probed from experiments diluted in toluene.

Carboxylic acid additives were employed to increase the efficiency of Mn(I)-catalysis using terminal alkynes, while inhibiting reactions with acrylates (Chapter 4). Mechanistic studies revealed that a change in catalyst resting-state explains the different effects. TRIR spectroscopy allowed for the observation of the protonation by carboxylic acids, leading to an observation of the steps underpinning the CMD/AMLA-6 mechanism.

Investigation into the fluorine-induced regioselectivity of Mn(I)-mediated C–H bond functionalisation of 2-phenylpyridines showed that the cyclomanganation reaction is kinetically driven and irreversible. Addition of benzoic acid led to a reversible mechanism, where the regioselectivity is thermodynamically controlled. It was additionally revealed that the regioselectivity likely arises from the relative thermodynamic stability of the manganacycles, where the trend follows the order: *ortho>meta>para* (with respect to the fluorine substituent).

List of Contents

List of Figures

List of Schemes

List of Tables

Acknowledgements

Firstly, I want to express my gratitude towards Ian Fairlamb and Jason Lynam for their excellent support and supervision. I much appreciate all the help and freedom I have been given during this project, which has been tremendously enjoyable and rewarding. I will always cherish my time working with the two of you and I wish you both the best for the future. I would also like to extend my thanks to my industrial supervisor Alan Robinson for being supportive of the project and especially the mechanistic aspect of the work.

I would like to thank the staff at the ULTRA facility (in particular Emma Gozzard, Ian Clark and Mike Towrie) for their help and support with the TRIR experiments. The RAL visits have been very enjoyable and one of the highlights of the PhD. I am grateful for the help and support I received during my placement at Syngenta from everyone in the Process Study Group and in particular Tom Corrie. I also want to thank James Donald and James Firth for their collaboration on the synthetic application of the photochemical work. The technical support I have received in York have been invaluable, so I want to especially acknowledge the support of Heather Fish (NMR), Karl Heaton (MS), Adrian Whitwood (XRD) and Graeme McAllister (CHN).

I would like to thank everybody that has had a positive impact on my project and time in York. There are too many to name individually, but there are a few that deserve a mention: Alan (for getting me to the point where I could do this PhD), Ben (for teaching me about the finer sides of British culture and for the time in Aucott Towers), Charlotte (for making sure it is even possible to work in the lab and that the ReactIR probe is clean), David (for the M&S trips and education about the true north), Evans (for always smiling and finding NMR tubes), Gayathri (for Suits and Hamilton), George Platt (for being a true Cheesehead and therefore always being there to discuss the latest NFL news), George Clarke (for knowing the exchange rate to the Swiss Franc at any given point), Jonny and Matthew (for the RAL banter), Josh (for a ton of help and always being up for a pint), Lampie (for being a Mark Petchey, who I admit is a great chemist), Lisa (for leaving us the best gift of all in BANG), Mary (for teaching all of us about large scale synthesis), Neda (for seeking after my failures in life), Neil (for being a contagiously positive and energetic person) and the excellent undergraduate and Erasmus students I had the pleasure to work with.

Jag skulle också vilja tacka mamma och pappa för all otrolig stöttning genom alla dessa år och Krille för all hjälp och inspiration som tillslut ledde till denna PhD. Farfar, Icki, Farmor och Christer har också hjälpt till med motivation och strävan efter större saker. Till slut så måste jag tacka mormor för sisun som jag har haft mycket nytta av under projektet.

Author's Declaration

I declare that this thesis is a presentation of original work and I am the sole author. This work has not previously been presented for an award at this, or any other, University. All sources are acknowledged as References.

Parts of this work have been reproduced in published papers, copies of which can be found in Appendix 1:

Hammarback, L. A.; Clark, I. P.; Sazanovich, I.; Towrie, M.; Robinson, A.; Clarke, F.; Meyer, S.; Fairlamb, I. J. S.; Lynam, J. M. Mapping out the key carbon-carbon bond forming steps in manganese-catalysed C–H functionalisation. *Nat. Catal.* **2018**, *1*, 830-840.

Hammarback, L. A.; Robinson, A.; Lynam, J. M.; Fairlamb, I. J. S. Mechanistic Insight into Catalytic Redox-Neutral C–H Bond Activation Involving Manganese(I) Carbonyls: Catalyst Activation, Turnover, and Deactivation Pathways Reveal an Intricate Network of Steps. *J. Am. Chem. Soc.* **2019**, *141*, 2316-2328.

Hammarback, L. A.; Robinson, A.; Lynam, J. M.; Fairlamb, I. J. S. Delineating the critical role of acid additives in Mn-catalysed C–H bond functionalisation processes. *Chem. Commun.* **2019**, *55*, 3211-3214.

Chapter 1: Introduction

1.1 Manganese Catalysis

Transition metal-mediated reactions has been an important tool for synthetic chemists for more than half a century. Nobel prizes has been awarded for this in 2010 (Pd-catalysed cross-coupling), 2005 (olefin metathesis), 2001 (asymmetric hydrogenation) and 1973 (sandwich compounds).[1] Though most major synthetic discoveries has been made using platinum group metals (PGMs), there is a large potential of more abundant and sustainable first row transition metals. Metals such as Mn,[2] Fe,[3] Cu,[4] Ni[5] and Co[6] has among other examples been successfully utilised in a wide-range of organic transformations both as alternatives to PGMs and as replacements.

Many studies have been conducted into the reactivity of manganese for use in catalytic reactions, with the development of Jacobsen's catalyst for enantioselective epoxidation being one of the most well-known examples.[7] Manganese-complexes have also been utilised in radical cyclisations, C–H bond oxidations, halogenations etc., where the large number of oxidation states for Mn (−3 to +7) partially enables its diverse reactivity.[2, 8] A recent discovery has been reported by Chirik, Knowles and co-workers on the generation of ammonia from a Mn(V)-nitride complex, mediated by photoredox catalysts in the presence of light.[9] This represents an intriguing possibility of a new methodology for the synthesis of ammonia and shows that an excited photoredox catalysts can interact with the manganese centre to promote further reactivity.

C–H bond functionalisation have over the past 2 decades become one of the most studied type of transition metal mediated processes.[10] It provides a large upside over processes such as traditional cross-coupling reactions, due to in general being more atom economic, generating less waste and being more cost effective. As for Mn-catalysis in general, there are many reported Mn-catalysed C–H bond functionalisation methodologies.[2] The direct amination of benzylic C–H bonds using iminoiodinanes and Mn(III)-catalyst **3**, is an example which has recently been reported by White and co-workers (**Scheme 1**).[11] This methodology provides an opportunity to directly and selectively form C–N bonds from benzylic C–H bonds, in the presence of other C–H bonds.

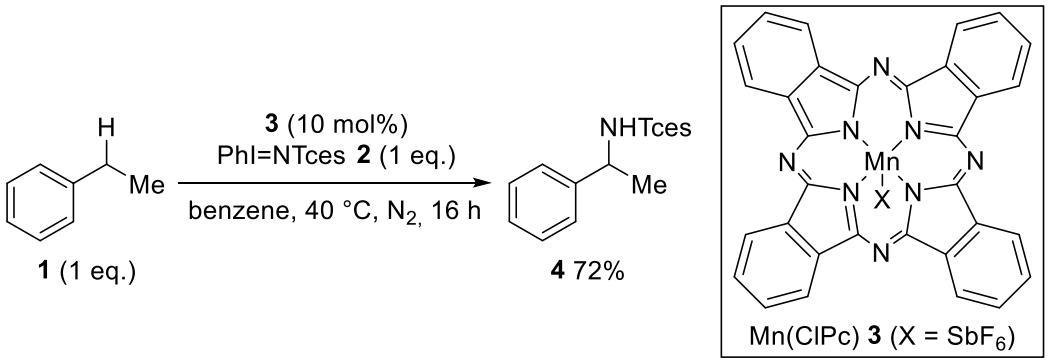

Scheme 1. Mn-catalysed amination of benzylic C–H bonds, reported by White and co-workers.[11]

1.2 Stoichiometric Mn(I)-Mediated C–H Bond Functionalisation

The reactivity of manganese carbonyl complexes has been studied extensively since the 1950s. There have been numerous studies conducted into from the reactivity of manganese anions, hydrides, halides, etc., with a wide range of different functional groups, in order to probe reactions such as C–H/F bond activation and C–Mn/C bond formation.[12] The reactions most relevant to the work presented within this thesis are *ortho*-directed cyclomanganation reactions of ligands containing suitable directing groups.

Bruce and co-workers reported the *ortho*-directed cyclometallation of azobenzene **5** using $MnMe(CO)_5$ **6** in 1970 (**Scheme 2**)[13] and this is commonly considered to be the first reported cyclomanganation reaction.[14] However, the resulting manganacycle **7** was reported by Heck two year earlier, where it was synthesised through reaction of manganese-anion **8** with azobenzene-containing palladacycle **9**.[15] As Heck's methodology did not involve Mn-mediated C–H bond activation, it is understandable that Bruce and co-workers are considered to have reported the first cyclomanganation. Neither studies probed further reactivity of the newly formed C–Mn bond, but Bruce and co-workers showed that Mn(I)-alkyl species can generate manganacycles directly from a sp^2-hybradised C–H bond in a regioselective fashion.

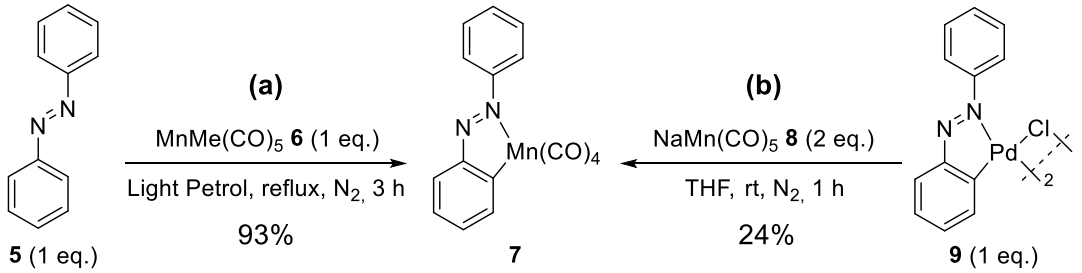

Scheme 2. First reported cyclomanganation reactions of azobenzene to manganacycle **7**. (a) Synthesis reported by Bruce and co-workers, using **6** as the manganese precursor.[13] (a) Synthesis reported by Heck, using **8** as the manganese precursor.[15]

The directing groups and C–H bonds on the ligand (to be cyclomanganated) has widely varied, with exotic examples such as triphenylphosphine/arsine oxides, sulfides and selenides reported (**Figure 1**).[16] *N*-containing directing groups are most commonly utilised, with examples including amines,[17] imines[18, 19] and *N*-heterocycles.[14, 17] The other main type of directing groups employed are the oxygen-containing derivatives, such as aldehydes,[20] ketones[20, 21] and amides.[20, 22] One of the main challenges of utilising the manganacycles in catalysis is to find a balance between the binding affinity and lability of the ligand, which allows for both binding of the substrate and release of the product post-functionalisation. Therefore, it is likely that several of the reported ligands are unsuitable for effective utilisation in catalysis, as the binding affinity will differ.

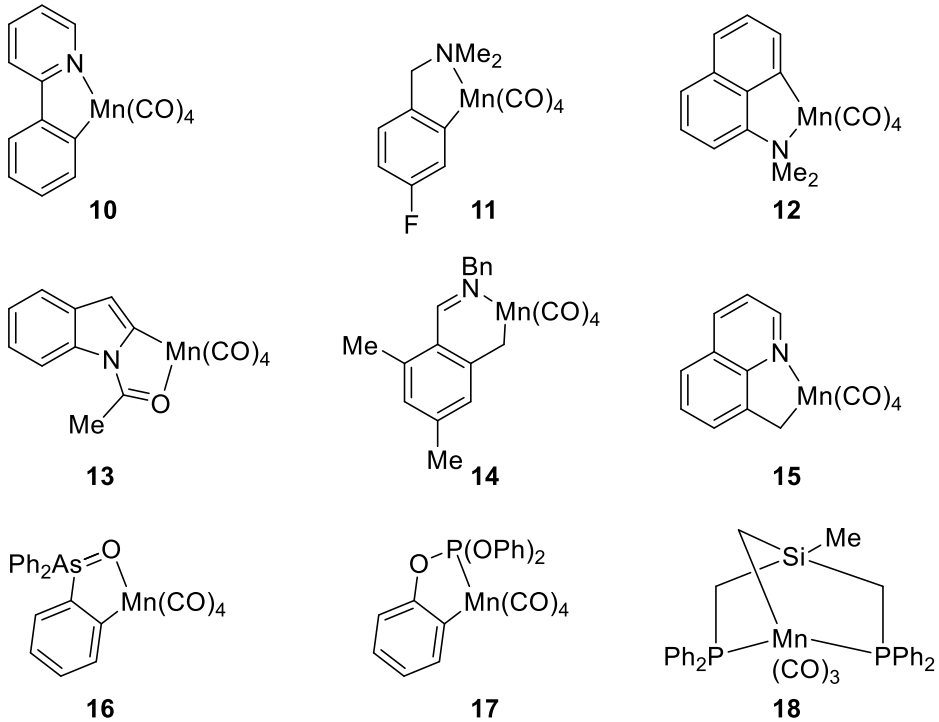

Figure 1. Examples of reported manganacycles; **10**,[23] **11**,[17] **12**,[17] **13**,[20] **14**,[19] **15**,[17] **16**,[24] **17**[25] and **18**.[26]

Interestingly, benzylic C–H bonds have also been activated to form the corresponding manganacycles,[19] though no catalytic utilisation has been found thus far. This is unexpected as Mn-alkyl species with no directing group (such as $MnBn(CO)_5$ **19** and $MnMe(CO)_5$ **6**) can perform a range of reactions.[12, 14] The stability of the benzylic manganacycles or preference for side-reactions could explain the lack of desired reactivity.

Even though no utilisation of the manganese complexes in catalytic reactions was reported prior to this millennium, there were studies conducted investigating the reactivity of the manganacycles towards various reagents. Liebeskind and co-workers reported the first insertion of an internal alkyne into a C–Mn bond, when reacting diphenylacetylene **21** with acetophenone-derived manganacycle **20** (**Scheme 3**).[27] Trimethylamine *N*-oxide initiated CO-loss, which allowed for the alkyne to coordinate and react to form cyclopentadiene **22**. The formation of **22** should proceed *via* the generation of a 7-membered insertion complex (such as examples shown in **Figure 2**), which can subsequently rearrange to form the cyclopentadiene derivative. The reactivity of unsaturated substrates with C–Mn bonds was previously reported by Wilford *et al*., studying the insertion of tetrafluoroethylene into the C–Mn bond of $MnPh(CO)_5$.[28]

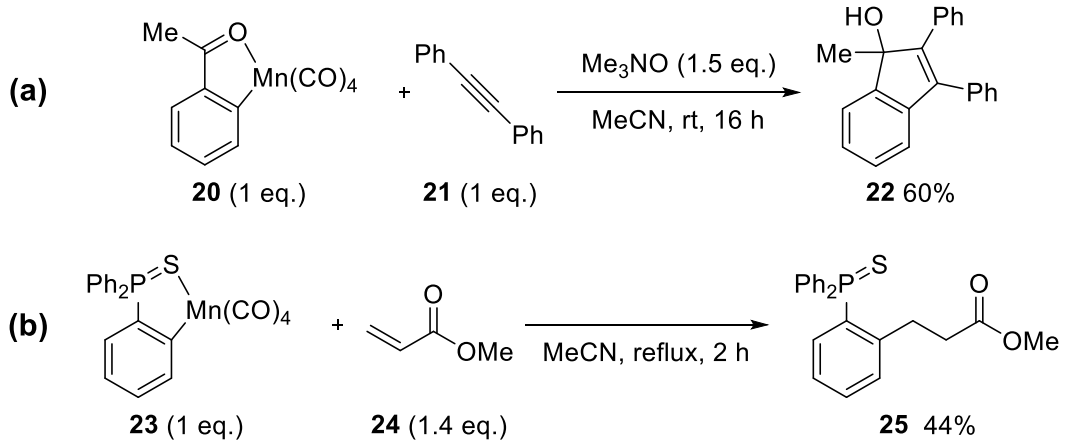

Scheme 3. Stoichiometric reactions between manganacycles with unsaturated substrates. (a) Reaction between diphenylacetylene and acetophenone-derived manganacycle **20**, reported by Liebeskind and co-workers.[27] (b) Reaction of methyl acrylate with sulfur-containing manganacycle **23**, reported by Nicholson and co-workers.[29]

Nicholson and co-workers have also conducted studies into the reactivity of manganacyclic C–Mn bonds, where the reaction of methyl acrylate with triphenylphosphine sulfide derived Mn-complex **23** (**Scheme 3**) is highly relevant to the work presented within this thesis.[29] The new C–C bond of alkyl product **25** is likely

formed according to the same C–Mn insertion mechanism as for Libeskind and co-workers. However, an extra hydrogen has been added to the product in this example. This means that one reagent in solution can transfer a proton, which is unexpected due to the relatively low acidity of the C–H bonds in solution. Other unexpected results on the insertion reactions with acrylates and alkenes, had already been reported by Nicholson and co-workers.[30] When studying the insertion on cyclomanganated chalcones, surprising hydrogen-transfer and cyclisations were reported for the acrylates and alkenes respectively.

Nicholson and co-workers synthesised 7-membered insertion complexes, to support the proposed mechanism of C–C bond formation (**Figure 2**). Triphenylphosphite derived complex **26** was generated by reaction of the 5-membered manganacycle with diphenylacetylene **21**. The successful synthesis of the 7-membered insertion complex highlights the relative stability of the complexes derived from internal alkynes, as no examples formed from terminal alkynes has been reported.[16] The reaction of dimethyl acetylenedicarboxylate with triphenylphosphine sulfide complex **23**, generated 7-membered insertion-complex **27**. Unexpectedly, decarboxylation occurred to generate an alkene-proton on the carbon bonded to the arene.[29] It is unclear if the decarboxylation took place before or after the C–C bond formation. The final example was reported Suarez and co-workers, where an imidazole-containing manganacycle was treated with **21** to form insertion-complex **28** (**Figure 2**).[31] This is the most relevant example for the subsequently developed catalytic reactions, where *N*-heterocycles are commonly employed.[32] The characterisation of the 7-memerbed insertion complexes supports the proposed mechanism of C–C bond formation in the catalytic reactions. Though, no mechanism investigations were performed to elucidate a more detailed mechanism of C–C bond formation.

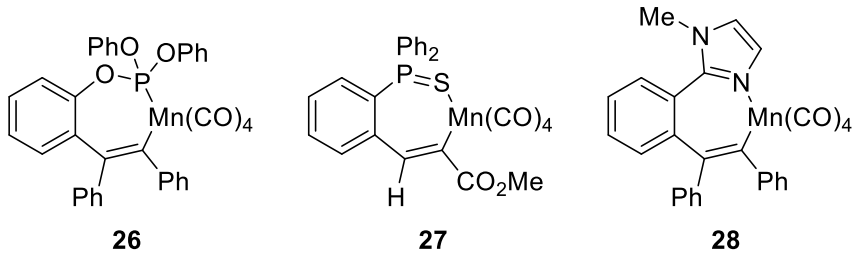

26 **27** **28**

Figure 2. 7-membered manganacycles **26**,[16] **27**[29] and **28**,[31] generated by stoichiometric reaction with internal alkynes.

1.3 Mn(I)-Catalysed C–H Bond Functionalisation

Even though the synthesis of manganese(I)-carbonyl complexes have been known for many decades and their reactivity has been probed, it was not until 2007 when Kuninobu and co-workers reported the first synthetic methodology using catalytic amounts of manganese (**Scheme 4**).[33] They employed $MnBr(CO)_5$ **31** as the Mn-precursor to activate the *ortho* C–H bond of 2-arylimidazoles, which subsequently reacted with aldehydes to form the corresponding alcohols. The initial reaction was however stoichiometric in manganese unless triethylsilane was added, which generated the silyl ether product and made the reaction catalytic in Mn. The high temperature (115 °C) and long reaction time (24 hours) are problematic aspects of this methodology, but it still highlights that Mn(I)-carbonyl catalysed C–H bond functionalisation is possible.

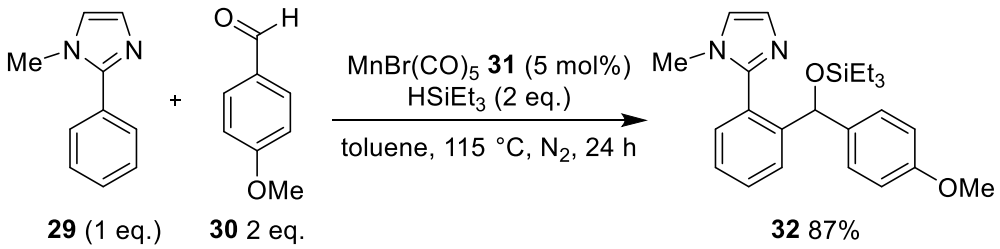

Scheme 4. Mn(I)-catalysed C–H bond functionalisation of 2-arylimidazoles with aldehydes, reported by Kuninobu and co-workers.[33]

Despite Kuninobu's publication, it took 6 years until the next reported example of a Mn(I)-catalysed reaction, when Wang and co-workers reported the C–H bond alkenylation of 2-phenylpyridines to yield the corresponding styrene derivatives (**Scheme 5**).[34] **31** was used once more as pre-catalyst and an amine base additive was required to generate alkene product **35**, as the C–H bond activation of 2-phenylpyridine **33** did not occur in the absence of base. The reaction tolerated a range of different 2-phenylpyridines and terminal alkynes, generating the corresponding alkene products in good yields. However, internal alkynes were found to be inactive and did not generate any of the desired alkene product under the reaction conditions. This inactivity could arise from the relatively high stability of the 7-membered insertion-complexes for internal compared to terminal alkynes.[31] An initial mechanistic investigation was conducted by Wang and co-workers, and it was combined with computational studies to generate a proposed mechanism, which is discussed in chapter 2.

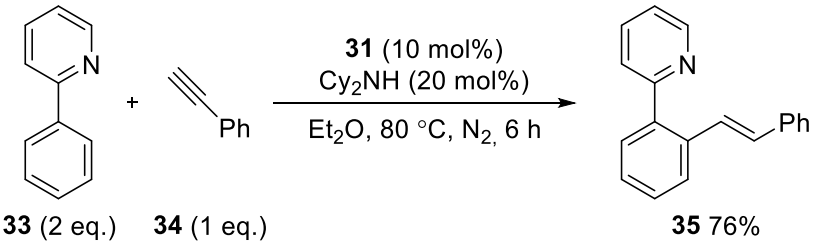

Scheme 5. Mn(I)-catalysed C–H bond alkenylation reaction, reported by Wang and co-workers.[34]

After their initial report, Wang and co-workers have expanded their contribution to the Mn(I)-catalysis field by subsequently reporting a range of new synthetic methodologies.[35] The most relevant to the work presented within this thesis is the reactions employing acrylates as the unsaturated substrate (**Scheme 6**),[36] which provided for a catalytic adaptation of the previously mentioned reactions of manganacycles with acrylates (**Scheme 3**). The desired alkyl products were generated in high yields, with **31** and Cy_2NH employed as pre-catalyst and base additive respectively. Interestingly, the ratio of unsaturated substrate to 2-phenylpyridine **33** differs from the alkenylation-methodology (1:2),[34] where the acrylates (1.5:1) are in excess. From preliminary mechanistic studies it was suggested that the conjugate acid of the amine base is responsible for the proton transfer event, which is surprising given the relatively low acidity of the ammonium protons.

1-(2-pyridyl)indoles have become commonly utilised in Mn(I)-catalysed C–H bond functionalisation due to their perceived increased reactivity[32] and one important example relating to this thesis is the reaction with isocyanates, which was reported by Ackermann and co-workers (**Scheme 6**).[37] The aminocarbonylation did not require any base additives, which was a difference to most other methodologies. This suggested that the isocyanate can act a base in the reaction, as no other significant alterations are made compared to other similar examples. It was also unclear how the proton transfer occurred and it was suggested HBr is responsible, though it is unlikely to be generated with many potential *N*-containing bases present in solution.

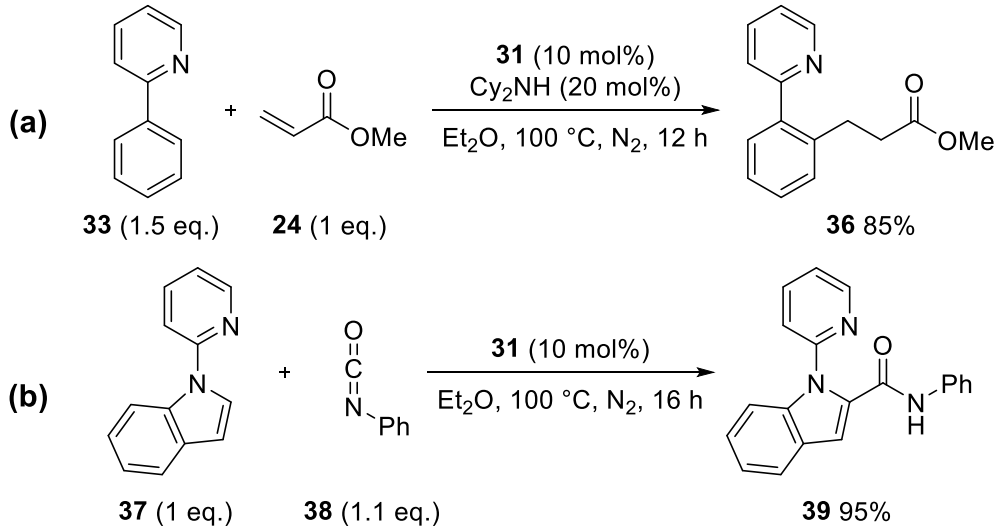

Scheme 6. Mn(I)-catalysed C–H bond functionalisation reactions of 2-pyridylarenes. (a) Reaction with acrylate **24**, reported by Wang and co-workers.[36] (b) Reaction with isocyanate **38**, reported by Ackermann and co-workers.[37]

Many other Mn(I)-catalysed C–H bond functionalisation reactions have been reported by a range of research groups (see examples in **Figure 3**), where the methodologies have a few common features.[32, 38] The formation of the new C–C/X bond have continuously been proposed to proceed through insertion into a C–Mn bond to form a 7-membered insertion complex. Separately form the reactions involving insertion into a C–Mn bond, there have been a range of other reactions catalysed by Mn(I)-carbonyl complexes.[2] Hydrosilylation,[39] direct arylation[40] and alkyne trimerization[41] are examples showing the versatility of the manganese-complexes.

$MnBr(CO)_5$ **31** or $Mn_2(CO)_{10}$ **40** have been utilised as pre-catalyst in the majority of the reported methodologies and there have been surprisingly few studies conducted into the thermal C–H bond activation mechanism for either manganese complex. This have likely influenced the suggested mechanism of pre-catalyst activation, where a manganacycle is commonly proposed to be generated directly from the pre-catalyst, even though this has mainly been observed for Mn-alkyl species.

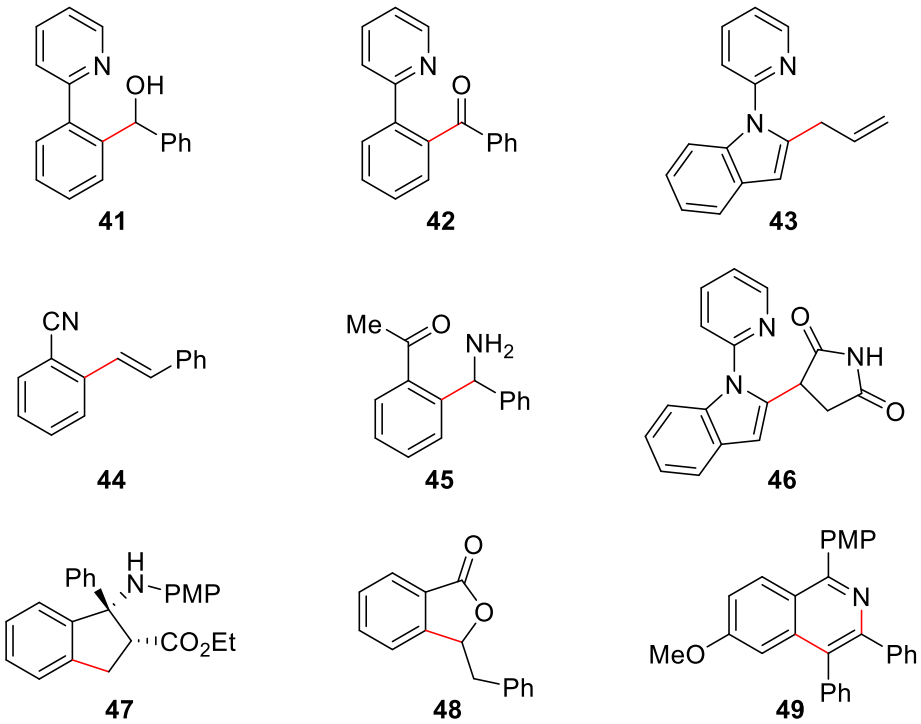

Figure 3. Examples of reported products formed by Mn(I)-catalysed C–H bond functionalisation; **41**,[42] **42**,[42] **43**,[43] **44**,[44] **45**,[45] **46**,[46] **47**,[47] **48**[48] and **49**.[49] Red bonds highlight the C–C/N bond formation mediated by the manganese.

Lynam, Fairlamb and co-workers have provided further mechanistic insight to Mn(I)-catalysed C–H bond functionalisation, when they characterised 2-pyrone derived 7-membered insertion complex **54** (**Scheme 7**).[50] The catalytic reaction between phenylacetylene **34** and 2-pyridyl-2-pyrones was found not to generate any of the desired alkene-product. Nevertheless, insertion-complex **54** was synthesised from the corresponding 5-membered manganacycle **50** using UV-light to dissociate one CO-ligand, to allow for coordination of **34**. Low temperatures hindered further reactivity, while reductive elimination to form **53** took place at room temperature. High temperatures were however required to produce **53** in the absence of UV-irradiation, highlighting that thermal CO-loss from the 5-membered manganacycle is difficult. It also shows that reductive elimination is preferred over protonation for the 2-pyrone system, which has also been utilised in the C–H bond functionalisation of an imine derivative.[49]

The desired alkene product **52** was generated (28%) if the reaction was performed in neat **34**, with the rest of the manganacycle forming unusual products from Diels-Alder reactions taking place with the excess alkyne. It seemed as the Diels-Alder reactions occurred on reductive elimination complex **53**, though a separate reaction of **53** in **34** was not performed to confirm this. Another unexpected product synthesised was

bicyclic product **55**, which was formed from a second insertion of **34** on the 7-membered insertion complex. This was only observed for a manganacycle with methoxy-substituted pyridine group (**51**), but the equivalent reactivity had previously been utilised by Lei, Li and co-workers while functionalising indoles.[51]

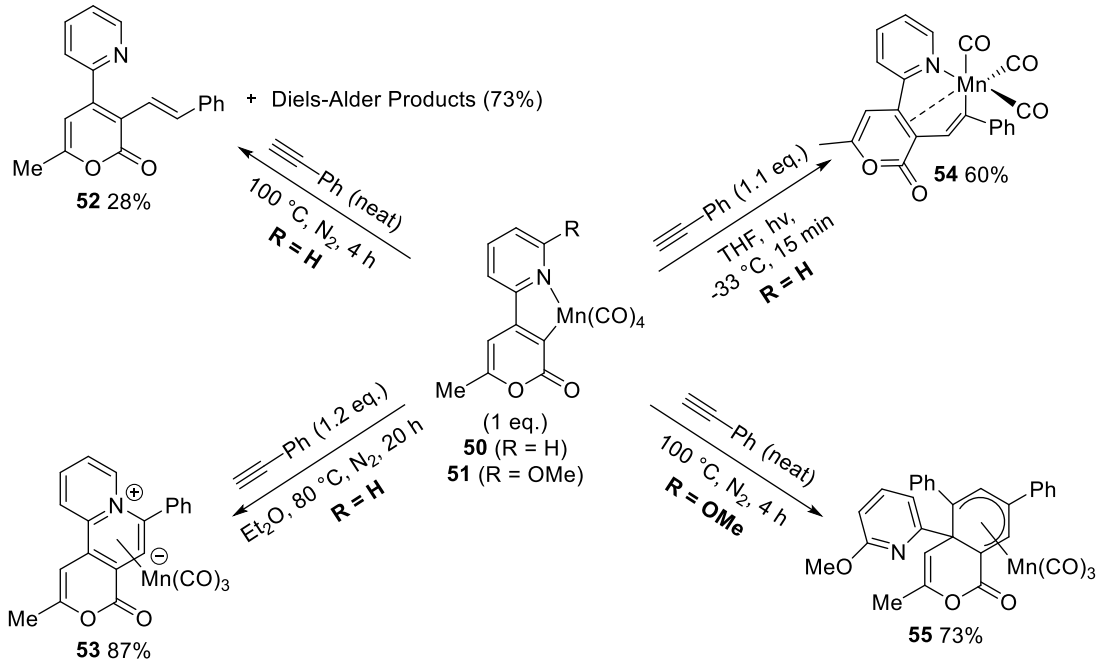

Scheme 7. Reactivity of cyclomanganated 4-(2-pyridyl)-2-pyrones with phenylacetylene, reported by Lynam, Fairlamb and co-workers.[50]

1.4 Alternative Synthesis of Styrene Derivatives

The functionalised styrene derivatives generated by Wang and co-workers[34] (**Scheme 5**) are the main type of products studied within this thesis. Styrene derivatives are important in a wide variety of application, where the main usage is in the synthesis of various polymers such as polystyrene, synthetic rubbers and medical grade resins.[52] Functionalisation of the styrene building blocks may allow for the generation of new polymers and materials with novel properties. Another use of styrene is as a starting material in further small molecule modifications, such as for example in transition metal mediated C–H bond alkylation,[53] hydrogenation[54] and cross-coupling reactions.[55] Styrene is also used as a building block in many common organic reactions, where examples range between hydroboration,[56] epoxidation[57] and halogenation reactions.[58] The styrene moiety can also be found in many natural products and drug molecules, such as in Naftifine[59] (antifungal drug) and Bexarotene[60] (for treating cutaneous T cell lymphoma). The natural products and drugs containing

styrene derivatives are mostly highly functionalised, which are therefore more challenging to synthesise than styrene.

Currently, commercial synthesis of styrene proceeds via multiple step pathways, such as initial Friedel-Crafts alkylation with subsequent dehydrogenation, yielding large excess of halogenated waste and often requiring higher reaction temperatures.[61] Additionally, there are many reported transition metal mediated methodologies to synthesise functionalised styrene derivatives, which forms the same C–C bond as in Wang and co-workers Mn(I)-example (**Scheme 5**). The Pd-catalysed Heck cross-coupling reaction is one of the most common examples used for this transformation, requiring the coupling of an alkene with a halogenated arene.[55] As well as the Friedel-Crafts alkylation, the Heck cross-coupling generates stoichiometric amounts of undesirable halogenated waste material. The main advantages of this approach, compared to Wang's methodology, is the generally low catalyst-loadings required (with examples using < 0.1 mol% Pd)[62] and high functional group tolerance.[55] However, the disadvantages include the undesired waste generation, poor atom economy and generally slightly higher reaction temperatures than that of the Mn(I)-catalysis.[55]

In addition to the examples using pre-functionalised arenes, there are a large amount of reported methodologies forming the same C–C bond via C–H bond functionalisation, using transition metals such as Ru, Rh, Pd, Pt and Co.[63] Fujiwara and co-workers reported in 2000 a mild alkenylation of benzenes using alkynes and $Pd(OAc)_2$ as the pre-catalyst.[64] As was the case with the Heck cross-coupling, Fujuwara's methodology employs low catalyst loadings (0.02-1 mol%), with the lower amounts reaching similar yields after extended reaction times. In addition to the low reaction temperatures (25 °C), the functionalisation of an aryl C–H bond without the need for a directing group provides further advantages to the Mn(I)-catalysis of Wang and co-workers. Though, the usage of halogenated solvent (CH_2Cl_2), extended reaction time (with low catalyst loading) and difficulty in selectively activating a desired C–H bond are problematic when compared to the manganese catalysed methodology. Another example of the direct functionalisation of a benzene C–H bond with ethylene to form styrene has been reported by Gunnoe and co-workers, where they used a diazobutadiene-containing Rh-catalyst.[61] This process requires the use of stoichiometric copper oxidant and high reaction temperatures (≤ 200 °C). The Rh-

catalyst is however used in very low amounts (1×10^{-3} mol%) and can produce the styrene in excellent yields (95%).

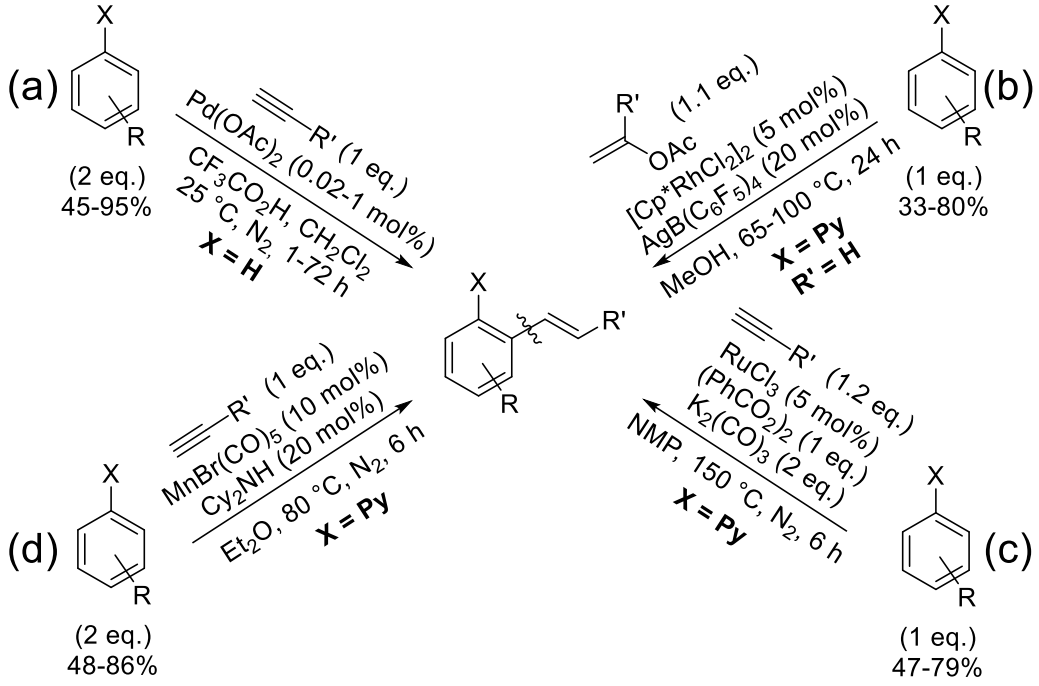

Scheme 8. Examples of transition metal-catalysed synthesis of functionalised styrene derivatives, using C–H bond functionalisation. (a) Pd-catalysed synthesis of styrene derivatives, reported by Fujiwara and co-workers.[64] (b) Rh-catalysed synthesis of styrene derivatives, reported by Ellman and co-worker.[65] (c) Ru-catalysed synthesis of styrene derivatives, reported by Zhang and co-workers.[66] (d) Mn-catalysed synthesis of styrene derivatives, reported by Wang and co-workers.[34]

There are also many examples of producing styrene derivatives using directing groups on the arene, and a few reports used the 2-phenylpyridine starting material as the case was in the Mn(I)-catalysis.[63] A report by Ellman and co-worker uses Rh-catalysis to couple 2-phenylpyridines with vinyl acetates at temperatures comparable to the Mn(I)-catalysis (65–100 °C).[65] The relatively high catalyst loadings (10 mol% Rh) and large amounts of silver additives (20 mol%) are problematic when compared to Wang's protocol,[34] using the same catalyst loading of Mn and an amine base additive. Zhang and co-workers have developed a Ru-catalysed methodology in forming alkenylated 2-phenylpyridines by coupling the same reagents as in Wang's Mn(I)-example.[66] The reaction used half the catalyst loading (5 mol%), but required higher reaction temperatures (150 °C) and an extra additive (benzoyl peroxide). Otherwise the reactions are comparable with similar yields and reaction times (6 hours). There are additionally several reported methodologies where the same C–C bond formation is made as the work mentioned above, but the directing group used (often containing N–H bonds) allows for a subsequent C–N bond to be formed.[67-70]

As previously shown, there are many methodologies reported for the synthesis of styrene derivatives in addition to the Mn(I)-catalysed example by Wang and co-workers.[34] There are advantages and disadvantages with all pathways, whether it is the reaction temperature, catalyst loading, use of additives or excess generation of waste material. Therefore, a methodology is best chosen based upon the priority of conditions for a particular process, where for example catalyst recyclability and functional group tolerance may be of high importance. However, Wang's methodology has the potential to be a competitive process as it uses an abundance earth metal which has a large potential as catalyst for organic transformations[2] and proceeds under relatively mild reaction conditions.[63] The process also generates relatively low amounts of halogenated waste (compared to when using halogenated arenes as substrates) and is atom economic when formally no additional atoms are found in the final product (besides from the two starting material). The lack of catalyst recyclability of the Mn-catalyst is problematic for the process efficiency, which also is the case for the high amounts of catalyst employed (10 mol%). A full analysis of all aspects of the reaction (cost efficiency, environmental impact, etc.) is required for the comparison to other methodologies to be made, and it should be noted that some aspects (for example availability of starting material or catalyst) may change with increased demand and this should also be taken into account.

The environmental impact the process is one of the most important aspects which needs to be considered in deciding on the suitability of employing a particular methodology. This is highly difficult to evaluate as a vast range of factors has an impact on the environment. For example, the catalyst mining, synthesis, recyclability, efficiency and toxicity of metal species in waste/products are all important when comparing transition metal catalysts. In the case of Wang's Mn(I)-catalysis, the use of toxic CO-ligands on large scale can be problematic when considering the safety aspects and the lack of catalyst recovery requires the pre-catalyst to be synthesised before each use. These problems can however be solved with design of improved pre-catalysts, which can be recycled and uses less toxic ligands. Detailed analysis for all reagents and solvents used in the process is required for the full environmental impact to be assessed and therefore to be compared to other competitive methodologies.

1.5 Mechanisms of C–H Bond Activation

There are several reaction mechanisms for transition metal mediated C–H bond activation, of which oxidative addition, electrophilic substitution and σ-bond metathesis are the main subdivisions.[71] The specific mechanism is not well defined for these descriptions and they mainly describe the overarching transformation that has taken place. σ-Complex Assisted Metathesis (σ-CAM) and Concerted Metallation-Deprotonation (CMD) or Ambiphilic Metal Ligand Activation (AMLA) are the mechanisms most applicable to the work presented within this thesis.

σ-Bond metathesis reactions have been known for many decades and the involvement of σ-complexes in the mechanism have been proposed for some examples.[72] However, the mechanism which now is referred to as σ-CAM was not proposed until the early 2000s by Sabo-Etienne, Perutz and co-workers.[73, 74] The σ-CAM mechanism for C–H bond activation starts with an initial σ-coordination of the C–H bond to form the corresponding σ-complex (**Scheme 9**). Thereafter, the hydrogen is transferred in a concerted fashion to the proton-acceptor, as the new C–M bond is generated. The new σ-complex generated can subsequently dissociate from the metal to complete the C–H bond activation step. The steps involved in the mechanism are reversible and the relative strength of the X–H bonds determines which M–X species is generated in the reaction.

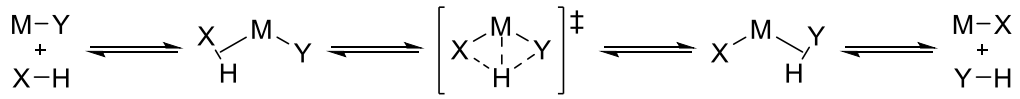

Scheme 9. General schematic view of transition metal mediated C–H bond activation according to the σ-CAM mechanism.[74]

The CMD and AMLA mechanisms were developed at a similar time as the σ-CAM mechanism, by Fagnou and co-workers (CMD)[75] and Davies, Macgregor and co-workers (AMLA).[76] The mechanisms are highly similar in practice and have been extensively studied,[71, 77] as well as proposed being involved in many transition metal catalysed C–H bond functionalisation reactions.[78] For the AMLA mechanism, a number following "AMLA" denotes the number of atoms involved in the transition state, with 6 being the most common number.

An almost identical mechanism to the CMD/AMLA-6 was reported by Ryabov on the cyclopalladation of benzylamines using palladium acetate, with the main difference of a proposed positive charge on the arene in the transition state (Wheland intermediate),

suggesting that an initial electrophilic addition is favourable.[79] Later computational studies by Davies, Macgregor and co-worker elucidated a similar mechanism (**Scheme 10**).[76] An agostic-interaction to the C–H bond was important in lowering its acidity, making CMD/AMLA more favourable than an initial electrophilic addition, before the acetate-ligand deprotonates the benzylamine in a concerted fashion. The newly formed acetic acid-complex is lower in energy than the starting acetate-species, meaning that the reverse reaction was unlikely to occur.

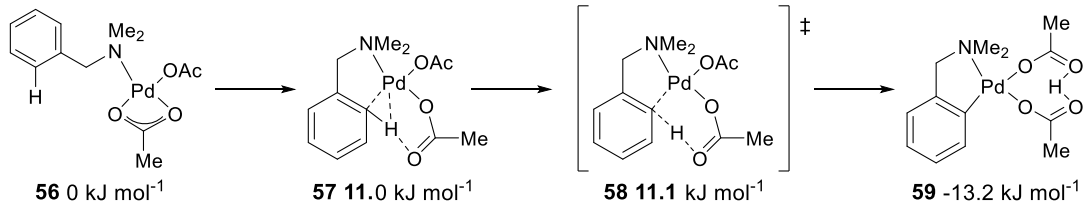

Scheme 10. Computationally determined CMD/AMLA-6 mechanism for the acetate-assisted cyclopalladation of benzylamines, reported by Davies, Macgregor and co-worker.[76]

The CMD/AMLA mechanism can be employed on a wide-range of substrates and does not require, for example, cyclometallation to occur nor the presence of specific ligands. It has commonly been proposed in direct arylation of both electron-rich/poor arenes and heterocycles.[77, 80] There are many similarities between the σ-CAM and CMD/AMLA mechanisms, with both mechanisms including a concreted proton-transfer step to form a new C–M bond. Both processes are also reversible in principle and the relative stability of the complexes and X–H bonds determines if the desired C–H bond activation will take place of not.

1.6 Project Aims and Objectives

The aim of this project is to develop a deeper understanding of the mechanism and underlying properties of Mn(I)-catalysed C–H bond functionalisation, and to use the findings in increasing the reaction efficiency. The following objectives were employed to achieve the aim of the project:

I. The utilisation of the distinct IR bands of the manganese-carbonyl complexes and other techniques, to elucidate a full reaction mechanism for Mn(I)-catalysed C–H bond alkenylation.
II. Exploit the photochemical properties of the manganese-carbonyl complexes in studying the C–C bond formation using time-resolved spectroscopy.

III. Investigate the effect of the conjugate acid and other acid additives in the Mn(I)-catalysed C–H bond functionalisation, using *in situ* and *ex situ* analytical techniques.

IV. Examine fluorine-induced regioselectivity in Mn(I)-mediated C–H bond functionalisation, using ^{19}F NMR and time-resolved spectroscopic techniques.

Chapter 2: Mechanism of Mn(I)-Catalysed C–H Bond Alkenylation

2.1 Background

2.1.1 Proposed Reaction Mechanisms

The synthetic methodology reported by Wang and co-workers in 2013 on the Mn(I)-catalysed C–H bond alkenylation reactions[34] (**Scheme 11**, see Chapter 1.3) is truly ground breaking for utilising an earth-abundant transition metal catalyst in performing this challenging chemical transformation, which most commonly employs platinum group metals (see more detail in Chapter 1.4). However, the mechanistic understanding of this reaction is limited, and current knowledge is based on insufficient experimental evidence and DFT-studies. Following this work by Wang, the many other research teams (*e.g.* Ackermann, Glorius, Kuninobu, Lynam-Fairlamb, etc.) undertaking the remaining synthetic challenges in this field have been basing their methodology development and proposed mechanisms on this assumed knowledge. The issues with this approach are obvious and without further mechanistic work to support or disprove the current mechanisms, there is a good chance that many synthetic methodologies and improvements goes undiscovered.

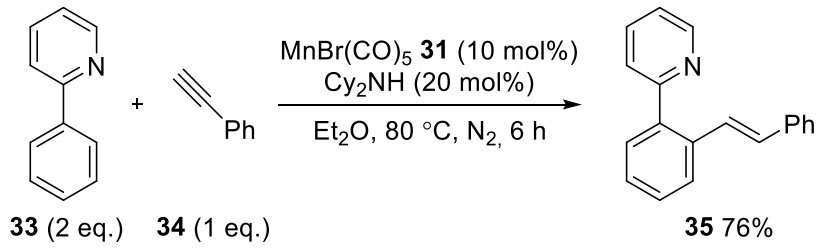

Scheme 11. Mn(I)-catalysed C–H bond alkenylation reaction to be studied within this chapter, reported by Wang and co-workers.[34]

In order for the remaining mechanistic challenges to be correctly elucidated, a detailed assessment of Wang's proposed mechanism[34] is required. Initially, the base-assisted activation of $MnBr(CO)_5$ **31** was supported by the stoichiometric preparation (31% yield of isolated product) of $Mn(ppy)(CO)_4$ **10** from **31** (1 eq.), **33** (1 eq.) and Cy_2NH (1 eq.), while the corresponding reaction with the terminal alkyne to form $Mn(\kappa_1\text{-}CCTol)(CO)_5$ **60** did not yield any observable product.

Compound **60** was obtainable in 55% yield, when **31** (1 eq.) and tolyl-alkyne **61** (1 eq.) was reacted in the presence of *n*-BuLi (1 eq.). However, this does not definitively exclude the manganese from initially reacting with the terminal alkyne, as the deprotonation mechanism for the different bases could differ. Whether loss of a CO-ligand is involved will have a major impact on the efficiency of reaction, depending of the ease of the subsequent recombination. The low efficiency of the cyclomanganation step (31%) also raises questions, as it suggests that the majority of the manganese is lost in the pre-catalyst activation pathway and the reaction is only promoted by ~ 3 mol% Mn (of the total 10 mol% Mn available). Still, **10** was found to be a capable pre-catalyst, while generating the organic product in 9% lower yield than under the standard reaction conditions. The lower catalytic competence, combined with the seemingly low amount of **10** formed in solution (~ 3 mol%) highlight the questions about **10** being a reaction intermediate, due to the seeming negative reaction order in **10**.

The proposed mechanism suggests that after pre-catalyst activation, the C–C bond formation takes place. This is projected to proceed through CO-dissociation, alkyne coordination to the Mn and subsequent insertion into the C–Mn bond to form a 7-membered manganacycle. The pathway is supported by literature examples of 7-membered manganacyle derivatives reported by Nicholson[16] (phosphite directing group) and Suárez[31] (imidazole directing group), where internal alkynes was used. No terminal alkyne complexes have been reported to this date. The efficient reaction of internal alkynes compared to the terminal analogues naturally poses the question of why the internal alkynes do not afford alkene product under seemingly standard reaction conditions.

Wang and co-workers did attempt to synthesise the 7-membered manganacycle using **61**, but instead found the unexpected formation of a doubly alkenylated 2-phenylpyridine compound isolated in 29% yield. An alkyne-assisted protonation pathway followed by Mn-alkynyl assisted C–H bond activation was suggested for the catalytic cycle. **60** was employed as a pre-catalyst to probe the proposed reaction mechanism. The reaction was found to yield relatively low amount of the mono-alkene product (63% yield of isolated product), when taking into account that the amount of active manganese should be about three times higher than in the standard reaction (note: assumed from the inefficient pre-catalyst activation). No kinetic or other

mechanistic studies were conducted, which are clearly needed in order for the validity of the proposed protonation mechanism to be probed and alternative identified.

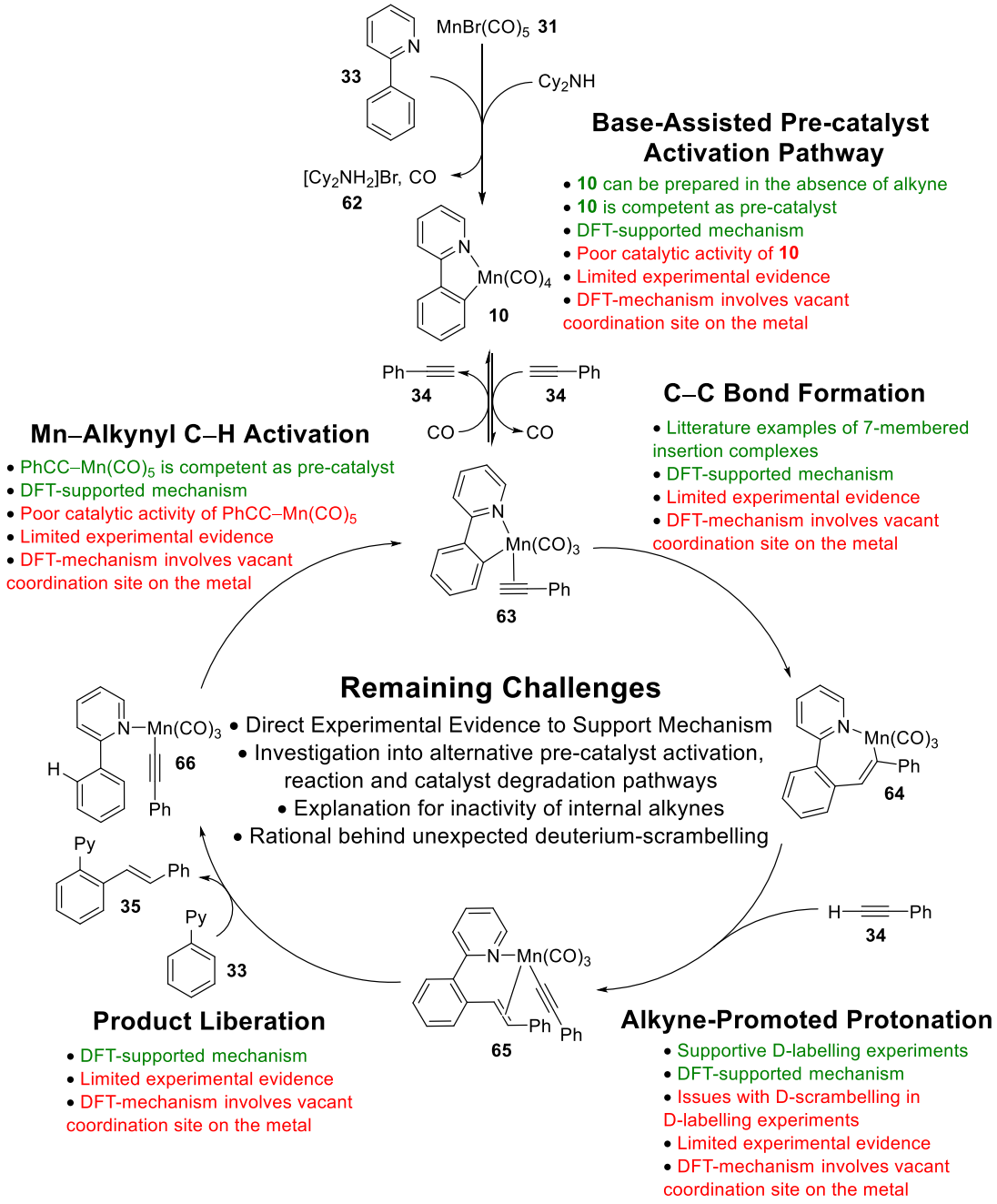

Scheme 12. Summary of proposed reaction mechanism by Wang and co-workers,[34] highlighting the issues and remaining challenges of understanding the full mechanism. Key; green = in support of mechanism, red = in disagreement with mechanism.

Deuterium-labelling studies were used to provide support for the mechanism. These studies indicated extensive scrambling of deuterium between the organic fragments. The incorporation of deuterium into both alkene positions, under standard reaction conditions was in accordance with the proposed mechanism, due to the alkyne C–H being repeatedly broken and reformed during the reaction. However, the extent of D-

incorporation was lower than expected (*i.e.* 50% ought to be achievable if one substrate is deuterated), suggesting a more complex mechanism. The system thus experienced extensive H-scrambling, highlighting the importance of further experiments, including appropriate control reactions being required for accurate conclusions to be drawn.

DFT-calculations were conducted to validate the proposed mechanism enabling further details about the various steps for the catalytic cycle(s) which had not been discovered. For example, it was found that the base-assisted cyclomanganation likely proceeded through a CMD mechanism, while the on-cycle C–H bond activation pass *via* a CMD/AMLA-4 pathway. The overall mechanism was supported by the DFT calculations, even if it should be noted that the common depiction of 16-electron manganese complexes with vacant coordination sites is slightly alarming. Even the presumptive resting state of the catalysis **66** (Mn-alkynyl complex with *N*-bound **33**) is one of these manganese complexes, and similar complexes have not been isolated to prove their competency as valid reaction intermediates.

Overall, there is a need for further experimental evidence for the mechanistic hypotheses underpinning this promising synthetic methodology. Obtaining such data by direct means is highly desired. In particular, the pre-catalyst activation, protonation, C–H bond activation and catalyst degradation pathways are of interest due to their high importance to the mechanism and efficiency of the reaction. The nature of the catalyst resting state is also of interest because of its impact on the rate of reaction and catalyst degradation, providing an obvious focal point for condition improvements. Additionally, the difference in reactivity between internal and terminal alkynes requires rational explanation, to aid in potential reaction improvements and translation of mechanistic understanding to other relevant systems. Finally, whether the apparent complexity of the reaction (*i.e.* derived from the D-labelling experiments) stems from a complicated reaction mechanism or innocent C–H bond scrambling should by default be determined if the full reaction mechanism has been determined.

2.1.2 Use of *In Operando* IR Monitoring in Mechanistic Studies

In operando (*in situ*) reaction monitoring techniques are some of the most important analytical techniques in the reaction mechanism elucidation of transition metal catalysed processes.[81] The direct observation of intermediates, as well as the

acquisition of reliable kinetic information, are of high importance for mechanistic investigations. Infrared (IR) spectroscopy provides excellent complementarity to other techniques, due to high peak-specificity and good correlation to bond strengths and electronic effects. *In situ* IR spectroscopic techniques have been used extensively in heterogeneous catalysis, while still being widely applicable to homogeneous systems.[81] IR spectroscopic analysis allows for both reaction kinetics and catalyst intermediate characterisation to be obtained in the same experiment with little to no manipulation of experimental data. It can also be employed on a wide range of timescales from hours or days to ultra-fast picosecond timescale.[82]

In situ IR spectroscopy has been an instrumental technique in the development of the RPKA (Reaction Progress Kinetic Analysis) methodology, reported by Blackmond in 2005.[83] The RPKA method creates a standard procedure of how to conduct mechanistic investigations, which can be used as an alternative to the procedures used within this thesis. Through the analysis of *in situ* generated kinetic data in a stepwise manner, the mechanism can be elucidated with minimal redundant experiments performed.

An example of the use of *in situ* IR spectroscopic reaction monitoring in the deduction of a complicated transition metal mediated reaction mechanism, is the work by Bray *et al.* on the Pd-catalysed cyanation of 4-bromo-2-pyridone **67** to form 4-cyano-2-pyridone **68** (**Scheme 13**).[84] In this study the C=O stretching mode of the 2-pyridone ring system provide an excellent IR spectroscopic handle for the *in operando* monitoring of the reaction progress. This allowed for a wide range of conditions to be screened so that reagent orders, catalyst heterogeneity, catalyst efficiency (TOF and TON), could be determined. The data obtained was combined into a full reaction mechanism where there are both hetero- and homogeneous catalytic cycles taking place and water concentration was found to be the crucial factor in the determination of which cycle is active in the reaction.

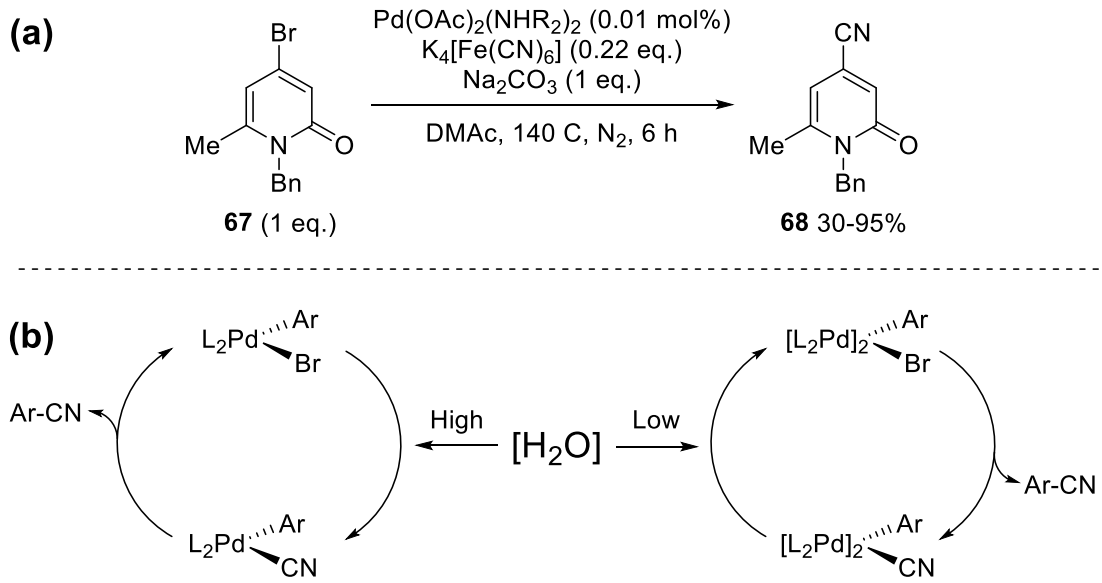

Scheme 13. (a) Reaction scheme of the Pd-catalysed cyanation of *N*-benzyl-4-bromo-6-methyl-2-pyidone reported by Bray *et al*.[84] (b) Simplified reaction mechanism highlighting impact of water concentration.

In the study reported by O'Brien and co-workers in 2011 on the asymmetric Pd-catalysed α-arylation of N-Boc pyrrolidone, several long-lived intermediates were observed and the kinetics of their formation and depletion could be obtained using *in operando* IR spectroscopy (**Scheme 14**).[85] After the initial addition of *s*-BuLi, the lithiated pyrrolidine intermediate could be seen forming more quickly than expected (complete within 60 minutes) in accordance with previous methodologies. Thereafter, several zincated species were observed, following addition of $ZnCl_2$ to the solution and heating to 20 °C. The final Negishi cross-coupling step with bromobenzene could also be monitored, where the product formation was observed without any Pd-intermediates appearing in the IR spectra. This still shows that *in situ* IR spectroscopic analysis can allow for the observation of several different reaction intermediates and kinetic information for their formation and depletion.

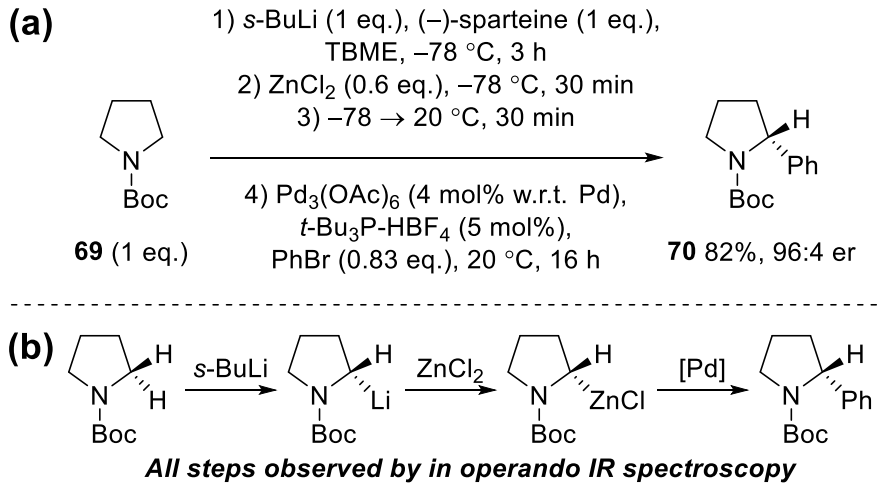

Scheme 14. (a) Reaction scheme of the asymmetric Pd-catalysed Negishi cross-coupling reaction reported by O'Brien and co-workers.[85] (b) Reaction intermediates observed by *in operando* IR spectroscopy.

A study by Lei and co-workers employed *in situ* IR spectroscopy for the direct observation of key intermediates in the copper-catalysed arylation of β-diketones.[86] This study found $[Cu(acac)_2]^-$ to be the active catalyst in the system through its presence in the IR spectra. This finding was further supported by additional experimental data and DFT-calculations. Off-cycle Cu-species could also be observed and characterised through this study.

In situ IR spectroscopic analysis for the study of reaction mechanisms has also been utilised in metal carbonyl catalysed reactions, with the hydroformylation of alkenes being a good example. Both Co and Rh have been utilised as catalysts for this reaction, however, the Co derivative was the first transition metal-catalysed transformation employed on an industrial scale in 1938.[87] Even as early as 1974, Whyman employed *in situ* IR spectroscopy to observe reaction intermediates, such as $HCo(CO)_3(PBu_3)$, from the distinct IR bands exhibited by metal carbonyl complexes.[88, 89] Many subsequent IR spectroscopic studies have been performed through the years, leading to the formulation of the currently accepted reaction mechanism of cobalt-catalysed hydroformylation reactions (**Scheme 15**).[90] Similar *in situ* IR spectroscopic studies have also been performed on the analogous rhodium system, with some early work by Garland and co-workers.[91]

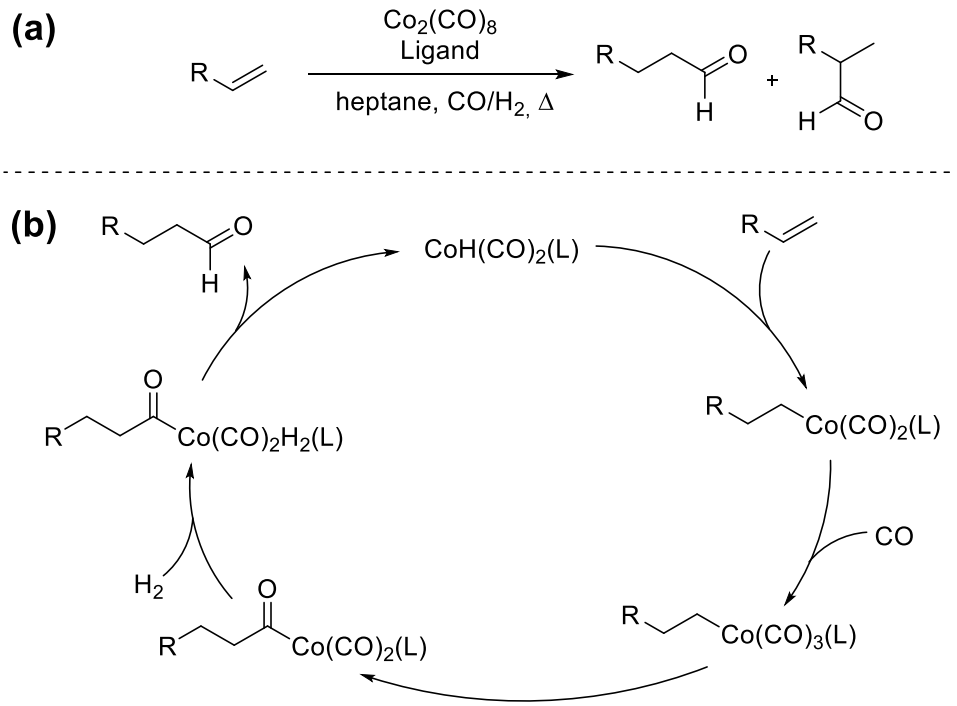

Scheme 15. (a) General reaction scheme for cobalt-catalysed hydroformylation of alkenes. (b) Generally accepted mechanism of the hydroformylation of alkenes.[90]

Another catalytically relevant study into metal carbonyl systems can be found in early work by Eischens *et al.* in 1954, on the chemisorption of CO gas onto Cu, Pt, Pd and Ni surfaces.[92] The IR spectra for the various materials showed how the CO absorbs to the surface and the various C–M bond strengths is inferred from the respective band locations.

2.2 IR Monitoring of Mn(I)-Catalysed C–H Alkenylation

2.2.1 Investigation under Standard Reaction Conditions

To investigate the mechanism of Mn(I)-catalysed C–H alkenylation, *in operando* IR monitoring (ReactIR™) was chosen as a suitable technique for this purpose. Metal carbonyls are well-known for their strong and distinct signals in the IR spectrum, where the peak location has been widely utilized to observe and rational steric and electronic effects on metal centres.[93] Therefore, the predicted changes to the manganese catalyst should be observable by IR spectroscopy, in a more clear and distinct fashion than alternative techniques such as NMR spectroscopy, mass spectrometry or UV/Vis spectroscopy. Organic fragments may also be observable by the *in operando* IR technique, meaning that there is potential for direct monitoring of the reaction kinetics without the need for external sampling.

When monitoring the changes to the IR bands in the metal carbonyl region using *in operando* IR spectroscopy, bands were mainly attributed to common species by comparing kinetic traces of peaks and time of appearance and/or disappearance (when kinetic traces were not obtainable due to spectral overlap). Unknown species in the solution were assigned by comparison to the IR spectrum of a structurally similar species or the predicted IR spectrum by DFT calculations (performed by Dr Jason M. Lynam) or group theory. The kinetic trace of a species in combination with the knowledge of other reaction intermediates in the solution also supported these assignments.

Initially, the coupling of 2-phenylpyridine **33** (2 eq.) and phenylacetylene **34** (1 eq.), using $MnBr(CO)_5$ **31** (10 mol%) as pre-catalyst and Cy_2NH (20 mol%) as additive, was investigated (**Scheme 11**). The reaction was monitored using a Mettler-Toledo ReactIR^{TM} instrument (IC10) with Si probe (1 min collection interval, ± 4 cm^{-1} peak resolution), at 100 °C under an argon atmosphere. *n*-Bu_2O was chosen as a solvent substitute for Et_2O (due to safety concerns arising from the high reaction temperature), while the reaction was performed in wet solvent, as the reaction conversion had proven unaffected by surplus water (76% conversion to **35**). The reaction solvent was heated to reaction temperature under the argon atmosphere (added through deoxygenating *via* balloon) without any of the reagents, for the collection an appropriate solvent reference to be possible. Thereafter, the reagents were added in the order **33**, **34**, Cy_2NH and **31**, to avoid any unwanted degradation or reactions taking place with the manganese catalyst before reaction monitoring is initiated. These reaction conditions are hereafter referred to as the standard conditions.

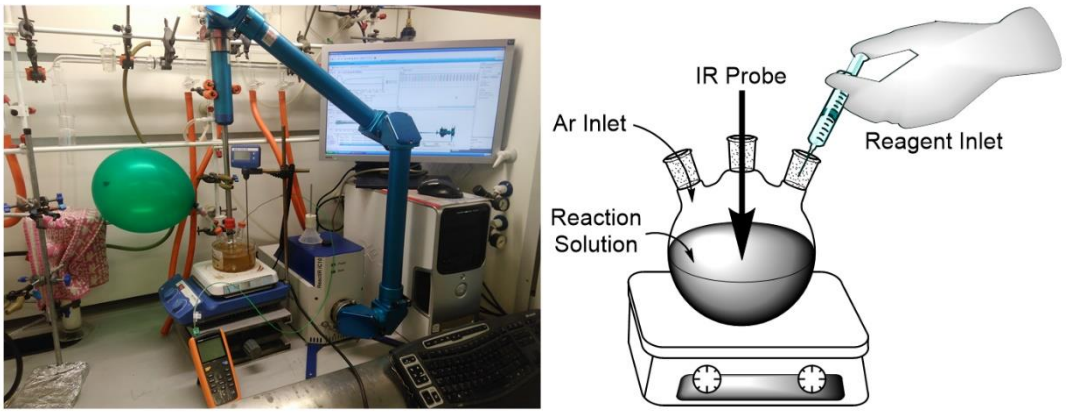

Figure 4. Picture and schematic view of *in operando* IR spectroscopic monitoring setup.

The reaction initiates immediately after the addition of the **31**, where an increase in temperature (typically 1–3 °C, observed by internal thermocouple) and gas evolution can be observed. Within the metal carbonyl region (2150–1850 cm^{-1}) there are several new manganese-carbonyl containing species formed within the first minute of the reaction (**Figure 5**). From the kinetic trace, **31** (band at 2054 cm^{-1}) remains in the reaction mixture for three minutes, showing that the manganese pre-catalyst is rapidly consumed and is as expected not a resting state of the catalysis.

Kinetic information of the formation of **35** could be obtained using *ex situ* ^{1}H NMR spectroscopic analysis, where aliquots were immediately cooled, diluted in $CDCl_3$ and filtered through a Celite® pad before recording the NMR spectra. Reaction progress can also be directly obtained from the IR spectra, but due to poor resolution the NMR spectroscopic assay was chosen for kinetic analysis. **35** can be seen forming in an exponential fashion in a reaction that lasts for about 30 minutes before tailing off (k = $1.8 \pm 0.4 \times 10^{-3}$ s^{-1} at 100 °C), which may be due to the extensive catalyst degradation observed. The rate throughout the reaction was also obtained, where a typical curve can be seen of the rate decreasing as the reaction progressed, arising from a combination of both lower substrate and catalyst concentrations. Of the newly formed complexes in the reaction, there is one tetracarbonyl manganese species which show high similarity to **10**. However, closer inspection of the spectrum reveals that there is a slight difference between these two species and the new complex **71** (bands at 2071, 1987 (br) and 1943 cm^{-1} compared to 2078, 1996, 1982 and 1941 cm^{-1} for **10**) is most likely a manganacycle of high structural similarity to **10**. This species is consumed at $k = 1.9 \pm 0.2 \times 10^{-3}$ s^{-1} (at 100 °C), which is concomitant with the formation of the organic product **35** ($k = 1.8 \pm 0.4 \times 10^{-3}$ s^{-1} at 100 °C), indicating that **71** is the identity of the catalyst resting state. Further experiments are however required for that to be confirmed.

The inability to observe **10** in solution may arise from it being transient in the reaction and consumed at too high a rate, making it undetectable on the timescale of the experiment (1 min). It could alternatively indicate a different pre-catalyst activation pathway, which does not involve the formation of **10**. Such an mechanism is not unlikely due to the relatively high thermal stability of the tetracarbonyl manganacycle (**10** can be prepared in refluxing hydrocarbon solvents, such as toluene, petrol, hexane and heptane)[23, 94], combined with the fast reaction time of about 30 minutes.

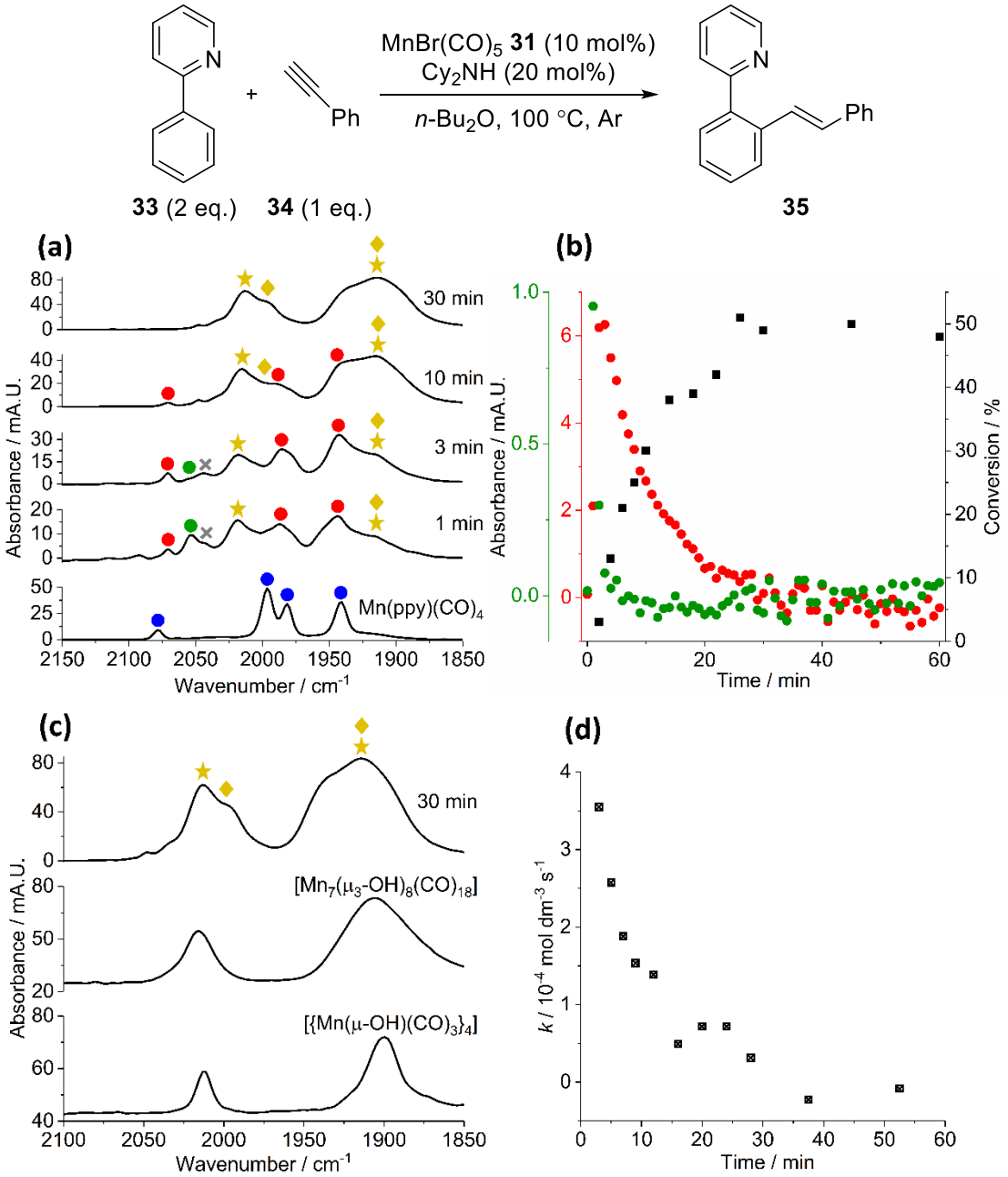

Figure 5. *In operando* IR study of the reaction between **34** and **33** using **31** as pre-catalyst with Cy_2NH as additive. (a) IR spectra of the reaction in the metal carbonyl region at various timepoints and a reference spectrum of **10**. Key; blue circle = **10**, green circle = **31**, red circle = **71**, grey cross = unknown Mn-carbonyl species and gold star/diamond = Mn degradation complex. Reaction conditions (in order of addition); *n*-Bu_2O (10 ml), **33** (8.32 mmol, 2 eq.), **34** (4.16 mmol, 1 eq.), Cy_2NH (0.83 mmol, 20 mol%) and **31** (0.42 mmol, 10 mol%) at 100 °C under argon atmosphere. (b) Kinetic plot of the formation of alkene product **35** (black squares, determined by *ex situ* ^{1}H NMR spectroscopy) and the formation and depletion of **31** (green circles, band at 2054 cm^{-1}) and **71** (red circles, band at 2071 cm^{-1}), extracted from (a). (c) Comparison between *in situ* IR spectra at 30 minutes and two different Mn-hydroxyl clusters. (d) Change of rate of reaction over time using a 4-point smoothening function.

There are two tricarbonyl manganese species with large absorption coefficients appearing during the reaction as the other species deplete, strongly suggesting that these complexes are a result of catalyst degradation. Tricarbonyl manganese-hydroxyl clusters has been reported by Clerk and Zaworotko[95] and exhibit strikingly similar IR

bands to the degradation complexes in this reaction. To probe the validity of this tentative assignment, two Mn-hydroxyl clusters [(Mn(μ-OH)$(CO)_3)_4$] **72** and [Mn_7(μ$_3$-OH)$_8(CO)_{18}$] **73** were synthesised.[95] IR spectra of the clusters in *n*-Bu_2O were recorded at the reaction temperature and compared to a late timepoint spectrum of the reaction (30 min). This proved that there is a good similarity between the clusters (**72** = 2012 and 1900 cm^{-1}, **73** = 2016 and 1906 cm^{-1}) and the degradation complexes (2013 and 1915 cm^{-1} for the main species), though they are not the same species. **72** and **73** also proved not to be catalytically competent and did not produce any **35** under the reaction conditions.

Carbonyl-containing Ru-alkynyl clusters have been reported by Low and co-workers, which was synthesised by reaction with terminal alkynes[96]. It is possible that similar Mn-alkynyl clusters might be formed in the Mn(I)-catalysis as well, as Mn-alkynyl species are proposed to be key intermediates in Wang's mechanism. However, attempts to isolate and further characterise the degradation complexes proved unfruitful. Due to the reasons mentioned *vide supra*, it is highly likely that the complexes are a variety of manganese-tricarbonyl clusters of which both Mn-hydroxyl and Mn-alkynyl derivatives are possible. The broadness of the peaks supports that a mixture of species might be formed in the solution.

2.2.2 Determination of Reaction Order in Reagents

To obtain further information of the Mn(I)-catalysed C–H bond alkenenylation, the reaction order of the reagents was determined. If the previously proposed mechanism is correct, then the reaction should most likely be first-order in alkyne **34** as only one alkyne is involved in any one step (in some steps there are both an alkyne and newly formed alkene), except from the product liberation. **33** will be zero-order, unless the product liberation is rate-determining as it will be first-order in that instance. There should finally be a zero-order dependence of Cy_2NH due to it only being involved in initial catalyst activation, not proposed to be involved in the generation of product. The reaction order in catalyst would be difficult to obtain, due to the extensive catalyst deactivation evident throughout the duration of the reaction. Therefore, no order in $MnBr(CO)_5$ was determined.

Initially, the order in 2-phenylpyridine **33** was determined through the use of an excess of alkyne **34** (6 eq.) to obtain pseudo-first order reaction conditions (**Figure 6**). A higher equivalence of alkyne could not be employed due to the corresponding loss of solvent. Observed rate constants (k_{obs}) was used as a measure of reaction rates and was determined by ^{1}H NMR spectroscopic analysis. After varying the equivalence of **33** between 1 and 3, a reaction order of 0.87 ± 0.06 was obtained. It is an unexpected order, which leads to the creation of two alternative explanations. The determination of the order could be inaccurate and the reaction is in reality first order, but that is significantly outside the error of the experiment and is therefore unlikely. Alternatively, the reaction is more complicated than previously envisaged and contain two or more competing mechanisms, which utilise **33** in different amounts.

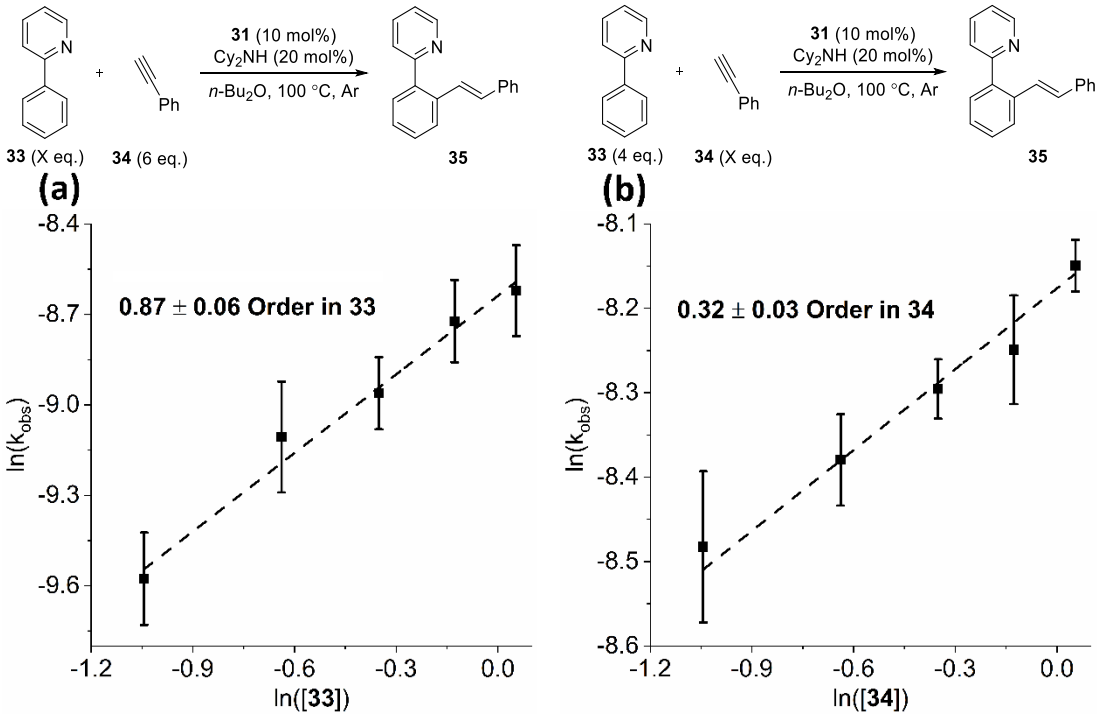

Figure 6. (a) Reaction order determination for **33** using an excess **34** (6 eq.) and amount of **33** was varied between 1–3 eq. The linear fit gave an order of 0.32 ± 0.03 (R^2 = 0.98). (b) Reaction order determination for **34** using an excess **33** (4 eq.) and amount of **34** was varied between 0.5–2 eq. The linear fit gave an order of 0.87 ± 0.06 (R^2 = 0.99).

In the determination of the reaction order in alkyne **34**, an excess of **33** (4 eq.) was used to obtain pseudo-first order conditions (**Figure 6**). Again, using a larger excess of **33** was not possible due to the corresponding solvent loss. The equivalence of alkyne was varied between 0.5 and 2 to give an order in **34** of 0.32 ± 0.03, further supporting the hypothesis of two or more competing reaction mechanisms. A partial reaction order can arise from heterogeneous catalysis, in which, for example, nanoparticular metal catalysts are generated *in situ*.[84] However, this is unlikely in this

case and it is more than likely that the reaction is more complicated than previously thought.

The final reagent for which the reaction order can determined is the amine base Cy_2NH, which was varied between 5 and 80 mol%, at the same time as the substrate concentrations remains as in the standard conditions (1 eq. **34** and 2 eq. **33**). Interestingly, a simple linear dependence of $\ln(k_{obs})$ over $\ln([Cy_2NH])$ was not obtained in this study (**Figure 7**). The rate increases with increasing $[Cy_2NH]$ at low concentration, while a rate-independence of $[Cy_2NH]$ was found at higher concentrations. This can be more clearly seen in the plot of k_{obs} vs. Cy_2NH:**31** ratio, where 20 mol% (Cy_2NH:**31** = 2) of the base is optimal for the reaction. The unusual shape of the curve again suggests that there is a more complicated reaction mechanism than was previously proposed. Alternatively, it could mean that the pre-catalyst activation pathway is interfering with the monitoring of the rate of reaction, through being slow compared to the active catalysis.

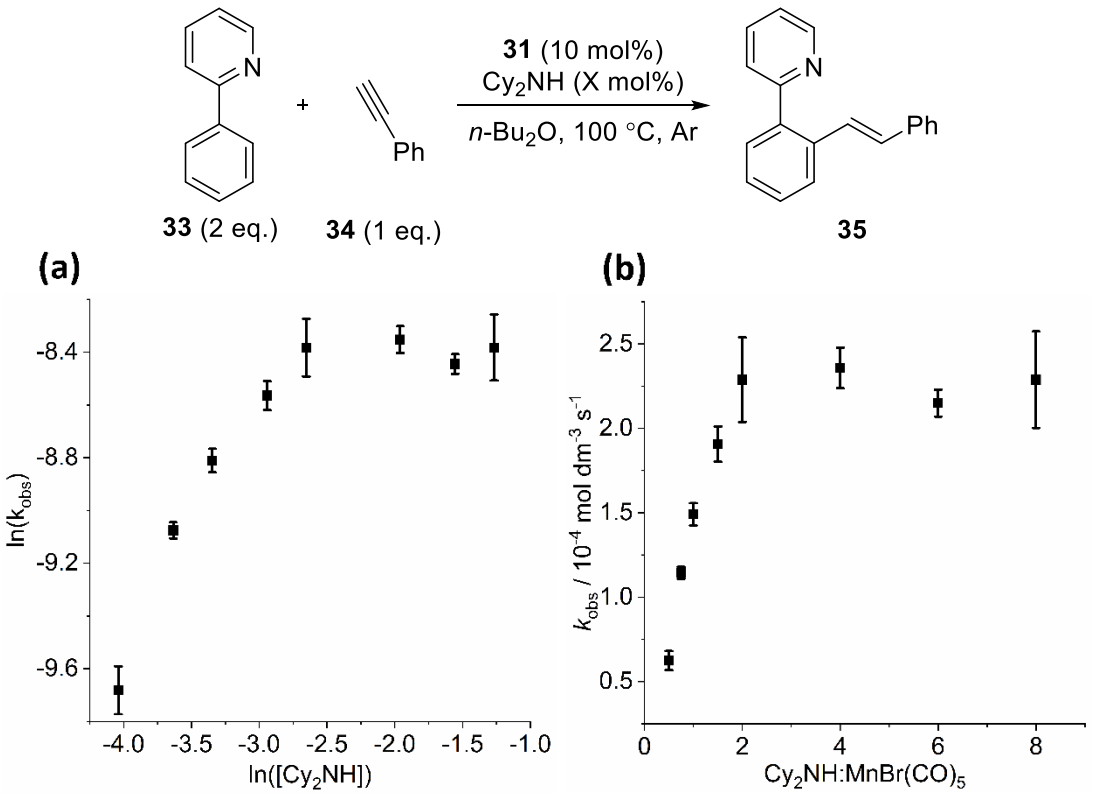

Figure 7. (a) Reaction order determination for Cy_2NH under standard reaction conditions. (b) Effect of the base to manganese ratio, where a 2:1 ratio is found to give the optimal reaction rate.

In summary, it has been determined that the reaction order in reagents **33**, **34** and Cy_2NH, are all complicated, inferring the operation of a complex mechanism, perhaps involving multiple mechanisms taking place. Critically, the pre-catalyst activation

could be interfering in the order determination. Thus, further experimental evidence is required for more precise elucidation of the reaction mechanism operative under standard conditions.

2.2.3 Variation of Manganese Pre-Catalyst

In an attempt to avoid the pre-catalyst activation step, the reaction was performed using **10** as pre-catalyst (**Figure 8**). This study should provide additional evidence for the validity of **10** being an intermediate in the entrance into the catalytic cycle. Despite the low yielding cyclomanganation step starting from **31** and Cy_2NH (31% as shown by Wang and co-workers[34]), 10 mol% pre-catalyst loading was employed to allow for direct comparison to the standard conditions.

Complex **10** could be seen depleting throughout the reaction between **33** (2 eq.) and **34** (1 eq.), using **10** (10 mol%) as pre-catalyst (**Figure 8**). This outcome suggests it is unlikely as an intermediate in the standard reaction, as it cannot be observed under those conditions. Nevertheless, the amount of **10** depletes at a rate of $5.4 \pm 0.5\ 10^{-3}\ s^{-1}$ (at 100 °C), which coincides with the appearance of **71** ($k = 6.1 \pm 0.8\ 10^{-3}\ s^{-1}$ at 100 °C). Once more, the consumption of **71** ($k = 1.1 \pm 0.1\ 10^{-3}\ s^{-1}$ at 100 °C) matches the rate of product **35** generation ($k = 1.2 \pm 0.3\ 10^{-3}\ s^{-1}$ at 100 °C). It becomes obvious that **10** is the pre-catalyst and **71** the catalyst resting state in this reaction.

The rate of formation of **71** is clearly slower in this reaction ($k = 6.1 \pm 0.8\ 10^{-3}\ s^{-1}$ at 100 °C) than starting from **31** and Cy_2NH, which is too fast for the rate to be accurately determined. This creates a paradox if the proposed mechanism is correct, as **10** cannot react slower than **31**, if **10** is formed as an intermediate in the activation of **31**. The generation of **35** is also slightly slower using **10** ($k_{obs} = 2.6 \pm 0.3 \times 10^{-4}$ mol $dm^{-3}\ s^{-1}$ at 100 °C for **31** and $k_{obs} = 1.8 \pm 0.1 \times 10^{-4}$ mol $dm^{-3}\ s^{-1}$ at 100 °C for **10**), which is unexpected for the above-mentioned reason of the inefficient cyclomanganation reaction to form **10**. The rate of product formation throughout the reaction follows a similar trend as observed for **31**, where it decays over time as the reagents are consumed.

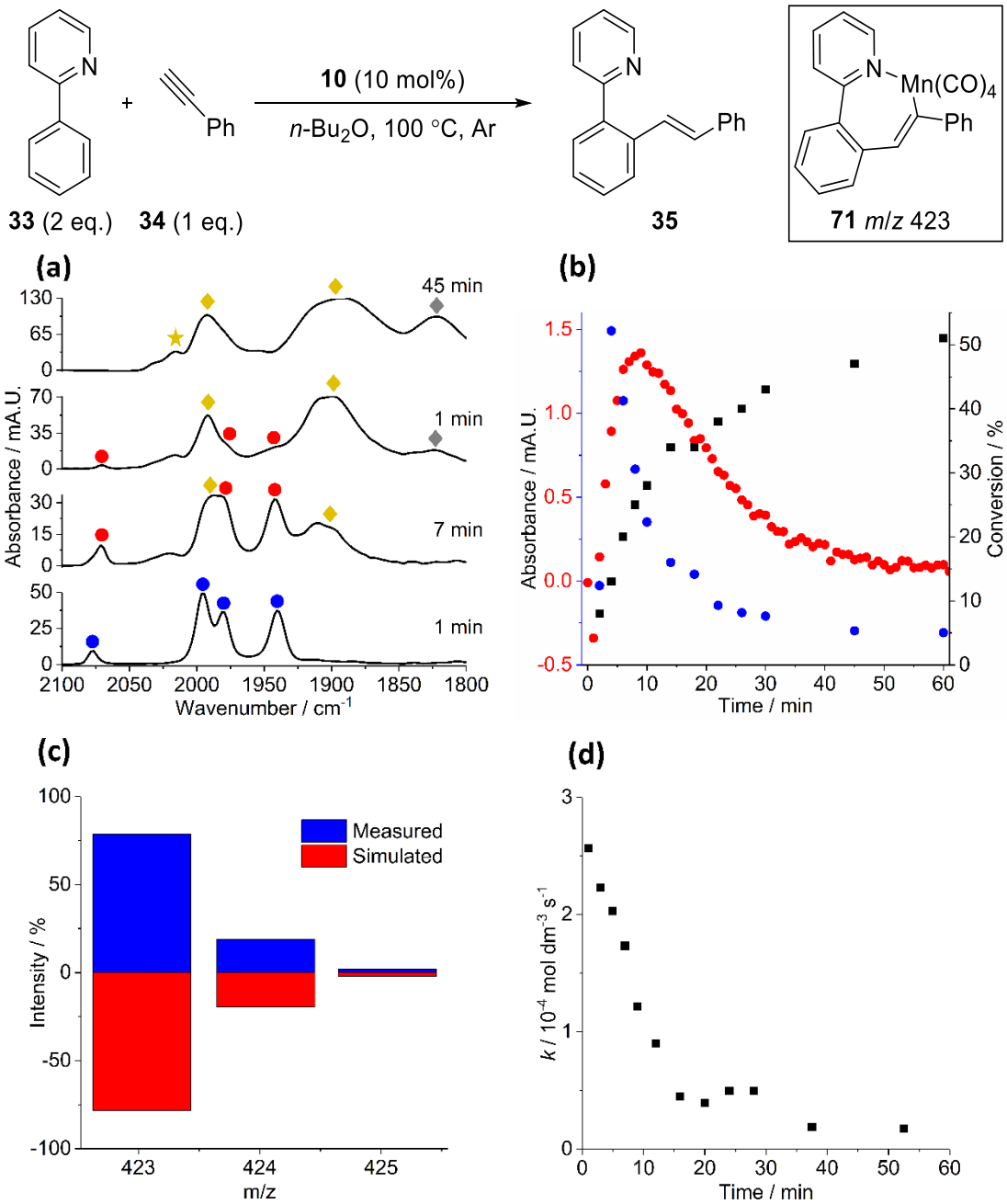

Figure 8. *In operando* IR study of the reaction between **34** and **33** using **10** as pre-catalyst. (a) IR spectra of the reaction in the metal carbonyl region at various timepoints. Key; blue circle = **10**, red circle = **71**, grey cross = unknown Mn-carbonyl species and gold star/diamond = Mn degradation complexes. Reaction conditions (in order of addition); *n*-Bu_2O (10 ml), **33** (8.32 mmol, 2 eq.), **34** (4.16 mmol, 1 eq.) and **10** (0.42 mmol, 10 mol%) at 100 °C under argon atmosphere. (b) Kinetic plot of the formation of alkene product **35** (black squares, determined by *ex situ* ^{1}H NMR spectroscopy), the depletion of **10** (blue circles, band at 2078 cm^{-1}) and the formation and depletion of **71** (red circles, band at 2071 cm^{-1}), extracted from (a). (c) Comparison between measured and simulated masses obtained from LIFDI-MS analysis. (d) Change of rate of reaction over time using a 4-point smoothening function.

An attempt to find the identity of **71** was conducted using mass spectrometry and LIFDI-ionisation (LIFDI-MS), which is a mild technique well suited for the observation of transition metal complexes. In the LIFDI-MS spectrum a species corresponding to the tetracarbonyl version of the 7-membered insertion complex (peak

at 423.03 m/z) is observed, which is formed after C–C bond formation and recombination with the displaced CO-ligand. The tricarbonyl derivative can also be seen, but in a less intense peak. It is easy to envisage that **71** is the species observed in the LIFDI-MS, due to the IR bands expected to be very similar to **10** and the tricarbonyl derivative being an anticipated intermediate in the reaction. If the protonation is slow and C–C bond formation is fast, it is not unlikely that the spare CO in solution can coordinate to the manganese. The binding of CO should be more favourable than π-coordination to an alkyne and was calculated to be 79 kJ mol^{-1} stronger (all DFT-calculations in this chapter was performed by Dr Jason M. Lynam).

The degradation species which was present in the reaction using **31** and Cy_2NH was formed in this reaction as well (distinct peaks at 2015 and 1993 cm^{-1}), though in different amounts. This suggests that the active catalysis proceeds through the same mechanism(s) independent of pre-catalyst, while the preference of a specific mechanism or degradation pathway is affected by the reaction conditions employed. The presence of Cy_2NH and HBr-derived compounds may be the reason for this observed difference. There is also a previously unobserved band appearing at 1821 cm^{-1} in the reaction employing **10** as pre-catalyst, likely corresponding to a degradation species unobtainable from **31** for the reasons mentioned above.

$MnBn(CO)_5$ **19** is a well-known precursor for cyclomanganation reactions[14] and is therefore much more likely to form **10** as a reaction intermediate compared to **31**. **71** is observed forming (k = 5.4 ± 1.6 10^{-3} s^{-1} at 100 °C) as **19** is consumed (k = 6.1 ± 0.4 10^{-3} s^{-1} at 100 °C), in the reaction between **33** (2 eq.) and **34** (1 eq.). Once more, no formation of any intermediate species, such as **10**, is observed in the solution (**Figure 9**). It is of note that the rate of formation of **71** is within error for both **19** and **10** (k = 5.4 ± 1.6 10^{-3} s^{-1} at 100 °C and 6.1 ± 0.8 10^{-3} s^{-1} at 100 °C respectively), with **31** being faster (formation complete within 3 minutes). At first glance this might indicate that the reaction proceeds *via* **10**, but cyclomangantion using $MnBn(CO)_5$ to form **10** usually takes several hours to complete, so it would be unlikely that this step would not affect the rate of the process. Interestingly, for the rate of depletion of **71**, **19** (k = 1.5 ± 0.2 10^{-3} s^{-1} at 100 °C) is in the middle between **31** (k = 1.9 ± 0.2 × 10^{-3} s^{-1} at 100 °C) and **10** (k = 1.1 ± 0.1 10^{-3} s^{-1} at 100 °C), highlighting that **31** and Cy_2NH provide a more efficient catalyst system.

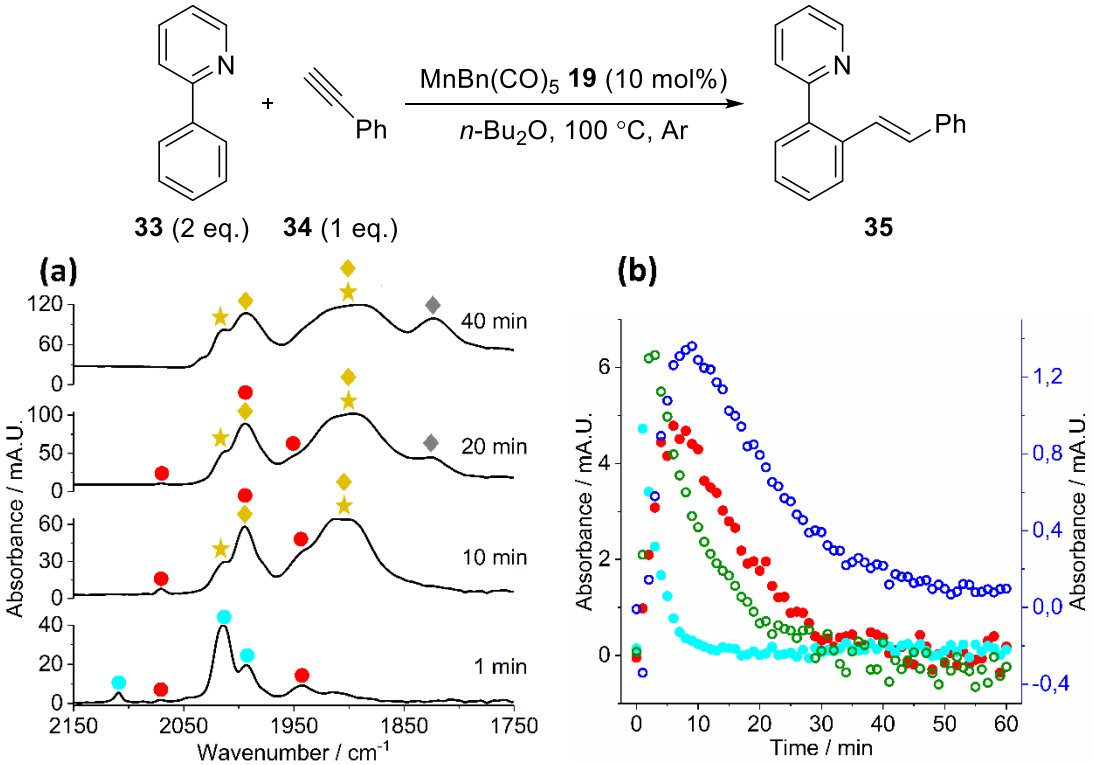

Figure 9. *In operando* IR study of the reaction between **34** and **33** using **19** as pre-catalyst. (a) IR spectra of the reaction in the metal carbonyl region at various timepoints. Key; cyan circle = **19**, red circle = **71**, grey diamond = unknown Mn-carbonyl species and gold star/diamond = Mn degradation complexes. Reaction conditions (in order of addition); *n*-Bu_2O (10 ml), **33** (8.32 mmol, 2 eq.), **34** (4.16 mmol, 1 eq.) and **19** (0.42 mmol, 10 mol%) at 100 °C under argon atmosphere. (b) Kinetic plot of the depletion of **19** (cyan circles, band at 2109 cm^{-1}) and the formation and depletion of **71** (band at 2071 cm^{-1}) from the different pre-catalysts (red circles = **19**, green hollow circles = **31** and blue hollow circles = **10**).

The catalyst degradation complexes discussed *vide supra* are once again generated in this reaction, together with the unknown species at 1821 cm^{-1}. This further supports a similarity in mechanism to that of using **10** as pre-catalyst. However, the ratio between the different species is different and the observed similarity is much more likely to arise from the lack of Cy_2NH and "HBr" in solution than pre-catalyst activation proceeding *via* a common pathway.

One further pre-catalyst was tested in the reaction, $Mn_2(CO)_{10}$ **40** is widely used as pre-catalyst in Mn(I)-catalysed C–H bond functionalisation[35] and also for the alkenylation reaction yielding 58% of **35**.[34] Only 22% conversion was observed in the reaction between **33** (2 eq.) and **34** (1 eq.) using **40** (10 mol%) as pre-catalyst and Cy_2NH (20 mol%) as additive, suggesting a more water sensitive reaction than observed with the other pre-catalysts. No new manganese carbonyl containing species could be observed in the IR spectra and the product formation show a linear zero-order curve. This is unexpected and indicates that the reaction mechanism is different for

this complex than the others, possibly involving manganese-radicals. However, this warrants further investigation for any conclusions to be drawn.

2.3 Investigation of Pre-Catalyst Activation Pathway

2.3.1 Selective Monitoring of Pre-Catalyst Activation

Either the generation of **71** from **31**, or the subsequent formation of the organic product **35**, is higher in energy, demanding the high reaction temperatures employed in the reaction. Even though **71** is observed as a reaction intermediate, one must take into account the many turnovers a catalyst must make in the reaction. The temperature was lowered to investigate if **71** could be selectively synthesised and potentially isolated. The initial temperature was set to 40 °C and was thereafter increased by increments of 10 °C. At 40 °C no formation of **71** could be observed, while a slow generation occurred at 50 °C and a relatively quick transformation occurred at 60 °C. **71** remained in solution for a significant duration of time at 60 °C without noticeable degradation taking place, leading to future investigations being performed at 60 °C. It should be noted that efforts to isolate **71** from the reaction solution proved challenging and no successful attempts were made.

The reaction between **33** (2 eq.) and **34** (1 eq.) using **31** as precursor (10 mol%) with Cy_2NH (20 mol%), starting at 60 °C under an argon atmosphere (**Figure 10**), showed the aforementioned **71** forming and remaining in solution. Through crude ^1H NMR spectroscopy a similar compound to the organic product **35** could be seen at 8% conversion, containing an alkene proton (7.04 ppm) close to the position of **35** (7.07 ppm). The rate of formation of **71** ($k = 3.6 \pm 0.8 \times 10^{-3}$ s^{-1} at 60 °C) matches the depletion of **31** ($k = 3.4 \pm 0.7 \times 10^{-3}$ s^{-1} at 60 °C) and no transient intermediates could be observed. The lack of observation of **10** in solution further invalidates **10** being a reaction intermediate, in particularly as the rate of formation and depletion of **10** cannot be quicker at 60 °C than 100 °C which would be necessary if it is an unobservable intermediate. There are degradation complexes formed in the solution as well, which grows in as the reaction progresses.

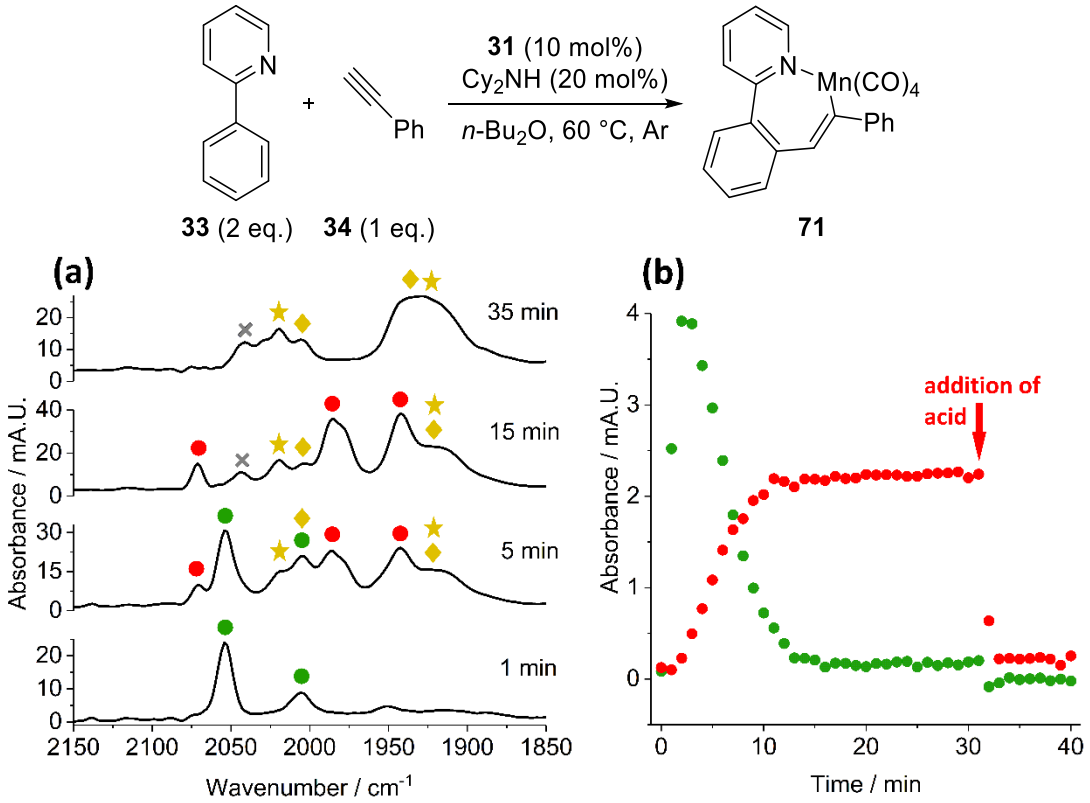

Figure 10. *In operando* IR study of the reaction between **34** and **33** under standard reaction conditions at 60 °C. (a) IR spectra of the reaction in the metal carbonyl region at various timepoints. Key; green circle = **31**, red circle = **71**, grey cross = unknown Mn-carbonyl species and gold star/diamond = Mn degradation complexes. Reaction conditions (in order of addition); *n*-Bu_2O (10 ml), **33** (8.32 mmol, 2 eq.), **34** (4.16 mmol, 1 eq.), Cy_2NH (0.83 mmol, 20 mol%) and **31** (0.42 mmol, 10 mol%) at 60 °C under argon atmosphere. Propionic acid (1.25 mmol, 0.3 eq.) was added after 30 minutes. (b) Kinetic plot of the formation of the depletion of **31** (green circles, band at 2054 cm^{-1}) and the formation and depletion of **71** (red circles, band at 2071 cm^{-1}), extracted from (a).

If **71** is the tetracarbonyl derivative of 7-membered insertion complex **64**, then it is likely to be sensitive to acid additives. The addition of propionic acid (3 eq. with respect to Mn) led to rapid decomposition of **71** and formation of **35** at 5% conversion, further supporting the assignment of **71** being the tetracarbonyl insertion complex post C–C bond formation. The 8% conversion to the insertion complex is much cleaner than the cyclomanganation methodology with Cy_2NH as previously shown by Wang and co-workers,[34] providing a rational for the efficient catalysis taking place under the standard reaction conditions.

Reagents were removed from the reaction in order to further probe the precise mechanism of pre-catalyst activation. Firstly, the reaction was performed without Cy_2NH, using **33** (2 eq.), **34** (1 eq.) and **31** (10 mol%) at 60 °C (**Figure 11**). As expected, no formation of **71** took place while **31** was seen slowly degrading, leading to the addition of Cy_2NH (20 mol%) after 25 minutes. No kinetic information could be obtained for this slow degradation due to the addition of the amine base before the

degradation of **31** was complete. The base additive did allow for the generation of **71**, which formed at the same rate as previously seen under the standard conditions at 60 °C (k = 4.2 ± 0.7 × 10^{-3} s^{-1} at 60 °C and k = 3.6 ± 0.8 × 10^{-3} s^{-1} at 60 °C respectively). This experiment highlights the proposed necessity of the base additive in the pre-catalyst activation step.

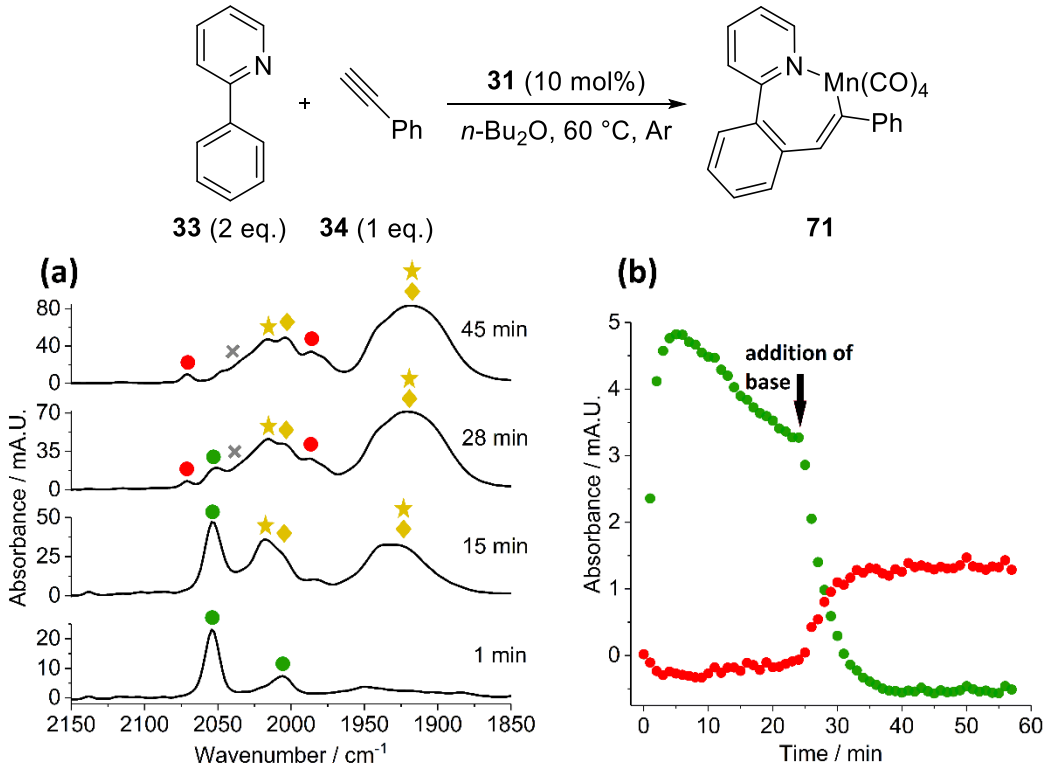

Figure 11. *In operando* IR study of the reaction between **34** and **33** using **31** as Mn-precursor and no base additive at 60 °C. (a) IR spectra of the reaction in the metal carbonyl region at various timepoints. Key; green circle = **31**, red circle = **71**, grey cross = unknown Mn-carbonyl species and gold star/diamond = Mn degradation complexes. Reaction conditions (in order of addition); *n*-Bu_2O (10 ml), **33** (8.32 mmol, 2 eq.), **34** (4.16 mmol, 1 eq.) and **31** (0.42 mmol, 10 mol%) at 60 °C under argon atmosphere. Cy_2NH (0.83 mmol, 20 mol%) was added after 25 minutes. (b) Kinetic plot of the formation of the depletion of **31** (green circles, band at 2054 cm^{-1}) and the formation and depletion of **71** (red circles, band at 2071 cm^{-1}), extracted from (a).

Next the alkyne **34** was removed from the solution (**Figure 12**) to force the reaction to proceed through the formation of **10**, in addition to rationalise the reportedly low efficiency of this step.[34] Apart from the manganacycle, a degradation complex (bands at 2025 and 1918 (br) cm^{-1}) is formed, which grows over time in a much slower fashion than **10**, indicating it is formed post cyclomanganation or in a separate process altogether. In a separate experiment it was found that this species is generated from simply heating of **10** in *n*-Bu_2O.

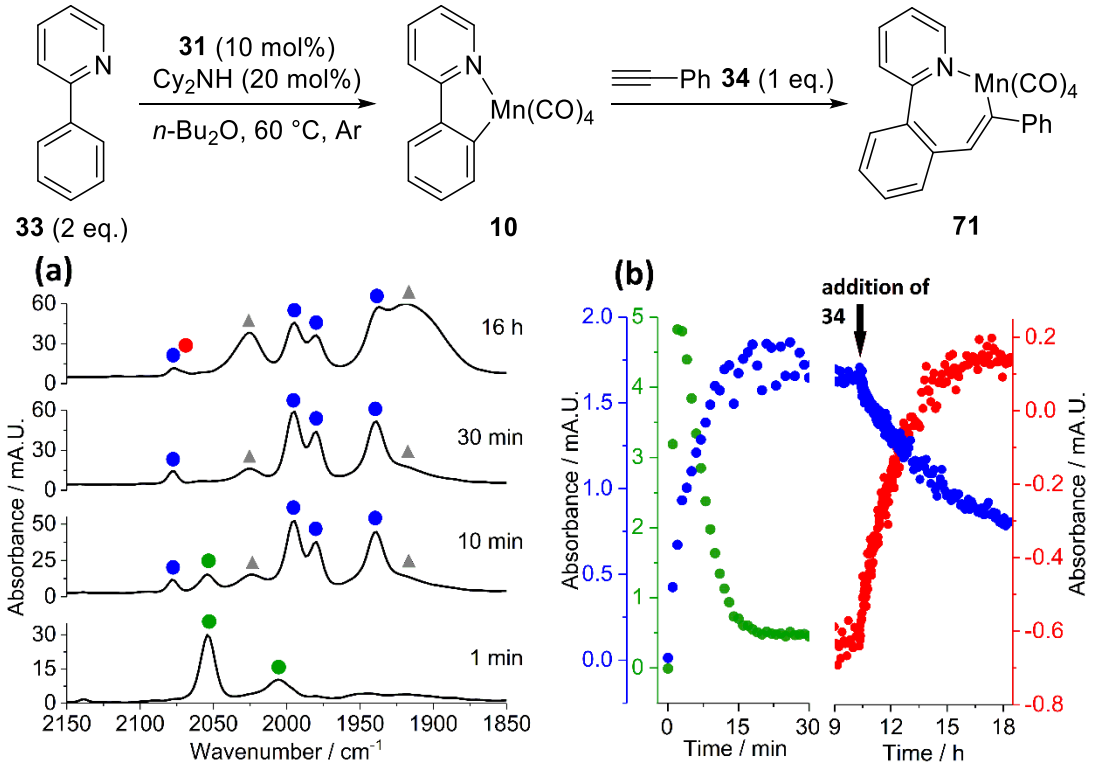

Figure 12. *In operando* IR study of the reaction without **34**, using **31** as Mn-precursor at 60 °C. (a) IR spectra of the reaction in the metal carbonyl region at various timepoints. Key; green circle = **31**, blue circle = **10**, red circle = **71** and grey triangle = unknown Mn-carbonyl species. Reaction conditions (in order of addition); *n*-Bu_2O (10 ml), **33** (8.32 mmol, 2 eq.), Cy_2NH (0.83 mmol, 20 mol%) and **31** (0.42 mmol, 10 mol%) at 60 °C under argon atmosphere. **34** (4.16 mmol, 1 eq.) was added after 10 hours. (b) Kinetic plot of the formation of the depletion of **31** (green circles, band at 2054 cm^{-1}), the formation of the depletion of **10** (blue circles, band at 2078 cm^{-1}) and the formation and depletion of **71** (red circles, band at 2071 cm^{-1}), extracted from (a).

The rate of cyclomanganation ($k = 3.2 \pm 0.8 \times 10^{-3}$ s^{-1} at 60 °C) is roughly the same as the rate of formation of **71** with **34** present ($k = 3.6 \pm 0.8 \times 10^{-3}$ s^{-1} at 60 °C). The rate of C–C bond formation from **10** has already been established to be slow ($k = 1.8 \pm 0.4 \times 10^{-3}$ s^{-1} at 100 °C) relative to the cyclomanganation, but **34** (1 eq.) was still added to this reaction from which the rate could be determined at 60 °C. At this temperature the rate of **71** formation was found to be $k = 1.25 \pm 0.06 \times 10^{-4}$ s^{-1} (at 60 °C), meaning that **10** would be observed under the standard reaction if it is an intermediate in the pre-catalyst activation. However, it does not elucidate whether the manganese initially reacts with **34** or **33**.

The reaction was thereafter performed in the absence of **33** at 60 °C (**Figure 13**), where neither **71** nor **10** can be formed. **31** was found to still be consumed at a fast rate ($k = 5.4 \pm 0.3 \times 10^{-3}$ s^{-1} at 60 °C), which is twice that of reaction with **33** instead of the alkyne ($k = 2.9 \pm 0.4 \times 10^{-3}$ s^{-1} at 60 °C). This shows that even though the pyridyl **33** is expected to be a better ligand, the alkyne **34** is seemingly reacting faster with the

manganese, also despite **33** being in excess (2:1). The degradation complexes observed in the reaction are those found under the standard reaction conditions at 60 °C, and kinetic traces shows that they are formed directly from **31** with no observable transient intermediates.

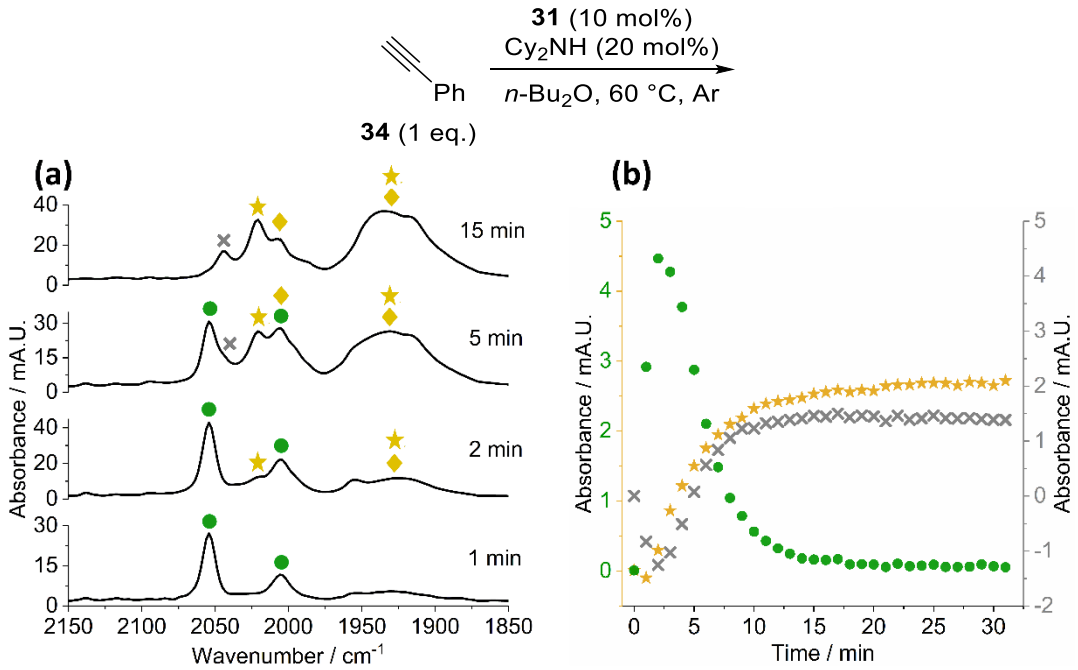

Figure 13. *In operando* IR study of the reaction without **33**, using **31** as Mn-precursor at 60 °C. (a) IR spectra of the reaction in the metal carbonyl region at various timepoints. Key; green circle = **31**, grey cross = unknown Mn-carbonyl species and gold star/diamond = Mn degradation complexes. Reaction conditions (in order of addition); *n*-Bu_2O (10 ml), **34** (4.16 mmol, 1 eq.), Cy_2NH (0.83 mmol, 20 mol%) and **31** (0.42 mmol, 10 mol%) at 60 °C under argon atmosphere. (b) Kinetic plot of the formation of the depletion of **31** (green circles, band at 2054 cm^{-1}) and the formation of two new manganese species (grey crosses, band at 2044 cm^{-1} and gold stars, band at 2022 cm^{-1}), extracted from (a).

The reaction was performed without both substrates to probe the interaction between the base and manganese, coupled with an attempt to detect further reaction intermediates (**Figure 14**). In this reaction using **31** and Cy_2NH under catalytic conditions at 60 °C, it was found that **31** is consumed much slower ($k = 4.9 \pm 0.2 \times 10^{-4}$ s^{-1} at 60 °C) than in previous reactions ($k = 5.4 \pm 0.3 \times 10^{-3}$ s^{-1} at 60 °C with **34** added and $k = 2.9 \pm 0.4 \times 10^{-3}$ s^{-1} at 60 °C with **33** added). This shows that a substrate (**34** or **33**) in combination with Cy_2NH is required for rapid reaction with **31**, as removing the substrates or the base significantly slows down the pre-catalyst consumption.

When the spectra obtained from the various reactions is compared (**Figure 14**), the reaction without the alkyne **34** is distinctly different in the degradation complexes formed. Only the reaction without **33** allows for the formation of the same species as

observed in the standard reaction at 60 °C, supporting the activation pathway proceeding through initial reaction with the alkyne.

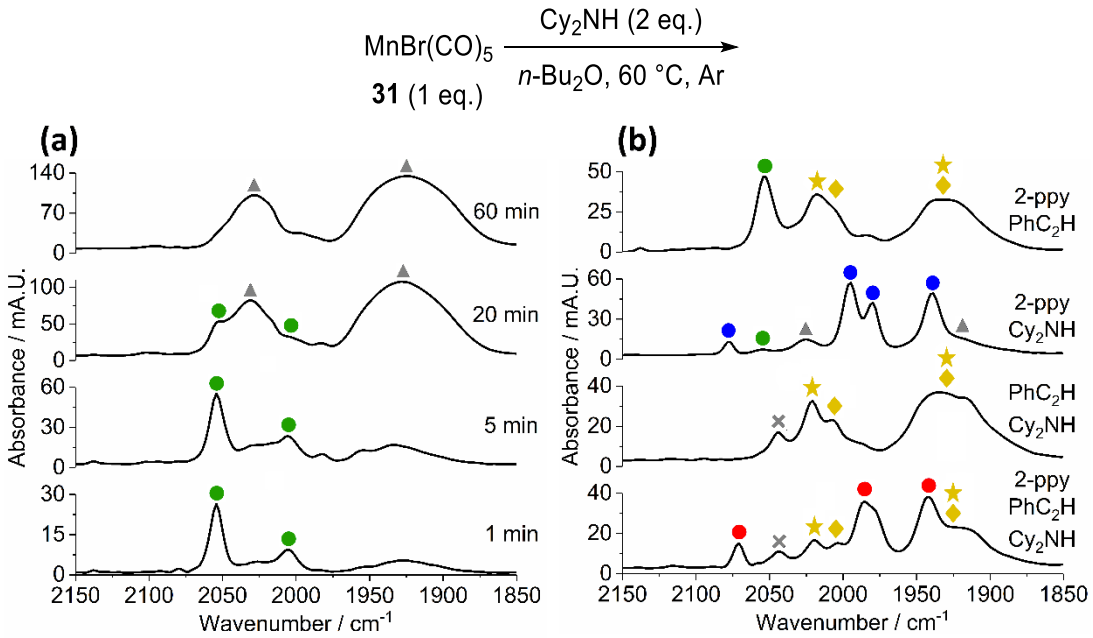

Figure 14. *In operando* IR study of the reaction without **34** and **33** using **31** as Mn-precursor at 60 °C. (a) IR spectra of the reaction in the metal carbonyl region at various timepoints. Key; green circle = **31** and grey triangle = unknown Mn-carbonyl species. Reaction conditions (in order of addition); *n*-Bu_2O (10 ml), Cy_2NH (0.83 mmol, 20 mol%) and **31** (0.42 mmol, 10 mol%) at 60 °C under argon atmosphere. (b) Comparison of the IR spectra taken at 15 minutes under various reaction conditions.

In addition, the manganese is clearly not able to activate either of the C–H bonds without additives. This likely arise due to limitations of the σ-CAM mechanism, where the bromide is a poor proton acceptor. The energy of the H–Br σ-complex is, for example, predicted (by DFT-calculations) to be 163 kJ mol^{-1} higher than the corresponding H–Bn complex, leading to an unfavourable reaction. In the reaction conducted without exogenous base CO is released from **31** allowing for the coordination of a substrate which cannot react further, except for in degradation pathways. The lack of observation of [MnBr(substrate)$(CO)_4$] intermediates, joint with the slow manganese degradation suggest that the substrate binding is reversible with an opportunity to degrade. Cy_2NH should also be able to reversibly coordinate to form a [MnBr(Cy_2NH)$(CO)_4$] species in the same manner as for **33** and **34**.

Pentacarbonyl Mn-alkynyl complex **60** was synthesised to probe the activation pathway proceeding through initial reaction with the alkyne. Therefore, the reaction between **33** (2 eq.) and **34** (1 eq.) was performed using **60** (10 mol%) as precursor (**Figure 15**), with no base required due to the initial C–H activation already taken

place. **60** was found to be remarkably stable as **71** is formed slowly over the course of 3 hours ($k = 2.3 \pm 1.3 \times 10^{-4}$ s^{-1} at 60 °C compared to $k = 3.6 \pm 0.8 \times 10^{-3}$ s^{-1} at 60 °C starting from **31**). The slow reaction rate must arise from the high stability of the pre-catalyst, as the degradation processes are also slow. Therefore, the initial CO-loss is likely rate determining and no useful kinetic information can be obtained from this experiment. Due to the small amount of **71** in solution, acetic acid was added to confirm the presence of the complex.

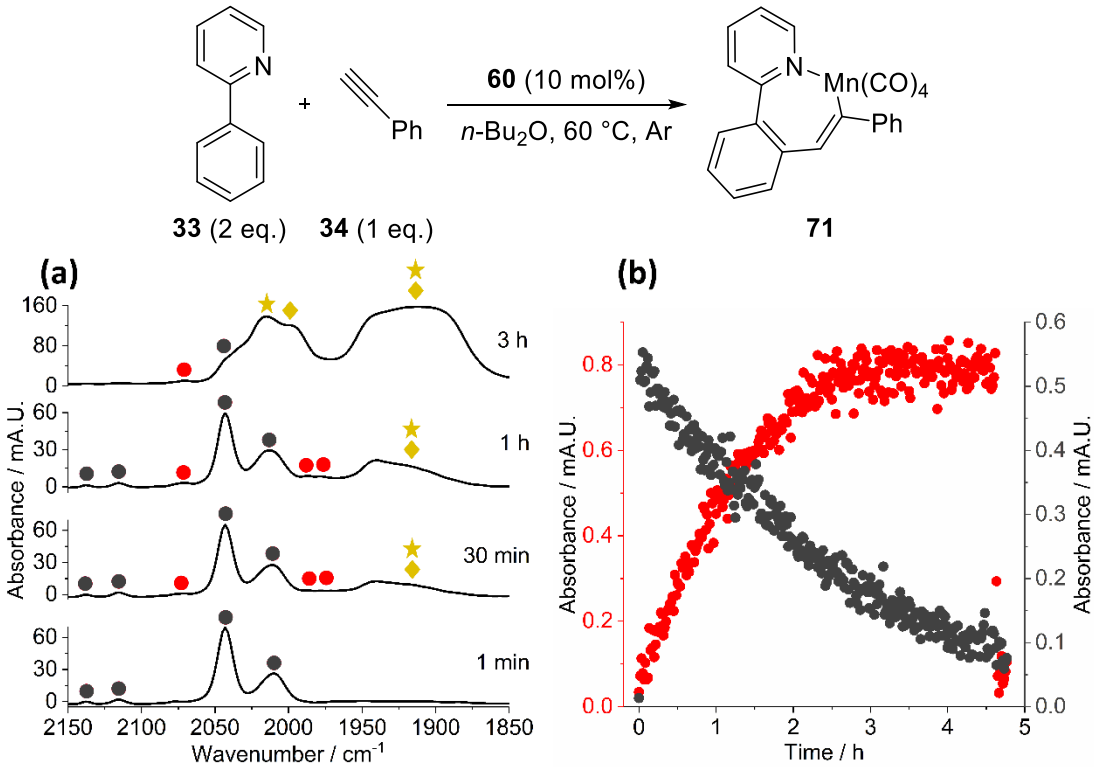

Figure 15. *In operando* IR study of the reaction between **34** and **33** using **60** as Mn-precursor at 60 °C. (a) IR spectra of the reaction in the metal carbonyl region at various timepoints. Key; dark grey circle = **60**, red circle = **71** and gold star/diamond = Mn degradation complexes. Reaction conditions (in order of addition); *n*-Bu_2O (10 ml), **33** (8.32 mmol, 2 eq.), **34** (4.16 mmol, 1 eq.) and **60** (0.42 mmol, 10 mol%) at 60 °C under argon atmosphere. Acetic acid (4.16 mmol, 1 eq.) was added after 4.5 hours. (b) Kinetic plot of the depletion of **60** (dark grey circles, band at 2138 cm^{-1}) and the formation and depletion of **71** (red circles, band at 2071 cm^{-1}), extracted from (a).

The thermal degradation of the pre-catalyst **31** in *n*-Bu_2O at 100 °C was also investigated (**Figure 16**). The reaction revealed an interesting observation, where a clean spectrum of $Mn_2(CO)_{10}$ **40** was obtained within an hour of heating. **31** quickly reacted to form two new species within 4 minutes, one is an unknown tricarbonyl complex at 2028 and 1940 cm^{-1}. The other complex is a tetracarbonyl species at 2101, 2046, 2015 and 1981 cm^{-1}, which correlate well to the literature values for the dimer $[Mn(\mu_2\text{-}Br)(CO)_4]_2$ **74** (2099, 2042, 2011, 1975 cm^{-1}).[97] This dimeric manganese

complex is synthesised through the simple heating of **31** in hydrocarbon solvent, which supports the structural assignment of **74**.

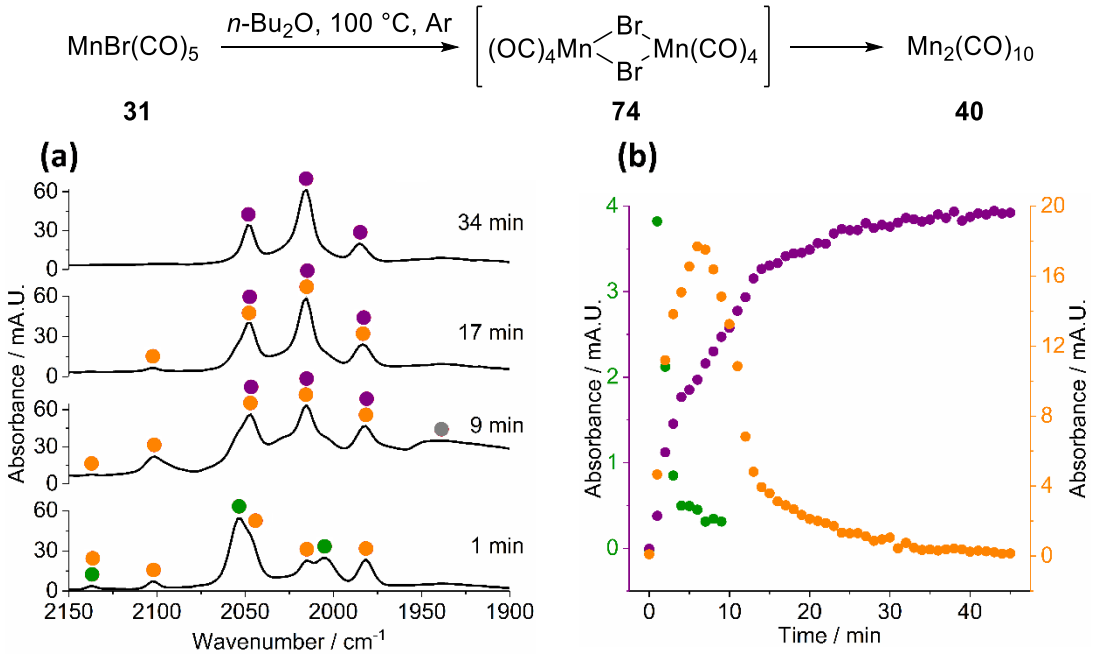

Figure 16. *In operando* IR study of the heating **31** in *n*-Bu_2O at 60 °C. (a) IR spectra of the reaction in the metal carbonyl region at various timepoints. Key; green circle = **31**, orange circle = **74** and purple circle = **40**. Reaction conditions (in order of addition); *n*-Bu_2O (10 ml) and **31** (0.42 mmol, 1 eq.) at 60 °C under argon atmosphere. (b) Kinetic plot of the depletion of **31** (green circles, band at 2154 cm^{-1}), the formation and depletion of **74** (orange circles, band at 2102 cm^{-1}) and the formation of **40** (purple circles, band at 2013 cm^{-1}), extracted from (a).

Species **74** can thereafter react further in the ultimate formation of $Mn_2(CO)_{10}$ **40**. Due to the substantial spectral overlap between **74** and **40** no kinetic information of **40** formation can be obtained. The observed formation of the manganese-dimer shows the reason for why **40** is formed under these conditions. The consumption of **74** presumably leads to the degradation of a significant portion of the manganese, possibly through the formation of $MnBr_2$ or MnO_2. There is a requirement of surplus CO, which is why a plausible version of the reaction can be described as; $2[MnBr(CO)_4]_2 \rightarrow 2MnBr_2 + Mn_2(CO)_{10} + 6CO$. Further studies are required to determine the exact mechanism of this process.

2.3.2 Deuterium-Labelling Experiments

To supplement the investigation, *vide supra*, deuterium-labelling studies were conducted under the reaction conditions at 60 °C. If the pre-catalyst activation proceeds *via* initial cyclomangnation of **33**, then there should be no kinetic isotope effect (KIE) nor deuterium-erosion in **35** (after addition of acid) if **34**-D is used in the

reaction. However, the opposite is true if the reaction proceeds through reaction with the alkyne first. The reversed trend to **34**-D is expected when **33**-D_5 is used.

Initially, the reaction using **33** (2 eq.), **31** (10 mol%) and Cy_2NH (20 mol%) was treated with **34**-D (1 eq., 96% D) in *n*-Bu_2O at 60 °C under an argon atmosphere (**Figure 17**). As expected, **71** is seen forming in the IR spectra, concomitantly with the anticipated manganese complexes formed by degradation. The rate of formation was found to be identical with the reaction using **34**-H, which infers a KIE of 1. At first glance this is in support of the previously proposed mechanism, where the alkyne C–H bond is not broken until the protonation step of the catalytic cycle. Even though that is true, a KIE for the Mn-alkynyl pathway might not be expected either. The KIE arises from the H/D-effects on the rate determining step of the reaction, which for an Mn-alkynyl pathway is likely taking place after the initial activation of the alkyne C–H bond (following initial alkyne-manganese coordination). Therefore, a distinct differentiation between the two different activation pathways cannot be determined based on the KIE obtained.

After the completion of the reaction and addition of AcOH (1 eq.), the organic product **35** was isolated by flash column chromatography to determine the amount of deuterium-incorporation into the two alkene positions. It can be seen that there is 76% deuterium at the C1 position, where either 0 or 100% was expected (0% for initial reaction with **34**, and 100% with **33**). The alkyne-exchange in the π-coordinated complex Mn(ppy)(**34**)$(CO)_3$ **63** (which is formed as an intermediate regardless of activation pathway) can explain the unexpected D-incorporation. If exchange is rapid, a substantial amount of deuterium in the product is expected. A small amount of deuterium (8%) can be observed in the C2-position and ^2H NMR spectroscopy was additionally recorded to confirm the observed deuterium-incorporation.

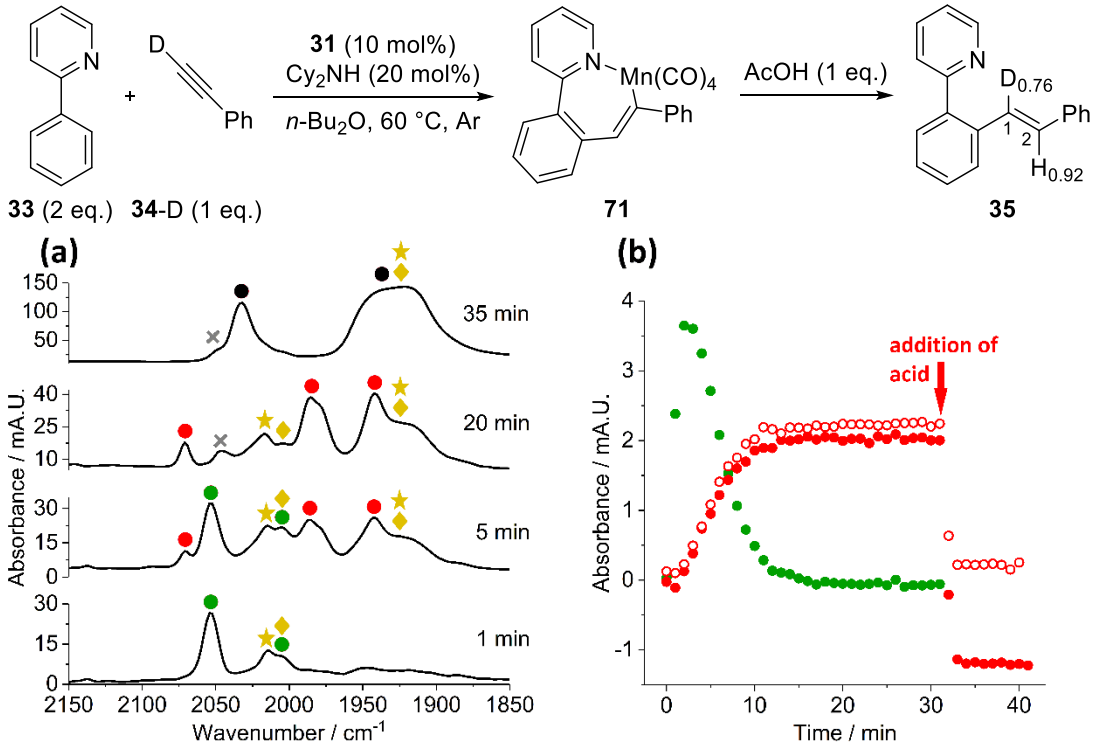

Figure 17. *In operando* IR study of the reaction between **34**-D and **33** under standard reaction conditions at 60 °C. (a) IR spectra of the reaction in the metal carbonyl region at various timepoints. Key; green circle = **31**, red circle = **71**, grey cross = unknown Mn-carbonyl species, black circle = unknown Mn-carbonyl species and gold star/diamond = Mn degradation complexes. Reaction conditions (in order of addition); *n*-Bu_2O (10 ml), **33** (8.32 mmol, 2 eq.), **34**-D (4.16 mmol, 1 eq.), Cy_2NH (0.83 mmol, 20 mol%) and **31** (0.42 mmol, 10 mol%) at 60 °C under argon atmosphere. Acetic acid (4.16 mmol, 1 eq.) was added after 30 minutes. (b) Kinetic plot of the formation of the depletion of **31** (green circles, band at 2054 cm^{-1}) and the formation and depletion of **71** from both **34**-D (red circles, band at 2071 cm^{-1}), extracted from (a), and **34** (hollow red circles).

When the reaction using **34** (1 eq.), **31** (10 mol%) and Cy_2NH (20 mol%) in *n*-Bu_2O at 60 °C under an argon atmosphere was treated with **33**-D_5 (2 eq., >99% D), **71** was found to form in smaller amounts than previously observed (**Figure 18**). A KIE of 1.29 ± 0.16 was obtained, possibly indicating a secondary KIE in this system where the C–H bond is not broken in the rate determining step yet still has an impact. However, it could also suggest a very small primary KIE, as values around 1.3 has previously been used to rationalise both primary and secondary KIEs.[98, 99] The CO-loss from **63** is likely either the rate determining (which might be affected by the H/D-exchange leading to a secondary effect) or a competitive step (lowering the value of the primary KIE) in the Mn-alkynyl pathway. Further mechanistic evidence is required to determine if the effect is primary or secondary. Nevertheless, this supports of an activation pathway which proceeds *via* initial reaction with the alkyne, as it is likely that the cyclomanganation of **33** would have a much larger primary KIE.

Following the addition of acetic acid and isolation of **35**, no deuterium incorporation was observed at the C2-position. The 37% incorporation observed could on the other hand be seen at the C1-position, again differing from the predicted 0 or 100% (0% for initial reaction with **33**, and 100% with **34**). The exchange of alkyne-ligand on **63** could again explain this observation. The differential between predicted and measure D-incorporation in the two experiments are similar (76 and 63%), consistent with a mechanism that is affected by alkyne exchange from the surrounding solution. It could also be possible that the lower than expected deuterium incorporation could arise from a D/H-exchange taking place before the alkyne reacting with the manganese. Taken together, the deuterium-labelling experiments are still in support of the mechanism with initial reaction with the alkyne to proceed *via* a Mn-alkynyl complex.

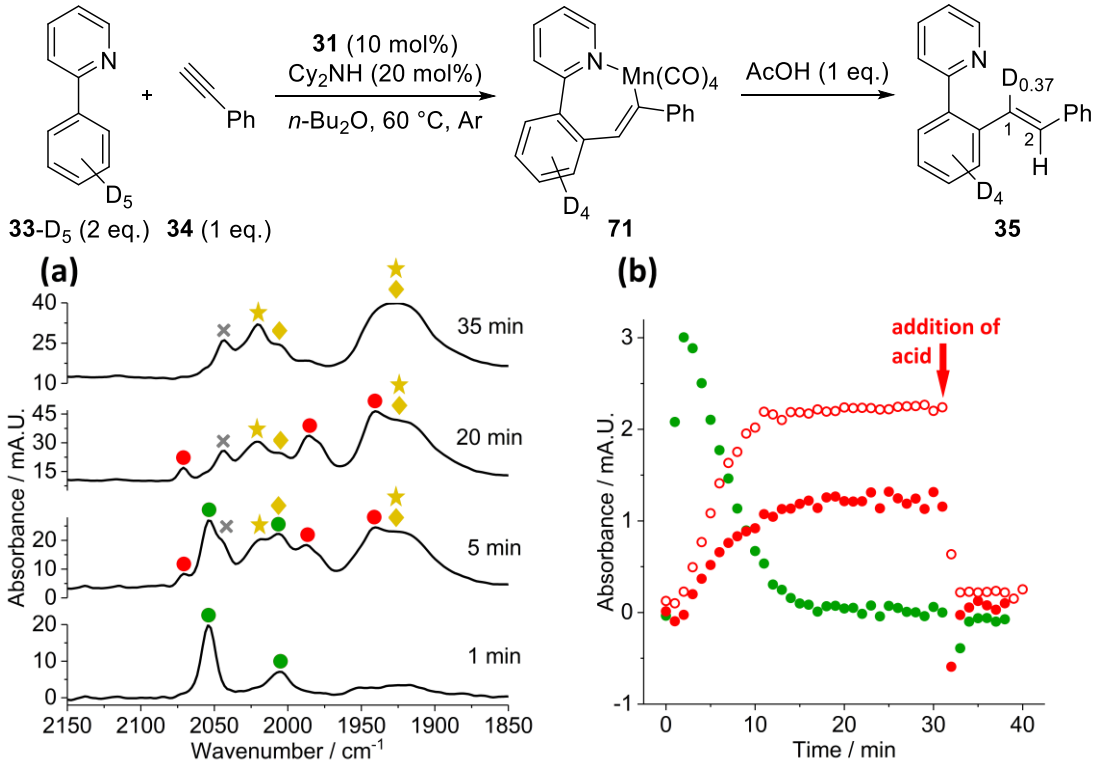

Figure 18. *In operando* IR study of the reaction between **34** and **33**-D_5 under standard reaction conditions at 60 °C. (a) IR spectra of the reaction in the metal carbonyl region at various timepoints. Key; green circle = **31**, red circle = **71**, grey cross = unknown Mn-carbonyl species and gold star/diamond = Mn degradation complexes. Reaction conditions (in order of addition); *n*-Bu_2O (10 ml), **33**-D_5 (8.32 mmol, 2 eq.), **34** (4.16 mmol, 1 eq.), Cy_2NH (0.83 mmol, 20 mol%) and **31** (0.42 mmol, 10 mol%) at 60 °C under argon atmosphere. Acetic acid (4.16 mmol, 1 eq.) was added after 30 minutes. (b) Kinetic plot of the formation of the depletion of **31** (green circles, band at 2054 cm^{-1}) and the formation and depletion of **71** from both **33**-D_5 (red circles, band at 2071 cm^{-1}), extracted from (a), and **33** (hollow red circles).

2.4 Investigation of Protonation Pathways

2.4.1 Examination through Stoichiometric Reactions

Following the pre-catalyst activation investigation, the focus shifted towards the catalytic cycle itself. The reaction step involving the depletion of the rate determining state is a suitable starting point for the investigation into the mechanism of catalysis. The protonation pathway has therefore been studied, and the identity of the proton source requires identification and verification. A relatively straight-forward way to test the viability of various substrates as the proton source, was to perform stoichiometric (with respect to Mn) reactions and thereby limiting the manganese to less than one turnover. Variations in reagent amounts should affect product generation and thereby the ability of a substrate to perform the protonation can be elucidated. The reactions were also run using **10** as the Mn-precursor to avoid implications of pre-catalyst activation and the compulsory addition of **33**.

Initially, the reaction between **10** (1 eq.) and **34** (1 eq.) was performed in *n*-Bu_2O at 100 °C under an argon atmosphere, where the conversion was determined by *ex situ* ^{1}H NMR spectroscopic analysis of the crude reaction mixture after 30 minutes (**Figure 19**). If the alkyne is responsible for the protonation, then 50% conversion to **35** would be the maximum for this reaction. However, only 7% of **35** was observed, while full consumption of **10** has occurred and the remaining 2-phenylpyridine was found in two unknown compounds and free **33**. First is the doubly-alkenylated 2-phenylpyridine **76**, which was isolated by flash column chromatography (in a separate experiment) and is the result from the manganese enabling a further turnover. Compound **76** was formed with 5% conversion in this reaction.

The second unknown compound exhibited four highly distinct peaks in the ^{1}H NMR spectra (6.57, 5.70, 4.16 and 3.23 ppm), which are even more shielded than the observed alkene proton (6.88 ppm). Distinct IR CO-stretching bands were also observed by analysis of the crude reaction mixture (1983 and 1896 cm^{-1}), suggesting the presence of a "$Mn(CO)_3$" moiety. This compound (**75**) was isolated as a brown solid through crystallisation from CH_2Cl_2/pentane, where both the ^{1}H NMR and IR stretching bands were retained. After obtaining supporting characterisation data (^{13}C NMR spectroscopy, ESI-mass spectrometry and melting point), **75** was assigned as being the reductive elimination complex formed from the tricarbonyl insertion

complex **77**. A manganese-tricarbonyl anion is still coordinated to the pyridinium cation generated from the reductive elimination, rationalising the large shielding of the pyridinium protons in the ^{1}H NMR spectrum.

Next, the equivalents of **34** was increased to assess the viability of the terminal alkyne as a proton source to be probed. Performing the reaction using two equivalents of the alkyne allowed for a slight increase in the generation of **35** to 12% conversion, while the amount of **76** significantly increased to 25%. The amount of the reductive elimination product **75** did decrease to 64%, arising from the protonation taking place more readily. When the equivalents were increased to four, the observed trend continued where **35** (17%) and **76** (51%) both boasted higher conversions. The conversion to **75** thus significantly decreased to 32%, leading to **76** being the major product of the reaction.

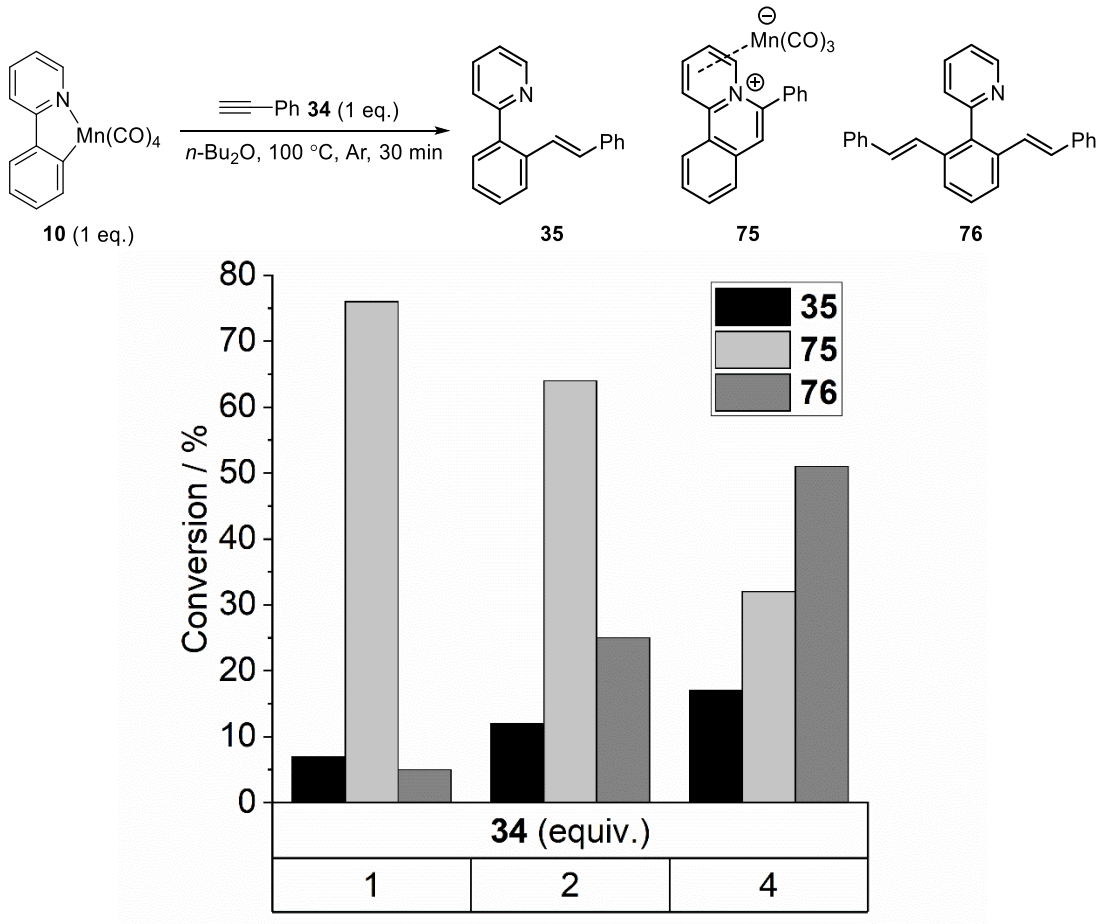

Figure 19. The effect of increasing amount of **34** in the stoichiometric reaction between **10** and **34**. Reaction conditions; **10** (0.025 mmol, 1 eq.), **34** (0.025–0.100 mmol, 1–4 eq.) and *n*-Bu_2O (0.6 ml) at 100 °C under argon atmosphere for 30 minutes.

The trend emerging is one where the alkyne can perform the proton transfer to form the desired organic product **35**. However, the formation of 17% **35** using four

equivalents of alkyne is inadequate for **34** to solely be responsible for the protonation. The large amount of double-alkene product **76** formed under these conditions further supports the analysis, as none can be seen under catalytic conditions. There must be something in the solution which hinders the reaction from forming **76**. Species **33** could be responsible and can accelerate product liberation through competitive binding to the manganese. The reductive elimination complex **75** only appears to be formed when there is a small amount of accessible proton source in solution, making the reductive elimination pathway competitive.

To study the viability of 2-phenylpyridine **33** as a proton source, the reaction was performed using **10** (1 eq.), **34** (1 eq.) and **33** (1.15 eq., determined by ^{1}H NMR spectroscopy) in *n*-Bu_2O at 100 °C under an argon atmosphere (**Figure 20**). The generation of **35** significantly increased to 59% conversion in this reaction, signalling a large impact of **33** on the efficiency of the protonation step. 53% of **75** was generated and the total conversion was over 100% due to the limitation of the experiment set by the one equivalent of **34** used. No doubly-alkenylated compound **76** could be seen, partially explaining the large increase in **35** formation.

It is unclear if the positive effect of **33** on the reaction arises from the protonation event itself or from the product liberation step. To deconvolute this, pyridine (1 eq.) replaced **33** as an additive, achieving 22% of **35** and 68% of **75**. Again, no formation of **76** was observed, leading to the conclusion that the 2-phenylpyridine has a large impact on both steps within the mechanism. The large increase in **35** formation is mostly due to its proton transfer capability, while the lack of **76** generation must arise from the product liberation ability.

The final proton source to be tested was H_2O, due to its presence in the wet reaction solvent and relatively acidic protons compared to **34** and **33**. Running the reaction between **10** (1 eq.) and **34** (1 eq.) with additional H_2O (10 eq.) added leads to a large increase in **35** formation (42%). **76** is still formed (9%) in the reaction, while the reductive elimination product **75** is only generated in 44% conversion. This result confirms that water is capable of performing the protonation in the reaction, while finding the competitive coordination in the product liberation step difficult.

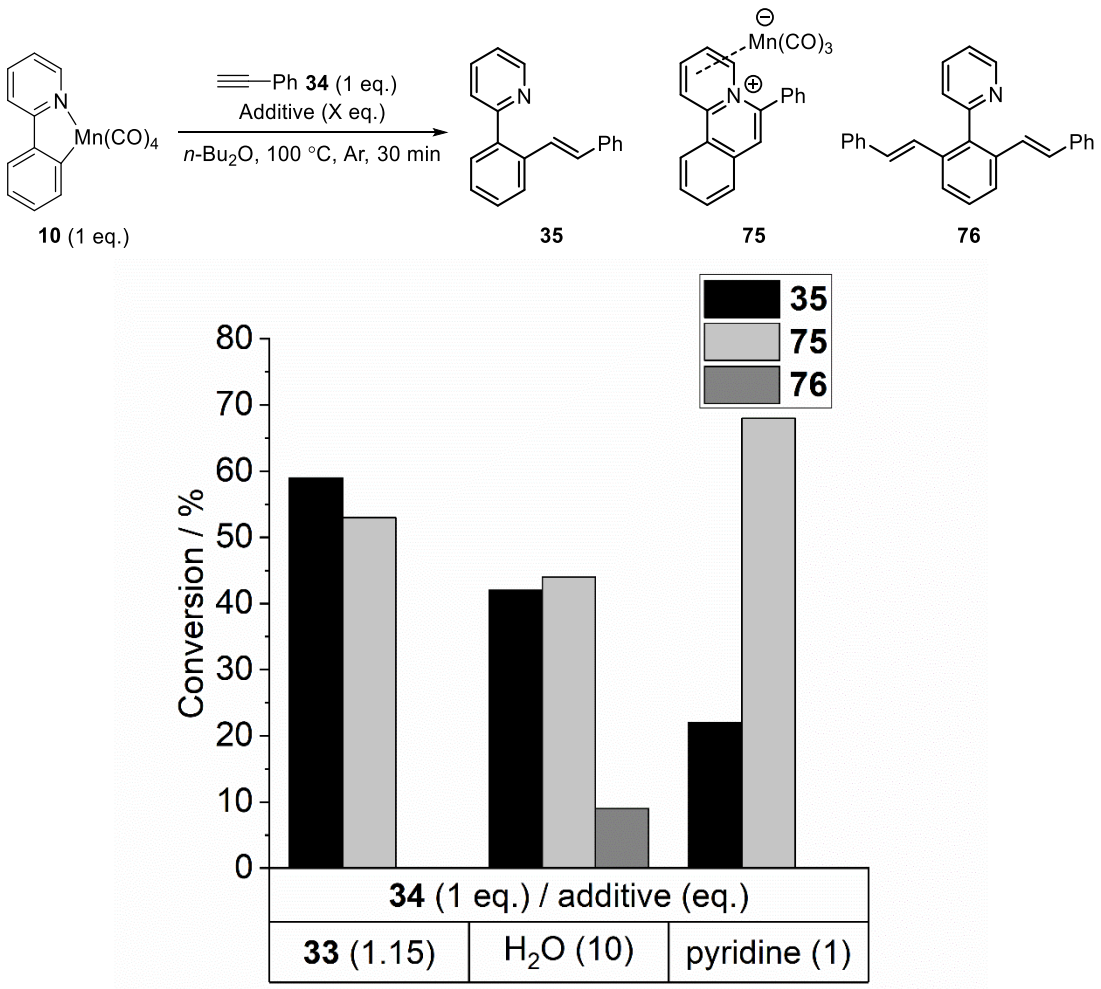

Figure 20. The effect of external additives in the stoichiometric reaction between **10** and **34**. Reaction conditions; **10** (0.025 mmol, 1 eq.), **34** (0.025 mmol, 1 eq.), *n*-Bu_2O (0.6 ml) and H_2O (0.25 mmol, 10 eq.) or **33** (0.029 mmol, 1.15 eq.) or pyridine (0.025 mmol, 1 eq.) at 100 °C under argon for 30 minutes.

2.4.2 Deuterium-Labelling Studies

To confirm the ability of the three reagents (**34**, **33** and H_2O) to act as acids in the reaction, deuterium-labelling experiments were conducted. Employing deuterated additives allows for the monitoring of the deuterium incorporation into the relevant alkene position, and thereby providing supportive evidence for the different protonation pathways.

Initially, the reaction between **10** (1 eq.) and **34**-D (4 eq., 96% D) was performed in *n*-Bu_2O at 100 °C (**Scheme 16**). The organic products formed post-protonation (**35** and **76**) were isolated by flash column chromatography and characterised with ^1H and ^2H NMR spectroscopy. The generation of **35** mirrored the result seen using **34** (17 and 21% respectively), while formation of **76** was lowered to 29% (51% using **34**) and **75** increased to 50% conversion (32% using **34**). This shift in observed conversion might

arise from the deuterated analogue finding the protonation step more difficult than the protio-derivative. This infers that **75** becomes favoured as the reductive elimination is more competitive in this reaction. Comparing the rates of protonation and reductive elimination can allow for the confirmation of this hypothesis.

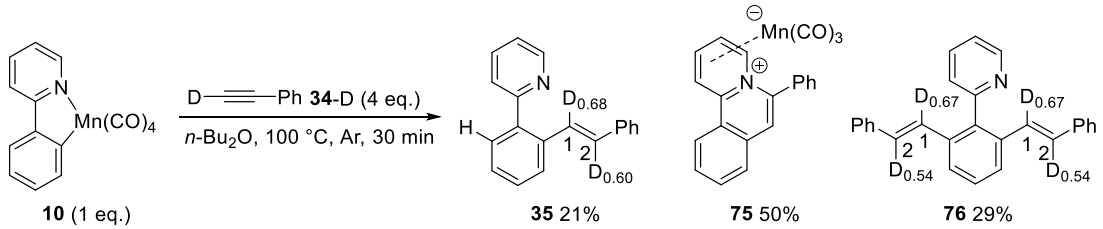

Scheme 16. Stoichiometric reaction between **10** and **34**-D and observation of the deuterium-incorporation into the organic products.

The deuterium-incorporation into **35** and **76** was monitored and a mixture of deuterated alkene-positions were observed. In **35** 60% D was found in the C2-position, supporting the capability of **34** to perform protonation in the reaction. Unexpectedly, there was 65% D observed at the C1-position, which indicated a reversibility of the protonation step. This reversibility allows for the subsequent C–H bond activation to take place on both the alkene (reversed protonation) and on the arene (towards double alkenylation), leading to H/D exchange to take place. A similar deuterium distribution was observed in **76** (67% D in C1 and 54% D C2), arising for the reasons stated above.

Utilising **33**-D_5 (1 eq.) in the reaction between **10** (1 eq.) and **34** (1 eq.), afforded a similar amount of **76** (60%, 53% using **33**) and **75** (2%, 0% using **33**). The amount of the desired alkene product **35** was however significantly lowered to 29% (59% using **33**). This reduction is likely the result of a KIE, which makes protonation more challenging for the substrate.

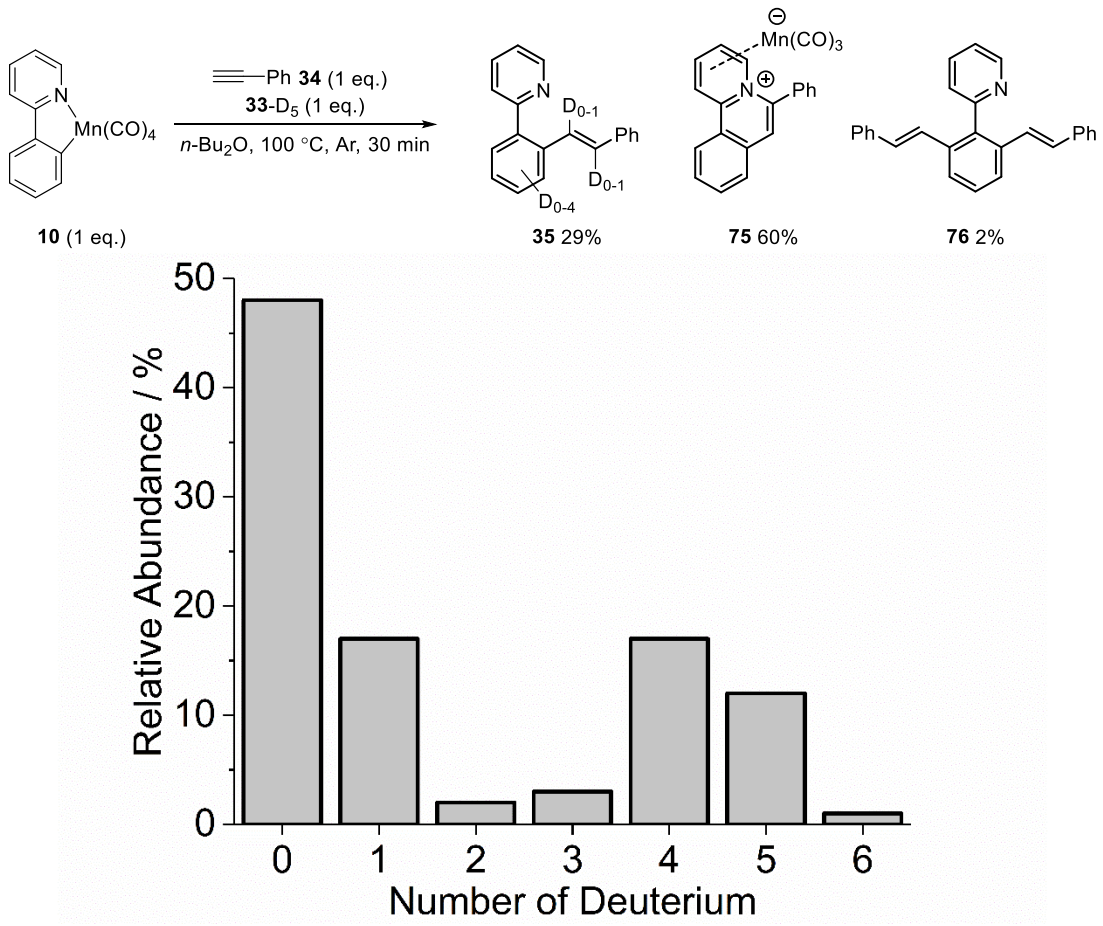

Figure 21. Stoichiometric reaction between **10**, **34** and **33**-D_5 and determination of the deuterium-incorporation into the organic products by ESI-MS.

The monitoring of D-incorporation becomes challenging due to the large amount of aromatic C–D bonds in the product. Therefore ESI-MS was utilised to perform this task, where a plot of the relative abundance (%) of the possible isomers can be obtained from the peak intensities. In this plot the most abundant configuration contains no deuterium atoms (*m*/*z* 257.1204, 48% abundance, 14% conversion), whereas the desired product with one deuterium is present in 17% abundance (5% conversion). The products containing four (*m*/*z* 261.1456) and five (*m*/*z* 262.1518) deuterium atoms exhibit a similar trend (17 and 12% abundance, 5 and 3% conversion, respectively), where the extra deuterium originate from **33**-D_5 being incorporated into the reaction. The deuterium-labelling observed is supportive of the ability of **33** to perform the protonation step in the reaction, while the competition by **34** and H_2O most likely is responsible for the reduced incorporation observed.

The final additive to be tested was H_2O, whereas D_2O (10 eq.) was added to the reaction between **10** (1 eq.) and **34** (1 eq.) at 100 °C (**Scheme 17**). This reaction showed large similarities to the protio-version, for the generation of **35** (52%, 42% using H_2O),

76 (8%, 9% using H_2O) and **75** (40%, 44% using H_2O). The deuterium-labelling resulted as expected in no incorporation into the C1-position and a large amount in the C2-position (83%). This is in strong support of water being involved in the protonation step within the catalysis.

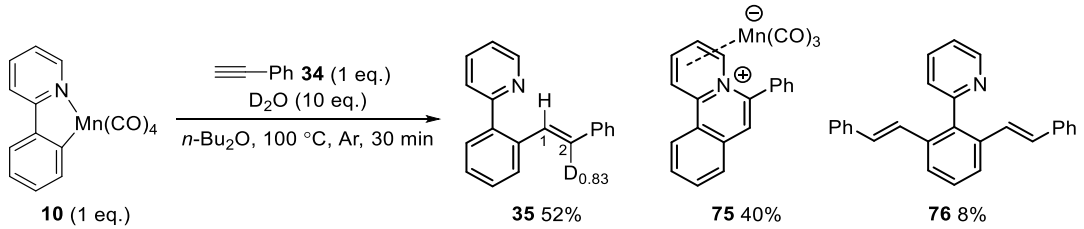

Scheme 17. Stoichiometric reaction between **10**, **34** and H_2O and determination of the deuterium-incorporation into the organic products.

2.4.3 Computational Studies

The involvement of three different proton sources in the reaction, automatically creates three different catalytic cycles. It is highly unlikely that these cycles converge before the common alkyne-coordinated Mn(κ$_2$-ppy)(**34**)$(CO)_3$ is formed. It is difficult to experimentally determine the full catalytic cycles due to the lack of observable intermediates and direct kinetic information. The mechanism of the catalytic cycles involving **34**, **33** and H_2O were instead investigated using DFT-calculations. The computational approach may allow for the exclusion of certain reaction pathways (with experimental support) while providing supporting evidence for others, even though caution should be taken with the application of gas-phase calculations to solution-phase reactions. The validity of the computational model used is discussed in Chapter 3.3.1.

The catalytic cycle resulting from protonation by the terminal alkyne was investigated using **10** as a reference point (**Scheme 18**). The C–C bond is initially formed through the predicted pathway reported by Wang,[34] where initial alkyne-coordination is followed by insertion into the C–Mn bond. After the formation of the 7-membered insertion complex, the tetracarbonyl version **71** is significantly lower in energy than tricarbonyl **77** (ΔG = -51 and -16 kJ mol^{-1} respectively) This shows why **71** is observed as the catalyst resting state. Nevertheless, **77** arises from the calculations as being the divergence point, where the catalyst can proceed through either protonation, reductive elimination or double insertion, *i.e.* where the fate of the products formed is decided.

Using **34** as the substrate leads to a high energy transition state **TS$_{77\text{-}75}$** (ΔG = +106 kJ mol^{-1}) and product **75** (ΔG = +67 kJ mol^{-1}) for the reductive elimination pathway. This is significantly larger than the highest energy transition state **TS$_{79\text{-}65}$** (ΔG = +80 kJ mol^{-1}) in the protonation pathway by the terminal alkyne, highlighting why forcing stoichiometric reaction conditions are required for **75** to be generated.

The protonation pathway for **34** (from **77**) starts with formation of the alkyne-bound complex **78** (ΔG = +46 kJ mol^{-1}), before rearrangement to bind as a σ-complex to the terminal C–H bond in complex **79** (ΔG = +69 kJ mol^{-1}) occurs. This place the proton in position to be transferred across the C–Mn bond through transition state **TS$_{79\text{-}65}$** (ΔG = +80 kJ mol^{-1}). The energy suggested by theory explains the high temperatures required for the protonation to proceed experimentally. The proton-transfer finally generate Mn-alkynyl species **65**, with product **35** still κ_2-bound to the manganese. **65** is lower in energy (ΔG = -49 kJ mol^{-1}) by 33 kJ mol^{-1} than **77**, suggesting protonation could be irreversible. However, the similar energy of **TS$_{77\text{-}75}$** to the required input energy needed to reverse the protonation (ΔG = 122 and 129 kJ mol^{-1} respectively) shows that proton transfer can be reversed in the reaction.

The protonation step by **33** is initiated by the *N*-coordination of the 2-phenylpyridine to form complex **80** (ΔG = +18 kJ mol^{-1}). Thereafter the rearrangement to form a σ-complex to an *ortho* C–H bond in **81** (ΔG = +51 kJ mol^{-1}) occurs, before the subsequent proton transfer event takes place *via* transition state **TS$_{81\text{-}82}$** (ΔG = +84 kJ mol^{-1}). After protonation the alkene product **35** is still bound as a σ-complex in **82** (ΔG = -19 kJ mol^{-1}), which is replaced by a low energy π-complex **83** (ΔG = -16 kJ mol^{-1}). The final complex to be formed in these calculations is the *N*-bound complex (ΔG = -54 kJ mol^{-1}) and as expected is the thermodynamically most favourable configuration. The relatively high energy of **82** suggests that this process is reversible as the activation barrier for reverse proton transfer is 3 kJ mol^{-1} lower in energy.

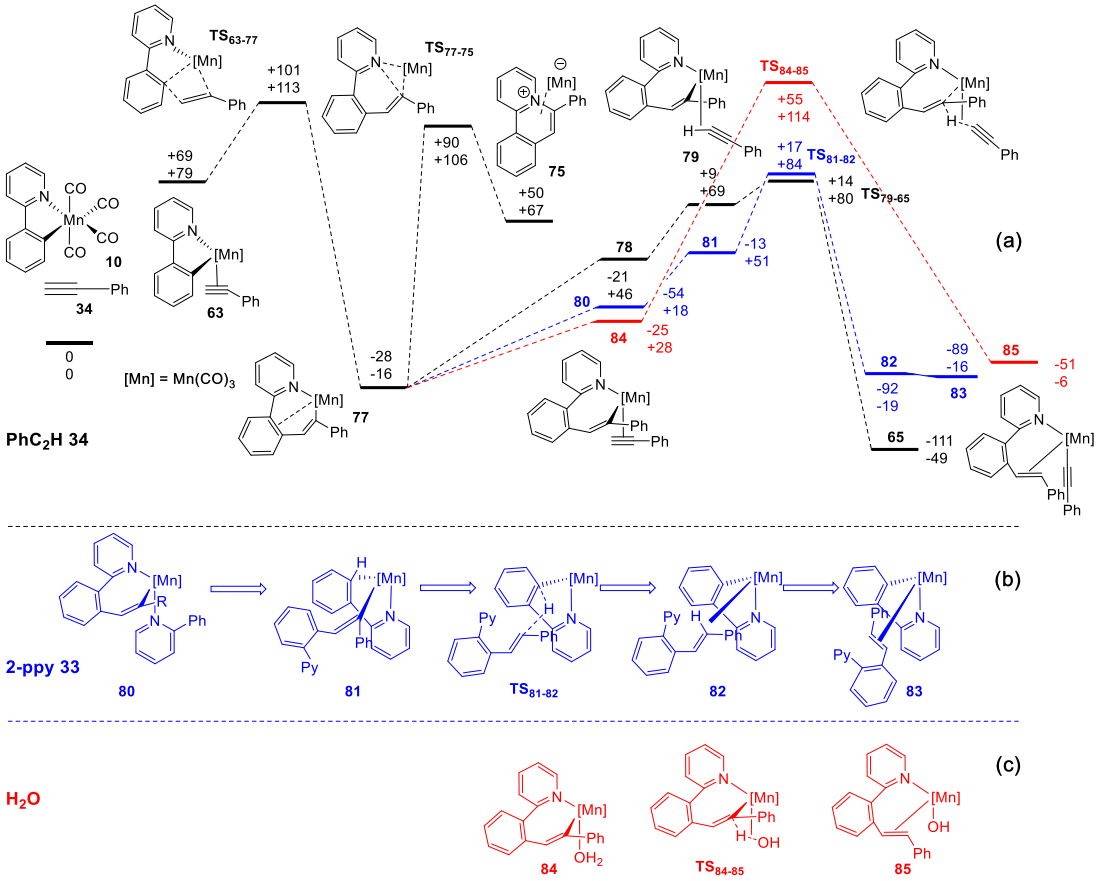

Scheme 18. DFT-calculated protonation pathways for **34**, **33** and H_2O. Calculations were performed at the (RI-)BP86/SV(P) level. Energies are zero-point energy-corrected energies (top) and Gibbs energies at 298 K (bottom) in kJ mol^{-1}. (a) C–C bond formation step from **10** and **34**, followed by all three possible protonation pathways and structures relating to **34**. A comparison to the reductive elimination pathway for **34** is also included. (b) Structures relating to the protonation pathway mediated by **33**. (c) Structures relating to the protonation pathway mediated by H_2O.

H_2O is also found to be an efficient ligand in initial binding to the manganese to form *O*-bound complex **84** (ΔG = +28 kJ mol^{-1}). No rearrangement is required for the proton transfer, thus the process proceeds through high energy transition state **TS84-85** (ΔG = +112 kJ mol^{-1}) to form hydroxyl-complex **85** (ΔG = -8 kJ mol^{-1}). The high energy transition state is problematic for this pathway to be competitive, but it is still possible that it occurs when enough water is present in solution. The process should also be reversible as the reverse proton transfer is 8 kJ mol^{-1} lower in energy.

2.5 Reaction with Internal Alkyne

The ability of **33** and H_2O to perform the protonation in the reaction raises questions about why the internal alkynes are not productive in the formation of the alkene product **89**. Whether the lack of reactivity arises from inability to take part in the proton transfer step (accepting the proton from **33** or H_2O), inhibition of the manganese

catalyst or inability for the pre-catalyst activation step to proceed, will have a large impact on the understanding of the catalytic system. Therefore, studies into this "unreactive" system were conducted.

The reaction between **33** (2 eq.) and diphenylacetylene **21** (1 eq.) was performed under the standard reaction conditions using **31** (10 mol%) as pre-catalyst (**Figure 22**). Species **31** was again rapidly consumed in the reaction (< 3 min) and replaced by a few new species, of which one is a transient unknown tricarbonyl manganese complex (band at 1991, 1907 and 1897 cm^{-1}). **10** can, as expected, be observed in the reaction (distinct peak at 2078 cm^{-1}) next to a species which resembles **71**. This species was tentatively assigned as tetracarbonyl insertion complex **91**, formed post C–C bond formation with **21** (distinct band at 2069 cm^{-1}). These two manganese complexes exhibit similar reaction rates, in the rapid formation and subsequent depletion on 10–20 minute timescale, from which a new tricarbonyl complex **86** is generated. There was still a minor species remaining after the reaction was seemingly complete but has transformed into **86** after several hours, rendering only **86** present in the IR spectrum.

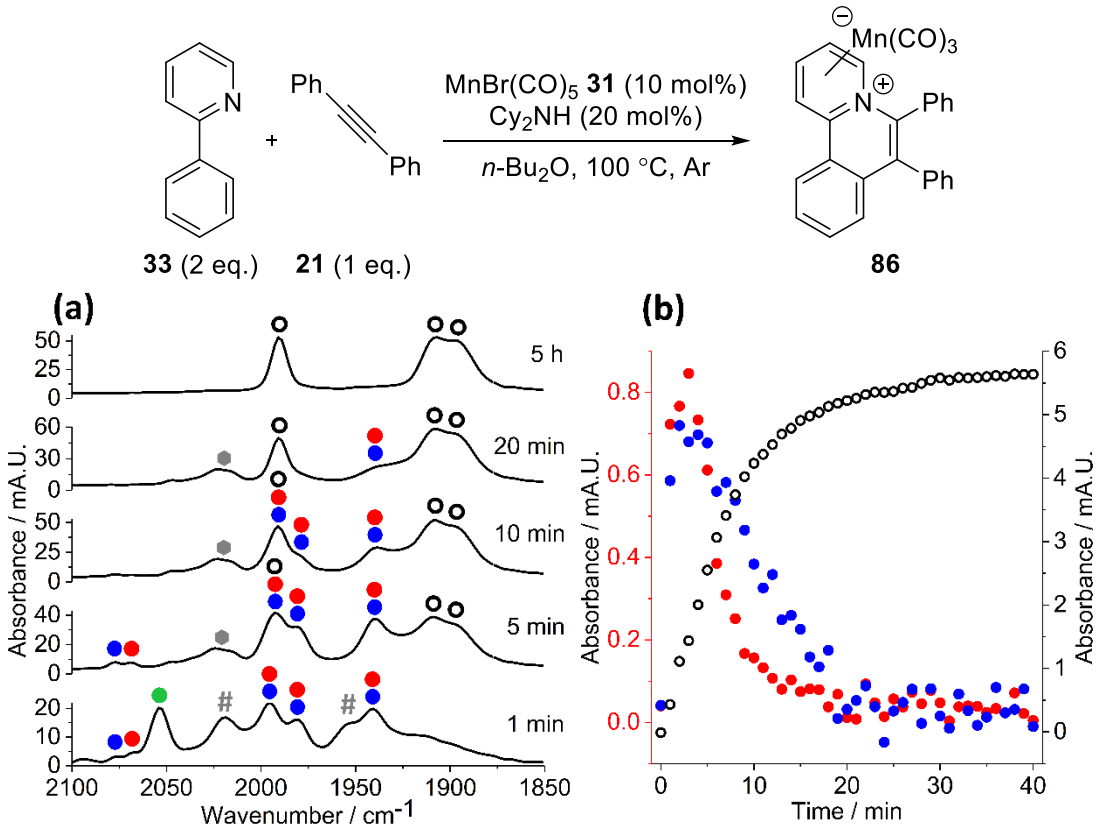

Figure 22. *In operando* IR study of the reaction between **33** and **21** using **31** as pre-catalyst with Cy_2NH as additive. (a) IR spectra of the reaction in the metal carbonyl region at various timepoints. Key; blue circle = **10**, green circle = **31**, red circle = **91**, hollow black circles = **86** and grey cross/hash = unknown Mn-carbonyl species. Reaction conditions (in order of addition); *n*-Bu_2O (10 ml), **33** (8.32 mmol, 2 eq.), **21** (4.16 mmol, 1 eq.), Cy_2NH (0.83 mmol, 20 mol%) and **31** (0.42 mmol, 10 mol%) at 100 °C under

argon atmosphere. (b) Kinetic plot of the formation of reductive elimination product **86** (hollow black circles, band at 1897 cm^{-1}) and the formation and depletion of **10** (blue circles, band at 2078 cm^{-1}) and **71** (red circles, band at 2071 cm^{-1}), extracted from (a).

This new tricarbonyl complex **86** show a large resemblance to the reductive elimination complex for the terminal alkyne and was successfully isolated by crystallisation from CH_2Cl_2/pentane. It was found to be stable where strong acid (HCl) or silica gel was required for degradation of the complex. The distinctive ^1H NMR spectroscopic peaks for the pyridinium-protons are present and an X-ray structure was solved for this complex (**Figure 23**), where it was confirmed that the manganese tricarbonyl anion has emerged as coordinated to the pyridinium ring. Mn–C bond distances confirms that the four C–H atoms in the pyridinium are coordinated to the manganese. This Mn-coordination allows for the planar pyridinium ring to distort and form a boat-conformation, suggesting a loss of aromaticity.

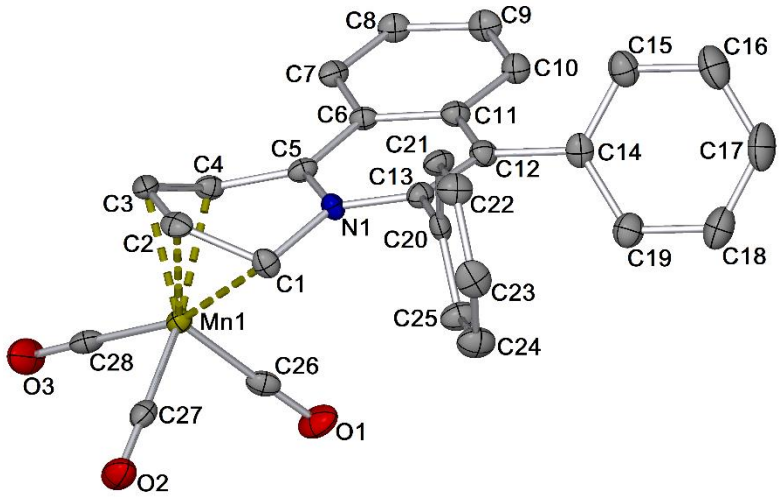

Figure 23. X-ray crystallographic structure of reductive elimination complex **86**.

The rate of consumption of the manganese intermediates provide insight into the relative ease of the reductive elimination process. The slower rate of decay and linearity for **10** ($k = 2.0 \pm 0.4 \times 10^{-3}$ s^{-1} at 100 °C) compared to **91** ($k = 5.1 \pm 0.6 \times 10^{-3}$ s^{-1} at 100 °C), indicates that the reductive elimination proceeds at a slightly quicker rate than the C–C bond formation. Therefore, the consumption of **10** (CO-loss) becomes rate determining for the formation of the reductive elimination complex ($k = 2.4 \pm 0.1 \times 10^{-3}$ s^{-1} at 100 °C).

Additionally, DFT-calculations were employed to explore the rationale behind the preference for reductive elimination over any protonation pathways. Starting from the tricarbonyl manganese insertion complex, the transition state for reductive elimination

and protonation by 2-phenylpyridine **33** (+123 kJ mol^{-1} and +104 kJ mol^{-1} respectively) were found to be highly similar as when using terminal alkyne **34** (**Scheme 18**). Therefore, no insight into why the reductive elimination is favoured for the internal alkyne were obtainable through the DFT-calculations.

The reaction was repeated using **10** (10 mol%) as the pre-catalyst and no amine base additive was employed (**Figure 24**). The cleanliness of the IR spectrum recorded is quite striking, where only **10**, **91** and **86** can be observed, suggesting complete conversion with respect to manganese. The rate of formation of **86** (k = 2.4 ± 0.1 × 10^{-3} s^{-1} at 100 °C) is identical (within error) to the reaction starting from **31** (k = 2.4 ± 0.1 × 10^{-3} s^{-1} at 100 °C). This result supports the rapid base-assisted cyclomanganation pathway to form **10** from **31**, proceeding *via* tetracarbonyl manganese intermediates, suggesting that **10** is a reaction intermediate rather than an off-cycle species. This also highlights that **10** should be observed in the reactions using the terminal alkynes, if the pre-catalyst activation pathway proceeds through this manganacycle.

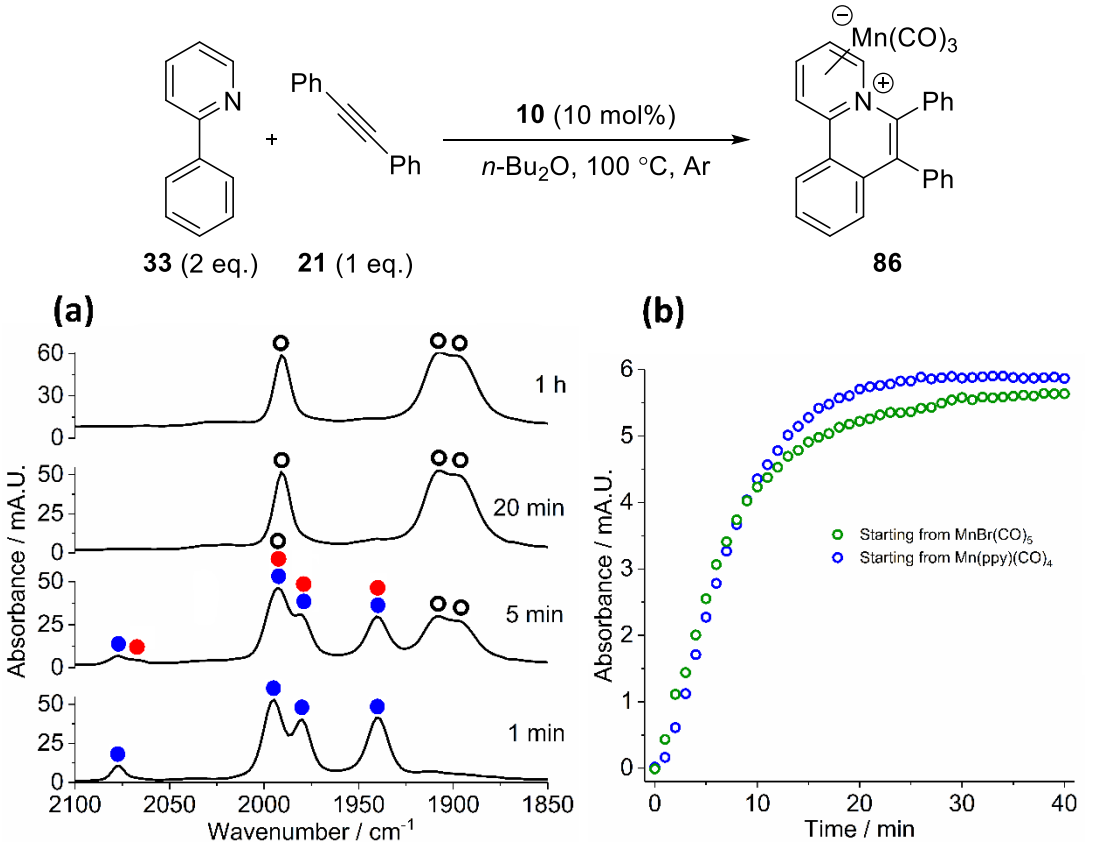

Figure 24. *In operando* IR study of the reaction between **33** and **21** using **10** as pre-catalyst. (a) IR spectra of the reaction in the metal carbonyl region at various timepoints. Key; blue circle = **10**, red circle = **91** and hollow black circles = **86**. Reaction conditions (in order of addition); *n*-Bu_2O (10 ml), **33** (8.32 mmol, 2 eq.), **21** (4.16 mmol, 1 eq.) and **10** (0.42 mmol, 10 mol%) at 100 °C under argon atmosphere. (b) Kinetic plot of the formation of reductive elimination product **86** for both precursors **10** (hollow black circles, band at 1897 cm^{-1}) and **31** (hollow green circles).

Monitoring the reaction between **33** (2 eq.) and **21** (1 eq.) at 60 °C using **31** (10 mol%) and Cy_2NH (20 mol%), produced a significantly slower reaction profile (reaction complete after ~ 5 hours) but the reductive elimination product **86** was still produced. This shows that the reductive elimination for internal alkynes is even more favourable and readily accessible than the protonation and reductive elimination pathways for the terminal alkynes. Small amounts of new degradation complexes could be observed at longer times, most likely arising due to the slow C–C bond formation. These are not common with those observed for the terminal alkyne under the same reaction conditions.

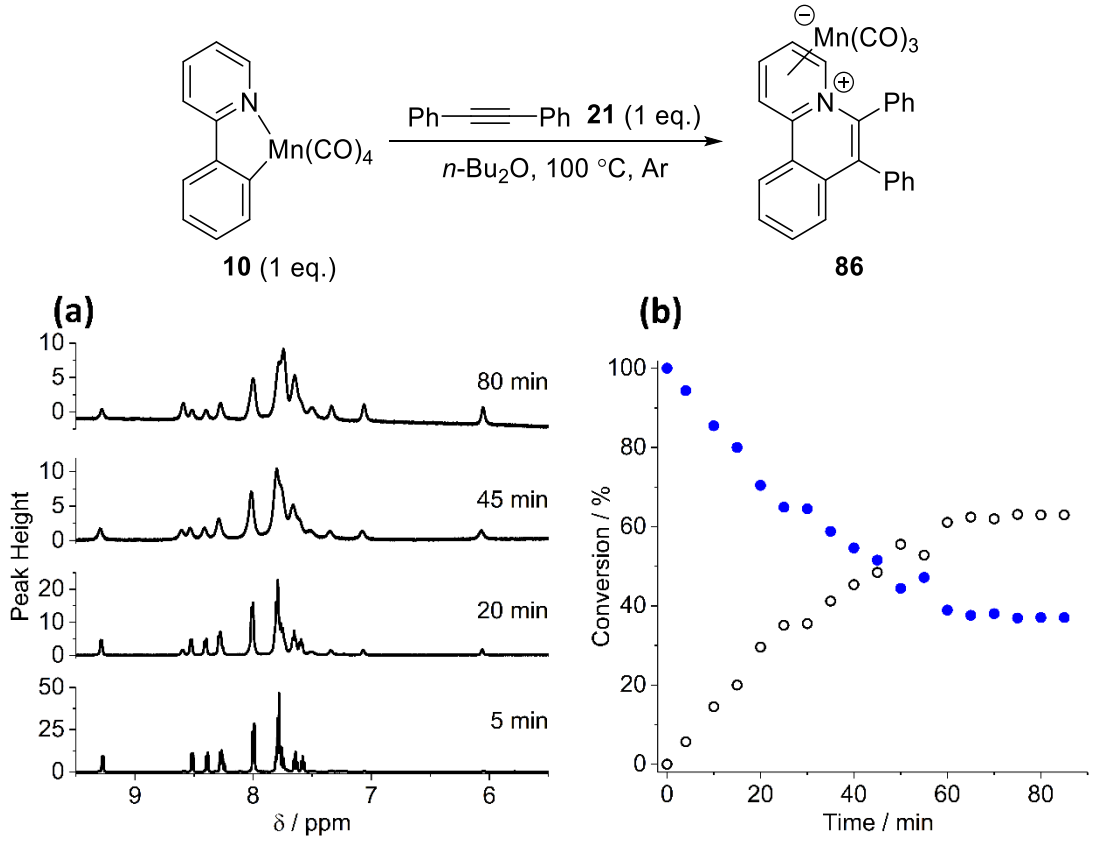

Figure 25. Stoichiometric reaction between **10** and **21** at 100 °C in *n*-Bu_2O, monitored by *in situ* ^1H NMR spectroscopy. (a) Unlocked ^1H NMR spectra in the aromatic region through the reaction progress. (b) Kinetic trace for the depletion of **10** (blue circles) and formation of **86** (hollow black circles), extracted from (a).

The C–C bond formation step was also monitored using *in situ* NMR spectroscopy, where a Young's tap NMR tube containing the reaction mixture was inserted into the NMR spectrometer and heated to 100 °C. Recording ^1H NMR spectra every 5 minutes allowed for the observation of the reductive elimination product **86** forming (**Figure 25**). The kinetic curve halts at 62%, which is likely caused by the lack of stirring in solution. More important is the lack of paramagnetic manganese species generated.

These complexes are readily formed under standard reaction conditions and this experiment shows that the pre-catalyst activation and protonation pathways are most likely the cause for these species forming, with only minor loss of resolution within the ^{1}H NMR spectrum occurring.

2.6 Formulation of a Full Reaction Mechanism

2.6.1 Analysis of Results

The various parts of the reaction mechanism have been investigated in this study and links to the previously proposed mechanism have been made, leading to both supporting and contradictive results. The outcomes from these experiments can be compiled in the generation of a full reaction mechanism for the Mn(I)-catalysed C–H bond alkenylation, using both terminal and internal alkynes.

Firstly, understanding the pre-catalyst activation pathway is important for future pre-catalyst development, among other reasons. Wang and co-workers proposed a pre-catalyst activation that proceeds through initial C–H bond activation of the 2-phenylpyridine **33**.[34] This proposal has been widely accepted as a general pre-catalyst activation pathway in the Mn(I)-catalysed C–H bond functionalisation field.[32] The main supporting experimental data for this pathway is the ability of **33** to cyclomanganate in the presence of amine base Cy_2NH to form $Mn(ppy)(CO)_4$ **10**.

The existence of a base-mediated cyclomanganation step was confirmed in this study, where the *in operando* IR spectroscopic data show a rapid ($k = 3.2 \pm 0.8 \times 10^{-3}$ s^{-1}, at 60 °C) C–H bond activation step. However, the addition of phenylacetylene **34** to this solution resulted in sluggish ($k = 1.25 \pm 0.06 \times 10^{-4}$ s^{-1}, at 60 °C) C–C bond formation. For obvious reasons this raises doubts in the validity of this being the pre-catalyst activation pathway in this reaction, when the initial C–C bond formation with all reagents present is significantly quicker ($k = 3.6 \pm 0.8 \times 10^{-3}$ s^{-1}, at 60 °C). Additional doubts arise from the lack of **10** observed in the standard reaction at both 60 and 100 °C, while showing the formation and depletion of 7-membered insertion complex and resting state **71** instead.

As a rationale for the slow C–C bond formation, questions might arise about the reaction proceeding directly to a tricarbonyl manganese species instead of the

tetracarbonyl **10**. However, DFT-calculations support a mechanism proceeding *via* a tetracarbonyl pathway, which does not require a second CO-loss from the precursor $MnBr(CO)_5$ **31**. Additionally, in the event of a $Mn(ppy)(S)(CO)_3$ species forming in the reaction, there will be a competition between **34** (C–C bond formation) and CO (**10** formation) for the substitution of the solvent ligand. CO is a much stronger ligand than both **34** and the internal alkyne **21**, which are predicted (through DFT-calculations) to be much weaker ligands than CO (+79 and +81 kJ mol^{-1} respectively). This means that even if a tricarbonyl cyclomanganation mechanism is correct, the formation of **10** would still occur and it should be observed in many of the reactions conducted.

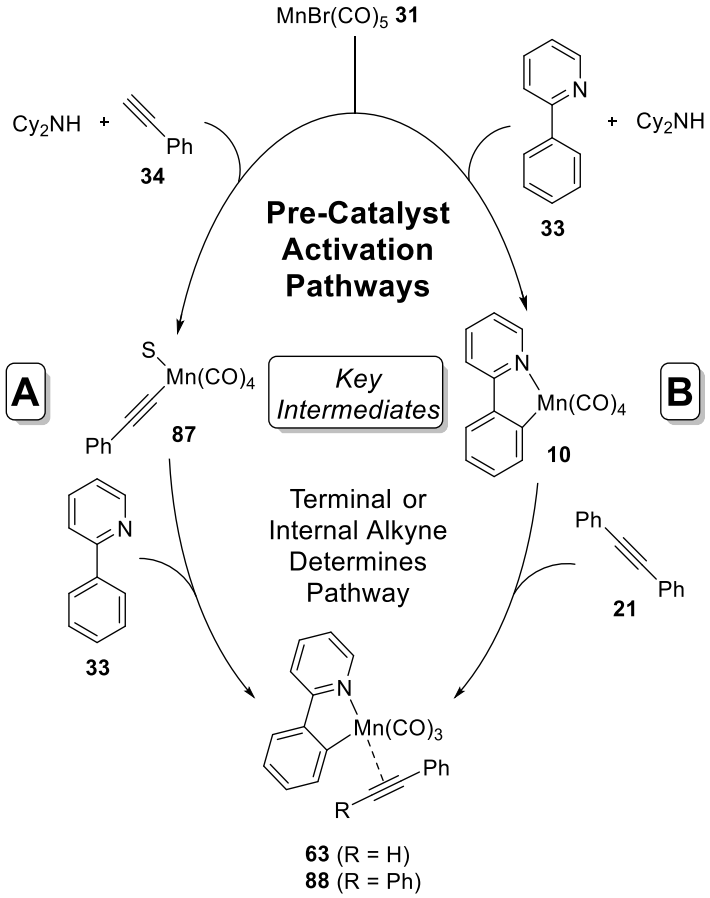

Scheme 19. Simplified pre-catalyst activation pathways identified in this study.

An alternative pre-catalyst activation pathway must be occurring, where either Cy_2NH and/or **34** are involved from the start. The reaction between **31** and Cy_2NH at 60 °C disproved the initial formation of a manganese-amine complex, due to a slow reaction (consumption of **31**; $k = 4.9 \pm 0.2 \times 10^{-4}$ s^{-1} at 60 °C) between the two reagents being observed, forming species that are not observable under the standard conditions at the same temperature. The reaction under standard conditions at 60 °C, withholding the

base-additive, proved that Cy_2NH is required in the initial pre-catalyst activation. This means that the combination between terminal alkyne **34** and Cy_2NH is most likely responsible for the rapid pre-catalyst activation.

Performing the standard reaction at 60 °C in the absence of **33** leads to the rapid consumption of **31**, even faster than with **33** in the solution ($k = 5.4 \pm 0.3 \times 10^{-3}$ s^{-1} at 60 °C and $k = 3.4 \pm 0.7 \times 10^{-3}$ s^{-1} at 60 °C respectively). The process is also quicker than the base-assisted cyclomanganation of **33** ($k = 3.2 \pm 0.8 \times 10^{-3}$ s^{-1} at 60 °C), which explains why the pre-catalyst activation pathway proceeds *via* initial reaction with the terminal alkyne. The degradation species observed in this reaction match those seen under the standard conditions, further supporting reaction with **34** being the initial pre-catalyst activation step. The slower rate under standard conditions indicates that the initial substrate binding is reversible, as **33** is expected to bind better than **34** and is additionally in excess (2:1). As the subsequent C–H bond activation is evidently faster for the terminal alkyne than the 2-phenylpyridine, a preference for a pathway involving the formation of Mn-alkynyl species is evident. Interestingly, none of the manganese species appear to proceed *via* the cyclomanganation pathway as even small amounts of **10** or corresponding degradation complexes should be observed in the various experiments performed.

Potentially impacting the initial C–H bond activation, is the unexpected deuterium-labelling studies performed for the pre-catalyst activation pathway where loss/gain on the C1 alkene position took place. These reactions suggests that C–H bond activation might be reversible but likely not readily, due to the intermolecular nature and low acidity of the conjugate ammonium acid. However, this cannot be completely excluded without further examination. A more probable explanation of the unexpected results is the possible exchange of alkyne ligand from the alkyne-coordinated complex **63** formed after the second C–H bond activation. Nonetheless, these results do not support the cyclomanganation activation pathway, as no H/D-erosion should be observed regardless of potential alkyne-exchange processes.

Under the standard reaction conditions at 100 °C, **10** can, as expected, not be observed. Instead **71** forms and disappears as the reaction progresses, exhibiting the same behaviour as the reaction at 60 °C but at a faster rate. The reaction utilising **10** as pre-catalyst with no base additive showed a significantly slower rate of formation and

depletion of **71**, again supporting the Mn-alkynyl activation pathway. Even the known cyclomanganation precursor $MnBn(CO)_5$ **19** is found to proceed *via* the alternative activation pathway, though in a slightly slower fashion. These results show that the mechanistic interpretation made at 60 °C holds true even at higher reaction temperatures.

As a final comment on the pre-catalyst activation pathway, it should be mentioned that the involvement of a Mn-alkynyl pathway is not necessarily thermodynamically preferred, but the preference arises instead from the process being kinetically driven. There is a narrow difference between the two pathways, which means that small alterations to the substrates may have a large impact on the pre-catalyst activation.

The reaction with internal alkyne **21** under the standard reaction conditions is found to proceed with **10** being a reaction intermediate to eventually form the reductive elimination product **86** (**Scheme 19**). In this reaction there is no choice of pre-catalyst activation pathway and the only accessible version is utilised. In the reaction, both **10** and **91** are observed forming and disappearing as the reaction progresses, with slower rate of depletion for **10** ($k = 2.0 \pm 0.4 \times 10^{-3}$ s^{-1} at 100 °C for **10** and $k = 5.1 \pm 0.6 \times 10^{-3}$ s^{-1} at 100 °C for **91**). This means that the reductive elimination and C–C bond formation is of similar rate, with the former being slightly faster. The overall reaction time of roughly 20 minutes shows that a reaction progressing through the initial cyclomanganation pathway does not necessarily need to exhibit a significantly slower reaction rate.

The reaction using **10** as the pre-catalyst exhibit nearly identical formation of **86**, highlighting the C–C bond formation being much slower than the initial C–H bond activation for this pathway. This again supports that **10** should have been observed in the reactions with the terminal alkyne, if this was a true reaction intermediate in those cases.

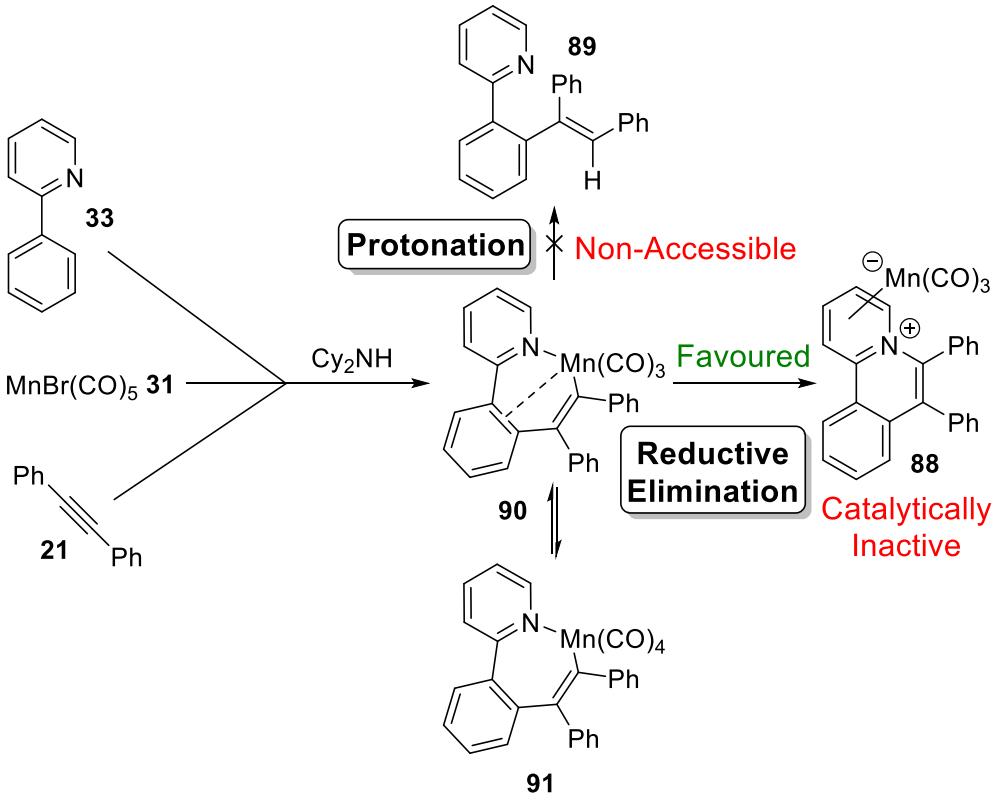

Scheme 20. Reaction pathway for internal alkynes.

Through both the experimental results mentioned above and supplementary DFT-calculations, the rational for the internal alkyne being unproductive in the desired alkenylation reaction is due to the strong preference for the reductive elimination (**Scheme 20**). The reductive elimination is energetically favourable compared to the protonation pathways, which combined with the process being intramolecular makes the protonation pathways inaccessible using any reagents in this methodology (see progress made in Chapter 4). In contrast, the reductive elimination for the terminal alkyne is substantially higher in energy than the protonation pathways and is only accessible under forcing stoichiometric conditions.

The mechanism of the C–C bond formation step, preceding any protonation or reductive elimination pathways, is thought to proceed *via* the previously proposed mechanism,[34] where the alkyne is π-coordinated to a "Mn(κ_2-ppy)$(CO)_3$" moiety before inserting in a concerted fashion into the C–Mn bond. This directly generates the tricarbonyl manganese insertion complex, which rapidly converts to the tetracarbonyl resting state in **71** or **91**. DFT-calculations support this mechanism, in addition to the extensive studies on these and related C–C bond formations discussed in Chapter 3.

The second of the main alterations to Wang's proposed mechanism[34] (in addition to the pre-catalyst activation pathway) is the addition of two further catalytic cycles. Through stoichiometric reactions between manganacycle **10** and terminal alkyne **34**, the protonation pathway by the alkyne was validated, though the observed efficiency was found to be lower than expected if it is the sole acid in the reaction. The addition of **33** and H_2O (in separate experiments) showed that both 2-phenylpyridine and water are more than capable to perform the protonation step (**Scheme 21**). These results were supported by deuterium labelling-experiments, where the incorporation of deuterium into the C2 alkene position occurred using deuterated additives. Computational studies were also employed and revealed that all three pathways are achievable in the reaction, with the protonation by water being higher in energy than the other two.

It is clear from these results that there are three distinct protonation pathways in the reaction, yet the ability of these to proceed through a subsequent C–H activation step is not necessarily certain. It does appear from the results that the alkyne is able to complete the catalytic cycle, due to the large formation of the double alkene product **76** under stoichiometric conditions. The C–H bond activation step results directly from the proton transfer for **33**, while the ability of the water (Mn-OH species) to perform this task is not confirmed. However, it is easily envisaged that the resulting Mn-hydroxyl complex formed post protonation can perform the C–H bond activation. This needs further experimental support, such as isolation and testing of one of the Mn-OH intermediates, to allow for the confirmation of this reaction pathway. The invalidation of this mechanism is, however, not possible for the same reasons stated.

The presence of three different catalytic cycles explains the reaction orders for **33** (0.87 ± 0.06) and **34** (0.32 ± 0.03). The quantities of each reagent required differs in each of the catalytic cycles, leading to complex orders as a result. If the cycles were to be investigated individually, the preference for each cycle can be linked back to the order obtained, requiring further studies to be performed.

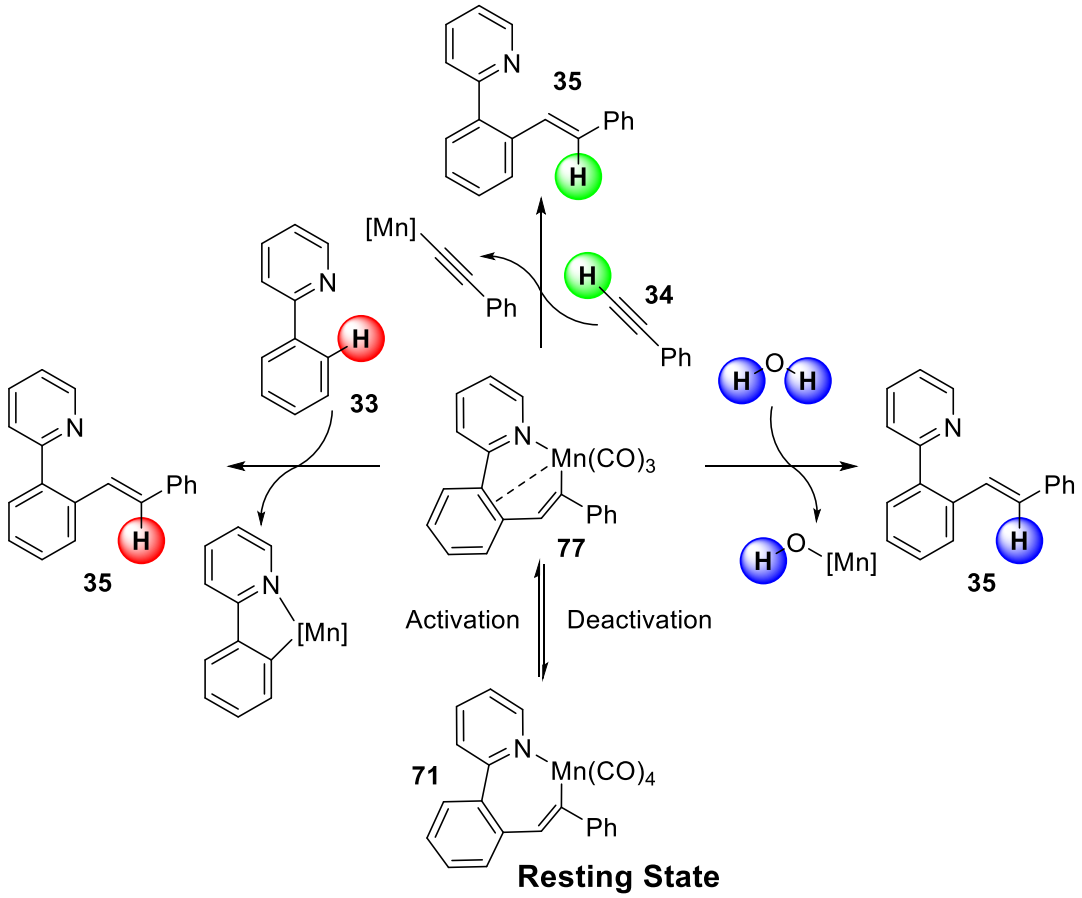

Scheme 21. Simplified scheme of the possible protonation pathways in the Mn(I)-catalysed C–H alkenylation reaction.

The final part of the mechanism that has been studied is the catalyst degradation process, which previously has not been investigated in detail. It was found that the degradation species in the reaction show large similarities in the IR stretching bands to the Mn-hydroxyl clusters. Such species were independently synthesised and compared to the reaction solution. The clusters can easily be envisaged forming as side-products from the H_2O catalytic cycle, but could alternatively form by from interference of water in the other cycles. The broadness of the bands indicates a mixture of Mn-hydroxyl cluster species being present, which is expected due to a number of different configurations being possible. They are also not formed until the protonation pathways are accessible, as the reactions at 60 °C showed no formation of these species. Of note is the lack of isolated and characterised species from the reaction, meaning that the presence of the proposed clusters cannot be definitively proven. However, the resemblance of the IR bands and the formation as a result from the catalytic cycles, is enough for a tentative assignment of these degraded catalyst species being Mn-hydroxyl clusters.

As mentioned, these Mn-hydroxyl clusters are not formed at lower reaction temperatures, with new species being observed instead. Through the exclusion of reagents from the standard reaction at 60 °C, it could be seen that they are not formed when reacting with 2-phenylpyridine **33** in the absence of the alkyne. Additionally, they were not formed under standard reaction conditions for the internal alkyne at 60 °C, but only when the terminal alkyne and Cy_2NH was present. This suggests that these species are formed from the initial C–H bond activation step of the terminal alkyne and is likely arising from the degradation of the alkynyl-complex Mn(S)(**34**)$(CO)_4$ **87**. Mn-alkynyl clusters are likely the endpoint in these degradation pathways and similar compounds are known for other transition metals, supporting a tentative assignment of these as Mn-clusters. They should also be formed under the standard reaction conditions as **87** is an intermediate in the terminal alkyne catalytic cycle.

2.6.2 Description of Mechanism

The reaction between **33** (2 eq.) and **34** (1 eq.) employing Cy_2NH (20 mol%) and **31** (10 mol%) as the pre-catalyst must start with a CO-loss to form a solvated MnBr(S)$(CO)_4$ species **92**, which may thereafter proceed through three different pathways (**Scheme 22**). Any of **33**, **34** or Cy_2NH can coordinate to the manganese, where Cy_2NH is unproductive and will cause degradation to occur but is present in relatively small quantities. The coordination should be reversible and can thereby allow for the terminal alkyne to preferentially react, even though the coordination should favour the 2-phenylpyridine.

In Pathway A, the initial C–H activation of the terminal alkyne (not accessible for internal alkynes) proceed *via* a alkyne-coordinated MnBr(**34**)$(CO)_4$ complex **93**, where the acidity of the terminal C–H bond should be significantly increased. Cy_2NH aids in the deprotonation of this species to form Mn-alkynyl complex **87**, which leads to the formal loss of $[Cy_2NH_2]Br$ **62**. **87** is likely prone to degradation to form Mn-alkynyl clusters, but may also *N*-coordinate a 2-phenylpyridine ligand to form complex Mn(**34**)(**33**)$(CO)_4$ **94**. From this tetracarbonyl species, CO-loss is required before the *ortho*-C–H bond (on **33**) can coordinate *via* a σ-complex. The proton is thereafter transferred to the alkyne through the σ-CAM mechanism to form species **63**, where

the alkyne is coordinated to the manganese and the 2-phenylpyridine is cyclomanganated. This species marks completion of the pre-catalyst activation *via* Pathway A and can proceed to react further.

In contrast, Pathway B proceed by initial coordination of the 2-phenylpyridine to form MnBr(**33**)$(CO)_4$ **95**, which requires Cy_2NH to perform the C–H bond activation and in the process release the bromide, formally generating **62**. The C–H activation proceeds concerted *via* a CMD-type mechanism to eventually form Mn(ppy)$(CO)_4$ **10**. This reaction intermediate can thereafter release one of its CO-ligands and π-coordinate an alkyne to form species **63**, converging the two pre-catalyst activation pathways. It should be noted that the terminal alkynes show a preference for Pathway A, exhibiting favourable rates. The internal alkynes cannot proceed *via* this pathway and are thereby limited to the slower Pathway B.

Following formation of intermediate **63**, the alkyne can insert into the C–Mn bond to generate tricarbonyl insertion-complex **77**, which is in equilibrium with the tetracarbonyl derivative **71**. The latter species is the energetically more favourable configuration and is the off-cycle resting state of the catalysis. For further reaction steps to proceed, one of the CO-ligands must be lost for a vacant coordination site and a reactive 16-electron complex to be generated.

There are four possibilities in which **77** can react further (excluding CO-coordination), deriving from three different protonation pathways and catalytic cycles. Firstly, **77** can react with another terminal alkyne, in which the alkyne π-coordinate (**78**) then form a σ-complex (**79**) to the terminal C–H bond. This σ-complex can transfer its proton in a reversible fashion to the alkynyl-ligand, generating the alkene- and alkynyl-bound manganese complex **65** (cycle 1). Following release of the organic alkene product a solvent molecule can coordinate to generate species **87**, from which the C–H bond activation will proceed *via* the same mechanism as pre-catalyst activation Pathway A.

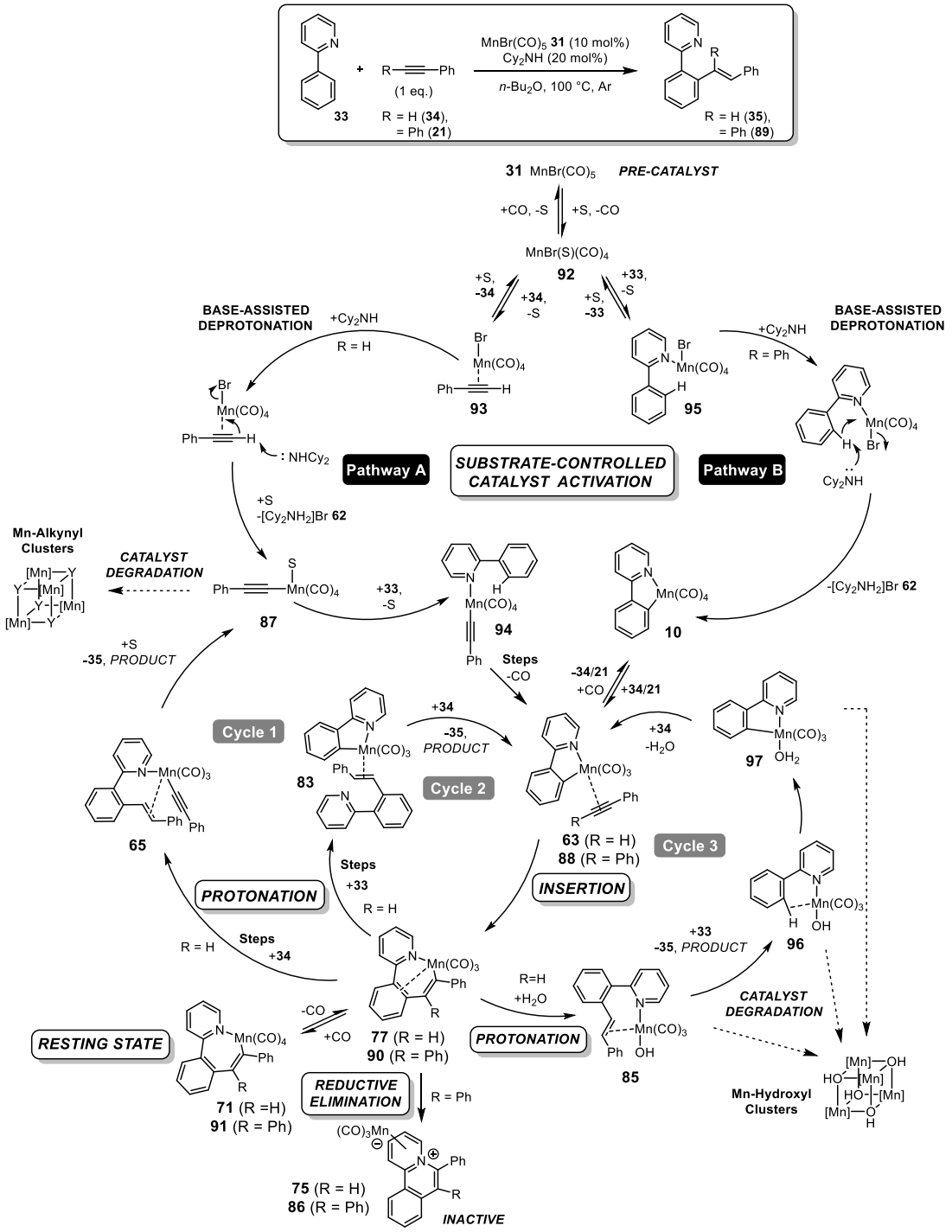

Scheme 22. Reaction mechanism of Mn(I)-catalysed C–H alkenylation.

The second catalytic cycle (cycle 2) involves initial reaction with 2-phenylpyridine, where the *N*-coordinated complex **80** is formed, before rearranging to the σ-complex **81**. After the proton has been transferred to the alkynyl-ligand, the "new" 2-phenylpyridine has become cyclomanganated. Product release, followed by coordination of an alkyne is only required to regenerate **63**, completing the catalytic cycle.

The third cycle (cycle 3) is that of H_2O, in which the water coordinate to **77** forming complex **84**. The reversible proton transfer thereafter takes place generating complex **85**, where the alkene product still is coordinated to the manganese. After product release and 2-phenylpyridine coordination, the *N*-bound σ-complex **96** can transfer a proton to the hydroxyl-ligand, forming water and facilitating cyclomanganation of the 2-phenylpyridine. All these tricarbonyl water/hydroxyl-complexes are prone to degradation to form Mn-hydroxyl clusters. Following ligand exchange between the water and an alkyne, **63** is regenerated and the cycle is completed.

The final reaction pathway of **77** is the reductive elimination to form the corresponding tricyclic pyridinium complex with a manganese-tricarbonyl anion still coordinated. This pathway is the preferred pathway for internal alkynes, outcompeting the above-mentioned catalytic cycles. The reductive elimination for the terminal alkynes is only accessible through limiting the rate of protonation, rendering the reductive elimination competitive.

In conclusion, the remaining mechanistic challenges identified for Mn(I)-catalysed C–H alkenylation have been met. Through this study different substrate-controlled pre-catalyst activation pathways has been observed. Direct experimental evidence to support the proposed catalytic cycle, in addition to two new catalytic cycles has been obtained. All of the catalytic cycles are unfavourable for the internal alkynes and reductive elimination is preferred. The observation of several reversible reaction steps explains the observed deuterium-scrambling in this complex catalyst system.

Chapter 3: Direct Observation of C–C Bond Formation and Related Processes

3.1 Background

3.1.1 Time-Resolved InfraRed (TRIR) Spectroscopy

Time-resolved infrared (TRIR) spectroscopy is a powerful analytical technique that allows for the monitoring of physical, chemical and biological processes taking place on as low as sub-picosecond timescale.[100] IR spectroscopy is highly suitable for ultra-fast measurements due to its high temporal resolution, which is much greater than, for example NMR spectroscopy. Additionally, metal carbonyls are good reporters due to their high intensity and discrete vibrational transitions in a region (2150-1800 cm^{-1}) removed from most other measured IR bands.

One of the challenges in ultra-fast time-resolved spectroscopy is the precision in time determination and the initiation of the process to be observed. Using photolysis to initiate the reaction is advantageous due to the ease in controlling the sample irradiation and high precision lasers are often used in "pump-probe" experimental setups.[100] Irradiation can induce a range of processes due to the reactivity of the generated excited state, such as non-dissociative fluorescence or phosphorescence and ligand dissociation to promote further reactivity. The pump pulse (often UV/Vis) is used to excite or activate the sample to be studied and the probe pulse observes the changes in the IR spectrum. By varying the delay between these two beams, the evolution of the sample over a number of timescales can be monitored.

A further challenge is vibrational relaxation or cooling, which poses a large problem for femtosecond TRIR experiments due to resulting in extensive peak-broadening. Transition metal complexes typically cool on picosecond timescales and this effect arises from the excited state complex being vibrationally "hot", where the molecule occupying many different vibrational states.[101] Due to the vibrational energy well being anharmonic and the energy differences between the lower vibrational states is higher than higher energy states, the IR bands typically shifts to higher wavenumbers and sharpen as they cool. The excess energy is mostly transferred to the surrounding solvent and ends with all the vibrationally excited molecules in their ground state. The nature of the complex and solvent used affects the rate of relaxation and therefore the

earliest times when useful TRIR spectroscopic data can be obtained for other processes. For example, HCl in xenon relaxes on second timescale[102] and for transition metal complex $W(CO)_6$ it takes less than 1 nanosecond to cool.[103]

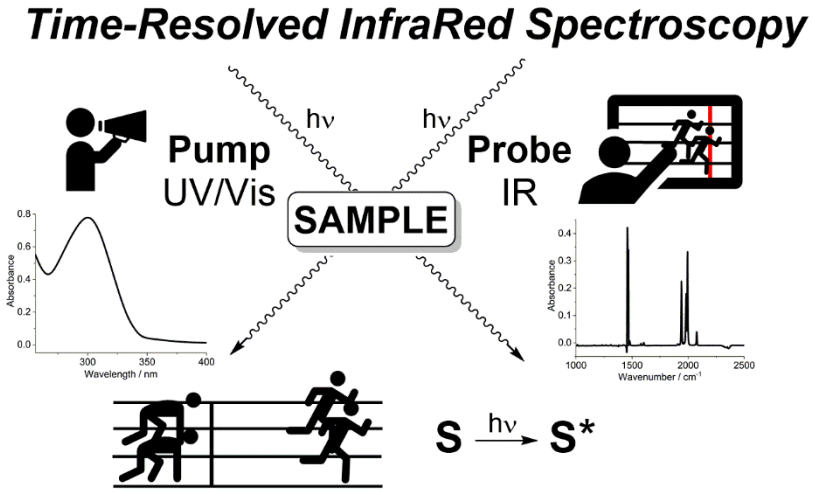

Figure 26. Basic concept of time-resolved infrared (TRIR) spectroscopy.

There are alternative techniques more suitable for the monitoring of processes on femtosecond timescales, such as transient-absorpotion (TA) spectroscopy and laser mass spectrometry.[104] Both techniques are not affected by vibrational cooling or other disruptive events taking place at short times. They can provide information on electronic transitions and chemical composition, though there are limitation which does not exist with IR spectroscopy. For example, there are issues with resolution in UV/Vis-spectroscopy and the lack of structural information that can be obtained from either technique. Therefore, a mixture of these techniques provides a powerful method for the observation of chemical processes taking place on short timescales.

The range of pump-probe delays that can be observed in a single experiment is another issue in TRIR spectroscopy. Time-delays above nanoseconds are often achieved using electronic delays,[105] while shorter times require high-precision optical delay lines.[106] There are several examples of instrumental setups that can achieve both of these types of delays in the same experiment,[107-110] with Time-Resolved Multiple Probe Spectroscopy (TR^MPS) being the most relevant example to the work presented within this thesis.[82, 111] The operation of TR^MPS functions *via* a "pump-probe-probe-probe…" configuration, where the initial pump beam is followed by several probe beams (with distinct time-delays between them) before the next pump beam arrives. This means that an optical delay line can adjust and achieve the short timescale data, while the electronic delay attains the longer times (**Figure 27**).

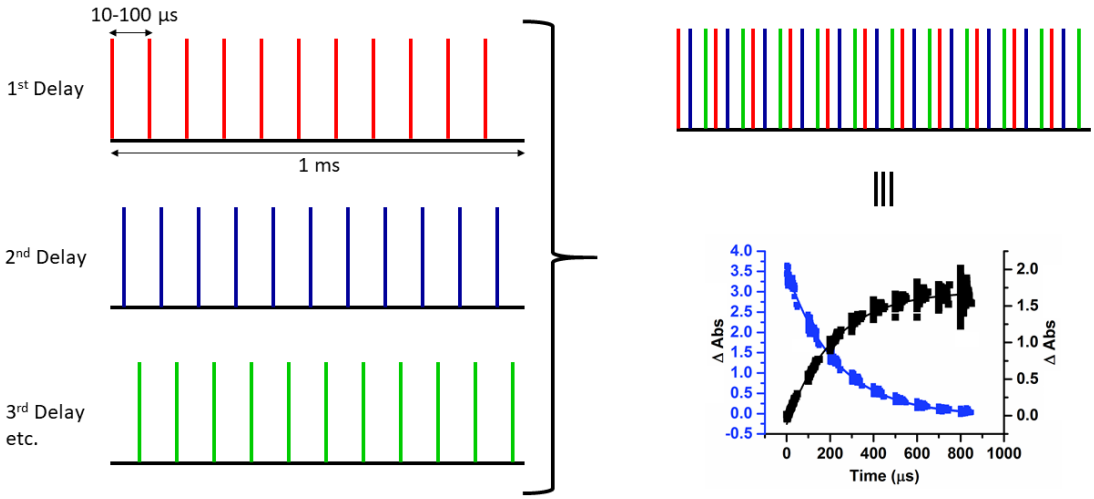

Figure 27. Simplified schematic view of time-resolved multiple probe spectroscopy (TR^{M}PS), where each coloured line represents a measured IR spectrum.

The times achievable by TR^{M}PS stretches over 9 orders of magnitude, which is greater than other reported TRIR systems.[82] There have been several studies utilising TR^{M}PS[112-114] and one example that Towrie and co-workers have used to illustrate its proficiency, is the UV-photolysis of $W(CO)_6$ in heptane.[111] In this experiment, CO-dissociation from $W(CO)_6$ took place on sub-picosecond timescale and was too fast to be observed. However, the vibrational cooling of the corresponding heptane-coordinated complex, $W(CO)_5$(heptane), took place over long picoseconds. This complex remained stable in solution before being replaced by water, to generate $W(CO)_5(H_2O)$ over the first hundred microseconds. The full range of times achievable with TR^{M}PS was required for the two processes to be observed in the same experiment.

TRIR spectroscopy has also been utilised to study more catalytically relevant systems, such as in the formation of rhenium σ-complexes, an observation which is of high importance for the σ-CAM mechanism. George and co-workers have using TRIR spectroscopy studied examples of $Re(\eta^5\text{-}C_5H_5)(CO)_2(R)$ (R = Me, Et, heptane) σ-complexes, generated by UV-photolysis of $Re(\eta^5\text{-}C_5H_5)(CO)_3$ **98** (**Scheme 23**).[115, 116] These complexes were found to be relatively stable, but a rapid return to the starting complex was observed in the presence of excess CO. It was also observed in a subsequent study that the initial binding to the rhenium consisted of an equilibrium between the σ-complex and the corresponding alkyl hydride complex.[117] The latter complex must be formed *via* a reversible oxidative addition and induces a shift to higher wavenumber of the rhenium-carbonyl bands in the IR spectra.

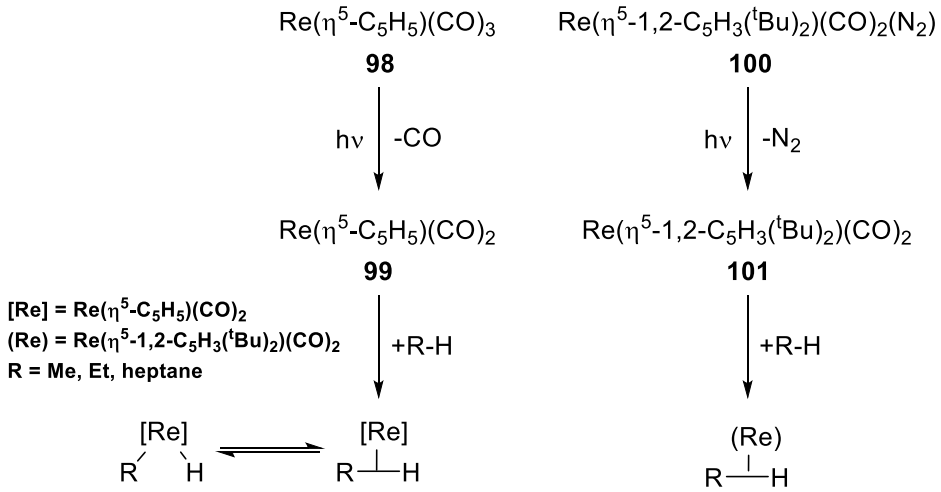

Scheme 23. Agostic rhenium-alkyl complexes observed using TRIR spectroscopy, reported by Calladine *et al.*[118]

In 2010 Calladine *et al.* reported that σ-complexes could be selectively generated if the rhenium precursor was changed to $Re(\eta^5\text{-}1,2\text{-}C_5H_3(^tBu)_2)(CO)_2(N_2)$ **100** (**Scheme 23**).[118] Initial photolysis induce the release of the N_2-ligand, with the CO-ligands remining bound throughout the experiments. The relatively poor binding ability of N_2, combined with the vast excess of the alkyl solvent, lead to the formation of the desired σ-complex. The change of the Cp-ligand increased the lifetime of the σ-complexes, which meant that they could be characterised by NMR spectroscopy. The high stability of the σ-complex may explain why the oxidative addition across the C–H bond is not observed for this system.

The mechanism of the hydrogenation of norbornadiene (NBD) to form norbornene (NBN), catalysed by chromium, tungsten and molybdenum carbonyl complexes has been studied by Poliakoff and co-workers (**Scheme 24**). TRIR spectroscopy was used as a key technique in this study.[119, 120] Norbornene is useful in catalysis, not at least as an additive in the Pd-catalysed Catellani reaction.[121] Poliakoff and co-workers managed to show that NBD-coordinated metal-dihydrogen complexes are formed from UV-irradiation of $M(NBD)(CO)_4$. The H_2 is bonded in a nonclassical manner (σ-complex) and the complexes are stable if produced at –90 °C, but degrade at higher temperatures.

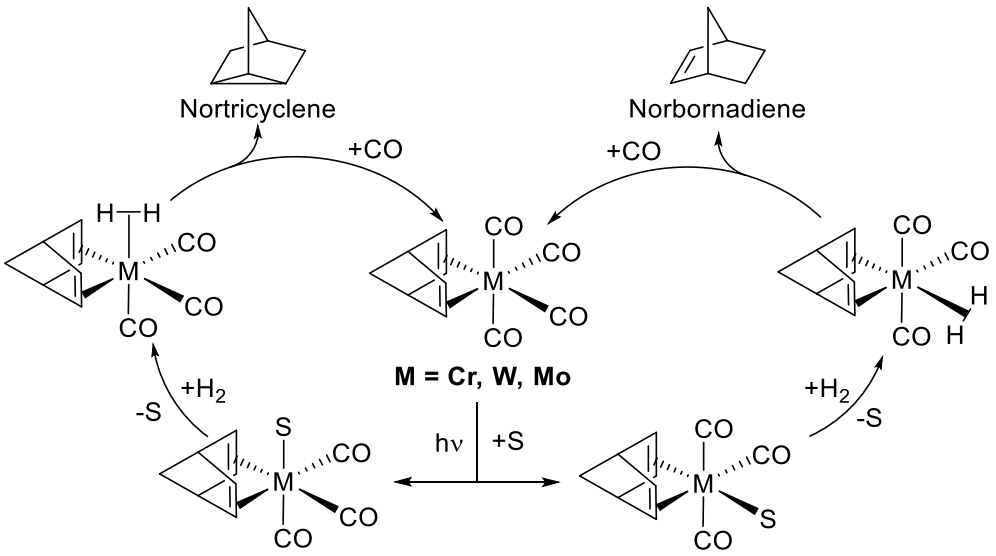

Scheme 24. Simplified mechanism proposed by Poliakoff and co-workers on the transition metal-catalysed hydrogenation of norbornadiene, which TRIR spectroscopy was an instrumental part in the investigation.[119, 120]

Using TRIR spectroscopy, Poliakoff and co-workers probed the kinetics of the processes taking place following photolysis of the $M(NBD)(CO)_4$ complexes. Times from microseconds was measured giving the kinetic trace of the solvated $Mn(NBD)(CO)_3(S)$ forming. The subsequent substitution by another NBD-ligand was shown to be a part of the catalytic cycle. Additionally, the hydrogenation step is thought to proceed from a σ-complex bound H_2 complex in a concerted fashion, where the mer- or fac-binding to the metal determines whether the desired norbornene (mer) or undesired nortricyclene (fac) is generated.

TRIR spectroscopy has also been used in the monitoring of the light-induced C–H activation step performed by Rh-carbodiimide complexes, reported by George and co-workers (**Scheme 25**).[122] After initial excitation of Tp*Rh(CNMe)(carbodiimide) **102** (Tp* = tris(3,5-dimethyl-1-pyrazolyl)borate), the carbodiimide ligand was released and the alkyl solvent coordinated through hydrogen-bonding interactions (**103**). In heptane, this complex was found to deplete on longer picosecond timescales as an transient alkane-intermediate **104** was formed. The oxidative addition across the C–H bond thereafter took place to generate Tp*Rh(CNMe)(H)(C_7H_{15}) **105**. The rate of this transformation was found to depend on both the length of the alkyl chain and on the co-ligand, where CO exhibit quicker rates than isocyanides. Computational studies were employed to support and expand on the TRIR spectroscopic results and they combined to give a full reaction mechanism of C–H activation by the rhodium-complex.

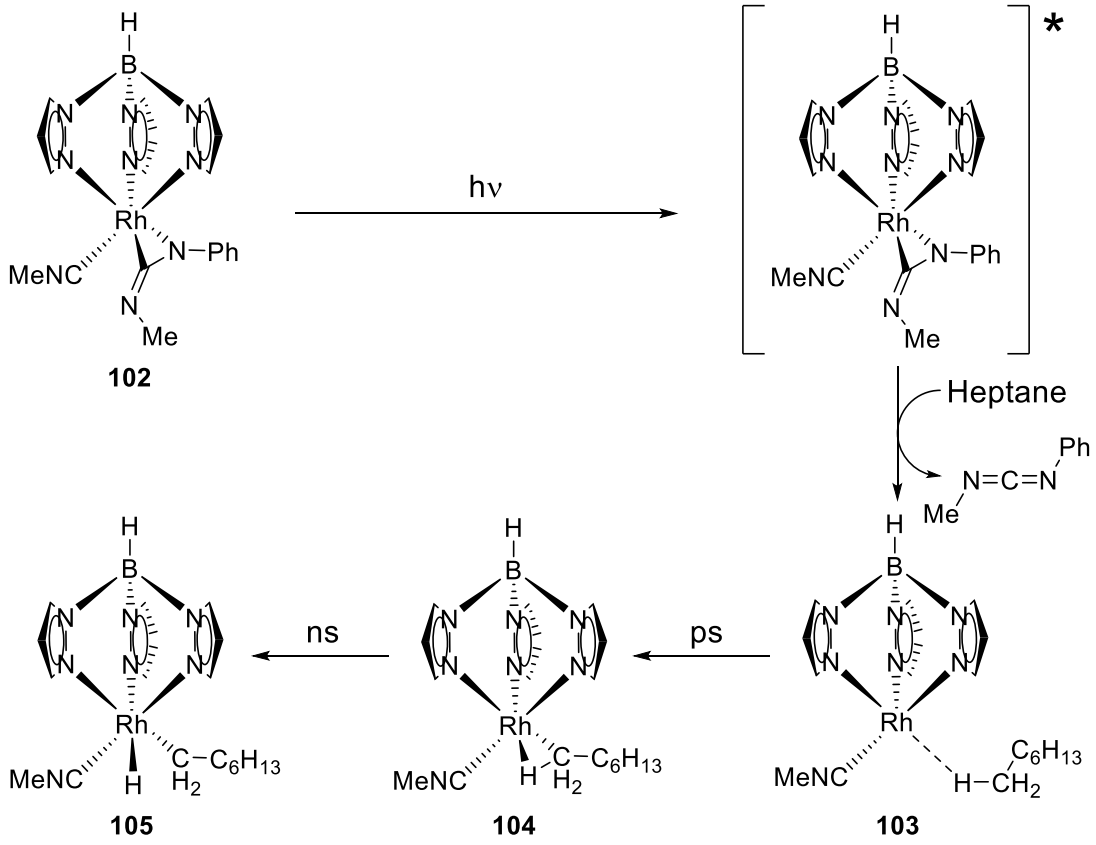

Scheme 25. Photochemical, Rh-mediated terminal C–H activation of heptane, reported by George and co-workers.[122]

The photochemistry of Cr(bpy)(CO)$_4$ **106** has been extensively studied and is of highly importance to the work within this thesis, as it is isoelectronic and structurally similar to the Mn(I)-complexes. Vlček and co-workers have shown through TRIR and TA spectroscopy (**Scheme 26**) that two triplet excited states (MLCT) are formed from an initially generated singlet excited state (MLCT).[123, 124] The formation of these two triplet states takes place on mid to longer femtosecond timescale,[125] while the recovery to the ground state occurs over short to mid picoseconds.

It is possible for CO-dissociation to also occur form the singlet excited state due to decreased fac-C–Cr bond strength[126] and solvents such as CH_2Cl_2 has been observed coordinating to the chromium-centre on sub-picosecond timescales.[123] Even though CO-loss is a minor process in this particular system, it is typically the major process for metal-carbonyl complexes.[127] Low-lying vacant orbitals of the bpy-ligand provides a more favourable formation of the non-dissociative excited states, rather than the CO-dissociative states which most commonly the lowest-lying orbitals for metal-carbonyl complexes.[128]

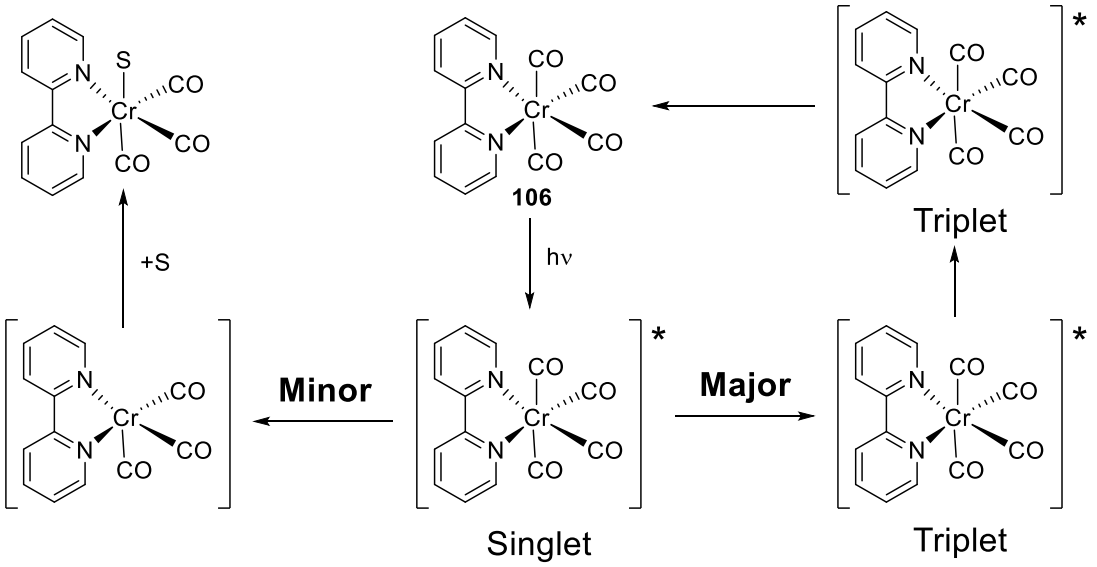

Scheme 26. Reaction pathways following UV-irradiation of **106**, reported by Vlček and co-workers.[123, 124]

3.1.2 TRIR Spectroscopic Studies of Manganaese-Complexes

Photodissociation of carbonyl ligands on Mn(I)-complexes has been investigated using TRIR spectroscopy by Aucott *et al.*,[129, 130] where solvent-substitution on Mn(ppy)(CO)$_4$ **10** was the focus. It was known from previous work that near-UV light (355 nm) is suitable for CO-dissociation, as this complex has been investigated as a potential carbon-monoxide-releasing molecule (photo-CO-RM).[131]

The photodissociation occurs *via* an initial excitation to form a singlet excited state *via* a metal-to-ligand charge transfer (MLCT, **Scheme 27**). This short-lived complex was not observed in any of the TRIR experiments and therefore is concluded to have a lifetime shorter than 0.5 picoseconds. Nevertheless, the excited manganacycle has two different pathways through which it can react, where the first is a spin-orbit coupling pathway to form a triplet excited state. The relaxation of the triplet excited state is slow due to the spin-forbidden transition and can therefore be observed in the experiments. However, for **10** it is formed as a major species in solution, while for other manganacycles it is generated in larger quantities. For example, for an azobenzene-derived manganacycle, the triplet excited state is the dominant pathway and vastly outcompetes any CO-dissociative processes.[129]

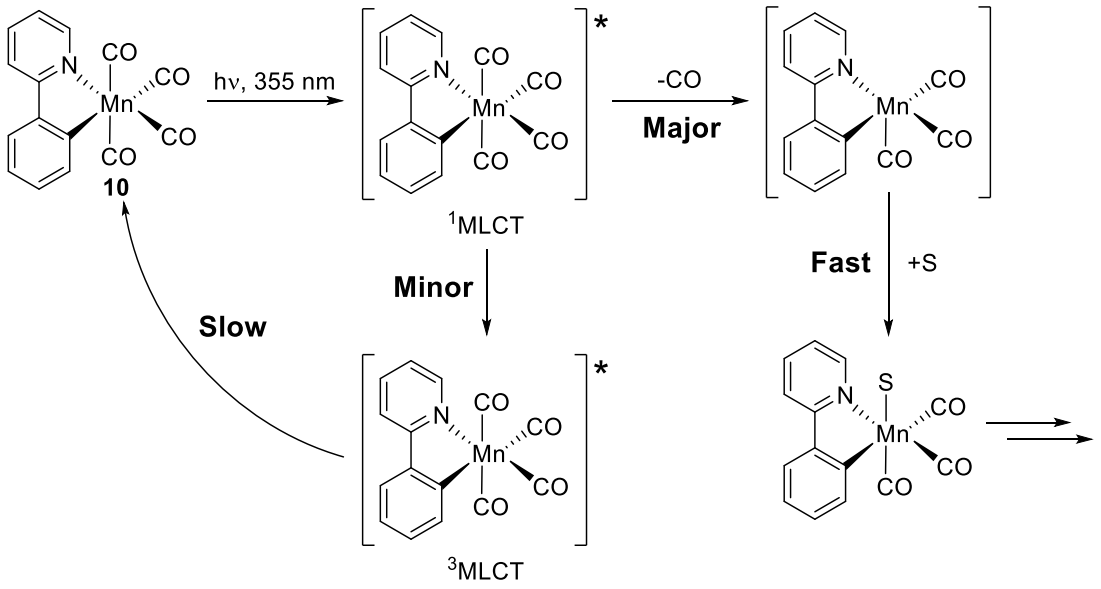

Scheme 27. Initial reaction pathways of Mn(ppy)(CO)$_4$ **10** following irradiation (355 nm), reported by Aucott *et al.*[130]

The second reaction pathway from the singlet excited state is dissociation of a facial CO-ligand to form a 16-electron complex with a vacant coordination site on the manganese. This complex is highly reactive, and the lifetime is again too short for it to be observed *via* TRIR spectroscopy. Instead the manganese binds to the solvent in which the experiment is performed, to form a more stable 18-electron complex (**Scheme 27**). The mode of binding differs depending on the solvent and the CO dissociated is always axial.

When the photolysis experiment was performed in MeCN, only one species could be observed in the TRIR spectroscopic data (**Scheme 28**). This species was assigned to be *N*-coordinated MeCN-complex **115** and is remarkably stable, as it remains for several hours in solution (measured by separate *in operando* IR spectroscopy).[129]

The binding mode differs in other heteroatom-containing solvents such as THF, where initially σ-complex **112** is formed (**Scheme 28**). The regioselectivity of the THF-coordination could not be determined. The σ-complex was observed to rearrange (several 10s of ps) to the more stable O-bound species **113**, where no further transformations could be observed on the timescale of the experiment (< 1 ms). *n*-Bu_2O was found to react in a similar fashion as THF, initially forming σ-complex **110**, which rearranges on longer picosecond timescales to form the stable O-bound complex **111**. DMSO is expected at first glance to behave similar to THF or *n*-Bu_2O, as it contains C–H bonds that can form σ-complexes and an oxygen atom which can form

a more stable configuration. The experiment in DMSO did find an initial σ-complex in **107**, which formed both S- and O-bound complexes **109** or **108**. Due to there being no change in concentration for neither complex after their formation, it was concluded that the binding is irreversible over the timescale studied.

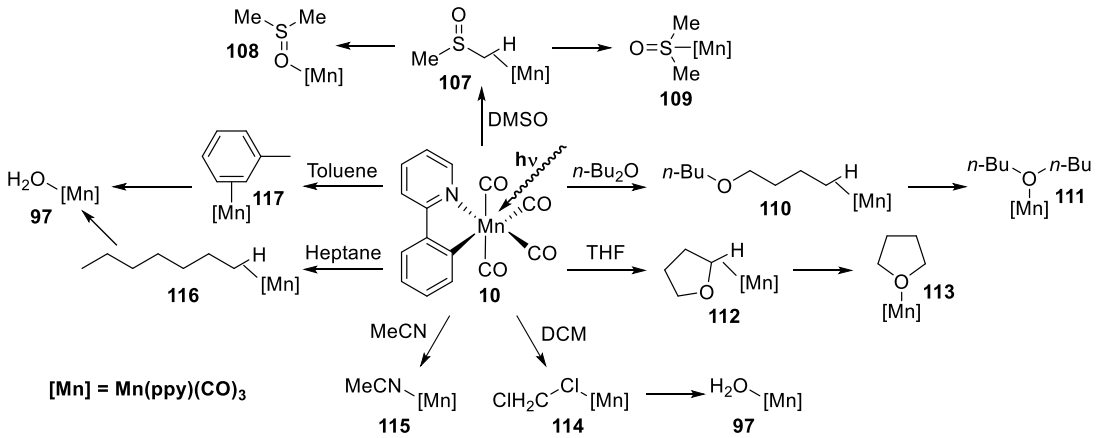

Scheme 28. Reactivity of $Mn(ppy)(CO)_4$ **10** in various solvents after 355 nm irradiation, reported by Aucott *et al*.[129]

A larger difference in reactivity was found when the photolysis was performed in hydrocarbon solvents, toluene and heptane. In heptane, an initial C–H σ-complex **116** was formed and was thought to be a mixture of regioisomers. As expected, these complexes are not stable and water is observed to substitute the heptane to bind to the manganese. This complex (**97**) remained in solution for the remainder of the experiment. This highlights the kinetically controlled initial binding, while thermodynamics determines the configuration of longer-lived species. The experiment in toluene proceeds similarly to heptane but is initially coordinated through a π-coordination to the arene, before forming **97**. The final solvent of interest is DCM, where Cl-coordinated complex **114** is formed at early times and is thereafter followed by the generation of **97**.

Another example of TRIR being utilised to study the photochemistry of Mn(I)-complexes was reported by Ford and co-worker (**Scheme 29**), on the near UV photolysis of manganese-acyl complex **118**.[132] Irradiation of **118** using 355 nm light is known to yield $MnMe(CO)_5$ **6**, resulting from the reverse of the migrationary insertion reaction, which commonly is used to synthesise the manganese acyl precursor. However, the mechanism of this reaction is not clear and therefore TRIR was utilised to study this system.

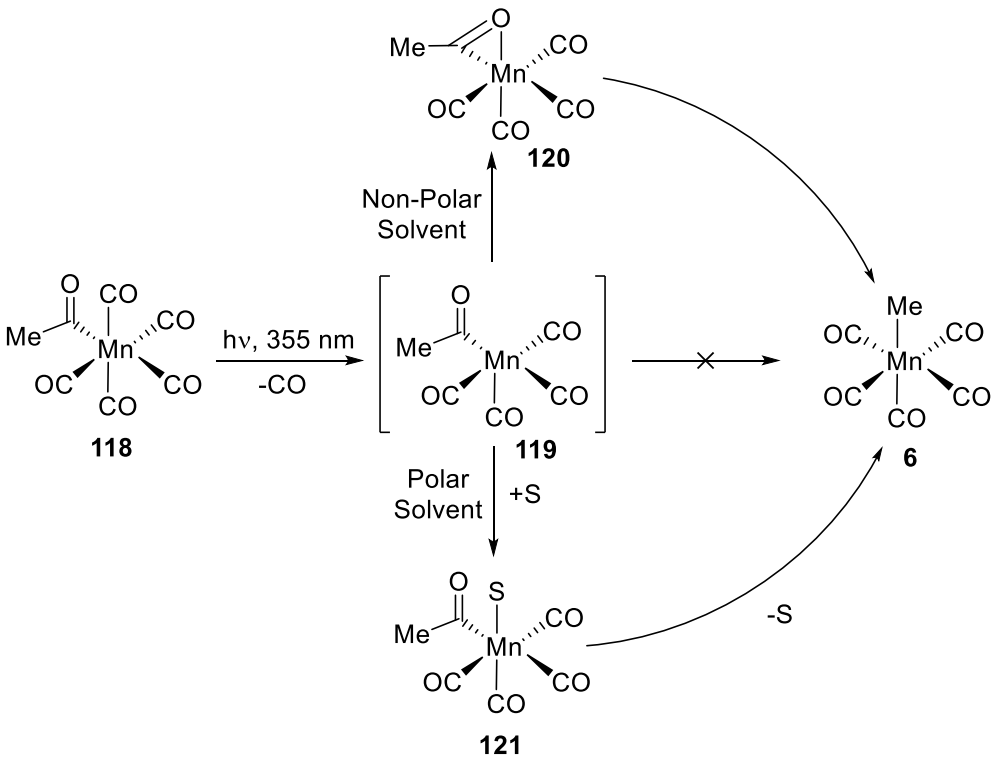

Scheme 29. Solvent dependence in the methyl migration from Mn-acyl complex **118** upon 355 nm irradiation, reported by Ford and co-workers.[132]

The TRIR studies found a solvent dependent reaction mechanism, where non-polar hydrocarbon solvents do not coordinate to the manganese after the initial CO-loss. It is however highly likely that an initial solvent-binding occur, as the first obtained timepoint was after ~150 ns in this reaction setup. Nevertheless, the first observed species was the bridged acyl-complex **120**, where the oxygen is coordinated to the Mn-centre. Thereafter, the methyl migration occurs slowly and time-resolved optical (TRO) spectroscopy was required for the kinetics to be monitored.

In polar solvents, such as THF, the solvent-coordination outcompetes the acyl-bridged complex and therefore the solvent-adduct was observed in these TRIR experiments. This could also arise from the THF-complex being stable enough not to readily lose its solvent-ligand. The rate of methyl migration was surprisingly found to be only slightly dependent on the solvent used. For example, cyclohexane and THF exhibit the same rate of migration ($k = 9.0 \pm 0.9$ s^{-1} and $k = 9.3 \pm 1.9$ s^{-1} respectively).

The photochemistry of $Mn_2(CO)_{10}$ **40** has undergone thorough investigations and is has been shown that there are two competitive pathways upon photolysis. The preference of each pathway depends on the wavelength of light used. The first pathway is the CO-dissociation from **40** to form $Mn_2(CO)_9$ **122**, with bridging carbonyl

ligands.[133, 134] The second pathway is the Mn–Mn bond cleavage of **40**, which generates two $^{\bullet}Mn(CO)_5$ **124** radicals.[135]

It has been found that a wavelength around the λ_{max} (345 nm),[136] generates both species simultaneously. Flash photolysis experiment,[135] TRIR spectroscopy,[137] transient-absorption (TA) spectroscopy[136, 138, 139] and ultra-fast mass spectrometry[140] have been used to probe this dynamic behaviour. The rates for these two processes compared to the rate of recombination has been measured and has resulted in more detailed mechanistic understanding of the two processes.

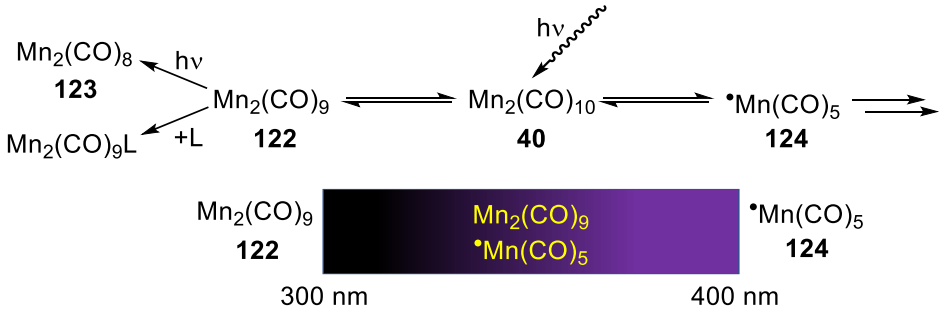

Scheme 30. Wavelength dependence on the ratio of **122** and **124** formation and their subsequent reactivity.

Owrutsky and co-workers found through TRIR spectroscopic studies using 400 nm light, that **124** is almost exclusively formed under these conditions.[141] They also found that the radical species is relatively stable and does not deplete within the 500 ps window of their experimental setup.

CO-dissociation becomes more favoured the lower wavelength used, as seen by Weitz and co-workers. They used 351, 248 and 193 nm light to excite **40** in the gas-phase.[137] It should be noted that they believe that most of the radical **124** is formed from internal excitation, meaning that only CO-dissociation occurs in higher energy light. It has been shown through TRIR spectroscopy and photolysis at 310 nm, that CO-dissociation to give **122** is the sole process taking place when performed in solution.[142] Treatment of **122** with ligands, such as a phosphines or pyridines, yielded $Mn_2(CO)_9L$ complexes (L = phosphine or pyridine).[133, 143] The formation of $Mn_2(CO)_9(py)$ can directly be observed by TRIR spectroscopy from photolysis of **40** in pyridine.[142] The addition of a second photolysis pump at 532 nm (with 30 us delay after initial 355 nm irradiation) following generation of $Mn_2(CO)_9$ **122**, yields another CO-dissociation to form $Mn_2(CO)_8$ **123**.[144]

3.2 Instrumentation

TRIR spectroscopy can be employed in several different experimental setups, as done in the examples discussed previously. In this study, Time-Resolved Multiple Probe Spectroscopy ($TR^{M}PS$) is used to achieve timepoints from sub-picosecond to millisecond timescales. Many different wavelengths of the pump (to irradiate sample) can be achieved, but mostly 355 or 400 nm was used. The choice of wavelength was based on the absorption band of the CO-dissociative UV/Vis-band for the individual manganese-complexes studied. The tuning of the laser pulse is performed by an optical parametric amplifier (OPA). Infrared light was used in the probe beam, to generate *in situ* IR spectra of the solution at desired timepoints. The infrared beam is split into two, with one being the reference beam to allow for correcting for variations in the laser pulse intensity between different datapoints (**Scheme 31**).

To avoid photolysis of photoproducts, the concentration of the manganese-complexes must be sufficiently low, while still being high enough to give sharp spectra with good signal-to-noise ratio. For the same reason, the reaction mixture must also be flowed through the IR cell, which is continuously rastered. The flow is generated by a peristaltic pump and the solution is recycled from the solution reservoir to the cell and back (**Scheme 31**). All reactions are performed under ambient conditions, unless otherwise stated.

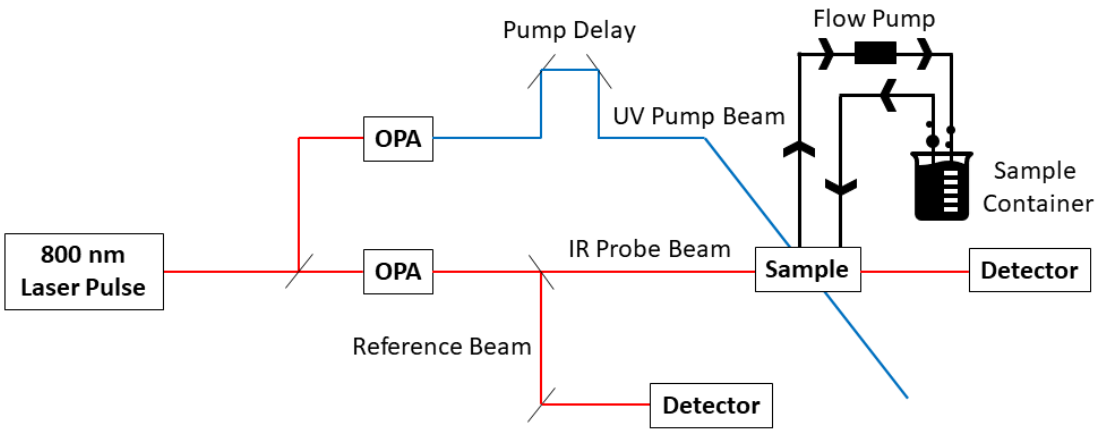

Scheme 31. Schematic view of the experimental setup for TRIR Spectroscopy.

The timing of the pump and probe beams are controlled by both electronic and optical delays, where the optical delays are responsible for shorter sub-nanosecond times and the electronic delays achieve the microsecond times. A combination of the two delays are used for nanosecond timescales. The main difference between the two experimental setups used within this thesis (ULTRA A and LIFEtime) is the length

between each pump and probe in the "pump-probe-probe-probe..." sequence, mentioned earlier. The pump for both setups runs at a 1 kHz repetition rate, arriving every 1 millisecond. For ULTRA A, the repetition rate of the probe is 10 kHz, meaning that the probe arrives every 100 microseconds (10 probes per pump). In the LIFEtime setup, the repetition rate is much higher (100 kHz), leading to repeated delays every 10 microseconds. This repetition results in clustering of datapoints appearing in the kinetic trace at longer times. A noise pattern can often be observed in the clustered data points, which arises from a timing issue with the optical delay line between each probe beam (in the "pump-probe-probe-probe..." sequence). The noise pattern is larger when monitoring weak IR bands. The IR spectra reported are difference spectra obtained by subtraction of a background spectra recorded, leading to lost species being negative and newly formed species positive in the change of absorbance.

As a result of different laser pulse lengths being used for the experimental setups, the spectral window that can be monitored is smaller for LIFEtime (180 fs pulse length gives ~250 cm^{-1} spectral window) than for ULTRA A (40 fs pulse length gives ~500 cm^{-1} spectral window). This does in some cases lead to a second experiment being required when not all IR bands of interest can be collected. In both cases, two detectors (measuring the IR spectrum in pixels) are used for the experiment and an overlap between them ensures that an accurate IR spectrum is generated. Known calibration samples (such as $W(CO)_6$, 1,4-dioxane, polystyrene and/or known bleach bands in the experiment) were used to determine the wavenumber for each pixel recorded.

3.3 Monitoring C–C Bond Formation using Phenylacetylene

3.3.1 C–C Bond Formation in Neat Alkyne

TRIR spectroscopy is a highly suitable technique for the monitoring of the Mn(I)-catalysed C–H bond functionalisation processes studied within this thesis. As previously mentioned (Chapter 3.1.2), **10** and other Mn(I)-carbonyl complexes tend to strongly prefer CO-loss to non-dissociative pathways upon irradiation of UV-light. As mentioned in Chapter 2.6, CO-dissociation is key in most steps within both the pre-catalyst activation and catalytic cycles of the Mn(I)-catalysis, providing a good opportunity to use TRIR spectroscopy to study the reaction mechanism in further detail.

There are at least some steps involved in the pre-catalyst activation pathway which require heat and rely on Mn–Br (rather than Mn–CO) bond cleavage. Hence, $MnBr(CO)_5$ **31** is not a suitable starting point for monitoring the catalysis. Instead **10** was identified as a near ideal starting point, as the conditions under which CO-dissociation is achieved are known and this process leads directly into the catalytic cycles. Even if **10** is not a reaction intermediate in the catalysis using terminal alkynes, the "$Mn(ppy)(CO)_3$" moiety generated is. Replacing the solvent in the photolysis experiments previously discussed with a terminal alkyne such as phenylacetylene **34**, should result in CO-dissociation, alkyne coordination with the potential to observe the C–C bond formation. Kinetic information and observation of further reaction intermediates may be obtained for this reaction as well.

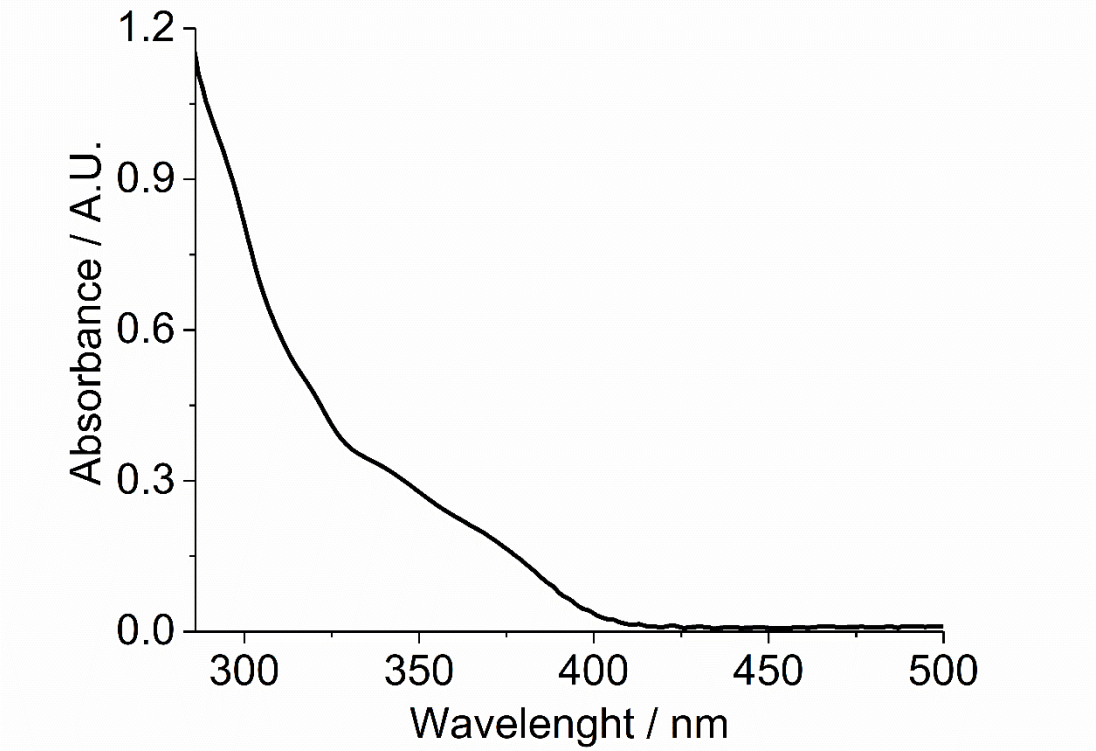

Figure 28. UV/Vis spectrum of **10** in toluene (8×10^{-5} mol dm^{-3}).

From previous experiments[129] it has been found that a manganese concentration of 1.5–2.0 × 10^{-3} mol dm^{-3} is optimal for strong IR bands to be obtained and for other processes such as photolysis of photoproducts not to occur. 355 nm light was chosen as it has previously been shown that it allows for close to selective CO-dissociation in the photolysis of **1**, with little to no triplet excited state formation.[129] Higher (400 nm) and lower wavelengths (310 nm) generated weaker signals in the IR spectra and thus 355 nm light was utilised in these experiment. Therefore, a solution of **10** (1.84 × 10^{-3}

mol dm^{-3}) in neat phenylacetylene was photolysed using 355 nm light in the ULTRA A experimental setup (**Figure 29**). As expected, there are bleaches (2067, 1988, 1973 and 1933 cm^{-1}) present at even the shortest time (500 fs) and remaining throughout the duration of the experiment (1 ms). These bands correspond to the loss of **10** following photolysis. The bleaches appear to recover at longer times, but does so in the same fashion as the positive bands and this effect arise for several reasons. For example the physical removal of sample (by the flow) from the detection spot lowers the observed peak intensity and this can be adjusted for by normalisation.[82]

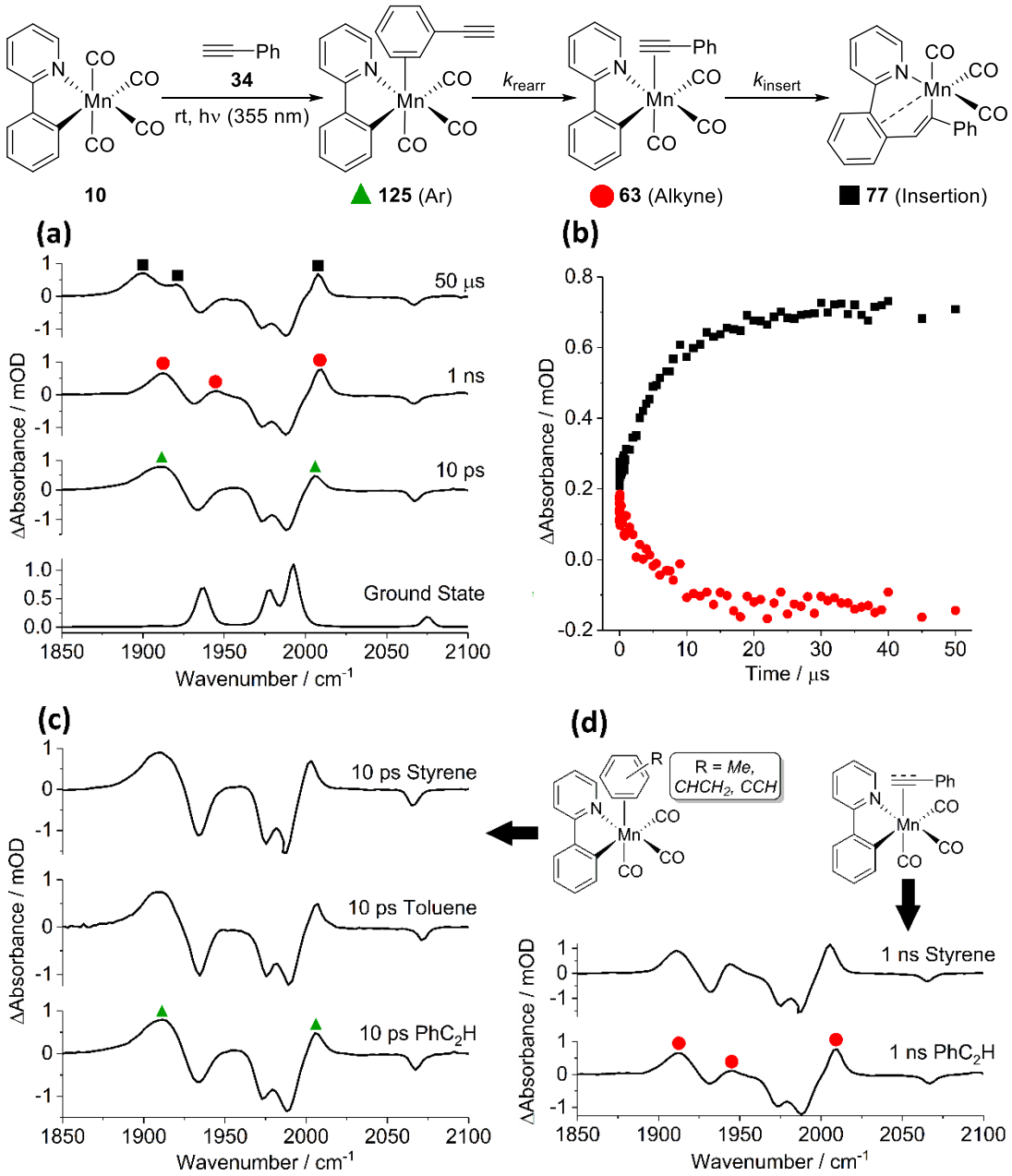

Figure 29. TRIR study of the photolysis of **10** in neat **34** ([**10**] = 1.84 × 10^{-3} mol dm^{-3}), showing the formation of various species after irradiation. (a) IR spectra of the reaction showing the metal carbonyl region at various timepoints. Negative bleach bands correspond to the loss of **10** after irradiation. The green triangle at 1912 cm^{-1} marks a broad signal corresponding to two overlapping IR bands. (b) Kinetic

plot of the formation of **77** (black squares, band at 1896 cm^{-1}) and depletion of **63** (red circles, band at 1941 cm^{-1}), extracted from (a). (c) Comparison of IR spectra recorded 10 ps after irradiation (in separate experiments) of **10** in **34**, toluene and styrene. (d) Comparison of IR spectra recorded 1 ns after irradiation (in separate experiments) of **10** in **34** and styrene.

At picosecond timescales a species, **125**, was observed in the IR spectra with positive bands at 2006 and 1912 (br) cm^{-1}. These bands sharpen over the early picoseconds, which most likely due to vibrational cooling and is on the same timescale as previously observed for this manganacycle.[130] The bands also slightly shift to higher wavenumbers due to the Mn–CO bond becoming slightly stronger as the complex relaxes, reflecting the anharmonic nature of the vibrational energy well.

To determine how **34** have bound to the manganese, control reactions in neat toluene and styrene was performed. Styrene should behave in a similar manner to **34**, when it comes to the mode of binding to the manganese. It can be seen that the complexes formed at early times (10 ps) in all three experiments are highly similar (**Table 1**). Toluene has already been shown to bind through the π-system[129, 130] and it is therefore likely that **34** and styrene does so as well. Additionally, a σ-complex should shift the IR bands as seen for solvents such as THF or heptane (**Table 1**). DFT-predicted (all DFT-calculations in this chapter were performed by Dr Jason M. Lynam) IR frequencies support the assignment of **125** being an arene-bound phenylacetylene-complex. It is therefore concluded that the initial binding of **34** after CO-dissociation proceed *via* a kinetically selective arene-coordination. It should be noted that the predicted IR bands were normalised according to the equation 0.7333x + 567.5 (x = IR band to be normalised), which was obtained from a linear regression of a combination of all predicted and experimental IR frequencies.

125 transforms into a new species **63** (bands at 2009, 1944 and 1912 cm^{-1}) within the first nanosecond of the experiment, where the rate was determined using an exponential growth function ($k_{rearr} = 3.8 \pm 0.7 \times 10^9$ s^{-1} at room temperature). The new species should be a more thermodynamically stable complex and therefore it is not believed to be a σ-complex. There are instead two main alternatives for the identity of **63**, either an alkyne-coordinated complex or the 7-membered manganacycle **77**, where the C–C bond formation has occurred. When comparing the IR bands of **63** with the bands in styrene at 1 nanosecond, a near identical fit is observed (2006, 1943 and 1911 cm^{-1}). The band at 1944 cm^{-1} is highly distinct and has not been observed with any solvents previously used with this manganacycle.[129] The large shift of the bands to

higher wavenumber is consistent with this assignment due to the π-accepting nature of the alkyne-ligand, which reduces back-bonding to the carbonyl ligands. This shift is also consistent with the DFT-predicted IR bands, and therefore **63** was assigned as an alkyne-coordinated complex.

Table 1. Observed (o) and predicted (p) IR bands for the various intermediates formed during photolysis of **10** in **34** and other relevant solvents. Calculations were performed at the (RI-)BP86/SV(P) level.

Entry	Substrate	Ar_o / cm^{-1}	Ar_p / cm^{-1}	$Alkyne_o$ / cm^{-1}	$Alkyne_p$ / cm^{-1}	$Insertion_o$ / cm^{-1}	$Insertion_p$ / cm^{-1}
1	PhC_2H **34**	2006, 1912 (br)	1996, 1915, 1893	2009, 1944, 1912	2010, 1941, 1915	2008, 1922, 1899	2003, 1925, 1893
2	Styrene	2003, 1910 (br)	1995, 1912, 1892	2006, 1943, 1911	2006, 1935, 1902	N/A	N/A
3	Toluene	2004, 1907 (br)	1992, 1910, 1880	N/A	N/A	N/A	N/A
4	THF (agostic)	2011, 1912 (br)	1998, 1914, 1889	N/A	N/A	N/A	N/A
5	Heptane (agostic)	2019, 1933, 1923	2005, 1921, 1899	N/A	N/A	N/A	N/A

Over the next few hundreds of nanoseconds, the bands for **63** can be seen being replaced by a new complex (2008, 1912 and 1899 cm^{-1}, $k_{insert} = 1.35 \pm 0.09 \times 10^5$ s^{-1} at room temperature) which remains in solution for the remainder of the experiment, without any detected degradation. This new species exhibits a shift in the IR bands back to lower wavenumbers, corresponding to the loss of the alkyne-coordination. The insertion of the alkyne into the Mn–C bond is the most obvious reaction that may have taken place and the DFT-predicted bands are in agreement with an assignment of complex **77**. There are no similar IR bands reported for similar complexes, inferring

that a direct comparison of IR bands is not possible in this case. Nevertheless, this experiment has shown that the C–C bond formation and reaction intermediates proposed for Mn(I)-catalysed C–H bond functionalisation can be observed using TRIR spectroscopy.

The validity of the computational model utilised was also investigated, in order to confirm accuracy of the predicted IR bands, structure shapes and their respective energies. Firstly, the computationally predicted bond lengths were compared experimental values (obtained from X-ray crystallographic strucutres) for three different 2-arylpyridine-derivatives (**Table 2**). A good correlation was observed between the predicted and observed data, indicating a good accuracy of the computational model in predicting the structures of the types of molecules used within this thesis. Secondly, the predicted and experimental (more detail in Chapter 3.7.2) energy barriers of C–C bond formation were compared between three 2-arylpyridine-complexes **10**, pyrone-derivative **50** and pyridone-derivative **129** (more details about the C–C bond formation step for **50** and **129** are described in Chapter 3.4). It was found that the experimental values (**10** = 44 kJ mol^{-1}, **50** = 39 kJ mol^{-1}, **129** = 34 kJ mol^{-1}) were larger than the predicted values (**10** = 34 kJ mol^{-1}, **50** = 26 kJ mol^{-1}, **129** = 20 kJ mol^{-1}), but the very similar change in energy between the different complexes (for both values) shows a good correlation between the computational model and the predicted energies of the structures. Finally, the consistent correlation between the predicted and observed IR bands (for example those shown in **Table 1**) supports a good accuracy of the computational model to predict the IR bands of the types of structures used within this thesis. Due to the structural similarity between the structures calculated in this chapter and those in Chapter 2, the same assessment of the validity of the computational approach is applicable there. If calculations were to be performed on other structures than the manganese-complexes, a new evaluation of the validity of the computational model is required.

Table 2. Predicted ($_p$) and observed ($_o$) bond lengths for three different 2-arylpyridine derived complexes. Calculations were performed at the (RI-)BP86/SV(P) level. Observed bond lengths were obtained from X-ray crystallographic structures of **10**,[145] pyrone-derivative **50**,[50] and indole-derivative **130**.[146]

Entry	Complex	Mn–CO_{ax} / Å	Mn–CO_{eq} / Å	Mn–C_{Ar} / Å	Mn–N_{py} / Å
1	**10$_o$**	1.845(18)	1.809(2)	2.066(16)	2.066(15)
2	**10$_p$**	1.842	1.797	2.069	2.164
3	**50$_o$**	1.866(3)	1.817(3)	2.042(2)	2.065(19)
4	**50$_p$**	1.844	1.820	2.047	2.091
5	**130$_o$**	1.841(19)	1.807(17)	2.014(17)	2.058(14)
6	**130$_p$**	1.847	1.801	2.025	2.087

3.3.2 C–C Bond Formation in Toluene Solution

The observation made above of the various intermediates involved in the C–C bond formation is of high value and provide direct information of the various reaction steps. However, the neat alkyne solvent used does not accurately mirror the catalysis, nor does it allow for substantial changes to the reaction conditions to further investigate the reactivity of the various intermediates. Therefore, it is desired to perform the reaction in a co-solvent, which ideally should not be interfering with the desired reaction. Toluene was chosen as solvent due to its similarity to **34** and poor binding affinity to the manganese, as seen by the prompt substitution by water.

A TRIR-experiment was conducted with 355 nm irradiation of **10** and **34** dissolved in toluene ([**10**] = 1.70×10^{-3} mol dm^{-3} and [**34**] = 0.05 mol dm^{-3}), where the alkyne is present in excess (30 equivalents, **Figure 30**). Initially, a species with IR bands at 2004 and 1907 (br) cm^{-1} is formed, which cannot be distinguished between the toluene or **34** arene-bound complexes due to their spectral similarity. The 200-fold excess of toluene to **34** in the reaction makes it highly likely that the species formed consist mostly of toluene-coordinated complex **117**. The rate of depletion of this species (k_{sub} = $3.9 \pm 0.6 \times 10^6$ s^{-1} at room temperature) is three orders of magnitude slower than that in neat alkyne (k_{rearr} = $3.8 \pm 0.7 \times 10^9$ s^{-1} at room temperature), further supporting the assignment of **117** being the initial reaction intermediate.

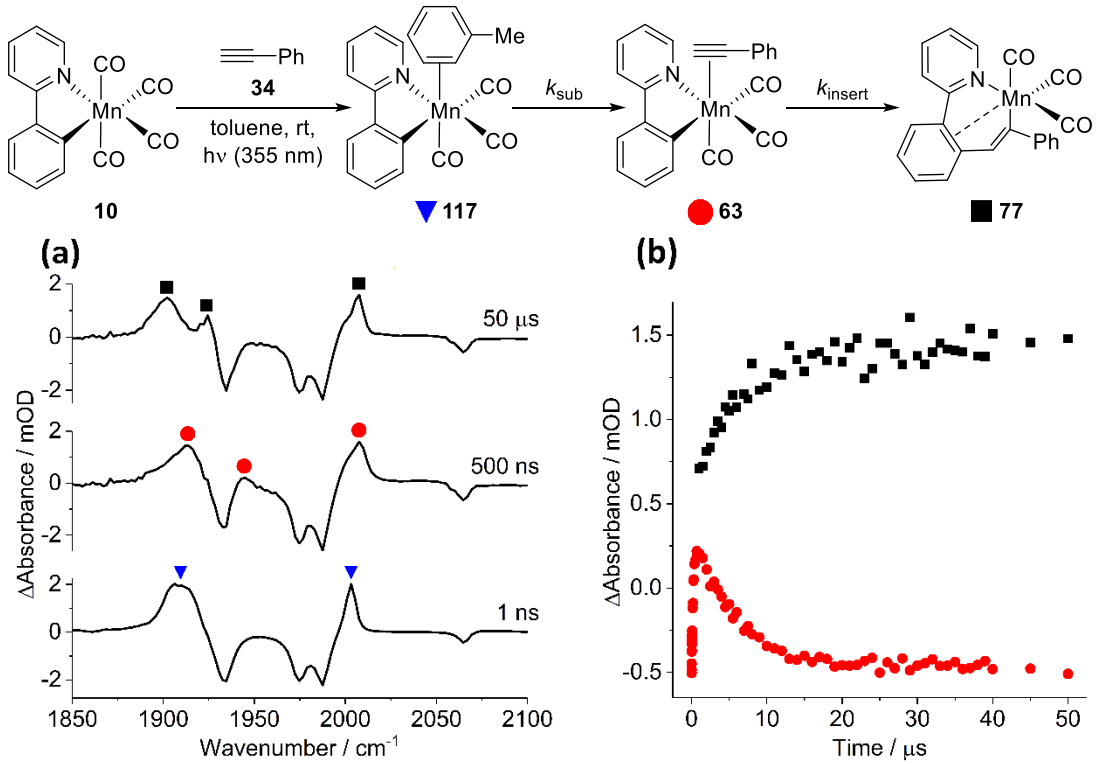

Figure 30. TRIR study of the photolysis of **10** and **34** in toluene ([**10**] = 1.70 × 10^{-3} mol dm^{-3} and [**34**] = 0.05 mol dm^{-3}), showing the formation of various species after irradiation. (a) IR spectra of the reaction showing the metal carbonyl region at various timepoints. Negative bleach bands correspond to the loss of **10** after irradiation. (b) Kinetic plot of the formation of **77** (black squares, band at 1899 cm^{-1}) and depletion of **63** (red circles, band at 1940 cm^{-1}), extracted from (a).

117 is replaced by alkyne-complex **63**, which subsequently inserts into the C–Mn bond on a microsecond timescale. The IR bands for both intermediates are virtually identical to the species observed in neat **34**. The rate of insertion (k_{insert} = 1.7 ± 0.3 × 10^5 s^{-1} at room temperature) is statistically identical to the rate in neat alkyne (k_{insert} = 1.35 ± 0.09 × 10^5 s^{-1} at room temperature), which is consistent with a unimolecular mechanism for this reaction step. The kinetic trace of the formation and decay of **63** could be fitted to an exponential growth and decay function, while the growth of **77** was fitted once more to an exponential growth function. The observation of the insertion under dilute and more catalytically relevant conditions, provide relevant information about the overall reaction mechanism. For example, the C–C bond formation is very rapid (assuming no interference of other species in solution) following initial CO-loss and supports the observation of this step not being rate-determining in the catalytic cycles.

The amount of **34** was varied (0.02–0.92 mol dm^{-3}) to probe the concentration dependence on the rates of substitution and insertion (**Figure 31**). Increasing [**34**] leads to a linear enhancement on the rate of substitution, due to the mechanism being

bimolecular. This means that a higher concentration of substrate is more competitive in binding to the manganese, leading to the increased rate. The rate of insertion on the other hand remains constant with increased [**34**], confirming the unimolecular nature of this step. Increasing the amount of substrate does not change the rate, as the substrate is already bound to the metal and therefore cannot be impacted by external influence under these conditions.

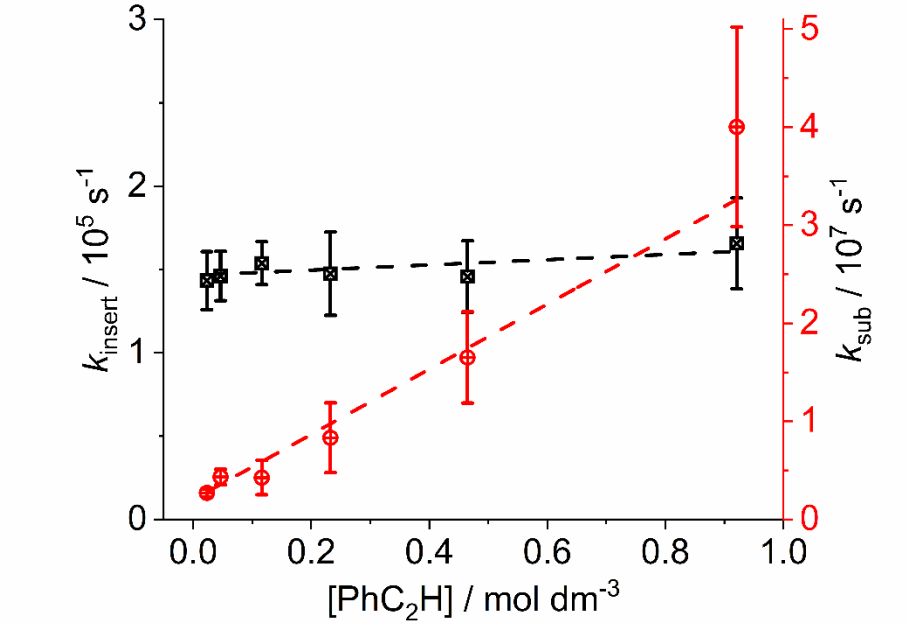

Figure 31. Concentration dependence of **34** on the rate of substitution (k_{sub}, red circles) and insertion (k_{insert}, black squares) in the photolysis of **10** in **34**/toluene solution ([**10**] = 1.89 × 10^{-3} mol dm^{-3} and [**34**] = 0.02–0.92 mol dm^{-3}). Slope of linear regression for k_{sub} = 3.32 ± 0.54 × 10^7 (R^2 = 0.91) and k_{insert} = 1.56 ± 0.96 × 10^4 (R^2 = 0.40).

The selective generation of the tricarbonyl insertion complex **77**, provide an opportunity to form alkenylated 2-phenylpyridine **35**. The only step remaining is the protonation, which can be aided by addition of acid additives. Initially, **10** (1 eq.) and **34** (2 eq.) was irradiated with 400 nm light for 3 hours, using a 5 W LED light source on a continuous 2 minutes on/off cycle (**Table 3**). Surprisingly, **35** could be detected in the crude reaction mixture (21%), showing that the reagents are capable of performing the protonation even at room temperature. The reaction was performed in *n*-Bu_2O, which shows that the strongly coordinating solvent still allows for alkyne coordination and subsequent insertion into the Mn–C bond. A control reaction was performed without the photolysis, showing no formation of **35**.

Table 3. Condition screening in the light-induced formation of alkene **35** from **10** and **34**.

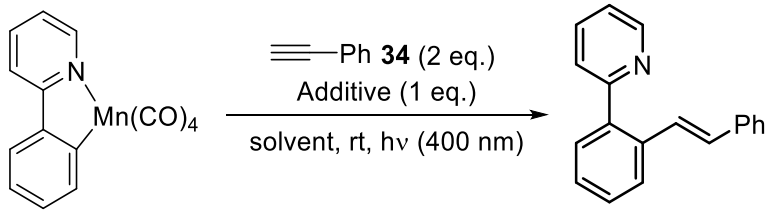

10 (1 eq.) **35**

Entry	Additive	Solvent	Time / h	Conversion / %[1]
1	None	*n*-Bu_2O	3	21
2	$PhCO_2H$	*n*-Bu_2O	3	59
3	$PhCO_2H$	*n*-Bu_2O	16	67
4	$PhCO_2H$	*n*-Bu_2O	48	81
5	$EtCO_2H$	*n*-Bu_2O	3	45
6	$PhCO_2H$	Toluene	3	50
7[2]	$PhCO_2H$	*n*-Bu_2O	3	0

[1]Determined by ^{1}H NMR spectroscopy. [2]Reaction performed without irradiation.

The conversion to **35** was, as expected, improved by the addition of an equivalent of benzoic acid (59%). Change to propionic acid did not improve the efficiency of the reaction (45%) nor did substitution of the solvent to toluene (50%). Increasing the duration of the reaction leads to an enhancement in the observed conversion to **35**, where both 16 and 48 hours exhibited increasing product formation to 67% and 81% respectively. This shows that **35** can be generated in good conversion under mild reaction conditions. Though the reaction is stoichiometric rather than catalytic, it still shows the possibility to utilise photochemical initiation to enhance the efficiency of the Mn(I)-catalysis. Further studies are required to fully utilise this concept in the development of a synthetically useful protocol for mild Mn(I)-catalysed C–H bond functionalisation.

3.3.3 C–C Bond Formation Under Catalytic Conditions

The ability to monitor the C–C bond formation step diluted in toluene provided an opportunity to probe the reaction intermediates and their respective kinetic traces. The intention of this experiment was to determine the exact speciation under catalytic conditions. 2-phenylpyridine **33** is required in the solution to achieve this but

understanding the interaction between the pyridine and the manganese is important, before **34** is added to the solution.

An TRIR-experiment was performed using 355 nm light of **10** and **33** in toluene (**Figure 32**, [**10**] = 1.94 × 10^{-3} mol dm^{-3} and [**33**] = 0.23 mol dm^{-3}). This allows the corresponding IR bands to be obtained of *N*-bound 2-phenylpyridine-complex **126**, which is expected to be the lowest energy conformation of the product. First, toluene-complex **117** was formed (2005 and 1909 (br) cm^{-1}), before being replaced by a new species at 1996, 1904 and 1887 cm^{-1}. This new species is different from water-complex **97** (2003, 1905 and 1893 cm^{-1}) and exhibits two orders of magnitude faster rate of formation (k_{sub} = 1.2 ± 0.2 × 10^{7} s^{-1} at room temperature), leading to the assignment of this species being expected complex **126**.

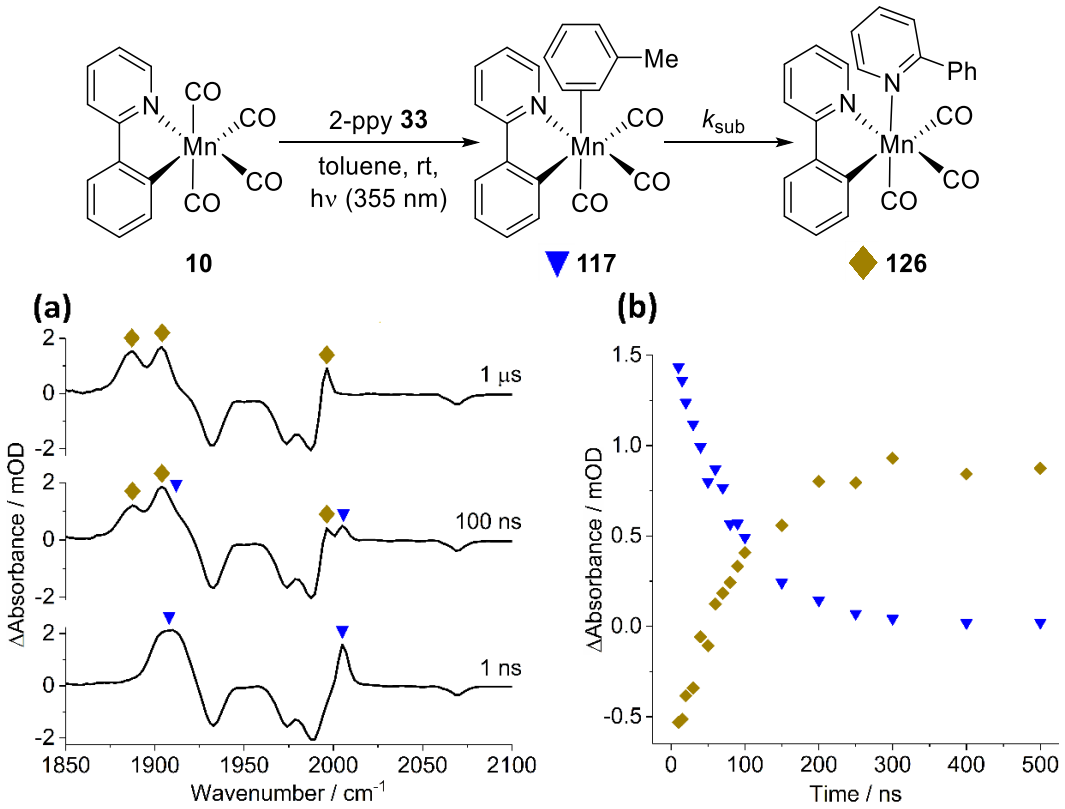

Figure 32. TRIR study of the photolysis of **10** and **33** in toluene ([**10**] = 1.94 × 10^{-3} mol dm^{-3} and [**33**] = 0.23 mol dm^{-3}), showing the formation of various species after irradiation. (a) IR spectra of the reaction showing the metal carbonyl region at various timepoints. Negative bleach bands correspond to the loss of **10** after irradiation. (b) Kinetic plot of the formation of **126** (brown diamonds, band at 1996 cm^{-1}) and depletion of **117** (blue triangles, band at 2005 cm^{-1}), extracted from (a).

Phenylacetylene **34** was added to the reaction in equimolar amounts to **33**, to probe the effect of the pyridine on the binding affinity and influence on C–C bond formation (**Figure 33**). Toluene-complex **117** (2005 and 1908 (br) cm^{-1}) was seen being replaced by both **126** (1996, 1904 and 1887 cm^{-1}) and **63** (2010 and 1944 cm^{-1}) over the first

100 nanoseconds, exhibiting similar rate of formation (k_{sub} = 2.0 ± 0.4 × 10^7 s^{-1} at room temperature for **126** and 3.6 ± 0.6 × 10^7 s^{-1} at room temperature for **63**). In the proposed parallel reaction pathway, the rate of formation of both complexes should be the same, but the rates might have been altered by other factors, such as different interaction with water in the toluene. Higher quality data may aid to definitively determine that this step is a parallel reaction. Furthermore, the exact ratio of the two complexes cannot be determined without their respective absorption coefficients.

Thereafter, **63** proceeds through the C–C bond formation step to form insertion complex **77** and the rate (k_{insert} = 2.0 ± 0.3 × 10^5 s^{-1} at room temperature) is similar to the previously obtained rates for this transformation. **126** was observed in the solution for the remainder of the experiment, without any new species detected. The extended kinetic traces (**Figure 160**) also does not show any formation of new species, though it seems as the complex disappears after 0.5 ms. This effect resulted from a combination of reasons such as that the sample had flowed away from the laser beam and that the reference spectrum was recorded at the end of the experiment, both lowering the signal strength and increasing the signal to noise ratio. Since no new species is observed and the kinetic traces does not show interconversion of **126** to insertion complex **77**, it is concluded that **126** is formed in the reaction and remains unreacted on the timescale of this experiment.

The reaction was repeated under conditions in which the ratios of a catalytic reaction was mirrored (**10** = 0.1 eq., **34** = 1 eq., **33** = 2 eq.). The C–C bond formation could be observed taking place in this reaction, but more **126** is generated than in the previous experiment, limiting the quality of the kinetic information that can be gained from this experiment. It does still show direct evidence that the proposed mechanism of C–C bond formation in the Mn(I)-catalysed C–H bond alkenylation is possible and proceeds under catalytic conditions. There is an interference on the efficiency of the reaction step by the 2-phenylpyridine, but this will likely not pose a problem for the overall reaction as exchange with the alkyne is likely taking place on longer timescales at a sufficiently high rate.

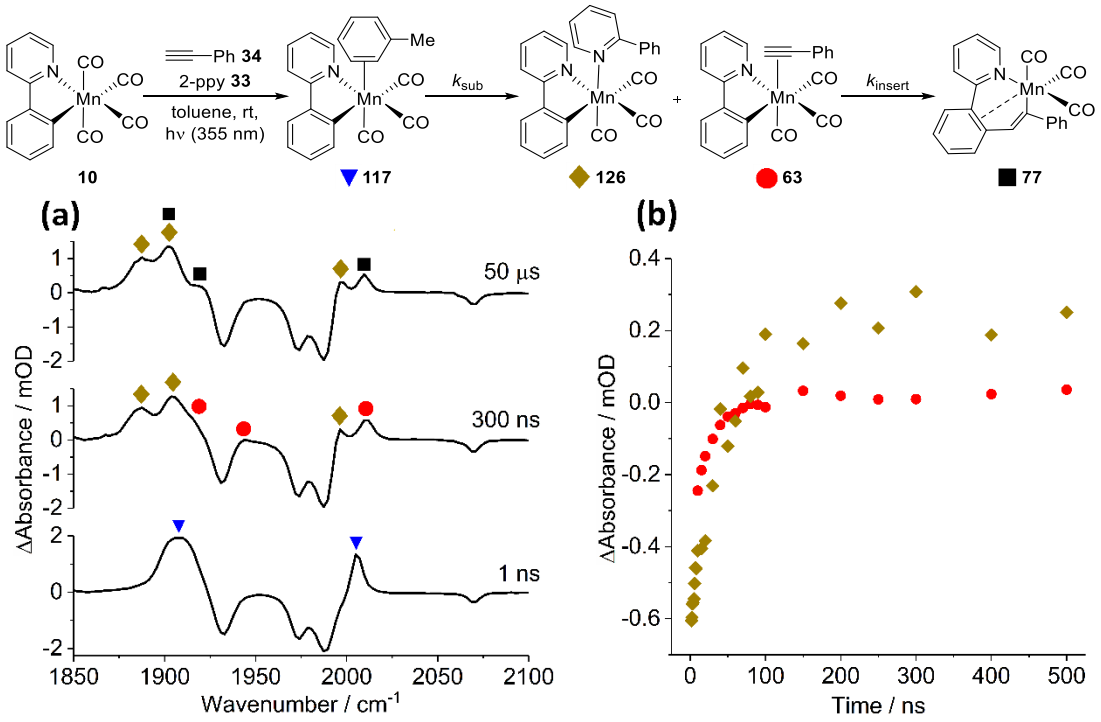

Figure 33. TRIR study of the photolysis of **10**, **34** and **33** in toluene ([**10**] = 1.94 × 10^{-3} mol dm^{-3}, [**34**] = 0.23 mol dm^{-3} and [**33**] = 0.23 mol dm^{-3}), showing the formation of various species after irradiation. (a) IR spectra of the reaction showing the metal carbonyl region at various timepoints. Negative bleach bands correspond to the loss of **10** after irradiation. (b) Kinetic plot of the formation of **126** (brown diamonds, band at 1996 cm^{-1}) and **63** (red circles, band at 1943 cm^{-1}), extracted from (a).

3.4 Effect of Changing Manganacycle

3.4.1 C–C Bond Formation with 2-Arylpyridine Complexes

Modifications of the 2-phenylpyridine ligand was made to probe the generality and factors affecting C–C bond formation. Initially, the phenyl group was exchanged for heterocyclic systems, such as the 2-pyrone (**50**) and 2-pyridone (**129**, synthesised by Francis Clarke) derivatives. These heterocycles have already been reported affecting the reactivity under the Mn(I)-catalysed C–H bond alkenylation conditions, with neither derivative generating the desired alkene-product.[50, 147] Furthermore, Lynam, Fairlamb and co-workers have photochemically produced and characterised the corresponding tricarbonyl insertion complex **54** for the 2-pyrone system,[50] showing that the C–C bond formation should be observable with TRIR spectroscopy.

To monitor the reported C–C bond formation, 2-pyrone-derivative **50** were photolysed in neat **34** ([**50**] = 1.81 × 10^{-3} mol dm^{-3}) using the ULTRA A experimental setup (**Figure 34**). The arene-bound complex **127** (2011, 1931 and 1913 cm^{-1}) was observed from the earliest timepoints and show a shift to higher wavenumbers, compared to the

corresponding complex for **10** (2006 and 1912 (br) cm^{-1}). It was thereafter replaced by alkyne-complex **128** (2014, 1961 and 1925 cm^{-1}) at a comparable rate to **10** (k_{rearr} = 3.0 ± 0.6 × 10^9 s^{-1} at room temperature for **128** and k_{rearr} = 3.8 ± 0.7 × 10^9 s^{-1} at room temperature for **10**). The subsequent insertion step to form 7-membered insertion complex **54** (2008, 1932 and 1908), was marked by the shift back to lower wavenumbers. The rate of insertion is almost an order of magnitude faster for the 2-pyrone-derivative (k_{insert} = 1.04 ± 0.02 × 10^6 s^{-1} at room temperature) than for **10** (k_{insert} = 1.35 ± 0.09 × 10^5 s^{-1} at room temperature).

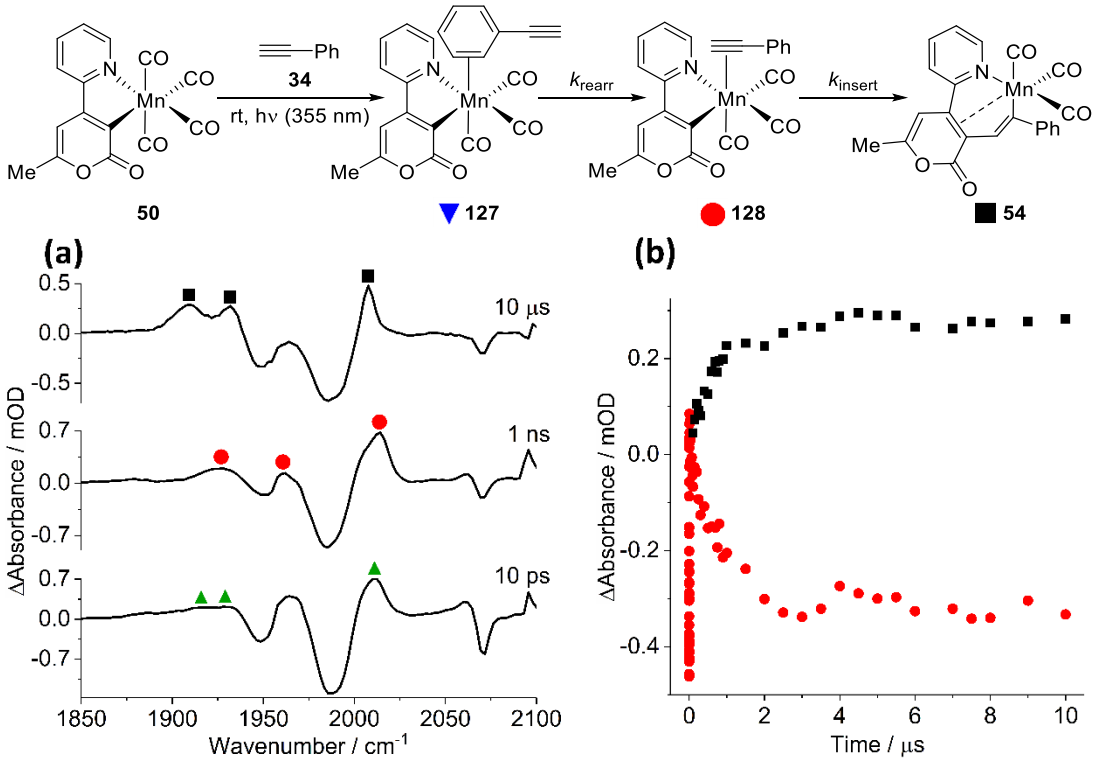

Figure 34. TRIR study of the photolysis of **50** in neat **34** ([**50**] = 1.81 × 10^{-3} mol dm^{-3}), showing the formation of various species after irradiation. (a) IR spectra of the reaction showing the metal carbonyl region at various timepoints. Negative bleach bands correspond to the loss of **50** after irradiation. (b) Kinetic plot of the formation and depletion of **128** (red circles, bleach band at 1948 cm^{-1}) and **54** (black squares, band at 1908 cm^{-1}), extracted from (a).

The ligand was changed to 2-pyridone-derivative **129** and the TRIR experiment was repeated ([**129**] = 1.78 × 10^{-3} mol dm^{-3}). The arene- and alkyne-bound complexes were formed as expected, but the rate of rearrangement (k_{rearr} = 2.0 ± 0.5 × 10^{10} s^{-1} at room temperature) is an order of magnitude faster than observed for the other two complexes. This suggests that either the arene-complex is destabilised, or the alkyne-complex is further stabilised compared to the other two systems studied.

The rate of insertion into the C–Mn bond forming the corresponding insertion-complex (2003, 1925 and 1900 cm^{-1}, k_{insert} = 7.5 ± 1.3 × 10^6 s^{-1} at room temperature) is even

faster for the 2-pyridone-derivative than for **50**. This means that the obtained rate of insertion follows the trend; 2-pyridone > 2-pyrone > phenyl (**Table 4**). This was supported by DFT-calculations, where the calculated energy barriers follow the same trend.

Table 4. Observed IR bands of alkyne and insertion complexes, with corresponding rates of formation for TRIR experiments of various 2-arylpyridine complexes in neat **34** ([Complex] = 1.78–2.22 × 10^{-3} mol dm^{-3}).

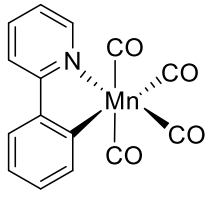

10

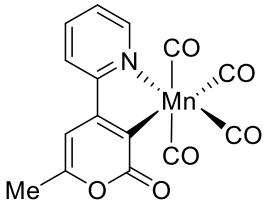

50

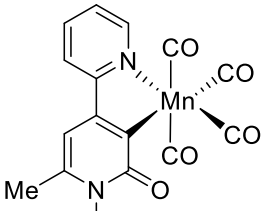

129

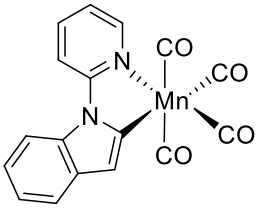

130

Entry	Complex	Alkyne / cm^{-1}	k_{rearr} / 10^{10} s^{-1}	Insertion / cm^{-1}	k_{insert} / 10^{5} s^{-1}
1	**10**	2009, 1944 and 1912	0.38 ± 0.07	2008, 1922 and 1899	1.35 ± 0.09
2	**50**	2014, 1961 and 1925	0.30 ± 0.06	2008, 1932 and 1908	10.43 ± 0.15
3	**129**	2011, 1949 and 1919	2.03 ± 0.50	2003, 1925 and 1900	74.60 ± 12.8
4	**130**	2017, 1931 and 1922	5.87 ± 0.96	2010 and 1909 (br)	0.20 ± 0.01

Lastly, pyridyl-indole complex **130** (synthesised by Stephanie Meyer) was employed as it has been widely utilised in Mn(I)-catalysed C–H bond functionalisation.[32] The TRIR experiment with **130** in neat **34** ([**130**] = 2.22 × 10^{-3} mol dm^{-3}), allows for a direct comparison of the reactivity between the indole- and phenyl-derivatives. The rearrangement from the initial arene-complex (2015 and 1920 (br) cm^{-1}) to the corresponding alkyne-complex (2017, 1931 and 1922 cm^{-1}) took place at the fastest rate (k_{rearr} = 5.9 ± 0.9 × 10^{10} s^{-1} at room temperature) of all substrates studied. Thus, indicating that the arene-complex is less stable or the activation barrier is lower compared to the other manganacycles.

Interestingly, the rate of insertion (k_{insert} = 2.00 ± 0.08 × 10^{4} s^{-1} at room temperature) to form the 7-membered insertion-complex (2010 and 1909 (br) cm^{-1}) is significantly

slower than for the other derivatives, with **129** exhibiting more than 350 times higher rate. It seems as a slower rate of insertion is indicative of a more suitable substrate for the Mn(I)-catalysis. Studies into the other steps of the catalytic cycles are required to accurately determine the rationale behind this trend.

3.4.2 Modifying the Directing Group

The second modifiable segment of the 2-phenylpyridine ligand is the pyridine directing group. As previously mentioned, there are other reported directing group that has been employed in Mn(I)-catalysed C–H bond functionalisation, but these are limited to groups such as *N*-heterocycles, imines and carbonyls.[32] The number of viable directing groups for cyclomanganation are greater than those reported under catalytic conditions.[32, 148] It is unclear from where this difference arises and warrants further investigation.

In Wang and co-workers report of the Mn(I)-catalysed C–H bond alkenylation, the pyridine directing group was substituted in several different positions.[34] However, the lack of substitution at the 6-position is striking, especially with the unusual reactivity exhibited by 6-subsituted pyridyl-pyrones, as reported by Lynam, Fairlamb and co-workers.[50] Therefore, two different 6-substituted 2-phenylpyridines, 2-methoxy-6-phenylpyridine **131** and 2,6-diphenylpyridine **132**, were further investigated. It was noticed that reacting either ligand (2 eq.) with **34** (1 eq.) in the presence of **31** (10 mol%) and Cy_2NH (20 mol%) in *n*-Bu_2O at 80 °C, did not generate the desired alkene-product. The corresponding 5-membered manganacycles **133** and **134** could, however, be synthesised *via* stoichiometric reaction with $MnBn(CO)_5$ **1**.

TRIR spectroscopy can be used to show whether the C–C bond formation step is responsible for the lack of productivity under catalytic conditions. Separate experiments were performed between **133**/**134** and **34**, diluted in toluene ([**133**] = 2.01 × 10^{-3} mol dm^{-3}, [**134**] = 1.78 × 10^{-3} mol dm^{-3} and [**34**] = 0.23 mol dm^{-3}) with 355 nm irradiation (**Table 5**). Both complexes showed initial formation of the toluene-bound arene-complex (2009, 1911 and 1897 cm^{-1} for **133** and 2010, 1914 and 1897 cm^{-1} for **134**), which was confirmed by separate experiments in toluene.

The subsequent formation of the alkyne-bound complexes (2015, 1941 and 1907 cm^{-1} for **133** and 2012, 1941 and 1908 cm^{-1} for **134**) exhibited an interesting trend in the rate of substitution, where the rate increases with larger steric bulk of the substituent.

It is likely that steric clashes between the bound solvent and the 6-substituent arise. This is based on a model in which the loss of solvent is rate controlling, leading to a faster rate of toluene dissociation.

Table 5. Observed IR bands of alkyne and insertion complexes, with corresponding rates of formation for TRIR experiments of 6-substituted 2-phenylpyridine complexes with **34** in toluene ([Complex] = 1.78–2.01 × 10^{-3} mol dm^{-3} and [**34**] = 0.23 mol dm^{-3}).

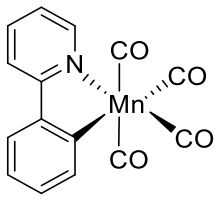

10

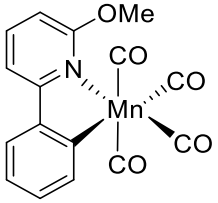

133

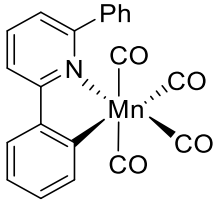

134

Entry	Complex	Alkyne / cm^{-1}	k_{sub} / 10^7 s^{-1}	Insertion / cm^{-1}	k_{insert} / 10^5 s^{-1}
1	**10**	2009, 1944 and 1912	0.83 ± 0.36	2008, 1922 and 1899	1.47 ± 0.25
2	**133**	2015, 1941 and 1907	2.74 ± 0.48	2012, 1915 and 1906	1.54 ± 0.06
3	**134**	2012, 1941 and 1908	5.53 ± 0.65	2012, 1915 and 1908	1.99 ± 0.13

Despite of the different steric bulk of the substituents, the rate of insertion to form the corresponding insertion-complex (2012, 1915 and 1906 cm^{-1} for **133** and 2012, 1915 and 1908 cm^{-1} for **134**) remained very similar. This highlights a lack of steric or electronic influence of the 6-substituent on this step.

From these studies it can be concluded that the lack of reactivity observed for 6-substituted 2-phenylpyridines does not arise from an inability to insert into the C–Mn bond. Steric interactions between the 6-substituent and the proton sources during the protonation step is a more likely reason behind the lack of reactivity. Further studies into the protonation pathways for these substrates are required to be confirmed this.

The pyridine was changed for an imine directing group to see if there are differences in reactivity depending on the type of *N*-containing directing group. Thus, an TRIR spectroscopic experiment was performed between **135** (synthesised by Dr Joshua T. W. Bray) in neat **34** ([**135**] = 2.06 × 10^{-3} mol dm^{-3}) using 355 photolysis (**Figure 35**).

As expected, arene-bound complex **136** (2007 and 1908 (br) cm^{-1}) is initially formed, before rearranging to form alkyne-complex **137** (2009, 1943 and 1908 cm^{-1}), signified by the shift to higher wavenumbers. The rate of rearrangement (k_{rearr} = 1.4 ± 0.3 × 10^{10} s^{-1} at room temperature) is almost an order of magnitude higher than observed for **10** (k_{rearr} = 3.8 ± 0.7 × 10^{9} s^{-1} at room temperature). This infers a lower energy barrier between the two complexes, which may arise from the arene-complex being more unstable.

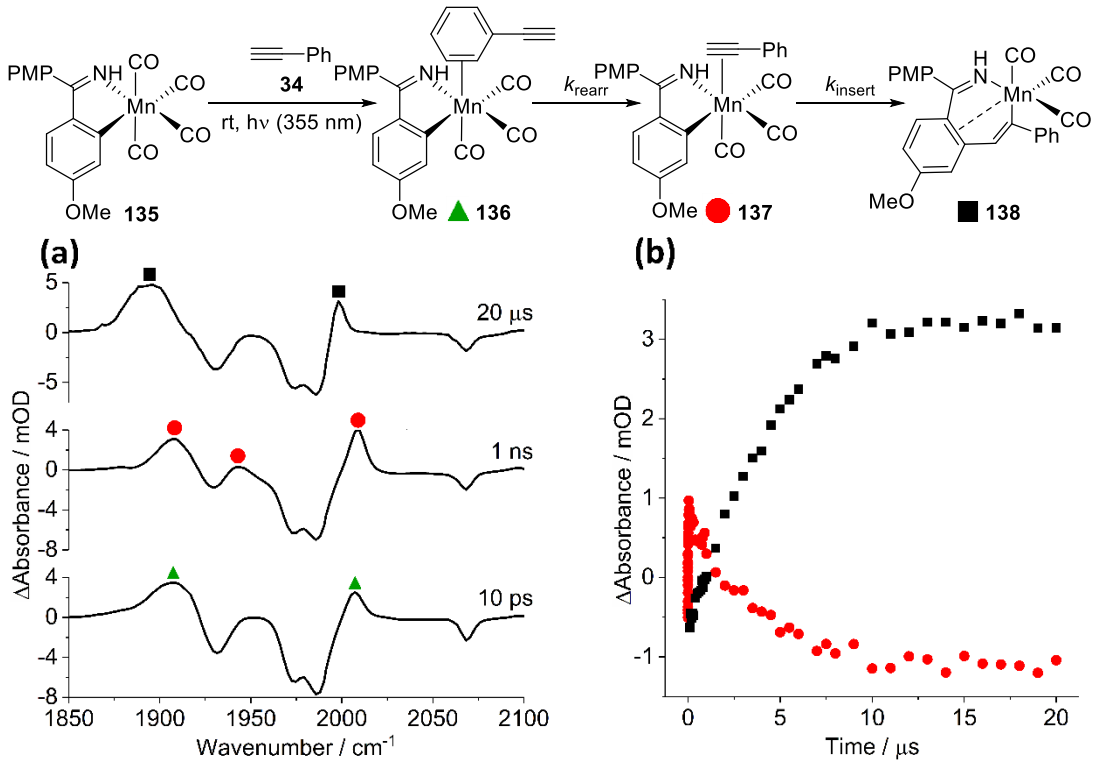

Figure 35. TRIR study of the photolysis of **135** in neat **34** ([**135**] = 2.06 × 10^{-3} mol dm^{-3}), showing the formation of various species after irradiation. (a) IR spectra of the reaction showing the metal carbonyl region at various timepoints. Negative bleach bands correspond to the loss of **135** after irradiation. (b) Kinetic plot of the formation and depletion of **137** (red circles, band at 1943 cm^{-1}) and **138** (black squares, band at 1998 cm^{-1}), extracted from (a).

The shift back to lower wavenumbers marks the formation of insertion-complex **138** (1998 and 1984 (br) cm^{-1}), which remains in solution for the remaining time of the experiment. This means that no reductive elimination to form the corresponding isoquinoline can be observed on the timescale of the experiment. The rate of insertion (k_{insert} = 2.4 ± 0.2 × 10^{5} s^{-1}) is slightly faster than for **10** (k_{insert} = 1.35 ± 0.09 × 10^{5} s^{-1} at room temperature), again showing that it seems as the rate of insertion is indicative on the success of the directing group in catalysis.

Moving to an acetophenone ligand with a carbonyl directing group, which has been successfully used in Mn(I)-catalysed C–H bond functionalisation.[45, 149] Acetophenone-

containing manganacycle **20** was synthesised and employed in an TRIR experiment with **34** diluted in toluene ([**20**] = 1.68 × 10^{-3} mol dm^{-3} and [**34**] = 0.23 mol dm^{-3}) and was irradiated using 355 nm light (**Figure 36**). A similar behaviour was observed for this complex as for the other complexes studied, where initially toluene-complex **139** was formed (2018, 1921 and 1903 cm^{-1}). Thereafter, rearrangement to form alkyne-complex **140** (2023, 1950 and 1914 cm^{-1}) took place at a comparable rate (k_{sub} = 6 ± 1 × 10^6 s^{-1} at room temperature) to what was observed for **10** (k_{sub} = 3.9 ± 0.6 × 10^6 s^{-1} at room temperature).

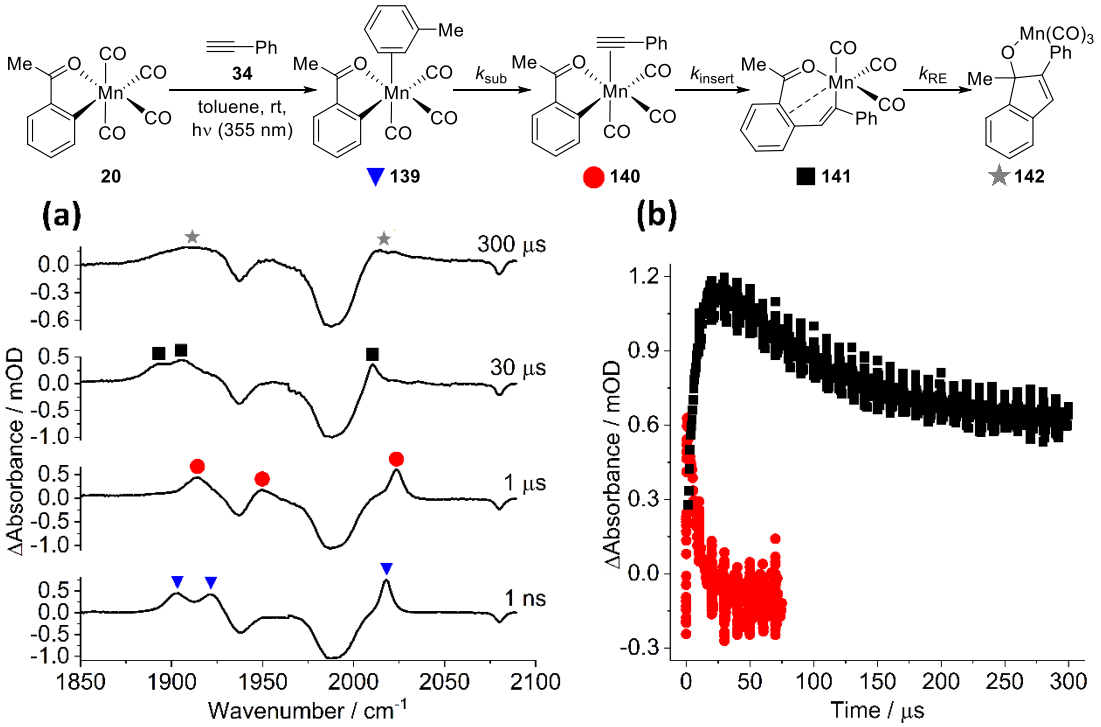

Figure 36. TRIR study of the photolysis of **20** and **34** in toluene ([**20**] = 1.68 × 10^{-3} mol dm^{-3} and [**34**] = 0.23 mol dm^{-3}), showing the formation of various species after irradiation. (a) IR spectra of the reaction showing the metal carbonyl region at various timepoints. Negative bleach bands correspond to the loss of **20** after irradiation. (b) Kinetic plot of the formation and depletion of **140** (red circles, band at 1950 cm^{-1}) and **141** (black squares, band at 1894 cm^{-1}), extracted from (a).

Next, the insertion into the C–Mn bond took place to form insertion-complex **141** (2010, 1906 and 1894 cm^{-1}), where the rate of insertion (k_{insert} = 1.99 ± 0.03 × 10^5 s^{-1} at room temperature) was comparable to the rate for **10** (k_{insert} = 1.5 ± 0.3 × 10^5 s^{-1} at room temperature). This shows that the carbonyl and pyridine directing groups act very similar in the C–C bond formation, again indicating that the rate of insertion is not very fast for catalytically relevant directing groups.

Surprisingly, **141** is not observed remaining in solution for the residual time of the experiment. Instead, it can be seen depleting to form a new species with IR bands at similar wavenumbers (2016 (br) and 1913 (br) cm^{-1}), indicating a further reaction

taking place. It is unlikely that coordination of **34** or toluene is taking place as this process has not been observed for any other manganacycles. Reductive elimination is a more likely process that can take place without the requirement of external influences and would lead to the formation of a manganese-tricarbonyl anion. However, this anion is unlikely to exhibit similar wavenumbers to **141** and an analogous reaction has already been reported generating the cyclopentadiene.[27] Therefore, the final step is tentatively assigned as being cyclopentadiene **142** (k_{RE} = 1.02 ± 0.03 × 10^4 s^{-1} at room temperature), formed following nucleophilic attack of the C–Mn onto the carbonyl. Probing the concentration dependence of this step can further support this assignment, as this reaction should be concentration-independent with respect to all components in solution.

3.5 C–C Bond Formation with Other Alkynes

3.5.1 Probing Substituent Effects

Exchanging the phenylacetylene for other alkynes allows for investigation into steric and electronic effects of the alkyne-substituents. Therefore, cyclohexylacetylene **143** ([**143**] = 0.23 mol dm^{-3}) was employed in a TRIR experiment with **10** ([**10**] = 1.89 × 10^{-3} mol dm^{-3}), using 355 nm irradiation (**Figure 37**). The bulkier cyclohexyl substituent might influence the rate of formation for some of the intermediates in the reaction.

After the initial formation of toluene-complex **117**, the alkyne-coordinated complex **144** is observed with IR bands (2010, 1944 and 1908 cm^{-1}) similar to the phenyl derivative (2009, 1944 and 1912 cm^{-1}). The rate of formation of **144** (k_{sub} = 6 ± 1 × 10^6 s^{-1} at room temperature) is within error the same as for **34** (k_{sub} = 8 ± 4 × 10^6 s^{-1} at room temperature), indicating that the steric bulk of the substituent on the alkyne plays a limited role in the initial binding to the manganese. The rate of insertion on the other hand to form insertion complex **145** (2006, 1920 and 1890 cm^{-1}) show a distinct dependence on the alkyne-substituent, with phenyl derivative **34** (k_{insert} = 1.5 ± 0.3 × 10^5 s^{-1} at room temperature) exhibiting an order of magnitude faster rate than cyclohexyl derivative **143** (k_{insert} = 0.13 ± 0.01 × 10^5 s^{-1} at room temperature). This difference could arise from the steric clashes in the insertion-complex between the

bulkier cyclohexyl group and the carbonyl ligands on the manganese, leading to more difficult C–Mn bond formation and therefore slower kinetics.

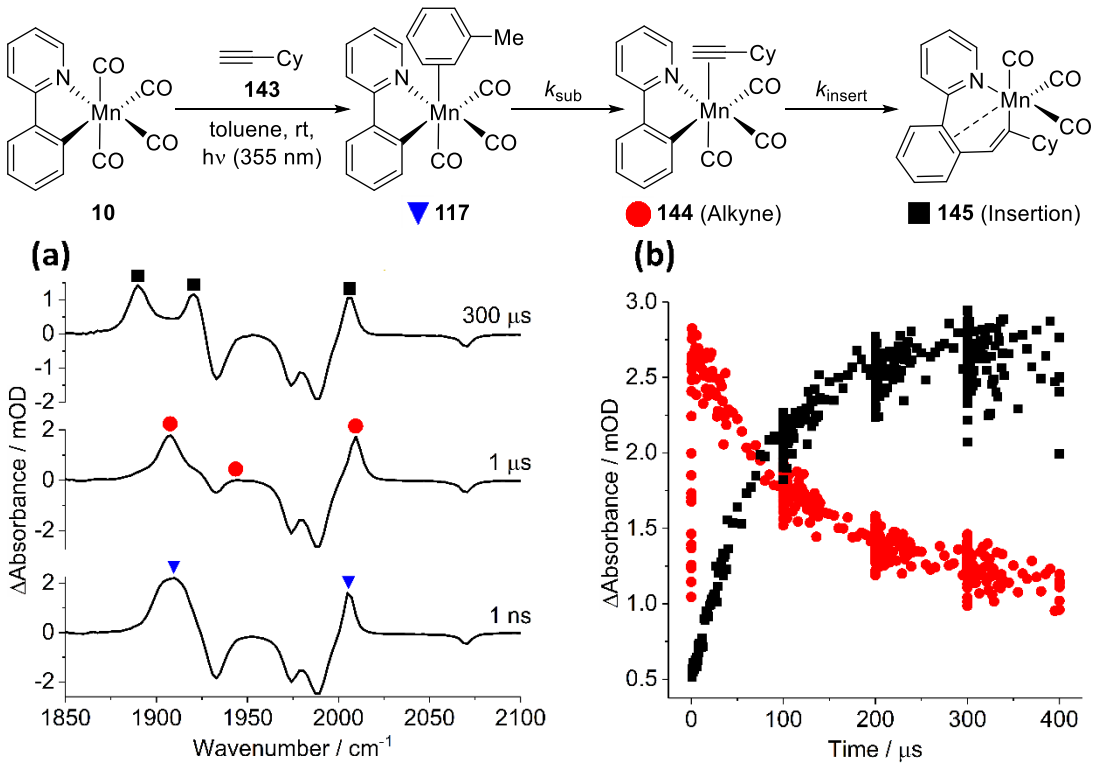

Figure 37. TRIR study of the photolysis of **10** and **143** in toluene ([**10**] = 1.56 × 10^{-3} mol dm^{-3} and [**143**] = 0.23 mol dm^{-3}), showing the formation of various species after irradiation. (a) IR spectra of the reaction showing the metal carbonyl region at various timepoints. Negative bleach bands correspond to the loss of **10** after irradiation. (b) Kinetic plot of the formation of **145** (black squares, band at 1890 cm^{-1}) and formation and depletion of **144** (red circles, band at 2010 cm^{-1}), extracted from (a).

Ester-containing terminal alkyne propargyl benzoate **146** has been utilised as a substrate in Mn(I)-catalysed C–H alkenylation, as reported by Wang and co-workers.[34] The carbonyl might be able to coordinate to the manganese and thereby influence the rate of insertion and coordination modes of the alkyne during the reaction. The reaction was performed in neat **146** ([**10**] = 1.89 × 10^{-3} mol dm^{-3}) to allow for the observation of all the reaction intermediates and their binding to the manganese.

146 can be seen behaving very similarly to **34** (**Table 6**), forming the corresponding intermediates, with no observation of *O*-bound species in solution. The rate of formation (k_{rearr} = 1.1 ± 0.2 × 10^{10} s^{-1} at room temperature) of the alkyne-coordinated complex (2012, 1947 and 1909 cm^{-1}) is faster than observed for **34** (k_{rearr} = 3.8 ± 0.7 × 10^{9} s^{-1} at room temperature). This is unexpected due to the initial binding to the arene, which is located at a much greater distance away from the terminal alkyne in **146**. Nevertheless, the rate of insertion is within error the same between the two alkynes,

showing that there is limited electronic, steric or coordinating influences by the ester-containing substituent.

Table 6. Observed IR bands of alkyne and insertion complexes, with corresponding rates of formation for the TRIR experiments with a range of alkynes ([**10**] = 1.89 × 10^{-3} mol dm^{-3} and [Alkyne] = 0.23 mol dm^{-3}).

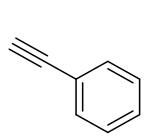

34

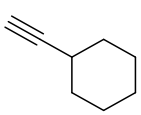

143

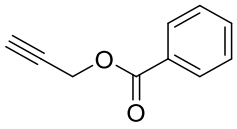

146

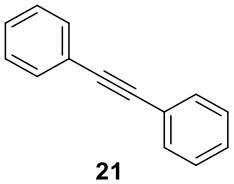

21

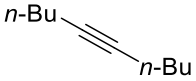

147

Entry	Substrate	Alkyne / cm^{-1}	k_{sub} / 10^6 s^{-1}	Insertion / cm^{-1}	k_{insert} / 10^5 s^{-1}
1	**34**	2009, 1944 and 1912	8.32 ± 3.56	2008, 1922 and 1899	1.47 ± 0.25
2	**143**	2010, 1944 and 1908	6.65 ± 1.15	2006, 1920 and 1890	0.13 ± 0.01
3	**146**[1]	2012, 1947 and 1909	1.13 ± 0.18 × 10^4	2001, 1903 and 1892	1.79 ± 0.49
4	**21**	2004, 1943 and 1912	11.95 ± 2.08	2003, 1904 and 1893	0.57 ± 0.06
5	**147**	2006, 1925 and 1906	4.36 ± 1.49	Not Observed	Not Observed

[1]Performed in neat alkyne.

The internal alkyne diphenylacetylene **21** proceed, as seen previously (Chapter 2), to form the new C–C bond under catalytic conditions. Employing it in a TRIR experiment allows for the observation of any differences in behaviour to the terminal analogue. The experiment was performed diluted in toluene ([**10**] = 1.89 × 10^{-3} mol dm^{-3} and [**21**] = 0.23 mol dm^{-3}) with 355 nm irradiation.

The formation of the alkyne-bound complex (2004, 1943 and 1912 cm^{-1}) does not show much difference in rate of formation between the two alkynes **21** (k_{sub} = 1.1 ± 0.2 × 10^7 s^{-1} at room temperature) and **34** (k_{sub} = 0.8 ± 0.4 × 10^7 s^{-1} at room temperature), showing a negligible effect on the steric bulk of the substrate. However, the rate of insertion differs, where the insertion complex (2003, 1904 and 1893 cm^{-1}) is formed at a slower rate for **21** (k_{insert} = 0.57 ± 0.06 × 10^5 s^{-1} at room temperature)

than for **34** (k_{insert} = 1.5 ± 0.3 × 10^5 s^{-1} at room temperature), placing **21** in the middle between **34** and **143** in rate of insertion.

The exchange of the phenyl groups on **21** to *n*-hexyl chains leads to some unexpected reactivity (**Table 6**). The TRIR experiment with dec-5-yne **147** and **10** diluted in toluene ([**10**] = 1.89 × 10^{-3} mol dm^{-3} and [**147**] = 0.23 mol dm^{-3}), showed the formation of the corresponding alkyne-complex (2006, 1925 and 1906 cm^{-1}). Thereafter, no other species were observed, and the alkyne-complex remained in solution for the remainder of the experiment. The insertion should take place at longer times than can be observed in the experiment, but it does highlight that the alkyl-chains have strong deactivating effects on the rate of C–C bond formation.

3.5.2 Hammett Plot

To assess electronic effects on the rate of C–C bond formation, a correlation according to the Hammett equation ($\log(k_R/k_H) = \sigma\rho$) could be generated, assuming a linear free energy relation. The phenylacetylene was *para*-substituted with a range of different substituents for which individual TRIR experiments diluted in toluene with **10** ([**10**] = 1.89 × 10^{-3} mol dm^{-3} and [Alkyne] = 0.23 mol dm^{-3}) was performed (**Figure 38**). To obtain the results from the Hammett plot, $\log(k_R/k_H)$ (R = NMe_2, OMe, F, CO_2Me and CF_3) was plotted against the corresponding σ_p-values.

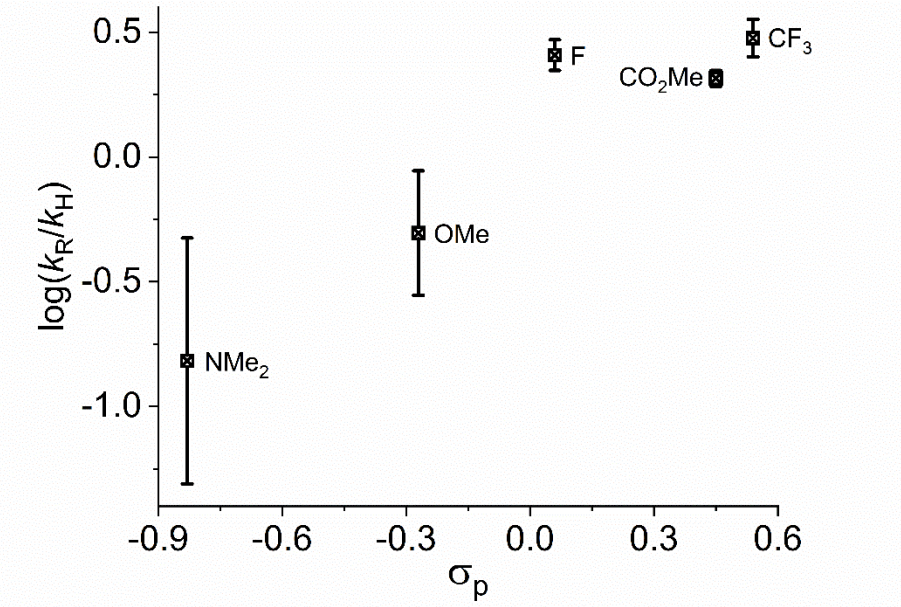

Figure 38. Hammett plot based on k_{insert} for various *para*-substituted phenylacetylene derivatives ($HCCC_6H_4R$, R = NMe_2, OMe, F, CO_2Me and CF_3) reacting with **10** ([**10**] = 1.89 × 10^{-3} mol dm^{-3} and [Alkyne] = 0.23 mol dm^{-3}). Linear regression without error bars gave a slope of 0.94 ± 0.19 (R^2 = 0.89).

It can initially be seen that a non-linear trend is generated, with slower rates observed for electron-donating substituents. If the fluorine-substituent is considered as an outlier, a linear correlation is observed with a slope of 0.92 ± 0.04 (R^2 = 1.00). It is, however, not clear from the performed experiments if this is the true trend of the experiment and more substituents, such as trimethylsilyl or phenyl, with similar σ_p-value to F can be employed. The fluorine-substituent being an outlier would be consistent with the rates observed for CF_3 and CO_2Me, as all three exhibit higher rates than the standard substrate **34**. Nonetheless, it clear that electron-withdrawing substituents increases the rate of the C–C bond formation step.

Large errors can be observed for the slower electron-donating substrates, which is a result from the error propagation performed when dividing a smaller value by one larger. For example, the rate of insertion (k_{insert}) for the NMe_2-substituted alkyne exhibit the second smallest percentage error of all six experiments. It is therefore easily envisaged why Hammett plots are often generated without error bars for the individual values.[150]

The electron-withdrawing substituents should through resonance make the terminal carbon of the alkyne more electron deficient, while in turn increasing a partial negative charge on the other alkyne-carbon. This should allow the terminal carbon to react more efficiently with the electron-rich C–Mn carbon, which should be more electronegative than the manganese metal. The other alkyne carbon will as a result interact better with the manganese centre. Both of these reasons will make for a more efficient interaction with the manganacycle, and thereby increase the rate of reaction which is observed. It is possible that the –I and +M effects of fluorine can influence the rate in an unexpected manner. The rational for the slower rate of reaction of electron-donating substituents are the same as for the higher rate for electron-withdrawing substituents. Thus, the C–C bond formation is best viewed as nucleophilic attack by the carbon of the 2-ppy ligand onto an electrophilic alkyne-bound carbon.

3.6 Reactions with Acrylates and Alkenes

3.6.1 C–C Bond Formation in Neat Acrylate

Besides the alkynes, there are many other unsaturated substrates that has been utilised in Mn(I)-catalysed C–H bond functionalisation.[32] Activated alkenes, such as acrylates,

is one example that has been successfully employed.[36] The carbonyl group is vital to the reactivity and it should be possible using TRIR spectroscopy to probe the interactions between the acrylate and the manganese, during the C–C bond formation process. Therefore, an experiment was performed using 355 nm irradiation of **10** in neat *n*-butyl acrylate **148** ([**10**] = 1.79 × 10^{-3} mol dm^{-3}) using the ULTRA A experimental setup (**Figure 39**).

At short times (ps) a species at 2007, 1910 and 1894 cm^{-1} was observed, which show large similarities to the IR bands generated in alkane solvents, such as heptane (2019, 1933 and 1923 cm^{-1}).[130] Therefore, it is assigned as being σ-complex **149**, where the C–H bond to which the manganese is coordinated cannot be precisely determined. Over the first nanosecond, **149** depletes and is replaced by two new species, which marks a large change from the experiments with terminal alkynes.

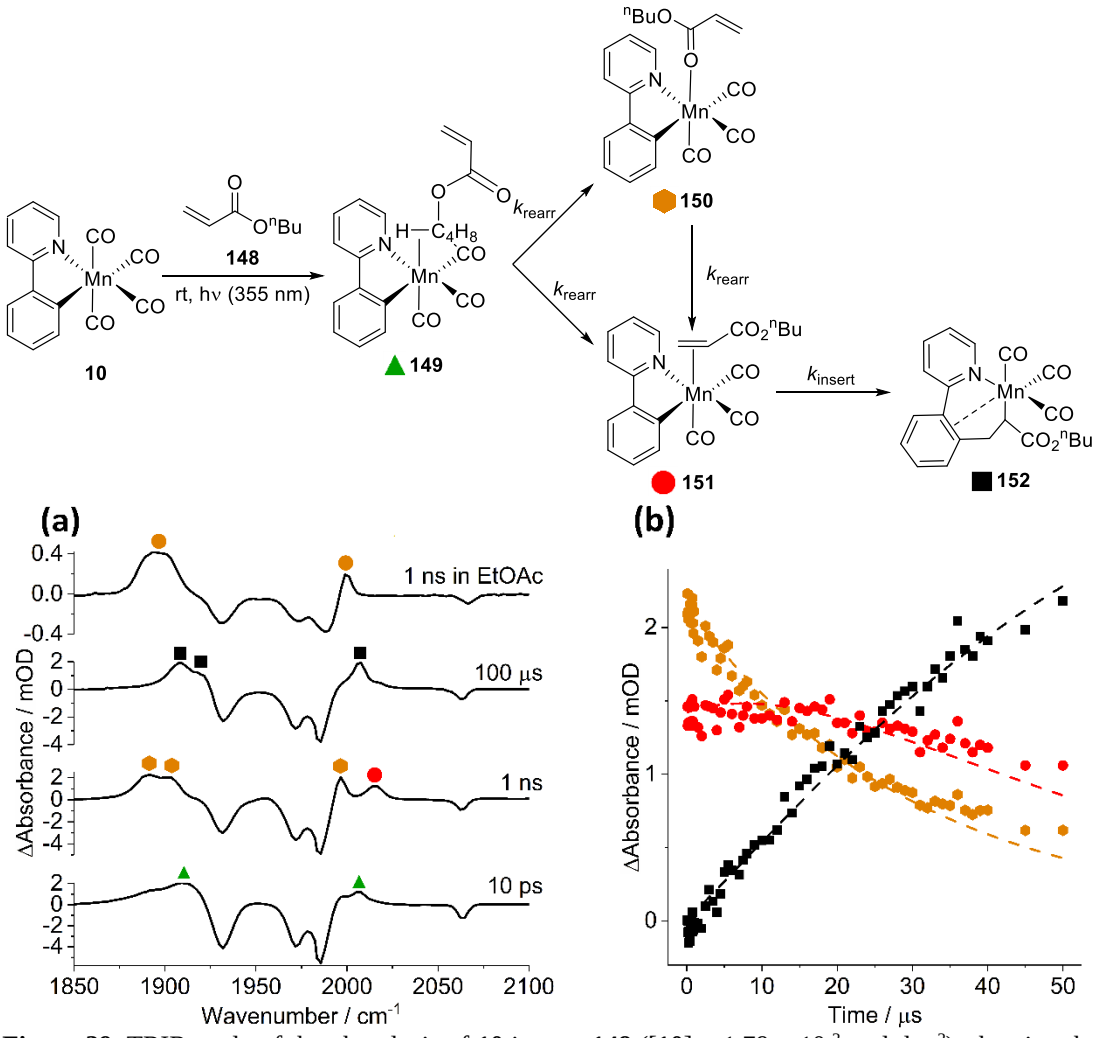

Figure 39. TRIR study of the photolysis of **10** in neat **148** ([**10**] = 1.79 × 10^{-3} mol dm^{-3}), showing the formation of various species after irradiation. (a) IR spectra of the reaction showing the metal carbonyl region at various timepoints and a comparison to the *O*-bound ethyl acetate-complex generated in a separate experiment (orange circles). Negative bleach bands correspond to the loss of **10** after

irradiation. (b) Kinetic plot of the formation of **152** (black squares, band at 2008 cm^{-1}) and depletion of **150** (orange hexagons, band at 1997 cm^{-1}) and **151** (red circles, band at 2017 cm^{-1}), extracted from (a). Dotted lines are kinetic traces obtained from COPASI modelling.

The first species (1997, 1903 and 1890 cm^{-1}) show remarkable similarities to the *O*-bound ethyl acetate complex (1999 and 1896 (br) cm^{-1}), formed following irradiation in ethyl acetate solvent (**Figure 39**). Hence, the manganese is likely coordinated to the carbonyl oxygen, generating *O*-bound complex **150**. Only one IR band can be distinguished for the second species (2017 cm^{-1}), due to spectral overlap with **150** or the bleach bands. The shift to higher wavenumber is consistent with the coordination to the alkene, forming alkene-complex **151**. The difference in magnitude of the shift compared to styrene arise from the acrylate being a better π-acceptor, due to being more electron-deficient. The rate of formation of **150** (k_{rearr} = 2.9 ± 0.6 × 10^{10} s^{-1} at room temperature) and **151** (k_{rearr} = 2.7 ± 0.8 × 10^{10} s^{-1} at room temperature), shows that the rearrangement from σ-complex **149** is unselective and binds to both positions at the same rate.

An interesting insight into the initial binding of the acrylate was found based on the reaction performed in neat ethyl acrylate. The corresponding species as seen in *n*-butyl acrylate was observed, but the rate of depletion of the initial σ-complex (k_{rearr} = 6.0 ± 0.5 × 10^{10} s^{-1} at room temperature and 5.0 ± 0.7 × 10^{10} s^{-1} at room temperature) is about twice the rate observed in **148**. Therefore, it is likely that the manganese binds to the end of the alkyl group and chain-walks to form either of the *O*- or alkene-bound complexes. The difference in chain length agrees with the rate-differential observed.

As the reaction progresses both **150** and **151** are replaced by one single species (2008, 1920 and 1894 cm^{-1}), taking place over longer microsecond timescales (k_{insert} = 3.62 ± 0.01 × 10^{4} s^{-1} at room temperature). The shift to lower wavenumbers is consistent with the insertion into the C–Mn bond to form 7-membered insertion complex **152**. This does not occur for styrene, further supporting the C–C bond formation taking place. DFT-calculated energy barriers agree with the observed reactivity, where there is a difference of 14 kJ mol^{-1} between **148** (41 kJ mol^{-1}) and styrene (55 kJ mol^{-1}).

How the two complexes **150** and **151** turn into **152** is not clear from the data obtained and further kinetic analysis is required. From DFT-calculations is was concluded that the C–C bond formation cannot take place straight from *O*-bound complex **150**, while it is possible from alkene-complex **151**. Kinetic modelling was performed using the

COPASI software program, which allows for both parameter estimation (i.e. reaction rate) and kinetic simulation (predict kinetic trace based on rate constants). By inserting the IR intensities and estimating the various rate constants for several different plausible reaction pathways, the most likely mechanism may be identified. The goodness of fit was used as a measure of the validity for the different pathways and was obtained from the coefficient of variation and standard deviation. The proposed mechanisms include various ways that the three complexes, **150**, **151** and **152**, can be related and whether the pathways are reversible or not (**Table 7**).

From the parameter estimation, relatively large values of both the coefficient of variation and standard deviation are obtained for the mechanisms with reversible pathways. Therefore, it is unlikely that any of the steps within the reaction are reversible and is consistent with the mechanism of C–C bond formation observed for the alkynes. The mechanism where **150** have to generate **151** before the insertion into the C–Mn bond can occur, exhibit rate constants with acceptable goodness of fit, supporting this proposed mechanism. As a control, the reverse mechanism was modelled, with poor goodness of fit as a result. It is therefore concluded from the kinetic modelling that *O*-bound complex **150** has to rearrange to alkene-complex **151**, before the C–C bond formation step can occur (**Figure 39**).

The reaction in neat acrylate was repeated with imine-complex **135** and indole-complex **130**, to observe if the reactivity of **148** is applicable to other substrates. Initially, the corresponding σ-complexes are observed forming (2009 and 1907 (br) cm^{-1} for **135** and 2014, 1917 (br) cm^{-1} for **130**) and they are consumed at a similar rate (k_{rearr} = 1.3 ± 0.6 × 10^{10} s^{-1} at room temperature for **135** and k_{rearr} = 1.8 ± 0.3 × 10^{10} s^{-1} at room temperature for **130**) as **149**. The *O*- (1998, 1899 and 1890 cm^{-1} for **135** and 2010 and 1908 (br) cm^{-1} for **130**) and alkene-bound (2019 and 1955 cm^{-1} for **135** and 2028 cm^{-1} for **130**) complexes are thereafter generated. In the case of indole derivative **130**, the formation of the insertion complex (2012, 1922 and 1908 cm^{-1}) follows in the same manner as seen for **10**, with a slower rate of insertion (k_{insert} = 8.2 ± 0.31× 10^{3} s^{-1} at room temperature). This slower rate of insertion is consistent with the trend observed for the C–C bond formation using **34** (**Table 4**).

Table 7. Kinetic data obtained from modelling in COPASI for a variety of possible reaction pathways in the formation of **152** from **150** and **151**. Goodness of the fit was obtained from the coefficient of variation (C. V.) and standard deviation.

150 $\xrightarrow{k_1}$ **151** $\xrightarrow{k_3}$ **152**

k	***k*$_{calc}$ / 10^4 s^{-1}**	**C. V.**	**Standard Deviation**
k_1	2.59	1.98	0.51
k_2	-	-	-
k_3	2.66	1.60	0.43
k_4	-	-	-

150 $\underset{k_2}{\overset{k_1}{\rightleftharpoons}}$ **151** $\xrightarrow{k_3}$ **152**

k	***k*$_{calc}$ / 10^4 s^{-1}**	**C. V.**	**Standard Deviation**
k_1	4.19	12.29	5.15
k_2	1.51	31.61	4.77
k_3	2.62	1.64	0.43
k_4	-	-	-

151 $\xrightarrow{k_2}$ **150** $\xrightarrow{k_5}$ **152**

k_1	***k*$_{calc}$ / 10^4 s^{-1}**	**C. V.**	**Standard Deviation**
k_2	1.32	26.04	0.34
k_3	-	-	-
k_4	-	-	-
k_5	2.74	1.57	0.43

150 $\underset{}{\overset{k_1}{\rightleftharpoons}}$ **151** $\underset{k_4}{\overset{k_3}{\rightleftharpoons}}$ **152**

k	***k*$_{calc}$ / 10^4 s^{-1}**	**C. V.**	**Standard Deviation**
k_1	2.64	1.88	0.50
k_2	-	-	-
k_3	3.90	6.21	2.42
k_4	1.51	18.56	2.81

150 $\underset{k_2}{\overset{k_1}{\rightleftharpoons}}$ **151** $\underset{k_4}{\overset{k_3}{\rightleftharpoons}}$ **152**

k	***k*$_{calc}$ / 10^4 s^{-1}**	**C. V.**	**Standard Deviation**
k_1	5.11	9.67	4.94
k_2	2.32	19.62	4.55
k_3	4.22	5.70	2.40
k_4	1.99	14.12	2.82

Interestingly, imine derivative **135** show two new species (2014, 2003 and 1907 (br) cm^{-1}) forming following the loss of the alkene-complex. The rate of loss of this species should mirror the C–C bond formation (k_{insert} = 1.32 ± 0.06 × 10^4 s^{-1} at room temperature) and is similar to the experiment using **10**. The identity of the unknown species cannot be definitively determined based on this experiment, but can be

speculated being the corresponding isoquinoline formed *via* reductive elimination of the insertion complex.

3.6.2 C–C Bond Formation in Toluene Solution

To probe the effect of solvent on the C–C bond formation, an TRIR experiment was performed between **10** and **148** diluted in toluene ([**10**] = 1.89 × 10^{-3} mol dm^{-3} and [**148**] = 0.46 mol dm^{-3}) using the ULTRA A experimental setup (**Figure 40**). As seen in the experiments performed with **34**, the only species formed that is different than in neat acrylate is the initial formation of toluene-complex **117** (2005 and 1908 (br) cm^{-1}). Thereafter, *O*-bound complex **150** (2001, 1903 and 1890 cm^{-1}) and alkene-complex **151** (2021 cm^{-1}) are generated, but at a reduced rate (k_{sub} = 1.5 ± 0.3 × 10^{7} s^{-1} at room temperature). These complexes disappear at longer times to be replaced by insertion complex **152** (2011, 1920 and 1907 cm^{-1}), in the same fashion as observed previously (k_{insert} = 3.1 ± 0.6 × 10^{4} s^{-1} at room temperature). This shows that the behaviour of the acrylate is the same whether it is neat **148** or diluted in toluene, with the initial solvent-complex being the exception.

To further probe the various steps and intermediates, several experiments were performed at a range of **148** concentrations ([**148**] = 0.05–0.91 mol dm^{-3}). The depletion rate of toluene-complex **117** was found to be dependent on the concentration of acrylate, showing a linear increase in rate with higher concentration of **148**. This arises from the bimolecular nature of this reaction step, as seen for the terminal alkynes. As expected, the rate of insertion is independent of acrylate concentration, due to the step being unimolecular. The same independence on the rate of loss of *O*-bound complex **150** was observed and infers that the rearrangement to form **151** does not require exchange with the surrounding solvated acrylate.

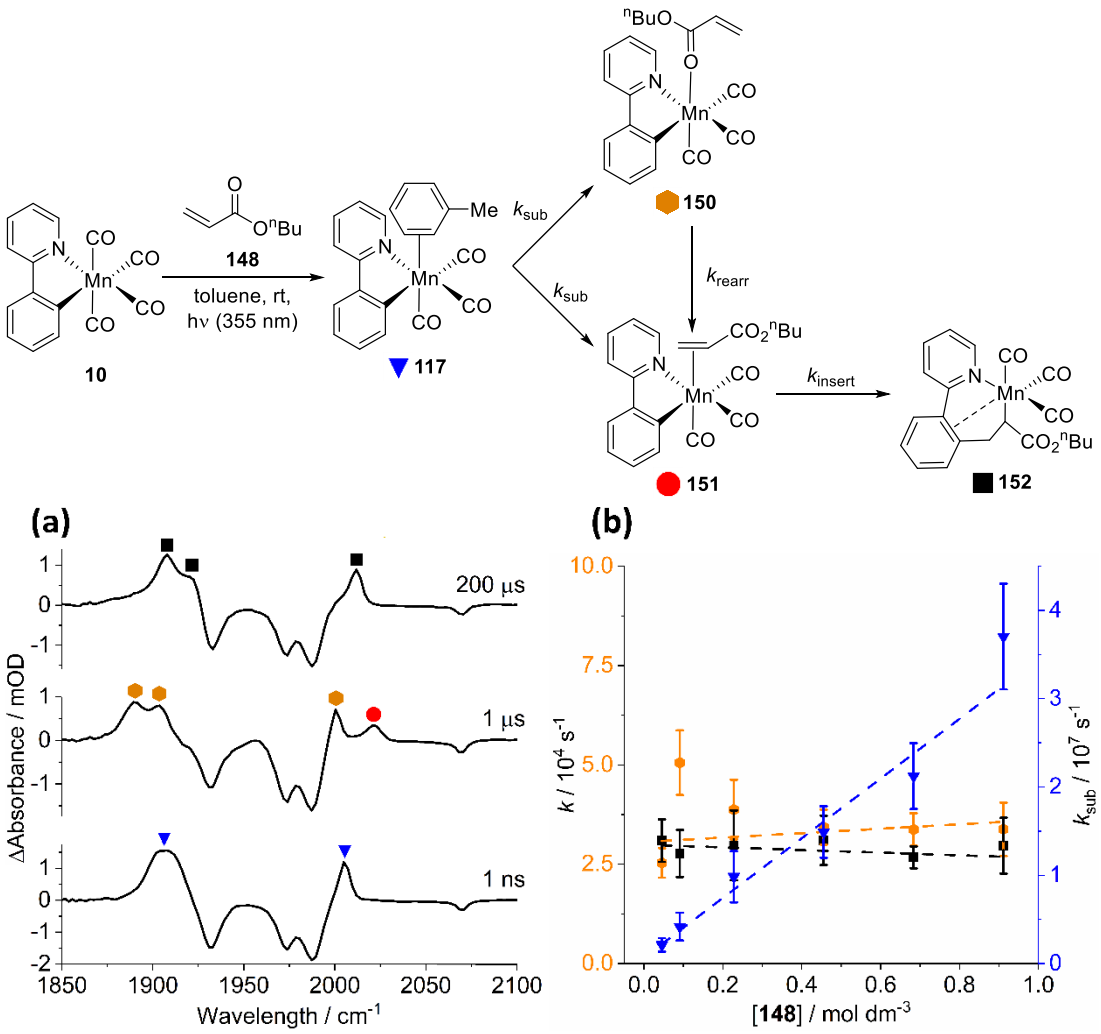

Figure 40. TRIR study of the photolysis of **10** and **148** in toluene ([**10**] = 1.89 × 10^{-3} mol dm^{-3} and [**148**] = 0.46 mol dm^{-3}), showing the formation of various species after irradiation. (a) IR spectra of the reaction showing the metal carbonyl region at various timepoints. Negative bleach bands correspond to the loss of **10** after irradiation. (b) Concentration dependence on the rate of loss of **117** (k_{sub}, blue triangles), loss of **150** (orange hexagons) and gain of **152** (k_{insert}, black squares), determined in separate experiments. Slope of linear regression for k_{sub} = 3.38 ± 0.27 × 10^{7} (R^2 = 0.98), k_{rearr} = 0.56 ± 1.01 × 10^{4} (R^2 = 0.07) and k_{insert} = −3.33 ± 2.68 × 10^{3} (R^2 = 0.28).

33 was added to the experiment with **10** and **148** in toluene ([**10**] = 1.89 × 10^{-3} mol dm^{-3}, [**148**] = 1.91 × 10^{-2} mol dm^{-3} and [**33**] = 3.96 × 10^{-2} mol dm^{-3}), to produce a more catalytically relevant reaction mixture (**Figure 41**). The initial toluene-complex **117** (2005 and 1908 (br) cm^{-1}) was seen disappearing over the first microsecond, to form alkene-complex **151** (2020 cm^{-1}) and *N*-coordinated 2-phenylpyridine complex **126** (1996, 1903 and 1888 cm^{-1}). It is possible that *O*-bound complex **150** is generated, but it cannot be observed due to overlap of the bands with **126**.

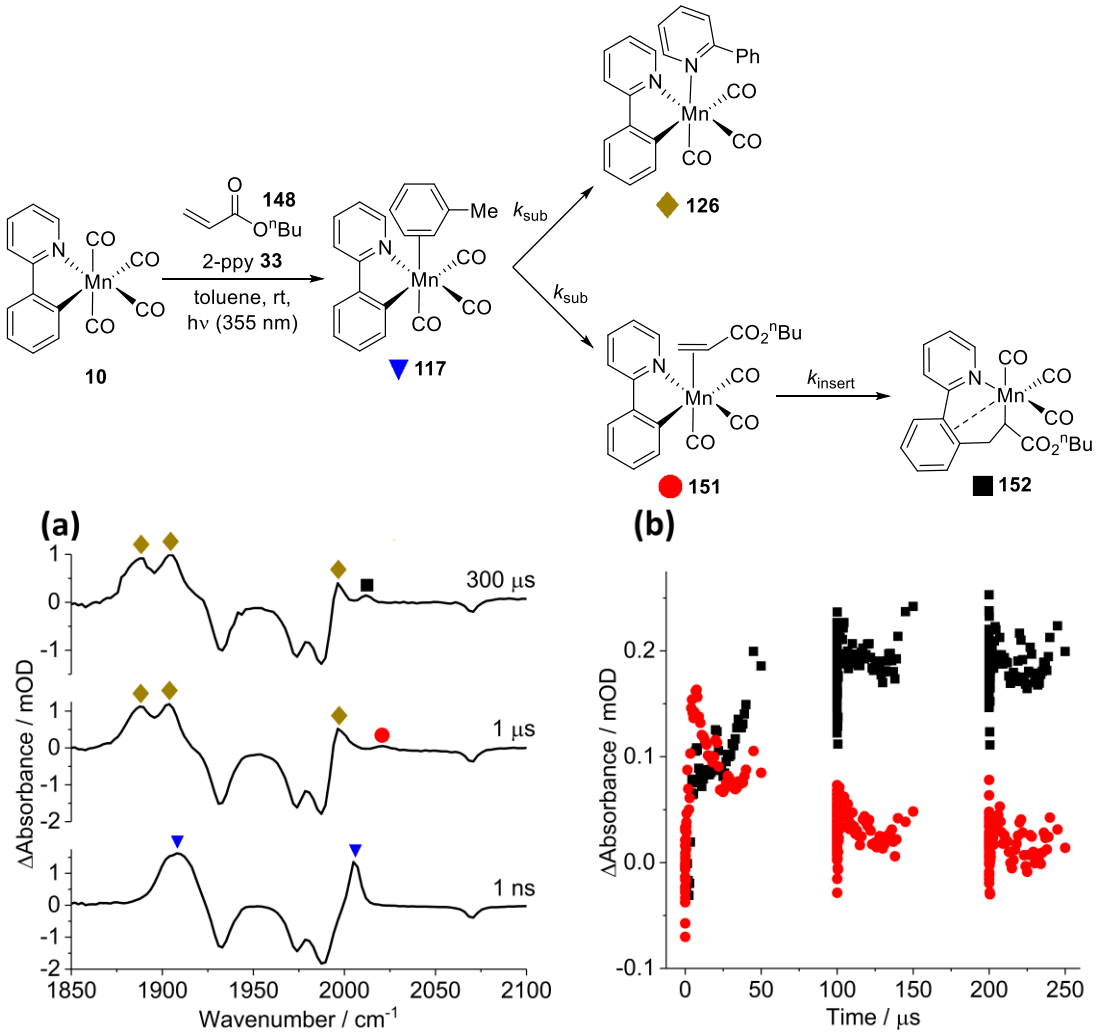

Figure 41. TRIR study of the photolysis of **10**, **148** and **33** in toluene ([**10**] = 1.89 × 10^{-3} mol dm^{-3}, [**148**] = 1.91 × 10^{-2} mol dm^{-3} and [**33**] = 3.96 × 10^{-2} mol dm^{-3}), showing the formation of various species after irradiation. (a) IR spectra of the reaction showing the metal carbonyl region at various timepoints. Negative bleach bands correspond to the loss of **10** after irradiation. (b) Kinetic plot of the formation and depletion of **151** (red circles, band at 2020 cm^{-1}) and formation of **152** (black squares, band at 2011 cm^{-1}), extracted from (a).

151 disappears to form **152** (2011 cm^{-1}) towards the longer microsecond times, exhibiting a rate of insertion (k_{insert} = 2.3 ± 0.4 × 10^4 s^{-1} at room temperature) which is comparable to the previously observed rates for this step. **126** is observed remaining throughout the remainder of the reaction, showing that the exchange of the pyridine-ligand is not taking place on the timescale of the experiment. Overall, this experiment shows that **33** have an impact on the efficiency of the C–C bond formation, but as previously stated it is unlikely to be negative for the overall catalytic reaction due to the fast rate of this reaction step.

3.6.3 Fluorinated alkene

The higher efficiency of acrylates in the C–C bond formation than the other alkenes studied, inspired the utilisation of other alkene substrates. Perfluorinated alkenes, such as perfluoro-1-decene **153**, has been successfully employed in Mn(I)-catalysed C–H bond functionalisation (**Scheme 32**).[151]

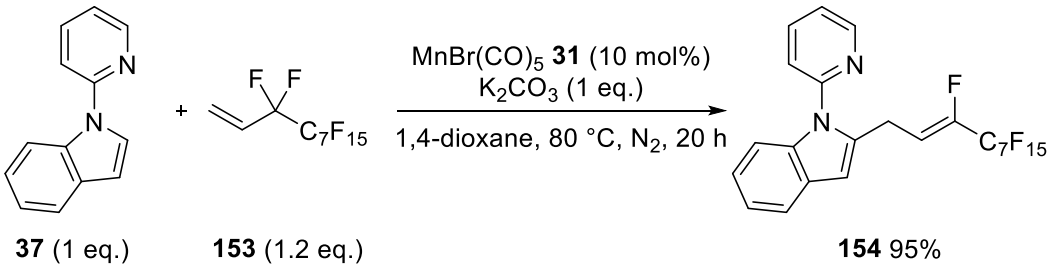

Scheme 32. Mn(I)-catalysed C–H bond allylation using perfluorinated alkenes, reported by Ackermann and co-workers.[151]

An TRIR experiment with the ULTRA A setup was performed between **10** and **153**, diluted in toluene ([**10**] = 1.94 × 10^{-3} mol dm^{-3} and [**153**] = 0.23 mol dm^{-3}) to probe the C–C bond formation for the alkene. After the initial formation of toluene-complex **117**, a distinct shift of the IR bands to higher wavenumbers marked the formation of alkene-complex **155** (2028, 1944 and 1891 cm^{-1}). The rate of substitution (k_{sub} = 2.0 ± 0.5 × 10^6 s^{-1} at room temperature) is about an order of magnitude slower than observed in the analogous experiment with *n*-butyl acrylate **148**, which could arise from the additional carbonyl group on the acrylate increasing the binding affinity.

The IR bands can be seen on microsecond timescale shifting back to lower wavenumbers (2016, 1910 and 1891 cm^{-1}), signifying the C–C bond formation taking place to form insertion complex **156**. The rate of the insertion (k_{insert} = 1.3 ± 0.2 × 10^5 s^{-1} at room temperature) is within error the same as observed for **34**, which showcases the large impact of the fluorine substituents, as styrene cannot be observed forming the C–C bond for the duration of the experiment.

Replacing **153** with 1-decene (0.18 mol dm^{-3}) in the TRIR experiment, lead to a reaction where the C–C bond formation was not observed. Instead the alkene-complex (2019, 1948 and 1913 cm^{-1}) remained in solution until the end of the experiment. This further highlights the large impact of the fluorine-substituents on the reactivity of the alkene.

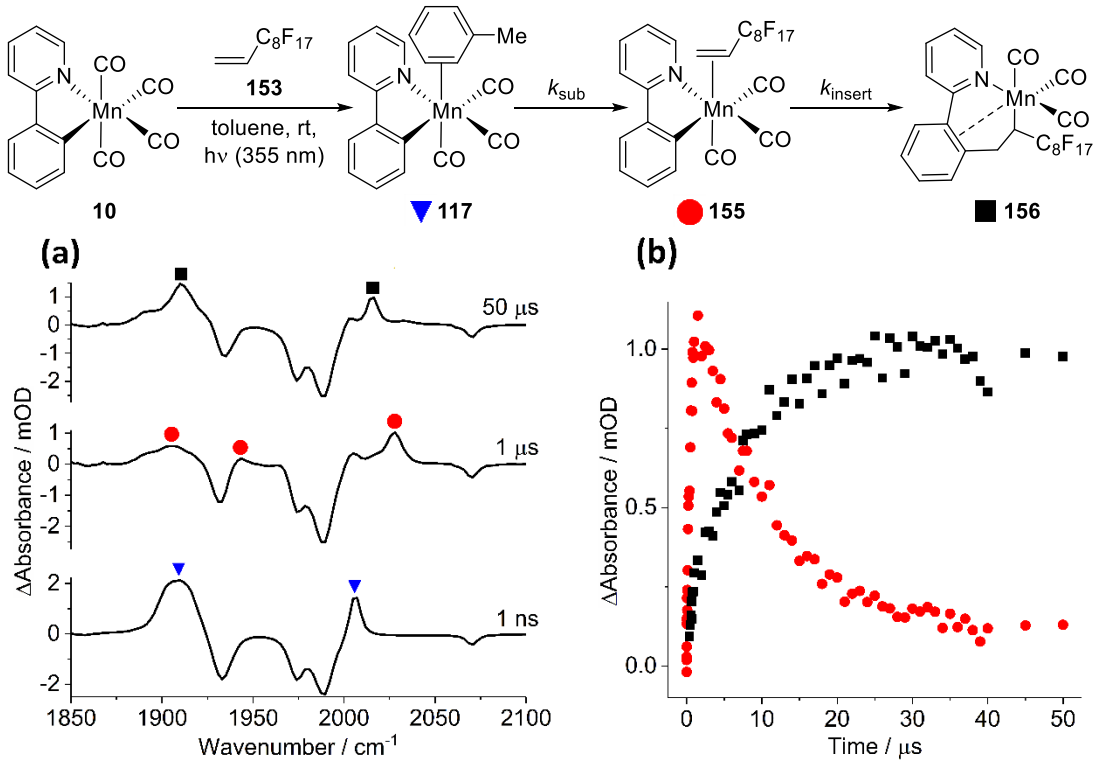

Figure 42. TRIR study of the photolysis of **10** and **153** in toluene ([**10**] = 1.94 × 10^{-3} mol dm^{-3} and [**153**] = 0.23 mol dm^{-3}), showing the formation of various species after irradiation. (a) IR spectra of the reaction showing the metal carbonyl region at various timepoints. Negative bleach bands correspond to the loss of **10** after irradiation. (b) Kinetic plot of the formation and depletion of **155** (red circles, band at 2028 cm^{-1}) and formation of **156** (black squares, band at 2016 cm^{-1}), extracted from (a).

3.7 Other Substrates

3.7.1 Hexyl Isocyanate and Other Carbonyls

As previously mentioned, there are many other substrates utilised in Mn(I)-catalysed C–H bond functionalisation reactions,[32] where the C–C bond formation is of interest. Isocyanates are examples of substrates utilised in these reactions[37] and the many heteroatoms raises questions about how they coordinate to the manganese. Therefore, an TRIR experiment between hexyl isocyanate **157** and **10** ([**10**] = 1.79 × 10^{-3} mol dm^{-3}) was monitored using the ULTRA experimental setup (**Figure 43**). Two different species, **158** (2009 and 1910 (br) cm^{-1}) and **159** (2003, 1913 and 1897 cm^{-1}), are observed at the earliest times measured. Due to the similarity of the IR bands to the σ-complex formed in heptane (2019, 1933 and 1923 cm^{-1}), **158** is assigned as being the corresponding σ-complex bound to the alkyl-chain. **158** is observed converting into **159** (k_{rearr} = 1.9 ± 0.3 × 10^{10} s^{-1} at room temperature) as the experiment progresses and only **159** is present in the IR spectrum after 10 nanoseconds.

159 proceeds to deplete in favour of a new complex, **160** (2001, 1913 and 1897 cm^{-1}), which exhibit remarkable similar IR bands to its predecessor. The rate of the interconversion cannot be determined due to the large spectral overlap and similar intensity of the bands. However, the loss of **160** to form the final complex in the reaction (k_{insert} = 4.34 ± 0.02 × 10^3 s^{-1} at room temperature), **161** (2029, 1946 and 1921 cm^{-1}), which is assigned as the insertion complex formed post C–C bond formation. It can be seen that the C–C bond formation for the isocyanate is significantly slower than the other substrates investigated, with for example **34** inserting about 30 times faster.

The assignment of **159** and **160** provides a challenge due to the similar IR bands. Nevertheless, the *N*-bound complex is predicted to be lower in energy than the corresponding *O*-bound complex. Therefore, **159** and **160** are assigned as being the *O*-bound and *N*-bound complex respectively.

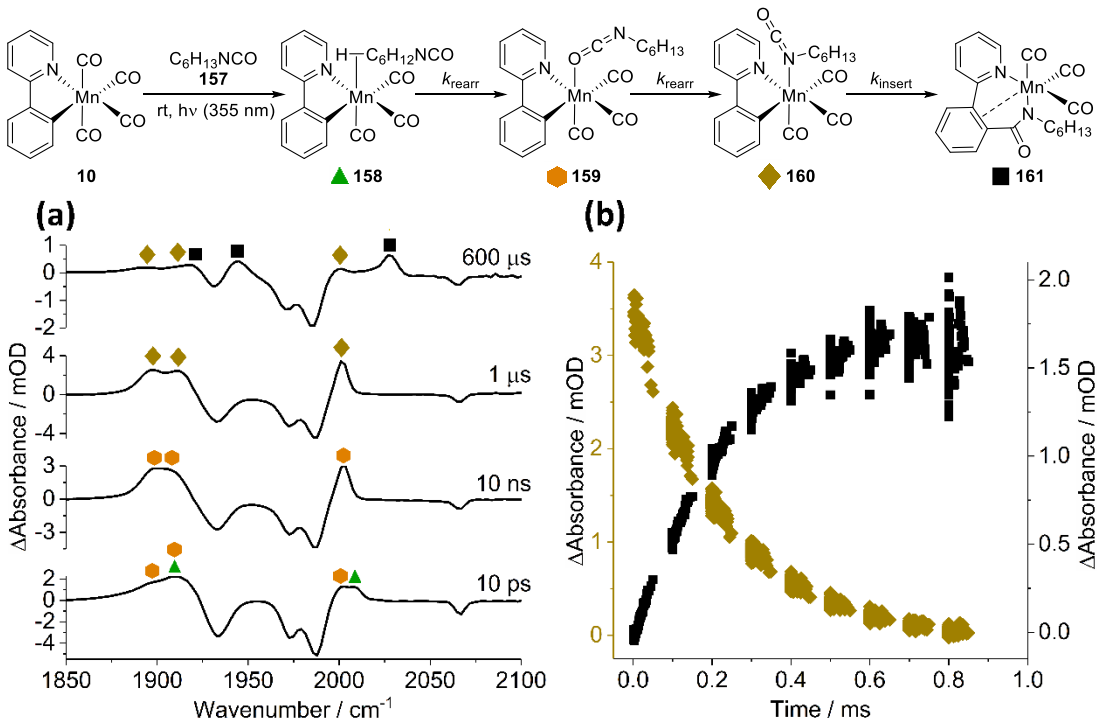

Figure 43. TRIR study of the photolysis of **10** in neat **157** ([**10**] = 1.79 × 10^{-3} mol dm^{-3}), showing the formation of various species after irradiation. (a) IR spectra of the reaction showing the metal carbonyl region at various timepoints. Negative bleach bands correspond to the loss of **10** after irradiation. (b) Kinetic plot of the depletion of **160** (brown diamonds, band at 2001 cm^{-1}) and formation of **161** (black squares, band at 2029 cm^{-1}), extracted from (a).

Another carbonyl species, benzaldehyde was used as simple carbonyls have also been used as substrate in Mn(I)-catalysed C–H bond functionalisation.[33, 42] An TRIR experiment of **10** in neat benzaldehyde ([**10**] = 1.79 × 10^{-3} mol dm^{-3}) was performed using a 355 nm pump beam. As observed previously, the arene-bound complex (2006 and 1905 (br) cm^{-1}) was initially observed before rearranging to the *O*-bound complex

(1994, 1905 and 1891 cm^{-1}). It should also be noted that an additional band at 1818 cm^{-1} was observed and was assigned as a benzoyl radical, forming as a photoproduct of benzaldehyde without the need of any interaction with the manganese.[152] The *O*-bound complex is present through the remainder of the experiment and the C–C bond formation can therefore not be observed for this substrate. This is supported by a relatively large predicted barrier of insertion (48 kJ mol^{-1}). It is still possible that the benzaldehyde can insert into the C–Mn bond, but the rate of insertion is too slow for this to be observed on the timescale of the experiment.

3.7.2 Correlation Between Experimental and Predicted Energy Barriers

The Eyring equation (**Equation 1**) allows for quantification of the correlation between the rate of reaction and energy barrier of the particular step. Therefore, experimental $\Delta G^{\ddagger}_{298}$-values can be determined directly from the rate of the reactions, while computational energy barriers are found using DFT-calculations. For these calculations an assumed transmission coefficient of 1 (full conversion across energy barrier) was utilised. The experimental and computational values should form a straight line if the reactions proceed as predicted, though the values can differ as the computational values are obtained in the gas-phase. Solvent was corrected for in the calculations with the COSMO dielectric continuum model.[153]

$$k = \frac{\kappa k_B T}{h} e^{-\frac{\Delta G^{\ddagger}}{RT}}$$

Equation 1. Eyring equation.

The computationally predicted $\Delta G^{\ddagger}_{298}$-values values are found to be lower than the experimental values (**Figure 44**), which has been observed previously and could arise due to certain factors being difficult to model.[154] Nevertheless, a linear trend is observed between the two $\Delta G^{\ddagger}_{298}$ values for the C–C bond formation, supporting the assignment of the process taking place. The trend of pyrones and pyridones reacting faster than the phenyl analogue is mirrored in the computational data as well. It can also be seen that the substrates that did not insert into the C–Mn bond have a larger activation barrier and therefore cannot form the C–C bond on the timescale of the experiment. However, this does not determine whether or not the C–C bond formation will take place on longer timescales than measured in the experiment.

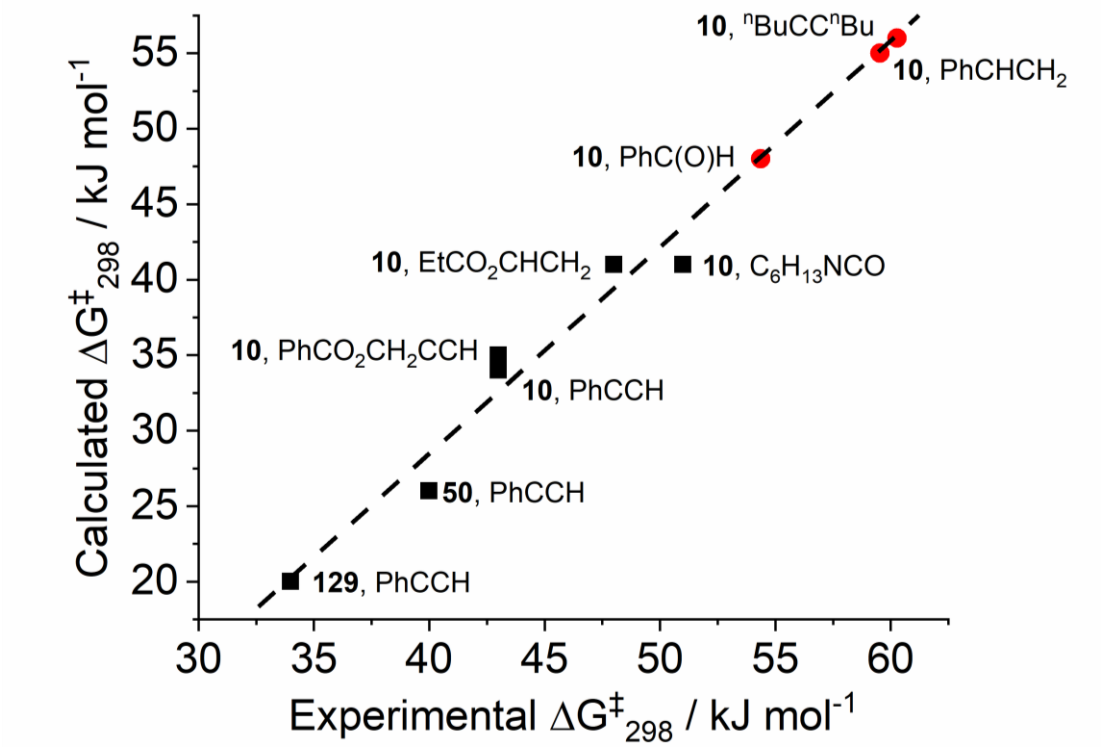

Figure 44. Correlation between the predicted and experimental $\Delta G^{\ddagger}_{298}$-values for the C–C bond formation step studied by TRIR spectroscopy. Calculations were performed at the (RI-)BP86/SV(P) level. Slope of linear regression for experimentally determined points was 1.35 ± 0.18 (R^2 = 0.93). Red dots are not experimentally detected and the predicted rates are extrapolated onto the linear correlation.

Chapter 4: Effect of Acid Additives in Mn(I)-Catalysed C–H Bond Functionalisation

4.1 Background

The role of the 2-phenylpyridine, terminal alkyne and manganese catalyst in the Mn(I)-catalysed C–H bond alkenylation have been described in Chapter 2. The importance of the amine base additive in the pre-catalyst activation step was also elucidated, but further impacts of the base or its conjugate acid may still be occurring. The extensive scrambling of deuterium in D-labelling studies[34] and the unusual reaction order in Cy_2NH (Chapter 2), suggests that the amine may affect the reaction in unexpected ways. Additionally, the lower conversion to alkene product **35** observed when starting the reactions from $Mn(ppy)(CO)_4$ **10** rather than $MnBr(CO)_5$ **31** and Cy_2NH, indicates that it is possible the conjugate acid ($[Cy_2NH_2]Br$ **62**) may influence the reaction. Therefore, it is also conceivable that stronger acid additives might have an even more pronounced effect on the reaction.

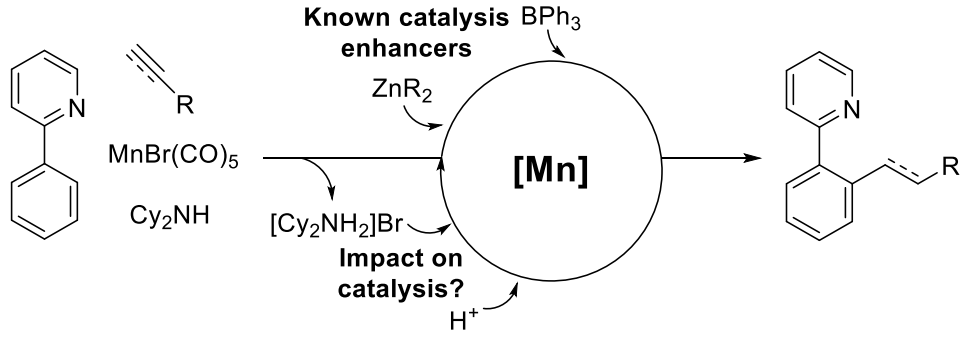

Scheme 33. Highlighting the possible impact on the reactions by the amine base's conjugate acid or other acids, in comparison to previously known enhancers in BPh_3[48] and ZnR_2[42] additives.

Acid additives have already found use in Mn(I)-catalysed C–H bond functionalisation processes, with the work by Lei, Li and co-workers[51] being an excellent example of this (**Scheme 34**). They found that in the C2-selective alkenylation of *N*-(2-pyrimidine)indole **162**, benzoic acid was required in catalytic amounts (20 mol%) to form alkene product **163**. Carbazole **164**, formed from double insertion of the terminal alkyne, was the only isolatable product (18%) in the absence of the acid additive. This most likely arise from energetically unfavourable protonation pathways and more accessible side-reactions taking place instead. This was observed for internal alkynes in Chapter 2.5 and previously for pyridyl-2-pyrone derivatives.[50] Interestingly, H_2 and

styrene are both observed forming in the reaction and **34** still remains as the limiting reagent (1.5 eq.), and were not used in excess for optimisation of **164**.

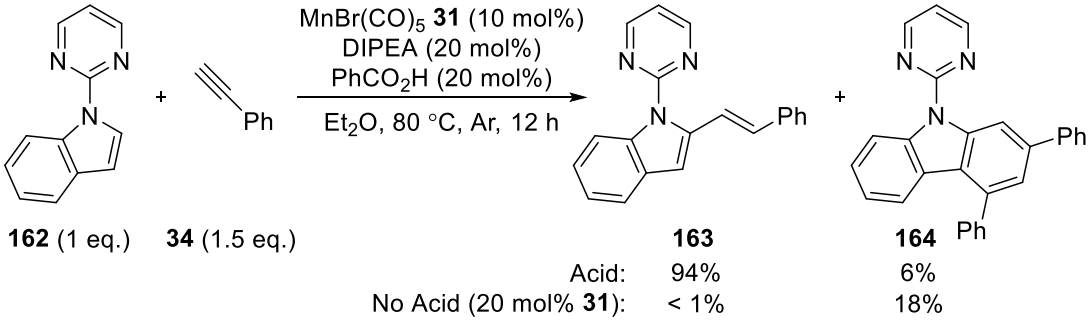

Scheme 34. Mn(I)-catalysed C–H bond functionalisation of *N*-(2-pyrimidine)indole where benzoic acid selects between the generation of alkene **163** or carbazole **164**, reported by Lei, Li and co-workers.[51]

A similar example of a Mn(I)-catalysed reaction influenced by an acid additive is the alkenylation or allenelation of *N*-(2-pyridyl)indole **37**, reported by Ackermann and co-workers (**Scheme 35**).[155] This methodology was performed in flow, allowing for shorter reaction times. Cyclic carbonate-containing terminal alkyne **165** was used as unsaturated substrate and **31** as pre-catalyst. With no additives employed, allene **167** was the major product formed in 63% yield of isolated product, while alkene **166** was only found in trace quantities. Not requiring any base additive, this reaction shows a distinct difference from similar methodologies, which need base in order for the catalyst to be activated.[35] Again, the unfavoured protonation pathway led to no formation of the alkenylated indole **166** and instead allowed for the generation of **167** through the extrication of CO. To aid in the protonation step, the addition of acetic acid (20 mol%) led to the selective formation of **166** in 95% yield of isolated product.

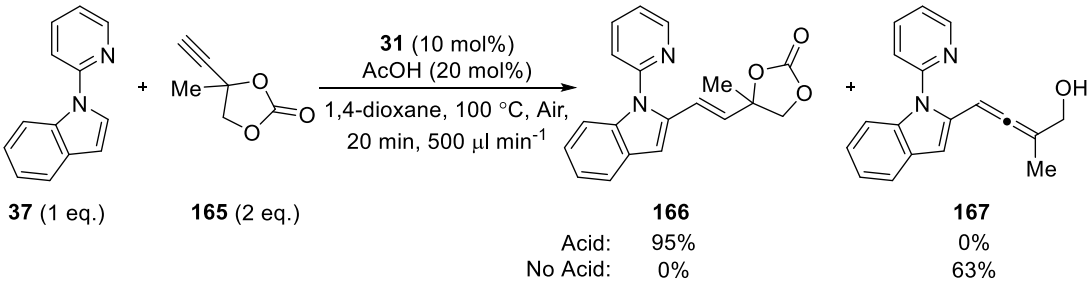

Scheme 35. Mn(I)-catalysed C–H bond alkenylation and allylation of *N*-(2-pyridyl)indole performed in flow, reported by Ackermann and co-workers.[155]

A manganese-carboxylate species may be formed in the reactions with carboxylic acid additives (or if generated *in situ*), providing a proton transfer step following the CMD/AMLA-6 mechanism. The feasibility of C–H bond activation mediated by a manganese acetate complex, has been studied by Dang and co-worker.[156] They used

DFT-calculations to understand the factors controlling a competition between hydroarylation and cyclisation, for an Mn(I)-catalysed C–H bond functionalisation with NaOAc as base additive, which was reported by Rueping and co-workers (**Scheme 36**).[157] Cavallo, Rueping and co-workers had previously shown that the activation of $MnBr(CO)_5$ **31** to form a manganese-acetate species is possible,[158] which meant that Dang and co-worker's calculations started from this point. It was shown that the subsequent C–H bond activation of indole **162** proceed *via* a CMD/AMLA-6 mechanism, highlighting the feasibility of manganese acetate species being productive in the catalysis.

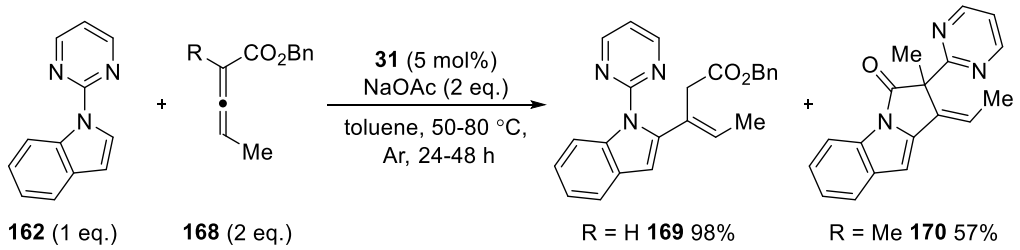

Scheme 36. Mn(I)-catalysed C–H bond functionalisation of *N*-(2-pyrimidine)indole where the R-group selects between an hydroarylation and cyclisation pathway, reported by Rueping and co-workers.[157]

There is a rich enough history of acid additives affecting Mn(I)-catalysed C–H functionalisation processes and intrigue in how the amine base (or its conjugate acid) may impact the catalytic reactions, for a further investigation to be performed. If the full role of the base and/or acid additive can be understood in these reactions, there is a large potential of reaction optimisation and new reactivities to be discovered.

4.2 Investigation into the Effect of Acid Additives in Mn(I)-Catalysed C–H Functionalisation

4.2.1 Amine-Derived Conjugate Acid Additives in Mn(I)-Catalysis

$Mn(ppy)(CO)_4$ **10**, was chosen as pre-catalyst to avoid interference of the initial base-mediated C–H activation, and thereby allow for a more straightforward investigation into the effect of the ammonium conjugate acid on the Mn(I)-catalysis. The reactions were performed at 100 °C, under argon atmosphere in microwave vials using the standard reaction conditions described in the experimental section (Chapter 7) unless otherwise stated. As previously mentioned (Chapter 2.2.3), employing **10** as pre-catalyst (10 mol%) in the reaction of alkyne **34** (1 eq.) with 2-phenylpyridine **33** (2

eq.) with no extra additives, led to a relatively low conversion to alkenylated 2-phenylpyridine **35** (55%, determined by ^{1}H NMR spectroscopy). This was a reduction of 23% compared to the same reaction, using $MnBr(CO)_5$ **31** (10 mol%) as the pre-catalyst and Cy_2NH (20 mol%) as base additive. Aside from the pre-catalyst activation pathway (Chapter 2.6), the main difference between these two reaction conditions is the *in situ* generation of the conjugate acid of the amine base, which may be responsible for the difference in reactivity observed.

Cy_2NH and its conjugate acid derivatives (with varying anion) were screened as additives in the C–H bond alkenylation, employing **10** as pre-catalyst (**Figure 45**). Addition of Cy_2NH to the reaction did not affect the outcome and yielded 58% conversion to **35**. This is consistent with the amine base only being required in the initial pre-catalyst activation and therefore having no impact on the efficiency of the C–H bond activation steps, once the manganese has entered the catalytic cycles. The conjugate acid formally generated following initial C–H bond activation, $[Cy_2NH_2]Br$ **62**, was employed as an additive and the conversion to **35** remained unchanged at 53%. The observed lack of reactivity supports **62** not being involved in the protonation of the C–Mn bond, which has been proposed and supported by DFT calculations from Wang and co-workers.[34] Changes in anion to other halides (Cl **171** or I **172**) or pseudohalide (BF_4 **173**) provided no improvements on the conversion, affording 49% (**171**), 51% (**172**) and 57% (**173**) conversion to **35**.

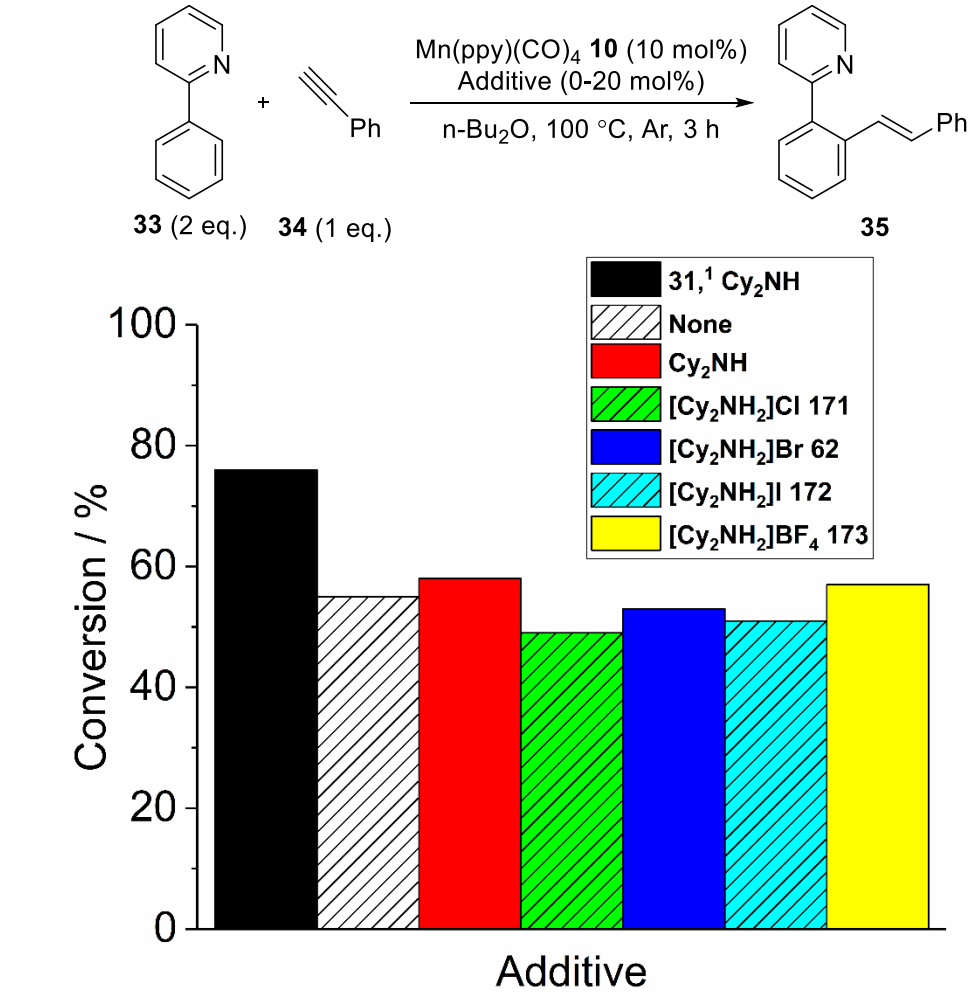

Figure 45. The effect of base or conjugate acid additives in the reaction between **34** and **33**. Reaction conditions: **34** (0.25 mmol, 1 eq.), **33** (0.5 mmol, 2 eq.), **10** (0.025 mmol, 10 mol%), additive (0.05 mmol, 20 mol%) and *n*-Bu_2O (0.6 ml) at 100 °C under argon for 3 h. $^1MnBr(CO)_5$ **31** used instead of **10** as pre-catalyst.

A more pronounced effect of the ammonium salts was observed with a different alkyne, propargyl benzoate **146**, which formed alkenylated 2-phenylpyridine **174** (**Figure 46**). The reaction of **146** (1 eq.) with **33** (2 eq.), using **10** (10 mol%) as pre-catalyst afforded a relatively low conversion to product (7%). At first glance this hinted towards the manganese being unable to fully proceed through the catalytic cycle to complete a turnover, but alternate reasons such as extensive catalyst deactivation could also be responsible. Consistent with the reaction using alkyne **34**, the reaction employing **31** (10 mol%) and Cy_2NH (20 mol%) yielded a higher conversion to **174** at 48%. The addition of Cy_2NH (20 mol%) to the reaction using pre-catalyst **10** did not affect the conversion to the alkene product (8%). However, the addition of conjugate acid **62** resulted in almost an order of magnitude increase in formation of **174** (63%). This significant boost in product generation, revealed a non-innocent role of the ammonium salt in the catalysis for alkyne **146**. It is uncertain where this effect

arise from, and why there was seemingly no impact of **62** on the reaction using alkyne **34**.

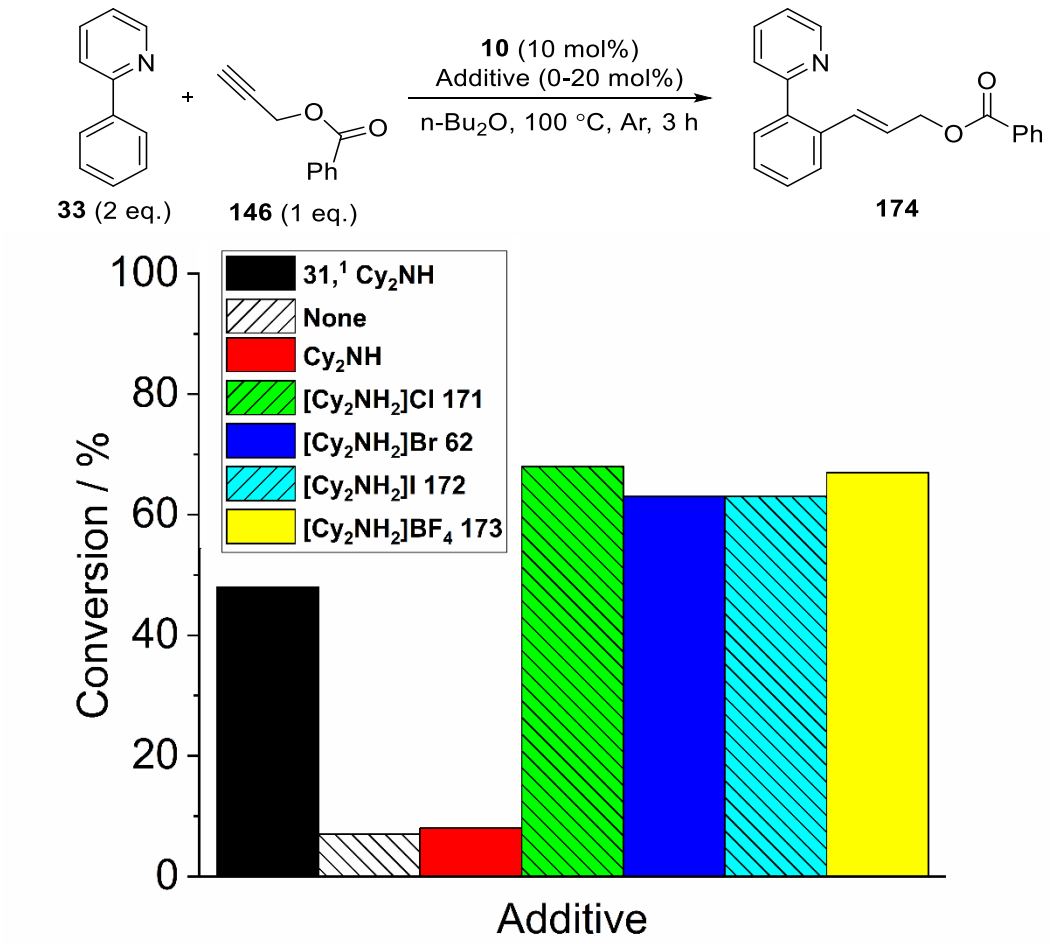

Figure 46. The effect of base or conjugate acid additives in the reaction between **146** and **33**. Reaction conditions: **146** (0.25 mmol, 1 eq.), **33** (0.5 mmol, 2 eq.), **10** (0.025 mmol, 10 mol%), additive (0.05 mmol, 20 mol%) and *n*-Bu_2O (0.6 ml) at 100 °C under argon for 3 h. $^1MnBr(CO)_5$ **31** used instead of **10** as pre-catalyst.

To test whether the anion or the ammonium cation is responsible for the enhancing effect, [*n*-Bu_4N]Br (TBAB) was used as an additive to remove any impact from the protons of the ammonium cation. Surprisingly, the reaction was inhibited and no formation of **174** could be observed under these reaction conditions, inferring that the positive effect arises from the ammonium cation. At the same time, there was a surprising negative impact of the bromine anion in the reaction. If the positive effect is linked to the ammonium protons, the removal of these should not have a negative impact on the reaction and the conversion to **174** would remain in the higher single digits. The formation of [*n*-Bu_4N][$MnBr_2(CO)_4$] is one possible rationale for the lack of reactivity, and can be synthesised from **31** when reacted with tetraalkylammonium bromides.[159] Nonetheless, the anion of the conjugate acid was found not to impact the

conversion to **174** (**Figure 46**), using ammonium salts **171** (68%), **172** (63%) and **173** (67%) as additives. Unexpectedly, the ammonium salt **173** did not change the observed conversion (67%), given the lower nucleophilicity of the tetrafluoroborate anion compared to the halides. The lack of effect of the anion and reactivity of the TBAB suggested that the protons of the ammonium salt were responsible for the positive effect, though why this is was still unknown.

Strangely, $MnBn(CO)_5$ **19** exhibited some unexpected results as a pre-catalyst, for example, giving the same conversion to **174** (48%) as when using **31** with Cy_2NH. As **19** generates toluene as a by-product from C–H bond activation while entering into the catalytic cycles, the conversion to product should have been equal or similar to the reaction employing **10** as pre-catalyst (7%). However, a similar impact as previously observed on the conversion to **174** occurred when **173** (20 mol%) was added to the reaction, which might indicate that the pre-catalyst activation is cleaner for **19** than for **31**. Another interesting result was that the reaction using alkyne **34**, generated 49% conversion to **35**, which is a large decrease compared to the reaction using **31** with Cy_2NH (76%).

In the 2014 publication by Wang and co-workers,[36] on employing acrylates (activated alkenes) in the functionalisation of 2-phenylpyridines, it was suggested that the conjugate acid of the amine base (**62**) was responsible for transferring the proton to the 7-membered insertion complex **152**. Therefore, it is easily envisaged that the role of **62** in the reaction of propargyl benzoate **146** should be reprised when acrylates are used. Due to the relatively low volatility (b.p. of 145 °C), *n*-Butyl acrylate **148** was chosen as unsaturated substrate. As with the terminal alkynes, the conversion to alkylated 2-phenylpyridine **175** (**Figure 47**) was lower using **10** (44%) as pre-catalyst than with **31** and Cy_2NH (79%). When **10** was used in tandem with Cy_2NH (20 mol%), the conversion remained unchanged at 46%. Surprisingly, the conversion to **175** was suppressed by the addition of ammonium salt **62** (27%). Change of halide anion to Cl (**171**) or I (**172**) did not have a large impact and slightly lowered the observed conversion (20% and 19% respectively). However, using the less coordinating tetrafluroborate analogue **173** led to only a minor decrease in conversion to 40%, indicating that the nucleophilicity or basicity of the anion might be important for catalyst inhibition/degradation.

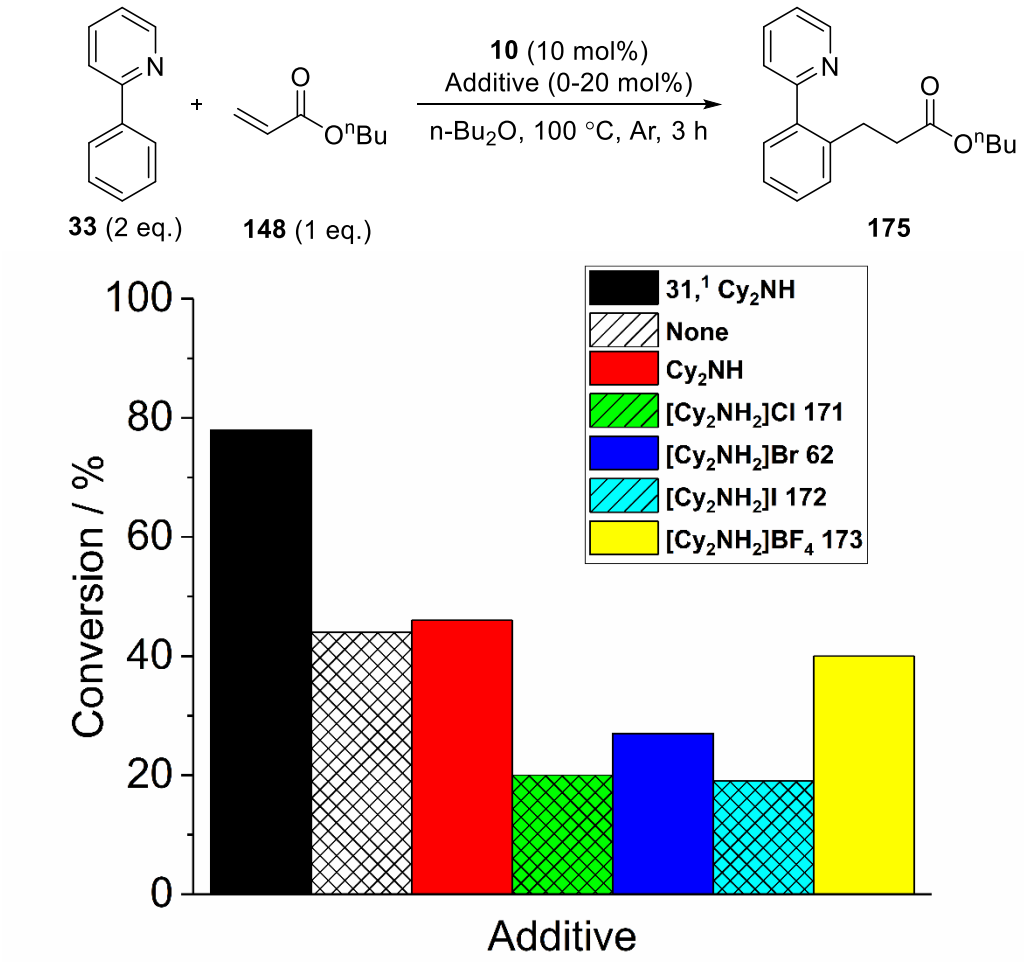

Figure 47. The effect of base or conjugate acid additives in the reaction between **148** and **33**. Reaction conditions: **148** (0.25 mmol, 1 eq.), **33** (0.5 mmol, 2 eq.), **10** (0.025 mmol, 10 mol%), additive (0.05 mmol, 20 mol%) and *n*-Bu_2O (0.6 ml) at 100 °C under argon for 3 h. $^1MnBr(CO)_5$ **31** used instead of **10** as pre-catalyst.

4.2.2 *In Operando* IR Studies on the Conjugate Acid Additive Effect for Propargyl Benzoate

To explain the positive (**146**), negative (**148**) and negligible (**34**) effects of the conjugate acid additives, *in operando* IR studies were conducted using a Mettler Toledo ReactIR® instrument with Si-probe. As in Chapter 2, the reactions were monitored in the metal carbonyl region (2150–1800 cm^{-1}), observing any changes occurring during the reaction. Initially, the reaction conditions using no conjugate acid additive was studied (using both **31** and **10** as pre-catalysts) for propargyl benzoate **146**, as a benchmark for the reactions with the ammonium salts to be compared with.

In the reaction (**Figure 48**) of **146** (1 eq.) and **33** (2 eq.) using **31** (10 mol%) and Cy_2NH (20 mol%) at 100 °C under an argon atmosphere, a rapid consumption of **31** was observed (<3 min) without any detection of **10**. This is consistent with the

alternative pre-catalyst activation pathway for terminal alkynes, proceeding *via* Mn-alkynyl complexes (see Chapter 2.6). The formation of a new transient tetracarbonyl manganese species was seen in the same position (2071 cm^{-1}) as 7-membered insertion complex **71** (2071 cm^{-1}, see chapter 2.2.3), indicating a rapid formation of the corresponding 7-membered tetracarbonyl manganese insertion complex for **146**. Another tetracarbonyl manganese species with observed peaks at 2086, 2039 and 1980 cm^{-1}, appeared and thereafter disappeared in tandem with the organic product **174** forming. This species exhibited similar IR spectroscopic bands and reaction kinetics, though it was not successfully isolated and identified. An unknown tricarbonyl manganese species (2010, 1944 and 1927 cm^{-1}) was also observed forming early in the reaction and slowly degraded over time, while still remaining at the end of the reaction. There was one major degradation complex seen in this reaction, a tricarbonyl manganese species at 2022 and 1906 cm^{-1} which showed large similarities to the Mn-hydroxyl clusters in Chapter 2 (2012 and 1900 cm^{-1} for **72**, 2017 and 1905 cm^{-1} for **73**).

Changing pre-catalyst in the same reaction to **10** (10 mol%, **Figure 49**) led to a significantly slower consumption of the pre-catalyst than for **31**, consistent with the results for phenyl acetylene **34** (Chapter 2). Neither the tetracarbonyl manganese insertion complex, nor the unknown species (distinct IR band at 2086 cm^{-1}) was observed forming in this experiment and instead **10** was seen depleting on the same timescale as organic product **174** formed. The lack of accumulation of a 7-membered insertion complex was likely a result of the reaction not being catalytic in manganese (10% observed conversion to **174**), and the rate determining step most likely being the thermal CO-loss from **10**. Interestingly, the timescale of the reaction was similar for both pre-catalysts (~20 min for both **10** and **31**), though the rate of product formation for **10** was roughly 5 times slower than for **31** (**Figure 50**). This suggested a role of the conjugate acid in allowing for catalyst turnover and thereby enhancement of the observed rate of product formation. Two degradation complexes can be observed forming as **10** is consumed in the reaction (distinct IR bands at 2014 and 2022 cm^{-1}), of which the latter was observed in the reaction using **31** as discussed *vide supra*.

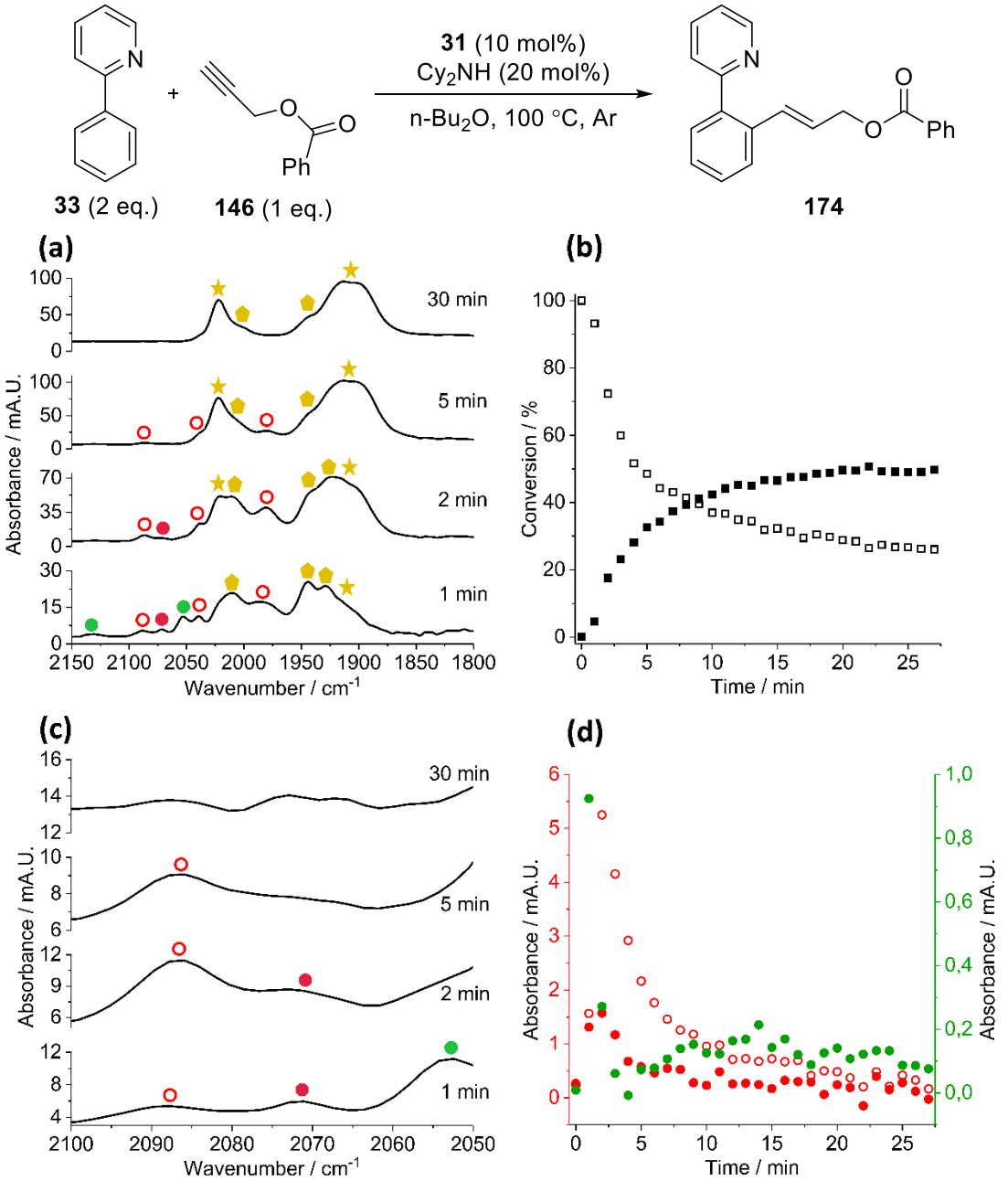

Figure 48. *In operando* IR study of the reaction between **146** and **33** using **31** as pre-catalyst. (a) IR spectra showing the metal carbonyl region at various timepoints. Key; green circle = **31**, red circle = 7-memberd tetracarbonyl manganese insertion complex, red hollow circle = unknown manganese carbonyl species, gold star/pentagon = Mn degradation complex, possibly a Mn-hydroxy cluster. (b) Kinetic plot of the consumption of **33** (hollow squares, band at 1735 cm^{-1}) and formation of alkenylated product **174** (black squares, band at 1726 cm^{-1}). (c) Expansion of the region 2100–2050 cm^{-1} in (a). Key; see (a). (d) Kinetic plot of the formation and consumption of the various manganese species in the region 2100–2050 cm^{-1}. Key; see (a). Reaction conditions (in order of addition): *n*-Bu_2O (10 ml), **33** (8.32 mmol, 2 eq.), **146** (4.16 mmol, 1 eq.), Cy_2NH (0.83 mmol, 20 mol%) and **31** (0.416 mmol, 10 mol%) at 100 °C under argon.

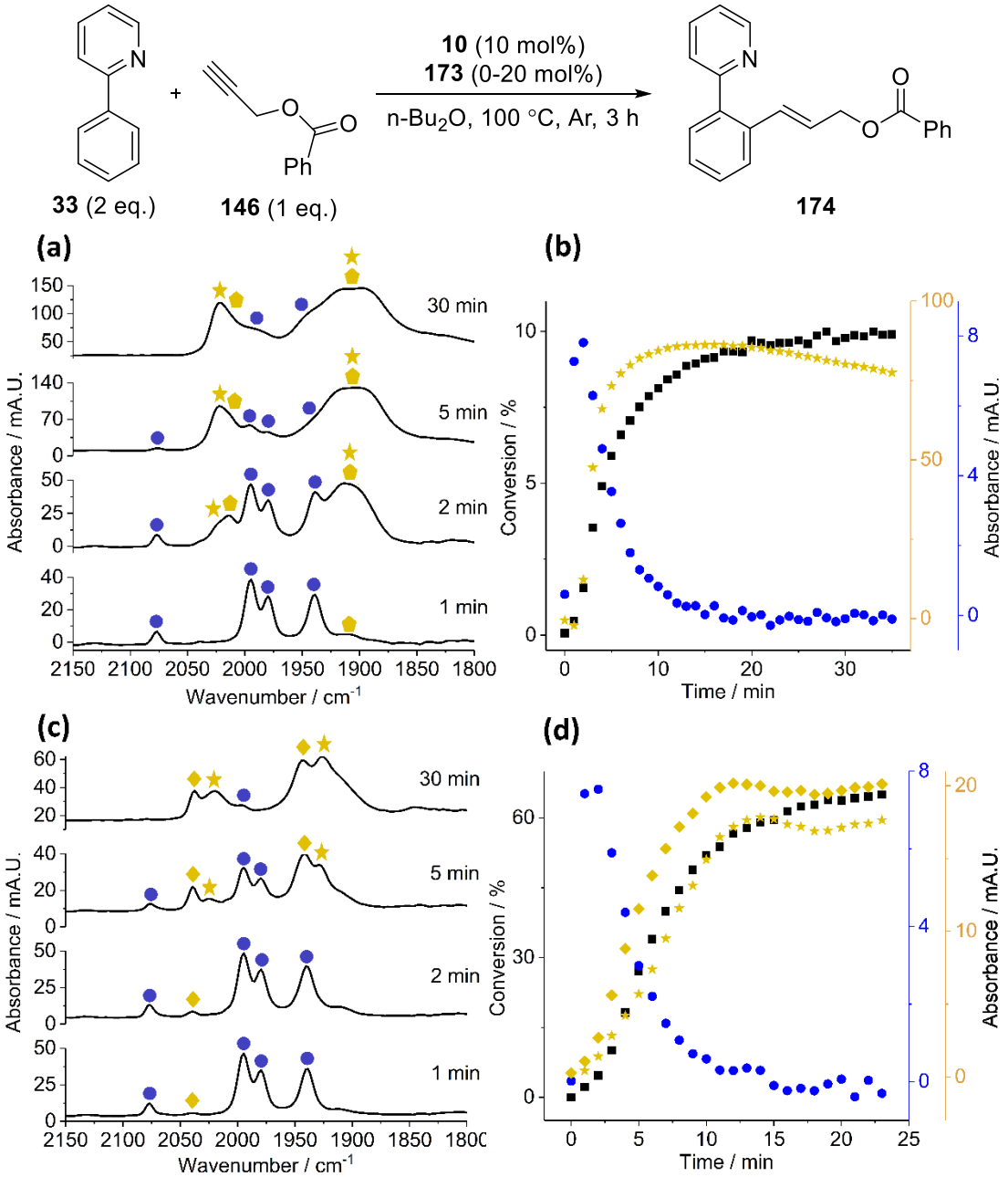

Figure 49. *In operando* IR study of the reaction between **146** and **33** using **10** as pre-catalyst with/without the addition of **173**. (a) IR spectra of the reaction with no additive showing the metal carbonyl region at various timepoints. Key; blue circle = **10**, gold star/pentagon = Mn degradation complex, possibly a Mn-hydroxy cluster. Reaction conditions (in order of addition): *n*-Bu_2O (10 ml), **33** (8.32 mmol, 2 eq.), **146** (4.16 mmol, 1 eq.) and **10** (0.416 mmol, 10 mol%) at 100 °C under argon. (b) Kinetic plot of the formation of alkenylated product **174** (black squares, determined by *ex situ* ^{1}H NMR spectroscopy), formation and depletion of **10** (blue circles, band at 2078 cm^{-1}) and the formation of one degradation complex (gold star, band at 2022 cm^{-1}), extracted from (a). (c) IR spectra of the reaction with **173** added showing the metal carbonyl region at various timepoints. Key; blue circle = **10**, gold diamond = Mn degradation complex, possibly a Mn-hydroxy cluster. Reaction conditions (in order of addition): *n*-Bu_2O (10 ml), **33** (8.32 mmol, 2 eq.), **146** (4.16 mmol, 1 eq.), **173** (0.83 mmol, 20 mol%) and **10** (0.416 mmol, 10 mol%) at 100 °C under argon. (d) Kinetic plot of the formation of alkenylated product **174** (black squares, determined by *ex situ* ^{1}H NMR spectroscopy), formation and depletion of **10** (blue circles, band at 2078 cm^{-1}) and the formation of both degradation complexes (gold diamond/star, band at 2038 and 2022 cm^{-1} respectively), extracted from (c).

When $[Cy_2NH_2]BF_4$ **173** (20 mol%) was added to the reaction using **10** (10 mol%) as pre-catalyst (**Figure 49**), the duration of the reaction remained around 20 minutes in length, with the expected increase in product conversion observed. The observed rate of product generation ($5.2 \pm 0.2 \times 10^{-4}$ mol dm^{-3} s^{-1} at 100 °C) increased to an identical value (within error) to the reaction utilising **31** and Cy_2NH (**Figure 50**), highlighting the impact of the conjugate acid on the rate of reaction. The overall increase in conversion to **174** with **10** seemed, to be a result of less manganese being lost through the catalyst activation pathway, though with identical reaction mechanism.

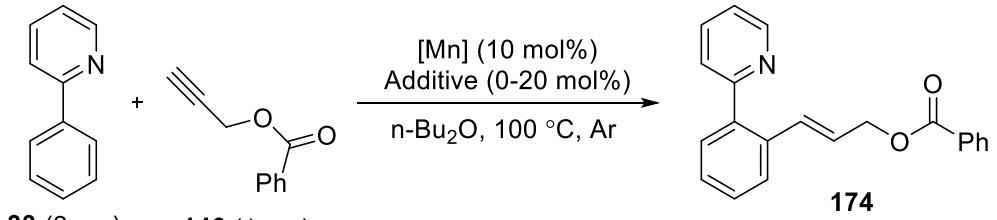

[Mn]	Additive	k_{obs} / 10^{-4} mol dm^{-3} s^{-1} (at 100 °C)
$MnBr(CO)_5$	Cy_2NH	5.2 ± 0.5
$Mn(ppy)(CO)_4$	None	0.99 ± 0.06
$Mn(ppy)(CO)_4$	$[Cy_2NH_2]BF_4$	5.2 ± 0.2

Figure 50. Observed rate constants (k_{obs}) for the reaction between **146** and **33** using either **10** or **31** as pre-catalysts with/without additives.

A distinct difference in the formation of the manganese degradation complexes was also observed. The previously detected species at 2022 cm^{-1} was still formed, while the complex at 2014 cm^{-1} did not appear, though it was replaced by a new species at 2038 cm^{-1}. This is a complex which surprisingly was not observed in the reaction using **31** and Cy_2NH (in which $[Cy_2NH_2]Br$ **62** should form), leading to the assumption that the BF_4 anion likely has an effect on the formation of this species. Therefore, it is likely that the generation of the species with distinct peaks at 2010, 2014 and 2038 cm^{-1} was determined by the anion in the reaction (Br^-, OH^- or BF_4^-).

4.2.3 *In Operando* IR Studies on the Conjugate Acid Additive Effect for *n*-Butyl Acrylate

To explain the negative effects of the conjugate acids on the reaction of butyl acrylate **148** with **33**, an investigation into the mechanism of these reactions was conducted. Initially, the reaction between *n*-butyl acrylate **148** (1 eq.) and **34** (1.5 eq.), mediated by **31** (10 mol%) and Cy_2NH (20 mol%) in *n*-Bu_2O at 100 °C under argon atmosphere was studied using *in operando* IR spectroscopy (**Figure 51**). **31** was rapidly consumed

(~3 min) after initiation of the reaction, which coincided with the formation and depletion of a new transient species with a distinct peak at 2093 cm^{-1}. As the two manganese carbonyl species disappears, **10** was forming in their place, suggesting that the specie at 2093 cm^{-1} was either an intermediate in the cyclomanganation mechanism or an off-cycle complex. A cationic manganese carbonyl complex with a 2-ppy ligand, was a species that could be formed following a loss of the bromide and would likely be one of the more stable species in the cyclomanganation mechanism. The formation of **10** in the reaction provided for a substantial difference in pre-catalyst activation mechanism from the terminal alkynes. This suggested that the alkene protons of the acrylate were not acidic enough to activate the manganese through a Mn-alkenyl complex.

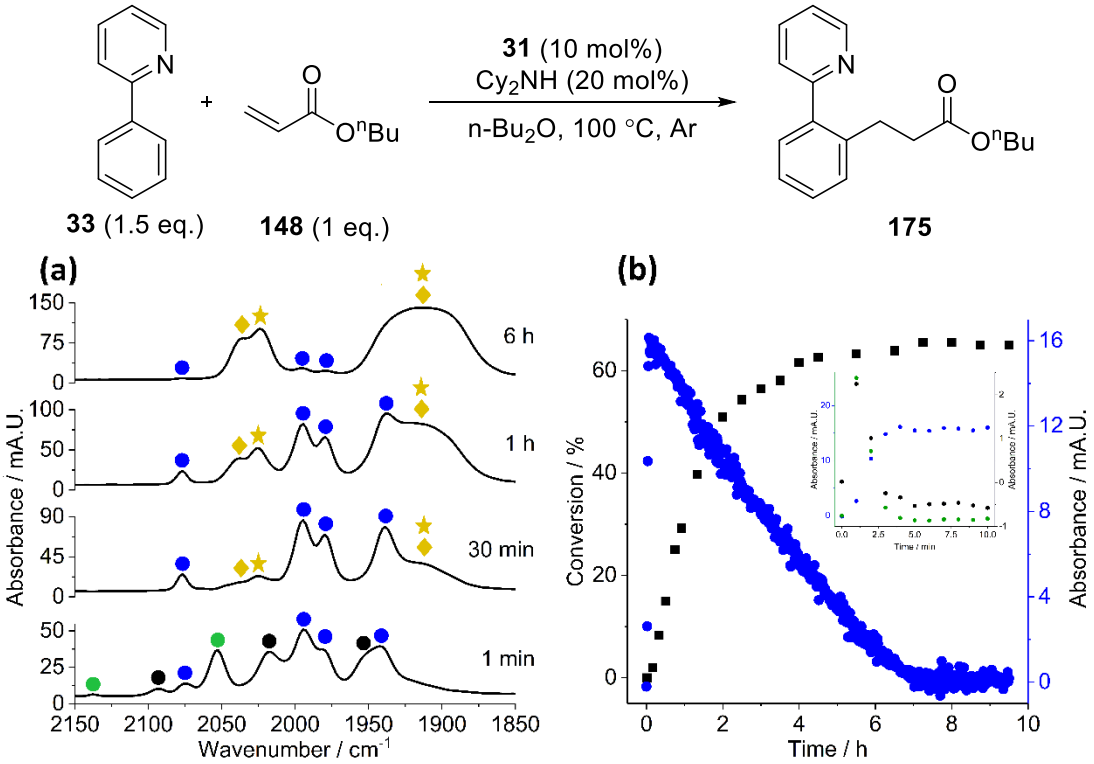

Figure 51. *In operando* IR study of the reaction between **148** and **33** using **31** as pre-catalyst. (a) IR spectra showing the metal carbonyl region at various timepoints. Key; green circle = **31**, blue circle = **10**, black circle = unknown transient manganese carbonyl species, gold star/diamond = Mn degradation complex, possibly a Mn-hydroxy cluster. (b) Kinetic plot at long and short timescales of the formation of alkenylated product **175** (black squares, determined by *ex situ* ^{1}H NMR spectroscopy) and formation and depletion of **10** (blue circles, band at 2078 cm^{-1}), **31** (green circles, band at 2054 cm^{-1}) and the unknown metal carbonyl species (black circles, band at 2093 cm^{-1}). Reaction conditions (in order of addition): *n*-Bu_2O (10 ml), **33** (15.0 mmol, 1.5 eq.), **148** (10.0 mmol, 1 eq.), Cy_2NH (2.0 mmol, 20 mol%) and **31** (1.0 mmol, 10 mol%) at 100 °C under argon.

Surprisingly, no species corresponding to a 7-membered insertion complex was observed in the reaction. Two degradation species (2025 and 2038 cm^{-1}) can be seen forming as **10** depletes and these complexes are strikingly similar to those formed

when ammonium salt **173** (20 mol%) was added to the reaction using alkyne **146** (1 eq., **Figure 49**). This indicated that degradation species were highly similar and does not involve the unsaturated substrate in their structure. The linear depletion of **10** may arise from the high concentration of the reaction and relatively low solubility of the manganese complex, which combined with the decreased rate of reaction over time, could lead to increased degradation of the manganese. The lack of other active manganese complexes observed in solution suggests that **10** is an off-cycle resting state of the reaction, which is in contrast to the terminal alkynes where the 7-membered tetracarbonyl insertion complex is the resting state of catalysis.

The organic product **175** formed as **10** was consumed and stopped forming when only degradation complexes remained in the metal carbonyl region of the IR spectrum. The duration of the reactions employing **148** was significantly longer than for the terminal alkynes (~20 times).

Following the understanding that **10** is the catalyst resting state when using acrylate **148**, the reaction was performed using **10** (10 mol%) as pre-catalyst with a 1:2 ratio of **148** to **33**, in order to simulate the experiments with and without conjugate acid additives added (**Figure 52**). In the reaction with no additive, a similar behaviour of **10** was observed (as with an excess of the acrylate), with a linear depletion as the reaction progressed. Apart from **10**, the two degradation complexes seen under standard conditions (using **31** and Cy_2NH) were observed forming as the only new manganese carbonyl species in solution. The similarity between the reactions using **10** or **31** as pre-catalysts, provide further evidence of the catalyst activation pathway under these conditions proceed through an initial C–H bond activation on 2-phenylpyridine **33** to generate **10**.

Addition of **62** (20 mol%) to the reaction changed the IR profile significantly (**Figure 52**). Firstly, the organic carbonyl stretches at 1732 cm^{-1} (**148**) and 1742 cm^{-1} (**175**), allowed for the monitoring of product formation directly from the IR spectra. The observed rate of reaction was almost halved when **62** was added (k_{obs} = 0.82 ± 0.04 × 10^{-4} mol dm^{-3} s^{-1} at 100 °C with **62** and k_{obs} = 1.34 ± 0.04 × 10^{-4} mol dm^{-3} s^{-1} at 100 °C with no **62** added), consistent with the lower conversion to product **174**. Both rates of product formation were similar to the rate observed for the reaction with alkyne **146**, using **10** as pre-catalyst (k_{obs} = 0.99 ± 0.06 × 10^{-4} mol dm^{-3} s^{-1} at 100 °C), which

suggested that CO-dissociation from **10** was rate determining under these reaction conditions.

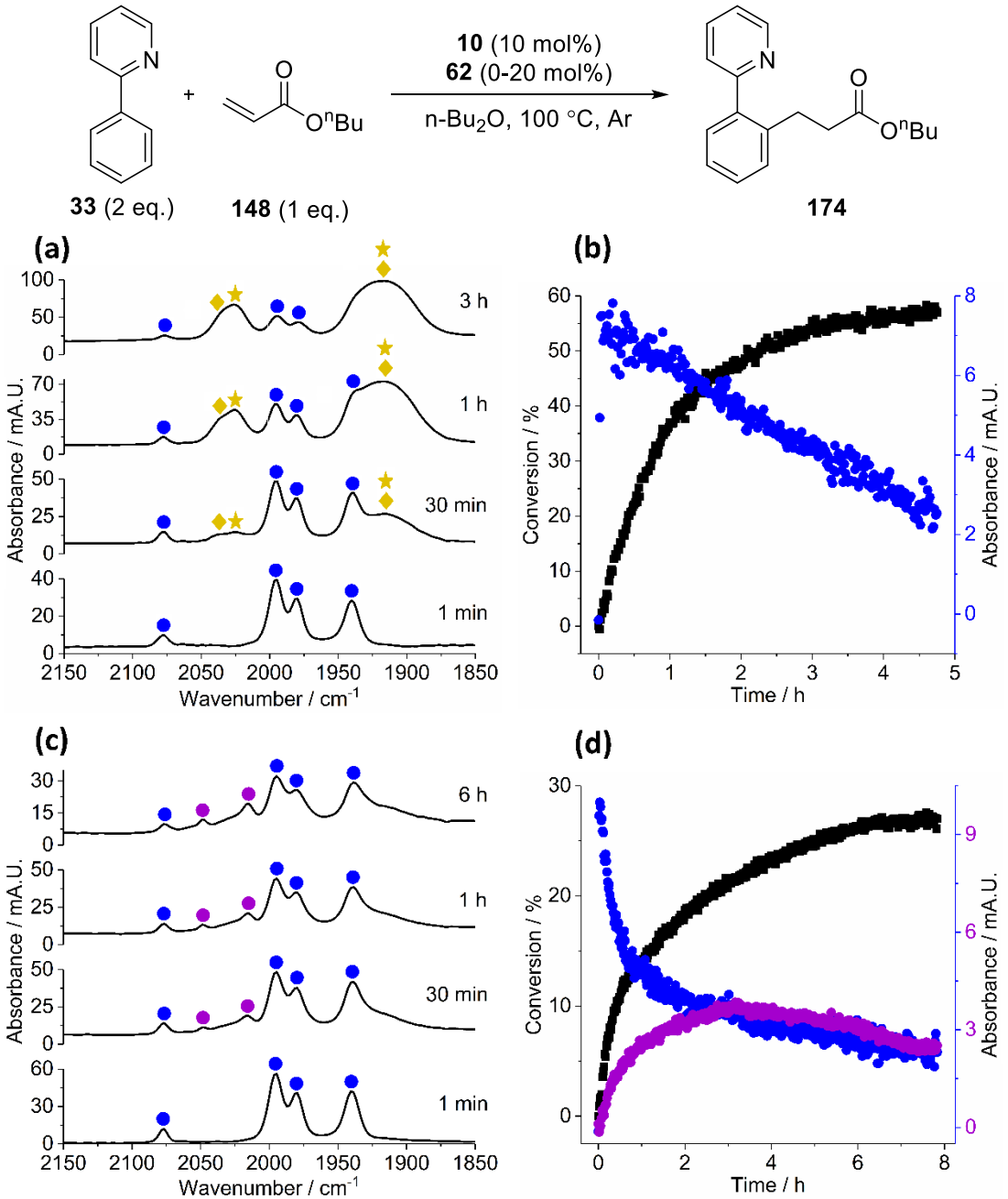

Figure 52. *In operando* IR study of the reaction between **148** and **33** using **10** as pre-catalyst with/without the addition of **62**. (a) IR spectra of the reaction with no additive showing the metal carbonyl region at various timepoints. Key; blue circle = **10**, gold star/diamond = Mn degradation complex, possibly a Mn-hydroxy cluster. Reaction conditions (in order of addition): *n*-Bu_2O (10 ml), **33** (8.32 mmol, 2 eq.), **148** (4.16 mmol, 1 eq.) and **10** (0.416 mmol, 10 mol%) at 100 °C under argon. (b) Kinetic plot of the formation of alkenylated product **175** (black squares, band at 1742 cm^{-1}), formation and depletion of **10** (blue circles, band at 2078 cm^{-1}), extracted from (a). (c) IR spectra of the reaction with **62** added showing the metal carbonyl region at various timepoints. Key; blue circle = **10**, purple circle = **40**. Reaction conditions (in order of addition): *n*-Bu_2O (10 ml), **33** (8.32 mmol, 2 eq.), **148** (4.16 mmol, 1 eq.), **62** (0.83 mmol, 20 mol%) and **10** (0.416 mmol, 10 mol%) at 100 °C under argon. (d) Kinetic plot of the formation of alkenylated product **175** (black squares, determined by *ex situ* ^1H NMR spectroscopy), formation and depletion of **10** (blue circles, band at 2078 cm^{-1}) and the formation and depletion of **40** (purple circles, band at 2047 cm^{-1}), extracted from (c).

Secondly, the previously described degradation complexes were not seen in any larger amounts, and a new species was instead formed at 2047 and 2013 cm^{-1}, corresponding to $Mn_2(CO)_{10}$ **40**. The shape of the depletion of **10** also changed to form an exponential decay over time, which coincided with the formation of **40**. This likely means that **40** was formed as a result from protiodemetallation of **10**, generating free **33** and a new manganese species that is more prone to further degradation to eventually form **40**.

The formation of **40**, combined with **10** being the catalyst resting state, therefore explains why the addition of $[Cy_2NH_2]X$ (X = Cl, Br or I) had a negative impact on the catalysis, in comparison to the terminal alkynes. The higher undesirable acid sensitivity of the catalyst resting state, led to a more extensive decomposition of the manganese than observed for the terminal alkynes. This takes place while not generating any of the desired product, which generated the negative effect observed. It is not clear from the studies conducted why the catalyst resting state differs between the substrates and further investigations are required for this to be determined.

4.2.4 Scope of Acid Additives in Mn(I)-Catalysed C–H Bond Functionalisation

The nature of the acid additive utilised in the C–H bond functionalisation discussed *vide supra* might impact on lowering catalyst degradation, and possibly aid in the protonation step of the 7-membered insertion complexes in the catalytic cycles. To test this hypothesis, strong acids HX (where X = Cl, Br, I or BF_4) were added (20 mol%) to the reaction mediated by **10** (10 mol%, **Figure 53**). Addition of HCl led to no enhancement in the formation of **174** (5% conversion), while the stronger acids HBr and HI resulted in inhibition the catalysis and only trace **174** was observed (≤ 1%). The lack of reactivity of the halogen derivatives likely stem from protiodemetallation readily occurring on the manganacycles (such as **10**), resulting in the formation of manganese tetracarbonyl halides which require base additives to active the C–H bonds in solution. However, the positive acid effect returned when HBF_4•OEt_2 was employed, affording 62% conversion to **174**. The non-coordinating nature of the BF_4 anion presumably prohibits the formation of manganese boron containing compounds, and instead allow for the suppression of catalyst degradation pathways as seen for the conjugate acid additives.

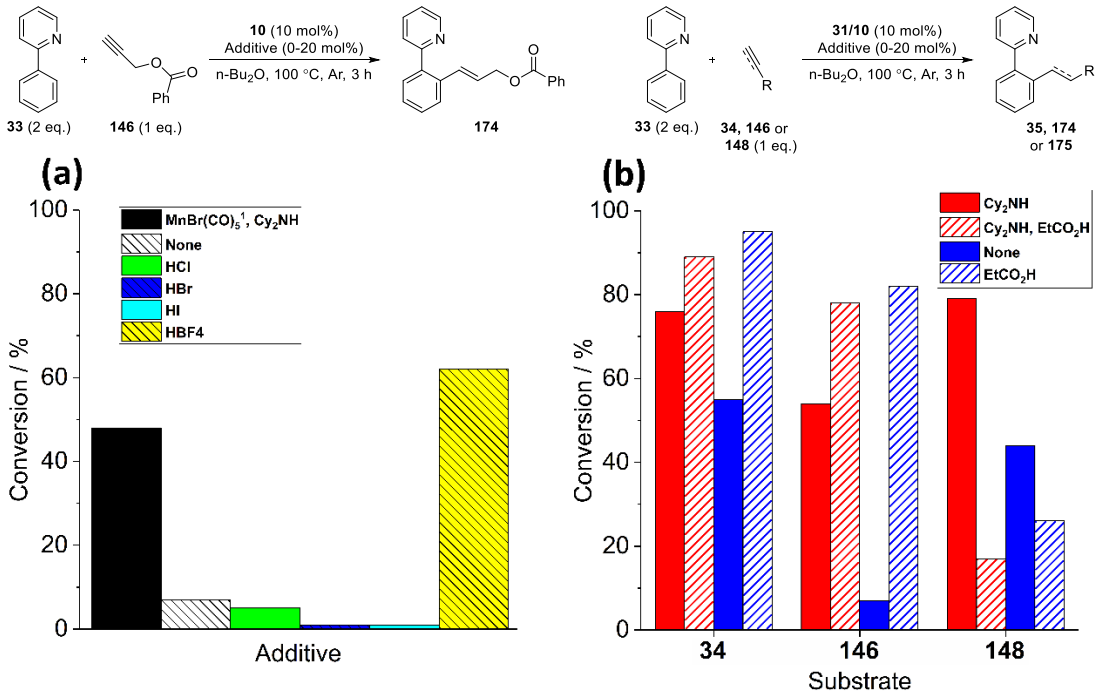

Figure 53. [1]**31** used instead of **10** as pre-catalyst. (a) The effect of strong acid additives in the reaction between **146** and **33**. Reaction conditions: **146** (0.25 mmol, 1 eq.), **33** (0.5 mmol, 2 eq.), **10** (0.025 mmol, 10 mol%), additive (0.05 mmol, 20 mol%) and *n*-Bu_2O (0.6 ml) at 100 °C under argon for 3 h. (b) The effect of carboxylic acid additives in the reaction between **146** and **33** using either **31** or **10** as pre-catalyst.

Establishing that there is a limit on the nucleophilicity of the conjugate base to the acid additive, carboxylic acid additives were explored. A manganese carbonyl acetate species should be able to readily activate C–H bonds,[156] which means that hypothetically the carboxylic proton source could aid the reaction in three main modes of action;

1. The inhibition of catalyst degradation pathways, prolonging the catalyst lifetime.
2. The protonation step of the catalysis, increasing rate of reaction.
3. Mediating the subsequent C–H activation step post-protonation.

Performing the reaction with **10** (10 mol%) and $EtCO_2H$ (20 mol%), added to the reaction of propargyl benzoate **146** (1 eq.) with **33** (2 eq.), significantly enhanced the conversion to **174** (82% compared to 7% without additive). Since both acetate and amine bases are active under catalytic reactions,[34] the addition of propionic acid to the reaction employing **31** and Cy_2NH should not inhibit the initial C–H activation. Performing the reaction using **31** (10 mol%) with both Cy_2NH (20 mol%) and propionic acid (20 mol%) added, still yielded the product **174** in high conversion (78%).

The exploration of the effect of propionic acid in the catalysis was expanded to phenyl acetylene **34** and butyl acrylate **148**. The formation of product **35** was enhanced to 95% in the reaction using **10**, which is an improvement of 40% to the reaction with no additives added. The same trend was seen in the system using **31** and Cy_2NH (89%), both results marking a discrepancy from the earlier trend observed for the conjugate acid additives (which showed no impact on the catalysis with **34**). **148** did however continue the previous trend, in which the acid additives have a negative impact on the catalysis. Addition of propionic acid to the reactions employing either **10** or **31** (with Cy_2NH) as pre-catalysts, had a large negative impact yielding the product **175** in 26% and 17% respectively.

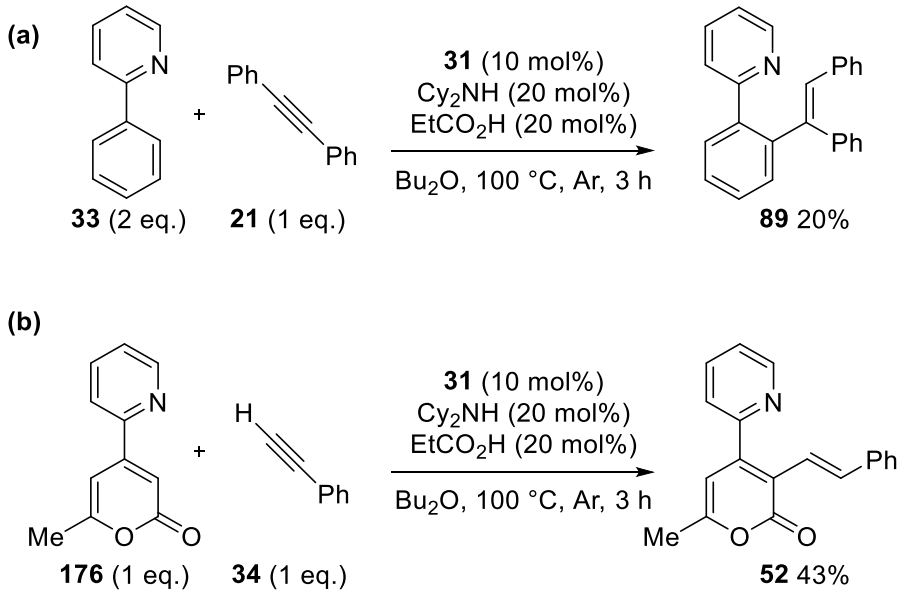

Scheme 37. Synthesis of alkenylated 2-phenylpyridines unachievable using standard reaction conditions. (a) Reaction between **21** and **33** with propionic acid added, generating the alkene product **89**. (b) Reaction between **34** and **176** with propionic acid added, generating the alkene product **52**.

The positive effects of the addition of propionic acid on the alkyne substrates, and its potential to aid in the protonation of unreactive (under standard conditions) 7-membered insertion complexes, led to attempts to perform the alkenylation reaction using an internal alkyne and a previously unreactive (toward protonation pathways) 2-pyridyl-2-pyrone derivate (**Scheme 37**). For the reaction between **33** (2 eq.) and diphenylacetylene **21** (1 eq.), using **31** (10 mol%) and Cy_2NH (20 mol%) in *n*-Bu_2O at 100 °C under argon atmosphere, the addition of propionic acid (20 mol%) gave 20% yield of the isolated product **89**. Another positive impact of propionic acid (20 mol%) was observed in the reaction using 2-(2-pyridyl)-6-methyl-2-pyrone **176** (2 eq.) with **34** (1 eq.) using **31** (10 mol%) and Cy_2NH (20 mol%), where alkenylated 2-pyrone **52**

was isolated in 43% yield. Despite the low to modest yields observed, this was still an example of synthetic methodology improvement, which was only possible through the understanding of the reaction mechanism.

4.2.5 Development of "On-Water" Reaction Conditions

Following the positive impact of the acid additives and the viable protonation ability of H_2O (see Chapter 2.6), it was thought that water might have a similar influence on the reactions as the acids. To probe this, a reaction of **146** (1 eq.) and **33** (2 eq.) in water at 100 °C was performed using $MnBn(CO)_5$ **19** (10 mol%) as pre-catalyst, to avoid the use of the amine base additive (**Figure 54**). This methodology led to good yield (69%) of isolated **174**. An inert atmosphere was not necessary, and it was found that the reaction can proceed under ambient air. The addition of propionic acid (20 mol%) to this reaction did not influence the yield (70%), which still is a 22% improvement over the procedure using inert atmosphere and organic solvent (*n*-Bu_2O). When the manganese pre-catalyst were changed to $MnBr(CO)_5$ **31** (10 mol%), the reaction yield remained fairly high at 53%, and did not require any addition of external base additives. The lack of need for base additives might arise from the *in situ* formation of a $MnOH(CO)_4X$ (where X = CO, H_2O, **33**, **146** or formation of a dimeric complex) species, which is more active towards C–H bond activation. Propionic acid (20 mol%) had a slight positive impact on raising the yield of isolated product to 61%.

To test whether the reactions *vide supra* are influenced by the solvation in the water, or if the reactions are in effect being run in neat substrates, the solubility of the reagents in water was tested. Small amounts of the reagents were transferred into an NMR tube before D_2O was added. Thereafter, ^1H NMR was recorded at 25, 40, 50, 60, 70, 80 and 90 °C to observe if the reagent is soluble in water, as it should appear in the NMR spectra. None of **146**, **34**, **33** and **10** were found to be soluble in D_2O, strongly suggesting that the reaction is being run neat. However, when the reaction between **146** (1 eq.) and **33** (2 eq.), with **10** (10 mol%) added was performed without any solvent added (both **146** and **33** are liquids) the reaction only gave 30% conversion. The low conversion to **174** suggests that there might be an influence of either the excess water that will be present, or that the water at the solvent interfaces might be more activated to aid in the protonation step. The "on-water" effect has previously been reported by

Sharpless and co-workers in the preparation of 1,2-diazetidines, where low solubility of the reagents significantly enhanced the rate of product formation (even compared reaction in neat substrates).[160]

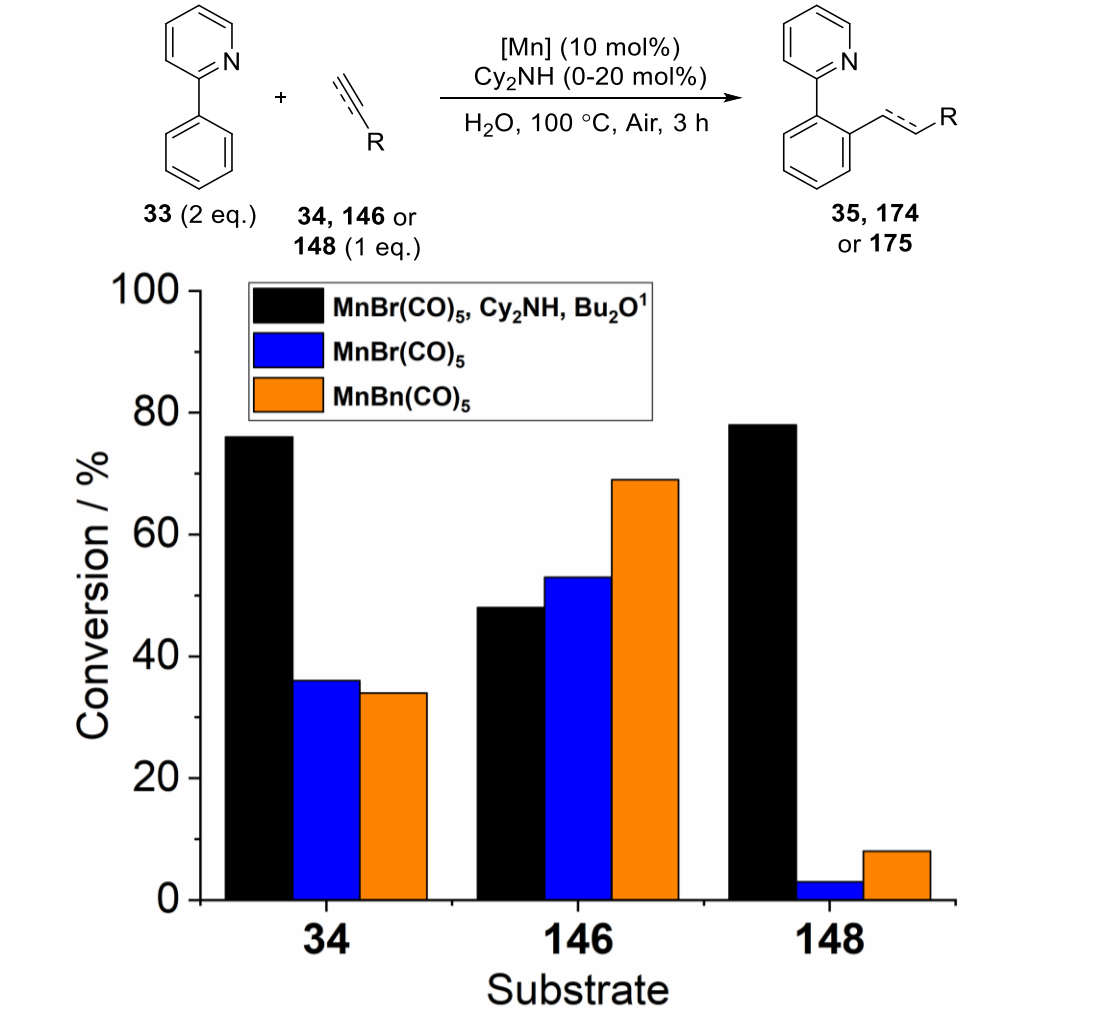

Figure 54. $^{1}Bu_2O$ used as solvent instead of H_2O. The effect of using H_2O as solvent in the reaction between various unsaturated substrates and **33**. Reaction conditions: unsaturated substrate (0.25 mmol, 1 eq.), **33** (0.5 mmol, 2 eq.), [Mn] (0.025 mmol, 10 mol%), additive (0.05 mmol, 20 mol%) and H_2O (0.6 ml) at 100 °C under air for 3 h.

Unexpectedly, the yield of the reactions employing **34** as the unsaturated substrate and **31** or **19** as pre-catalysts only reached 36% and 34% respectively. This constitutes a lowering of the yield by 42% for **31**, compared to the reaction in organic solvent and under inert atmosphere. The negative effect could be a result from a different composition of the solvent interface or that the reaction using **34** is more sensitive to degradation into manganese hydroxyl-clusters. As expected, low conversion to product was observed when the reaction was performed with acrylate **148**, only generating the product **175** in 3% and 8% respectively for **31** and **19** as pre-catalysts.

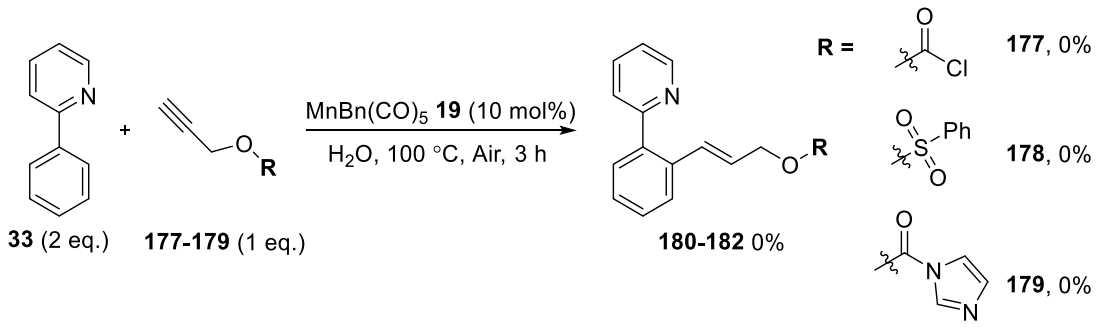

Scheme 38. Effect of changing the unsaturated substrate to alkynes structurally similar to propargyl benzoate, in the reaction employing H_2O as solvent.

To probe the applicability of the propargyl benzoate substrate **146**, similar substrates were employed (**Scheme 38**). Unfortunately, the use of acid chloride derived, propargyl chloroformate **177**, yielded no formation of the desired alkenylated product. No product formation could also be seen for the sulfonate derived propargyl benzenesulfonate **178** and the imidazole containing propargyl 1H-imidazole-1-carboxylate **179**. The lack of reactivity in structurally similar systems to propargyl benzoate suggest that there is an issue with them being more water soluble or that the positive effect for **146** is of a remarkably high substrate specificity.

4.3 Monitoring Protonation Mechanism using Time-Resolved IR Spectroscopy

4.3.1 Protonation Mechanism on Tetracarbonyl Manganese 2-Phenylpyridines

To study the mechanism of protonation by the carboxylic acid additives in further detail than in Chapter 4.2, Time-Resolved Infra-Red (TRIR) spectroscopy was identified as a suitable technique. As a proof of concept, the protiodemetallation of $Mn(ppy)(CO)_4$ **10** by acetic acid to form free 2-phenylpyridine was studied (**Scheme 39**). The photolysis of **10** using 355 nm light should dissociate one CO-ligand to give a *fac*-$[Mn(ppy)(CO)_3L]$ (**Chapter 3**), where L is an acetic acid ligand if performed in neat substrate. The initial coordination should take place on sub-picosecond timescale as previously observed for other substrates (**Chapter 3**). The mode of binding will likely proceed through the most kinetically favoured configuration, before the first timepoint is obtained (0.5 ps). The subsequent rearrangement to form a more energetically favourable structure (provided the kinetically and thermodynamically

preferred structures are different) should take place within the observable time window (0.5 ps – 1 ms). If one of the formed configurations place the OH group in a suitable position to interact with the **C**–Mn, the proton transfer event might also be detected in the experiment.

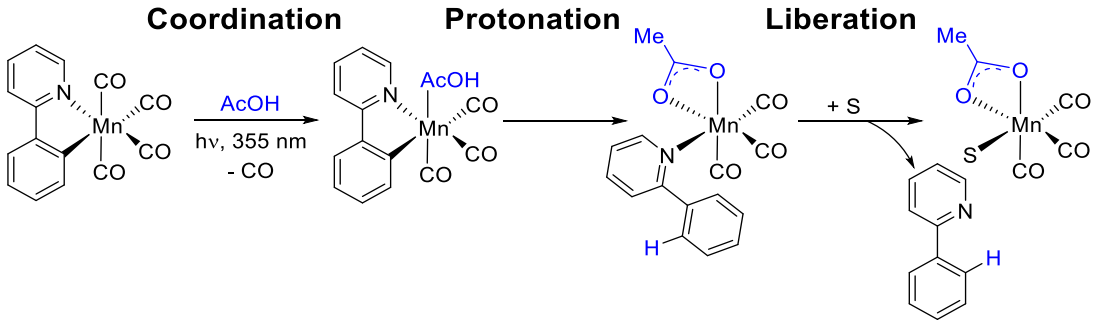

Scheme 39. Proposed mode of action for the acid degradation of Mn(ppy)(CO)$_4$ **10** under photolysis conditions.

To probe the hypothesis, **10** was dissolved in acetic acid (1.74×10^{-3} mol dm^{-3}), irradiated using 355 nm light and probed using TRIR spectroscopy (LIFEtime experimental setup, **Figure 55**). Initially, a σ-complex bound acetic acid complex **183** (bands at 2012 and 1911 cm^{-1}) was assigned, due to the similarity to other complexes, such as σ-complex bound ethyl acrylate species (bands at 2011, 1914 and 1897 cm^{-1}, **Chapter 3.6.1**). This complex rapidly rearranged to form a new species **184** (bands at 2003 and 1903 cm^{-1}) over the first few 10's of picoseconds ($k_1 = 5.2 \pm 0.7 \times 10^{10}$ s^{-1} at room temperature). The bands were similar to the O-bound ethyl acetate complex (bands at 2001, 1904 and 1895 cm^{-1}), leading to the assignment of **184** as the O-bound acetic acid complex, where the OH is uncoordinated. The similar rate of formation of the O-bound species for both AcOH and EtOAc ($5.2 \pm 0.7 \times 10^{10}$ s^{-1} at room temperature and $8 \pm 1 \times 10^{10}$ s^{-1} at room temperature respectively) also supported the structural assignment.

A new tricarbonyl manganese species **185** (bands at 2011 and 1892 cm^{-1}) formed and remained in solution during the depletion of **184** ($k_2 = 1.3 \pm 0.1 \times 10^{8}$ s^{-1} at room temperature). Unfortunately, no kinetic trace for **185** could be obtained due to spectral overlap. The reason for the low amounts of **185** formed was the rapid consumption to form tricarbonyl manganese complex **186** (bands at 2041, 1947 and 1925 cm^{-1}, $k_3 = 1.3 \pm 0.1 \times 10^{8}$ s^{-1} at room temperature). The long lifetime of the final photoproduct **186**, in combination with the large shift in the IR frequencies, led to an assignment of this being the acetate-bound complex formed following proton transfer. Seeing that

184 and **186** were the expected structures pre- and post-protonation, joint with the rapid rate of consumption of **185**, infers that **185** was an intermediate either immediately prior or after the protonation event. The proton transfer event and subsequent rearrangement to generate **186** should be relatively quick, meaning that **185** most likely was an intermediate pre-protonation. On this basis, **185** was tentatively assigned to be a complex where the H is hydrogen-bonded to the **C**-Mn.

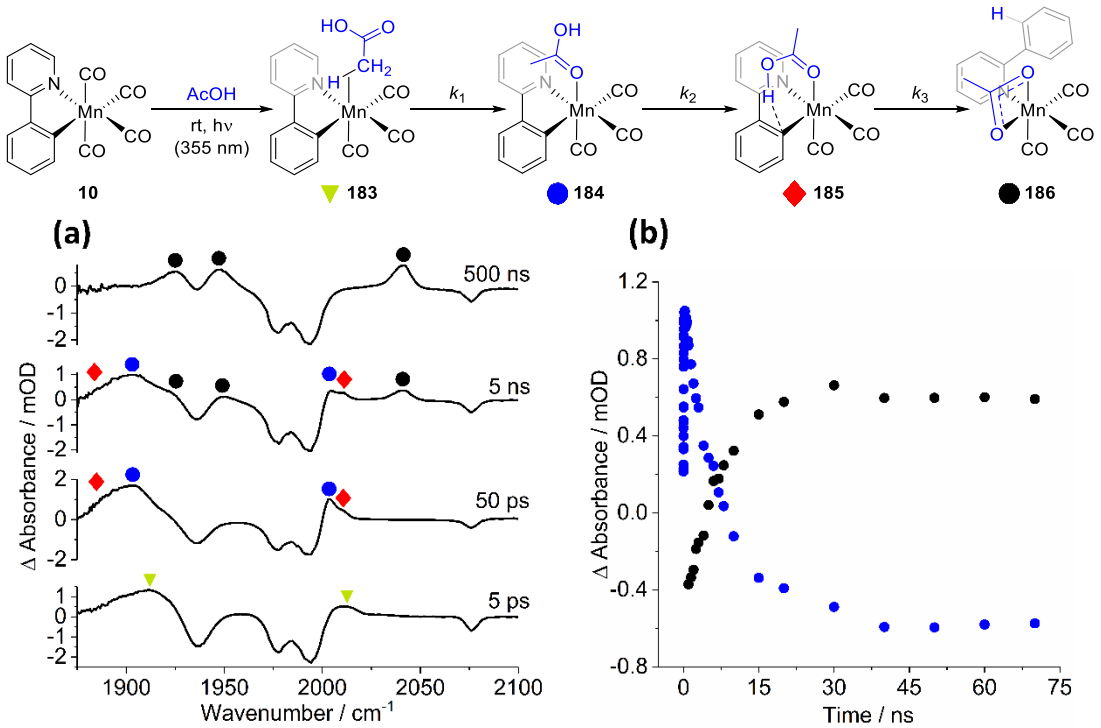

Figure 55. TRIR study of the photolysis of **10** in neat acetic acid (1.74×10^{-3} mol dm^{-3}), showing the formation of the various species in solution after irradiation. (a) IR spectra of the reaction showing the metal carbonyl region at various timepoints. Negative bleach bands correspond the loss of **10** after irradiation. (b) Kinetic plot of the formation of **186** (black circles, band at 2041 cm^{-1}), formation and depletion of **184** (blue circles, band at 2003 cm^{-1}), extracted from (a).

The full mechanism of the proton transfer event was evaluated using DFT-calculations (all DFT-calculations in this chapter was performed by Dr. Jason M. Lynam, **Scheme 40**), showing that the process most likely proceeded from hydrogen-bonded complex **185**, supporting the structural assignment made previously. This complex transferred the proton to the **C**–Mn, where the low-lying transition state **187** ($\Delta G^{\ddagger}$ = +14 kJ mol^{-1}) explained the rapid reaction rate. Following the completed proton transfer, the resulting σ-complex **188** was isomerised to form the observed manganese acetate tricarbonyl species **186**. **186** was significantly lower in energy than **185** (24 kJ mol^{-1}), clarifying why the equilibrium favours **186**.

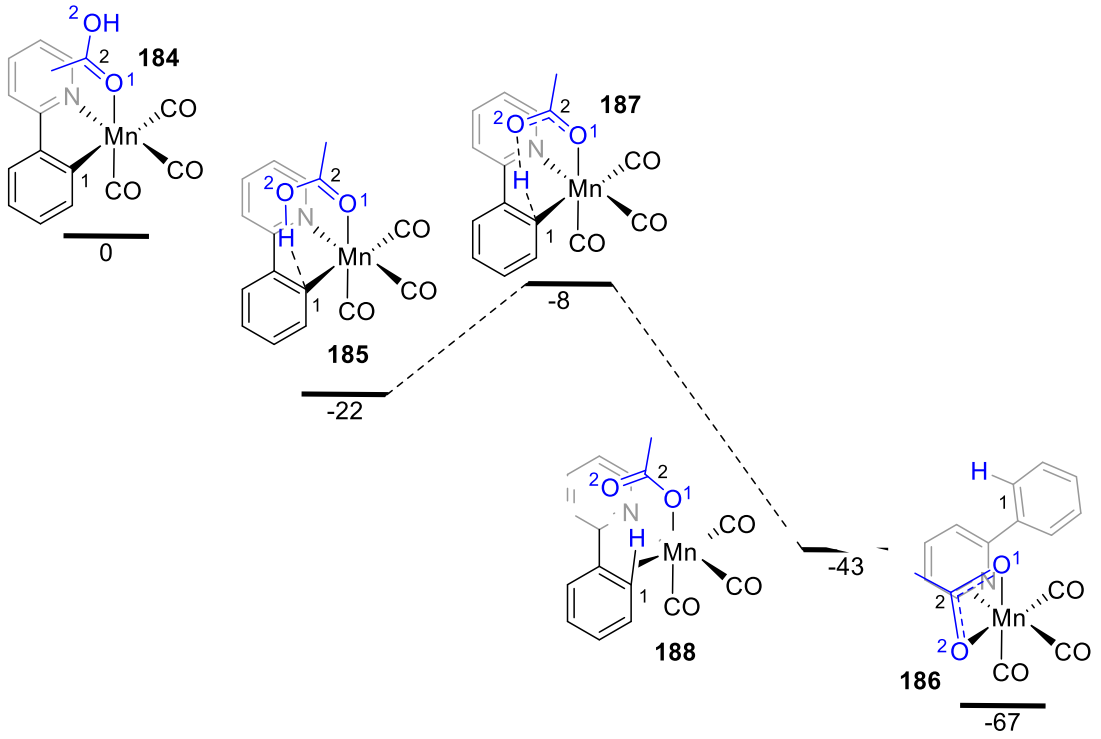

Scheme 40. DFT-calculated (performed by Dr. Jason M. Lynam) mechanism for the protonation of **10** by acetic acid. Energies are free energies in kJ mol^{-1} at 298 K. Calculations were performed at the (RI-)BP86/SV(P) level.

The bond lengths of the DFT-calculated structures were examined to gain information into the nature of the various bonds, in particular the C–O bonds as they experience significant changes during the proton transfer (**Table 8**). It can be seen that there was a clear C=O and C–OH bond division for both complex **184** (O^1 1.23 = Å and O^2 = 1.35 Å) and **185** (O^1–C^2 = 1.24 Å and O^2–C^2 = 1.32 Å), where the hydrogen was still formally bound to the oxygen and provided no distortion to the expected bonding in the acetic acid molecule. Transition state **187** did however show that the bond lengths for both C–O bonds were the same (O^1–C^2 = 1.27 Å and O^2–C^2 = 1.28 Å) and therefore should be depicted as being conjugated as in an κ_1-acetate type complex. Following proton transfer, the C–O bond lengths went back to being different (O^1–C^2 = 1.30 Å and O^2–C^2 = 1.24 Å), this time with the former hydroxy C–O bond being of the double bond character. A conjugate system is regained after the rearrangement to form the final acetate bound complex **186** (O^1–C^2 = 1.28 Å and O^2–C^2 = 1.28 Å).

Table 8. Key DFT-calculated bond lengths of intermediates involved in protonation of **10** by acetic acid. Calculations were performed at the (RI-)BP86/SV(P) level.

Entry	Bond	184 / Å	185 / Å	187 / Å	188 / Å	186 / Å
1	C^1–Mn	2.05	2.07	2.19	2.44	3.55
2	O^1–Mn	2.12	2.13	2.08	2.02	2.09
3	C^2–O^1	1.23	1.24	1.27	1.30	1.28
4	C^2–O^2	1.35	1.32	1.28	1.24	1.28
5	O^2–H	0.98	1.03	1.28	1.93	2.13
6	C^1–H	5.18	1.84	1.37	1.14	1.10

The protiodemetallation of **10** by AcOH was performed at half the concentration of manganese, to ensure the correct assignment of **186** and to make sure it was not a manganese acetate tricarbonyl dimer ($[Mn(\kappa_1\text{-}OAc)(CO)_3]_2$). The rate of proton transfer (k_3) should be first order in manganese (the limiting reagent), due to the pseudo-first order conditions under which the reaction is run. The observed rate for the reaction at half concentration did show a decrease in k_3 ($1.5 \pm 0.3 \times 10^8$ s^{-1} at room temperature compared to $1.3 \pm 0.1 \times 10^8$ s^{-1} at room temperature, under standard concentration), corresponding to the reaction being first order in manganese. Due to k_3 being relatively fast, the rate of dimerization must be faster than the diffusion controlled rate.

Two acids, propionic acid ($EtCO_2H$) and butyric acid (n-$PrCO_2H$), with varied alkyl chain length were employed instead of AcOH, as they should exhibit similar acidity (**Table 9**). The rate of the initial rearrangement (k_1) was similar for all the acids, with slightly lowered rates as the chain length increased. This could arise from the manganese initially binding to a terminal C–H bond, before chain walking towards the carbonyl oxygen as seen in neat acrylates (see Chapter 3.6.1). There was however a large difference in behaviour in the formation of the hydrogen-bonded complex, where propionic acid rearranged more than an order of magnitude faster than acetic acid (k_2 = $3.6 \pm 1.0 \times 10^9$ s^{-1} at room temperature and $0.13 \pm 0.01 \times 10^9$ s^{-1} at room temperature respectively). Where this difference originated from is unclear and requires further studies to be determined. The value of k_2 for butyric acid could not be determined due to spectral overlap. The rate of the final proton transfer step showed a linear increase with increasing alkyl chain length with a range of rates between 1.27–3.12 s^{-1}. It is

unclear where this slight increase in rate could arise from, but it is possible that a longer chain somehow through steric effects lowers the activation barrier for this step.

Table 9. Rates of the protonation steps (of **10**) at room temperature by carboxylic acids with varying chain length.

Entry	Acid	k_1 / 10^{10} s^{-1}	k_2 / 10^{9} s^{-1}	k_3 / 10^{8} s^{-1}
1	Acetic acid	5.2 ± 0.7	0.13 ± 0.01	1.3 ± 0.1
2	Propionic acid	5 ± 2	3.6 ± 1.0	2.5 ± 0.5
3	Butyric acid	3 ± 1	–[1]	3.1 ± 0.6

[1]Not obtainable due to spectral overlap.

4.3.2 Kinetic Isotope and Ligand Effects on Protonation Mechanism

The experiment in neat AcOH was repeated with AcOD, in order for the kinetic isotope effect (KIE) of the various steps to be determined (**Figure 56**). Firstly, no spectroscopic information could be obtained above 1970 cm^{-1} due to the absorbance of AcOD, and the KIE for the first two steps (k_1 and k_2) was not be determined due to spectral overlap. A large KIE of 5.8 ± 1.0 was observed for the proton transfer (k_3 = 2.2 ± 0.3 s^{-1} at room temperature in AcOD), indicating that the O–H bond is broken in this step. The information gained from the KIE experiment further supported that for the first time the direct observation of the relevant intermediates and kinetic information had been obtained of a proton transfer process, in accordance with the CMD/AMLA-6 mechanism. The observations also support the assignment of **185** being the H-bonded complex pre-protonation, as its depletion should involve O–H bond breakage.

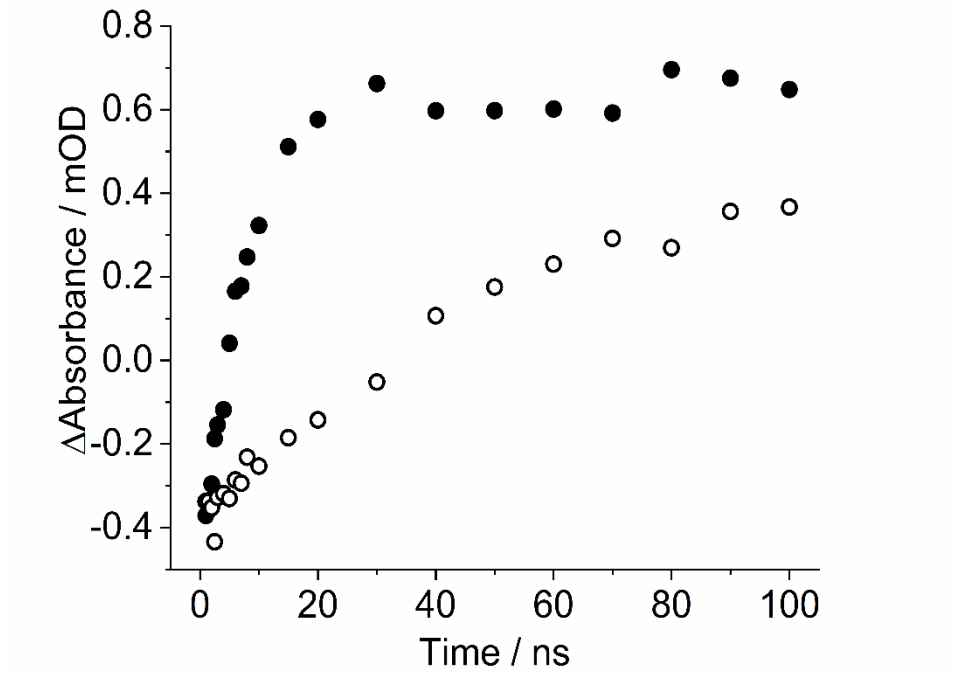

Figure 56. Kinetic trace of k_3 in the TRIR monitored protiodemetallation of **10** with AcOH (closed black circles) and AcOD (open black circles).

The photolysis experiment in neat AcOH was expanded to include other manganacycles to investigate if the protiodemetallation mechanism were generally applicable or specific for the 2-phenylpyridine derivative (**Table 10**). Surprisingly, changing the phenyl group to a 2-pyrone (**50**) or 2-pyridone (**129**), led to a substantially lower rate of protonation by almost two orders of magnitude ($3.4 \pm 0.6 \times 10^6$ s^{-1} at room temperature and $4.8 \pm 0.7 \times 10^6$ s^{-1} at room temperature respectively). This impact on changing the arene was inconsistent with the expected trend of rates (**129** > **50** > **10**), based on the relative nucleophilicity of the arene, as previously observed for the insertion of alkyne **34** into the C–Mn bond (Chapter 3.4.1). It should be noted that **129** reacted faster than **50**, following the trend of the insertion chemistry. This suggests that the phenyl ring somehow reacted differently than the other two ring systems. It is also possible that the additional heteroatoms present in **50** and **129** provide an interfering effect on the proton transfer event, possibly through H-bond acceptance. Kinetic information on the formation of the species preceding proton transfer was not obtained due to spectral overlap, rendering it difficult to precisely determine the reason for the unexpected behaviour. The large KIEs observed (5.6 ± 1.6 and 4.1 ± 0.7 for **50** and **129** respectively) and large similarity of IR stretching band (distinctive peak at 2041 and 2042 cm^{-1} for **50** and **129** respectively), confirmed that the H-transfer (through a CMD/AMLA-6 mechanism) to form the expected manganese acetate tricarbonyl complex, was the final step for **50** and **129** as well.

Table 10. Rates of protonation at room temperature in neat AcOH obtained for various manganacycles.

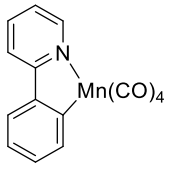

10

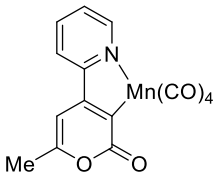

50

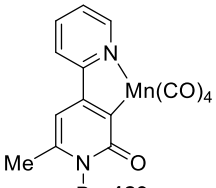

129

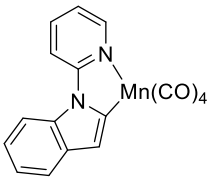

130

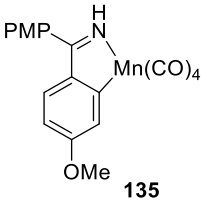

135

Entry	Complex	k_1 / 10^{10} s^{-1}	k_2 / 10^8 s^{-1}	k_3 / 10^7 s^{-1}	KIE (k_3)
1	**10**	5.2 ± 0.7	1.3 ± 0.1	13 ± 1	5.8 ± 1.0
2	**50**	–[1]	–[1]	0.34 ± 0.06	5.6 ± 1.6
3	**129**	–[1]	–[1]	0.48 ± 0.07	4.1 ± 0.7
4	**130**	0.12 ± 0.02	7 ± 2	9 ± 3	3.4 ± 1.4
5	**135**	5 ± 1	–[1]	28 ± 3	4.1 ± 0.7

[1]Not obtainable due to spectral overlap.

N-(2-pyridyl)indole **130** demonstrated a similar reactivity as previously observed for the insertion of **34** into the C–Mn bond (see **Chapter 3.4.1**), where the crucial C–Mn bond breaking step is slower than for **10** ($k_3 = 9 \pm 3 \times 10^7$ s^{-1} at room temperature and $1.3 \pm 0.1 \times 10^8$ s^{-1} at room temperature respectively, **Table 10**). The initial rearrangement of the σ-complex bound species to form the O-bound complex (with free OH), was again slower for indole **130** than for the phenyl derivative ($k_1 = 1.2 \pm 0.2 \times 10^9$ s^{-1} at room temperature and $5.2 \pm 0.7 \times 10^{10}$ s^{-1} at room temperature respectively). Surprisingly, the rearrangement to form the hydrogen-bonded complex was quicker for the indole ($k_2 = 7 \pm 2 \times 10^8$ s^{-1} at room temperature, compared to $1.3 \pm 0.1 \times 10^8$ s^{-1} at room temperature for **10**), which combined with the slow proton transfer suggested a significant stabilisation of the hydrogen-bonded intermediate. The kinetic isotope effect was also slightly lower at 3.4 ± 1.4, while still being large enough to show that O–H bond breakage took place in the final step.

The usage of imine containing manganacycle **135** led to a strong resemblance in behaviour to **10** (**Table 10**). The initial rearrangement step (k_1) was virtually identical ($5 \pm 1 \times 10^{10}$ at room temperature, compared to $5.2 \pm 0.7 \times 10^{10}$ s^{-1} at room temperature for **10**) and the final proton transfer step was slightly quicker for **135** ($2.8 \pm 0.4 \times 10^8$ at room temperature compared to $1.3 \pm 0.1 \times 10^8$ s^{-1} at room temperature for **10**). This was consistent with both pyridines and imines exhibiting similar catalytic activity. Kinetic information for the rearrangement to form the hydrogen-bonded complex was

not obtainable due to spectral overlap. The KIE of 4.1 ± 0.7 was slightly lower than for **10** and might arise from the reasons discussed above for the indole derivative **130**.

4.3.3 Protonation Mechanism in Toluene Solution

To simulate a more catalytically relevant environment, the protonation of **10** by AcOH was performed in toluene solution ([**10**] = 1.89 × 10^{-3} mol dm^{-3}, [AcOH] = 0.79 mol dm^{-3} (418 eq. with respect to Mn), **Figure 57**). A toluene complex should form at early times, before the acetic acid can substitute for Mn-binding. The number of steps of the protonation (k_1–k_3) that is observable will, depend on how long it takes for the acetic acid to substitute the toluene.

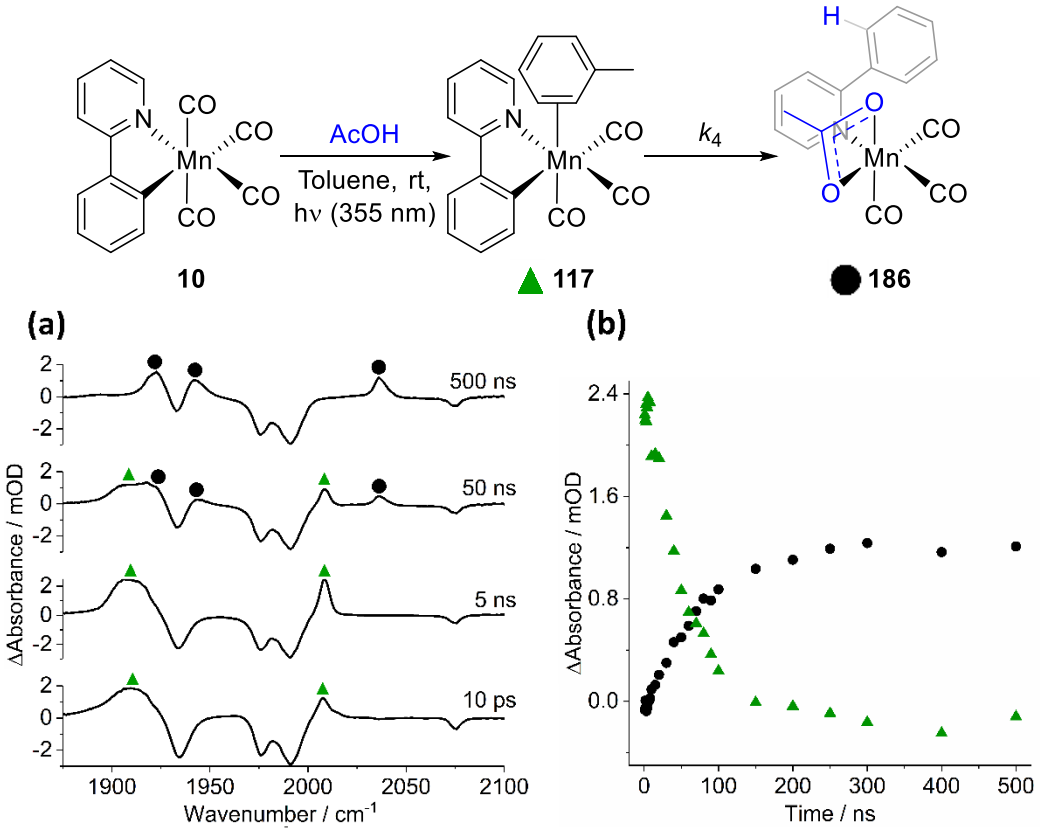

Figure 57. TRIR study of the photolysis of **10** in AcOH/toluene solution ([**10**] = 1.89 × 10^{-3} mol dm^{-3}, [AcOH] = 0.79 mol dm^{-3}), showing the formation of the various species in solution after irradiation. (a) IR spectra of the reaction showing the metal carbonyl region at various timepoints. Negative bleach bands correspond the loss of **10** after irradiation. (b) Kinetic plot of the formation of **186** (black circles, band at 2041 cm^{-1}) and depletion of **117** (green triangles, band at 2008 cm^{-1}), extracted from (a).

Initially, toluene-bound complex **117** was observed (bands at 2008 and 1909 cm^{-1}). Towards longer nanosecond timescales, this complex was replaced by the acetate-bound tricarbonyl manganese complex **186** (bands at 2036, 1942 and 1922 cm^{-1}). This demonstrated that the substitution was slow compared to the rearrangement steps observed in neat AcOH, which is why the other short-lived intermediates was not

detected. The substitution being rate determining was reflected in the rate of formation of **186** (k_4 = 1.27 ± 0.09 × 10^7 s^{-1} at room temperature), which was an order of magnitude slower than in neat AcOH (k_4 = 1.3 ± 0.1 × 10^8 s^{-1} at room temperature). The fingerprint region (1450-1800 cm^{-1}) were also monitored to observe the organic carbonyl stretches. A bleach band corresponding to the loss of AcOH was seen growing over time. This band could not be detected in neat AcOH due to saturation of the bleach band. Unfortunately, no IR bands were observed for the acetate-bound species **186**.

The slow substitution of the toluene-ligand in the experiment, relative to the protonation event itself means that there should be a concentration dependence of acetic acid on the rate of formation of **186** (k_4). In order to probe this, the concentration of AcOH in solution was varied (0.04–0.79 mol dm^{-3}) and resulted in the expected rate increase of **186** formation with increasing [AcOH] (**Figure 58**). Firstly, the increasing rate of k_4 with higher [AcOH] suggested that the rate determining step of k_4 was the substitution of toluene by acetic acid, which means that further details of the proton transfer step was not obtainable. The graph obtained may show a slight curvature, which could indicate that AcOH is not rate determining at very high acid concentrations. However, it was difficult to distinguish this from the expected linear plot using this data and experiments at higher [AcOH] could aid in the determination of the curvature of the plot. If the plot was assumed to be linear, the second order rate constant for the reaction could be determined (by a linear regression of k_4 vs. [AcOH]) to be 1.7 ± 0.2 × 10^7 mol^{-1} dm^3 s^{-1} (at room temperature). No solid acid additives were used to obtain further information about substituent effects (on for example benzoic acids) or KIE determination, as the relevant data could only be obtained in neat (liquid) acids.

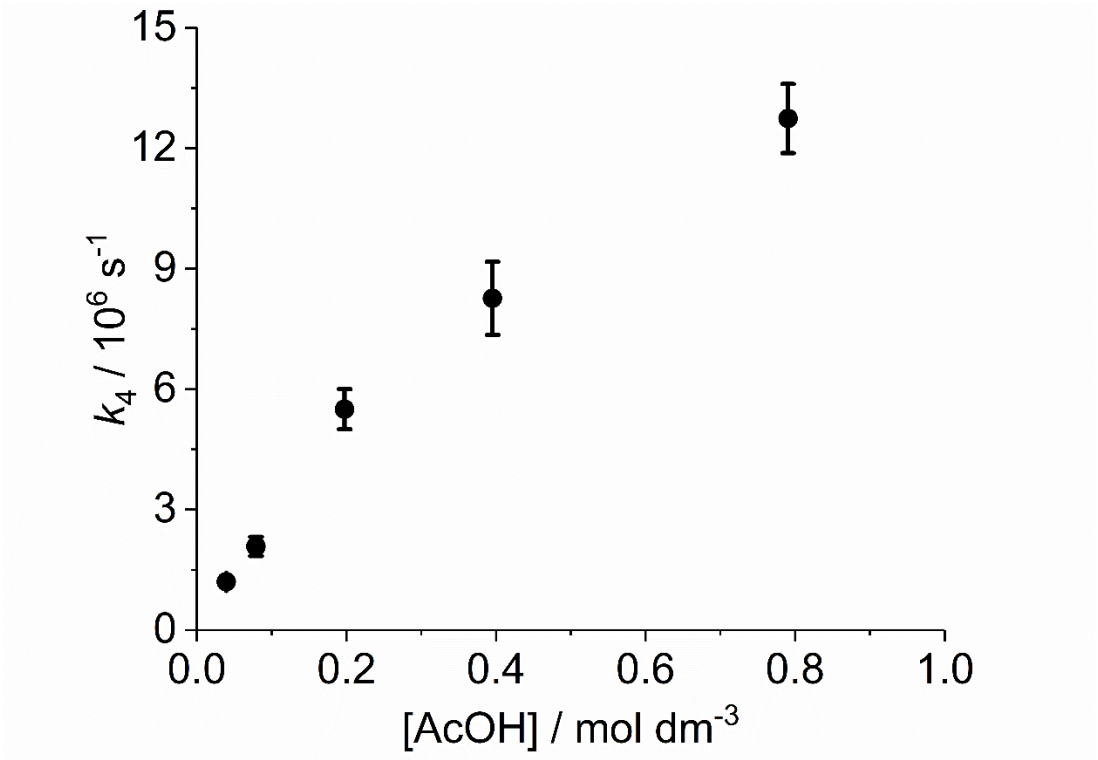

Figure 58. Dependence of acetic acid concentration in toluene on the rate of formation of **186** from the photolysis of **10**. Slope of linear regression is 1.71 ± 0.22 × 10^7 (R^2 = 0.95) and error bars are the 95% confidence limits from the exponential growth fit of the formation of **186**.

4.3.4 Protonation Following C–C Bond Formation

The ability to observe **186** post proton transfer, inspired attempts to directly monitor the protonation mechanism taking place in the alkenylation reactions with carboxylic acid additives *vide supra*. Therefore, an experiment with carefully chosen concentrations of both a terminal alkyne and acetic acid in a toluene solution should theoretically contain (at different times) intermediates of all three substrates. Initially, a toluene-bound complex should form before being substituted by either of the two substrates. **186** is formed in the case of acetic acid binding, while 7-membered insertion complex **77** will be generated if the alkyne binds first. In the latter case, acetic acid can still perform the protonation step on the **77**, generating the organic alkene product **35**.

As it was envisaged that an improper substrate ratio might lead to undesired protonation directly of **10** (leading to formation of **186**), the TRIR experiment was performed using a large excess of **34** (compared to AcOH) diluted in toluene ([**10**] = 1.90 × 10^{-3} mol dm^{-3}, [**34**] = 1.37 mol dm^{-3} and [AcOH] = 0.06 mol dm^{-3}, **Figure 59**). A ratio of 22:1 (**34**/AcOH) ensured that the manganese initially proceeds *via* C–Mn

insertion of the alkyne, before protonation can take place. Firstly, the formation of toluene-bound complex **117** (bands at 2010 and 1896 cm^{-1}) was observed, followed by the substitution by **34** to form the alkyne-bound complex **63** (bands at 2016, 1937 and 1900 cm^{-1}). After subsequent insertion into the C–Mn bond to form insertion complex **77** (bands at 2015, 1913 and 1883 cm^{-1}) a new complex (**189**) displaying a large shift in the manganese carbonyl bands (2040, 1936 and 1909 cm^{-1}) was observed. This new species was generated on the longer microsecond timescale ($t_{1/2} \approx 100$ µs, $k_7 = 9.90 \pm 0.06 \times 10^3$ s^{-1} at room temperature) and was assigned to be the desired "Mn(κ_2-OAc)$(CO)_3$" moiety to which the organic fragment **35** still is *N*-bound to the metal centre, due to its spectral similarity to **186** (2036, 1942 and 1922 cm^{-1}).

The process of monitoring the solvent coordination, substitution by **34**, C–C bond formation and proton transfer from AcOH, all in one experiment, pushed the limit of what is currently possible using TRIR spectroscopy, with the entire experimental time range being required for this task.

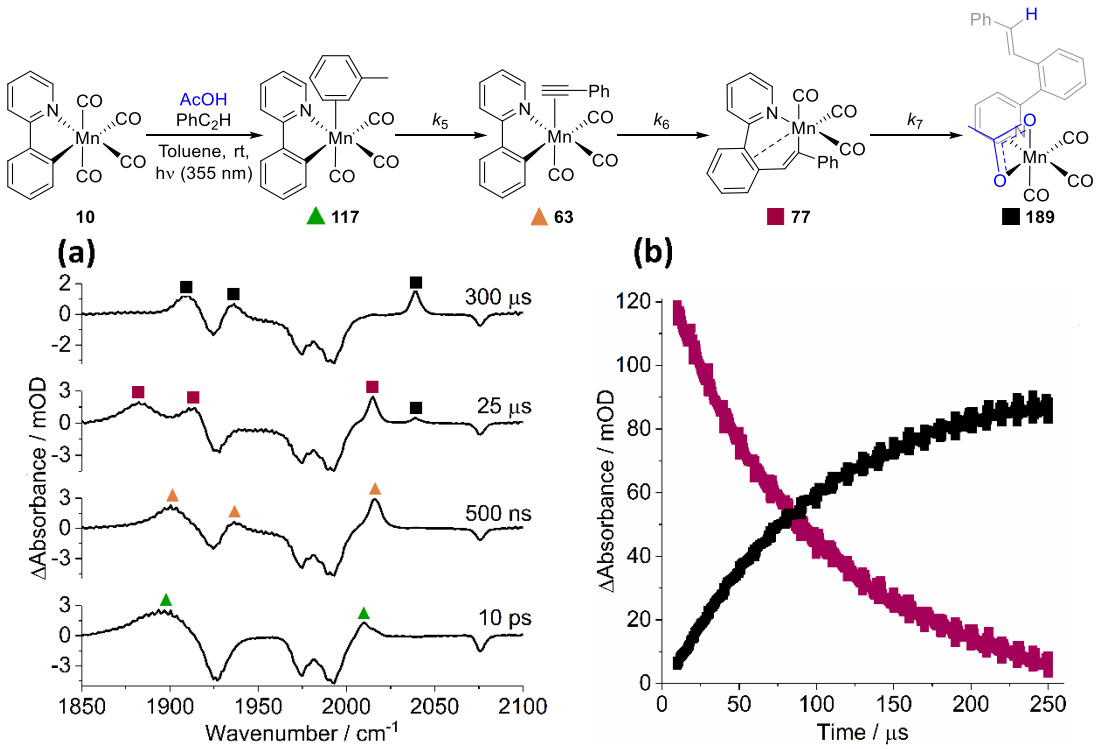

Figure 59. TRIR study of the photolysis of **10** in AcOH/**34**/toluene solution ([**10**] = 1.90×10^{-3} mol dm^{-3}, [**34**] = 1.37 mol dm^{-3} and [AcOH] = 0.06 mol dm^{-3}), showing the formation of the various species in solution after irradiation. (a) IR spectra of the reaction showing the metal carbonyl region at various timepoints. Negative bleach bands correspond the loss of **10** after irradiation. (b) Kinetic plot of the formation of **189** (black squares, band at 2040 cm^{-1}) and depletion of **77** (purple squares, band at 2015 cm^{-1}), extracted from (a).

The concentration dependence of the different substrates was investigated to further support the proposed line of events (**Figure 60**). The rate of protonation (k_7) remained

unchanged when the concentration of **34** was varied (0.46–2.28 mol dm^{-3}) with constant [AcOH] (6.26 × 10^{-2} mol dm^{-3}), indicating a zero-order dependence of **34**. This supported the proposed mechanism, as there should be no involvement of **34** in the final step. A linear increase in the observed rate (k_7) was found when the acetic acid concentration was varied (6.26–62.56 × 10^{-3} mol dm^{-3}) and [**34**] kept constant (1.37 mol dm^{-3}). This trend provided confirmation for the proposed mechanism, where the proton transfer itself was not observed, and the substitution by the AcOH was instead rate determining. From this data a second order rate constant of k = 1.5 ± 0.1 × 10^5 mol^{-1} dm^3 s^{-1} (at room temperature) could be determined.

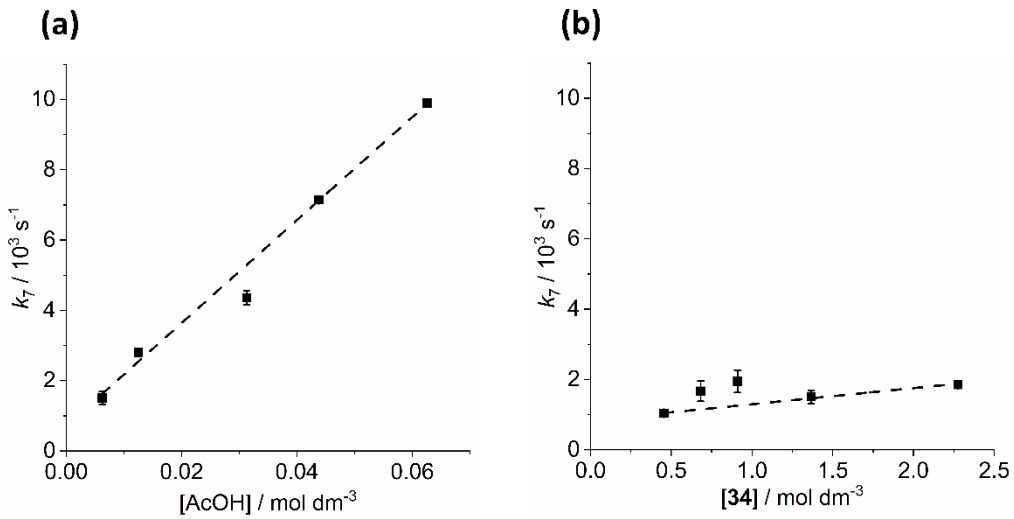

Figure 60. Substrate concentration impact on the rate of protonation (k_7), following C–C bond formation (at room temperature). (a) Rate of protonation on varying [AcOH], with constant [**34**] (1.37 mol dm^{-3}) and [**10**] (1.90 × 10^{-3} mol dm^{-3}). Slope of linear regression is 1.46 ± 0.07 × 10^5 (R^2 = 0.99). (b) Rate of protonation on varying [**34**], with constant [AcOH] (6.26 × 10^{-3} mol dm^{-3}) and [**10**] (1.90 × 10^{-3} mol dm^{-3}). Slope of linear regression is 4.60 ± 0.92 × 10^2 (R^2 = 0.89).

The direct observation of the protonation mechanism for AcOH and lack thereof for the other catalytically relevant substrates (**33**, terminal alkynes, H_2O, acrylates etc.), supported a mode of action of the carboxylic acid additives in Mn(I)-catalysed C–H bond functionalisation, which consisted of protonation assistance, followed by a C–H activation step proceeding through a CMD/AMLA-6 mechanism.

Chapter 5: Fluorine-Induced Regioselectivity in C–Mn and C–C Bond Formation

5.1 Background

The generation of highly regioselective reactions poses one of the major challenges in transition metal catalysed C–H bond functionalisation processes, especially if utilised in complicated target molecule synthesis, where issues are bound to arise. There are currently many strategies to solve this problem, with one of the most common being the incorporation of metal directing groups. In the case of functionalisation of sp^2-hybridised C–H bonds, containing *ortho*-directing groups (as studied within this thesis), the main regioselectivity issue that may arise is when using *meta*-substituted substrates. This reaction can provide two different products, through *ortho* (C_o) or *para* (C_p) C–H bond functionalisation (with respect to the *meta*-substituent).

Fluorine has been utilised as a non-coordinating directing group, where the electronegative nature of the fluorine atom was originally used as an explanation for the observed effects. However, studies by Eisenstein, Clot, Perutz and co-workers revealed that the C–M bond strength is strongly affected by the fluorine substituent (**Figure 61**). In a pair of studies on light-induced C–H bond activation of fluorobenzene by a rhenium-carbonyl complex, the C–Re bond strength was correlated to the observed regioselectivity of the reaction.[161, 162] It was found that the most energetically beneficial position was *ortho* to the fluorine (**192**), while the *meta*-position (**191**) was slightly more stable than the *para*-position (**190**).

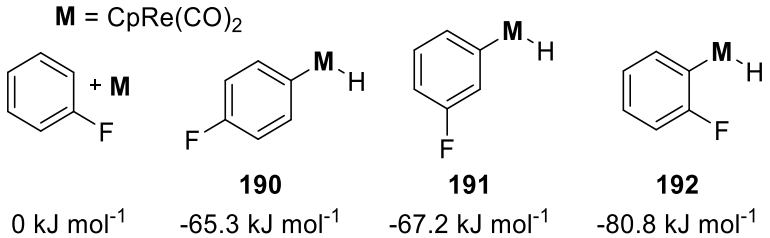

Figure 61. Relative stability of the various regioisomers formed from the Re-mediated C–H bond activation of fluorobenzene, reported by Eisenstein, Perutz and co-workers.[161]

The stability of the corresponding radical species (from C–Re bond breakage) was used as rational for the observed trend in C–Re bond strengthens, as the reverse stability trend was observed compared to the rhenium-complexes *vide supra*. Additionally, it was found that the stronger C–H bond is preferentially broken due to

the stronger C–Re bond formed. It was found that with additional *ortho*-fluorine substituents, the bond dissociation energy is increased and so is therefore the stability of the Re-complexes. The investigation of the *ortho*-fluorine effect has subsequently been studied further and been expanded to other transition metals.[163]

The preference for C–H bond activation *ortho* to fluorine on fluorobenzenes have been further investigated by Jones, Perutz and co-workers, studying formation of rhodium-arene complexes (**Scheme 41**).[164] Interestingly, the reaction between 1,3-difluorobenzene **193** and non-fluorinated rhodium-arene complex **194** at an elevated temperature (67 °C), allowed for arene-substitution to generate fluoro-arene complexes **195** and **196** in a 5:1 ratio. Complex **195** had one *ortho*- and one *para*-fluorine substituent, while **196** had two *meta*-fluorine substituents, neither being the expected product (**197**) with two *ortho*-fluorine substituents. However, increasing the temperature (to 78 °C) led to the expected formation of **197**, suggesting a discrepancy between the kinetic and thermodynamic products. It seemed as that the weaker C–H bonds are initially activated, before slowly equilibrating to the more thermodynamically stable isomer in **197**.

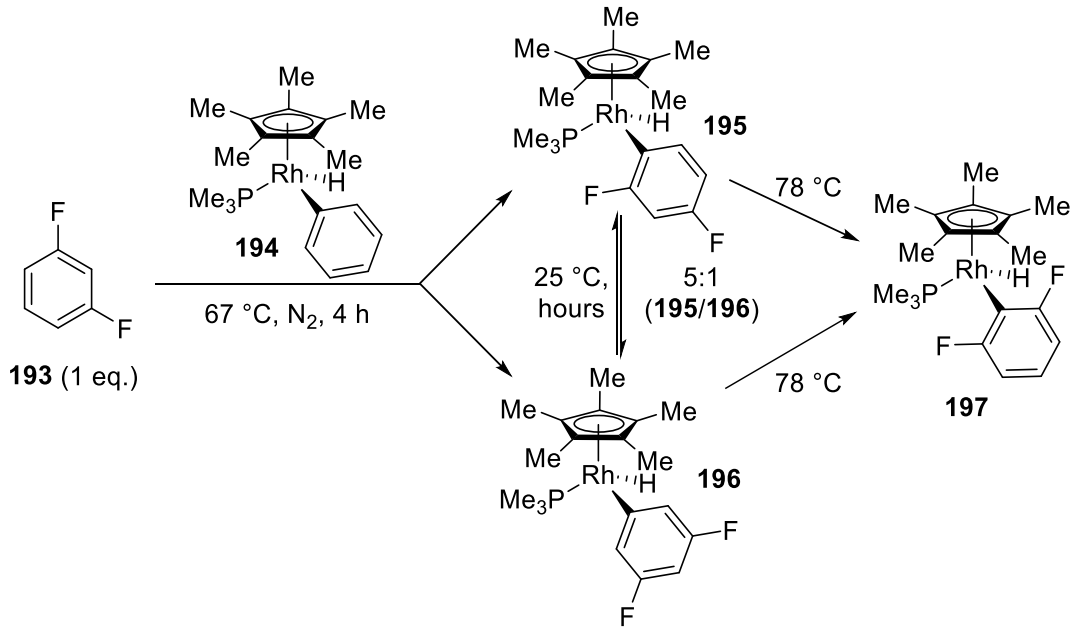

Scheme 41. Kinetic and thermodynamic control on the fluorine-induced regioselectivity of rhodium-mediated C–H bond activation of fluorobenzenes, reported by Jones, Perutz and co-workers.[164]

The observed regioselectivity in the rhenium-example above, have been exploited by Fagnou and co-workers in the Pd-catalysed C–H bond arylation of **193** (**Scheme 42**). In this reaction the thermodynamically preferred product **199** (with two *ortho*-fluorine substituents) was formed in high yield (85%), while no mono-arylation at any of the

other positions was observed. Eisenstein, Perutz and co-workers have subsequently showed *via* DFT-calculations that the *ortho*-fluorine substituent lowers the activation barriers for C–H bond activation,[165] which was predicted to proceed *via* a CMD mechanism.[80]

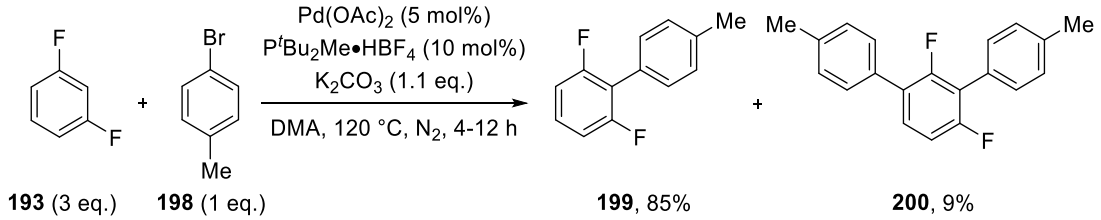

193 (3 eq.) **198** (1 eq.) **199**, 85% **200**, 9%

Scheme 42. Fluorine-induced regioselectivity in the Pd-catalysed C–H bond arylation of fluorobenzenes, reported by Fagnou and co-workers.[75]

The *ortho*-fluorine effect has additionally been observed in the formation of Mn(I)-complexes containing a second, more traditional, directing group. As previously mentioned, the most effective manner in studying this effect is in the stoichiometric generation of the cyclometallated complexes. Studies into the regioselectivity of cyclomangnation reactions have been performed by various research teams since the 1970s, and fluorine has been found to exhibit the reversed preference to that of most other substituents.

Bruce *et al.* studied the $MnMe(CO)_5$ **6** mediated cyclomanganation of substituted azobenzenes and monitored the regioselectivity of the reactions (**Table 11**).[166] They compared the observed regioselectivity with that seen for the equivalent cyclopalladation. The utilisation of phenyl (on the non-substituted arene) derivatives led to extensive C–H bond activation on the phenyl-ring and secondary competition processes, which complicated the translation into useful regioselectivity data. Therefore, the results obtained using pentafluorophenyl-substituted derivatives gave more direct insight into the regioselectivity, as no C–F bond activation was observed.

Table 11. Selected examples of the regioselectivity in the cyclomanganation of substituted azobenzenes, reported by Bruce *et al.*[166]

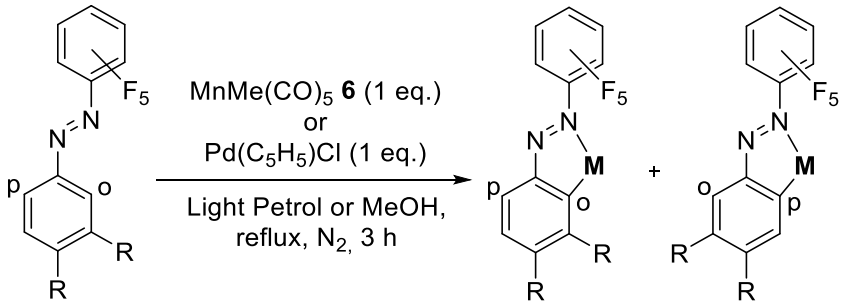

201-202 **203-206** **207-210**

Entry	Substrate	R	M	C_o / %	C_p / %
1	**201**	F	$Mn(CO)_4$	100 (**203**)	0 (**207**)
2	**201**	F	$Pd(\eta^5\text{-}C_5H_5)$	1 (**204**)	99 (**208**)
3	**202**	Me	$Mn(CO)_4$	0 (**205**)	100 (**209**)
4	**202**	Me	$Pd(\eta^5\text{-}C_5H_5)$	0 (**206**)	100 (**210**)

It was found in *meta*-fluorinated derivative **201** that the manganese has an intrinsic preference for the C_o-position, leading to the exclusive formation of the C_o-complex **203** quantitatively. The opposite selectivity was observed for the cyclopalladation, forming C_p-complex **208** in vast excess to C_o-complex **204** (99% and 1% respectively). The palladium continued to be selective for the C_p-position, when employing the methyl-substituted derivate **202**, forming **210** quantitatively. The manganese also exhibited a preference for the C_p-position, in stark contrast to the fluorinated substrate. C_p-complex **209** was found as the sole product in the reaction, with no observable degradation taking place. A trend emerging from this study is that the manganese prefers electron-poor C–H bonds, while palladium activates electron-rich C–H bonds. This is likely due to a difference in mechanism of cyclometallation.

Liebeskind *et al*. conducted an investigation into the regioselectivity of cyclomangnation of *meta*-substituted acetophenones (**Table 12**).[27] A wide range of substituents were employed and an interesting trend of the halogens was observed. Fluorine showed a large preference for the C_o-position (as seen above), generating a 4.5:1 ratio of C_o/C_p (**218**/**225**). Change to chlorine, essentially removed any regioselectivity, while bromine made the C_p-complex the major product in the reaction

(0.69:1, C_o/C_p). This observation leads to the speculation that higher electronegativity induces a selectivity for the C_o-position.

Table 12. Regioselectivity in the cyclomanganation of substituted acetophenones, reported by Liebeskind *et al*.[27]

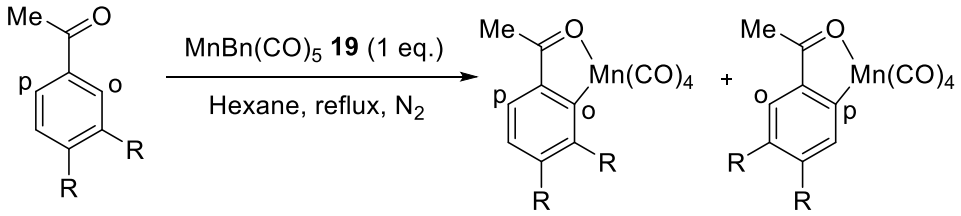

211-217 **218-224** **225-231**

Entry	Substrate	R	C_o / %	C_p / %	C_o/C_p
1	**211**	F	70 (**218**)	16 (**225**)	4.54:1
2	**212**	Cl	44 (**219**)	42 (**226**)	1.05:1
3	**213**	Br	27 (**220**)	38 (**227**)	0.69:1
4	**214**	Me	0 (**221**)	77 (**228**)	0:1
5	**215**	OMe	63 (**222**)	31 (**229**)	2.07:1
6	**216**	CF_3	0 (**223**)	85 (**230**)	0:1
7	**217**	CN	0 (**224**)	11 (**231**)	0:1

The same effect of a methyl-substituent, as seen by Bruce *et al*.,[166] was observed in the selective generation of C_p-complex **228**, presumably arising from the previously mentioned reasons. Methoxy-substituents returned the *ortho*-selectivity to the system, forming **222** in a 2.07:1 ratio to C_p-complex **229**. This trend was also observed by Kaesz and co-workers,[21] though they did not investigate any fluorine-substituents. The final two substituents investigated by Liebekind *et al*. were trifluoromethyl and cyano groups, both exhibiting complete selectivity for their respective C_p-complexes.

Pfeffer *et al.* reported that the aromatic substituent influences the regioselectivity of the cyclomanganation for benzyl amines (**Table 13**), without fluorine being employed.[17] Performing the reaction between **19** and 3,4-dimethylbenzyl-*N*,*N*-dimethylamine **232**, a preference for C_p-complex **232** was observed at a 2:1 ratio to the C_o-complex **234**. Changing the methyl for a methoxy substituent led to a reversal in regioselectivity, making C_o-complex **235** the major complex in the reaction (3:1 ratio to the C_p-complex **237**). The observed regioselectivity was found to be

independent of the reaction time, suggesting that either the reaction is irreversible, very fast or the kinetic and thermodynamic preference is identical.

Table 13. Regioselectivity in the cyclomanganation of substituted benzyl amines, reported by Pfeffer *et al.*[17]

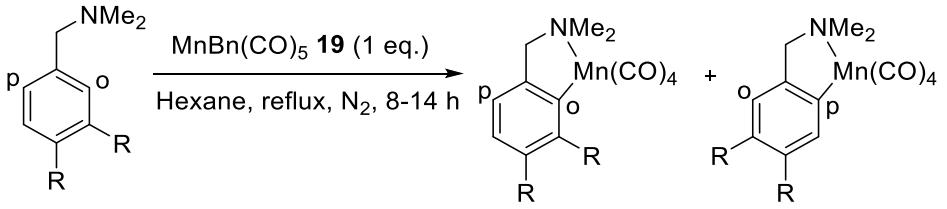

232, **233** **234**, **235** **236**, **237**

Entry	Substrate	R	C_o / %	C_p / %	C_o/C_p
1	**232**	Me	29 (**234**)	59 (**236**)	1:2
2	**233**	OMe	52 (**235**)	17 (**237**)	3:1

A similar substituent effect relating to regioselectivity has been reported by Rourke and co-workers, specifically in the cyclomanganation of *meta*-substituted imine-containing benzenes.[167] Again, no fluorinated substrates were employed, but the same preference of the C_o-complex (2.6:1, C_o/C_p) was observed with a methoxy-substituent. Using a nitro-substituent led to a reversal in regioselectivity, with a 1:5.5 ratio (C_o/C_p). Additionally, it was found that the electron-donating methoxy-substituent, increases the reaction rate, while the electron-withdrawing nitro-substituent had a negative impact.

The observation of a strong influence of fluorine substituents on the resulting regioselectivity has also been made by Bishop and Jordan (working within the Fairlamb research group) when studying the cyclomanganation by $MnBn(CO)_5$ **19** of fluorinated benzylamine derivatives (**Table 14**), building on the work by Pfeffer *et al.*[168, 169] It was found that the generated manganacycles could be isolated and show a relatively strong preference for the C_o-position (>90%). Unfortunately, the regioisomers could not be separated, while X-ray crystallographic structures was obtained for three C_o-complexes. The efficiency of the reactions was moderate with the yield of the isolated complexes ranging from 50–65%.

Table 14. Regioselectivity in the cyclomanganation of fluorinated benzylamine derivatives by Jordan.[169]

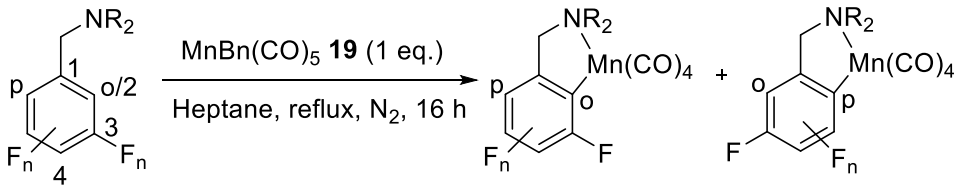

238-241 **242-245** **246-249**

Entry	Ligand	R_2	F_n	Yield[1] / %	C_o/C_p
1	**238**	Me_2	3	55	9:1 (**242**/**246**)
2	**239**	Me_2	3,4	52	99:1 (**243**/**247**)
3	**240**	$CH_2C_2H_4CH_2$	3	62	93:7 (**244**/**248**)
4	**241**	$CH_2C_2H_4CH_2$	3,4	53	92:8 (**245**/**249**)

[1]Yield of isolated product.

Through reaction pathways determined by theory (using DFT-calculations), it was speculated that the C_p-complexes should be kinetically preferred, exhibiting a lower energy barrier of formation. In contrast, the C_o-complexes is more thermodynamically stable and therefore becomes the major product in the reaction. This contradicted the result on similar benzylamine derivatives reported by Pfeffer *et al*.,[17] discussed above. To probe this hypothesis, initial kinetic studies were conducted by Clarke, but the data obtained from these studies was not sufficient to confirm or contradict the initial reversible formation of the C_p-complexes.[147]

The regioselectivity of the corresponding cyclopalladation has also been investigated by Milani *et al*., where the *ortho*-position is disfavoured.[170] Utilisation of Li_2PdCl_4 as the Pd-source, leads to the selective formation of dinuclear C_p-complex **252**. However, using palladium acetate yielded no selectivity and the two regioisomeric complexes **251** and **253** formed in equal amounts. The mechanism of C–H bond activation was different for the two Pd-precursors, where S_EAr (Li_2PdCl_4) and CMD ($Pd_3(OAc)_6$) were the two mechanisms. The competition between a favourable *ortho*-fluorine substituent for the CMD mechanism and unfavourable lone pair interaction with the bridging ligands, was seen as the primary reason for the observed regioselectivity.

Table 15. Regioselectivity in the cyclopalladation of fluorinated benzylamine derivatives, reported by Milani *et al*.[170]

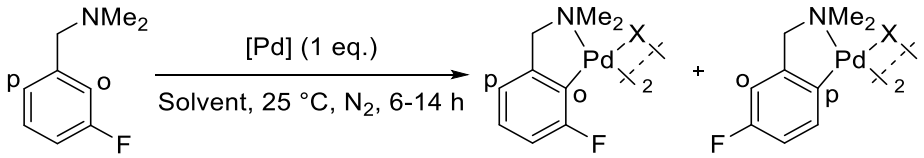

238 (2 eq.) **250**, **251** **252**, **253**

Entry	[Pd]	Solvent	C_o / %	C_p / %
1	1/3 $Pd_3(OAc)_6$	MeCN	40 (**250**)	36 (**252**)
2	Li_2PdCl_4	MeOH	0 (**251**)	76 (**253**)

The cyclomanganation of *meta*-fluorinated 2-phenylpyridine derivatives has been studied by Clarke (working in the Fairlamb research group).[147] Through a solvent screen it was found that the efficiency and regioselectivity of the reaction was highly dependent on the reaction solvent (**Figure 62**). It was the catalytically relevant and utilised solvents (toluene and DCE) which gave the highest conversions at 91% and 97% respectively. The regioselectivity was also consistent between the two solvents at a 3.3:1 ratio of **255**/**256** (C_o/C_p). Lower boiling point hydrocarbon solvents such as heptane and hexane yielded lesser quantities of the manganacycles but exhibit a large difference in the observed regioselectivity. Methanol was shown, as expected, not to be an efficient solvent for the reaction (11% conversion to **255**), but exclusively forms C_o-complex **255**.

The regioisomers could not be separated by flash column chromatography and characterised in isolation, but the reactions in toluene and DCE revealed enticing opportunities for the reaction kinetics to be monitored. The large amount of **256** could either arise from a slow reversibility of the C_p-Mn bond formation or from the reaction being less thermodynamically biased for the C_o-complex **255**. Further studies are required for this to be determined.

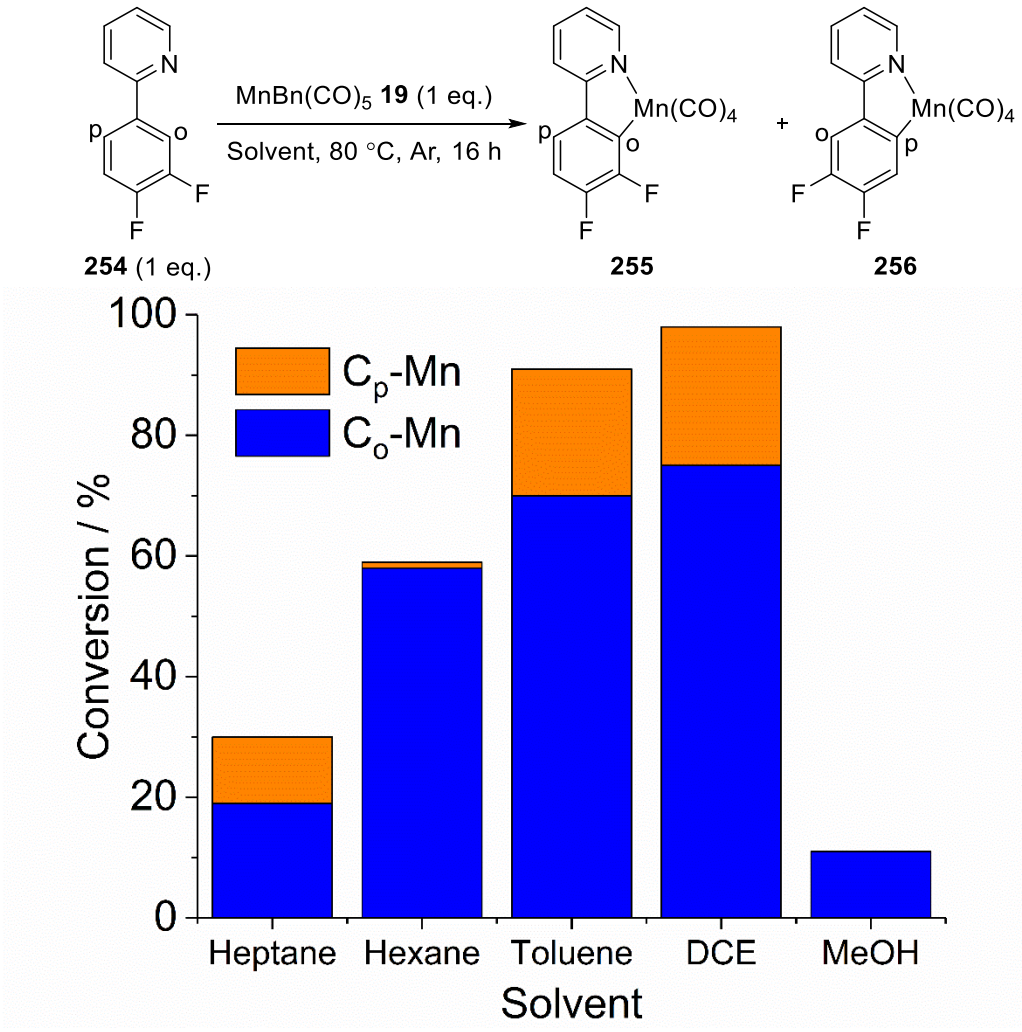

Figure 62. Solvent screen for the cyclomanganation of fluorinated 2-phenylpyridines by Clarke.[147]

5.2 Regioselectivity in C–Mn Bond Formation

5.2.1 Isolation and Characterisation of Regioisomers

The preliminary focus of this study was to repeat the reactions on the 2-phenylpyridine manganese complexes (**255** and **256**), initially performed by Clarke, so that kinetic information for the cyclomanganation processes could be obtained. However, before this could be done the relevant complexes should preferably be isolated and properly characterised. Two different fluorinated 2-phenylpyridines, **254** and **257**, were chosen to be studied and synthesised using a Suzuki-Miyaura cross-coupling methodology.

Reacting **257** (1 eq.) with **19** (1 eq.) in toluene (dry and deoxygenated) at 80 °C, yielded the manganacycles cleanly from the starting material (determined by ^{19}F NMR spectroscopy). The two manganese complexes **258** and **259** could be separated by flash column chromatography despite of small separation of R_f-values, though at relatively

low yields (40 and 30% respectively). The remaining material was collected as co-eluted fractions, with the majority consisting of **258**. Repeating the reaction with the difluorinated compound **254** showed a similar behaviour, with **255** and **256** being isolated in low yields (34 and 17% respectively) and most material co-eluted.

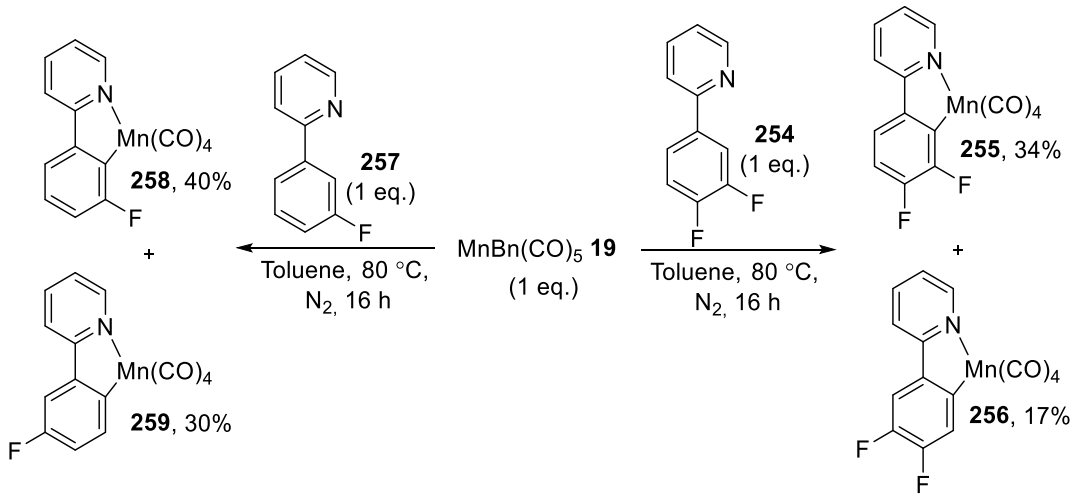

Scheme 43. Synthesis of the fluorinated manganacycles studied from *meta*-fluorinated substrates **257** and **254**.

Similar IR stretching bands were exhibited by all of the manganese complexes (**Table 16**), highlighting the minor effect of the fluorine substituents on the electron-richness of the metal centre. This was also consistent with the C–Mn bond lengths observed from the X-ray crystallographic structures obtained for **255**, **258** and **259**, which does not change for any of the manganacycles. The bond angles and Mn–CO bond lengths were also constant between the different manganese complexes and overall showed a remarkable similarity in the apparent nature of the 'Mn(CO)$_4$' moiety.

To be used as a control substrate, C$_m$-complex **261** was synthesised in good yield (96%) from the *para*-fluorinated 2-phenylpyridine **260**. Interestingly, if the reaction was performed in refluxing hexane, the product could be obtained by filtration due to not being soluble in the solvent and precipitating out of the solution. Again, no large differences could be seen within the metal carbonyl bands in the IR spectrum, while a single crystal X-ray structure was not obtained for this manganese complex (**261**).

Table 16. Key characterisation data for the various manganacycles synthesised.

Enty	Complex	IR[1] / cm^{-1}	^{19}F-NMR[2]	C–Mn / Å
1	**258**	2081, 1995 (br), 1942	−86.3	2.0557(18)
2	**259**	2077, 1992 (br), 1934	−121.4	2.0510(17)
3	**255**	2084, 1999 (br), 1946	−112.4, −135.5	2.0501(12)
4	**256**	2080, 1996 (br), 1938	−137.1, −146.3	Not Obtained
5	**261**	2078, 1994 (br), 1936	−110.9	Not Obtained

[1]Metal carbonyl bands only. [2]Reported in parts per million (ppm). [4]Determined by single crystal X-ray crystallographic diffraction methods.

The lack of electronic differences at the metal centres, was at first glance incompatible with the observed regioselectivity of these cyclomanganation reactions. However, the differential may instead arise from electronic changes on the ligand rather than the metal, in turn creating a change in selectivity. The ^{19}F NMR signals showed a difference between the regioisomeric manganese complexes, where the more fluorine signals exhibit a shielding trend of **259**>**260**>**258**. It was highly likely that another effect was behind the observed regioselectivity, as electronic changes to the phenyl-ring should affect the C–Mn bond length and the metal carbonyl bands, even if only marginally.

5.2.2 *In Situ* Monitoring of Standard Cyclomanganation Reaction

^{19}F NMR spectroscopy was identified as a suitable technique to monitor the reaction kinetics for the cyclomanganation reactions due to the distinct fluorine signals corresponding to the complexes, making it easy to separate the information for both regioisomers. *In operando* IR spectroscopy used throughout this thesis, was not appropriate as the regioisomers exhibit similar IR stretching bands, which will create large spectral overlap and difficulties in deconvolution of the data in the metal carbonyl region.

The reactions were performed in a Young's tap NMR tube (inside the NMR spectrometer), to avoid temperature fluctuations, minimise human error and ease the handling of the reaction. The concentration of the reaction was kept constant to the previous work at 0.05 mol dm^{-3}. The reagents were added under N_2, at room temperature and the toluene was dry and deoxygenated. A room temperature ^{19}F NMR spectrum was recorded to obtain the zero-time, before the spectrometer was heated to 80 °C. The time started after the addition of the NMR sample to the spectrometer, once at temperature. ^{19}F NMR spectra was recorded every 5 minutes for the duration of the experiment, unless otherwise stated. $PhCF_3$ was selected as an internal standard, as it does not influence the reaction nor overlap with any of the observed peaks required for analysis in these experiments.

Initially, the reaction between **257** (1 eq.) and **19** (1 eq.) was performed at 80 °C in toluene under a nitrogen atmosphere (**Figure 63**). As expected, the reaction preferably generated the C_o-product **258** in a 2.89:1 ratio, in a reaction where both products can be seen forming over *ca*. 20 hours. No transient intermediates could be observed in the ^{19}F NMR spectra. The rate of reaction slows down as the reaction proceeds in a typical non-linear fashion, while the ratio between the two regioisomers remains constant throughout the reaction for both substrates.

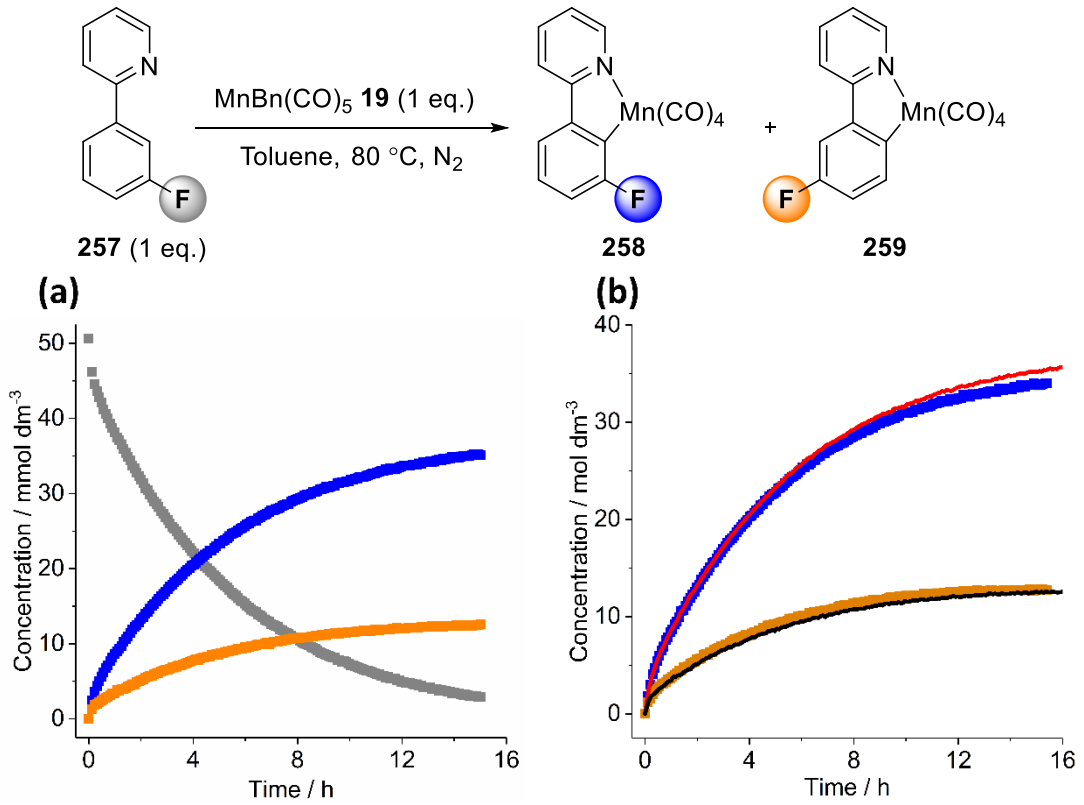

Figure 63. *In situ* ^{19}F NMR spectroscopic monitoring of the cyclomanganation of **257**. (a) Kinetic plot of the reaction between **257** (1 eq.) and **19** (1 eq.) in toluene at 80 °C, using $PhCF_3$ as internal standard. (b) Kinetic plot of the reaction between **257** (1.5 eq.) and **19** (1 eq.) in toluene at 80 °C, using $PhCF_3$ as internal standard. Red line (**258**) and black line (**259**) are the reaction profile in (a).

The kinetic data supported the expected parallel formation of the two products as the observed rate of formation of **258** and **259** were highly similar (k_{obs} = 5.09 ± 0.04 × 10^{-5} s^{-1} at 80 °C (formation of **258**) and k_{obs} = 5.78 ± 0.07 × 10^{-5} s^{-1} at 80 °C (formation of **259**)), especially when compared to the final product ratio. The different amount formed of each product arises from the rate constants being different for the two parallel steps and further studies are required to determine the rate constants of each step. The observed rate of two parallel reactions (starting from the same starting material) should be identical to the rate observed for loss of the starting material[171] and the rate of loss of **257** (k_{obs} = 5.20 ± 0.07 × 10^{-5} s^{-1} at 80 °C) were similar, further supporting the presence of a parallel reaction pathway.

To probe if the lack of observable reversibility in this system arises from the lack of non-bound **257**, the reaction was performed under the same conditions using an excess of **257** (1.5 eq., **Figure 63**). A highly similar reaction profile to when using 1 equivalent of **257** was observed and indicated a zero-order dependence in the 2-phenylpyridine (**257**). The initial activation of the manganese (possibly CO-loss from

19) was likely the rate determining process of the reaction and therefore the reaction rate was set independently of the ligand.

Table 17. Observed rate constants (k_{obs}) at 80 °C for the cyclomanganation of fluorinated 2-phenylpyridines (Ligand).

Entry	Ligand (eq.)	$k_{obs(o)}$ / 10^{-5} s^{-1}	$k_{obs(p)}$ / 10^{-5} s^{-1}	$k_{obs(SM)}$ / 10^{-5} s^{-1}	C_o/C_p
1	**257** (1)	5.1 ± 0.6	5.6 ± 0.1	5.20 ± 0.07	2.89
2	**257** (1.5)	5.24 ± 0.06	6.0 ± 0.1	5.44 ± 0.07	2.63
3	**254** (1)	5.94 ± 0.08	6.15 ± 0.02	5.92 ± 0.09	2.28
4	**254** (2)	5.88 ± 0.05	6.3 ± 0.1	6.24 ± 0.06	2.45
5	**260** (1)	6.36[1] ± 0.07	N/A	6.36 ± 0.07	N/A

[1] Only one rate obtainable (k_m).

The behaviour observed for **257** was repeated for the reactions employing **254** (**Figure 64**), but with a small difference in the C_o/C_p ratio. Again, the observed rates of both products were similar to the loss of starting material (**Table 17**), in line with two parallel reactions pathways. The addition of an extra equivalent of **254** gave a similar profile, but with a difference at the end of the reactions. This was likely due to slightly too much manganese starting material being added to the reaction with additional **254**. The reaction was performed for a prolonged time (40 hours) and it could be seen that a very slow interconversion between the two regioisomeric isomers occurred, for which residual water in the solvent was likely responsible for. Preliminary studies highlight that performing the reaction in wet solvent increases the extent of regioisomeric interconversion taking place over longer reaction times. The overall rate of reaction was similar between the mono- and di-fluorinated substrates (**257** and **254**), which is consistent with the ligand not being a part of the rate determining step of the reaction.

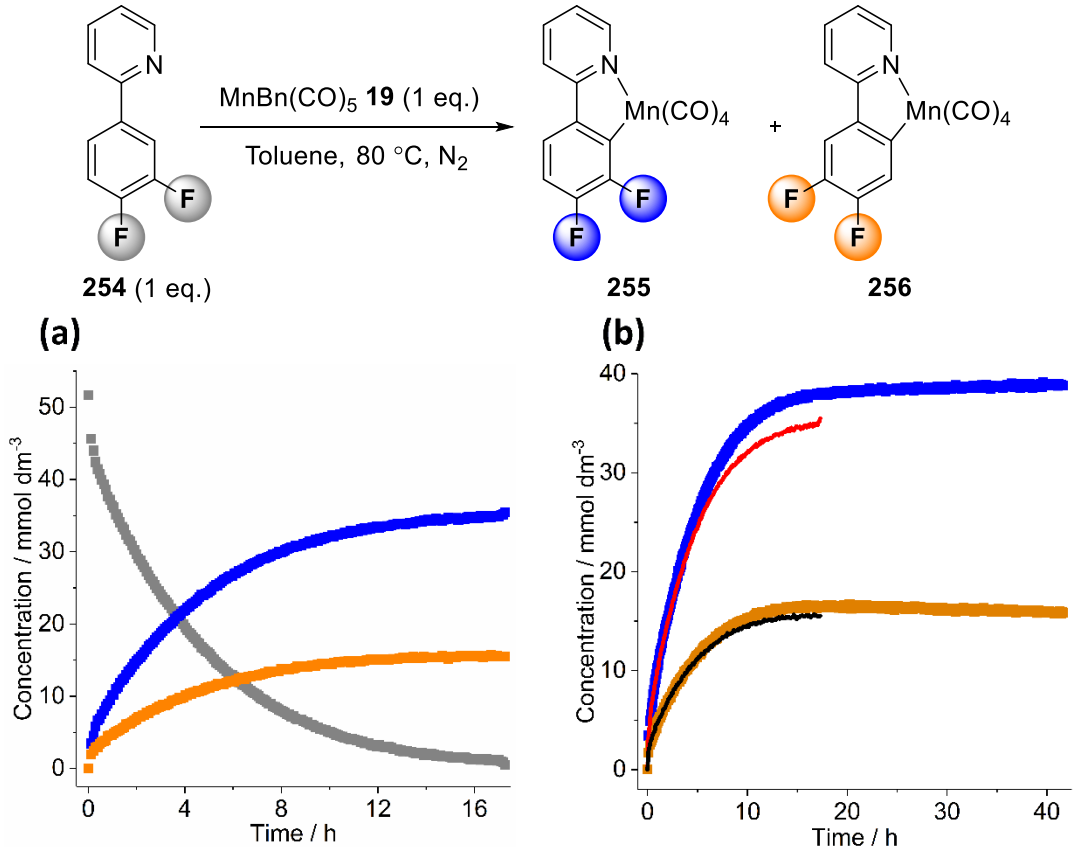

Figure 64. *In situ* ^{19}F NMR spectroscopic monitoring of the cyclomanganation of **254**. (a) Kinetic plot of the reaction between **254** (1 eq.) and **19** (1 eq.) in toluene at 80 °C, using $PhCF_3$ as internal standard. (b) Kinetic plot of the reaction between **254** (2 eq.) and **19** (1 eq.) in toluene at 80 °C, using $PhCF_3$ as internal standard. Red line (**255**) and black line (**256**) are the reaction profile in (a).

The cyclomanganation of *meta*-fluorinated substrate **260** was also monitored at 80 °C under a nitrogen atmosphere. The observed rate of this process were similar to the rates for both other ligands (**254** and **257**) in previous experiments (**Table 17**). Again, no transient reaction intermediates could be observed in these data.

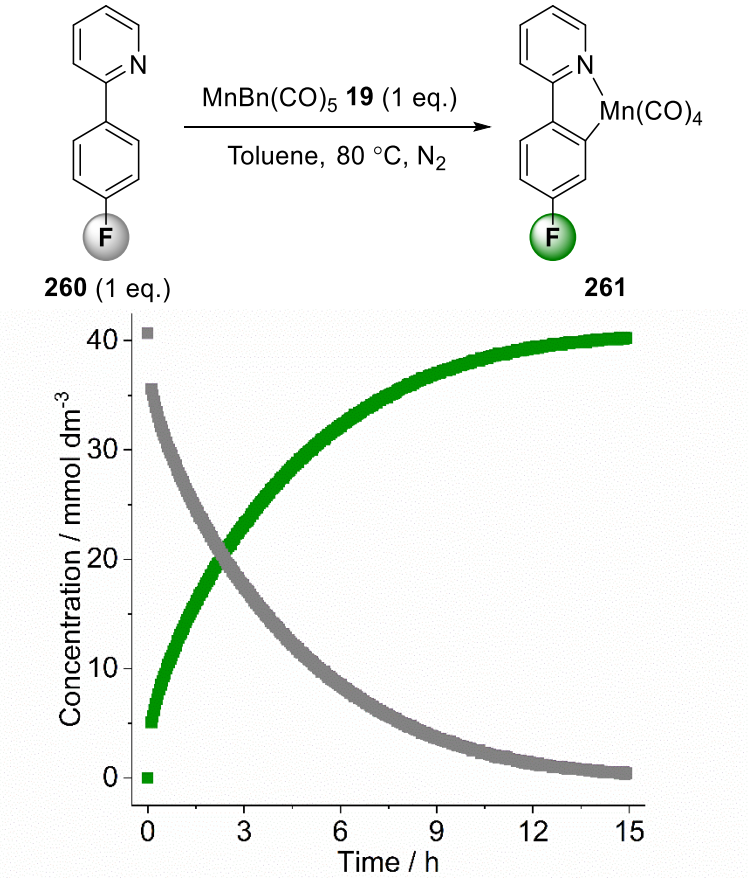

Figure 65. Kinetic plot from the *in situ* ^{19}F NMR spectroscopic monitoring of the reaction between **260** (1 eq.) and **19** (1 eq.) in toluene at 80 °C, using $PhCF_3$ as internal standard.

5.2.3 Impact of Acid Additives on Regioselectivity

Carboxylic acids were identified as suitable additives to further probe the reaction mechanism, due to the experimental evidence hinting towards an irreversible mechanism (see further discussion in Chapter 5.2.4). Several carboxylic acid additives have been successfully employed in proton transfer steps within this thesis (see Chapter 2 and 4), including the protonation of $Mn(ppy)(CO)_4$ **10** *via* a CMD/AMLA-6 pathway. The protonation mechanism of **10** should be reversible (as seen in the productive catalysis with acid additives), meaning that acid additives should make the regioselectivity thermodynamically determined and should only require catalytic amount of acid employed. Therefore, the C_o/C_p ratio ought to change with the addition of acid, as an irreversible reaction is kinetically driven and is highly unlikely to be identical to the thermodynamic selectivity.

To the reaction between **257** (1 eq.) and **19** (1 eq.) at 80 °C in toluene under a nitrogen atmosphere, was added benzoic acid (0.1 eq.) and was monitored using *in situ* ^{19}F

NMR spectroscopic analysis (**Figure 66**). A pronounced difference in the kinetic traces after addition of the acid was observed, with C_o-complex **258** becoming the dominant product generated, at a 16.90:1 ratio (**258**/**259**). There was also unreacted starting material **257** left in solution at the end of the reaction.

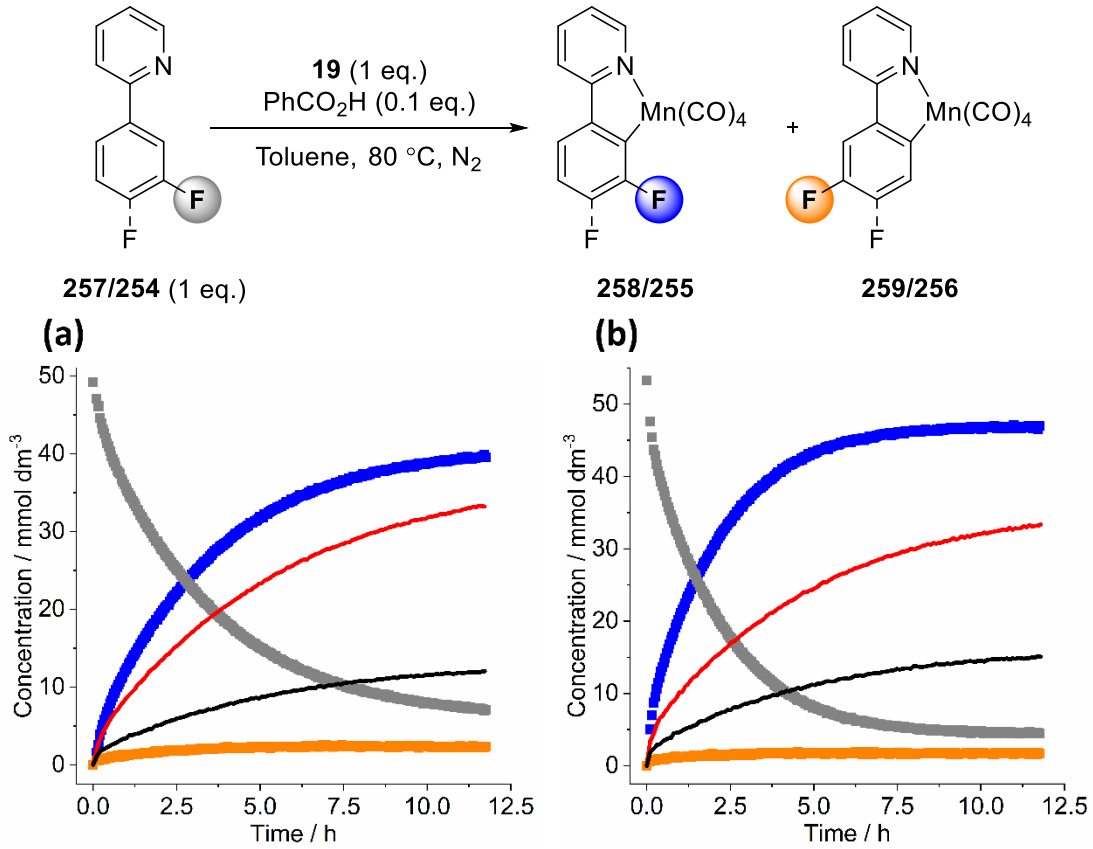

Figure 66. *In situ* ^{19}F NMR spectroscopic monitoring of the effect of benzoic acid on the observed regioselectivity of the cyclomanganation reaction of **257**. (a) Kinetic plot of the reaction between **257** (1 eq.), **19** (1 eq.) and benzoic acid (0.1 eq.) in toluene at 80 °C, using $PhCF_3$ as internal standard. Red line (**258**) and black line (**259**) are the reaction profile with no acid added. (b) Kinetic plot of the reaction between **254** (2 eq.), **19** (1 eq.) and benzoic acid (0.1 eq.) in toluene at 80 °C, using $PhCF_3$ as internal standard. Red line (**255**) and black line (**256**) are the reaction profile with no acid added.

The same effect was observed for the difluorinated substrate **254** (1 eq.) after addition of benzoic acid (**Figure 66**) and C_o-complex **255** forms at 29 times higher amount that C_p-complex **256**. The determined regioselectivity in the reactions employing acid additives contain a large uncertainty due to the minor amounts of the C_p-complexes (**259** and **256**) formed, which means that small errors in the C_p-integrals translates to large errors in the calculated selectivity. The trend of the C_o-complexes being strongly preferred under these conditions, was nonetheless trustworthy.

Comparing the reaction rates with and without acid additives, showed that the observed rate for the loss of starting material (**257** and **254**) increased by a factor of 1.6 (**257**) and 2.3 (**254**) with 0.1 equivalence benzoic acid added (**Table 18**). The rate

of formation for the C_p-complexes (**259** and **256**) showed larger discrepancies from the other rates (starting material and C_o-complexes) than without any additives, which most likely arises due to the very small quantities formed.

Table 18. Observed rate constants (k_{obs}) at 80 °C for the cyclomanganation of fluorinated 2-phenylpyridines (Ligand) with acid additives. All reactions are performed using one equivalent of the ligand and manganese precursor **19**.

Entry	Ligand	Additive (eq.)	$k_{obs(o)}$ / 10^{-4} s^{-1}	$k_{obs(p)}$ / 10^{-5} s^{-1}	$k_{obs(SM)}$ / 10^{-4} s^{-1}	C_o/C_p
1	**257**	None	0.51 ± 0.06	5.55 ± 0.10	0.52 ± 0.07	2.89
2	**257**	$PhCO_2H$ (0.1)	0.81 ± 0.01	1.51 ± 0.07	0.83 ± 0.01	16.90
3	**257**	4-F-$PhCO_2H$ (0.5)	1.5 ± 0.2	1.75 ± 0.12	1.5 ± 0.1	21.46
4	**257**	4-F-$PhCO_2H$ (1)[1]	23 ± 1	42 ± 14	20 ± 2	23.87
5	**254**	None	0.59 ± 0.01	0.62 ± 0.01	0.59 ± 0.01	2.28
6	**254**	$PhCO_2H$ (0.1)	1.33 ± 0.01	2.5 ± 0.2	1.34 ± 0.01	29.21

[1]Pre-heated for 2.25 hours.

It can be envisaged that the benzoic acid could protiodemetallate the benzyl group, generating toluene and a Mn(I)-benzoate carbonyl complex. Therefore, 4-fluoro-benzoic acid was employed, as the fluorine-handle should allow for the observation of these complexes. A larger amount of the acid than the 0.1 equivalence used previously, was preferred to make detection of new species easier.

The reaction between **257** (1 eq.), **19** (1 eq.) and 4-fluoro-benzoic acid (0.5 eq.) at 80 °C in toluene under a nitrogen atmosphere was monitored by *in situ* ^{19}F NMR spectroscopy (**Figure 67**). Once more, a fast reaction profile was observed, with a large selectivity for **258** over **259** (21.46:1). More of the free ligand **257** could be observed (28%) than in previous reactions. Interestingly, the fluorine peak for 4-fluoro-benzoic acid was observed splitting to form a new species, with a significant amount of the benzoic acid remaining. The new peak was seen drifting downfield as

the reaction progresses, widening in the process, which could barely be detected upon reaction completion.

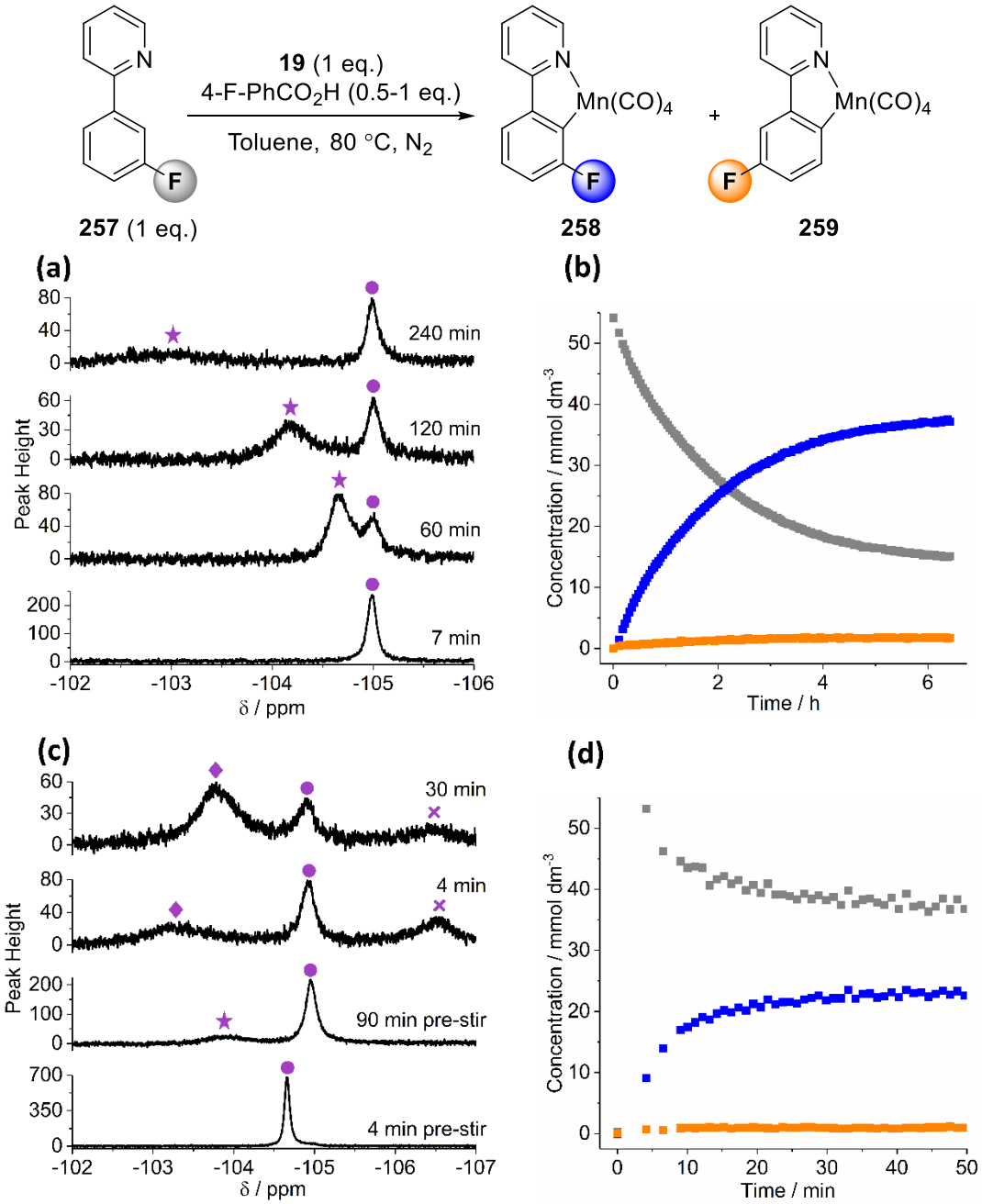

Figure 67. *In situ* ^{19}F NMR spectroscopic monitoring of the effect of 4-fluoro-benzoic acid on the observed regioselectivity of the cyclomanganation reaction of **257**. (a) ^{19}F NMR spectra of the reaction between **257** (1 eq.), **19** (1 eq.) and 4-fluoro-benzoic acid (0.5 eq.) in toluene at 80 °C, using $PhCF_3$ as internal standard. Key; purple circle = 4-fluorobenzoic acid and purple star = unknown 4-fluoro-benzoic acid derived compound. (b) Kinetic plot of **257** derived products (**258** and **259**), extracted from (a). (c) ^{19}F NMR spectra of the reaction employing 2.25 hours pre-stirring between **19** (1 eq.) and 4-fluoro-benzoic acid (1 eq.) in toluene at 80 °C using $PhCF_3$ as internal standard, before **257** (1 eq.) was added to the reaction. Key; purple circle = 4-fluorobenzoic acid, purple star = unknown 4-fluoro-benzoic acid derived compound also observed in (a) and purple diamond/cross = unknown 4-fluoro-benzoic acid derived compounds not previously observed. (d) Kinetic plot of **257** derived products (**258** and **259**) after addition of **257**, extracted from (c).

Compound **19** (1 eq.) and 4-fluoro-benzoic acid (1 eq.) was pre-heated at 80 °C in toluene under a nitrogen atmosphere for 2.25 hours (**Figure 67**) to further probe any initial reactions taking place between the manganese complex **19** and the benzoic acid. It was seen in the ^{19}F NMR spectra that the unknown species formed previously was present and again drifted downfield as time progressed. Addition of **257** (1 eq.) after 2.25 hours led to a significant change in the ^{19}F NMR spectrum. A species around the location of the unknown split peak was formed, which was either the same complex behaving differently upon addition of the ligand or a new complex altogether. The latter was more likely as it was seen shifting upfield (relative to its starting position) as the reaction progressed. There were several new species generated following addition of **257**, where a short-lived species at −106.5 ppm and another longer-lived compound at −111.8 ppm was observed. Attempts to isolate and further characterise any of these species formed in the reaction between **19** and the benzoic acid were unsuccessful.

The formation of **258** was again much preferred over **259**, with only trace amounts being formed of the later. The rate of **258** formation increased by an order of magnitude through pre-heating and increased amount of acid added. However, the total amount of manganacycle (**258** and **259**) formed was reduced compared to the other reactions, with 70% of **257** remaining in solution.

To further probe the reversibility induced by the acid additive, **259** (1 eq.) was initially heated at 80 °C in toluene under a nitrogen atmosphere for 4.25 hours (**Figure 68**). This experiment showcased the high thermal stability of **259**, with only trace amounts degrading, likely due to trace water in the solvent. Benzoic acid (0.5 eq.) was added after 4.25 hours and subsequent interconversion to **258** was observed. Interestingly, **257** was initially generated after the addition of the acid, before the observation of **258**. The amount of **257** remained constant and was consistent with the amount of acid present, while the rest of the ligand resided in **258**.

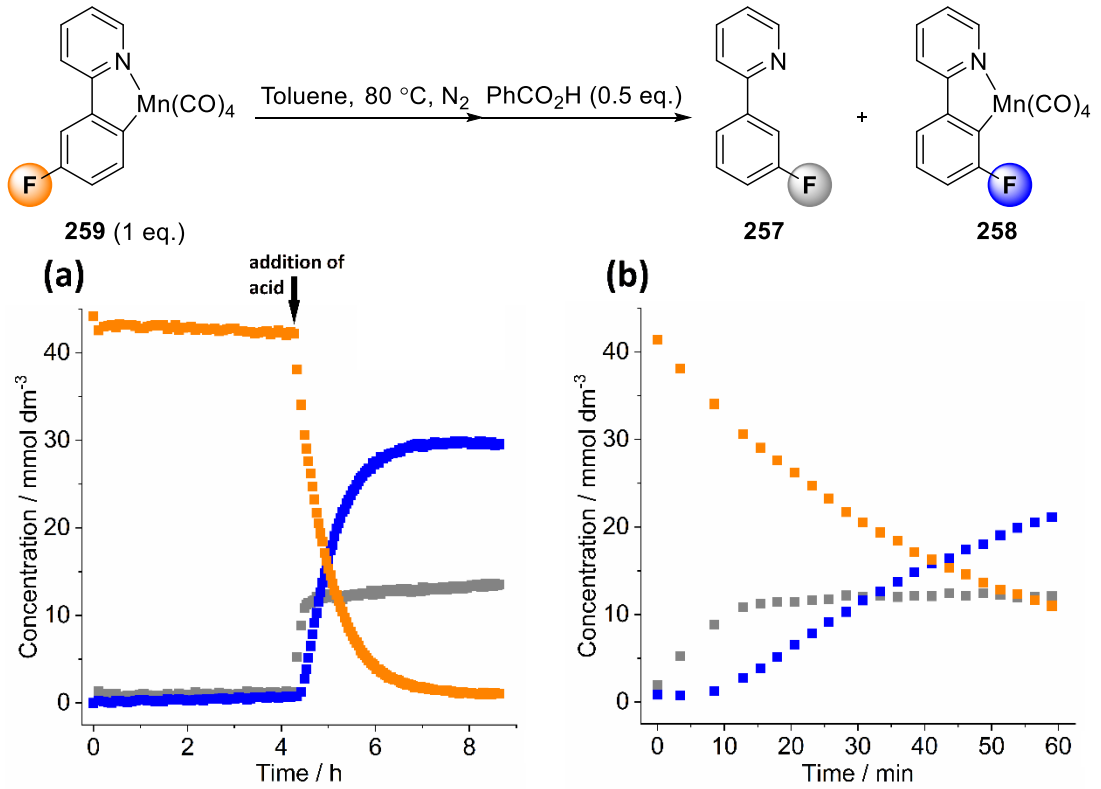

Figure 68. *In situ* ^{19}F NMR spectroscopic monitoring of the thermal stability of **259** and the effect of addition of benzoic acid. (a) Kinetic plot of the heating of **257** (1 eq.) in toluene at 80 °C using $PhCF_3$ as internal standard, with benzoic acid (0.5 eq.) added after 4.25 hours. (b) Kinetic plot of the first 60 minutes after addition of benzoic acid (0.5 eq.).

Further experimental evidence is required to support a mechanistic proposal into the mechanism of the reversibility induced by acid additives. Therefore, a reaction between **257** (1 eq.) and **19** (1 eq.) was initially performed at 80 °C in toluene under a nitrogen atmosphere (**Figure 69**), which generated a mixture of both **258** and **259**, as previously observed. Thereafter, **260** (0.55 eq.) and benzoic acid (0.5 eq.) was added to the reaction mixture, leading to a rapid depletion of both **258** and **259**. The quantity of **258** stabilised over time and remained as the major complex, while both **257** and **261** appeared in the solution.

To probe whether the reaction system was in an equilibrium, 3.7 equivalents of **260** was added to the solution after 21.5 hours reaction time. This resulted in making **261** the major Mn-species in solution and lowered the amount of **258** by the corresponding amount. The ratio between **258** and **261** provides information into the relative thermodynamic stability of the complexes, assuming the system was in an equilibrium. After the first addition of **260** (0.55 eq.), the ratio of **257**/**260** (counting both bound and unbound ligand) was 1.8:1, while the ratio of **258**/**261** at equilibrium was 2.6:1.

Following the second addition of **260** (3.7 eq.), the ratios changed to 0.235:1 (**257**/**260**) and 0.375:1 (**258**/**261**). In both cases **259** was only present in trace quantities.

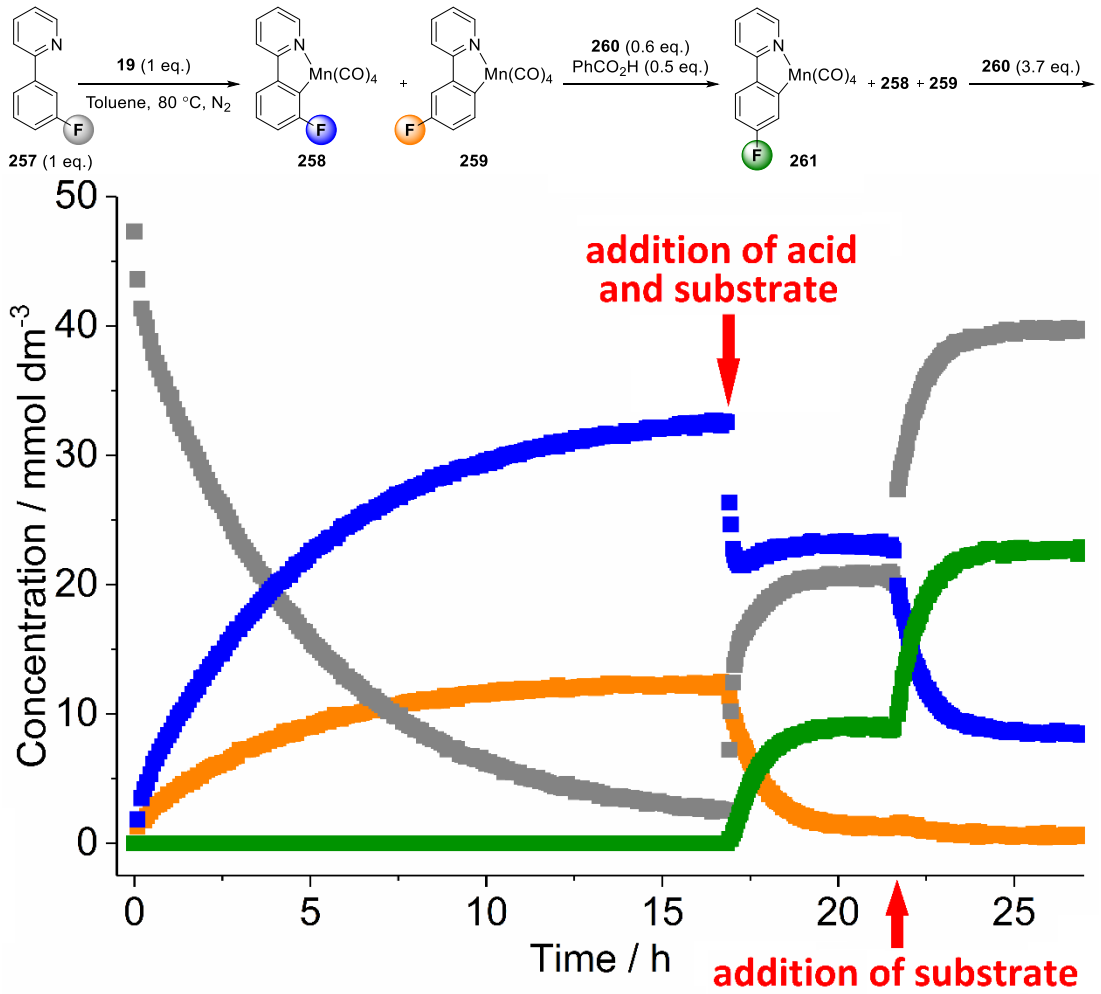

Figure 69. Kinetic plot from the *in situ* ^{19}F NMR spectroscopic monitoring of the cyclomanganation of **257** (1 eq.) with **19** (1 eq.) in toluene at 80 °C using $PhCF_3$ as internal standard, with benzoic acid (0.5 eq.) and **260** (0.55 eq.) added after 17 hours. Further **260** (3.7 eq.) was added after 21.5 hours. **260** was omitted from the plot for clarity reasons.

5.2.4 Mechanistic Implications of Acid Additives

The results observed in this study were not enough to identify all of the species involved in the reactions, but still it gave some important insights into the key steps of the mechanism of cyclomanganation (**Scheme 44**). The cyclomanganation of **257** by **19** without acid additives exhibited a rate-independence in **257** and no reaction intermediates containing **257** could be observed. This suggested both that the reaction order in **257** is zero and that that the activation of the manganese from **19** is rate-determining, presumably through initial thermal CO-loss. A stable intermediate containing **257** (that would likely be observable) must be formed for **257** to be involved

in the rate determining step of the reaction, while still exhibiting a zero-order dependence.

The most convincing result to support an irreversible cyclomanganation mechanism (in addition to the effect of benzoic acid added) arises from the heating of C_p-complex **259** (**Figure 68**). This experiment shows that **259** is thermally stable and should have interconverted to **258** in about a 3:1 ratio (**258**/**259**) if the reaction is reversible. Therefore, it can be concluded that the standard cyclomanganation of **257**/**254** was irreversible and that the observed regioselectivity must be kinetically determined. This meant that C_o-complexes were kinetically preferred over C_p-complexes, which was opposite to that hypothesised for the analogous benzylamines.[168]

The addition of sub-stoichiometric amounts of benzoic acid to the reaction drastically changed the observed regioselectivity to produce only trace quantities of the C_o-complex. This effect can either arise from the reaction becoming reversible with the addition of the acid additive, or from the rate of cyclomanganation (k_o and k_p) being significantly altered by the acid additive.

The rate of the overall reaction also increased by 1.6 (**257**) and 2.3 (**254**) times compared to the reaction without benzoic acid. The acid should have no influence on the rate if it only impacts the actual cyclomanganation step, meaning that the acid must interact with the manganese in the activation step. The large increased rate observed when pre-stirring **19** with 4-fluoro-benzoic acid, further supports this proposal. If a Mn-benzoate complex was generated from the protiodemetallation of the benzyl ligand (to form toluene), the mechanism is expected to proceed *via* a CMD/AMLA-6 mechanism, which therefore seems to be faster than the σ-CAM mechanism without additives.

The utilisation of 4-fluorobenzoic acid (0.5 eq.) led to the formation of a new species from the benzoic acid (in the ^{19}F NMR spectra) during the cyclomanganation of **257**. The formation of this species during pre-heating of the benzoic acid with **19**, supports an interaction of the acid with the manganese pre-reaction with the 2-phenylpyridine and might influence the rate of cyclomanganation (k_o and k_p). The extent of the interaction may be limited, as a large quantity of the benzoic acid remained unreacted at the end of the pre-stir. The identity of the generated species remains unknown due to unsuccessful isolation attempts and identification using other techniques. However,

the low amounts formed of the new species can be explained by it being highly air and moisture sensitive, but this would require the benzoic acid to be regenerated following degradation.

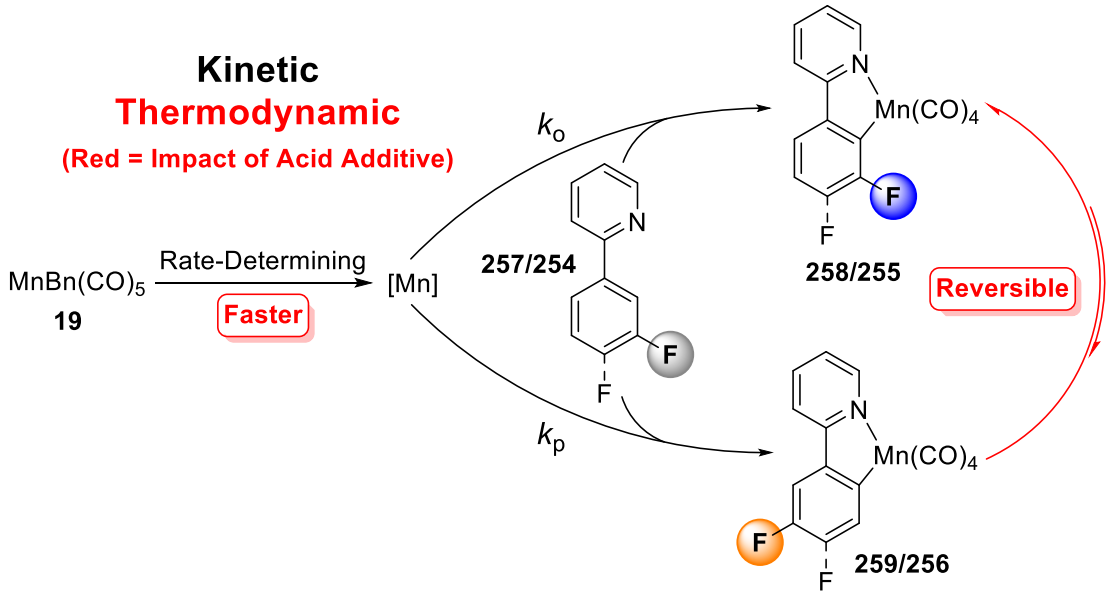

Scheme 44. Mechanistic impact of carboxylic acid additives on the cyclomanganation of fluorinated 2-phenylpyridines.

In addition to the reactions employing 4-fluorobenzoic acid suggesting at least a partial interaction between the acid and the manganese, it seems as the rate of cyclomanganation is increased with the addition. The extent of the impact is however difficult to determine in a reversible process and the experiment in which **259** is treated with benzoic acid (0.5 eq., **Figure 68**) strongly support the reaction being reversible in the presence of the acid.

The constant concentration of non-coordinated ligand **257**, following benzoic acid addition, is a common feature of all the reactions employing the acid additive. It suggests that the reaction is in an equilibrium between the two manganacycles (**258** and **259**) and **257**, as at equilibrium the quantity of each Mn-complex is determined by its relative thermodynamic stability. This means that if a Mn-benzoate complex generated (from protiodemetallation of a manganacycle) is stable enough, it should be present in solution and thus uncoordinated **257** as well. Complete consumption of **257** was observed with no addition of acid, while addition of 0.1 equivalents (benzoic acid) showed 5% of **257** remaining in solution. Thus, addition of 0.5 and 1 equivalents of 4-fluorobenzoic acid exhibited 28% and 70% respectively of **257** at the end of the reaction; the latter reaction may be lowered due to increased degradation. The

correlation between larger amount of acid used leading to more **257** observed at the end of the reaction, is consistent with the proposed mechanism.

The formation of uncoordinated **257** before **258**, after the addition of the benzoic acid to the reaction with **259** (**Figure 68**), have implications for the mechanism to interconvert between the species. Even though the protiodemetallation step likely proceeds *via* an intramolecular CMD/AMLA-6 mechanism, the initial presence of non-coordinated ligand suggest that the mechanism overall is intermolecular. This could arise from formation of a Mn(**257**)(benzoate)$(CO)_3$ complex after protonation *post factum*, which can easily be envisaged to substitute the **257**-ligand at a faster rate than the coordination and subsequent activation of the C–H bond. Therefore, non-coordinated **257** was generated at a faster rate initially than **258**. However, no further **257** should be formed after reaching its equilibrium concentration, explaining the constant concentration of **257** in solution after ~10 minutes.

Another experiment that supports an intermolecular reaction mechanism is the addition of benzoic acid and **260** to the completed cyclomanganation of **257** (**Figure 69**). The subsequent formation of **261** must proceed *via* an intermolecular mechanism, but this does not infer anything about the mechanism of interconversion between **258** and **259**. This experiment provides additional evidence for the reaction being reversible in the formation of the manganacycles, as the reaction consumes both C_o- and C_p-complexes.

The competitive formation of the three manganacycles (**258**, **259** and **261**) in this experiment (**Figure 69**) provide insight into the relative thermodynamic stability between the complexes. C_p-complex **259** is clearly the least stable complex due to the minor amounts generated under reversible and thermodynamic conditions. C_o-complex **258** can be seen being formed preferable over the C_m-complex **261** after the first addition of **260**, as the ratio of **258**/**261** (2.6:1, counting both bound and unbound ligand for **261**) is larger than **257**/**260** (1.8:1, counting both bound and unbound ligand for **260**). The same trend can be seen after the second addition of **260** as well, with the ratios being 0.375:1 (**258**/**261**) and 0.235:1 (**257**/**260**). Therefore, **257** can be concluded being 1.4–1.6 times more stable than **261** and the general stability trend of the complexes emerges as $C_o > C_m >> C_p$.

5.3 Regioselectivity in Catalytically Relevant Systems

5.3.1 *In Operando* IR Monitoring of Catalytic Reaction

It was desired to apply the gained mechanistic knowledge in improving the regioselectivity of Mn-mediated C–H bond activation of fluorinated 2-phenylpyridines into more synthetically useful systems, such as the alkenylation reaction reported by Wang and co-workers[34] discussed in previous chapters. In that report, **257** was employed as a substrate, solely yielding C_o-product **262** (60%). The selective generation of **257** suggested a reversibility in the C–H bond activation step, unless the regioselectivity in C–H bond activation is intrinsically different than that observed for the cyclomanganation reactions.

To find a rational for the reported regioselectivity, an investigation into the mechanism is warranted. Initially the reaction between **257** (2 eq.) and **34** (1 eq.), mediated by **31** (10 mol%) and Cy_2NH (20 mol%) in dry and deoxygenated toluene under a nitrogen atmosphere, was performed to enable isolation of the organic products. Compound **262** was, as expected, found as the major reaction product, with 68% yield of isolated product, following flash chromatography. Unexpectedly, the other regioisomeric alkene **263** (C_p) was isolated as a minor product (9% yield of isolated product). The appearance of the C_p-product **263** may stem from the different solvent used (Et_2O vs. toluene) or from simply not being identified previously.

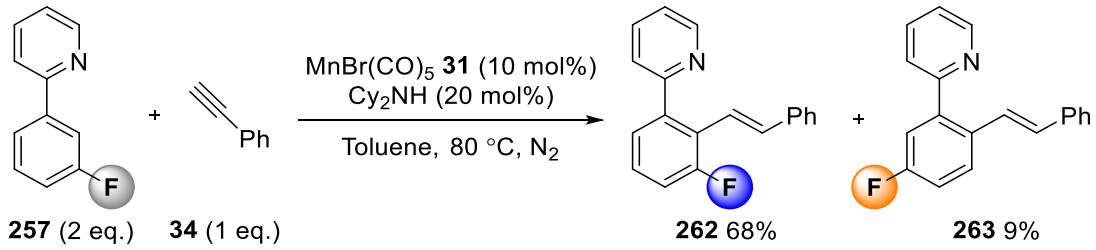

Scheme 45. Mn(I)-catalysed C–H bond alkenylation of fluorinated 2-phenylpyridine **257**.

Nevertheless, the reaction clearly generated both regioisomers and was therefore monitored by *in operando* IR spectroscopy (**Figure 70**), coupled with *ex situ* ^{19}F NMR spectroscopy. The latter technique allowed for the observation of the various species containing the 2-phenylpyridine moiety and can be correlated with the IR spectroscopic data to aid in assignment of the IR stretching bands and separation of C_o- and C_p-species. The *ex situ* samples were stored and recorded under an inert nitrogen atmosphere, to avoid any degradation of oxygen sensitive species.

Both organic products, **262** and **263**, can be monitored using ^{19}F NMR spectroscopy and therefore kinetic information for the regioselectivity could be obtained, as seen previously for the cyclomanganation reactions. C_o-product **262** was strongly preferred in the reaction generating a 9.24:1 ratio of C_o/C_p. The reaction profile for both products was normalised by division of the concentration by the final concentration ($[X]/[X]_\infty$), producing a graph which allowed for the direct comparison of the reaction profile of the two regioisomeric products. The corresponding curves for both **262** and **263** were identical, suggesting that the observed preference of **262** formation is intrinsic of the reaction and does not arise from secondary isomerisation processes. An IR deformation band (970 cm^{-1}) correlating to the alkene product forming, was observed growing during the reaction and shows the same normalised reaction profile as both the regioisomers. It should be noted that it is not clear from the obtained data whether the C–H bond activation is reversible or not under catalytic conditions, and further studies are required for this to be conclusively determined.

Compound **31** together with a new tetracarbonyl manganese complex (bands at 2071, 1982 (br) and 1943 cm^{-1}) was observed in the IR spectrum after 1 minute. The latter species was assigned as being the 7-membered tetracarbonyl manganese insertion complex **264**, due to high similarity to the non-fluorinated derivative **71** (bands at 2071, 1987 (br) and 1943 cm^{-1}). Interestingly, an induction period of a few minutes could be observed in the formation of both alkene products (**262** and **263**). The induction period was concomitant with the formation of **264** and another unknown Mn-carbonyl species (identified at 2043 cm^{-1}), which was visible in larger amounts after 5 minutes. This unknown species was thereafter consumed in the reaction and the IR stretching band depletes concomitant with organic product formation (**262** and **263**).

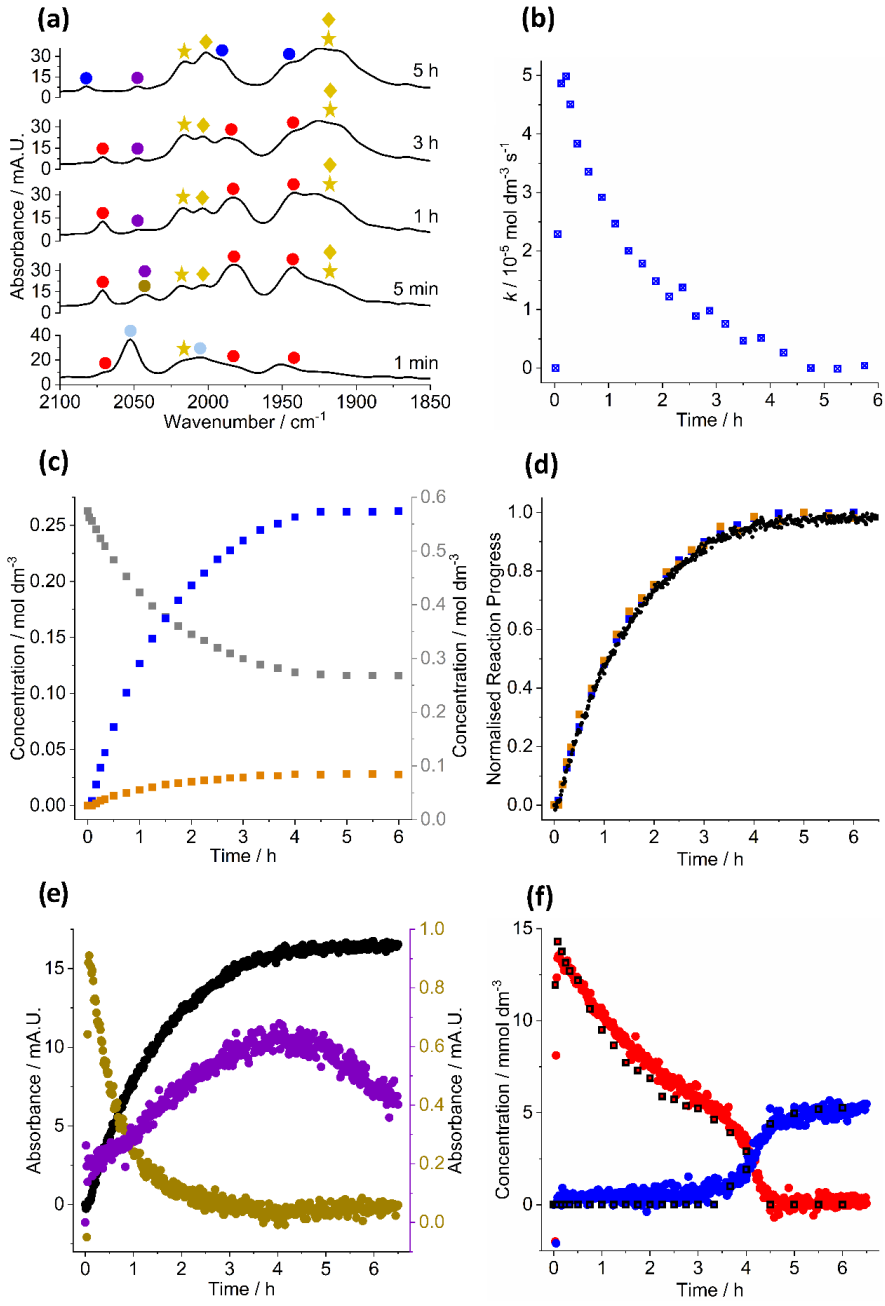

Figure 70. *In operando* IR and *ex situ* ^{19}F NMR study of the reaction between **34** and **257** using **31** as pre-catalyst with Cy_2NH as additive (**Scheme 45**). (a) IR spectra of the reaction in the metal carbonyl region at various timepoints. Key; pale blue circle = **31**, red circle = 7-membered tetracarbonyl manganese insertion complex **264**, blue circle = **258**, purple circle = **40**, dark yellow circle = unknown Mn-carbonyl species and gold star/diamond = Mn degradation complex. Reaction conditions (in order of addition); Toluene (10 ml), **257** (8.32 mmol, 2 eq.), **34** (4.16 mmol, 1 eq.), Cy_2NH (0.83 mmol, 20 mol%) and **31** (0.42 mmol, 10 mol%) at 80 °C under nitrogen atmosphere. (b) Change in the rate of formation of alkene product **262** (determined by *ex situ* ^{19}F NMR spectroscopy) over the course of the reaction. (c) Kinetic plot of the formation of alkene products **262** (blue squares, determined by *ex situ* ^{19}F NMR spectroscopy) and **263** (orange squares, determined by *ex situ* ^{19}F NMR spectroscopy), coupled with the depletion of **257** (grey squares, determined by *ex situ* ^{19}F NMR spectroscopy). (d) Normalised reaction progress for **262** (for key see (c)), **263** (for key see (c)) and the IR observed product generation (black circles, band at 970 cm^{-1}). (e) Formation and depletion of the unknown Mn-carbonyl species (dark yellow circles, band at 2043 cm^{-1}) and **40** (purple circles, band at 2047 cm^{-1}), with the formation of alkene products (black circles, band at 970 cm^{-1}). (f) Formation and depletion of 7-membered tetracarbonyl manganese insertion complex **264** (red circles, band at 2071 cm^{-1} and black/red squares, determined by *ex situ* ^{19}F NMR spectroscopy) and the formation of **258** (blue circles, band at 2084 cm^{-1} and black/blue squares, determined by *ex situ* ^{19}F NMR spectroscopy).

264 was tentatively assigned in the ^{19}F NMR spectra (−115 ppm) due to the high similarity of the behaviour of this peak to the reaction profile obtained from the IR spectroscopy. This was likely the C_o-derivative due to the strong preference of the C_o-species in the reaction. Tetracarbonyl manganese insertion complex **264** remained present in the reaction solution to the end of productive catalysis, whereas the unknown species (2043 cm^{-1}) disappeared. Afterwards, **264** was rapidly consumed as the reaction had presumably consumed all the alkyne, with the manganese only being able to proceed through one final protonation process. This resulted in the formation of **258**, as seen in both the IR and ^{19}F NMR spectroscopic data, further highlighting the high C_o-selectivity in the system as no **259** could be observed. Additionally, this result is in agreement with the mechanism proposed in Chapter 2, since only **257** or H_2O can be responsible for the final protonation step in this reaction. The alkyne **34** cannot perform the final protonation step, due to the subsequent insertion into the C–Mn bond should still take place in this case.

The lack of observation of a catalyst resting state in the formation of **263**, indicate a more rapid reaction for the C_o-derivatives. The cyclomanganation step likely sets the regioselectivity of the reaction, as this is similar to that of the stoichiometric reactions. It remains unclear whether the reaction step is reversible and why the C_p-product **263** forms in relatively high amounts, compared to the selectivity of cyclomanganation at the end of the reaction. A reversible formation of the 5-membered manganacycles (**258** and **259**) could lead to a misleading selectivity, where the regioselectivity under productive catalysis is different than under stoichiometric conditions (as under the final catalyst turnover).

Interestingly, a new peak was observed forming during the reaction at 2047 cm^{-1}, which is of high similarity to $Mn_2(CO)_{10}$ **40** and was therefore tentatively assigned as this complex. The other IR bands for **40** could not be deconvoluted due to extensive spectral overlap. **40** was seen increasing until the completion of the catalysis, at which point its depletion was noted. Further studies are required to determine if **40** is a part of the catalysis, a degradation species or takes part in a different process.

Catalyst degradation manganese complexes appeared alongside the productive catalysis. These manganese complexes (with two distinct bands at 2017 and 2004 cm^{-1}) show a large similarity to the reaction using non-fluorinated **33** (2020 and 2006 cm^{-1}

at 60 °C in *n*-Bu_2O) and was therefore assigned to be the corresponding species. Isolation or further characterisation of the degradation complexes is required, but it seemed from the similarity of the IR stretching bands that the 2-phenylpyridine ligand was not incorporated into the complexes. This is in support of the assignment of these complexes being various Mn-hydroxyl and Mn-alkynyl clusters.

5.3.2 Rate of C–C Bond Formation for Regioisomeric Manganacycles

Cyclomanganation reactions has mainly been utilised in the investigation into the fluorine-induced regioselectivity to this point. In principle, the C–Mn bond breakage can reveal as much information about the regioselectivity as the bond formation process, where the relative thermodynamic stability of the C_o-, C_m- and C_p-complexes has already been determined for monosubstituted manganacycles. The differences in thermodynamic stability should translate into the rate of C–C bond formation, where the least stable complex reacts fastest due to a more reactive C–Mn bond.

TRIR spectroscopy provide, as seen previously (Chapter 3), the ability to obtain rates of C–C bond formation without interference of other reaction steps. Therefore, **258** was photolysed in neat **34** ([**258**] = 1.89×10^{-3} mol dm^{-3}) using a 355 nm pump to release one of the CO-ligands and initiate the C–C bond formation process (**Figure 71**). The reaction proceeded in the same manner as for the non-fluorinated substrate **10**. Initially, the arene-bound complex **265** was observed (2016 and 1915 (br) cm^{-1}), followed by the alkyne-coordinated species **266** (2018, 1955 and 1923 cm^{-1}), which subsequently inserted into the C–Mn bond to form insertion complex **267** (2013, 1924 and 1897 cm^{-1}). The experiments employing the other four manganacycles (**259**, **255**, **256** and **261**) within this work proceeded *via* the same line of events (**Table 19**). All the TRIR experiment within this chapter was performed using the LIFEtime experimental setup.

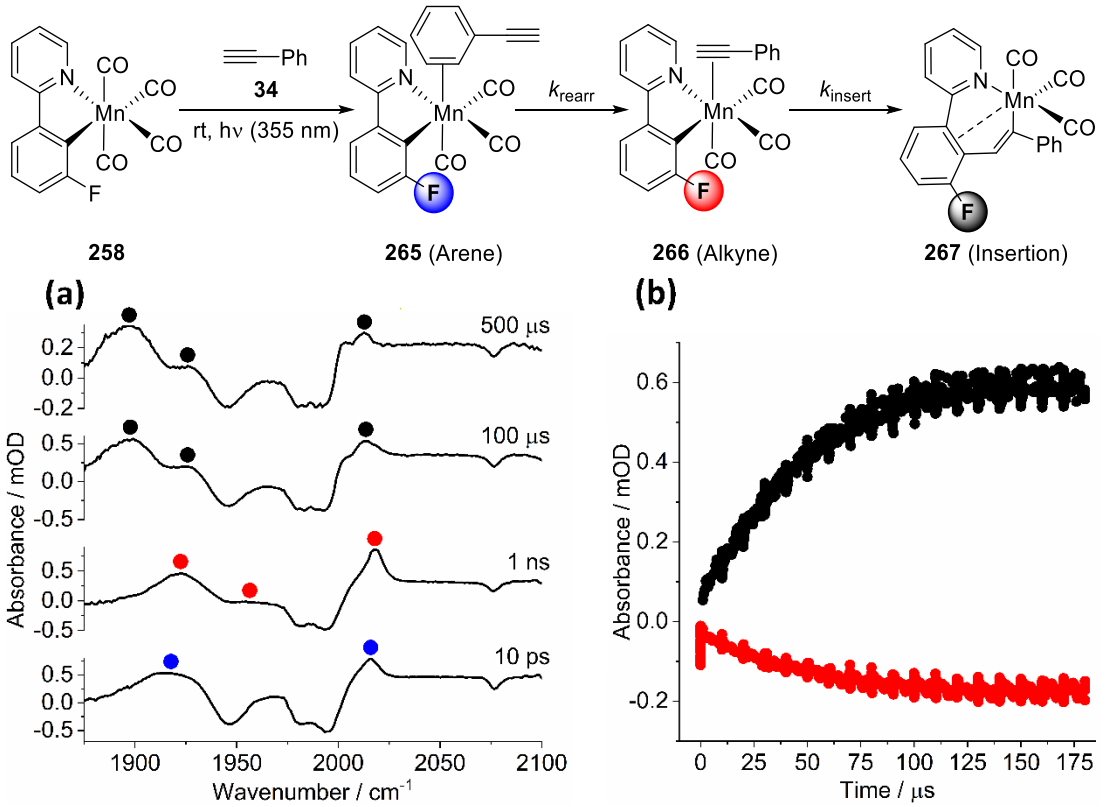

Figure 71. TRIR study of the photolysis of **258** in neat **34** ([**258**] = 1.75 × 10^{-3} mol dm^{-3}), showing the formation of the various species in solution after irradiation. (a) IR spectra of the reaction showing the metal carbonyl region at various timepoints. Negative bleach bands correspond the loss of **258** after irradiation. (b) Kinetic plot of the formation of **267** (black circles, band at 1897 cm^{-1}) and depletion of **266** (red circles, band at 1955 cm^{-1}), extracted from (a).

Unexpectedly, a new species with an IR stretching band at 2002 cm^{-1} was seen forming at longer times in the reactions. The location of the new species was roughly the same in all the experiments and formed in larger quantities for the C_p-complexes than for the C_o-derivatives. The band was overlapping with the bleach band, as was confirmed by subtraction of the bleaches. The formation of the unknown species occurred alongside the insertion step and the rate of formation seemed to change according to changes in k_{insert}. Therefore, it was unlikely that the unknown species was formed from the insertion complex, unless the two species was in an equilibrium with each other. The larger amounts formed for the C_p-complexes suggested that the *ortho*-fluorine effect affects the rate of formation of the unknown species, more than the rate of C–C bond formation. The identity of the unknown species requires further studies to be accurately determined.

Large changes in the rate of insertion into the C–Mn bond (k_{insert}) were observed between the different substrates (**Table 19**). Firstly, a clear dependence on the amount of fluorine substituents in the system was found, where non-fluorinated derivative **10**

(k_{insert} = 1.35 ± 0.09 10^5 s^{-1} at room temperature) showed more than twice as high rate compared to C_p-complex **259** (k_{insert} = 5.7 ± 0.2 10^4 s^{-1} at room temperature, second fastest substrate), who in turn is faster than difluorinated complex **256** (k_{insert} = 1.86 ± 0.05 10^4 s^{-1} at room temperature). A similar dependence was observed for the C_o-complexes, though it should be noted that an excessive 15-point smoothening function was required to obtain the rate of insertion for **255**.

Table 19. TRIR spectroscopic data and rate constants obtained (at room temperature) from the photolysis of the manganacycles in neat **34**.

Entry	Complex	Arene / cm^{-1}	Alkyne / cm^{-1}	k_{rearr} / 10^9 s^{-1}	Insertion / cm^{-1}	k_{insert} / 10^4 s^{-1}
1	**10**	2006 and 1912 (br)	2009, 1944 and 1912	3.8 ± 0.7	2008, 1922 and 1899	13.5 ± 0.9
2	**258**	2016 and 1915 (br)	2018, 1955 and 1923	3.0 ± 0.3[1]	2013, 1924 and 1897	2.21 ± 0.04
3	**255**	2019 and 1918 (br)	2020, 1968 and 1925	1.7 ± 0.6[1]	2021, 1925 and 1897	0.36 ± 0.01[2]
4	**261**	2011 and 1913 (br)	2014, 1950 and 1916	2.3 ± 0.5[1]	2012, 1923 and 1898	3.5 ± 0.1
5	**259**	2009 and 1910 (br)	2013, 1948 and 1912	2.9 ± 0.4[1]	2011, 1920 and 1897	5.7 ± 0.2
6	**256**	2012 and 1915 (br)	2015, 1953 and 1917	1.7 ± 0.4[1]	2013, 1921 and 1895	1.86 ± 0.05[1]

[1]Data treated with a 6-point smoothening function. [2]Data treated with a 15-point smoothening function.

The position of the fluorine on the arene (with respect to the manganese) had an impact on the rate of C–C bond formation, where C_p (**259**, k_{insert} = 5.7 ± 0.2 10^4 s^{-1} at room temperature) was faster than C_m (**261**, k_{insert} = 3.5 ± 0.1 10^4 s^{-1} at room temperature) and C_o was the slowest (**258**, k_{insert} = 2.21 ± 0.04 10^4 s^{-1} at room temperature). These rates support the previously determined thermodynamic stability trend of the

manganese complexes (**258**, **259** and **261**, Chapter 5.2.4) and was consistent with an *ortho*-fluorine effect, where the C_o-position is stabilised and C_p-position destabilised (relative to the C_m-complex). **261** inserted 1.59 ± 0.03 times faster than **258**, matching the previously determined thermodynamic stability of C_o being 1.4–1.6 more stable than C_p.

Table 20. Reaction scheme of the photolysis of the manganacycles in toluene, with TRIR spectroscopic data and rate constants obtained (at room temperature).

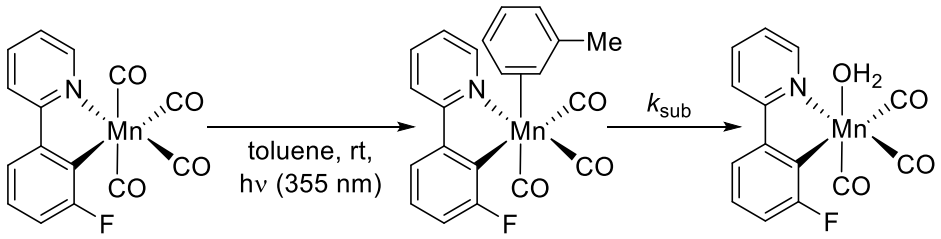

258 **268** (Toluene) **269** (Water)

Entry	Complex	Tol / cm^{-1}	Water / cm^{-1}	k_{sub} / 10^5 s^{-1}
1	**10**	2004 and 1907 (br)	2003, 1905 and 1893	2.1 ± 0.4
2	**258**	2015, 1929 and 1909	2012, 1920 and 1896	1.58 ± 0.04
3	**255**	2018, 1933 and 1914	2015, 1923 and 1901	1.14 ± 0.04
4	**261**	2009 and 1912 (br)	2006, 1906 and 1893	1.27 ± 0.03
5	**259**	2008 and 1909 (br)	2005, 1906 and 1893	2.4 ± 0.2
6	**256**	2008 and 1915 (br)	2008, 1909 and 1898	0.96 ± 0.03

To further validate the experimental results in neat **34** and to observe the rate of insertion in more catalytically relevant system, it was desired to perform the reactions diluted in toluene. Firstly, the manganacycles were irradiated in toluene to obtain the location of the IR bands for the toluene-adduct and observe its behaviour (**Table 20**). The complexes behaved in a similar manner to that of **10** in the initial formation of toluene-complex **268**, followed by the substitution by water from the surrounding solvent. The rate of this process was not dependent on the position or amount of

fluorine-substituents and the rate of substitution was generally in the rage of k_{sub} = 1–2.5 × 10^5 s^{-1} (at room temperature).

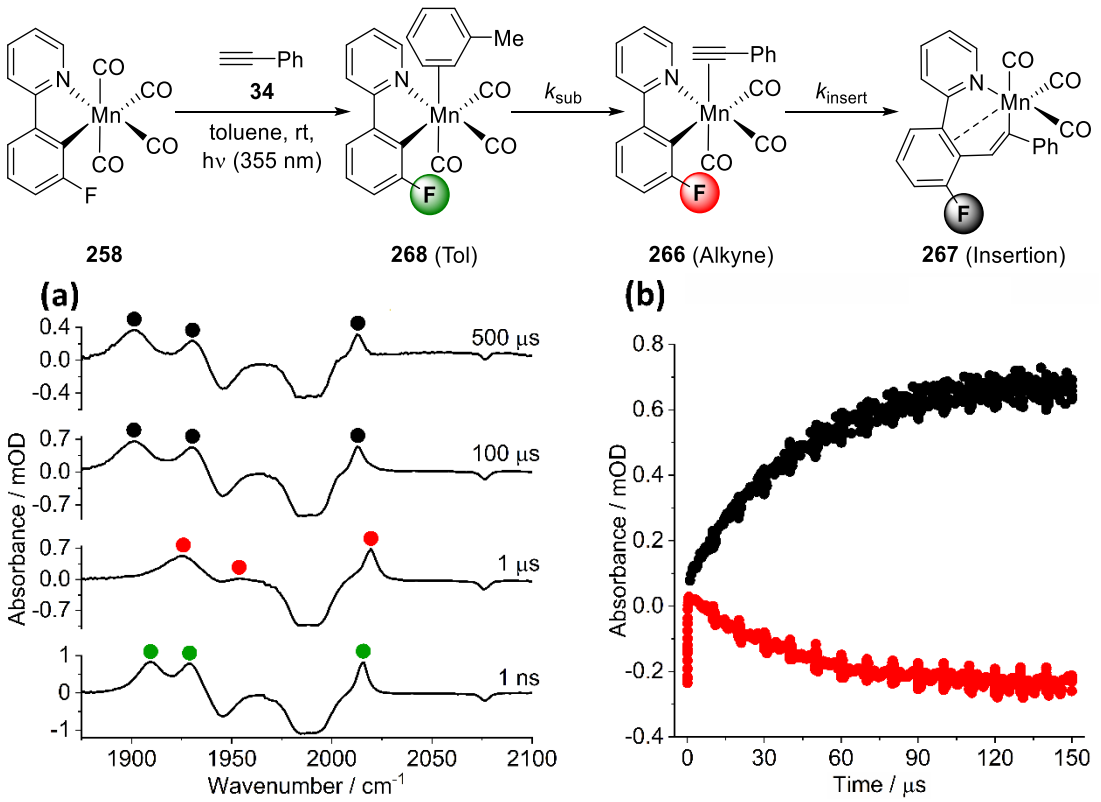

Figure 72. TRIR study of the photolysis of **258** in **34**/toluene solution ([**258**] = 1.75 × 10^{-3} mol dm^{-3} and [**34**] = 0.27 mol dm^{-3}), showing the formation of the various species in solution after irradiation. (a) IR spectra of the reaction showing the metal carbonyl region at various timepoints. Negative bleach bands correspond the loss of **258** after irradiation. (b) Kinetic plot of the formation of **267** (black circles, band at 1901 cm^{-1}) and depletion of **266** (red circles, band at 1954 cm^{-1}), extracted from (a).

Alkyne **34** was added to the toluene solution ([**34**] = 0.27 mol dm^{-3}) and the TRIR spectroscopic experiments repeated (**Figure 72**). The expected initial formation of toluene-complex **268** was observed, from which the substitution by **34** took place to form alkyne-complex **266** instead. No dependence on the fluorine-substituents was observed (**Table 21**) and all substrates proceeded through the subsequent insertion step. The rate of insertion followed the same trend observed in neat alkyne, where the rate decreases with more fluorine-substituents. The impact of regioselectivity continued, with C_p-complex **259** reacting the fastest. **261** inserted 1.72 ± 0.03 times faster than **258**, again supporting the relative thermodynamic stability of the complexes. The experiments also showed that C_o-complex **258** inserts 3.21 ± 0.06 times faster than C_p-complex **259**. This should correlate to the relative stability of the complexes, though it was smaller than what is observed for the stoichiometric cyclomanganation reactions previously studied.

Table 21. TRIR spectroscopic data and rate constants obtained (at room temperature) from the photolysis of the manganacycles in **34**/toluene solution ([**34**] = 0.27 mol dm^{-3}).

Entry	Complex	Tol / cm^{-1}	Alkyne / cm^{-1}	k_{sub} / 10^7 s^{-1}	Insertion / cm^{-1}	k_{insert} / 10^4 s^{-1}
1	**10**[1]	2004 and 1907 (br)	2008, 1940 and 1909	0.39 ± 0.06	2006, 1917 and 1990	16 ± 3
2	**258**	2015, 1929 and 1909	2020, 1954 and 1925	1.1 ± 0.1	2013, 1930 and 1901	2.39 ± 0.05
3	**255**	2017, 1932 and 1914	2022, 1963 and 1928	0.5 ± 0.1	2016, 1931 and 1903	0.72 ± 0.02[2,3]
4	**261**	2009 and 1912 (br)	2015, 1950 and 1918	0.71 ± 0.09	2012, 1929 and 1902	4.10 ± 0.08
5	**259**	2008 and 1909 (br)	2013, 1946 and 1916	1.0 ± 0.2	2012, 1927 and 1900	7.7 ± 0.4
6	**256**	2011 and 1914 (br)	2016, 1951 and 1919	6.3 ± 0.8	2014, 1929 and 1902	1.88 ± 0.04[4]

[1][**34**] = 0.05 mol dm^{-3}. [2]Data treated with a 15-point smoothening function. [3]Determined using loss of alkyne-complex. [4]Data treated with a 6-point smoothening function.

Chapter 6: Conclusions and Future Work

6.1 Conclusions

The research presented within this thesis has focused on understanding the mechanism and properties influencing the reactivity of Mn(I)-mediated C–H bond functionalisation. IR spectroscopy has proven to be invaluable in the monitoring of the reactions, which has been performed on timescales from pico- to kiloseconds. In particular, the utilisation of TRIR spectroscopy in the direct observation of intermediates and kinetics of individual steps within the catalytic cycle, is something that has not previously been reported in the literature.

A more traditional mechanistic investigation was performed into Mn(I)-catalysed C–H bond alkenylations (**Scheme 46**), where *in operando* IR spectroscopy was used as the main analytical technique. It allowed for the direct monitoring of the longer-lived manganese species in solution and thereby elucidation of the pre-catalyst activation pathways. It was found that pre-catalyst activation is substrate-dependent, with internal alkynes proceeding *via* the previously proposed mechanism of initial formation of manganacycle **10**.[34] However, terminal alkynes proceeded *via* initial C–H bond breakage of the alkynyl-hydrogen to form a manganese alkynyl-complex. This complex can thereafter cyclomanganate the 2-phenylpyridine ligand, allowing entry into the catalytic cycles without generating **10**. The higher rate of reaction of **31** with the alkyne compared to the 2-phenylpyridine is presumably the reason for terminal alkynes preferring the latter mechanism.

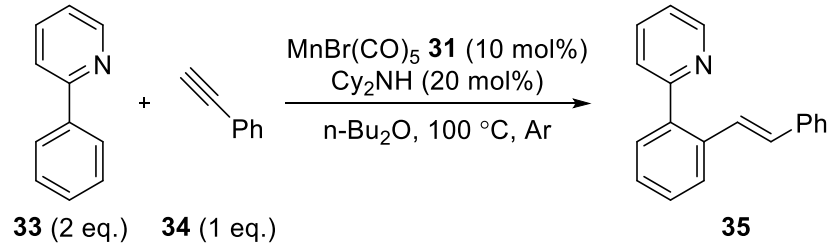

Scheme 46. Mn(I)-catalysed C–H bond alkenylation reaction studied within this chapter, originally reported by Wang and co-workers.[34]

The protonation pathways to generate alkene product **35** from 7-membered manganese insertion complex **77**, were probed using stoichiometric reactions starting from **10**, where the amount of alkyne and additives were varied. Through these studies it was found that the alkyne, 2-phenylpyridine and water are all capable of performing the

proton transfer event. This added to the proposed mechanism by Wang and co-workers, which was limited to the process involving the terminal alkyne as the proton source.[34] DFT-calculations showed that these reaction pathways are all preferential compared to reductive elimination or double insertion. This was not the case for internal alkynes as the reductive elimination is dominant and the corresponding pyridinium salt was cleanly generated, which highlighted why these substrates was reported as inactive under catalytic conditions.[34]

The C–C bond formation step of the mechanism was studied using TRIR spectroscopy and photochemical initiation (**Scheme 47**). Photolysis of **10** dissociated one of the CO-ligands and allowed for the binding of the alkyne-substrate. It was found that phenylacetylene **34** prefers initial π-coordination to the phenyl ring (**125**) and was observed at the earliest timescales (0.5 ps). On nanosecond timescale, a rearrangement took place to form alkyne-complex **63**, which thereafter transformed into insertion-complex **77** over microsecond times, confirming the proposed reaction pathway for C–C bond formation.[34] The experiment was repeated in toluene solution, where the main difference was the initial formation of a toluene-bound complex, replacing complex **125**. The rate constants of the steps could be obtained and through changing the concentration of **34**, it was found that the substitution of toluene was dependent on [**34**]. The rate of insertion was however independent on the alkyne concentration, due to this step being unimolecular.

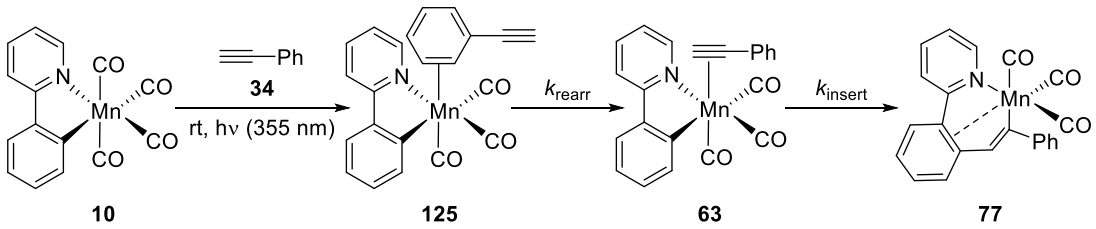

Scheme 47. Reaction mechanism of C–C bond formation in neat **34**, deduced by TRIR spectroscopy.

Further experiments were performed to probe the reactivity of both the manganacycle and unsaturated substrate. Electronic differences on the phenyl ring of **34** did affect the rate of insertion, while trend emerged in which slower rates of C–C bond formation were observed for the manganacycles mainly used in catalytic methodologies.[32] Steric bulk on the 2-phenylpyridine ligand did not seem to affect the rate of insertion, though in some cases the rate of rearrangement to the alkyne-complex was impacted. Moving to acrylates as the unsaturated substrate led to the observation of two separate reaction

pathways, in the formation of *O*- and alkene-bound complexes. Both pathways converged into the alkene-complex which could insert into the C–Mn bond, suggesting that in general, the addition of heteroatoms to the unsaturated substrate does not affect the ability to insert into the C–Mn bond. Unproductive substrates in the Mn(I)-catalysis, such as styrene[36] and benzaldehyde,[42] could be seen forming their respective alkene- and *O*-bound complexes. These complexes did not insert to form the new C–C bond, providing a rationale for their lack of reactivity under catalytic conditions. Additionally, the rate of insertion could be directly correlated to the DFT-calculated energy barriers for the respective C–C bond formation steps, which showed that DFT-calculations can accurately determine if an insertion into the C–Mn bond will occur. These studies show in conclusion that TRIR spectroscopy is a highly suitable technique to study the nature of the short-lived intermediates involved in the C–C bond formation.

Carboxylic acid additives, such as propionic acid, has been shown within this thesis to have a major impact on the efficiency of the Mn(I)-catalysis studied. It was found that for terminal alkynes **34** and **146** it had a positive effect, almost doubling the conversion to alkene product **174**. The rationale for this positive effect is the effective protonation of C–Mn bonds by the carboxylic acid, which was studied using TRIR spectroscopy. It was found that the acetic acid performs the proton transfer *via* the CMD/AMLA-6 mechanism, the intermediates and kinetics of which could be observed (**Scheme 48**). This was the first time that the short-lived intermediates in this process have been directly observed and provided experimental evidence to support the previously observed effects of carboxylic acid additives.[51, 155, 157]

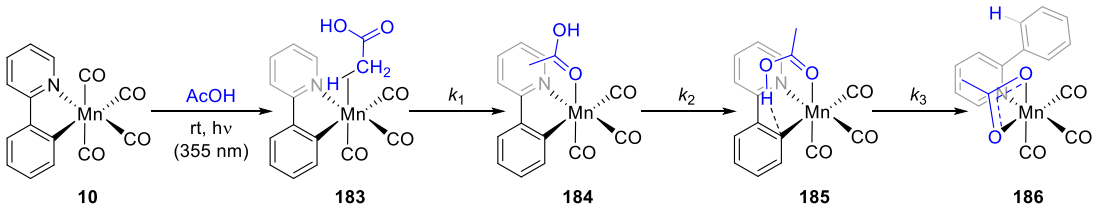

Scheme 48. CMD/AMLA-6 mechanism of C–H bond formation in neat acetic acid, deduced by TRIR spectroscopy.

The acid additives had a surprisingly negative effect of the reactions employing acrylates as substrates, lowering the conversion to product significantly. This effect arises as the resting state of catalysis was **10**, which was different to the reactions using terminal alkynes. Complex **10** degraded to catalytically inactive species if treated with

acid additives, leading to the lower conversions observed. This highlights the importance of mechanistic understanding, as seemingly similar reactions (with terminal alkynes and acrylates) can differ in critical ways. Nevertheless, the acid additives could be employed in the successful synthesis of alkene-products **89** and **52**, which cannot be generated using the standard reaction conditions as these intermediates are prone to reductive elimination.

Finally, the fluorine-induced regioselectivity on the Mn(I)-mediated C–H bond activation and functionalisation has been studied using ^{19}F NMR and TRIR spectroscopy. It was found through stoichiometric cyclomanganation reactions of two different fluorinated 2-phenylpyridines, **257** and **254**, that the *ortho*-position (C_o) was preferred in both cases. Due to the standard cyclomanganation reaction (with no additives) being irreversible it was concluded that this selectivity is kinetically determined. Benzoic acid generated a reversible reaction, where the selectivity became determined thermodynamically. Through competition experiments of **258** and **259** with C_m-complex **258**, it was found that the relative stability of the complexes follows a trend of; $C_o > C_m > C_p$. TRIR spectroscopic experiments were employed and the rates of insertion (k_{insert}) supported the relative stability trend of the manganacycles, as the C–Mn bond strength should affect the observed rate. The *ortho*-selectivity translates into the catalysis, where both regioisomermic products were found, contrary to previous reports.[34]

6.2 Future Work

6.2.1 Further Mechanistic Studies

The mechanistic studies within this thesis has found several different catalytic cycles of Mn(I)-catalysed C–H bond alkenylation, which can be affected by carboxylic acid additives. Though comprehensive, this study does not cover all aspects of the reaction mechanism, with especially catalyst degradation requiring further studies. The mapping of how the catalyst degrades, would allow for the development of methods to suppress these pathways and therefore increase the efficiency of the catalysis. Additionally, further studies into the double insertion and reductive elimination pathways can allow for methods to selectively generate each of the three main products in a given reaction system.

Investigating a large range of Mn(I)-catalysed C–H bond functionalisation processes allows for a database of mechanistic knowledge to be generated. As a result, trends emerge and the reactivity of (un)known compounds can be rationalised, new improved methodologies can be designed, and current methodologies optimised. The inactivity of 6-substituted 2-phenylpyridines in the catalysis can for example be solved and complicated systems with multiple functional groups selectively modified. The generality of activation pathways for the current and future pre-catalysts can be determined and thereby aid in the production of new and improved pre-catalysts. For example, the thermal activation of $Mn_2(CO)_{10}$ **40** under catalytic conditions is poorly understood and studies to explore this reactivity can lead to new reactivity being discovered.

Some of the ultimate aims to perform the reactions without a directing group and to functionalise sp^3-hybridised C–H bonds, will likely not be achievable without further understanding of the underpinning chemistry taking place. New pre-catalysts need to be designed, which does not require directing groups and is active enough to functionalise an alkyl C–H bond. The knowledge on which this design is based must arise from mechanistic understanding of how existing and future manganese complexes react.

6.2.2 TRIR Spectroscopy

There are a lot of room for expansion of the TRIR spectroscopic studies of manganese-carbonyl complexes. Many of the reported Mn(I)-catalysed C–H bond functionalisation processes have not been studied within this thesis. The properties underlying the C–C and C–X bond formation steps are important and by probing this step for a wider range of substrates, a more complete understanding can be obtained. Trends of reactivity and understanding of why some substrates are not viable for use in catalytic reactions, can be achieved through this expanded study.

New reactivity of the manganese-complexes can also be probed using TRIR-spectroscopy, where for example the selective CO-loss or radical formation from $Mn_2(CO)_{10}$ **40** can be studied in the reaction with new substrates, which could lead to new synthetically useful reactions. The formation of triplet excited states can also be exploited using this analytical technique, where the lifetime of the excited state can be

monitored. If a suitable long-lived triplet excited state is generated, its reactivity can be probed, and new synthetic procedures can be developed. Photoredox catalysis is a potential field of interest for the non-dissociative excited state chemistry.

This technique could also be exploited in the monitoring of other transition metal mediated transformations which are initiated by light. One of the main issues with many of the photochemically initiated reactions are that they do not contain good IR reporter groups and it may therefore be difficult to correctly identify intermediates forming in the reaction. The most obvious type of chemistry that can be monitored using TRIR spectroscopy is transition metal mediated photoredox catalysis, of which there have been a plethora of synthetic work reported in the past decade.[172] Monitoring of ruthenium or iridium 2,2-bipyridine complexes reacting with organic substrates upon irradiation can prove a powerful tool for the investigation of the mechanisms of these reactions. This type of studies has been conducted by Orr-Ewing and co-workers using organic photoredox catalysts.[173] There are additional transition metal catalysed reactions that can be investigated, such as Fe-catalysed amination of benzylic alcohols. The Fe-catalysts contain suitable IR active CO-ligands and the reactions has been shown to be photochemically initiated.[174]

6.2.3 Catalyst Design

The pre-catalysts utilised in Mn(I)-catalysed C–H bond functionalisation has to this point been limited to simple manganese carbonyl complexes, such as $MnBr(CO)_5$ **31** and $Mn_2(CO)_{10}$ **40**. This is a surprisingly small diversity, if compared to more established transition metal-mediated reactions, such as for example Pd-catalysed cross-coupling reactions.[1]

There are other Mn(I)-carbonyl complexes reported which provide an interesting starting ground for the development of new pre-catalysts. For example, 2,2-bipyridine and phosphine ligands has often been coordinated to Mn(I)-centres, which has been used in for example CO_2-reduction chemistry.[175] Cyclic and acyclic pentadienyl manganese tricarbonyl complexes[176] also provide an interesting alternative, contingent on the ability to dissociate the pentadienyl-ligand.

The most promising class of manganese-precursors are the *N*-heterocyclic carbene (NHC) containing Mn(I)-complexes. There a few reported manganese tricarbonyl

complexes with bidentate NHC-ligands.[177] The ease of modification of the steric and electronic properties of the NHC-ligands are the main attractive element for the utilisation of them in catalysis. Monodentate ligands are likely more useful, to avoid too strong coordination to be manganese and thereby hindering the catalysis from taking place.

A final way that new pre-catalysts can be generated is by the removal of the carbonyl-ligands. The synthesis of **40** is usually performed under high temperature and pressure of carbon monoxide, though it is possible to generate it at ambient pressure from Cp'Mn(CO)$_3$ (MMT).[178] Therefore, a new synthesis to avoid the use of the toxic CO-gas and harsh reaction conditions is desired and could possibly be achieved using electrochemical synthesis. The main issue with replacing the CO-ligands is the high oxidation potential of CO compared to most other ligands.[179] Therefore, it is difficult to keep the manganese from oxidising and is the major challenge to be overcome for this to be successful.

6.2.4 *Ortho*-Fluorine Effect

Further investigation into the *ortho*-fluorine effect observed within this thesis, can allow for the underlying rationale behind the effect to be determined. That the effect is kinetically determined under standard conditions has been concluded, but why the thermodynamically preferred product also is kinetically preferred is still unknown. Additionally, the exact reasons why the C–Mn bond is seemingly stronger for the *ortho*-complex is also undetermined and further computational and experimental studies could shed light on this issue. The understanding of these issues can also allow for the rationale behind the selectivity observed for other substituents, such as methyl and methoxy. In addition, through understanding the factors governing the regioselectivity, the observed kinetic selectivity could potentially be reversed. This could have a major impact on the C–H bond functionalisation reactions, as the minor product could be generated in greater amounts and thereby improving the usefulness of the methodology.

Chapter 7: Experimental

7.1 General Experimental Information

Solvents and Reagents

Commercially sourced reagents were purchased from Acros Organics, Alfa Aesar, Fluorochem, or Sigma-Aldrich and used as received unless otherwise stated. Dicyclohexylamine was deoxygenated with N_2 under sonication and stored in a solvent ampule under N_2. Dry THF, CH_2Cl_2, hexane, toluene and MeCN were obtained from a Pure Solv MD-7 solvent system and stored under nitrogen. THF was also degassed by bubbling N_2 through the solvent under sonication. Petroleum ether refers to the fraction of petroleum that is collected at 40−60 °C. Reactions requiring anhydrous conditions were carried out using Schlenk techniques (high vacuum, liquid nitrogen trap on a standard in-house built dual line). Room-temperature upper and lower limits are stated as 13−25 °C, but typically 21 °C was recorded.

Compound **129** and **130** were synthesised by Francis Clarke and Stephanie Meyer respectively.[146] Compound **135** was synthesised by Dr Joshua Bray and characterisation data were in accordance with the literature.[49]

Chromatography

Thin-layer chromatography (TLC) was carried out using Merck 5554 aluminum-backed silica plates (silica gel 60 F254), and spots were visualized using UV light (254 nm). Where necessary, plates were stained and heated with potassium permanganate, anisaldehyde, or vanillin as appropriate. Retention factors (R_f) are reported along with the solvent system used in parenthesis. Flash column chromatography was performed according to the method reported by Still et al.[180] using Fluorochem silica gel 60 (particle size 40−63 μm) and a solvent system as stated in the text.

Melting Points

Melting points were recorded using a Stuart digital SMP3 machine using a temperature ramp of 3 °C min^{-1}.

Infrared Spectroscopy

Infrared spectra were obtained using a Unicam Research Series FTIR (KBr IR) or a Bruker APLHA-Platinum FTIR Spectrometer with a platinum−diamond ATR sampling module. Where indicated, reactions were monitored in situ using a Mettler Toledo ReactIR ic10 with a K6 conduit SiComp (silicon) probe and MCT detector.

Time-Resolved Infrared Spectroscopy (ULTRA A)

The Time-Resolved Infrared (TRIR) Spectroscopic experiments were performed at the Central Laser Facility (Science & Technology Facilities Council (STFC), Rutherford Appleton Laboratories, Oxfordshire, UK) using the Time-Resolved Multiple Probe Spectroscopy ($TR^{M}PS$) at the ULTRA facility. The experiments were driven by a 10 kHz repetition rate Ti:Sapphire amplifier (Thales) as a probe source, producing 40 fs pulses at 800 nm. The Ti:Sapphire laser output was used to pump an Optical Parametric Amplifier (OPA, TOPAS; Light Conversion Ltd.) followed by an AgGaS 'Difference-frequency mixing' stage, which produced a tuneable mid-infrared probe beam of ~500 cm^{-1} useable bandwidth. The IR probe beam was split to form reference and probe beams, which were passed through spectrographs onto Mercury Cadmium Telluride (MCT) array detectors (InfraRed Associates). The probe beam spot size at sample was around 80 µm × 80 µm. High speed data acquisition systems (Quantum Detectors) allowed 10 kHz acquisition and processing of the probe and reference pulses to generate a pump-on/pump-off IR absorption difference signal. The excitation source for the TRIR experiments was the output of the 1 kHz Ti:Sapphire amplifier (Spectra-Physics Spitfire XP; 100 fs pulse length) equipped with another TOPAS OPA. The pulse energy at the sample was attenuated down to 1 µJ and forced down to a spot size around 150 µm × 150 µm. Both ULTRA and Spitfire amplifiers were optically synchronised by sharing the same seed from a 68 MHz Ti:Sapphire oscillator. The seed beam was delayed with an optical delay line before the 1 kHz amplifier to accommodate for the 100 fs – 14.7 ns time delays between the pump and probe. For times beyond 14.7 ns and up to 100 µs, subsequent seed pulses were selected from the 68 MHz seed pulse train accompanied by the appropriate setting of the optical delay line. The polarization of the excitation beam at sample was set to 54.7° with respect to the probe.

Data was collected using pump-probe delays ranging from 0.5 ps to 850 μs. Data was acquired with the pump laser on (pump-on) and also under essentially identical conditions with the pump laser off (pump-off). Subtraction of the pump-off data from the pump-on data allowed for removal of electrical noise.

Time-Resolved Infrared Spectroscopy (LIFEtime)

The Time-Resolved Infrared (TRIR) Spectroscopic experiments were performed at the Central Laser Facility (Science & Technology Facilities Council (STFC), Rutherford Appleton Laboratories, Oxfordshire, UK) using the Time-Resolved Multiple Probe Spectroscopy ($TR^{M}PS$) at the ULTRA facility. The experiments were driven by a 100 kHz repetition rate Yb:KGW amplifier (Pharos) as pump source, producing 260 fs pulses at 1030 nm. The laser output was used to pump a BBO-based 515 nm pumped Optical Parametric Amplifier (OPA). The pump beam was collimated, travelled along a programmable optical delay line (0-16 ns 1200 mm long double pass), then focused onto the sample. The probe beam sources from a 100 kHz repetition rate YB:KGW amplifier(Pharos) producing 6W, 180 fs pulses at 1030 nm, driving two 3 W BBO/KTA based OPAs. The two Pharos sources shared an 80 MHz oscillator, allowing pump-probe delay steps of 12.5 ns. The probe beam was split to provide probe and reference pulses. The probe beams were collimated, synchronised by a fixed optical delay, and focused by a gold parabolic mirror onto the sample. The probe beam spot size at sample was around 180 μm × 180 μm. The three beams were overlapped on the sample using a 50 μm pinhole. The probe beams were measured by two separate 128-element detectors. To go beyond 12.5 ns, subsequent seed pulses can be selected from the 80 MHz oscillator.

Data were collected using pump-probe delays ranging from 1 ps to 988.5 μs.

Nuclear Magnetic Resonance Spectroscopy

NMR spectra were obtained in the solvent indicated using a JEOL ECX400 or JEOL ECS400 spectrometer (400, 128, 101 and 376 MHz for ^{1}H, ^{11}B, ^{13}C and ^{19}F respectively) or a Bruker 500 (500, 125 and 470 MHz for ^{1}H, ^{13}C and ^{19}F respectively). Chemical shifts are reported in parts per million and were referenced to the residual

non-deuterated solvent of the deuterated solvent used ($CHCl_3$ TMH = 7.26 and TMC = 77.16 ($CDCl_3$), $CDHCl_2$ TMH = 5.31 and TMC = 54.0 (CD_2Cl_2), ^1H and ^{13}C, respectively). Spectra were typically run at a temperature of 298 (for $CDCl_3$) or 295 K (for CD_2Cl_2). All ^{13}C NMR spectra were obtained with ^1H decoupling. NMR spectra were processed using MestReNova software (versions 11.0.3-18688, 2017 and 12.0.3-21384, 2018). For the ^1H NMR spectra, the resolution varies from 0.15 to 0.5 Hz; the coupling constants have been quoted to ±0.5 Hz in all cases for consistency. ^1H NMR chemical shifts are reported to two decimal places, and ^{13}C NMR chemical shifts are reported to one decimal place.

Mass Spectrometry

Electrospray ionisation (ESI) mass spectrometry (MS) spectra were measured using a Bruker Daltronics micrOTOF MS, Agilent series 1200LC with electrospray ionization (ESI and APCI) or on a Thermo LCQ using electrospray ionization, with <5 ppm error recorded for all HRMS samples. Liquid induction field desorption ionisation (LIFDI) and electron impact (EI) mass spectrometry was carried out using a Waters GCT Premier MS Agilent 7890A GC. Mass spectral data are quoted as the mass to charge ratio (m/z) in Daltons along with the relative peak height in brackets (base peak = 100). High resolution mass spectra (HRMS) are reported with <5 ppm error.

7.2 General Procedures

7.2.1 Synthetic Procedures

General Procedure A: Mn(I)-Catalysed C–H Bond Alkenylation/Alkylation

Adapted from literature procedure.[34] To a microwave vial equipped with a stirrer bar were added the manganese complex, 2-phenylpyridine, the unsaturated substrate and any supplementary additives. *n*-Bu_2O (2.4 ml $mmol^{-1}$) was then added, and the solution deoxygenated with argon balloon before heating to the desired temperature. After the reaction completion and subsequent cooling, the crude material was purified by flash column chromatography to afford the product.

General Procedure B: Photochemical Alkenylation of 2-Phenylpyridine

To a microwave vial equipped with a stirrer bar was added $Mn(ppy)(CO)_4$, phenylacetylene, any additives and *n*-Bu_2O (1 ml $mmol^{-1}$). The reaction mixture was irradiated at 400 nm using a 5 W LED light source for 3 hours (at 2 minutes intervals on/off). The solution was thereafter filtered through Celite®, diluted with CH_2Cl_2 (200 ml $mmol^{-1}$) and washed with saturated aqueous $NaHCO_3$ (150 ml $mmol^{-1}$). The organic layer was dried over $MgSO_4$ and the solvent removed *in vacuo*. A crude ^1H NMR spectrum was recorded for the conversion to product and the crude material was, if desired, purified by flash column chromatography.

General Procedure C: Synthesis of 5-Membered Manganacycles

Adapted from literature procedure.[181] To a Schlenk tube under nitrogen was added $MnBn(CO)_5$ (1 eq.), ligand to be cyclomanganated (1 eq.) and dry deoxygenated solvent. The reaction mixture was excluded from light and heated to reflux for 6-24 hours, until completion of the reaction given from monitoring by IR. When the reaction was complete, the reaction mixture was allowed to cool to room temperature and was filtered through cotton wool. CH_2Cl_2 was used to rinse the flask and cotton wool, before the solvent was removed under reduced pressure. The crude material was purified by flash column chromatography to afford the product. If significant amounts of silicon grease or oil was present, the material was dissolved in acetonitrile and washed with a small amount of hexane, before the acetonitrile layer was removed under reduced pressure.

General Procedure D: Synthesis of Dicyclohexylammonium Salts

To a 25 ml round bottomed flash equipped with stirrer bar was added dicyclohexylamine (1 eq.) and Et_2O (2 ml $mmol^{-1}$). The relevant acid (1 eq.) was thereafter added dropwise at room temperature and the reaction mixture was stirred for 30 minutes. After the reaction time the solid precipitate was collected by filtration and washed with Et_2O to afford the product.

General Procedure E: Suzuki-Miyaura Cross-Coupling Protocol

Adapted from literature procedure.[181] To a Schlenk tube under nitrogen was added the arylbromine (1.0 eq.), aryl boronic acid (1.5 eq.), $Pd_3(OAc)_6$ (0.5–2 mol% with respect to Pd), K_3PO_4 (2 eq.) and deoxygenated ethylene glycol (6 ml $mmol^{-1}$). The reaction was heated to 80 °C for 150 min or 16 hours and was thereafter allowed to cool to room temperature. Water (7.5 ml $mmol^{-1}$) and saturated brine (7.5 ml $mmol^{-1}$) was added and the product was extracted using CH_2Cl_2 (4 × 10 ml $mmol^{-1}$). The CH_2Cl_2 layers was dried over $MgSO_4$ and the solvent was removed under reduced pressure. The crude material was purified using flash column chromatography to yield the product.

General Procedure F: Mn(I)-Catalysed C–H Bond Alkenylation/Alkylation "On-Water"

To a pressure tube equipped with a stirrer bar were added the manganese complex, 2-phenylpyridine, the unsaturated substrate and any supplementary additives. H_2O (2.4 ml $mmol^{-1}$) was then added and the solution was heated to 100 °C for 3 hours. The solution was subsequently cooled and the crude material purified by flash column chromatography to afford the product.

7.2.2 Standard Mn(I)-Catalysed C–H Bond Functionalisation for Screening

Adapted from a literature procedure.[34] To a microwave vial equipped with a stirrer bar were added the manganese complex, 2-phenylpyridine, unsaturated substrate and any supplementary additives. *n*-Bu_2O (1 eq. = 0.025 mol dm^{-3}) was then added, and the solution deoxygenated with argon balloon before heating to the desired temperature. After the reaction completion and subsequent cooling, a crude ^1H NMR spectrum was recorded to give the conversion to product.

7.2.3 *In Operando* IR Spectroscopic Measurements

Reactions under Argon Atmosphere

A 100 ml three necked round-bottomed flask equipped with a stirrer bar was attached to the ReactIR silicon-tipped ATR-IR probe. A background spectrum was collected and *n*-Bu_2O (10 ml) was added before septa were attached to the side joints. Thereafter, an internal thermocouple was attached through a septum, and the solvent was deoxygenated with argon balloon. After the temperature had reached a steady level, a solvent background spectrum was recorded to be used as a reference for the experiment.

The sample measurements were thereafter started, and the desired amount of 2-phenylpyridine, the unsaturated substrate and any additives were added sequentially. Enough time for the IR bands to stabilise was ensured between each addition. Liquid reagents were added through a septum, while solids were added by rapid removal and replacement of the septum. The manganese complex was added as the final reagent by rapid removal and replacement of the septum, and the sides of the flask were washed with the reaction solution. IR spectra were recorded every 1 min, and specific peaks in the metal carbonyl region (~2150−1800 cm^{-1}; peak resolution = ± 4 cm^{-1}) were picked and monitored on an individual experiment basis. The data was exported into a Microsoft Excel document, where the relevant processing was performed. Graph plots were generated and curve fitting performed using OriginPro 2017 (SR2, b9.4.2.380) or 2018b (SR2, b9.5.5.409) software.

When ex situ ^1H NMR monitoring was necessary, aliquots of the reaction mixture were taken at appropriate time intervals. The aliquots were filtered through a Pasteur pipet (with cotton wool and Celite® filter pad) into an NMR tube. A ^1H NMR spectrum was recorded of the sample to provide the conversion to product, which could be cross-correlated with the changes recorded by IR spectroscopic analysis. If samples for LIFDI-MS were required, an appropriate amount of the reaction solution was taken and the LIFDI-MS spectrum was recorded as soon as possible.

When using deuterated substrates, the crude reaction mixture was purified by flash column chromatography to afford the desired product. Deuterium-incorporation was determined using both ^1H and ^2H NMR spectroscopy.

Reactions under Nitrogen Atmosphere

A 100 ml three necked round-bottomed flask equipped with a stirrer bar was attached to the ReactIR silicon-tipped ATR-IR probe and Schlenk line. The flask was evacuated and backfilled with nitrogen three times, before an atmosphere background spectrum was collected. Dry deoxygenated toluene (10 ml) was added through a septum with an internal thermocouple was attached. After the temperature had reached a steady level, a solvent background spectrum was recorded to be used as a reference for the experiment.

The sample measurements were thereafter started, and the desired amount of any reagents and additives were added sequentially. Enough time for the IR bands to stabilise was ensured between each addition. Liquid reagents were added through a septum, while solids were added by rapid removal and replacement of the septum. The manganese complex was added as the final reagent by rapid removal and replacement of the septum, and the sides of the flask were washed with the reaction solution. IR spectra were recorded every 1 min, and specific peaks in the metal carbonyl region (~2150−1800 cm^{-1}; peak resolution = ± 4 cm^{-1}) were picked and monitored on an individual experiment basis. The data was exported into a Microsoft Excel document, where the relevant processing was performed. Graph plots were generated and curve fitting performed using OriginPro 2017 (SR2, b9.4.2.380) or 2018b (SR2, b9.5.5.409) software.

When ex situ ^{19}F NMR monitoring was necessary, aliquots of the reaction mixture were taken at appropriate time intervals. The aliquots were added to a Young's tap NMR tube under N_2 atmosphere and diluted with dry deoxygenated toluene. A ^{19}F NMR spectrum was recorded of the sample to provide the conversion to the products, which could be cross-correlated with the changes recorded by IR spectroscopic analysis.

7.2.4 Thermal Stoichiometric Alkenylation Reactions

To a microwave vial equipped with a stir bar was added $Mn(ppy)(CO)_4$ (8 mg, 0.025 mmol, 1 eq.). As required by the individual experiment, phenylacetylene (0.025−0.100 mmol, 1−4 eq.), 2-phenylpyridine (0.029 mmol, 1.15 eq.) and pyridine (0.025 mmol, 1 eq.) was added as stock solutions in *n*-Bu_2O. H_2O was added with syringe (5 µl, 0.25

mmol, 10 eq.) and a total volume of 0.6 ml *n*-Bu_2O was ensured for the experiment. The solution was deoxygenated by argon balloon before heating at 100 °C for 30 min. After cooling the solvent was removed *in vacuo*, and a ^1H NMR spectrum was recorded of the crude material to determine the crude conversion to the product.

When using deuterated substrates, the crude reaction mixture was purified by flash column chromatography to afford the desired product. Deuterium-incorporation was determined using both ^1H and ^2H NMR spectroscopy.

7.2.5 *In Situ* ^{19}F NMR Measurements

To a Schlenk tube under N_2 was added the fluorinated 2-phenylpyridine, the manganese complex and any additives (1 eq. = 0.115 mmol). $PhCF_3$ (0.023 mmol, 0.2 eq.) was used as internal standard and added as a stock solution (0.2 ml) in dry deoxygenated toluene. Toluene (2.0 ml) was added to the solution and 0.6 ml of the solution was transferred to a Young's tap NMR tube under N_2 atmosphere. A room temperature ^{19}F NMR spectrum was recorded as a zero-point for the experiment. Thereafter, the NMR tube was removed from the spectrometer and the temperature increased to the chosen level. The start of the experiment is defined as when the NMR tube was added to the spectrometer after reaching temperature. ^{19}F NMR spectra was recorded at appropriate intervals for the duration of the reaction. If an additive was added during the reaction, the NMR was removed from the spectrometer and the additive added at room temperature under N_2 atmosphere. The NMR was thereafter added to the spectrometer, which was kept at temperature.

7.2.6 Time-Resolved IR Spectroscopic Measurements

This procedure applies to both the ULTRA A and LIFEtime experimental setups.

Solutions of the manganese complexes were prepared at concentrations around 15–25 × 10^{-3} mol dm^{-3}. The solution was flowed (and recycled) through a Harrick cell constantly using tubing, a peristaltic pump and a solution reservoir. Experiments were performed under air unless otherwise stated.

The resulting data from the experiments were manipulated by subtracting the reference data to obtain a difference spectrum, followed by a first- or second-order polynomial

fitting to the baseline (performed in the ULTRA View version 2 software). The data were then exported as a comma-separated variable file and imported into OriginPro 2017 (SR2, b9.4.2.380) or 2018b (SR2, b9.5.5.409). Spectral calibration was performed with suitable standard, such as 190 μm polystyrene, 1,4-dioxane or by using the known positions of the bleach bands. This allowed for detector pixels to be allocated to specific frequencies. The overlap in frequencies were removed manually. The data was thereafter analysed as desired in OriginPro 2017 (SR2, b9.4.2.380) or 2018b (SR2, b9.5.5.409). The peak values reported are the experimentally obtained values and are not deconvoluted to remove overlap with other peaks. Kinetic data were analysed using the *expgro*, *expdec* and *expgrowdec* functions within Origin and errors were reported as 95% confidence intervals.

7.2.7 Kinetic Modelling with COPASI

Kinetic modelling was performed with the COPASI 4.16 software program (Build 104).

IR spectroscopic intensities were taken from the baseline-corrected TRIR data and iterated against the proposed kinetic model (Chapter 3.6.1), to obtain the estimated rate constants. The model was performed with pump-probe delays of 1 to 50 μs. Initial concentrations were taken from the t = 1 μs spectrum and initial rate parameters were obtained from approximate first order fits. No constraints were applied to the subsequent estimation of the rate constants. Goodness of fit was obtained from the coefficient of variation and standard deviation.

To obtain a visual fit of the modelled rate constants, the IR spectroscopic intensities were scaled to account for the difference in response factor of the IR bands for the complexes. The data were thereafter modelled in COPASI with the desired model, using the estimated rate constants, to produce a calculated fit of the data which can be compared to the experimentally obtained IR spectroscopic intensities.

7.2.8 Computational Chemistry

All calculations were performed using the TURBOMOLE version 6.4 package using the resolution of identity (RI) approximation.[182-189]

The initial optimizations were performed at the (RI-)BP86/SV(P) level and was followed by frequency calculations at the same level. The transition states were located by performing an initial constrained minimisation (by freezing internal coordinates that change most during the reaction) of a structure close to the anticipated transition state. This was followed by a frequency calculation to identify the transition vector to follow during a subsequent transition state optimisation. Thereafter, a final frequency calculation was performed on the optimised transition state structure. All minima were confirmed as such by the absence of imaginary frequencies and all transition states were identified by the presence of only one imaginary frequency. Dynamic reaction coordinate analysis confirmed that the transition states were connected to the appropriate minima. Single-point calculations on the (RI-)BP86/SV(P)-optimised geometries were performed using the hybrid PBE0 functional and the flexible def2-TZVPP basis set. The (RI-)PBE0/def2-TZVPP self-consistent field energies were corrected for their zero point energies, thermal energies and entropies (obtained form the (RI-)BP86/SV(P)-level frequency calculations). No symmetry constraints were applied during the optimisation. Solvent corrections were applied with the COSMO dielectric continuum model[153] and dispersion effects modelled with Grimme's D3 method.[190, 191]

The calculated values for the IR bands were normalised to obtain more accurate and comparable (to experimental values) peak locations. Therefore, the calculated vales were plotted against the observed values for the same IR bands, giving rise to a linear trend increasing with increasing wavenumbers. A linear regression afforded the relationship between the calculated and experimental values to be 0.7333x + 567.5. The normalised values of the IR bands were obtained by inserting the calculated IR values into the equation above as x.

7.3 Synthetic Procedures and Compound Data

Laboratory notebook references are given for the individual experiments throughout this section, from which the synthetic procedure is given. Where a known compound is prepared using literature procedure, a literature reference is placed next to the compound name. If known, compounds are compared to literature analytical data and referenced accordingly.

Tetracarbonyl (2-(phenyl-κ,C2-pyridine-κ,N) manganese(I) (**10**)

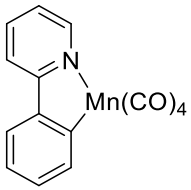

Synthesised using general procedure C from $MnBn(CO)_5$ (2.50 g, 9.15 mmol, 1 eq.), 2-phenylpyridine (1.33 ml, 1.45 g, 9.15 mmol, 1 eq.) and hexane (60 ml). Purification by flash column chromatography (petrol/CH_2Cl_2, 8:2, *v*/*v*) to afford a yellow crystalline solid (2.37 g, 81%).

Mp 114–115 °C (lit[181] 114 °C); R_f 0.26 (petrol/CH_2Cl_2, 8:2, *v*/*v*); ^{1}H NMR (500 MHz, $CDCl_3$, δ): 8.00 (d, *J* = 7.5 Hz, 1H), 7.89 (d, *J* = 8.0 Hz, 1H), 7.84–7.74 (m, 2H), 7.29 (dd, *J* = 7.5, 7.5 Hz, 1H), 7.19 (dd, *J* = 7.5, 7.5 Hz, 1H), 7.12 (dd, *J* = 6.5, 6.5 Hz, 1H); ^{13}C NMR (126 MHz, CDCl3, δ): 220.2, 214.3, 214.1, 174.9, 166.5, 154.0, 146.3, 141.8, 137.9, 130.4, 124.2, 124.1, 122.5, 119.4; LIFDI-MS *m*/*z* (ion, %): 321 ($[M]^+$, 100); IR (*n*-Bu_2O, solution, cm^{-1}): 2075, 1992, 1978, 1937, 1604, 1579, 1479.

The analytical data obtained were in accordance with the literature.[181]

Lab book reference number: LAH-5-230, LAH-6-360

Benzyl pentacarbonyl manganese(I) (**19**)

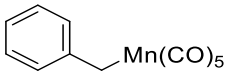

Adapted from literature procedure.[181] To a Schlenk tube under nitrogen was added mercury (12 ml). Sodium metal (1.18 g, 42.8 mmol, 4 eq.) was added in small pieces with high stirring to allow dissolution. In a separate Schlenk tube under nitrogen was added $Mn_2(CO)_{10}$ (4.16 g, 10.7 mmol, 1 eq.), followed by dry deoxygenated THF (80 ml). The THF solution was then transferred by cannula to the sodium amalgam, which was stirred for a further 3 hours. Benzyl chloride (2.47 ml, 2.71 g, 21.4 mmol, 2 eq.) was added to a separate Schlenk tube under nitrogen and placed in an ice bath. The Schlenk tube was put under vacuum with stirring for 30 seconds, before being

backfilled with nitrogen. At room temperature, the THF solution was transferred by cannula filtration to the benzyl chloride and stirred for 20 hours. The solution was thereafter filtered through a bed of Celite® and washed with Et_2O. The crude material was loaded onto silica gel and purified by flash column chromatography (petrol). Benzyl chloride impurities was removed under reduced pressure at 35 °C to yield a pale green crystalline solid (4.11 g, 67%).

Mp 114–115 °C (lit[181] 40 °C); R_f 0.33 (petrol); ^{1}H NMR (500 MHz, $CDCl_3$, δ): 7.24–7.12 (m, 4H), 7.05–6.94 (m, 1H); ^{13}C NMR (126 MHz, CDCl3, δ): 212.4, 210.0, 151.9, 128.8, 126.0, 123.6, 11.3; LIFDI-MS m/z (ion, %) 286 $[M]^+$; IR (CH_2Cl_2, solution, cm^{-1}): 2940, 2874, 2857, 2107, 2011, 1990, 1598, 1489, 1124.

The analytical data obtained were in accordance with the literature.[181]

Lab book reference number: LAH-6-343

Tetracarbonyl (2-(acetyl-κ,O)benzene-κ,C2) manganese(I) (20)

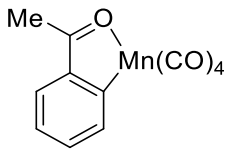

Synthesised using general procedure C from $MnBn(CO)_5$ (143 mg, 0.5 mmol, 1 eq.), acetophenone (58 µl, 0.5 mmol, 1 eq.) and hexane (10 ml). The crude material was purified by flash column chromatography (petrol/CH_2Cl_2, 9:1, *v*/*v*) to afford a yellow solid (79 mg, 55%).

Mp 116–117 °C dec; R_f 0.24 (petrol/CH_2Cl_2, 9:1, *v*/*v*); ^{1}H NMR (500 MHz, $CDCl_3$, δ): 7.40 (d, *J* = 7.5, 1H), 7.15 (d, *J* = 7.5 Hz, 2H), 6.72 (dd, *J* = 7.5, 7.5 Hz, 1H), 6.48 (dd, *J* = 7.5, 7.5 Hz, 1H); ^{13}C NMR (126 MHz, $CDCl_3$, δ): 220.4, 215.9, 212.2, 210.8, 192.8, 144.7, 140.9, 133.2, 131.0, 123.2, 23.9; LIFDI-MS *m*/*z* (ion, %): 286 ($[M]^+$, 100); LIFDI-HRMS *m*/*z*: 285.96780 $[M]^+$ (calculated for $C_{12}H_7NO_5Mn$ 285.96685); IR (CH_2Cl_2 solution, cm^{-1}): 2082, 1993, 1938, 1581, 1539, 1442, 1370, 1323.

The analytical data obtained were in accordance with the literature.[149]

Lab book reference number: LAH-12-923

2-(Pentadeuteriophenyl)pyridine (33-d_5)

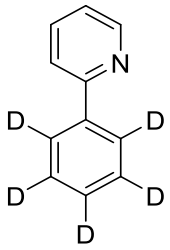

Adapted from literature procedure.[34] Synthesis of phenylboronic ester-d_5: To a Schlenk tube under nitrogen was added bromobenzene-d_5 (3.2 ml, 30 mmol, 1 eq.) and dry deoxygenated THF (120 ml). *n*-BuLi (2.5 M in hexanes, 14.4 ml, 36 mmol, 1.2 eq.) was added dropwise at −78°, and the solution was stirred for 1 hour. $B(OMe)_3$ (8.7 ml, 78 mmol, 2.6 eq.) was added, and the resulting mixture was stirred for a further hour, after warming to room temperature. The solution was acidified using HCl (10% *v*/*v* in H_2O) and extracted with Et_2O, and the organic layer was dried over $MgSO_4$, filtered, and concentrated *in vacuo* to give an off-white solid used without further purification.

To a Schlenk tube under nitrogen containing a stirred solution of the phenylboronic ester-d_5 (3.9 g, 25 mmol, 1.3 eq.), $Pd(PPh_3)_4$ (699 mg, 0.6 mmol, 3.2 mol%), and Na_2CO_3 (15 g, 186 mmol, 5.6 eq.) in dry deoxygenated toluene (72 ml), water (72 ml), and EtOH (14 ml), was added 2-bromopyridine (1.8 ml, 19 mmol, 1 eq.). The reaction mixture was refluxed for 20 hours before cooling to room temperature. Water was added and extracted with EtOAc. The organic layer was dried over $MgSO_4$, filtered, and concentrated *in vacuo*. The crude material was purified by flash column chromatography (petrol/EtOAc, 9:1, *v*/*v*) to yield a pale yellow liquid (2.84 g, 92%).

R_f 0.21 (petrol/EtOAc, 9:1, *v*/*v*); ^{1}H NMR (400 MHz, $CDCl_3$, δ): 8.70 (ddd, J = 5.0, 1.5, 1.5 Hz, 1H), 7.79−7.69 (m, 2H), 7.23 (ddd, J = 7.0, 5.0, 2.0 Hz, 1H); ^{13}C NMR (101 MHz, $CDCl_3$, δ): 157.6, 149.8, 139.3, 136.9, 128.5 (m, 2H coupling), 126.6 (m, ^{2}H coupling), 122.2, 120.7; ESI-MS *m*/*z* (ion, %): 161 ($[M+H]^+$, 100); ESI-HRMS *m*/*z*: 161.1119 $[M+H]^+$ (calculated for $C_{11}H_5D_5N$ 161.1122); IR (neat, ATR, cm^{-1}): 3052, 3012, 1595, 1569, 1470, 1433, 1382, 1332, 1300, 1246, 1153, 1098, 1055, 1015, 988, 908, 832, 820, 799, 750, 731, 642, 606, 552.

The analytical data obtained were in accordance with the literature.[34]

Lab book reference number: LAH-11-759

1-Deuterio(phenyl)acetylene (34-*d*)

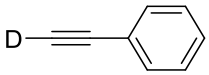

Adapted from literature procedure.[192] To a Schlenk tube under nitrogen were added phenylacetylene (2.75 ml, 25 mmol, 1 eq.), K_2CO_3 (5.18 g, 37.5 mmol, 1.5 eq.) and dry deoxygenated MeCN (60 ml). The solution was stirred at room temperature for 30 minutes before D_2O (11.30 ml, 625 mmol, 25 eq.) was added and stirred for a further hour. The reaction mixture was diluted with CH_2Cl_2 (60 ml), the organic layer was collected and dried over $MgSO_4$ and filtered followed by concentration *in vacuo*. The crude material was purified by distillation to yield a colourless liquid (1.14 g, 44%).

^{1}H NMR (400 MHz, $CDCl_3$, δ): 7.53−7.48 (m, 2H), 7.38−7.29 (m, 3H), 3.08 (s, 96% D-incorporation); ^{13}C NMR (101 MHz, CDCl3, δ): 132.3, 128.9, 128.4, 122.2, 83.3 (m, ^{2}H coupling), 77.03 (m, ^{2}H coupling); EI-GC-MS *m*/*z* (ion): 103 ($[C_8H_5D]^+$); EI-HRMS *m*/*z*: 103.0529 $[C_8H_5D]^+$ (calculated for C_8H_5D 103.0532); IR (neat, ATR, cm^{-1}): 3080, 3058, 2583, 1487, 1443, 1070, 1025, 917, 754, 689, 530, 483.

The analytical data obtained were in accordance with the literature.[192]

Lab book reference number: LAH-10-736

(*E*)-2-(2-Styrylphenyl)-pyridine (35)

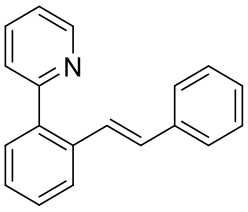

Method A: Synthesised using general procedure A from $MnBr(CO)_5$ (14 mg, 0.05 mmol, 10 mol%), Cy_2NH (20 µl, 18 mg, 0.10 mmol, 20 mol%), 2-phenylpyridine (0.14 ml, 0.16 g, 1.00 mmol, 2 eq.) and phenylacetylene (54 µl, 0.05 g, 0.50 mmol, 1 eq.).

Purification by flash column chromatography (petrol/Et_2O, 8:2, *v*/*v*) to afford a sticky oil (0.10 g, 79%).

Method B: Synthesised using general procedure B from $Mn(ppy)(CO)_4$ (32 mg, 0.1 mmol, 1 eq.), benzoic acid (12 mg, 0.1 mmol, 1 eq.) and phenylacetylene (22 µl, 20 mg, 0.2 mmol, 2 eq.). Purification by flash column chromatography (petrol/Et_2O, 7:3, *v*/*v*) to afford a sticky oil (14 mg, 53%).

Method C: Synthesised using general procedure F from $MnBn(CO)_5$ (7 mg, 0.025 mmol, 10 mol%), 2-phenylpyridine (70 µl, 76 mg, 0.5 mmol, 2 eq.) and phenylacetylene (27 µl, 25 mg, 0.25 mmol, 1 eq.). Purification by flash column chromatography (hexane/Et_2O, 7:3, *v*/*v*) to afford a sticky oil (27 mg, 34%).

R_f 0.12 (petrol/Et_2O, 8:2, *v*/*v*); ^1H NMR (500 MHz, $CDCl_3$, δ): 8.76 (ddd, *J* = 5.0, 2.0, 1.0 Hz, 1H), 7.79−7.72 (m, 2H), 7.57 (dd, *J* = 7.5, 1.5 Hz, 1H), 7.50−7.35 (m, 5H), 7.35−7.20 (m, 5H), 7.07 (d, *J* = 16.0 Hz, 1H); ^{13}C NMR (125 MHz, $CDCl_3$, δ): 159.0, 149.7, 139.7, 137.7, 136.1, 135.8, 130.4, 130.2, 128.8, 128.7, 127.8, 127.7, 127.7, 126.7, 126.4, 125.2, 122.0; ESI-MS *m*/*z* (ion, %): 258 ($[M+H]^+$, 100); ESI-HRMS *m*/*z*: 258.1277 $[M+H]^+$ (calculated for $C_{19}H_{16}N$ 258.1277); IR (neat, ATR, cm^{-1}) 3056, 3024, 1583, 1494, 1459, 1423, 1150, 1022, 960, 795, 749, 728, 690, 644, 616, 517.

The analytical data obtained were in accordance with the literature.[34]

Lab book reference number: LAH-8-548, LAH-9-624, LAH-8-531

Pyridyl pyrone tetracarbonyl (**50**)

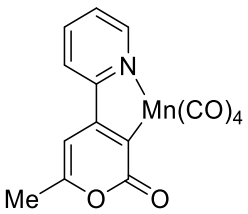

Synthesised using general procedure C from $MnBn(CO)_5$ (145 mg, 0.53 mmol, 1 eq.), 4-(2-pyridyl)-6-methyl-2-pyrone (100 mg, 0.53 mmol, 1 eq.) and hexane (10 ml). The crude material was purified by flash column chromatography (petrol/EtOAc, 7:3, *v*/*v*) to afford a yellow powder (32 mg, 71%).

Mp 168 °C dec (lit[50] 155–156 °C); R_f 0.15 (petrol/EtOAc, 7:3, *v*/*v*); ^{1}H NMR (500 MHz, $CDCl_3$, δ): 8.85 (d, *J* = 5.5, 1H), 7.90 (ddd, *J* = 8.0, 8.0, 1.5 Hz, 1H), 7.72 (d, *J* = 8.0, Hz, 1H), 7.30 (ddd, *J* = 7.5, 5.5, 1.5 Hz, 1H), 6.27 (s, 1H), 2.30 (s, 3H); ^{13}C NMR (126 MHz, $CDCl_3$, δ): 217.1, 214.5, 211.9, 168.7, 164.2, 164.0, 158.6, 156.4, 154.7, 138.4, 124.5, 121.8, 99.5, 20.0; LIFDI-MS *m*/*z* (ion, %): 353 ($[M]^+$, 100); LIFDI-HRMS *m*/*z*: 352.97208 $[M]^+$ (calculated for $C_{15}H_8NO_6Mn$ 352.97266); IR (CH_2Cl_2 solution, cm^{-1}): 2082, 1995, 1947, 1689, 1635, 1272.

The analytical data obtained were in accordance with the literature.[50]

Lab book reference number: LAH-7-372

6-Methyl-3-[(*E*)-2-phenylethenyl]-4-(pyridin-2-yl)-2H-pyran-2-one (**52**)

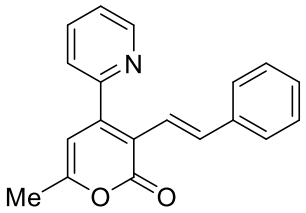

Synthesised using general procedure A from $MnBr(CO)_5$ (7 mg, 0.025 mmol, 10 mol%), 4-(2-pyridyl)-6-methyl-2-pyrone (47 mg, 0.25 mmol, 1 eq.), phenylacetylene (27 µl, 25 mg, 0.25 mmol, 1 eq.), dicyclohexylamine (10 µl, 9 mg, 0.05 mmol, 10 mol%) and $EtCO_2H$ (4 µl, 0.05 mmol, 20 mol%). The crude material was purified by flash column chromatography (petrol/toluene/EtOAc, 5.5:3:1.5, *v*/*v*) to afford a yellow solid (31 mg, 43%).

R_f 0.10 (petrol/toluene/EtOAc, 5.5:3:1.5, *v*/*v*); ^{1}H NMR (500 MHz, $CDCl_3$, δ): 8.79 (ddd, *J* = 5.0, 1.5, 1.0 Hz, 1H), 7.91 (d, *J* = 16.0 Hz, 1H), 7.80 (td, *J* = 7.5, 2.0 Hz, 1H), 7.49 (d, *J* = 8.0 Hz, 1H), 7.37 (ddd, *J* = 7.5, 5.0, 1.0 Hz, 1H), 7.35-7.32 (m, 2H), 7.31-7.25 (m, 2H), 7.24-7.19 (m, 1H), 6.90 (d, *J* = 16.0 Hz, 1H), 6.32 (s, 1H), 2.32 (s, 3H); ^{13}C NMR (125 MHz, $CDCl_3$, δ): 162.2, 159.3, 155.5, 150.4, 150.1, 137.9, 136.5, 135.3, 128.7, 128.0, 126.9, 125.2, 123.8, 120.7, 118.1, 106.5, 20.0; ESI-MS *m*/*z* (ion, %): 290 ($[M+H]^+$, 68), 312 ($[M+Na]^+$, 100); ESI-HRMS *m*/*z*: 290.1176 $[M+H]^+$ (calculated for $C_{18}H_{22}NO_2$ 290.1176); IR (solid-state, ATR, cm^{-1}): 3052, 2922, 2854,

1703, 1630, 1583, 1514, 1488, 1465, 1430, 1384, 1345, 1327, 1304, 1234, 1202, 1152, 1045, 1026, 988, 959, 882, 835, 797, 745, 673, 617, 580, 506.

The analytical data obtained were in accordance with the literature.[50]

Lab book reference number: LAH-11-826

(p-Tolylacetylide) pentacarbonyl manganese(I) (60)

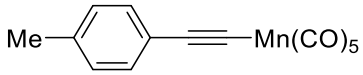

Adapted from literature procedure.[34] To a Schlenk tube under nitrogen were added 1-ethynyl-4-methylbenzene (0.57 ml, 4.5 mmol, 1 eq.) and THF (30 ml). *n*-BuLi (2.5 M in hexanes, 1.80 ml, 4.5 mmol, 1 eq.) was added dropwise to the solution at −78 °C and stirred for 30 minutes. A solution of $MnBr(CO)_5$ (1.24 g, 4.5 mmol, 1 eq.) in THF (60 ml) was added slowly *via* cannula and stirred at −78 °C for a further hour. The reaction mixture was warmed to room temperature, poured into water (45 ml) and extracted with CH_2Cl_2 (3 × 60 ml). The combined organic layers were dried over $MgSO_4$, filtered, and concentrated *in vacuo*. The crude material was purified by flash column chromatography (hexane/EtOAc, 99:1, *v*/*v*) to afford a yellow solid. The solid was dissolved in hexane and stirred over activated carbon for 10 minutes. Filtration through Celite® and concentration *in vacuo* yielded a white crystalline solid (0.45 g, 32%).

Mp 111–113 °C; R_f 0.19 (hexane/EtOAc, 99:1, *v*/*v*); ^{1}H NMR (500 MHz, CD_2Cl_2, δ): 7.24−7.20 (m, 2H), 7.05 (d, J = 9.0 Hz, 1H), 2.31 (s, 3H); ^{13}C NMR (126 MHz, CD_2Cl_2, δ): 208.4, 207.6, 136.6, 131.6, 129.3, 124.7, 117.0, 89.2, 21.6; LIFDI-MS *m*/*z* (ion, %): 310 ($[M]^+$, 100); IR (CH_2Cl_2, solution, cm^{-1}): 3006, 2136, 2110, 2040, 2010, 1739, 1436, 1366, 1273, 1217.

The analytical data obtained were in accordance with the literature.[34]

Lab book reference number: LAH-11-835, LAH-12-842

Dicyclohexylammonium bromide (62)

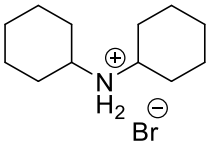

Synthesised using general procedure D from dicyclohexylamine (2.20 ml, 11.00 mmol, 1 eq.) and hydrobromic acid (48% in H_2O, 1.24 ml, 11.00 mmol, 1 eq.) to afford a white solid (2.13 g, 74%).

Mp 325–327 °C dec; ^{1}H NMR (400 MHz, $CDCl_3$, δ): 8.62 (s, 2H), 3.17 (t, *J* = 10.5 Hz, 2H), 2.24 (d, *J* = 12.5 Hz, 4H), 1.90–1.71 (m, 8H), 1.70–1.59 (m, 3H), 1.33–1.16 (m, 6H); ^{13}C NMR (101 MHz, $CDCl_3$, δ): 54.3, 29.3, 24.9, 24.9; ESI-MS *m*/*z* (ion, %): 182 ($[M]^+$, 100); ESI-HRMS *m*/*z*: 182.1903 $[M]^+$ (calc. for $C_{12}H_{24}N$ 182.1903); IR (solid-state, ATR, cm^{-1}): 2929, 2854, 2801, 2757, 2520, 2421, 2358, 1460, 1347, 1312, 1050, 1034, 919, 895, 857.

Lab book reference number: LAH-5-240

[(Mn(μ-OH)(CO)$_3$)$_4$] (72)

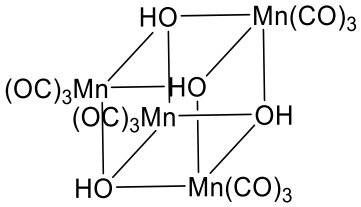

Adapted from literature procedure.[95] To a 50 ml round-bottom flask under ambient conditions was added $Mn_2(CO)_{10}$ (195 mg, 0.5 mmol, 1 eq.), trimethylamine *N*-oxide (333 mg, 3 mmol, 6 eq.) and THF (10 ml). The solution was stirred for 18 hours at room temperature, before the solvent was removed *in vacuo*. The crude material was recrystallized from hot toluene to yield a yellow powder (39 mg, 25%).

IR (KBr-disc, cm^{-1}): 3628, 3583, 3361, 2038, 2017, 1935, 1909, 1878, 1480, 1241, 951, 766, 645.

The analytical data obtained were in accordance with the literature.[95]

Lab book reference number: LAH-7-416

$[Mn_7(\mu_3\text{-}OH)_8(CO)_{18}]$ (73)

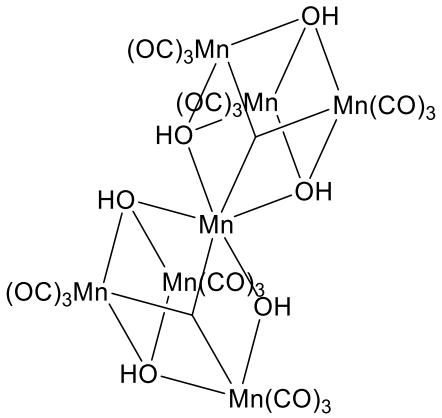

Adapted from literature procedure.[95] To a 50 ml round-bottom flask under ambient conditions was added $Mn_2(CO)_{10}$ (195 mg, 0.5 mmol, 1 eq.), trimethylamine *N*-oxide (333 mg, 3 mmol, 6 eq.), benzophenone (78 mg, 0.4 mmol, 0.8 eq.) and THF (10 ml). The solution was stirred for 18 hours at room temperature, before the solvent was removed *in vacuo*. The crude material was recrystallized from $CHCl_3$/hexane to yield a yellow powder (98 mg, 67%).

IR (KBr-disc, cm^{-1}): 3632, 3269, 2041, 2021, 1908, 1479, 952, 765, 691, 645, 513.

The analytical data obtained were in accordance with the literature.[95]

Lab book reference number: LAH-7-417

Reductive Elimination Product from PhC_2H (75)

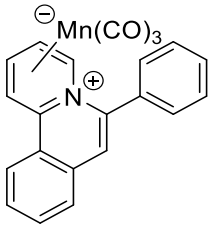

To a microwave vial equipped with a stirrer bar was added $Mn(ppy)(CO)_4$ (32 mg, 0.1 mmol, 1 eq.) and phenylacetylene (11 µl, 10 mg, 0.1 mmol, 1 eq.) was added as a stock solution in *n*-Bu_2O (3 ml, 0.042 mol dm^{-1}). The solution was deoxygenated with an argon balloon before heating to 100 °C for 30 min. After cooling, the solvent was

removed under reduced pressure and the product crystallized from CH_2Cl_2/pentane to afford the title compound as a brown solid (22 mg, 56%).

Mp 180−182 °C; ^{1}H NMR (500 MHz, CD_2Cl_2, δ): 8.01 (d, *J* = 8.5 Hz, 1H), 7.72 (dd, *J* = 7.5, 7.5 Hz, 1H), 7.61 (d, *J* = 8.0 Hz, 1H), 7.59−7.44 (m, 6H), 6.88 (s, 1H), 6.57 (s, 1H), 5.70 (s, 1H), 4.16 (d, *J* = 4.5 Hz, 1H), 3.23 (d, *J* = 5.5 Hz, 1H); ^{13}C NMR (125 MHz, CD_2Cl_2, δ): 167.9, 142.6, 135.5, 133.8, 133.7, 130.3, 129.7, 129.5, 129.4, 127.9, 126.0, 123.4, 118.3, 91.5, 78.8, 72.8, 50.4; ESI-MS *m*/*z* (ion, %): 256 ([M+H]$^+$, 100); ESI-HRMS *m*/*z*: 256.1121 [M+H]$^+$ (calculated for $C_{19}H_{14}N$ 256.1121); IR (CH_2Cl_2 solution, cm^{-1}) 1983, 1896, 1627, 1561, 1499, 1276, 1257.

Lab book reference number: LAH-11-791

2-(2,6-Di(*E*)-2-(2-styrylphenyl))pyridine (76)

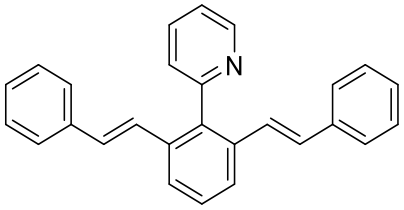

To a microwave vial equipped with stirrer bar were added Mn(ppy)$(CO)_4$ (32 mg, 0.1 mmol, 1 eq.) and phenylacetylene (44 µl, 0.4 mmol, 4 eq.). *n*-Bu_2O (2.4 ml) was then added, and the solution was deoxygenated using an argon balloon before heating to 100 °C for 30 minutes. After cooling, the crude material was purified by flash column chromatography (petrol/Et_2O, 8:2, *v*/*v*) to afford a yellow solid (8 mg, 22%).

R_f 0.20 (petrol/Et_2O, 8:2, *v*/*v*); ^{1}H NMR (500 MHz, CD_2Cl_2, δ): 8.79 (ddd, *J* = 5.0, 2.0, 1.0 Hz, 1H), 7.81 (ddd, *J* = 7.5, 7.5, 2.0 Hz, 1H), 7.73 (d, *J* = 8.0 Hz, 2H), 7.47 (dd, *J* = 8.0 Hz, 1H), 7.37 (ddd, *J* = 7.5, 5.0, 1.0 Hz, 1H), 7.33 (d, *J* = 7.5 Hz, 1H), 7.31−7.24 (m, 8H), 7.24−7.17 (m, 2H), 7.01 (d, *J* = 16.0 Hz, 2H), 6.76 (d, *J* = 16.0 Hz); ^{13}C NMR (125 MHz, CD_2Cl_2, δ): 158.6, 150.2, 139.6, 137.9, 137.0, 136.6, 130.5, 129.1, 129.0, 128.2, 127.5, 127.0, 126.9, 125.2, 122.8; ESI-MS *m*/*z* (ion, %): 360 ([M+H]$^+$, 100), 382 ([M+Na]$^+$, 4); ESI-HRMS *m*/*z*: 360.1746 [M+H]$^+$ (calculated for $C_{27}H_{22}N$ 360.1747); IR (solid-state, ATR, cm^{-1}): 3056, 3025, 2956, 2015, 1928, 1584, 1561, 1494, 1473, 1449, 1419, 1274, 1228, 1178, 1147, 1072, 1022, 958, 787, 748, 732, 689, 619.

The analytical data obtained were in accordance with the literature.[193]

Lab book reference number: LAH-11-792

Reductive Elimination Product from PhCCPh (86)

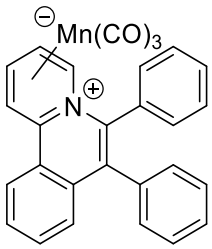

To a microwave vial equipped with a stirrer bar were added $Mn(ppy)(CO)_4$ (32 mg, 0.1 mmol, 1 eq.) and diphenylacetylene (17 mg, 0.1 mmol, 1 eq.). n-Bu_2O (3 ml) was then added, and the solution was deoxygenated using an argon balloon before heating to 100 °C for 30 minutes. After cooling, the solvent was removed under reduced pressure and the product crystallized from CH_2Cl_2/pentane to afford the title compound as a brown solid (41 mg, 86%).

Mp 202−204 °C; ^{1}H NMR (500 MHz, CD_2Cl_2, δ): 8.01 (d, *J* = 8.5 Hz, 1H), 7.72 (dd, *J* = 7.5, 7.5 Hz, 1H), 7.61 (d, *J* = 8.0 Hz, 1H), 7.59−7.44 (m, 6H), 6.88 (s, 1H), 6.57 (s, 1H), 5.70 (s, 1H), 4.16 (d, *J* = 4.5 Hz, 1H), 3.23 (d, *J* = 5.5 Hz, 1H); ^{13}C NMR (125 MHz, CD_2Cl_2, δ): 167.9, 142.6, 135.5, 133.8, 133.7, 130.3, 129.7, 129.5, 129.4, 127.9, 126.0, 123.4, 118.3, 91.5, 78.8, 72.8, 50.4; ESI-MS *m*/*z* (ion, %): 332 ($[M+H]^+$, 100); ESI-HRMS *m*/*z*: 332.1428 $[M+H]^+$ (calculated for $C_{25}H_{18}N$ 332.1434); IR (CH_2Cl_2 solution, cm^{-1}): 1982, 1894, 1614, 1561, 1504, 1426, 1274.

Lab book reference number: LAH-11-790

(*E*)-2-(2-(1,2-Diphenylvinyl)phenyl)pyridine (89)

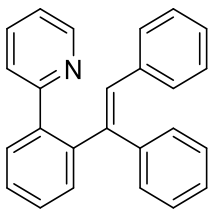

Synthesised using general procedure A from $MnBr(CO)_5$ (7 mg, 0.025 mmol, 10 mol%), 2-phenylpyridine (70 µl, 76 mg, 0.5 mmol, 2 eq.), diphenylacetylene (45 mg, 0.25 mmol, 1 eq.), dicyclohexylamine (10 µl, 9 mg, 0.05 mmol, 10 mol%) and $EtCO_2H$ (4 µl, 0.05 mmol, 20 mol%). The crude material was purified by flash column chromatography (petrol/EtOAc, 8:2, *v*/*v*) to afford a white solid (17 mg, 20%).

R_f 0.09 (petrol/EtOAc, 8:2, *v*/*v*); ^{1}H NMR (500 MHz, $CDCl_3$, δ): 8.46 (d, *J* = 5.0 Hz, 1H), 7.52-7.47 (m, 1H), 7.46-7.39 (m, 4H), 7.31 (d, *J* = 8.0 Hz, 1H), 7.14-7.07 (m, 3H), 7.06-6.96 (m, 6H), 6.94-6.89 (m, 2H), 6.66 (s, 1H); ^{13}C NMR (125 MHz, $CDCl_3$, δ): 159.8, 149.1, 143.6, 142.6, 140.6, 140.4, 137.7, 135.5, 131.2, 131.0, 130.4, 129.4, 128.3, 128.0, 127.9, 127.8, 126.9, 126.8, 124.5, 121.3; ESI-MS *m*/*z* (ion, %): 334 ($[M+H]^+$, 100); ESI-HRMS *m*/*z*: 334.1587 $[M+H]^+$ (calculated for $C_{18}H_{22}NO_2$ 334.1590); IR (solid-state, ATR, cm^{-1}): 3051, 3021, 1585, 1557, 1489, 1459, 1442, 1421, 1295, 1179, 1151, 1073, 1059, 1028, 990, 946, 914, 878, 793, 782, 743, 715, 697, 615, 591, 546, 513, 497.

The analytical data obtained were in accordance with the literature.[194]

Lab book reference number: LAH-11-801

2-Methoxy-6-phenylpyridine (131)

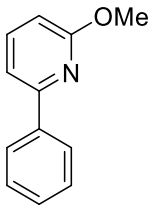

Synthesised using general procedure E from 2-bromo-6-methoxypyridine (2.5 ml, 3.76 g, 20.0 mmol, 1 eq.), phenylboronic acid (3.66 g, 30.0 mmol, 1.5 eq.) and $Pd_3(OAc)_6$ (23 mg, 0.03 mmol, 0.5 mol% with respect to Pd). The crude material was purified by flash column chromatography (petrol/Et_2O, 97.5:2.5, *v*/*v*) to afford a colourless oil (2.69 g, 73%).

R_f 0.28 (petrol/Et_2O, 97.5:2.5, *v*/*v*); ^{1}H NMR (400 MHz, $CDCl_3$, δ): 8.07–8.03 (m, 2H), 7.63 (dd, J = 8.0, 7.5 Hz, 1H), 7.49–7.44 (m, 2H), 7.42–7.37 (m, 1H), 7.35 (dd, J = 7.5, 0.5 Hz, 1H), 6.70 (dd, J = 8.0, 0.5 Hz, 1H), 4.05 (s, 3H); ^{13}C NMR (101 MHz,

$CDCl_3$, δ): 163.9, 154.8, 139.3, 139.2, 129.0, 128.7, 126.8, 112.9, 109.4, 53.4; ESI–MS *m*/*z* (ion, %): 186 ($[M+H]^+$, 100); ESI–HRMS *m*/*z*: 186.0910 (calc. for $C_{12}H_{12}NO$ 186.0913); IR (liquid–state): 3062, 2946, 2848, 1599, 1574, 1465, 1448, 1429, 1405, 1324, 1289, 1251, 1178, 1151, 1077, 1031, 1018, 986, 920, 878, 805, 760, 691, 659, 622, 607.

The analytical data obtained were in accordance with the literature.[195]

Lab book reference number: LAH-3-1, LAH-4-117

2,6-Diphenylpyridine (132)

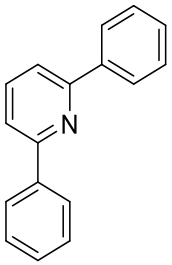

Synthesised using general procedure E from 2,6-dibromopyridine (2.37 g, 10.0 mmol, 1 eq.), phenylboronic acid (2.28 g, 15.0 mmol, 1.5 eq.) and $Pd_3(OAc)_6$ (12 mg, 0.02 mmol, 0.5 mol% with respect to Pd). The crude material was purified by flash column chromatography (petrol/Et_2O, 9:1, *v*/*v*) to afford a white solid (1.63 g, 93%).

R_f 0.33 (petrol/Et_2O, 9:1, *v*/*v*); ^1H NMR (400 MHz, $CDCl_3$, δ): 8.18–8.14 (m, 4H), 7.83 (dd, *J* = 8.5, 7.0 Hz, 1H), 7.70 (d, J = 7.5 Hz, 2H), 7.54–7.48 (m, 4H), 7.46–7.41 (m, 2H); ^{13}C NMR (101 MHz, $CDCl_3$, δ): 157.0, 139.6, 137.6, 129.1, 128.8, 127.1, 118.8; ESI–MS *m*/*z* (ion, %): 232 ($[M+H]^+$, 100), 254 ($[M+Na]^+$, 3); ESI–HRMS *m*/*z*: 232.1118 $[M+H]^+$ (calc. for $C_{17}H_{13}N$ 232.1121); IR (liquid–state): 3053, 3035, 1597, 1563, 1491, 1450, 1436, 1390, 1314, 1257, 1186, 1167, 1157, 1102, 1074, 1025, 987, 973, 924, 821, 775, 753, 739, 696, 626, 611.

The analytical data obtained were in accordance with the literature.[195]

Lab book reference number: LAH-3-11

Tetracarbonyl (2-methoxy-6-(phenyl-κ,C2)-pyridine-κ,N) manganese(I) (**133**)

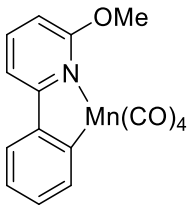

Synthesised using general procedure C from $MnBn(CO)_5$ (2.50 g, 9.15 mmol, 1 eq.), 2-methoxy-6-phenylpyridine (33 mg, 0.18 mmol, 1 eq.) and hexane (2.5 ml). The crude material was purified by flash column chromatography (petrol/Et_2O, 9:1, *v*/*v*) to afford a yellow solid (38 mg, 60%).

Mp 118–120 °C dec; R_f 0.02 (petrol/Et_2O, 9:1, *v*/*v*); ^{1}H NMR (500 MHz, $CDCl_3$, δ): 8.03 (d, *J* = 7.5 Hz, 1H), 7.81–7.73 (m, 2H), 7.54 (d, *J* = 8.0 Hz, 1H), 7.29–7.23 (m, 1H), 7.15 (dd, *J* = 7.5, 7.5, 1H), 6.58 (d, *J* = 8.0 Hz, 1H), 4.04 (s, 3H); ^{13}C NMR (126 MHz, $CDCl_3$, δ): 222.0, 214.8, 214.3, 175.9, 166.5, 166.2, 147.0, 130.0, 124.7, 123.8, 112.2, 102.6, 60.0; LIFDI-MS *m*/*z* (ion, %): 351 ($[M]^+$, 100); IR (CH_2Cl_2 solution, cm^{-1}): 2072, 1983, 1931, 1181, 1132, 1096, 1054, 1028, 1017, 1001.

Lab book reference number: LAH-3-7

Tetracarbonyl (2-(phenyl-κ,C2)-6-phenylpyridine-κ,N) manganese(I) (**134**)

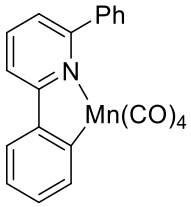

Synthesised using general procedure C from $MnBn(CO)_5$ (72 mg, 0.25 mmol, 1 eq.), 2,6-diphenylpyridine (58 mg, 0.25 mmol, 1 eq.) and hexane (5 ml). The crude material was purified by flash column chromatography (petrol/EtOAc, 9:1, *v*/*v*) to afford a yellow solid (56 mg, 57%).

Mp 132–133 °C dec; R_f 0.24 (petrol/EtOAc, 9:1, *v*/*v*); ^{1}H NMR (500 MHz, $CDCl_3$, δ): 8.01 (dd, *J* = 7.5, 1.5 Hz, 1H), 7.94 (dd, *J* = 8.0, 1.5 Hz, 1H), 7.85–7.79 (m, 2H), 7.56–7.51 (m, 3H), 7.43–7.39 (m, 2H), 7.29 (td, *J* = 7.5, 1.5 Hz, 1H), 7.20 (td, *J* = 7.5, 1.5 Hz, 1H), 7.29 (dd, *J* = 7.5, 1.5 Hz, 1H); ^{13}C NMR (126 MHz, $CDCl_3$, δ): 221.6, 214.6, 209.2, 175.0, 166.8, 165.6, 147.3, 143.7, 141.5, 137.5, 130.1, 129.7, 128.9, 128.7, 125.0, 124.0, 124.0, 117.9; LIFDI-MS *m*/*z* (ion, %): 397 ($[M]^+$, 100); LIFDI-HRMS *m*/*z*: 397.01389 $[M]^+$ (calculated for $C_{21}H_{12}NO_4Mn$ 397.01413); IR (CH_2Cl_2 solution, cm^{-1}): 2072, 1985, 1933, 1215, 1180.

Lab book reference number: LAH-12-922

Dicyclohexylammonium chloride (171)

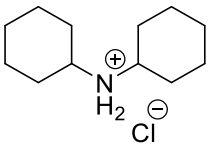

Synthesised using general procedure D from dicyclohexylamine (0.43 ml, 2.50 mmol, 1 eq.) and hydrochloric acid (37% in H_2O, 0.20 ml, 2.50 mmol, 1 eq.) to afford a white solid (0.54 g, quant.).

Mp 337–340 °C dec; ^{1}H NMR (400 MHz, $CDCl_3$, δ): 9.06 (s, 2H), 3.06 (t, *J* = 11.5 Hz, 2H), 2.20 (d, *J* = 12.0 Hz, 4H), 1.89–1.76 (m, 5H), 1.76–1.59 (m, 6H), 1.32–1.15 (m, 6H); ^{13}C NMR (101 MHz, $CDCl_3$, δ): 53.8, 29.3, 25.0, 24.9; ESI-MS *m*/*z* (ion, %): 182 ($[M]^+$, 100); ESI-HRMS *m*/*z*: 182.1907 $[M]^+$ (calculated for $C_{12}H_{24}N$ 182.1903); IR (solid-state, ATR, cm^{-1}): 2931, 2856, 2790, 2754, 2726, 2702, 2526, 2427, 2380, 1581, 1490, 1386, 1313, 1055, 1034, 965, 918, 894, 862.

Lab book reference number: LAH-5-247

Dicyclohexylammonium iodide (172)

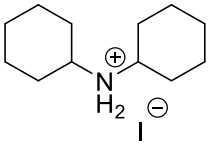

Synthesised using general procedure D from dicyclohexylamine (0.43 ml, 2.50 mmol, 1 eq.) and hydroiodic acid (57% in H_2O, 0.20 ml, 2.50 mmol, 1 eq.) to afford a white solid (0.59 g, 79%).

Mp 326–329 °C dec; ^{1}H NMR (400 MHz, $CDCl_3$, δ): 8.08 (s, 2H), 3.34 (tt, *J* = 12.0, 4.0 Hz, 2H), 2.29 (d, *J* = 11.0 Hz, 4H), 1.94–1.80 (m, 8H), 1.68 (d, *J* = 6,0 Hz, 2H), 1.34–1.18 (m, 7H); ^{13}C NMR (101 MHz, $CDCl_3$, δ): 54.8, 29.2, 24.9, 24.8; ESI-MS *m*/*z* (ion, %): 182 ($[M]^+$, 100); ESI-HRMS *m*/*z*: 182.1908 $[M]^+$ (calculated for $C_{12}H_{24}N$ 182.1903); IR (solid-state, ATR, cm^{-1}): 2933, 2857, 2823, 2730, 2514, 2412, 1571, 1450, 1388, 1314, 1160, 1032, 968, 850.

Lab book reference number: LAH-5-248

Dicyclohexylammonium tetrafluoroborate (173)

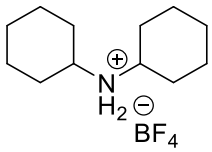

Synthesised using general procedure D with dicyclohexylamine (0.43 ml, 2.50 mmol, 1 eq.), tetrafluoroboric acid (48% in H_2O, 0.70 ml, 2.50 mmol, 1 eq.) to afford a white solid (0.45 g, 67%).

Mp 341–344 °C dec; ^{1}H NMR (400 MHz, $CDCl_3$, δ): 6.53 (m, 1H), 3.12 (tt, *J* = 11.5, 4.0 Hz, 2H), 2.06 (d, *J* = 12.5 Hz, 4H), 1.92–1.80 (m, 4H), 1.71–1.63 (m, 2H), 1.55–1.40 (m, 4H), 1.35–1.16 (m, 7H); ^{13}C NMR (101 MHz, $CDCl_3$, δ): 54.8, 29.2, 24.7, 24.7; ^{11}B NMR (128 MHz, $CDCl_3$, δ): −2.1; ^{19}F NMR (376 MHz, $CDCl_3$, δ): −146.3, −146.3; ESI-MS *m*/*z* (ion, %): 182 ($[M]^+$, 100); ESI-HRMS *m*/*z*: 182.1901 $[M]^+$ (calculated for $C_{12}H_{24}N$ 182.1903); IR (solid-state, ATR, cm^{-1}): 3175, 3126, 2938, 2861, 1601, 1456, 1389, 1315, 1096, 1002, 850, 767.

Lab book reference number: LAH-5-246

(*E*)-3-(2-(Pyridine-2-yl)phenyl)allyl benzoate (174)

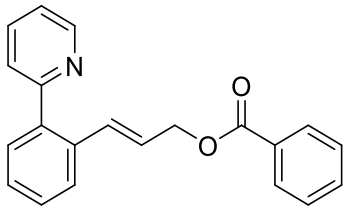

Method A: Synthesised using general procedure A from $MnBr(CO)_5$ (7 mg, 0.025 mmol, 10 mol%), Cy_2NH (10 µl, 9 mg, 0.05 mmol, 20 mol%), 2-phenylpyridine (70 µl, 76 mg, 0.5 mmol, 2 eq.) and propargyl benzoate (36 µl, 0.25 mmol, 1 eq.). The crude material was purified by flash column chromatography (hexane/Et_2O, 6:4, *v*/*v*) to afford a sticky oil (33 mg, 42%).

Method B: Synthesised using general procedure F from $MnBn(CO)_5$ (7 mg, 0.025 mmol, 10 mol%), 2-phenylpyridine (70 µl, 76 mg, 0.5 mmol, 2 eq.) and propargyl benzoate (36 µl, 40 mg, 0.25 mmol, 1 eq.). Purification by flash column chromatography (hexane/Et_2O, 7:3, *v*/*v*) to afford a sticky oil (35 mg, 70%).

R_f 0.12 (hexane/Et_2O, 6:4, *v*/*v*); ^{1}H NMR (500 MHz, $CDCl_3$, δ): 8.70 (ddd, *J* = 5.0, 2.0, 1.0 Hz, 1H), 8.05-8.00 (m, 2H), 7.71 (ddd, *J* = 7.5, 7.5, 2.0 Hz, 1H), 7.69-7.65 (m, 1H), 7.58-7.53 (m, 1H), 7.52-7.49 (m, 1H), 7.45-7.35 (m, 5H), 7.27-7.22 (m, 1H), 6.89 (d, *J* = 16.0 Hz, 1H), 6.37 (dt, *J* = 16.0, 6.0 Hz, 1H), 4.93 (dd, *J* = 6.0, 1.5 Hz, 2H); ^{13}C NMR (126 MHz, $CDCl_3$, δ): 166.4, 158.8, 149.5, 139.7, 136.2, 134.7, 133.1, 132.5, 130.3, 130.2, 129.8, 128.7, 128.5, 128.2, 126.6, 125.0, 124.7, 122.0, 65.6; ESI-MS *m*/*z* (ion, %): 316 ($[M]^+$, 100); ESI-HRMS *m*/*z*: 316.1336 $[M]^+$ (calculated for $C_{21}H_{18}NO_2$ 316.1332); IR (solid-state, ATR, cm^{-1}): 1715, 1584, 1570, 1425, 1376, 1265, 1175, 1106, 1069, 1024, 963, 795, 749, 708.

The analytical data obtained were in accordance with the literature.[34]

Lab book reference number: LAH-8-553, LAH-8-535

n-Butyl-3-(2-(pyridine-2-yl)phenyl)propanoate (175)

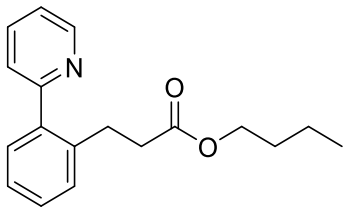

Method A: Synthesised using general procedure A from $MnBr(CO)_5$ (7 mg, 0.025 mmol, 10 mol%), Cy_2NH (10 µl, 9 mg, 0.05 mmol, 20 mol%), 2-phenylpyridine (70 µl, 76 mg, 0.5 mmol, 2 eq.) and *n*-butyl acrylate (36 µl, 0.25 mmol, 1 eq.). The crude material was purified by flash column chromatography (petrol/EtOAc, 8.5:1.5, *v*/*v*) to afford a sticky oil (0.39 g, 55%).

Method B: Synthesised using general procedure F from $MnBn(CO)_5$ (7 mg, 0.025 mmol, 10 mol%), 2-phenylpyridine (70 µl, 76 mg, 0.5 mmol, 2 eq.) and *n*-butyl acrylate (36 µl, 0.25 mmol, 1 eq.). Purification by flash column chromatography (petrol/EtOAc, 8.5:1.5, *v*/*v*) to afford a sticky oil (6 mg, 8%).

R_f 0.19 (petrol/EtOAc, 8.5:1.5, *v*/*v*); ^{1}H NMR (500 MHz, $CDCl_3$, δ): 8.67 (ddd, *J* = 5.0, 2.0, 1.0 Hz, 1H), 7.75 (ddd, *J* = 7.5, 7.5, 2.0 Hz, 1H), 7.40 (ddd, *J* = 8.0, 1.0, 1.0 Hz, 1H), 7.36–7.24 (m, 5H), 4.01 (t, *J* = 6.5 Hz, 2H), 3.07–3.02 (m, 2H), 2.55–2.50 (m, 2H), 1.57–1.51 (m, 2H), 1.35–1.27 (m, 2H), 0.90 (t, *J* = 7.5 Hz, 3H); ^{13}C NMR (125 MHz, $CDCl_3$, δ): 173.3, 160.1, 149.3, 140.6, 138.8, 136.5, 130.0, 129.9, 128.6, 126.5, 124.1, 121.9, 64.3, 35.9, 30.8, 28.7, 19.2, 13.8; ESI-MS *m*/*z* (ion, %): 284 ($[M+H]^+$, 100); ESI-HRMS *m*/*z*: 284.1650 $[M+H]^+$ (calculated for $C_{18}H_{22}NO_2$ 284.1645); IR (solid-state, ATR, cm^{-1}): 3350, 3056, 2957, 2930, 2872, 1729, 1650, 1586, 1518, 1470, 1426, 1387, 1306, 1230, 1176, 1113, 1025, 949, 814, 749, 696, 636, 502.

The analytical data obtained were in accordance with the literature.[36]

Lab book reference number: LAH-8-550, LAH-8-544

4-(2-pyridyl)-6-methyl-2-pyrone (176)[50]

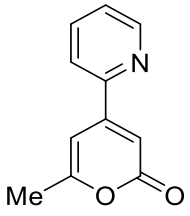

To a Schlenk tube under nitrogen were added 2-bromopyridine (0.52 ml, 0.87 g, 5.30 mmol, 1 eq.) and dry deoxygenated THF (28 ml), before being cooled to −78 °C. *n*-BuLi (1.5 M in hexanes, 3.0 ml, 5.83 mmol, 1.05 eq.) was added dropwise and stirred

for 30 minutes. In a separate Schlenk tube, $ZnCl_2$ (0.80 g, 5.83 mmol, 1.1 eq.) was placed under vacuum at cooled to −78 °C. The THF solution was transferred by cannula to the $ZnCl_2$ and stirred for 30 minutes while warming to room temperature. The reaction mixture was thereafter transferred by cannula to a separate Schlenk tube containing 4-bromo-6-methyl-2-pyrone (1.0 g, 5.30 mmol, 1 eq.) and $Pd(PPh_3)_4$ (306 mg, 0.27 mmol, 5 mol%) in dry deoxygenated THF (28 ml). The solution was stirred for 1 hour at 50 °C, before being quenched with saturated aqueous NH_4Cl (100 ml). The mixture was extracted with EtOAc (4 × 100 ml). The organic layers were combined, dried over $MgSO_4$, filtered and concentrated *in vacuo*. The crude material was purified by flash column chromatography (petrol/EtOAc, 6.5:3.5, *v*/*v*) to yield an off-white solid (0.79 g, 80%).

R_f 0.09 (petrol/EtOAc, 6.5:3.5, *v*/*v*); ^{1}H NMR (500 MHz, $CDCl_3$, δ): 8.73 (ddd, *J* = 5.0, 2.0, 1.0 Hz, 1H), 7.82 (ddd, *J* = 7.5, 7.5, 2.0 Hz, 1H), 7.74 (ddd, *J* = 8.0, 1.0, 1.0 Hz, 1H), 7.38 (ddd, *J* = 7.5, 5.0, 1.0 Hz, 1H), 6.82 (d, *J* = 1.5 Hz, 1H), 6.68 (d, *J* = 1.5 Hz, 1H), 2.34 (s, 3H); ^{13}C NMR (126 MHz, $CDCl_3$, δ): 163.8, 162.5, 153.7, 152.6, 150.2, 125.0, 121.6, 109.2, 102.4, 20.3; ESI-MS *m*/*z* (ion, %): 188 ($[M+H]^+$, 66), 210 ($[M+Na]^+$, 100); ESI-HRMS *m*/*z*: 188.0704 $[M+H]^+$ (calculated for $C_{11}H_{10}NO_2$ 188.0706); IR (solid-state, ATR, cm^{-1}): 3066, 2994, 2847, 1737, 1709, 1635, 1550, 1468, 1452, 1433, 1385, 1315, 1287, 1252, 1196, 1160, 1139, 1098, 1061, 1019, 992, 894, 876, 841, 785, 745, 724, 677, 621.

Lab book reference number: LAH-8-536, LAH-11-797

2-(3,4-Difluorophenyl)pyridine (254)

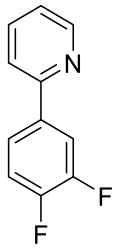

Synthesised using general procedure E from 2-bromopyridine (2.8 ml, 4.64 g, 29 mmol, 1 eq.), 3,4-difluorophenyl boronic acid (7.00 g, 44 mmol, 1.5 eq.) and $Pd_3(OAc)_6$ (196 mg, 0.3 mmol, 3 mol% with respect to Pd). The crude material was

purified by flash column chromatography (petrol/EtOAc, 8:2, *v*/*v*) to afford a white solid (4.23 g, 76%).

R_f 0.23 (petrol/EtOAc, 8:2, *v*/*v*); ^{1}H NMR (500 MHz, $CDCl_3$, δ): 8.71–8.64 (m, 1H), 7.92–7.83 (m, 1H), 7.79–7.69 (m, 2H), 7.67 (d, *J* = 7.5 Hz, 1H), 7.29–7.20 (m, 2H); ^{13}C NMR (126 MHz, $CDCl_3$, δ): 155.3, 151.4 (dd, *J* = 245.0, 8.0 Hz), 150.8 (dd, *J* = 251.5, 16.0 Hz), 149.9, 137.1, 136.6 (dd, *J* = 3.5, 5.5 Hz), 122.9 (dd, *J* = 3.5, 6.5 Hz), 122.7, 120.3, 117.6 (d, *J* = 17.5 Hz), 116.1 (d, *J* = 18.5 Hz); ^{19}F NMR (470 MHz, $CDCl_3$, δ): −137.4, −137.7; ESI-MS *m*/*z* (ion, %): 192 ($[M+H]^+$, 100); ESI-HRMS 192.0623 $[M+H]^+$ (calculated for $C_{11}H_8F_2N$ 192.0619); IR (solid-state, ATR, cm^{-1}): 3080, 3052, 3010, 1616, 1583, 1590, 1524, 1464, 1449, 1412, 1311, 1276, 1210, 1184, 1161, 1124, 1055, 1029, 990, 942, 903, 887, 820, 771, 739, 719, 629.

The analytical data obtained were in accordance with the literature.[196]

Lab book reference number: LAH-12-886

Tetracarbonyl (2-(2,3-difluorophenyl-κ,C6-pyridine-κ,N) manganese(I) (255)

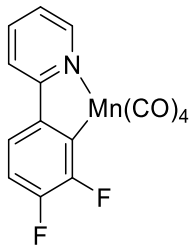

Synthesised using general procedure C from $MnBn(CO)_5$ (500 mg, 1.75 mmol, 1 eq.), 2-(3,4-difluorophenyl)pyridine (335 mg, 1.75 mmol, 1 eq.) and toluene (30 ml) at 80 °C. The crude material was purified by flash column chromatography (petrol/1,2-dichloroethane, 94:6, *v*/*v* and petrol/EtOAc/toluene, 85:7.5:7.5, *v*/*v*) to afford a yellow solid (0.23 g, 34%).

Mp 187–188 °C; R_f 0.17 (petrol/EtOAc/toluene, 85:7.5:7.5, *v*/*v*); ^{1}H NMR (500 MHz, CD_2Cl_2, δ): 8.76–8.72 (m, 1H), 7.88–7.82 (m, 2H), 7.64 (dd, *J* = 8.5, 4.0 Hz, 1H), 7.18 (ddd, *J* = 6.5, 5.5, 2.0 Hz, 1H), 7.00 (ddd, *J* = 10.0, 8.5, 8.0 Hz, 1H); ^{13}C NMR (126 MHz, CD_2Cl_2, δ): 218.7, 214.9, 213.0, 165.7, 160.6 (d, *J* = 45.5z Hz), 157.8 (dd, *J* =

230.5, 10.0 Hz), 154.6, 151.0 (dd, *J* = 256.5, 20.5), 143.8 (dd, *J* = 15.5, 3.5 Hz), 138.8, 123.4, 121.2 (dd, *J* = 6.0, 2.5 Hz), 120.3, 114.1 (d, *J* = 19.5 Hz); ^{19}F NMR (470 MHz, CD_2Cl_2, δ): −112.4, −135.5; LIFDI-MS *m*/*z* (ion, %): 357 ($[M]^+$, 100); LIFDI-HRMS *m*/*z*: 356.96505 $[M]^+$ (calculated for $C_{15}H_6NO_4F_2Mn$ 356.96399); IR (CH_2Cl_2 solution, cm^{-1}): 2084, 1999, 1946, 1597, 1462, 1441, 1385, 1272, 1258, 1162, 1123, 1079.

Lab book reference number: LAH-12-893(-2)

Tetracarbonyl (2-(3,4-difluorophenyl-κ,C6-pyridine-κ,N) manganese(I) (256)

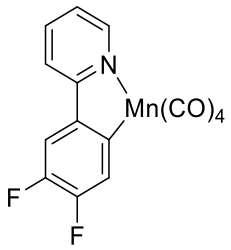

Synthesised using general procedure C from $MnBn(CO)_5$ (500 mg, 1.75 mmol, 1 eq.), 2-(3,4-difluorophenyl)pyridine (335 mg, 1.75 mmol, 1 eq.) and toluene (30 ml) at 80 °C. The crude material was purified by flash column chromatography (petrol/1,2-dichloroethane, 94:6, *v*/*v*) to afford a yellow solid (0.10 g, 17%).

Mp 154–156 °C; R_f 0.17 (petrol/1,2-dichloroethane, 94:6, *v*/*v*); ^{1}H NMR (500 MHz, CD_2Cl_2, δ): 8.72 (ddd, *J* = 5.5, 1.5, 1.0 Hz, 1H), 7.86 (ddd, *J* = 8.0, 7.5, 1.5 Hz, 1H), 7.77 (d, *J* = 8.0 Hz, 1H), 7.70 (dd, *J* = 10.0, 8.5 Hz, 1H), 7.65 (dd, *J* = 12.0, 7.5 Hz, 1H), 7.18 (ddd, *J* = 7.0, 5.5, 1.5 Hz, 1H); ^{13}C NMR (126 MHz, CD_2Cl_2, δ): 220.3, 214.3, 213.7, 171.4, 165.1 (dd, *J* = 4.5, 1.0 Hz), 154.7, 152.06 (dd, *J* = 256.5, 12.0 Hz), 149.2 (dd, *J* = 241.5, 14.0 Hz), 142.5 (dd, *J* = 5.0, 3.5 Hz), 138.9, 128.4 (d, *J* = 13.5 Hz), 123.4, 120.1, 113.2 (d, *J* = 17.5 Hz); ^{19}F NMR (470 MHz, CD_2Cl_2, δ): −137.1, −146.3; LIFDI-MS *m*/*z* (ion, %): 357 ($[M]^+$, 100); LIFDI-HRMS *m*/*z*: 356.96442 $[M]^+$ (calculated for $C_{15}H_6NO_4F_2Mn$ 356.96399); IR (CH_2Cl_2 solution, cm^{-1}): 2080, 1996, 1938, 1605, 1588, 1561, 1474, 1434, 1391, 1316, 1287, 1266, 1221, 1162.

Lab book reference number: LAH-12-893(-1)

2-(3-Fluorophenyl)pyridine (257)

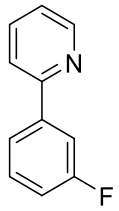

Synthesised using general procedure E from 2-bromopyridine (3.81 ml, 6.31 g, 40 mmol, 1 eq.), 3-fluorophenylboronic acid (8.40 g, 60 mmol, 1.5 eq.) and $Pd_3(OAc)_6$ (269 mg, 0.4 mmol, 3 mol% with respect to Pd). The crude material was purified by flash column chromatography (petrol/EtOAc, 8:2, v/v) to afford a pale yellow liquid (5.12 g, 74%).

R_f 0.12 (petrol/Et_2O, 8:2, *v*/*v*); ^{1}H NMR (400 MHz, $CDCl_3$, δ): 8.69 (ddd, *J* = 5.0, 2.0, 1.0 Hz, 1H), 7.79–7.67 (m, 4H), 7.46–7.39 (m, 1H), 7.27–7.22 (m, 1H), 7.13–7.07 (m, 1H); ^{13}C NMR (101 MHz, $CDCl_3$, δ): 163.4 (d, *J* = 245.5 Hz), 156.2 (d, *J* = 3.0 Hz), 149.9, 141.8 (d, *J* = 7.5 Hz), 137.0, 130.2 (d, J = 8.0 Hz), 122.8, 122.5 (d, *J* = 3.0 Hz), 120.7, 115.9 (d, *J* = 21.5 Hz), 114.0 (d, *J* = 22.5 Hz); ^{19}F NMR (376 MHz, $CDCl_3$, δ): −112.8; ESI-MS *m*/*z* (ion, %): 174 ($[M+H]^+$, 100); ESI-HRMS 174.0711 $[M+H]^+$ (calculated for $C_{11}H_9FN$ 174.0714); IR (solid-state, ATR, cm^{-1}): 3072, 3008, 1608, 1582, 1567, 1492, 1472, 1454, 1418, 1304, 1284, 1262, 1188, 1150, 1096, 1076, 991, 882, 766, 744, 725, 685, 639, 614, 601.

The analytical data obtained were in accordance with the literature.[197]

Lab book reference number: LAH-12-887

Tetracarbonyl (2-(2-fluorophenyl-κ,C6-pyridine-κ,N) manganese(I) (258)

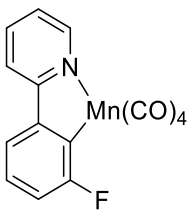

Synthesised using general procedure C from $MnBn(CO)_5$ (500 mg, 1.75 mmol, 1 eq.), 2-(3-fluorophenyl)pyridine (303 mg, 1.75 mmol, 1 eq.) and toluene (30 ml) at 80 °C. The crude material was purified by flash column chromatography (petrol/EtOAc, 9:1, *v*/*v*) to afford a yellow solid (0.26 g, 40%).

Mp 154–155 °C; R_f 0.23 (petrol/Et_2O, 9:1, *v*/*v*); ^{1}H NMR (500 MHz, $CDCl_3$, δ): 8.77 (d, *J* = 5.5 Hz, 1H), 7.90 (d, *J* = 8.0 Hz, 1H), 7.84–7.79 (m, 1H), 7.63 (d, *J* = 7.5 Hz, 1H), 7.21–7.13 (m, 2H), 7.03 (dd, *J* = 8.0, 6.5 Hz, 1H); ^{13}C NMR (126 MHz, $CDCl_3$, δ): 218.4, 214.7, 212.8, 171.4 (d, *J* = 233.0 Hz), 166.2, 156.2 (d, *J* = 49.5 Hz), 154.1, 148.7 (d, *J* = 17.0 Hz), 138.1, 126.1 (d, *J* = 7.5 Hz), 123.0, 120.3 (d, *J* = 2.5 Hz), 120.0, 116.1 (d, *J* = 31.0 Hz); ^{19}F NMR (470 MHz, $CDCl_3$, δ): −86.3; LIFDI-MS *m*/*z* (ion, %): 339 ($[M]^+$, 100); LIFDI-HRMS *m*/*z*: 338.97418 $[M]^+$ (calculated for $C_{15}H_7NO_4FMn$ 338.97341); IR (CH_2Cl_2 solution, cm^{-1}): 2081, 1995, 1942, 1605, 1567, 1484, 1439, 1400, 1315, 1302, 1265, 1257, 1211, 1172, 1084, 1015.

Lab book reference number: LAH-12-894(-1)

Tetracarbonyl (2-(4-fluorophenyl-κ,C2-pyridine-κ,N) manganese(I) (**259**)

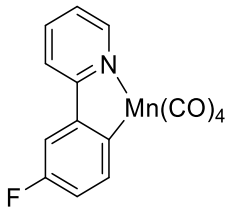

Synthesised using general procedure C from $MnBn(CO)_5$ (500 mg, 1.75 mmol, 1 eq.), 2-(3-fluorophenyl)pyridine (303 mg, 1.75 mmol, 1 eq.) and toluene (30 ml) at 80 °C. The crude material was purified by flash column chromatography (petrol/EtOAc, 9:1, *v*/*v*) to afford a yellow solid (0.20 g, 30%).

Mp 159–161 °C; R_f 0.30 (petrol/Et_2O, 9:1, *v*/*v*); ^{1}H NMR (500 MHz, $CDCl_3$, δ): 8.74 (ddd, *J* = 5.5, 1.0, 1.0 Hz, 1H), 7.89–7.80 (m, 3H), 7.49 (dd, *J* = 10.5, 2.5 Hz, 1H), 7.16 (ddd, *J* = 6.5, 5.5, 2.5 Hz, 1H), 7.07 (ddd, *J* = 9.5, 8.0, 2.5 Hz, 1H); ^{13}C NMR (126 MHz, $CDCl_3$, δ): 220.1, 214.0, 213.7, 167.3 (d, *J* = 2.5 Hz), 165.6 (d, *J* = 4.5 Hz), 162.1 (d, *J* = 240.0 Hz), 154.2, 146.7 (d, *J* = 6.0 Hz), 142.1 (d, *J* = 6.5 Hz), 138.2,

123.0, 119.7, 117.9 (d, *J* = 19.5 Hz), 111.1 (d, *J* = 21.0 Hz); ^{19}F NMR (470 MHz, $CDCl_3$, δ): −121.4; LIFDI-MS *m*/*z* (ion, %): 339 ($[M]^+$, 100); LIFDI-HRMS *m*/*z*: 338.97398 $[M]^+$ (calculated for $C_{15}H_7NO_4FMn$ 338.97341); IR (CH_2Cl_2 solution, cm^{-1}): 2077, 1992, 1934, 1603, 1560, 1480, 1463, 1427, 1314, 1271, 1257, 1229, 1188, 1160, 1014.

Lab book reference number: LAH-12-894(-2)

2-(4-Fluorophenyl)pyridine (260)

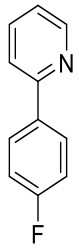

Synthesised using general procedure E from 2-bromopyridine (0.91 ml, 1.51 g, 9.5 mmol, 1 eq.), 4-fluorophenylboronic acid (2.00 g, 14.3 mmol, 1.5 eq.). The crude material was purified by flash column chromatography (petrol/EtOAc, 8:2, *v*/*v*) to afford a white solid (1.51 g, 92%).

R_f 0.26 (petrol/Et2O, 8:2, *v*/*v*); ^{1}H NMR (400 MHz, $CDCl_3$, δ): 8.67 (ddd, *J* = 5.0, 2.0, 1.0 Hz, 1H), 8.00–7.95 (m, 2H), 7.77–7.72 (m, 1H), 7.68 (dt, *J* = 8.0, 1.0 Hz, 1H), 7.22 (ddd, *J* = 7.5, 5.0, 1.0 Hz, 1H), 7.19–7.12 (m, 2H); ^{13}C NMR (101 MHz, $CDCl_3$, δ): 163.6 (d, *J* = 248.5 Hz), 156.6, 149.8, 137.0, 135.7 (d, *J* = 3.0 Hz), 128.8 (d, *J* = 8.5 Hz), 122.2, 120.4, 115.8 (d, *J* = 21.5 Hz); ^{19}F NMR (376 MHz, $CDCl_3$, δ): −113.1; ESI-MS *m*/*z* (ion, %): 174 ($[M+H]^+$, 100); ESI-HRMS 174.0713 $[M+H]^+$ (calculated for $C_{11}H_9N$ 174.0714); IR (solid-state, ATR, cm^{-1}): 3054, 3011, 1597, 1583, 1567, 1509, 1463, 1432, 1298, 1267, 1217, 1161, 1152, 1099, 1058, 1009, 989, 973, 844, 826, 771, 736, 705, 637, 618.

The analytical data obtained were in accordance with the literature.[198]

Lab book reference number: LAH-12-897

Tetracarbonyl (2-(3-fluorophenyl-κ,C6-pyridine-κ,N) manganese(I) (**261**)

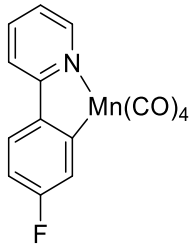

Synthesised using general procedure C from $MnBn(CO)_5$ (286 mg, 1.0 mmol, 1 eq.), 2-(4-fluorophenyl)pyridine (173 mg, 1.0 mmol, 1 eq.) and toluene (15 ml) at 80 °C. The crude material was purified by flash column chromatography (petrol/EtOAc, 85:15, *v*/*v*) to afford a yellow solid (0.32 g, 96%).

Mp 157–158 °C; R_f 0.27 (petrol/EtOAc, 85:15, *v*/*v*); ^{1}H NMR (500 MHz, $CDCl_3$, δ): 8.69 (dd, *J* = 5.5, 1.5 Hz, 1H), 7.82–7.78 (m, 2H), 7.76 (ddd, *J* = 8.5, 5.0, 1.5 Hz, 1H), 7.69 (ddd, *J* = 8.5, 2.5, 1.5 Hz, 1H), 7.14–7.08 (m, 1H), 6.88-6.82 (m, 1H); ^{13}C NMR (126 MHz, $CDCl_3$, δ): 219.8, 214.1, 213.4, 179.5 (d, *J* = 4.0 Hz), 165.5, 163.8 (d, *J* = 256.0 Hz), 154.0, 142.2 (d, *J* = 2.5 Hz), 138.1, 127.0 (d, *J* = 17.5 Hz), 125.4 (d, *J* = 8.5 Hz), 122.3, 119.3, 111.5 (d, *J* = 23.0 Hz); ^{19}F NMR (470 MHz, $CDCl_3$, δ): −110.9; LIFDI-MS *m*/*z* (ion, %): 339 ($[M]^+$, 100); LIFDI-HRMS *m*/*z*: 338.97310 $[M]^+$ (calculated for $C_{15}H_7NO_4FMn$ 338.97341); IR (CH_2Cl_2 solution, cm^{-1}): 2078, 1994, 1936, 1605, 1587, 1571, 1557, 1481, 1465, 1432, 1314, 1194, 1163.

Lab book reference number: LAH-12-907

(*E*)-2-(2-Styryl-3-fluorophenyl)-pyridine (**262**)

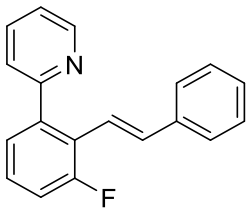

Adapted from literature procedure.[34] To a Schlenk tube under nitrogen were added $MnBr(CO)_5$ (14 mg, 0.05 mmol, 10 mol%), Cy_2NH (20 µl, 18 mg, 0.10 mmol, 20 mol%), 2-(3-fluorophenyl)pyridine (145 µl, 173 mg, 1.00 mmol, 2 eq.),

phenylacetylene (54 µl, 51 mg, 0.50 mmol, 1 eq.) and dry deoxygenated toluene (1.2 ml). The reaction solution was heated at 80 °C for 6 hours, before the solvent was removed *in vacuo*. The crude material was purified by flash column chromatography (toluene/CH_2Cl_2, 9:1, *v*/*v*) to yield the product as a sticky oil (91 mg, 66%).

R_f 0.12 (hexane/EtOAc, 95:5, *v*/*v*); ^{1}H NMR (500 MHz, $CDCl_3$, δ): 8.74 (ddd, *J* = 5.0, 2.0, 1.0 Hz, 1H), 7.74 (td, *J* = 7.5, 2.0 Hz, 1H), 7.45 (d, *J* = 8.0 Hz, 1H), 7.35–7.27 (m, 7H), 7.25–7.21 (m, 1H), 7.21–7.13 (m, 1H), 7.11 (d, *J* = 18.0 Hz, 1H), 6.94 (d, *J* = 16.5 Hz, 1H); ^{13}C NMR (126 MHz, $CDCl_3$, δ): 161.2 (d, *J* = 249.5 Hz), 158.4 (d, *J* = 3.0 Hz), 149.8, 142.2 (d, *J* = 3.5 Hz), 137.8, 136.2, 135.2 (d, *J* = 11.5), 128.7, 128.2 (d, *J* = 9.5 Hz), 127.9, 126.7, 126.2 (d, *J* = 3.0 Hz), 125.3, 123.9 (d, *J* = 12.5 Hz), 122.4, 121.2, 116.15 (d, *J* = 23.5 Hz); ^{19}F NMR (470 MHz, $CDCl_3$, δ): −114.8; ESI-MS *m*/*z* (ion, %): 276 ($[M+H]^+$, 100); ESI-HRMS *m*/*z*: 276.1178 $[M+H]^+$ (calculated for $C_{19}H_{15}FN$ 276.1183); IR (neat, ATR, cm^{-1}): 3057 , 3025, 1584, 1561, 1495, 1478, 1451, 1424, 1306, 1291, 1241, 1212, 1150, 1090, 1072, 1047, 991, 965, 916, 842, 803, 774, 750, 712, 689, 649, 625.

The analytical data obtained were in accordance with the literature.[34]

Lab book reference number: LAH-12-911

(*E*)-2-(3-Fluoro-6-styrylphenyl)-pyridine (263)

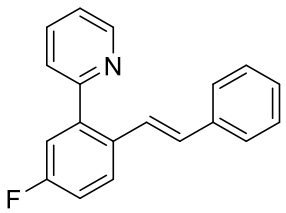

Adapted from literature procedure.[34] To a Schlenk tube under nitrogen were added $MnBr(CO)_5$ (14 mg, 0.05 mmol, 10 mol%), Cy_2NH (20 µl, 18 mg, 0.10 mmol, 20 mol%), 2-(3-fluorophenyl)pyridine (145 µl, 173 mg, 1.00 mmol, 2 eq.), phenylacetylene (54 µl, 51 mg, 0.50 mmol, 1 eq.) and dry deoxygenated toluene (1.2 ml). The reaction solution was heated at 80 °C for 6 hours, before the solvent was removed *in vacuo*. The crude material was purified by flash column chromatography (hexane/EtOAc, 97.5:2.5, *v*/*v*) to yield the product as a sticky oil (13 mg, 9%).

R_f 0.23 (hexane/EtOAc, 95:5, *v*/*v*); ^{1}H NMR (500 MHz, $CDCl_3$, δ): 8.76 (d, *J* = 4.0 Hz, 1H), 7.80–7.69 (m, 2H), 7.46 (d, *J* = 8.0 Hz, 1H), 7.38 (d, *J* = 7.0 Hz, 2H), 7.34–7.27 (m, 4H), 7.25–7.21 (m, 1H), 7.20–7.10 (m, 2H), 6.99 (d, *J* = 16.0 Hz, 1H); ^{13}C NMR (126 MHz, $CDCl_3$, δ): 162.3 (d, *J* = 247.5 Hz), 157.8 (d, *J* = 2.0 Hz), 149.9, 141.4 (d, *J* = 7.5 Hz), 137.6, 136.3, 132.1 (d, *J* = 3.5 Hz), 130.2 (d, *J* = 1.5 Hz), 128.8, 128.3 (d, *J* = 8.0 Hz), 127.8, 126.7, 125.1, 122.5, 117.0 (d, *J* = 22.5 Hz), 115.9 (d, *J* = 21.5 Hz); ^{19}F NMR (470 MHz, $CDCl_3$, δ): −114.5; ESI-MS *m*/*z* (ion, %): 276 ($[M+H]^+$, 100); ESI-HRMS *m*/*z*: 276.1183 $[M+H]^+$ (calculated for $C_{19}H_{15}FN$ 276.1183); IR (neat, ATR, cm^{-1}): 3057, 2926, 2853, 1582, 1564, 1496, 1462, 1427, 1306, 1286, 1246, 1196, 1175, 991, 961, 904, 876, 812, 785, 748, 721, 690, 648, 618, 601.

The analytical data obtained were in accordance with the literature.[199]

Lab book reference number: LAH-13-970

Appendix 1: Published Papers

The following section contains, in chronological order, papers which have been published in connection with the work described within this thesis.

1. Hammarback, L. A.; Clark, I. P.; Sazanovich, I.; Towrie, M.; Robinson, A.; Clarke, F.; Meyer, S.; Fairlamb, I. J. S.; Lynam, J. M. Mapping out the key carbon-carbon bond forming steps in manganese-catalysed C–H functionalisation. *Nat. Catal.* **2018**, *1*, 830-840.
2. Hammarback, L. A.; Robinson, A.; Lynam, J. M.; Fairlamb, I. J. S. Mechanistic Insight into Catalytic Redox-Neutral C–H Bond Activation Involving Manganese(I) Carbonyls: Catalyst Activation, Turnover, and Deactivation Pathways Reveal an Intricate Network of Steps. *J. Am. Chem. Soc.* **2019**, *141*, 2316-2328.
3. Hammarback, L. A.; Robinson, A.; Lynam, J. M.; Fairlamb, I. J. S. Delineating the critical role of acid additives in Mn-catalysed C–H bond functionalisation processes. *Chem. Commun.* **2019**, *55*, 3211-3214.

ARTICLES
https://doi.org/10.1038/s41929-018-0145-y
nature catalysis

Mapping out the key carbon–carbon bond-forming steps in Mn-catalysed C–H functionalization

L. Anders Hammarback[1], Ian P. Clark[2], Igor V. Sazanovich[2], Michael Towrie[2], Alan Robinson[3], Francis Clarke[1], Stephanie Meyer[1], Ian J. S. Fairlamb[1]* and Jason M. Lynam[1]*

Detailed understanding of the mechanistic processes that underpin transition metal-catalysed reactions allows for the rational and de novo development of complexes with enhanced activity, efficacy and wider substrate scope. Directly observing bond-cleaving and -forming events underpinning a catalytic reaction is non-trivial as the species that facilitate these steps are frequently short-lived and present at low concentrations. Here, we describe how the photochemical activation of a manganese precatalyst, [Mn(ppy)(CO)$_4$] (ppy = 2-phenylpyridine), results in selective loss of a carbonyl ligand simulating entry into the catalytic cycle for manganese-promoted C–H bond functionalization. Time-resolved infrared spectroscopy (on the ps–ms timescale) allows direct observation of the species responsible for the essential C–C bond formation step and an evaluation of the factors affecting its rate. This mechanistic information prompted the discovery of a new photochemically initiated manganese-promoted coupling of phenylacetylene with 2-phenylpyridine. This study provides unique insight into the mechanistic pathways underpinning catalysis by an Earth-abundant metal, manganese.

Transition metal-catalysed reactions play a central role in modern synthetic chemistry. A key advantage of such reagents is that detailed mechanistic investigations and/or structure–activity relationships permit the proposal of catalytic cycle(s) that can subsequently be used to rationally optimize catalyst structure, typically through judicious ligand selection and substrate matching. Studies that correlate ligand parameters with reaction kinetics, complemented with the observation of catalyst resting states, isotopic labelling and quantum chemical calculations (often using density functional theory (DFT)) are highly informative. The missing information is often the direct observation of the actual metal complexes involved within a catalytic cycle. Quantification of their behaviour can provide a precise understanding of the interplay between the different steps underpinning a given reaction, in addition highlighting subtle differences between substrates and co-ligands—specifically the balance between them. Such an approach is fraught with difficulty as observation of the short-lived key states within the catalytic cycle is, by definition, challenging. Furthermore, the individual steps within a catalytic process are likely to occur over different timescales, with, for example, substrate coordination occurring at a markedly different rate compared with subsequent C–C bond-forming events.

Time-resolved multiple-probe spectroscopy (TR^{M}PS)[1] permits the direct observation of molecular events over a wide timescale range (typically, fs to ms). This is made possible using a synchronized 1 kHz pump and 10 kHz probe lasers, together with integrated electronic and translational control over time delay. Photochemically initiated time-resolved spectroscopy enables the observation of short-lived and fundamentally important species; for example, alkane σ-complexes[2], enabling rationalization of organometallic mechanistic processes[3–5]. However, with an appropriate choice of catalyst system, TR^{M}PS has the potential to permit monitoring of a photo-initiated catalytic cycle by time-resolved infrared spectroscopy (TRIR) over nine orders of magnitude in time. Conducting the experiment in the presence of an appropriate substrate would enable the interaction between the ligand and the photo-activated catalyst to be observed, allowing insight into the nature and fate of catalytically relevant states to be obtained.

To demonstrate the feasibility of the proposed approach, manganese-catalysed C–H bond functionalizations were selected as the first exemplar of this methodology. Transition metal-catalysed direct functionalization of C–H bonds offers rapid and atom-efficient methods for structural elaboration[7]. Following the key developments in C–H functionalization methods using platinum group metals—notably, ruthenium[8], rhodium[9,10] and palladium[11]—there is an increasing desire to translate these synthetic methods to more sustainable Earth-abundant metals, such as manganese[12–15]. Simple precursors, such as [MnBr(CO)$_5$] or [Mn$_2$(CO)$_{10}$], may be employed to catalyse the formal insertion of unsaturated substrates (such as alkynes[16–23], alkenes[24–34], allenes[35–38], isocyanates[39] and carbonyl compounds[40–43]) into the C–H bond of heteroaromatic substrates (Fig. 1a)[44–46]. The heteroatom—typically nitrogen—plays a central role in the initial coordination of this substrate to the metal and directing the site of C–H functionalization.

The generally proposed mechanistic picture of manganese-catalysed C–H functionalization reactions (Fig. 1b), which use 2-phenylpyridine (ppy) as an exemplar substrate, involves cyclomanganation to give [Mn(ppy)(CO)$_4$] **1**. Subsequent loss of a carbonyl ligand results in the initial formation of solvent complex **I**: coordination of the unsaturated substrate to the metal gives **II**. This is followed by insertion of the unsaturated substrate (E=CR$_n$) into the Mn–C bond, resulting in the formation of metallocycle **III**. Protonation liberates the product and restarts the catalytic cycle. In a recent study, we demonstrated how low-temperature photolysis of **2**, which is structurally related to **1**, can be used to generate metallocycle **IV** (Fig. 1c)[47]. Complex **IV** may undergo reductive elimination to give **V** or liberate the alkenylated product **VI**, thus acting as a branching point in the reaction. Complex **1** was also successfully employed as a precatalyst, supporting its proposed role in catalysis[16].

[1]Department of Chemistry, University of York, York, UK. [2]Central Laser Facility, STFC Rutherford Appleton Laboratory, Didcot, UK. [3]Syngenta Crop Protection, Münchwilen, Switzerland. *e-mail: ian.fairlamb@york.ac.uk; jason.lynam@york.ac.uk

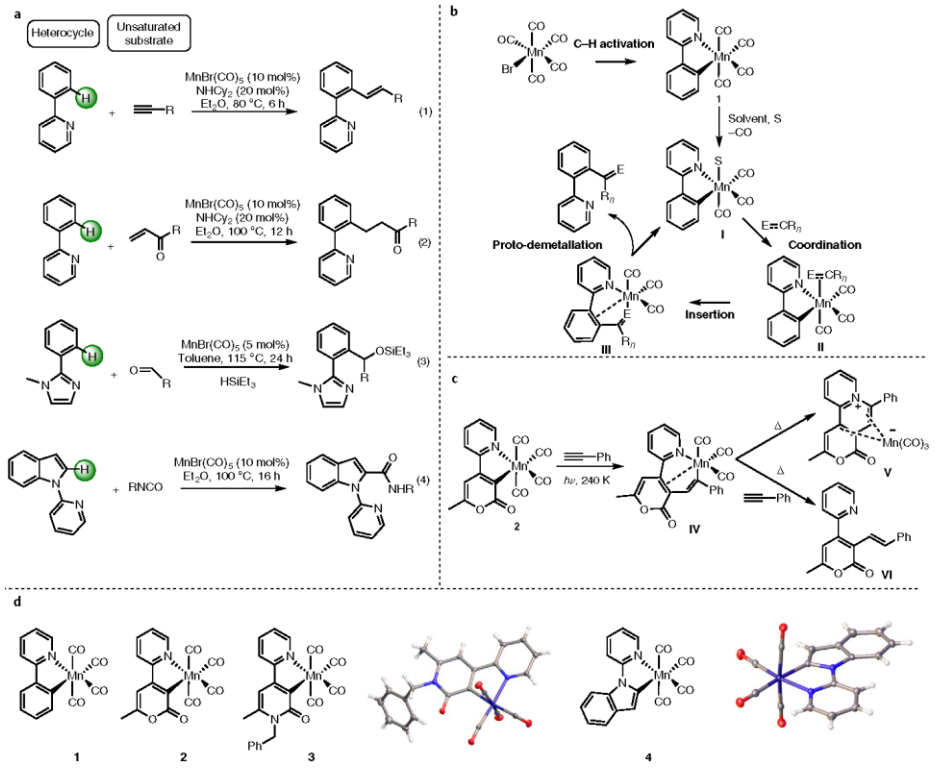

Fig. 1 | Summary of manganese-catalysed C–H functionalization reactions. a, Exemplar synthetic transformations from (1) ref [16], (2) ref. [24], (3) ref. [41] and (4) ref. [39]. **b**, Mechanistic steps proposed to underpin the catalytic cycle. **c**, Observation of a manganacycle intermediate from ref. [47], which acts as a branching point in catalysis to give either reductive elimination product **V** or, in the presence of alkyne, the product expected from a C–H functionalization reaction **VI** analogous to reaction (1) in **a**. **d**, Metal complexes employed in this study, including the molecular structures of **3** and **4** determined by single crystal X-ray diffraction.

Photolysis of **1** would result in photo-ejection of a CO ligand from the manganese, simulating the formation of **II** and entry into the catalytic cycle (Fig. 1b). The subsequent changes in the coordination environment at manganese will be reflected in the frequency and symmetry of the metal carbonyl stretching modes in the infrared spectrum (2,100–1,850 cm^{-1}). Difference spectra acquired using $TR^{M}PS$ will therefore provide quantitative and qualitative insight into the nature of ligand binding and the kinetics of C–C bond formation steps within the catalytic cycle.

The successful implementation of this strategy is now reported. The nature of the binding of alkynes (for example, PhC≡CH), alkenes (for example, $H_2C{=}CHCO_2{}^{n}Bu$), hexyl isocyanate and benzaldehyde to manganese is successfully demonstrated, with *n*-butyl acrylate showing unexpected competition between η^1(O) and η^2(C=C) binding modes. The kinetics of the subsequent C–C bond formation steps to give metallacycles related to **III** provide insight into the effect of different unsaturated substrates and cyclometallated ligands. The effects of the cyclometallated ligand on the insertion reaction have been further probed by substituting the 2-phenylpyridyl ligand in **1** for 4-(2′-pyridyl)-6-methyl-2-pyrone **2**, *N*-benzyl-4-(2′-pyridyl)-6-methylpyridin-2-one **3** and 1-(pyridine-2-yl)-1H-indole **4** (Fig. 1d), allowing electronic perturbations to be probed in the ring system, which contains the C–H bond undergoing activation and functionalization.

Results

Photochemically induced loss of CO from 1. Photolysis of **1** with a pump wavelength of 355 nm results in ultrafast (<0.5 ps) dissociation of a CO ligand and formation of *fac*-[Mn(ppy)$(CO)_3$(S)], where S is the solvent used for the experiment. Initial experiments were performed in neat unsaturated substrate; for example, alkyne, alkene or isocyanate, ensuring that following initial loss of CO from **1** only a single coordination event to Mn^{I} was viable. The resulting changes to the vibrational modes of the

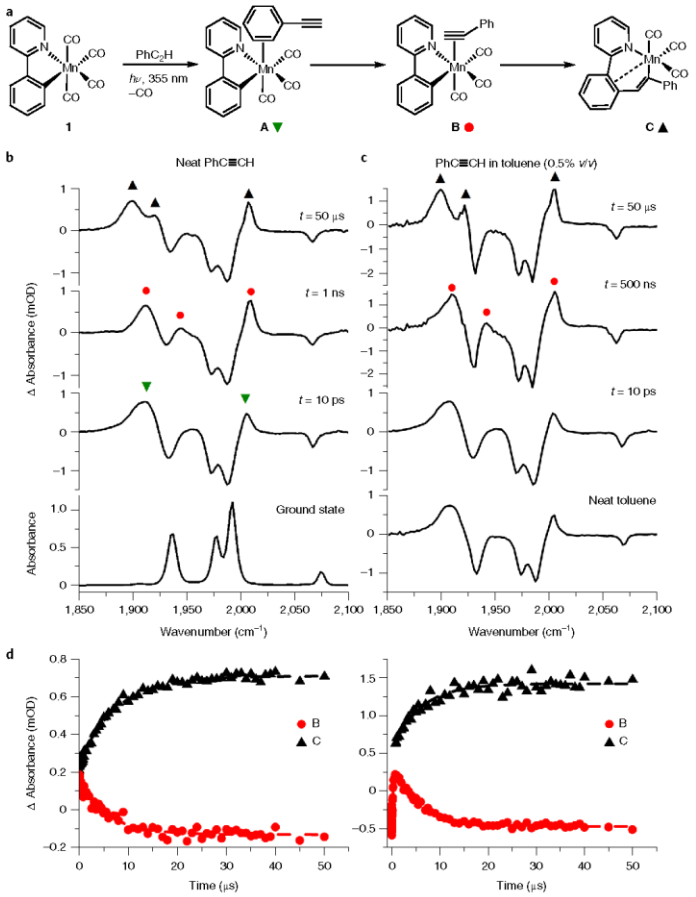

Fig. 2 | TRIR data for the reaction between 1 and PhC≡CH. **a**, Reaction scheme showing the proposed structures for intermediates **A**, **B** and **C**. **b**, TRIR data in the metal carbonyl region. The *y* axis shows the change in absorbance (mOD, milli-optical density). The negative peaks correspond to the bleach of the bands for **1**. The positive bands show the growth and change of intermediates. Data were acquired in a sealed flow system under ambient conditions. Spectra were recorded with pump–probe delays of 10 ps corresponding to **A** (bands at 1,912 and 2,006 cm^{-1}), 1 ns corresponding to **B** (bands at 1,912, 1,944 and 2,009 cm^{-1}) and 50 μs corresponding to **C** (bands at 1,899, 1,922 and 2,008 cm^{-1}). The bottom spectrum is the ground state spectrum of **1** in toluene solution. **c**, TRIR data for **1** in a toluene/phenylacetylene solution (0.5% *v*/*v*) recorded with pump–probe delays of 10 ps corresponding to [Mn(ppy)$(CO)_3$(toluene)] (bands at 1,907 and 2,004 cm^{-1}), 1 ns corresponding to **B** (bands at 1,914, 1,944 and 2,008 cm^{-1}) and 50 μs corresponding to **C** (bands at 1,901, 1,924 and 2,007 cm^{-1}). The bottom spectrum is a TRIR experiment performed on **1** in pure toluene solution (bands at 1,909 and 2,007 cm^{-1}). **d**, Left: kinetic plots for the reactions in neat phenylacetylene. Dashed lines show fits to exponential fits. Experimental data are shown for **B** (band at 1,945 cm^{-1}, $k = (1.67 \pm 0.28) \times 10^5\ s^{-1}$) and **C** (band at 1,898 cm^{-1}, $k = (1.35 \pm 0.09) \times 10^5\ s^{-1}$). Right: kinetic plots for the reactions in toluene/phenylacetylene solution (0.5% *v*/*v*). Dashed lines show fits to exponential growth and decay for **B** and exponential function for **C**). Experimental data are shown for **B** (band at 1,944 cm^{-1}, $k_{growth} = (3.85 \pm 1.24) \times 10^6\ s^{-1}$, $k_{decay} = (1.78 \pm 0.42) \times 10^5\ s^{-1}$) and **C** (band at 1,901 cm^{-1}, $k = (1.73 \pm 0.33) \times 10^5\ s^{-1}$).

metal carbonyl region (1,800–2,200 cm^{-1}) are diagnostic for the structural changes at the metal, although the high concentration of unsaturated substrate saturates the regions in the infrared spectrum where it absorbs, precluding the use of any diagnostic bands of the organic reagents to probe metal–ligand interactions. The difference spectra acquired after photolysis exhibited strong negative peaks corresponding to those for the ground state of **1** at around 1,940, 1,970, 1,990 and 2,070 cm^{-1} (Fig. 2b). This indicated

Table 1 | Tabulated rates of insertion, free energies of activation ($\Delta G^{\ddagger}_{298}$) at 298 K and DFT-calculated free energies of activation and free energies of reaction (ΔG_{298})

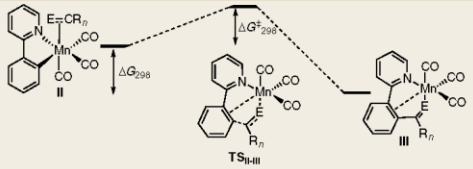

Complex	Substrate	k_{insert} (s^{-1})	$\Delta G^{\ddagger}_{298}$ ($kJ\,mol^{-1}$)	DFT-predicted $\Delta G^{\ddagger}_{298}$ ($kJ\,mol^{-1}$)	DFT-predicted ΔG_{298} ($kJ\,mol^{-1}$)
1	HC≡CPh	$(1.35\pm0.09)\times10^{5}$	44	34	−95
1	HC≡CPh[a]	$(1.63\pm0.18)\times10^{5}$	43	34	−95
1	HC≡CPh[b]	$(1.73\pm0.33)\times10^{5}$	43	34	−95
2	HC≡CPh	$(1.04\pm0.15)\times10^{6}$	39	26	−77
3	HC≡CPh	$(7.46\pm1.28)\times10^{6}$	34	20	−87
4	HC≡CPh	$(2.00\pm0.08)\times10^{4}$	48	42	−88
1	$HC{\equiv}CCH_2CO_2Ph$	$(1.79\pm0.49)\times10^{5}$	43	35	−102
1	$H_2C{=}CHPh$	N.O.	N.O.	55	−11
2	$H_2C{=}CHPh$	N.O.	N.O.	53	+7
3	$H_2C{=}CHPh$	N.O.	N.O.	46	−4
1	$H_2C{=}CHCO_2{}^{n}Bu$	$(3.62\pm0.01)\times10^{4}$	47	41	−47
1	HexNCO	$(4.38\pm0.02)\times10^{3}$	52	39	−57
1	PhC(O)H	N.O.	N.O.	48	−11

[a]6% *v*/*v* PhC≡CH in toluene solution. [b]0.5% *v*/*v* PhC≡CH in toluene solution. N.O., no insertion reaction observed. DFT-calculated energies are at the D3-PBE0/def2-TZVPP//BP86/SV(P) level with COSMO solvent correction and are relative to the appropriate complex II. In the case of the acrylate complexes, this is the O-bound form.

loss of the precursor and excluded any interference from a background thermal reaction in the TR^{M}PS experiment. Positive carbonyl stretching bands in the difference spectra indicate the generation of photoproducts, which—as evidenced by the change from four to three carbonyl bands—indicated that CO dissociation had occurred. In all cases, a high-energy band was observed at around 2,000 cm^{-1} corresponding to the symmetric stretching mode of the three CO ligands, whereas two asymmetric stretching modes were observed at lower energy as expected for *fac*-coordinated tricarbonyl compounds[48]. The experiments performed in neat substrate all displayed a similar pattern—at short timescales (<250 ps) following the pump pulse, unselective ligand binding (for example, through an alkyl chain or arene) to Mn^{I} occurred. These species then underwent a rearrangement to a thermodynamically preferable binding mode and, in certain cases, a subsequent insertion reaction was observed, the rate of which depended on the unsaturated substrate and cyclometallated ligand employed. Structural assignments were made based on comparisons with reference systems and predicted spectral changes from DFT.

Observation of alkyne binding to manganese and insertion into Mn–C bonds. TRIR spectra of **1** recorded using TR^{M}PS in neat PhC≡CH exhibited intense negative bands corresponding to bleaches of the carbonyl stretching vibrations of the ground state of **1** (Fig. 2b), and evidence was obtained for the formation of three different species over the timescale of the experiment (Fig. 2b). An initial photoproduct **A** with bands at 1,912 and 2,006 cm^{-1} was formed over the course of around 5 ps. Photoproduct **A** exhibited an exponential decay, $k=(3.83\pm0.73)\times10^{9}\,s^{-1}$ to give **B** with bands at 1,912, 1,944 and 2,009 cm^{-1}. **B** then converted to **C** (bands at 1,899, 1,922 and 2,008 cm^{-1}; $k=(1.35\pm0.09)\times10^{5}\,s^{-1}$).

These data are consistent with a pathway where the photo-ejection of CO from **1** results in an initial unselective binding of the alkyne to the metal. In a related study, we have shown that photolysis of **1** in solvents such as tetrahydrofuran or $^{n}Bu_2O$ can result in initial binding as a C–H σ-complex (B. J. Aucott et al., manuscript in preparation). Toluene appears to bind to Mn^{I} through its π-system. Comparison with the data obtained in toluene indicates that initial binding of PhC≡CH through the arene occurs. This is followed by isomerization to the thermodynamically more stable π-bound alkyne form **B**[49]. The blue shift in the infrared stretching bands for **B** compared with **A** is consistent with the presence of an η^2-(C≡C)-bound alkyne within the coordination sphere of Mn^{I}. The alkyne is an additional π-acceptor, which will reduce back-bonding to the three remaining carbonyl ligands; hence, the observed shift in stretching frequency for **B**. The formation of **C** corresponds to the insertion of the alkyne into the Mn–C bond, with the red shift in the infrared spectra consistent with the conversion of the π-accepting alkyne ligand to the seven-membered metallacycle in **C**. The rate of the insertion (**B** → **C**) at 298 K corresponds to a free energy of activation of 44 $kJ\,mol^{-1}$, which is in good agreement with that calculated by DFT (34 $kJ\,mol^{-1}$).

Repeating the experiment using a 0.5% *v*/*v* solution of PhC≡CH (Fig. 2c) in toluene provides additional support for the interpretation of the data. In this instance, the initial photoproduct corresponded to a π-bound toluene complex (B. J. Aucott et al., manuscript in preparation). The bands for **B** were then observed to grow in intensity ($k_{obs}=(3.85\pm0.63)\times10^{6}\,s^{-1}$), with subsequent conversion to **C**. The rate of this conversion to **C** was statistically identical to the experiment performed in neat PhC≡CH (Table 1), supporting the interpretation that this process is unimolecular in nature and does not arise from reactions with an additional molecule(s) of alkyne. Consistent with this explanation,

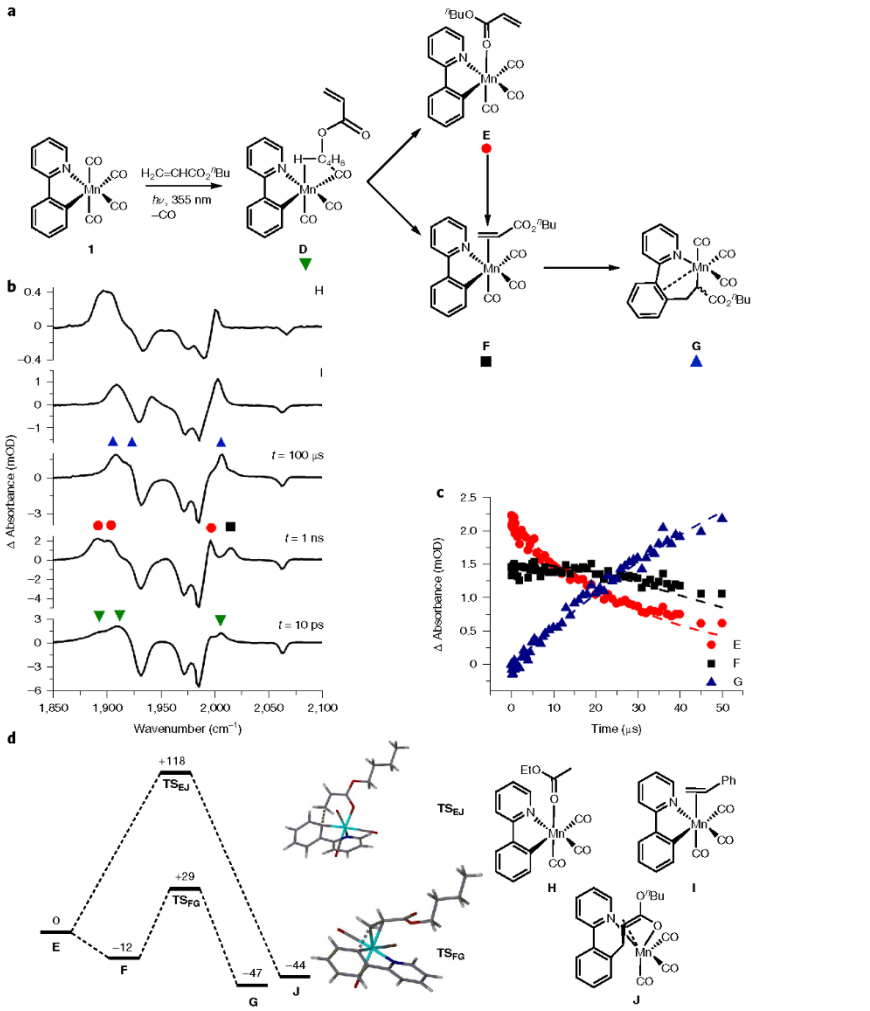

Fig. 3 | TRIR data for the reaction between 1 and $H_2C{=}CHCO_2{}^tBu$. **a**, Reaction scheme showing the proposed structures for intermediates **D**, **E**, **F** and **G**. **b**, TRIR data in the metal carbonyl region. The *y* axis shows the change in absorbance. The negative peaks correspond to the bleach of the bands for **1**. The positive bands show the growth and change of intermediates. Data were acquired in a sealed flow system under ambient conditions. Spectra were recorded with pump–probe delays of 10 ps corresponding to **D** (bands at 1,894, 1,910 and 2,007 cm^{-1}), 1 ns corresponding to **E** (bands at 1,890, 1,903 and 1,997 cm^{-1}) and **F** (band at 2,017 cm^{-1}), and 100 μs corresponding to **G** (bands at 1,908, 1,920 and 2,008 cm^{-1}). Reference spectra for complexes **H** and **I** prepared from the photolysis of **1** in neat ethyl acetate and styrene, respectively, were recorded with pump–probe delays of 1 ns. **c**, Kinetic plots showing the change in absorbance due to the loss of **E** (1,997 cm^{-1}) and **F** (2,017 cm^{-1}) and the growth of **G** (2,008 cm^{-1}). The dashed lines are fits to a kinetic model **E** → **F** → **G** with rate constants of **E** → **F** = (3.21 ± 0.01) × 10^4 s^{-1} and **F** → **G** = (3.62 ± 0.01) × 10^4 s^{-1}. **d**, Structures of complexes **H**–**J** and the DFT-calculated potential energy surface for the insertion of butyl acrylate into the Mn–C bond. Energies are Gibbs energies at 298.15 K at the D3-PBE0/def2-TZVPP//BP86/SV(P) level with COSMO solvent correction and are relative to **E**. TS_{EJ} and TS_{FG} are the **E** → **J** and **F** → **G** transition states, respectively.

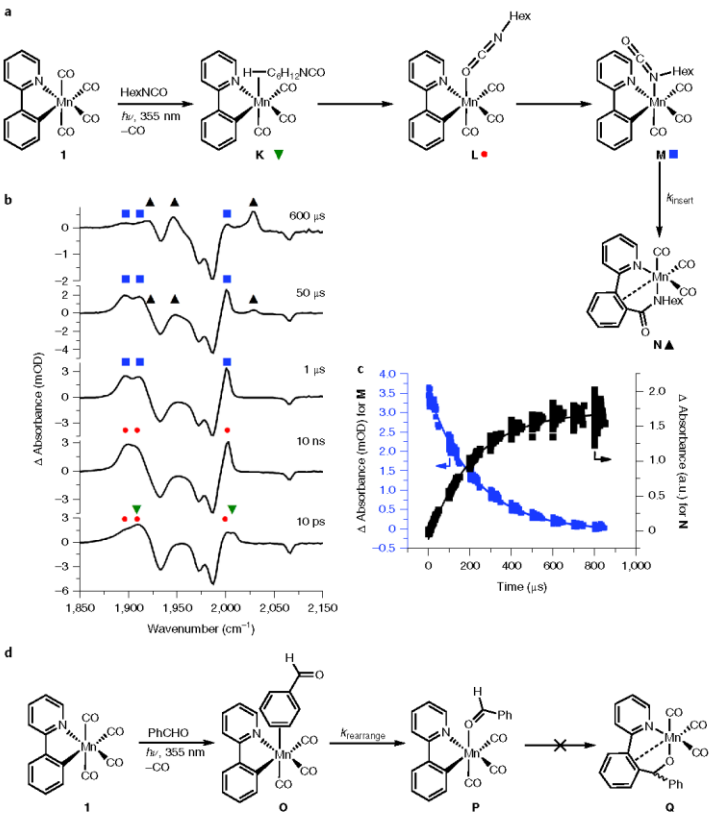

Fig. 4 | TRIR data for the reaction between 1 and HexNCO. a, Reaction scheme showing the proposed structures for intermediates **K**, **L**, **M** and **N**. **b**, TRIR data in the metal carbonyl region. The *y* axis shows the change in absorbance. The negative peaks correspond to the bleach of the bands for **1**. The positive bands show the growth and change of intermediates. Data were acquired in a sealed flow system under ambient conditions. Spectra were recorded with pump–probe delays of 10 ps corresponding to **K** (bands at 1,910 and 2,009 cm^{-1}) and **L** (bands at 1,898, 1,909 and 2,003 cm^{-1}), 1 µs corresponding to **M** (bands at 1,897, 1,913 and 2001 cm^{-1}), and at both 50 µs and 600 µs for **M** (bands at 1,897, 1913 and 2001 cm^{-1}) and **N** (bands at 1,921, 1,946 and 2,029 cm^{-1}). **c**, Double *y* axis plot showing the change in absorbance due to the loss of **M** (2,001 cm^{-1}, left-hand axis) and the growth of **N** (2,029 cm^{-1}, right-hand axis). The dashed lines are fits to exponential growth (**N**) and decay (**M**) functions. The data for **N** have been corrected for flow effects (see Supplementary Section 3.2). **d**, Reaction scheme showing the proposed structures for intermediates **O**, **P** and **Q**.

an experiment performed at an intermediate concentration of PhC≡CH (6% *v*/*v* in toluene; Supplementary Fig. 18) showed accelerated formation of **B** ($k_{obs} = (1.77 \pm 1.07) \times 10^7\ s^{-1}$), with a similar rate of conversion of **B** to **C** (Table 1).

The observation of alkyne coordination to Mn^I, coupled with the resulting insertion process in toluene solution, provides confidence that the results are pertinent to the catalytic systems. Furthermore, the data indicate that in reactions that are thermally promoted the coordination of the alkyne occurs extremely rapidly (on a µs timescale) following the initial loss of a CO ligand from **1**.

To ascertain the factors controlling the rate of alkyne insertion into the Mn–C bond, analogous experiments in neat PhC≡CH with compounds **2**, **3** and **4** were conducted (Supplementary Figs. 20, 22 and 24, respectively). Complex **4** is of particular interest as the indole-substituted substrate has been employed in a range of different manganese-catalysed reactions[20–23,29,34,38,39,42]. Spectral analysis demonstrated that the rate of alkyne insertion into the Mn–C bond decreased in the sequence **3** > **2** > **1** > **4**—a trend in behaviour that was predicted by DFT (Table 1). The behaviour of $HC{\equiv}CCH_2CO_2Ph$ (a substrate that can also be used in manganese-catalysed C–H functionalizations)[16] mirrored the observations for PhC≡CH (Supplementary Fig. 26). Initial binding to the phenyl group of the alkyne was seen, followed by migration to the η^2-C≡C-bound form: subsequent C–C bond formation by alkyne insertion

Table 2 | Photochemical generation of (*E*)-2-(2-styrylphenyl) pyridine 5 from 1 and PhC≡CH

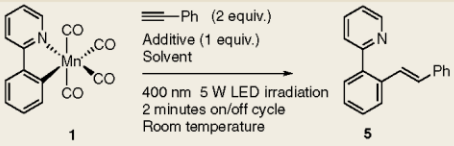

1 5

Entry	Solvent	Additive	Time (h)	Conversion to 5 (%)
1	Bu_2O	None	3	21
2	Bu_2O	$PhCO_2H$	3	59
3	Bu_2O	$PhCO_2H$	16	67
4	Bu_2O	$PhCO_2H$	48	81
5	Bu_2O	$EtCO_2H$	3	45
6	Toluene	$PhCO_2H$	3	50
7[a]	Bu_2O	$PhCO_2H$	16	0
8[b]	Bu_2O	$PhCO_2H$	3	0

[a]Reaction performed in the absence of 1. [b]Reaction performed without irradiation.

occurs at a similar rate to that for PhC≡CH (Table 1), consistent with the prediction from DFT. These data demonstrate that it is possible to use TR^{M}PS to directly activate Mn^{I}–carbonyl complexes and observe subsequent substrate binding and C–C bond formation steps that underpin the catalytic cycle.

Observation of alkene binding to manganese and insertion into Mn–C bonds. In addition to alkynes, polarized (activated) alkenes are viable unsaturated substrates for Mn^{I}-catalysed C–H functionalizations (Fig. 1a, reaction ii)[24,25]. The presence of the carbonyl group connected to the alkene is vital; substrates such as styrene are not viable[24]. Probing complexes **1**–**3** in *n*-butyl acrylate and **1** in ethyl acrylate, using TR^{M}PS, provided new insight into the key interactions between Mn^{I} and the substrates. The resulting spectra for **1** in neat *n*-butyl acrylate are presented in Fig. 3b.

Spectra recorded with short delays (<10 ps) exhibited broad features that sharpened (presumably as a result of vibrational cooling)[49] to give bands at 1,894, 1,910 and 2,007 cm^{-1}. Based on the similarity of these bands to those of the σ-alkane complex [Mn(ppy)(CO)$_3$(heptane)] (B. J. Aucott et al., manuscript in preparation), generated from the photolysis of **1** in neat heptane, this initial photoproduct was assigned as σ-complex **D**. Over the course of 100 ps, these stretching bands decreased in intensity to be replaced by those for **E** (1,890, 1,903 and 1,997 cm^{-1}) and **F** (2,017 cm^{-1}). Additional peaks for **F** may be obscured either by those of **E** or the bleach bands. The observed rate constants for the growth of **E** $(2.89 \pm 0.55) \times 10^{10}$ s^{-1} and **F** $(2.72 \pm 0.79) \times 10^{10}$ s^{-1} were statistically identical (Supplementary Figs. 28 and 29).

Insight into the nature of **E** and **F** was obtained from control experiments with ethyl acetate and styrene. Photolysis of **1** in neat ethyl acetate gave **H** (Fig. 3d), which showed bands essentially identical to **E**. Hence, the ligand was assigned an η^1(O)-substrate binding mode in both cases. The significant blue shift observed in the spectrum of **F** (2,017 cm^{-1}) is consistent with the introduction of a good π-acceptor ligand into the coordination sphere of Mn^{I}. Hence, the *n*-butyl acrylate ligand was assigned an η^2-C=C π-bonding mode in **F**. A smaller, but still significant, blue shift was observed in the η^2-C=C complex **I**, obtained on photolysis of **1** in neat styrene (bands at 1,911, 1,943 and 2,006 cm^{-1}). The smaller shift compared with **F** is expected as the more electron-deficient butyl acrylate is expected to be a better π-acceptor than styrene[50].

A related study of the photochemical reaction between **1** and ethyl acrylate demonstrated that the formation of analogous species of **E** and **F** from the corresponding σ-complex was more rapid $(k = (5.95 \pm 0.51) \times 10^{10}$ s^{-1} and $(4.96 \pm 0.71) \times 10^{10}$ s^{-1}, respectively; Supplementary Figs. 31 and 32). This is consistent with the initial binding of the manganese at the alkyl group of the acrylate before chain-walking to either the oxygen atom or alkene group. Presuming that the chain-walking is stochastic in nature, this would occur more rapidly in ethyl acrylate compared with the *n*-butyl analogue, due to the greater number of C–H bonds in the *n*-butyl analogue, as was observed[51].

Over the course of 100 μs, the bands for both **E** and **F** decreased in intensity to be replaced by those for a single new species **G** (1,908, 1,920 and 2,008 cm^{-1}). Kinetic modelling (Fig. 3c and Supplementary Discussion) of the resulting data indicated that a mechanistic process **E** → **F** → **G** was feasible, with the rate constants of both steps being similar.

These data allowed us to propose the mechanistic pathway for alkene insertion shown in Fig. 3a. A critical observation is that competitive η^1(O) and η^2(C=C) binding of the *n*-butyl acrylate is viable, but only η^2(C=C) binding leads to the product. This is consistent with DFT calculations indicating that there is a small difference in energy between **E** and **F**, and that the barrier to alkene insertion from **F** is greater than that for PhC≡CH. A transition state for C–C bond formation from **E** could be located (**TS$_{EI}$**; Fig. 3d), although the barrier was found to be too high (+118 kJ mol^{-1}) for the resulting process to be observed on the timescale of the experiments.

Wang and co-workers[34] have proposed that coordination of the ester functionality underpins the successful implementation of acrylates in the catalytic reaction (Fig. 1a, reaction ii). While it may be conjectured that our data show that the C–C bond formation occurs at a *fac*-Mn(CO)$_3$ complex, rather than the dicarbonyl complexes proposed by Wang, it is evident that that the ester group plays a central role in coordination to the metal. Styrene is not a viable substrate for the catalytic reaction. Indeed, no insertion into the Mn–C bond from η^2(C=C)-bound complex **I** was observed, reflecting the higher predicted barrier for this process (55 kJ mol^{-1}) compared with *n*-butyl acrylate (41 kJ mol^{-1}; Table 1).

Observation of isocyanate and benzaldehyde binding to Mn^{I} and insertion into Mn–C bonds. The insertion of isocyanates into an Mn–C bond has been proposed to be a key step in manganese-catalysed aminocarbonylation (Fig. 1a, reaction iv)[39]. The resulting TRIR study of **1** in hexyl isocyanate demonstrated the sequential formation of four photoproducts **K**, **L**, **M** and **N** (Fig. 4a). At short timescales (around 10 ps), both **K** and **L** were present (Fig. 4b). Subsequently, **K** converted to **L** $(k = (1.89 \pm 0.26) \times 10^{10}$ s$^{-1})$ and the pathway **L** → **M** → **N** was observed with the rate constant of the last step $k = (4.38 \pm 0.02) \times 10^{3}$ s^{-1}. Complex **K** was assigned as a C–H σ-complex based on its similarity to the spectrum of **D**. Product **N** was assigned as arising from insertion of the isocyanate into the Mn–C bond based on the observed blue shift in the three carbonyl bands (1,921, 1,946 and 2,029 cm^{-1}), mirroring those predicted computationally (Supplementary Table 1). The assignment of structures **L** (*O*-bound isocyanate) and **M** (*N*-bound isocyanate) was made on the basis that: (1) **M** is predicted to be at lower energy than **L** ($\Delta G_{298\ L\text{-}M} = -12$ kJ mol^{-1}); hence, **M** would not convert to **L**; and (2) an appropriate transition state for the conversion of **M** to **N** could be located at an energy ($\Delta G^{\ddagger}_{298\ M\text{-}N} = +39$ kJ mol^{-1}) consistent with the observed rate of reaction (Table 1). The predicted infrared stretching modes for **L** and **M** are similar, as are the experimental spectra; hence, they could not be used to distinguish between the two binding modes.

The conversion of **M** to **N** was proposed by Ackermann and co-workers[39] to be the rate-limiting step in manganese-catalysed aminocarbonylation and, although our data do not currently allow

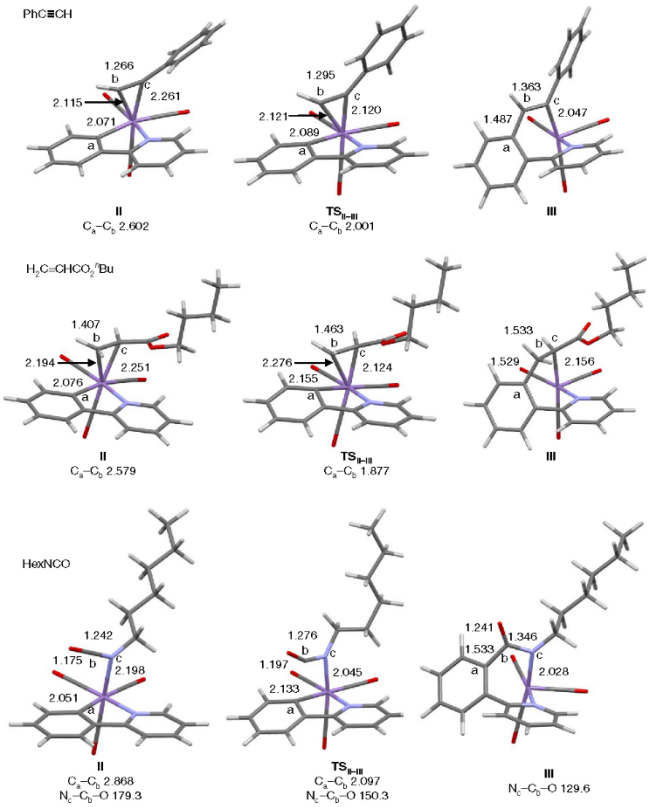

Fig. 5 | Analysis of experimental and DFT-calculated reaction kinetics. DFT-calculated structures of complexes **II**, **TS$_{II–III}$** and **III** for the reaction of **1** with PhC≡CH (top), $H_2C{=}CHCO_2{}^nBu$ (middle) and HexNCO (bottom). Selected bond lengths (Å) are given. In the case of PhC≡CH, **II** and **III** correspond to the experimentally observed species **B** and **C**; for $H_2C{=}CHCO_2{}^nBu$, they correspond to **F** and **G**, and for HexNCO, they correspond to **M** and **N**, respectively.

for a direct comparison with the rates of C–H activation, the insertion of the hexyl isocyanate is slower than PhC≡CH and acrylate substrates. A TR^{M}PS experiment on the reaction between **1** and benzaldehyde (Supplementary Fig. 33) was performed to mirror the manganese-catalysed insertion of an aldehyde into a C–H bond (Fig. 1a, reaction iii)[41,43]. In the same manner as the experiments conducted with PhC≡CH, a short-lived complex corresponding to the aryl-bound aldehyde photoproduct **O** was formed. Complex **O** then isomerized to **P**, in which the benzaldehyde was assigned an η^1(O)-binding mode based on the spectral similarity of both **E** and **H**. In these experiments, an additional band at 1,818 cm^{-1}, assigned to the benzoyl radical [PhCO]$^{\bullet}$[42], was observed, both in the presence and absence of **1**, consistent with this being a photoproduct of benzaldehyde (Supplementary Fig. 33). Complex **P** remained unchanged for the experiment duration (850 µs), indicating that any insertion into the Mn–C bond to give **Q** (Fig. 4) must be much slower than the experiment timescale. This deduction is supported by DFT calculations that show a larger barrier to insertion of benzaldehyde into the Mn–C bond (48 kJ mol^{-1}) compared with PhC≡CH, butyl acrylate and hexyl isocyanate.

In contrast with the reactions involving alkyne and activated alkene substrates, the manganese-catalysed addition of benzaldehyde to cyclometallated heteroaromatic substrates relies on the use of an additive[41,43]. For example, as shown in Fig. 1a (reaction iii), the coupling of 1-methyl-2-phenyl-1*H*-imidazole requires the use of a silane to trap the product. The DFT-calculated change in free energy for the formation of **Q** from **P** is the smallest in this study ($\Delta G_{298} = -11$ kJ mol^{-1}), demonstrating that there is only a small thermodynamic driving force for the C–C bond formation step, which may explain the requirement for the silane. Furthermore, $ZnBr_2$ is required to promote the coupling of 2-phenylpyridine with benzaldehyde, and it is proposed that the Lewis acid assists with the insertion step by increasing the electrophilicity of the aldehyde. Our data indicate that this insertion step would certainly be slower than that of alkynes and activated alkenes, and provide some support for this hypothesis.

A photochemically promoted alkenylation reaction. Given that the photodissociation of CO occurs readily at wavelengths of either 355 or 400 nm (B. J. Aucott et al., manuscript in preparation) and, for substrates such as PhC≡CH, the C–C bond formation is occurring on a sub-ms timescale, it was reasoned that the formation of the alkenylated product **5** from **1** could be initiated by light. Reaction optimization (Table 2) demonstrated that light-emitting diode (LED) irradiation (400 nm) of a room temperature $^{n}Bu_2O$ solution of **1** for 3 h in the presence of PhC≡CH (2 equiv.) and $PhCO_2H$ (1 equiv.) leads to 59% conversion to **5**: extending the irradiation to 48 h results in 81% conversion. No product was observed under the same conditions in the absence of LED irradiation, demonstrating the potential for a room temperature photochemically induced manganese-promoted alkenylation reaction. The discovery of what is the mildest Mn^{I}-prompted alkenylation was driven by the mechanistic information unearthed from this TRIR study.

Discussion

The kinetic data for the insertion steps for all the reactions studied are presented in Table 1, along with the DFT-predicted values for $\Delta G^{\ddagger}_{298}$ and ΔG_{298}. There is a direct correlation between the experimentally determined values for $\Delta G^{\ddagger}_{298}$ and those predicted by DFT. These data demonstrate that the barrier to insertion into the Mn–C bond of **1** increases in the series PhC≡CH ~ $HC{\equiv}CCH_2CO_2Ph$ < $H_2C{=}CHCO_2{}^{n}Bu$ ~ HexNCO << PhC(O)H < $H_2C{=}CHPh$: in the case of PhC≡CH, the rate of insertion increases in the series **3** < **2** < **1** < **4**.

As shown in Fig. 5, the DFT calculations reveal a common pathway for C–C bond formation in this series of complexes. Before C–C bond formation (state **II**; Fig. 5) the unsaturated ligand (alkyne, alkene or isocyanate) is aligned along the M–C axis of the 2-phenylpridine ligand. In the calculated transition state structures for C–C bond formation ($\mathbf{TS_{II\text{-}III}}$) for the alkyne and alkene examples, the Mn–C_b bond lengthens, as does the C_b–C_c bond; however, the Mn–C_c bond shortens. Similar effects are seen in the HexNCO example, with a shortening of the Mn–N_c bond and bending of the isocyanate ligand. In all three cases, the phenyl group of the 2-phenylpyridyl group deviates from planarity in the transition state and there is a notable lengthening of the Mn–C_a bond. Therefore, our experimental and computational data indicate a common low-energy pathway for C–C bond formation in these manganese-catalysed reactions, which is probably best viewed as a migratory insertion reaction supported by a low-spin d^6 $Mn(CO)_3$ fragment.

These experiments permitted the direct observation of C–C bond formation by insertion of unsaturated substrates into the Mn^{I}–C bond, within the coordination sphere of cyclometallated *fac*-$Mn(CO)_3$ complexes, indicating that it is a viable mechanistic pathway underpinning manganese-catalysed C–H functionalization reactions. The effects of different substrates and co-ligands within the coordination sphere of the metal have been quantified. Detailed information about substrate binding to Mn^{I} (for example, an unexpected η^1(O)-binding mode observed for acrylate substrates, and the reactions performed in toluene solution with PhC≡CH) have provided information about the kinetics of the coordination step of the cycle. Central to the success of this unique approach to the study of individual steps within a catalytic cycle is the versatility of TR^{M}PS, which permits the observation of processes occurring over a wide range of timescales, and of short-lived states that have only previously been predicted computationally.

Methods

Sample preparation. Compounds **1** (ref. [53]) and **2** (ref. [47]) were prepared following methods in the literature. The syntheses and characterization of **3** and **4** are described in the Supplementary Methods. Substrates were purchased from Sigma–Aldrich and used as supplied. Solutions of the manganese complexes were prepared at a concentration of around 1.88 mM in the appropriate substrate and flowed through a Harrick cell for the duration of the TRIR experiment.

TRIR measurements. The TRIR measurements were performed at the ULTRA[54] facility using the TR^{M}PS mode of operation[1] at the Central Laser Facility (Science and Technology Facilities Council Rutherford Appleton Laboratories). The experiments were driven by a 10 kHz repetition rate titanium sapphire amplifier (Thales) as a probe source, producing 40 fs pulses at 800 nm. The titanium sapphire laser output was used to pump an optical parametric amplifier (TOPAS; Light Conversion) followed by an AgGaS 'Difference-frequency mixing' stage, which produced a tuneable mid-infrared probe beam of ~500 cm^{-1} useable bandwidth. The infrared probe beam was split to form reference and probe beams, which were passed through spectrographs onto Mercury Cadmium Telluride array detectors (InfraRed Associates). The probe beam spot size at sample was around 80 μm × 80 μm. High-speed data-acquisition systems (Quantum Detectors) allowed 10 kHz acquisition and processing of the probe and reference pulses to generate a pump-on/pump-off infrared absorption difference signal. The excitation source for the TRIR experiments was the output of the 1 kHz titanium sapphire amplifier (Spectra-Physics Spitfire XP; 100 fs pulse length) equipped with another TOPAS optical parametric amplifier. The pulse energy at sample was attenuated down to 1 μJ and focused down to a spot size of around 150 μm × 150 μm). Both ULTRA and Spitfire amplifiers were optically synchronized by sharing the same seed from a 68 MHz titanium sapphire oscillator. The seed beam was delayed with an optical delay line before the 1 kHz amplifier to accommodate for the 100 fs–14.7 ns time delays between the pump and probe. To go beyond 14.7 ns and up to 100 μs, subsequent seed pulses were selected from the 68 MHz seed pulse train accompanied by the appropriate setting of the optical delay line. The polarization of the excitation beam at sample was set to 54.7° with respect to the probe.

Data were collected with pump–probe delays from 0.5 ps to 850 μs. Datasets were acquired with the pump laser on (pump-on) and also under essentially identical conditions with the pump laser off (pump-off). Subtraction of the pump-off data from the pump-on data allowed for a number of artefacts from electrical noise to be eliminated. The resulting data were then manipulated by first subtracting the reference data to obtain a difference spectrum and then performing a first- or second-order polynomial fitting to the baseline. The data were then exported as comma-separated variable files and imported into Origin. Spectral calibration was then performed with a 190 μm polystyrene standard allowing for detector pixels to be allocated to specific frequencies. The overlap in detection frequency between the two detectors was then removed manually. Kinetic data were obtained by fitting the intensities of selected peak maxima to appropriate functions within Origin. For the cases in which kinetic processes were occurring over long pump–probe delays (for example, greater than 1 ns), only the data with pump–probe delays of greater than 1 ns were typically considered. In addition, for the analysis of more rapid processes (<1 ns), only the data at short pump–probe delays were employed.

Data analysis. Spectra were initially processed to perform subtraction of reference spectra and baseline correction. The resulting data were then analysed in Origin and kinetic fits were performed with the ExpGro, ExpDec and ExpGroDec functions. Quoted errors are 95% confidence limits. Rate constants, k, were converted to free energies of action $\Delta G^{\ddagger}$ using the Eyring equation, where T was taken as 298 K, and the transmission coefficient, κ, of unity.

Computational chemistry. All calculations were performed using the TURBOMOLE version 6.4 package using the resolution of identity (RI) approximation[55–62].

Initial optimizations were performed at the (RI-)BP86/SV(P) level, followed by frequency calculations at the same level. Transition states were located by initially performing a constrained minimization (by freezing internal coordinates that change most during the reaction) of a structure close to the anticipated transition state. This was followed by a frequency calculation to identify the transition vector to follow during a subsequent transition state optimization. A final frequency calculation was then performed on the optimized transition state structure. All minima were confirmed as such by the absence of imaginary frequencies, and all transition states were identified by the presence of only one imaginary frequency. Dynamic reaction coordinate analysis confirmed that transition states were connected to the appropriate minima. Single-point calculations on the (RI-)BP86/SV(P)-optimized geometries were performed using the hybrid PBE0 functional and the flexible def2-TZVPP basis set. The (RI-)PBE0/def2-TZVPP self-consistent field energies were corrected for their zero point energies, thermal energies and entropies (obtained from the (RI-)BP86/SV(P)-level frequency calculations). No symmetry constraints were applied during the optimizations. Solvent corrections were applied with the COSMO dielectric continuum model[63] and dispersion effects modelled with Grimme's D3 method[64,65]. Energies, x, y and z coordinates and the first 50 lines of the vibrational spectra are presented in Supplementary Data 1.

Data availability

All data supporting this study are available on request from the University of York's York Research Database: https://doi.org/10.15124/46f25600-736a-408a-b498-8b7f6a5f3f2e. X-ray crystallography data for structures **3** and **4** are available free of charge from the Cambridge Crystallographic Data Centre (https://www.ccdc.cam.ac.uk/) under reference numbers 1815767 and 1844072, respectively.

Received: 25 January 2018; Accepted: 16 August 2018;
Published online: 8 October 2018

References

1. Greetham, G. M. et al. Time-resolved multiple probe spectroscopy. *Rev. Sci. Instrum.* **83**, 103107 (2012).
2. Calladine, J. A. et al. Photoinduced N_2 loss as a route to long-lived organometallic alkane complexes: a time-resolved IR and NMR study. *Chem. Sci.* **1**, 622–630 (2010).
3. Ford, P. C. From curiosity to applications. A personal perspective on inorganic photochemistry. *Chem. Sci.* **7**, 2964–2986 (2016).
4. Jackson, S. A., Hodges, P. M., Poliakoff, M., Turner, J. J. & Grevels, F. W. Infrared spectroscopic studies on the photocatalytic hydrogenation of norbornadiene by group 6 metal carbonyls. 1. The role of H_2 and the characterization of nonclassical dihydrogen complexes, (η^4-norbornadiene) $M(CO)_3(\eta^2\text{-}H_2)$. *J. Am. Chem. Soc.* **112**, 1221–1233 (1990).
5. Hodges, P. M. et al. Infrared spectroscopic studies on the photocatalytic hydrogenation of norbornadiene by group 6 metal carbonyls. 2. The role of the diene and the characterization of (η^4-norbornadiene)(η^2-norbornadiene) $M(CO)_3$ complexes. *J. Am. Chem. Soc.* **112**, 1234–1244 (1990).
6. Guan, J. et al. Probing the carbon–hydrogen activation of alkanes following photolysis of Tp′Rh(CNR)(carbodiimide): a computational and time-resolved infrared spectroscopic study. *J. Am. Chem. Soc.* **140**, 1842–1854 (2018).
7. Wencel-Delord, J. & Glorius, F. C–H bond activation enables the rapid construction and late-stage diversification of functional molecules. *Nat. Chem.* **5**, 369–375 (2013).
8. Arockiam, P. B., Bruneau, C. & Dixneuf, P. H. Ruthenium(II)-catalyzed C–H bond activation and functionalization. *Chem. Rev.* **112**, 5879–5918 (2012).
9. Song, G., Wang, F. & Li, X. C–C, C–O and C–N bond formation via rhodium(III)-catalyzed oxidative C–H activation. *Chem. Soc. Rev.* **41**, 3651–3678 (2012).
10. Colby, D. A., Bergman, R. G. & Ellman, J. A. Rhodium-catalyzed C–C bond formation via heteroatom-directed C–H bond activation. *Chem. Rev.* **110**, 624–655 (2010).
11. Lyons, T. W. & Sanford, M. S. Palladium-catalyzed ligand-directed C–H functionalization reactions. *Chem. Rev.* **110**, 1147–1169 (2010).
12. Pototschnig, G., Maulide, N. & Schnürch, M. Direct functionalization of C–H bonds by iron, nickel, and cobalt catalysis. *Chem. Eur. J.* **23**, 9206–9232 (2017).
13. Su, B., Cao, Z.-C. & Shi, Z.-J. Exploration of Earth-abundant transition metals (Fe, Co, and Ni) as catalysts in unreactive chemical bond activations. *Acc. Chem. Res.* **48**, 886–896 (2015).
14. Moselage, M., Li, J. & Ackermann, L. Cobalt-catalyzed C–H activation. *ACS Catal.* **6**, 498–525 (2016).
15. Shang, R., Ilies, L. & Nakamura, E. Iron-catalyzed C–H bond activation. *Chem. Rev.* **117**, 9086–9139 (2017).
16. Zhou, B., Chen, H. & Wang, C. Mn-catalyzed aromatic C–H alkenylation with terminal alkynes. *J. Am. Chem. Soc.* **135**, 1264–1267 (2013).
17. He, R., Huang, Z.-T., Zheng, Q.-Y. & Wang, C. Manganese-catalyzed dehydrogenative [4+2] annulation of N–H imines and alkynes by C–H/N–H activation. *Angew. Chem. Int. Ed.* **53**, 4950–4953 (2014).
18. Shi, L., Zhong, X., She, H., Lei, Z. & Li, F. Manganese catalyzed C–H functionalization of indoles with alkynes to synthesize bis/trisubstituted indolylalkenes and carbazoles: the acid is the key to control selectivity. *Chem. Commun.* **51**, 7136–7139 (2015).
19. Lu, Q. Q. et al. Redox-neutral manganese(I)-catalyzed C–H activation: traceless directing group enabled regioselective annulation. *Angew. Chem. Int. Ed.* **56**, 12778–12782 (2017).
20. Lu, Q. Q., Gressies, S., Klauck, F. J. R. & Glorius, F. Manganese(I)-catalyzed regioselective C–H allenylation: direct access to 2-allenylindoles. *Angew. Chem. Int. Ed.* **56**, 6660–6664 (2017).
21. Ruan, Z. X., Sauermann, N., Manoni, E. & Ackermann, L. Manganese-catalyzed C–H alkynylation: expedient peptide synthesis and modification. *Angew. Chem. Int. Ed.* **56**, 3172–3176 (2017).
22. Wang, H., Pesciaioli, F., Oliveira, J. C. A., Warratz, S. & Ackermann, L. Synergistic manganese(I) C–H activation catalysis in continuous flow: chemoselective hydroarylation. *Angew. Chem. Int. Ed.* **56**, 15063–15067 (2017).
23. Lu, Q. et al. Manganese(I)-catalyzed C–H (2-indolyl)methylation: expedient access to diheteroarylmethanes. *Angew. Chem. Int. Ed.* **57**, 1399–1403 (2018).
24. Zhou, B., Ma, P., Chen, H. & Wang, C. Amine-accelerated manganese-catalyzed aromatic C–H conjugate addition to α,β-unsaturated carbonyls. *Chem. Commun.* **50**, 14558–14561 (2014).
25. Liu, W., Zell, D., John, M. & Ackermann, L. Manganese-catalyzed synthesis of *cis*-β-amino acid esters through organometallic C–H activation of ketimines. *Angew. Chem. Int. Ed.* **54**, 4092–4096 (2015).
26. Cai, S. H. et al. Manganese-catalyzed synthesis of monofluoroalkenes via C–H activation and C–F cleavage. *Chem. Commun.* **53**, 8731–8734 (2017).
27. Liang, Y. F. et al. Methylenecyclopropane annulation by manganese(I)-catalyzed stereoselective C–H/C–C activation. *Angew. Chem. Int. Ed.* **56**, 9415–9419 (2017).
28. Liu, S. L. et al. An approach to 3-(indol-2-yl)succinimide derivatives by manganese catalyzed C–H activation. *Org. Lett.* **19**, 4042–4045 (2017).
29. Meyer, T. H. et al. Manganese(I)-catalyzed dispersion-enabled C–H/C–C activation. *Chem. Eur. J.* **23**, 5443–5447 (2017).
30. Ni, J. B., Zhao, H. C. & Zhang, A. Manganese(I)-catalyzed C–H 3,3-difluoroallylation of pyridones and indoles. *Org. Lett.* **19**, 3159–3162 (2017).
31. Wang, H., Lorion, M. M. & Ackermann, L. Air-stable manganese(I)-catalyzed C–H activation for decarboxylative C–H/C–O cleavages in water. *Angew. Chem. Int. Ed.* **56**, 6339–6342 (2017).
32. Zell, D. et al. C–F/C–H functionalization by manganese(I) catalysis: expedient (per)fluoro-allylations and alkenylations. *ACS Catal.* **7**, 4209–4213 (2017).
33. Liu, W., Richter, S. C., Zhang, Y. & Ackermann, L. Manganese(I)-catalyzed substitutive C–H allylation. *Angew. Chem. Int. Ed.* **55**, 7747–7750 (2016).
34. Lu, Q., Klauck, F. J. R. & Glorius, F. Manganese-catalyzed allylation via sequential C–H and C–C/C–Het bond activation. *Chem. Sci.* **8**, 3379–3383 (2017).
35. Chen, S. Y. et al. Manganese(I)-catalyzed regio- and stereoselective 1,2-diheteroarylation of allenes: combination of C–H activation and smiles rearrangement. *Angew. Chem. Int. Ed.* **56**, 9939–9943 (2017).
36. Chen, S. Y., Li, Q. J. & Wang, H. G. Manganese(I)-catalyzed direct C–H allylation of arenes with allenes. *J. Org. Chem.* **82**, 11173–11181 (2017).
37. Wang, C. M., Wang, A. & Rueping, M. Manganese-catalyzed C–H functionalizations: hydroarylations and alkenylations involving an unexpected heteroaryl shift. *Angew. Chem. Int. Ed.* **56**, 9935–9938 (2017).
38. Zhu, C., Schwarz, J. L., Cembellin, S., Gressies, S. & Glorius, F. Highly selective manganese(I)/Lewis acid cocatalyzed direct C–H propargylation using bromoallenes. *Angew. Chem. Int. Ed.* **57**, 437–441 (2018).
39. Liu, W., Bang, J., Zhang, Y. & Ackermann, L. Manganese(I)-catalyzed C–H aminocarbonylation of heteroarenes. *Angew. Chem. Int. Ed.* **54**, 14137–14140 (2015).
40. Zhou, B. W., Hu, Y. Y., Liu, T. & Wang, C. Y. Aromatic C–H addition of ketones to imines enabled by manganese catalysis. *Nat. Commun.* **8**, 1169 (2017).
41. Kuninobu, Y., Nishina, Y., Takeuchi, T. & Takai, K. Manganese-catalyzed insertion of aldehydes into a C–H bond. *Angew. Chem. Int. Ed.* **46**, 6518–6520 (2007).
42. Liang, Y.-F., Massignan, L., Liu, W. & Ackermann, L. Catalyst-guided C=Het hydroarylations by manganese-catalyzed additive-free C–H activation. *Chem. Eur. J.* **22**, 14856–14859 (2016).
43. Zhou, B., Hu, Y. & Wang, C. Manganese-catalyzed direct nucleophilic C(sp2)–H addition to aldehydes and nitriles. *Angew. Chem. Int. Ed.* **54**, 13659–13663 (2015).
44. Liu, W. & Ackermann, L. Manganese-catalyzed C–H activation. *ACS Catal.* **6**, 3743–3752 (2016).
45. Wang, C. Y. Manganese-mediated C–C bond formation via C–H activation: from stoichiometry to catalysis. *Synlett* **24**, 1606–1613 (2013).
46. Hu, Y., Zhou, B. & Wang, C. Inert C–H bond transformations enabled by organometallic manganese catalysis. *Acc. Chem. Res.* **51**, 816–827 (2018).
47. Yahaya, N. P. et al. Manganese(I)-catalyzed C–H activation: the key role of a 7-membered manganacycle in H-transfer and reductive elimination. *Angew. Chem. Int. Ed.* **55**, 12455–12459 (2016).
48. Farrell, I. R. et al. Direct observation of competitive ultrafast CO dissociation and relaxation of an MLCT excited state: picosecond time-resolved infrared spectroscopic study of $[Cr(CO)_4(2,2'\text{-bipyridine})]$. *Inorg. Chem.* **41**, 4318–4323 (2002).
49. Shanoski, J. E., Payne, C. K., Kling, M. F., Glascoe, E. A. & Harris, C. B. Ultrafast infrared mechanistic studies of the interaction of 1-hexyne with group 6 hexacarbonyl complexes. *Organometallics* **24**, 1852–1859 (2005).
50. Moulton, B. E. et al. A rationale for the linear correlation of aryl substituent effects in iron(0) tricarbonyl complexes containing α,β-unsaturated enone (chalcone) ligands. *Organometallics* **26**, 6354–6365 (2007).
51. Shanoski, J. E., Glascoe, E. A. & Harris, C. B. Ligand rearrangement reactions of $Cr(CO)_6$ in alcohol solutions: experiment and theory. *J. Phys. Chem. B* **110**, 996–1005 (2006).
52. Neville, A. G., Brown, C. E., Rayner, D. M., Lusztyk, J. & Ingold, K. U. First direct detection of transient organic free radicals in solution by time-resolved infrared spectroscopy. Kinetic studies on some acyl radicals. *J. Am. Chem. Soc.* **113**, 1869–1870 (1991).
53. Bruce, M. I., Goodall, B. L. & Matsuda, I. Cyclometallation reactions. XIII. Reactions of phenyl-substituted heterocyclic nitrogen-donor ligands. *Aust. J. Chem.* **28**, 1259–1264 (1975).
54. Greetham, G. M. et al. ULTRA: a unique instrument for time-resolved spectroscopy. *Appl. Spectrosc.* **64**, 1311–1319 (2010).

55. Császár, P. & Pulay, P. Geometry optimization by direct inversion in the iterative subspace. *J. Mol. Struct.* **114**, 31–34 (1984).
56. Ahlrichs, R., Bär, M., Häser, M., Horn, H. & Kölmel, C. Electronic structure calculations on workstation computers: the program system TURBOMOLE. *Chem. Phys. Lett.* **162**, 165–169 (1989).
57. Deglmann, P., Furche, F & Ahlrichs, R. An efficient implementation of second analytical derivatives for density functional methods. *Chem. Phys. Lett.* **362**, 511–518 (2002).
58. Deglmann, P., May, K., Furche, F. & Ahlrichs, R. Nuclear second analytical derivative calculations using auxiliary basis set expansions. *Chem. Phys. Lett.* **384**, 103–107 (2004).
59. Eichkorn, K., Treutler, O., Öhm, H., Häser, M. & Ahlrichs, R. Auxiliary basis sets to approximate Coulomb potentials. *Chem. Phys. Lett.* **240**, 283–290 (1995).
60. Eichkorn, K., Weigend, F., Treutler, O. & Ahlrichs, R. Auxiliary basis sets for main row atoms and transition metals and their use to approximate Coulomb potentials. *Theor. Chem. Acc.* **97**, 119–124 (1997).
61. Treutler, O. & Ahlrichs, R. Efficient molecular numerical integration schemes. *J. Chem. Phys.* **102**, 346–354 (1995).
62. von Arnim, M. & Ahlrichs, R. Geometry optimization in generalized natural internal coordinates. *J. Chem. Phys.* **111**, 9183–9190 (1999).
63. Klamt, A. & Schuurmann, G. COSMO: a new approach to dielectric screening in solvents with explicit expressions for the screening energy and its gradient. *J. Chem. Soc. Perk. Trans. 2* **1993**, 799–805 (1993).
64. Grimme, S., Antony, J., Ehrlich, S. & Krieg, H. A consistent and accurate ab initio parametrization of density functional dispersion correction (DFT-D) for the 94 elements H–Pu. *J. Chem. Phys.* **132**, 154104 (2010).
65. Grimme, S., Ehrlich, S. & Goerigk, L. Effect of the damping function in dispersion corrected density functional theory. *J. Comput. Chem.* **32**, 1456–1465 (2011).

Acknowledgements

We are grateful to Syngenta and the Engineering and Physical Sciences Research Council (CASE studentship to L.A.H. (EP/N509413/) and, for the computational equipment used in this study, EP/H011455/, and Engineering and Physical Sciences Research Council 'ENERGY' grant EP/K031589/1) for funding, as well as the Science and Technology Facilities Council for access to the ULTRA facilities at the Rutherford Appleton Laboratory. We thank A. Whitwood and R. Bean for the X-ray structure of compounds 3 and 4, D. Turnbull for a crystalline sample of 4, and R. Perutz for insightful comments on this work.

Author contributions

J.M.L. and I.J.S.F. conceived the experimental programme with input on project direction from A.R. The TRIR experiments were performed by L.A.H., J.M.L., I.J.S.F., I.P.C. and I.V.S. on instrumentation set-up and built by M.T. Compounds 1 and 2 were prepared by L.A.H. F.C. prepared compound 3. S.M. prepared compound 4. J.M.L. performed and analysed the DFT calculations. TRIR data were analysed by J.M.L., L.A.H., I.J.S.F., I.P.C. and M.T. J.M.L. wrote the paper with input from all authors.

Competing interests

The authors declare no competing interests

Additional information

Supplementary information is available for this paper at https://doi.org/10.1038/s41929-018-0145-y.

Reprints and permissions information is available at www.nature.com/reprints.

Correspondence and requests for materials should be addressed to I.J.S.F. or J.M.L.

Publisher's note: Springer Nature remains neutral with regard to jurisdictional claims in published maps and institutional affiliations.

JACS JOURNAL OF THE AMERICAN CHEMICAL SOCIETY
Article
Cite This: J. Am. Chem. Soc. 2019, 141, 2316−2328
pubs.acs.org/JACS

Mechanistic Insight into Catalytic Redox-Neutral C−H Bond Activation Involving Manganese(I) Carbonyls: Catalyst Activation, Turnover, and Deactivation Pathways Reveal an Intricate Network of Steps

L. Anders Hammarback,[†] Alan Robinson,[‡] Jason M. Lynam,*[,†] and Ian J. S. Fairlamb*[,†]

[†]Department of Chemistry, University of York, York, North Yorkshire YO10 5DD, United Kingdom
[‡]Syngenta Crop Protection AG, Breitenloh 5, Münchwilen 4333, Switzerland

Supporting Information

ABSTRACT: Manganese(I) carbonyl-catalyzed C−H bond functionalization of 2-phenylpyridine and related compounds containing suitable metal directing groups has recently emerged as a potentially useful synthetic methodology for the introduction of various groups to the ortho position of a benzene ring. Preliminary mechanistic studies have highlighted that these reactions could proceed via numerous different species and steps and, moreover, potentially different catalytic cycles. The primary requirement for typically 10 mol % catalyst, oftentimes the ubiquitous precursor catalyst, $BrMn(CO)_5$, has not yet been questioned nor significantly improved upon, suggesting catalytic deactivation may be a serious issue to be understood and resolved. Several critical questions are further raised by the species responsible for providing a source of protons in the protonation of vinyl−manganese(I) carbonyl intermediates. In this study, using a combination of experimental and theoretical methods, we provide comprehensive answers to the key mechanistic questions concerning the Mn(I) carbonyl-catalyzed C−H bond functionalization of 2-phenylpyridine and related compounds. Our results enable the explanation of alkyne substrate dependencies, i.e., internal versus terminal alkynes. We found that there are different catalyst activation pathways for $BrMn(CO)_5$, e.g., terminal alkynes lead to the generation of Mn^I−acetylide species, whose formation is reminiscent of Cu^I−acetylide species proposed to be of critical importance in Sonogashira cross-coupling processes. We have unequivocally established that alkyne, 2-phenylpyridine, and water can facilitate hydrogen transfer in the protonation step, leading to the liberation of protonated alkene products.

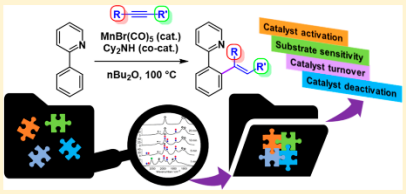

INTRODUCTION

Manganese is a versatile, earth-abundant element with considerable potential as a catalyst for applied chemical synthesis.[1] The organometallic chemistry of Mn^I has been a rich area of study for >40 years, e.g., cyclomanganation and stoichiometric reactions of manganacycles.[2] Catalysis has been slow to develop, but since Chen and Wang's publication in 2013,[3] the emergence of promising redox-neutral Mn^I-catalyzed C−H bond functionalization methodologies[4] involving cyclomanganation and formal insertion of various unsaturated substrates (e.g., alkenes,[5] alkynes,[6] carbonyls,[7] isocyanates,[8] cyanide reagents[9]) has been reported (Scheme 1a, e.g., **1** + **2** → **3**). Mn catalysis is complementary to transformations typically associated with platinum group metals (PGMs)[10] which coupled with other major breakthroughs in high oxidation state Mn catalysis[11] provides a promising platform to develop competitive processes. Critical to this endeavor is mechanistic information[4a] on the catalytic processes involving Mn^I. Indeed, mechanistic information for the Mn^I-catalyzed C−H functionalizations has been limited. While there are postulated mechanisms,[3,4a] experimental validation is required if catalyst design strategies/applications in more complicated target-orientated synthesis are to be more widely adopted.

The mechanistic steps for the C−H bond functionalization of the ubiquitous substrate, 2-phenylpyridine (ppy, **1**), are shown in Scheme 1b. Similar mechanistic hypotheses have been put forward,[4] with the key steps principally involving

- cyclomanganation/C−H bond activation at Mn^I to deliver manganacycle **4** (step 1),
- loss of CO and binding of an unsaturated acceptor substrate to Mn^I to give **5** (step 2),
- C−C bond formation by migratory insertion of the π-bound unsaturated substrate into a Mn−C bond leading to formation of a 7-membered manganacycle **6** (step 3), and
- protonation (protiodemanganation) of **6** to liberate organic product **3** with concomitant formation of manganacycle **4** (step 4).

Received: August 23, 2018
Published: January 30, 2019

DOI: 10.1021/jacs.8b09095
J. Am. Chem. Soc. 2019, 141, 2316−2328

Scheme 1. (a) Generic Mn-Catalyzed C−H Functionalization Reaction of 2-Phenyl Pyridine with Suitable Unsaturated Acceptor Substrate; (b) Generalized Catalytic Steps in the Postulated Mechanism

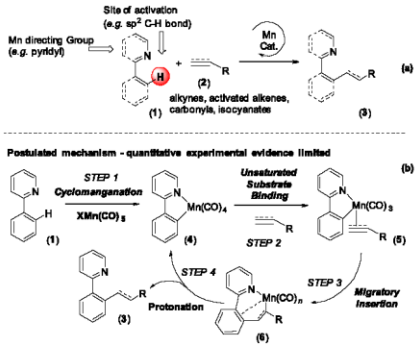

Our research team initially characterized a transient 7-membered manganacycle, containing a 2-pyrone ring system (relating to **6**), formed by alkyne insertion into a Mn−C bond (of **4**).[12] Subsequent studies employing time-resolved infrared spectroscopic analysis[13] have allowed us to directly observe the short-lived intermediates that are involved in the formation of **6** (Scheme 2).

Scheme 2. Time-Resolved IR Spectroscopic Analysis Enabling Characterization of Intermediates 5 and 6

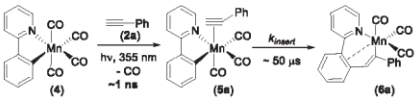

These findings taken together provide a detailed understanding of the process for alkyne insertion, i.e., steps 2 and 3 (Scheme 1b). We subsequently turned our attention (this study) to gathering critical mechanistic information, particularly kinetic data, concerning steps 1 and 4, which are key to productive catalysis. With a focus on the reactions of **1** + **2a**/**2b** → **3a**/**3b** (Scheme 3), our study described herein has been primed by asking the following questions.

(1) How does the generic precatalyst, $BrMn(CO)_5$, become activated under the catalytic conditions and what are the implications for step 1.

(2) What species is/are responsible for providing a source of protons in the protonation step 4.

Scheme 3. Key Reactions for Mechanistic Study

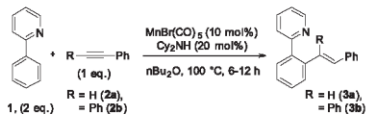

(3) What is the severity of catalyst deactivation, particularly as typically catalyst turnover numbers range from ca. 5 to 9.[3−9]

(4) What is the explanation for internal alkyne **2b** being unable to give alkenylated product **3b**.

An answer to question 3 is particularly important in terms of developing future catalyst design strategies. On the other hand, it is essential to understand at what stage internal alkynes such as **2b** are unable to complete a full catalytic cycle. Details concerning these questions are limited within the literature. Yet, clear answers are needed to meet the aspiration for Mn^I redox-neutral catalysis to become a competitive process to those currently employing PGMs.[4]

RESULTS AND DISCUSSION

The reactions given in Scheme 3 are both believed to involve manganacycle **4**.[3,12] We identified that the use of real-time infrared spectroscopic analysis (in situ IR on the second time scale), in operando, is useful for probing the different manganese carbonyl species formed during the C−H bond activation reactions, yielding qualitative information about manganese carbonyl speciation and quantitative kinetic data. Use of IR spectroscopic analysis for studying transient manganese carbonyl species has been validated in our previous studies.[14] For this mechanistic study, a Mettler-Toledo ReactIR instrument (IC10) with a Si probe was used (1 min scans, ± 4 cm^{-1}) to monitor changes in the manganese carbonyl IR bands in real time.

We first turned our attention to understanding the species that derive from reactions mediated by either the $BrMn(CO)_5$ precatalyst or the intermediate manganacycle **4** under the generalized reaction conditions given in Scheme 3. The changes in the IR spectral region of the manganese carbonyls for the reaction **1** + **2a** → **3a** catalyzed by $BrMn(CO)_5$ is shown in Figure 1a, accompanied by the kinetic information extracted from the data in Figure 1b. Analysis of the changes in the IR stretching bands shows rapid consumption of the $BrMn(CO)_5$ precatalyst, formation of the alkyne insertion complex **6a′** (independently verified by LIFDI MS as an intermediate, m/z = 423.0316, $[M^{\bullet+}]$), and Mn cluster species after only 1 min. After 3 min $BrMn(CO)_5$ is fully depleted. Note **6a′** is the tetracarbonyl manganese species associated with tricarbonyl manganese species **6** (i.e., **6a′** is acting as a reservoir for the active species **6a**). The maximum amount of **6a′** is observed at 3 min, which then decays exponentially [k_{obs} = (1.87 ± 0.18) × 10^{-3} s^{-1}] with concomitant formation of the alkenylated product **3a** (ex situ ^{1}H NMR analysis, k_{obs} (1.78 ± 0.43) × 10^{-3} s^{-1}). Curiously, the manganacycle **4** was not observed as an intermediate in this experiment, indicating that it was either not formed or too transient to be observed under the reaction conditions, i.e., manganacycle **4** is not an intermediate in this specific reaction or that alkyne insertion is rapid, compared with a base-assisted cyclomanganation step. Finally, after 1 min Mn clusters form, which dominate the carbonyl species observed in the IR spectra

The feasibility of manganacycle **4** as an intermediate in the reaction **1** + **2a** → **3a** was quantitatively assessed for its ability to act as a competent catalyst. The changes in the IR spectral region of the manganese carbonyls can be viewed in Figure 1c, which is accompanied by the kinetic information extracted from the data in Figure 1d. Analysis of the changes in the IR stretching bands shows the relatively slow consumption of **4** (no changes within 1

DOI: 10.1021/jacs.8b09995
J. Am. Chem. Soc. 2019, 141, 2316−2328

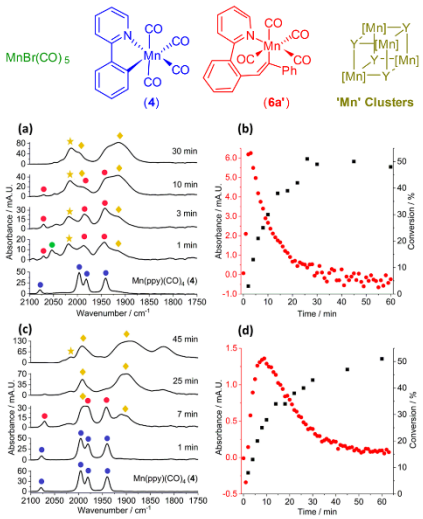

Figure 1. (a) IR spectral changes over time for the reaction of **1** + **2a** → **3a** catalyzed by $BrMn(CO)_5$ under conditions described in Scheme 3 {key: blue circle = **4**; red circle = **6a′**; green circle = $BrMn(CO)_5$; gold diamond/gold star = Mn carbonyl cluster species; [Mn] = $Mn(CO)_5$, Y = OH, alkynyl, see Discussion}. (b) Kinetic plot (extracted from a) showing the formation and loss of **6a′** (red circle) over time (in situ) in addition to percent conversion of organic product **3a** (black square) determined by ^{1}H NMR spectroscopic analysis (ex situ). (c) IR spectral changes over time for the reaction of **1** + **2a** → **3a** catalyzed by manganacycle **4**. (d) As for b (kinetic data extracted from c) (~30 min). These Mn clusters are catalytically inactive.[15]

min, in stark contrast to $BrMn(CO)_5$; kinetic details for this step are shown in the Supporting Information). Thus, after 7 min the formation of the alkyne insertion complex **6a′** and Mn carbonyl cluster species was observed, whose distribution appears different from the reaction mediated by $BrMn(CO)_5$. After ca. 10 min **4** is fully depleted, showing that this was the starting point for alkyne insertion, i.e., via loss of one CO ligand. Of particular note is the finding that the formation of **6a′** is slower in the reaction catalyzed by **4** than that catalyzed by $BrMn(CO)_5$, providing strong support for alternative pathways for catalyst activation, which enters into a common catalytic cycle.

The reaction **1** + **2a** → **3a** catalyzed by $BrMn(CO)_5$, under the standard conditions at 60 °C, allowed us to further gain more detail about the activation of the precatalyst species. Under these conditions no alkenylated product **3a** was observed, demonstrating that protonation is unfeasible at this temperature. Analysis of the changes in the IR stretching bands indicates a slower consumption of the $BrMn(CO)_5$ precatalyst than the reaction run at 100 °C. Again, formation of the alkyne insertion complex **6a′** is observed after 1 min, which after 12 min reaches a steady state, i.e., with full consumption of the $BrMn(CO)_5$ precatalyst. Propionic acid (3 equiv with respect to Mn; 30 mol %) was added at 32 min, resulting in complete loss of **6a′** and concomitant formation of product **3a** {5% yield, accounting for one-half of the original amount of $BrMn(CO)_5$ used; the remaining mass balance (loss) is accounted for through the formation of manganese carbonyl clusters, as observed in the IR spectra at 35 min}.[16] Finally, in keeping with the reaction run at 100 °C, we do not observe formation of manganacycle **4** on the time scale of the reaction.

We continued to investigate the reaction **1** + **2a** → **3a** catalyzed by $BrMn(CO)_5$ at 60 °C, omitting various components to assess their impact on the distribution of manganese carbonyl species present within the mixtures. Withholding the base, Cy_2NH, resulted in some degradation of $BrMn(CO)_5$ (hold time = 25 min) to give Mn carbonyl clusters with no formation of either manganacycle **4** or alkyne insertion complex **6a′** (Figure 3a). Addition of Cy_2NH triggers formation of **6a′** with concomitant loss of $BrMn(CO)_5$ (Figure 3b). The kinetic curves for this reaction mirror those seen in Figure 2b.

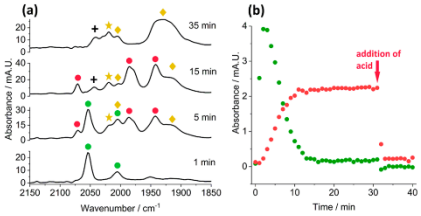

Figure 2. (a) IR spectral changes over time for the reaction of **1** + **2a** → **3a** catalyzed by $BrMn(CO)_5$ under conditions described in Scheme 3, run at 60 °C (key: as for Figure 1; + = unidentified manganese carbonyl species). (b) Kinetic plot (extracted from a) showing the formation and loss of **6a′** (red circle) over time (in situ) to form organic product **3a** {determined by ^{1}H NMR spectroscopic analysis (ex situ)}; initial growth of the bands for $BrMn(CO)_5$ are attributed to the dissolution of the solid into solution.

In the absence of alkyne **2a** we see rapid loss of $BrMn(CO)_5$ with concomitant formation of manganacycle **4** (Figure 3c and 3d). Another manganese carbonyl species forms in this reaction, as indicated by the black triangles. Addition of alkyne **2a** after 10 h results in loss of **4** and formation of **6a′**, although formation of the latter complex is slow, i.e., after a further 8 h reaction time, only a small amount is formed (where the reaction is halted).

Withholding 2-phenylpyridine **1** from the reaction we see formation of Mn carbonyl clusters within 5 min. After 15 min, an unidentified species is once again observed (indicated by + symbol), also seen in Figure 2a.

It is informative to compare the key IR spectral changes with the various components withheld from the reaction of **1** + **2a** → **3a** (Figure 3f). Withholding **1** demonstrates that formation of the unidentified species (+ symbol) is independent of it. Withholding Cy_2NH indicates that manganacycle **4** or alkyne insertion complex **6a′** is not formed. Catalyst degradation is the major dominating pathway, affording Mn carbonyl clusters that are dependent on the presence of alkyne **2a**. The point is reinforced by a different manganese carbonyl species forming (black triangle) in the absence of **2a**. The only conditions that give the same degraded Mn carbonyl clusters as the standard reaction conditions at 60 °C are the reaction without **1**.

DOI: 10.1021/jacs.8b09095
J. Am. Chem. Soc. 2019, 141, 2316−2328

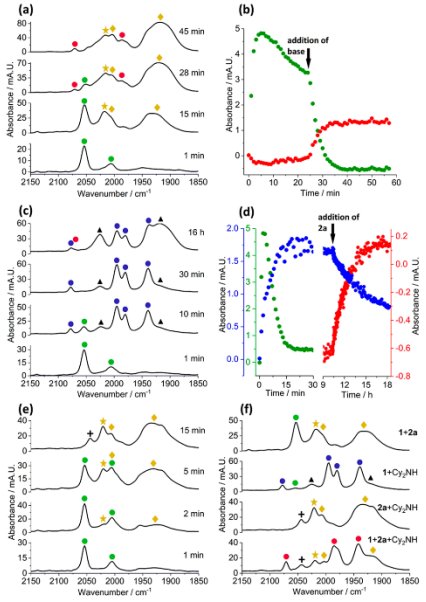

Figure 3. (a) IR spectral changes over time for the reaction of **1** + **2a** → **3a** catalyzed by $BrMn(CO)_5$ under conditions described in Scheme 3, run at 60 °C, withholding Cy_2NH for 25 min (key: as for Figure 1). (b) Kinetic plot (extracted from a) showing the loss of $BrMn(CO)_5$ (green circle) over time (in situ) due to degradation; initial growth of the bands for $BrMn(CO)_5$ (ca. 5 min) is attributed to dissolution of the solid into solution (also seen in d). Addition of Cy_2NH was made at 25 min. (c) As for a, withholding only alkyne **2a** for 10 h. (d) Kinetic plot (extracted from c) showing the loss of $BrMn(CO)_5$ (green circle) over time (in situ), followed by addition of **2a** at 10 h. (e) As for a, withholding only 2-phenylpyridine **1** (not added); + = unidentified manganese carbonyl species. (f) Comparative IR spectra (overlay) at 15 min reaction time for changes seen from Figures 2a, 3a, 3c, and 3e.

We further examined the interaction of $BrMn(CO)_5$ (1 equiv) and Cy_2NH (2 equiv) in nBu_2O at 60 °C for 20 min. Major and minor manganese carbonyl species are formed (see Supporting Information). The former shares similar IR bands to the species observed in Figure 3c, indicated by black triangles. The minor species are attributed to hydroxylated Mn carbonyl clusters.

In an earlier study experiments employing deuterium-labeled substrates were run under similar reaction conditions (100 °C, Et_2O) using 2-phenylpyridine **1** and propargyl benzoate instead of phenyl acetylene **2a**. This led to substantial deuterium scrambling among the alkenyl protons and the 2-phenyl group, highlighting the complexity of the complete reaction network. Furthermore, addition of D_2O to that system resulted in deuterium scrambling. We recognized that as our reaction run with **2a** at 60 °C stops at the alkyne insertion complex **6a′**, further useful data could be obtained for the catalyst activation step by running deuterium-labeling experiments in this system. Using the standard reaction conditions at 60 °C, two experiments were conducted (Scheme 4).

Scheme 4. Deuterium-Labeling Studies[a]

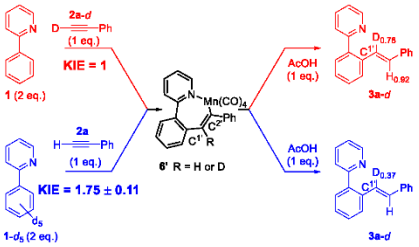

[a]Each reaction is mediated by $MnBr(CO)_5$ (10 mol %), Cy_2NH (20 mol %), in nBu_2O at 60 °C for 30 min.

In the first experiment, **1** (2 equiv) was reacted with **2a-*d*** (1 equiv), affording **6a′** (characterized by in situ IR). Treatment with acetic acid (1 equiv) afforded deuterated **3a**, with 78% deuterium incorporation at the C1′ position, showing some loss of deuterium from **2a-*d*** (a small amount if deuterium incorporation was also seen at C2′, ca. 8%). The kinetic isotopic effect (KIE) for this reaction was found to be 1 (i.e., identical kinetic curves, see Supporting Information). In the second experiment, the reaction of **1**-d_5 with **2a** cleanly gave **6a′**, with a KIE of 1.75 (±0.11). Quenching of **6a′** with acetic acid (1 equiv) gave product **3a**, with 37% deuterium incorporation at the C1′ position, supporting the formation of manganese alkynyl species activating the C−H bond in **1**. The small magnitude of the KIE reflects the C−H bond activation step as not rate determining, with CO loss during catalyst activation controlling the reaction kinetics.

Viability of Internal Alkyne 2b as a Substrate. We next turned our attention to understanding the reasons why internal alkyne **2b** does not deliver alkenylated product **3b**. From our results vide supra it appears that the terminal hydrogen in **2a** is activated at the Mn(I) center. However, clearly **2b** lacks this mode of activation. We examined the hypothetical reaction of **1** + **2b** → **3b** at 100 °C using in situ IR spectroscopic analysis (Figure 4). The IR spectral changes reveal a fast reaction to give both manganacycle **4** (blue circle) and alkyne insertion complex **6b′** (red circle) within 1 min. Complexes **4** and **6b′** are both formed and consumed at a similar rate. The formation of **4** stands in stark contrast to the reaction employing terminal alkyne **2a**. We also see a fraction of $BrMn(CO)_5$ remains after 1 min, but another new species is present (indicated by #) whose depletion is complete within 5 min. At this time point we observe formation of two new species (indicated by an asterisk, *) in addition to a major new product (indicated by an open circle), which is the only species remaining after 5 h, and assigned as the reductive elimination product **7b** (purified and characterized fully, including X-ray diffraction analysis of a single crystal). This result confirms that any protonation pathway is inaccessible for substrate **2b**. This is consistent with previous predictions made by Chen and Wang that the lack of a terminal hydrogen in **2b** explains the absence of alkene product **3b**. A separate stoichiometric reaction of **4** (1 equiv) with **2b** (1 equiv) in *n*-Bu_2O at 100 °C for 1.5 h led to the formation of **7b** (~60%,

DOI: 10.1021/jacs.8b09095
J. Am. Chem. Soc. 2019, 141, 2316−2328

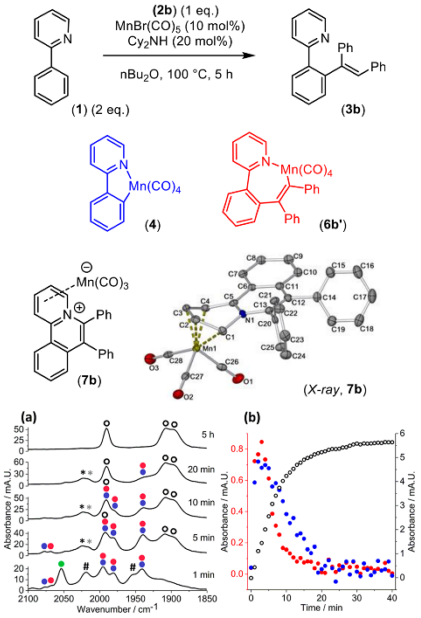

Figure 4. (a) IR spectral changes over time for reaction of **1** + **2b** → **3b** catalyzed by $BrMn(CO)_5$ under conditions described in Scheme 3, run at 100 °C (key: as for Figure 1). (b) Kinetic plot (extracted from a) showing loss of the manganacycle **4** (blue circle), alkyne insertion complex **6b′** (red circle), and new product **7b**; # = unidentified $Mn(CO)_3$ complex. Two species indicated by an asterisk (*) (in black and gray) are likely isomers of the reductive elimination product **7b**.

by in situ ^{1}H NMR reaction monitoring, nonstirred). The outcome confirms the clean conversion of **4** → **7b** and that no paramagnetic manganese species were formed.

Effect of $Cy_2NH/BrMn(CO)_5$ Ratio. It was anticipated that the ratio of Cy_2NH to $BrMn(CO)_5$ in the catalytic reaction could be critical to productive catalysis. From Chen and Wang's original study, a ratio of 2:1 $Cy_2NH/BrMn(CO)_5$ was employed. However, no alterations to this ratio were made, changes which may have, in part, a significant effect in the catalytic process. A total of eight separate reactions (**1** + **2a** → **3a** at 100 °C, under the standing conditions given in Scheme 3) were run with varying ratios of $Cy_2NH/BrMn(CO)_5$ from 0.5:1, 1:1, through to 8:1. The observed rates (k_{obs}) for each reaction were extracted from the kinetic data obtained by ex situ ^{1}H NMR; a plot of k_{obs} versus $Cy_2NH/BrMn(CO)_5$ is given in Figure 5.

Alteration of the $Cy_2NH/BrMn(CO)_5$ ratio from 0.5:1 to 2:1 led to a positive response in the rate of product **3a** formation—note that the response is nonlinear. Curiously, at a ratio of $Cy_2NH/BrMn(CO)_5$ of >2:1, no further enhancement in rate was observed, i.e., the optimal ratio is 2:1 $Cy_2NH/BrMn(CO)_5$.

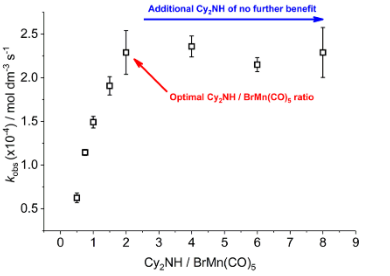

Figure 5. Plot of the dependence of $Cy_2NH/BrMn(CO)_5$ against k_{obs} extracted from kinetic data for the reaction **1** + **2a** → **3a**.

Further comments about this trend and outcome are given later in the Discussion section.

Protonation Pathways. Having identified and characterized the alkyne insertion complex **6a′** derived from both manganacycle **4** and $BrMn(CO)_5$, we recognized that the species responsible for protonation, i.e., delivery of the product **3a**, could be deduced, among other products. According to the original mechanistic proposal made by Chen and Wang, the alkyne **2a** is responsible for protonation of **6a′**. Thus, a reaction involving one equivalent each of **4** and **2a** ought to give a maximum of 50% product conversion (this assumes that alkyne insertion is the only pathway forward, which is supported by our reported time-resolved IR spectroscopic studies). Unexpectedly, reaction of **4** + **2a** gave only a small amount of the organic product **3a** (7%) (Figure 6a, see figure for reaction conditions) while consuming the majority of **4** (10% remaining). The major product was the reductive elimination product **7a** (76%). Compound **8a** was formed as a minor product (5%), resulting from double alkenylation. We note this is the first recording of the reductive elimination pathway becoming active employing a

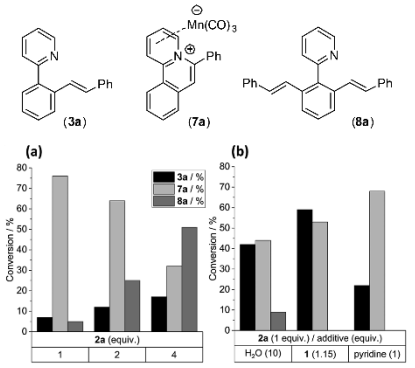

Figure 6. Examination of the protonation pathway for the reaction of **4** with **2a** and various additives at 100 °C, 0.5 h, under Ar atmosphere: (a) as a function of varying the amount of **2a**; (b) by variation of different additives, 2-phenylpyridine (**1**), H_2O, and pyridine.

DOI: 10.1021/jacs.8b09095
J. Am. Chem. Soc. 2019, 141, 2316−2328

Scheme 5. Computational Studies Using Density Functional theory (DFT) Methods[a]

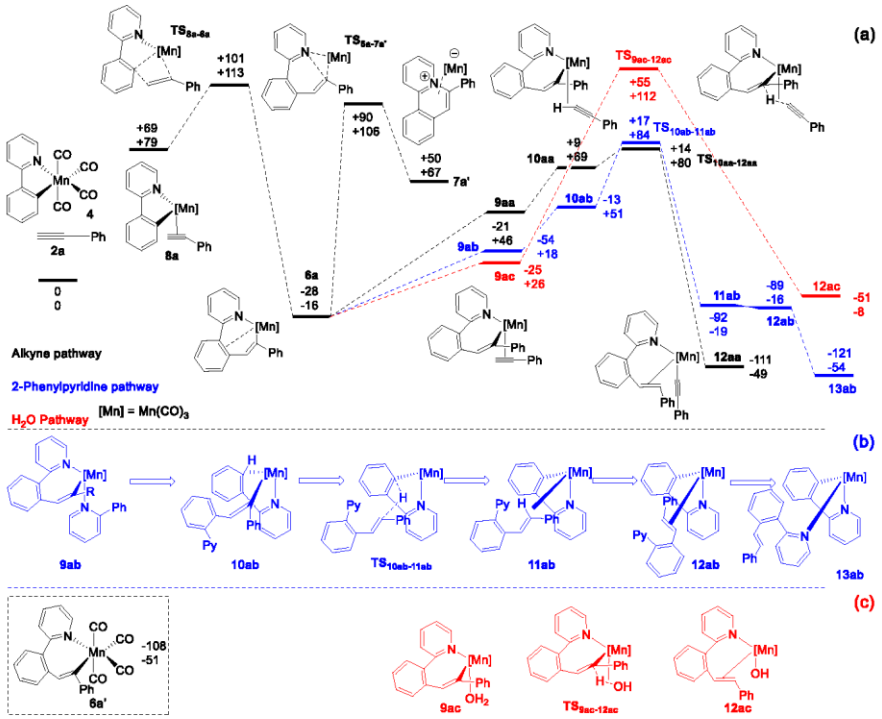

[a]Energies are zero-point energy-corrected electronic energies (top) and Gibbs energies at 298.15 K (bottom) in kJ mol^{-1}. [Mn] = *fac*-Mn(CO)$_3$.

terminal alkyne with manganacycle derived from **1**. Increasing the amount of **2a** to two equivalents resulted in full conversion of **4**, increased amounts of **8a** (25%; 64% **7a**), in addition to a slight increase in **3a** (12%). Addition of four equivalents of **2a** led to **8a** becoming the major product (51%) at the expense of **7a** (32%) with a small increase in **3a** also recorded (17%).

We further examined the role of other "proton" sources in the reaction of **2a** (1 equiv) with **4** (Figure 6b), all added at $t = 0$. Addition of 10 equivalents of water to the reaction mixture enabled more efficient protonation to give **3a** (42%); products **7a** and **8a** were still formed in 44% and 9% conversion, respectively. A similar distribution of products **3a** and **7a** was seen adding 2-phenylpyridine **1** as the proton source, formed with higher conversion. In this case, product **8a** was not formed under these reaction conditions, indicating that **1** competes with product **3a** for Mn coordination, resulting in diminished double alkenylation. Lastly, one equivalent of pyridine (lacking a suitable acidic proton) was added to the reaction, producing **7a** as the major product (68%) and **3a** as the minor product (22%). The result confirms that pyridine assists in product **3a** labalization, thwarting formation of **8a**, in keeping with the outcome resulting from addition of **1** to the reaction under otherwise identical conditions.

Replacing the substrate(s)/additive by their deuterated analogues (e.g., **2a**-*d*, **1**-d_5 and D_2O) allowed for monitoring of the deuterium content into product **3a** following the protonation step. Employing **2a**-*d* (4 equiv) in the reaction **4** + **2a** → **3a** + **7a** + **8a** gave deuterium incorporation into both alkene positions for **3a** (68% at C1′ and 60% at C2′) and **8a** (67% at C1′ and 54% at C2′), displaying the ability of **2a** to perform the protonation step. The loss of deuterium at the C1 spm′ position could arise from reversibility/instability of a manganese alkynyl species. No deuteration could be observed on the 2-phenylpyridine backbone. Regioselective deuterium incorporation at the C2′ position (83%) was achieved through the addition of D_2O (10 equiv) with no deuteration occurring at either the C1′ position or the 2-phenylpyridine backbone. Following the addition of **1**-d_5 (1 equiv) to the reaction, a mixture of deuterated analogues of **3a** was observed. The reaction was found to give lower conversion to **3a** (29%), as compared with the addition of the protio-analogue **1** (59%). The most abundant analogue (48% of isolated **3a**) showed no

DOI: 10.1021/jacs.8b09095
J. Am. Chem. Soc. 2019, 141, 2316−2328

Scheme 6. Substrate-Controlled Catalyst Activation, Insertion, and Protonation (SCAIP) Mechanism[a]

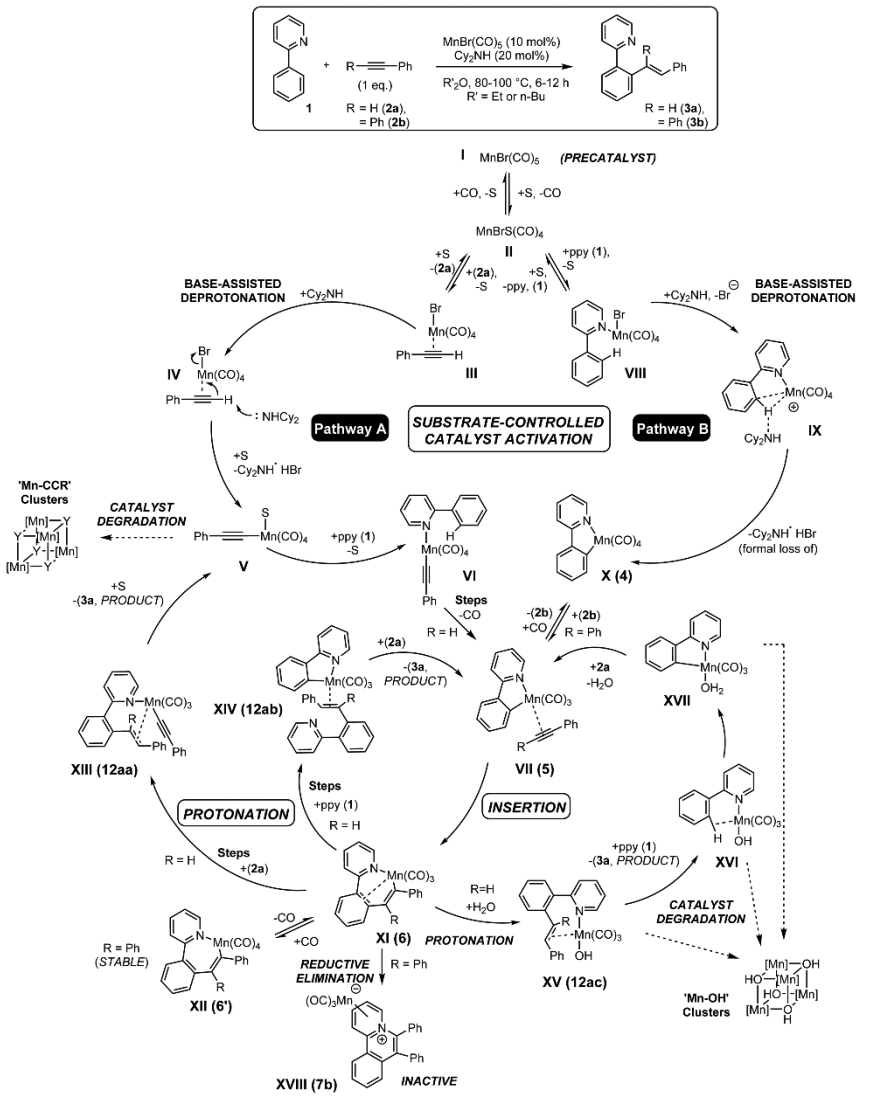

[a]Note: the proposed manganese clusters are representative of the high-order species present.

DOI: 10.1021/jacs.8b09095
J. Am. Chem. Soc. 2019, 141, 2316−2328

deuterium incorporation, while monodeuterated **3a** is present in 18% abundance. Incorporation of four and five deuterium's into the product was further seen (18% and 12% abundance, respectively).

Theoretical (DFT) Studies. Further insight into the key steps involved in Mn-catalyzed reactions was obtained using density functional theory (DFT); see Supporting Information for details of the methodology employed.

We modeled the reaction profile starting from the reaction of manganacycle **4** with phenylacetylene **2a** (Scheme 5). It is important to state that **4** is a useful reference state for our calculations as alkyne coordination and insertion, reductive elimination versus protonation (by either **1**, **2a** or water) steps could be compared. Loss of a CO ligand and coordination of alkyne **2a** leads to formation of **5a**, from which a feasible transition state structure could be located ($\mathbf{TS}_{\mathbf{8a-6a}}$) connecting to the 7-membered manganacycle **6a**. We previously observed this precise process using time-resolved infrared spectroscopy.[13] The energy of **6a** indicates that it is stable enough to be characterized either directly or indirectly (i.e., as **6a′**). Crucially, **6a** acts as the "anvil point" to either direct reductive elimination to give **7a′** or to protonation giving the final product complex vide infra. The transition state connecting **6a** to **7a** was identified as ($\mathbf{TS}_{\mathbf{6a\text{-}7a'}}$), which requires loss of the η^2-coordinated arene, revealing a 16-electron species, capable of a viable reductive elimination. We described previously the isomerization of **7a′** to **7a** (thermodynamically more stable) and the factors affecting the balance between protonation and reductive elimination from the anvil point complex **6a**.[12] The results illustrated in Figure 6 reinforce the argument that unless **6a** is intercepted by an appropriate proton source reductive elimination to give **7a** will occur.

Experimentally we determined that **6a** can be protonated by **1**, **2a**, and/or water. Three potential pathways that result in H transfer to **6a** and the generation of the product **3a** have been located. In the first instance, a second molecule of alkyne can bind to **6a** to give **9aa**, where a change of binding mode from η^2-C≡C to a C−H sigma complex gives **10aa**, which can then undergo a σ-CAM process[17] through $\mathbf{TS}_{\mathbf{10aa\text{-}12aa}}$ to give **12aa**, i.e., complex containing product **3a** (Scheme 5a).

An alternative pathway was also examined in which a second equivalent of **1** binds to **6a** to give **9ab**; a change in the coordination mode at the metalated 2-phenylpyridine would give sigma complex **10ab** (Scheme 5b). Thus, H transfer through $\mathbf{TS}_{\mathbf{10ab\text{-}11ab}}$ followed by a shift in binding mode would then ultimately give **13ab** in which the product is N bound to the Mn. Finally, H transfer can occur from the aqua manganese(I) complex **9ac** (Scheme 5c), which lies at +26 kJ mol^{-1}. Protonation by cleavage of the O−H bond involves a high-lying transition state $\mathbf{TS}_{\mathbf{9ac\text{-}12ac}}$ and then forming **12ac** (i.e., complex containing coordinated **3a**).

The calculations support a number of important mechanistic features, for example, the binding of PhC≡CH, 2-phenylpyridine, and water to the formally unsaturated complex **6a** is thermodynamically unfavorable in all cases; however tetracarbonyl **6a′** lies at −51 kJ mol^{-1}, implying that the binding of CO will readily occur, supporting its observation in the ReactIR studies. The energies of transition states $\mathbf{TS}_{\mathbf{10aa\text{-}12aa}}$ and $\mathbf{TS}_{\mathbf{10ab\text{-}11aa}}$ are similar (+80 and +84 kJ mol^{-1}, respectively), indicating that the energetic span for proton transfer from either PhC≡CH or 2-phenylpyridine to the alkenyl ligand in **6a** will be competitive. The transition state for proton transfer from water ($\mathbf{TS}_{\mathbf{9ac\text{-}12ac}}$ + 112 kJ mol^{-1}) is far higher, and the resulting complex with bound **3a** (**12ac**) is higher in energy than **6a**. This would indicate that under conditions when both PhC≡CH and 2-phenylpyridine are present, this pathway will be disfavored. However, when this is not the case (e.g., when **1**/**2a** are consumed) this pathway will become relevant, providing a potential explanation for the formation of hydroxy-containing manganese carbonyl clusters at longer reaction times.

Further experimental evidence for multiple protonation pathways is provided from a determination of order with respect to **1** and **2a** (under the standard reactions conditions at 100 °C; see Supporting Information for details). For 2-phenylpyridine **1** an order of 0.87 (±0.06) was determined, which is keeping with **1** acting as substrate and as a proton source for the protonation step. For phenylacetylene **2a** an unusual order of 0.32 (±0.03) was determined, indicating it being involved in multiple steps. Note: we cannot rule out that an aggregated Mn cluster containing terminal alkyne **2a** is acting as a reservoir for the reaction.

■ DISCUSSION

On the basis of the experimental and computational evidence presented in our study, coupled with the initial mechanistic data gathered previously, a mechanism for the catalytic C−H bond alkenylation of 2-phenylpyridine **1** by $BrMn(CO)_5$, with both terminal (**2a**) and internal alkynes (**2b**), can be stitched together to provide a unified reaction mechanism (Scheme 6). The ensuing discussion is based around the four main questions raised vide supra.

Activation of the Generic Precatalyst, $BrMn(CO)_5$. The question of how $BrMn(CO)_5$ becomes activated under catalytic conditions was answered by the reactions conducted at both 60 and 100 °C. This revealed that terminal alkyne **2a** reacts first with $BrMn(CO)_5$ in the presence of the base, Cy_2NH. Importantly, **2a** effectively outcompetes 2-phenylpyridine **1** in this step, which allows us to propose Pathway A (initially requiring **2a**) over Pathway B (initially requiring **1**) as the preferred one for precatalyst activation.

The first step in the mechanism involves initial loss of CO from $BrMn(CO)_5$ **I** to give solvated tetracarbonyl Mn^I species **II**. Entering Pathway A, displacement of solvent with **2a** gives η^2-alkyne Mn^I complex **III**, possessing a highly activated C−H bond that can be deprotonated by the mild base, Cy_2NH. The increased acidity of the C−H bond on p coordination of the alkyne to the metal shares a remarkable structural similarity with Cu^I species that are important in both Pd-catalyzed Sonogashira alkynylation chemistry and azide−alkyne "click" reactions.[18] Therefore, base deprotonation of **IV** leads to loss of $Cy_2NH{\cdot}HBr$, forming Mn^I−acetylide **V** (note: it was possible to synthesize a manganese(I) (*p*-tolylacetylide) pentacarbonyl complex (**14**) by independent synthesis[5]). In the presence and absence of **1** we found that Mn^I carbonyl clusters were formed with a similar distribution. Solvent displacement by **1** then reveals **VI**. A series of steps then takes **VI** through to the key intermediate Mn^I complex **VII** (**5**). The alternative Pathway B requires that **1** displaces a solvent molecule **II** → **VIII**, which upon action of Cy_2NH leads to arene deprotonation and bromide loss via **IX** to give manganacycle **X** (**4**); this was the mode of action proposed by Chen and Wang.

Experiments involving internal alkyne **2b** showed that Pathway B is viable (through the observation of **4** during the catalytic reaction by IR spectroscopic analysis) when Pathway A is inaccessible (i.e., **2b** not possessing an acidic proton). We note that withholding alkyne **2a**, i.e., forcing the catalyst activation to

DOI: 10.1021/jacs.8b09095
J. Am. Chem. Soc. 2019, 141, 2316−2328

occur through Pathway B, enabled characterization of manganacycle **4**; after **2a** was added alkyne insertion was remarkably slow.

The results of the isotopic-labeling experiments involving **1**-d_5 and **2a**-*d* (Scheme 4) show that activation of the C−H bond in **1** is conducted by an alkynyl manganese species. Thus, C−D bond cleavage in **2a**-*d* (reaction with **1**) is evidenced by loss of deuterium in the product **3a**-*d* (67% net transfer of deuterium). The reaction of **1**-d_5 and **2a** showed that deprotonation by the alkynyl manganese species occurred leading to protons being gained in the product **3a**-*d* (37% net transfer of deuterium). The magnitude of the KIE from each of the two isotopic-labeling experiments indicates that the C−H/C−D bond cleavage (in **1**) by the alkynyl manganese species appears to be rate determining. In addition, the KIE of 1.75 for the reaction of **1**-d_5 with **2a** leads us to conclude that CO loss is integral in the deprotonation pathway, i.e., deprotonation of **VI** to give **VII** (**5**) (Scheme 6). The discrepancies in observed deuterium incorporation likely arise from exchange of alkyne substrate with **VII** (**5**), with **2a**/**2a**-*d* at least being present in a 9-fold excess over the Mn catalyst (assuming the single consumption of **2a**/**2a**-*d* in the catalyst activation step; Pathway A).

Origin of the Proton in the Protonation (H Transfer) of XI (6). The experimental and theoretical calculations indicate that **1**, **2a**, and water are feasible sources of proton for the protonation of **XI** (**6**) (Figure 6 and Scheme 5). Stoichiometric reactions show that increasing the amount of **2a** leads to increasing product **3a** formation coupled with the formation of double alkenylation product **8a**. This is consistent with **2a** providing a source of proton, albeit not being the sole supply, i.e., **7a** is not observed under typical catalytic conditions.

The addition of **1** to these stoichiometric reactions lead to a significant increase in product **3a** formation while hindering the pathways that form **7a** and **8a**.

Through the addition of pyridine (as a substitute for the ligating properties of **1**) we could deduce the dual role of **1**, where its major role is as a proton source, and also its ability to libertate product **3a** from the final manganese species **XIII** (**12aa**). Finally, addition of water assists in the formation of product **3a**. All three pathways inferred by experiment are supported by the results of the DFT calculations (Scheme 5).

Catalyst Deactivation. To the best of our knowledge there are no reports concerning catalyst deactivation in Mn^I-catalyzed C−H bond functionalization processes. At the onset of our studies we had in mind that catalyst loadings had high (typically 10 mol %) reported transformations, with catalyst turnover numbers ranging from 5 to 9.[3−9] Our studies employing in situ IR spectroscopic analysis of reactions conducted at 60 and 100 °C showed formation of Mn^I carbonyl clusters within the first few minutes of substrate turnover. The formation of the Mn^I carbonyl clusters impacts greatly on substrate turnover, which explains the product **3a** conversions (ca. 50%). Finally, independently prepared hydroxylated Mn^I carbonyl clusters were found to be inactive catalyst species (reaction of **1** + **2a** → **3a**), demonstrating that they are not a reservoir of active "Y−$Mn^I(CO)_3$", where Y = OH or CCPh.

On the Poor Reactivity of Internal Alkyne 2b. The only examples of 1,2-diphenylacetylene **2b** being employed in Mn^I-catalyzed C−H bond functionalization chemistry involve the use of acid additives[6b] or rely on C−N reductive elimination processes.[6a] We demonstrated that manganacycle **4** and 7-membered alkyne insertion complex **6b** can be detected (by IR). As there are no accessible protons available (including from **1** and water) for the protonation step, we see liberation of reductive elimination product **7b**. This outcome is in keeping with the previously reported findings that diphenylacetylene **2b** enables the isolation and characterization of 7-membered manganacycles (Figure 7).

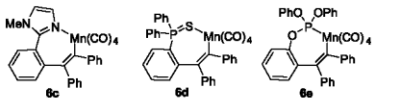

Figure 7. Previously reported stable 7-membered manganacycles **6c**−**e**, all forming through insertion of diphenylacetylene **2b** into a Mn−C bond of the corresponding manganacycle (relating to **4**).

■ CONCLUSION

Our mechanistic study has provided insight into the four key questions concerning catalytic C−H bond functionalization reactions mediated by manganese(I) carbonyl species. Our results explain why alkyne substrate dependencies, i.e., internal versus terminal alkynes, are observed in this chemistry and establish different catalyst activation pathways for $BrMn(CO)_5$. For terminal alkynes generation of Mn^I−acetylide species is highly likely, whose formation is reminiscent of Cu^I−acetylide species proposed to be important in traditional Sonogashira cross-coupling processes mediated by Pd/Cu.[19] This study unequivocally establishes that terminal alkyne, 2-phenylpyridine and water can facilitate hydrogen transfer in the protonation step leading to liberation of protonated alkene products in Mn^I-catalyzed C−H bond functionalization reactions. Finally, catalyst deactivation is currently an issue facing the development of Mn^I carbonyl catalysis involving the activation of C−H bonds; we determined that formation of Mn carbonyl clusters provides a dead end for catalysis. The development of new Mn^I catalysts able to thwart formation of such species will likely enable higher turnover numbers to be achieved, which is arguably critical for implementation of this promising C−H bond activation methodology in mainstream chemical synthesis.

■ EXPERIMENTAL SECTION

General Experimental and Instrumental Details. Reagents were purchased from Acros Organics, Alfa Aesar, Fluorochem, or Sigma-Aldrich and used as purchased unless otherwise stated. Dicyclohexylamine was degassed with N_2 under sonication and stored in a solvent ampule under N_2. Dry THF and MeCN were obtained from a Pure Solv MD-7 solvent system and stored under nitrogen. THF was also degassed by bubbling nitrogen through the solvent under sonication. Petroleum ether refers to the fraction of petroleum that is collected at 40−60 °C. Reactions requiring anhydrous conditions were carried out using Schlenk techniques (high vacuum, liquid nitrogen trap on a standard in-house built dual line). Room-temperature upper and lower limits are stated as 13−25 °C, but typically 21 °C was recorded.

Compound **4**[20] and Mn hydroxy cluster compounds[15] ([{$Mn(\mu_3$−$OH)(CO)_3\}_4$], and [$Mn_7(\mu_3$−$OH)_8(CO)_{18}$]) were prepared by literature methods.

Thin-layer chromatography (TLC) was carried out using Merck 5554 aluminum-backed silica plates (silica gel 60 F254), and spots were visualized using UV light (at 254 nm). Where necessary, plates were stained and heated with potassium permanganate, anisaldehyde, or vanillin as appropriate. Retention factors (R_f) are reported in parentheses along with the solvent system used. Flash column chromatography was performed according to the method reported by Still et al.[21] using Fluorochem silica gel 60 (particle size 40−63 μm) and a solvent system as stated in the text.

DOI: 10.1021/jacs.8b09095
J. Am. Chem. Soc. 2019, 141, 2316−2328

NMR spectra were obtained in the solvent indicated using a JEOL ECX400 or JEOL ECS400 spectrometer (400 and 101 MHz for ^{1}H and ^{13}C, respectively) or a Bruker 500 (500 and 125 MHz for ^{1}H and ^{13}C, respectively). Chemical shifts are reported in parts per million and were referenced to the residual nondeuterated solvent of the deuterated solvent used ($CHCl_3$ TMH = 7.26 and TMC = 77.16 ($CDCl_3$), $CDHCl_2$ TMH = 5.31 and TMC = 54.0 (CD_2Cl_2), ^{1}H and ^{13}C, respectively). Spectra were typically run at a temperature of 298 (for $CDCl_3$) or 295 K (for CD_2Cl_2). All ^{13}C NMR spectra were obtained with ^{1}H decoupling. NMR spectra were processed using MestReNova software (version 11.0.3-18688, 2017). The spectra given were typically saved as .emf files in MestReNova and inserted into a Microsoft Word document. For the ^{1}H NMR spectra, the resolution varies from 0.15 to 0.5 Hz; the coupling constants have been quoted to ±0.5 Hz in all cases for consistency. ^{1}H NMR chemical shifts are reported to two decimal places, and ^{13}C NMR chemical shifts are reported to one decimal place.

Infrared spectra were obtained using a Unicam Research Series FTIR (KBr IR) or a Bruker APLHA-Platinum FTIR Spectrometer with a platinum−diamond ATR sampling module. Where indicated, reactions were monitored in situ using a Mettler Toledo ReactIR ic_{10} with a K6 conduit SiComp (silicon) probe and MCT detector.

MS spectra were measured using a Bruker Daltronics micrOTOF MS, Agilent series 1200LC with electrospray ionization (ESI and APCI) or on a Thermo LCQ using electrospray ionization, with <5 ppm error recorded for all HRMS samples. LIFDI mass spectrometry was carried out using a Waters GCT Premier MS Agilent 7890A GC (usually for analysis of organometallic compounds when ESI or APCI are not satisfactory ionization methods). Mass spectral data are quoted as the m/z ratio along with the relative peak height in brackets (base peak = 100). Mass to charge ratios (m/z) are reported in Daltons. High-resolution mass spectra are reported with <5 ppm error.

Melting points were recorded using a Stuart digital SMP3 machine.

All DFT calculations were performed using the TURBOMOLE V6.4 package using the resolution of identity (RI) approximation.[22] Initial optimizations were performed at the (RI-)BP86/SV(P) level, followed by frequency calculations at the same level. Transition states were located by initially performing a constrained minimization (by freezing internal coordinates that change most during the reaction) of a structure close to the anticipated transition state. This was followed by a frequency calculation to identify the transition vector to follow during a subsequent transition state optimization. A final frequency calculation was then performed on the optimized transition-state structure. All minima were confirmed as such by the absence of imaginary frequencies, and all transition states were identified by the presence of only one imaginary frequency. Dynamic reaction coordinate analysis confirmed that transition states were connected to the appropriate minima. Finally, single-point calculations on the (RI)BP86/SV(P)-optimized geometries were performed using the hybrid PBE0 functional and the flexible def2-TZVPP basis set. The (RI)PBE0/def2-TZVPP SCF energies were corrected for their zero-point energies, thermal energies (ΔE), and entropies (obtained from the (RI-)BP86/SV(P)-level frequency calculations at 298.15 K, ΔG 298.15). Solvent correction for CH_2Cl_2 was applied with the COSMO dielectric continuum model[23] and dispersion effects modeled with Grimme's D3 method.[24] Calculated *XYZ* coordinates, single-point energies, and vibrational spectra are reported in the Supporting Information.

General Procedure for Reaction Monitoring Using in Situ IR Spectroscopic Analysis: General Procedure A. A 100 mL three necked round-bottomed flask equipped with a stir bar was attached to the ReactIR silicon-tipped ATR-IR probe. A background spectrum was collected and *n*-Bu_2O (10 mL) added before septa were attached to the side joints. Thereafter an internal thermocouple was attached through a septum, and the solvent was deoxygenated with an argon balloon. After the temperature had reached a steady level a solvent background spectrum was recorded to be used as a reference.

The sample measurements were thereafter started, and 2-phenylpyridine (**1**, 1.19 mL, 8.32 mmol, 2 equiv) was added through a septum. After the corresponding IR peaks had stabilized, phenylacetylene (**2a**, 0.45 mL, 4.16 mmol, 1 equiv) was added, followed by Cy_2NH (0.17 mL, 0.83 mmol, 20 mol %). $MnBr(CO)_5$ (114 mg, 0.42 mmol, 10 mol %) was added as the final reagent by rapid removal of the septum. IR spectra were recorded every 1 min, and specific peaks in the metal carbonyl region (~2150−1800 cm^{-1}; peak resolution = ± 4 cm^{-1}) were picked and monitored on individual experiment basis. The data was exported into a Microsoft Excel document, where the relevant processing was performed. Graph plots were generated and curve fitting performed using OriginPro 2017 software (SR2, b9.4.2.380).

When ex situ ^{1}NMR monitoring was necessary, aliquots (~50 μL, by microsyringe) of the reaction mixture were taken at appropriate time intervals. Aliquots were filtered through a Pasteur pipet (with cotton wool and Celite filter pad) into an NMR tube, after which a ^{1}H NMR spectrum was recorded of the sample to provide the product conversion, which could be cross-correlated with the changes recorded by IR spectroscopic analysis.

General Procedure for Stoichiometric Reactions: General Procedure B. To a microwave vial equipped with a stir bar was added $Mn(ppy)(CO)_4$ (**4**, 8 mg, 0.025 mmol, 1 equiv). Phenylacetylene (**2a**, 3 μL, 0.025 mmol, 1 equiv) was added as a stock solution in *n*-Bu_2O (0.6 mL, 0.042 mol dm^{-3}). The solution was deoxygenated by an argon balloon before heating at 100 °C for 30 min. After cooling the solvent was removed in vacuo, and the ^{1}H NMR spectrum was recorded of the crude material.

Characterization of Organic Products. *(E)-2-(2-Styrylphenyl)-pyridine* ***3a***. Adapted from a literature procedure.[3] To a microwave vial equipped with a stirbar were added $MnBr(CO)_5$ (14 mg, 0.05 mmol, 10 mol %), Cy_2NH (20 μL, 18 mg, 0.10 mmol, 20 mol %), 2-phenylpyridine (0.14 mL, 0.16 g, 1.00 mmol, 2 equiv), and phenylacetylene (54 μL, 0.05 g, 0.50 mmol, 1 equiv). nBu_2O (1.2 mL) was then added, and the solution was deoxygenated with an argon balloon before heating to 100 °C for 6 h. After cooling, the crude material was purified by flash column chromatography (petrol/Et_2O, 8:2, v/v) to afford a sticky oil (0.10 g, 79%).

R_f 0.12 (petrol/Et_2O, 8:2, *v*/*v*); ^{1}H NMR (500 MHz, $CDCl_3$, δ) 8.76 (ddd, J = 5.0, 2.0, 1.0 Hz, 1H), 7.79−7.72 (m, 2H), 7.57 (dd, J = 7.5, 1.5 Hz, 1H), 7.50−7.35 (m, 5H), 7.35−7.20 (m, 5H), 7.07 (d, J = 16.0 Hz, 1H); ^{13}C NMR (125 MHz, $CDCl_3$, δ) 159.0, 149.7, 139.7, 137.7, 136.1, 135.8, 130.4, 130.2, 128.8, 128.7, 127.8, 127.7, 127.7, 126.7, 126.4, 125.2, 122.0; ESI-MS m/z (ion, %) 258 ($[M + H]^+$, 100); ESI-HRMS m/z: 258.1277 $[M + H]^+$ (calcd for $C_{19}H_{16}N$ 258.1277); IR (neat, ATR, cm^{-1}) 3056, 3024, 1583, 1494, 1459, 1423, 1150, 1022, 960, 795, 749, 728, 690, 644, 616, 517.

Reductive Elimination Product ***7a***. Adapted from general procedure B. To a microwave vial equipped with a stir bar was added $Mn(ppy)(CO)_4$ (**4**, 32 mg, 0.1 mmol, 1 equiv), and phenylacetylene (11 μL, 10 mg, 0.1 mmol, 1 equiv) was added as a stock solution in nBu_2O (3 mL, 0.042 mol dm^{-1}). The solution was deoxygenated with an argon balloon before heating to 100 °C for 30 min. After cooling, the solvent was removed under reduced pressure and the product crystallized from CH_2Cl_2/pentane to afford the title compound as a brown solid (22 mg, 56%).

Mp 180−182 °C; ^{1}H NMR (500 MHz, CD_2Cl_2, δ) 8.01 (d, J = 8.5 Hz, 1H), 7.72 (dd, J = 7.5, 7.5 Hz, 1H), 7.61 (d, J = 8.0 Hz, 1H), 7.59−7.44 (m, 6H), 6.88 (s, 1H), 6.57 (s, 1H), 5.70 (s, 1H), 4.16 (d, J = 4.5 Hz, 1H), 3.23 (d, J = 5.5 Hz, 1H); ^{13}C NMR (125 MHz, CD_2Cl_2, δ) 167.9, 142.6, 135.5, 133.8, 133.7, 130.3, 129.7, 129.5, 129.4, 127.9, 126.0, 123.4, 118.3, 91.5, 78.8, 72.8, 50.4; ESI-MS m/z (ion, %): 256 ($[M + H]^+$, 100); ESI-HRMS m/z 256.1121 $[M + H]^+$ (calcd for $C_{19}H_{14}N$ 256.1121); IR (CH_2Cl_2 solution, cm^{-1}) 1983, 1896, 1627, 1561, 1499, 1276, 1257.

Reductive Elimination Product ***7b***. Adapted from general procedure B. To a microwave vial equipped with a stir bar weres added $Mn(ppy)(CO)_4$ (**4**, 32 mg, 0.1 mmol, 1 equiv) and diphenylacetylene (17 mg, 0.1 mmol, 1 equiv). Bu_2O (3 mL) was then added, and the solution was deoxygenated with an argon balloon before heating to 100 °C for 30 min. After cooling, the solvent was removed under reduced pressure and the product crystallized from CH_2Cl_2/pentane to afford the title compound as a brown solid (41 mg, 86%).

Mp 202−204 °C ; ^{1}H NMR (500 MHz, CD_2Cl_2, δ) 8.01 (d, J = 8.5 Hz, 1H), 7.72 (dd, J = 7.5, 7.5 Hz, 1H), 7.61 (d, J = 8.0 Hz, 1H), 7.59−

DOI: 10.1021/jacs.8b09095
J. Am. Chem. Soc. 2019, 141, 2316−2328

7.44 (m, 6H), 6.88 (s, 1H), 6.57 (s, 1H), 5.70 (s, 1H), 4.16 (d, J = 4.5 Hz, 1H), 3.23 (d, J = 5.5 Hz, 1H); ^{13}C NMR (125 MHz, CD_2Cl_2, δ) 167.9, 142.6, 135.5, 133.8, 133.7, 130.3, 129.7, 129.5, 129.4, 127.9, 126.0, 123.4, 118.3, 91.5, 78.8, 72.8, 50.4; ESI-MS m/z (ion, %) 332 ([M + H]$^+$, 100); ESI-HRMS m/z 332.1428 [M + H]$^+$ (calcd for $C_{25}H_{18}N$ 332.1434); IR (CH_2Cl_2 solution, cm^{-1}) 1982, 1894, 1614, 1561, 1504, 1426, 1274.

2-(2,6-Di(E)-2-(2-styrylphenyl))pyridine ***8a***. Adapted from general procedure B. To a microwave vial equipped with a stir bar were added Mn(ppy)(CO)$_4$ (**4**, 32 mg, 0.1 mmol, 1 equiv) and phenylacetylene (44 μL, 0.4 mmol, 4 equiv). Bu_2O (2.4 mL) was then added, and the solution was deoxygenated with an argon balloon before heating to 100 °C for 30 min. After cooling, the crude material was purified by flash column chromatography (petrol/Et_2O, 8:2, v/v) to afford a yellow solid (8 mg, 22%).

R_f 0.20 (petrol/Et_2O, 8:2, v/v); ^{1}H NMR (500 MHz, CD_2Cl_2, δ) 8.79 (ddd, J = 5.0, 2.0, 1.0 Hz, 1H), 7.81 (ddd, J = 7.5, 7.5, 2.0 Hz, 1H), 7.73 (d, J = 8.0 Hz, 2H), 7.47 (dd, J = 8.0 Hz, 1H), 7.37 (ddd, J = 7.5, 5.0, 1.0 Hz, 1H), 7.33 (d, J = 7.5 Hz, 1H), 7.31−7.24 (m, 8H), 7.24−7.17 (m, 2H), 7.01 (d, J = 16.0 Hz, 2H), 6.76 (d, J = 16.0 Hz); ^{13}C NMR (125 MHz, CD_2Cl_2, δ) 158.6, 150.2, 139.6, 137.9, 137.0, 136.6, 130.5, 129.1, 129.0, 128.2, 127.5, 127.0, 126.9, 125.2, 122.8; ESI-MS m/z (ion, %) 360 ([M + H]$^+$, 100), 382 ([M + Na]$^+$, 4); ESI-HRMS m/z 360.1746 [M + H]$^+$ (calcd for $C_{27}H_{22}N$ 360.1747); IR (solid-state, ATR, cm^{-1}) 3056, 3025, 2956, 2015, 1928, 1584, 1561, 1494, 1473, 1449, 1419, 1274, 1228, 1178, 1147, 1072, 1022, 958, 787, 748, 732, 689, 619.

2-(Pentadeuteriophenyl)pyridine ***1-d$_5$***. Adapted from the literature procedure.[3] Synthesis of phenylboronic ester-d_5: To a Schlenk tube under N_2 was added bromobenzene-d_5 (3.2 mL, 30 mmol, 1 equiv) and dry deoxygenated THF (120 mL). n-BuLi (2.5 M, 14.4 mL, 36 mmol, 1.2 equiv) was added dropwise at −78°, and the solution was stirred for 1 h. $B(OMe)_3$ (8.7 mL, 78 mmol, 2.6 equiv) was added, and the resulting mixture was stirred for a further 1 h, after warming to room temperature. The solution was acidified using HCl (10% in H_2O) and extracted with Et_2O, and the organic layer was dried over $MgSO_4$, filtered, and concentrated in vacuo to give an off-white solid used without further purification.

To a Schlenk tube under N_2 containing a stirred solution of phenylboronic ester-d_5 (3.9 g, 25 mmol, 1.3 equiv), Pd(PPh$_3$)$_4$ (699 mg, 0.6 mmol, 3.2 mol %), and Na_2CO_3 (15 g, 186 mmol, 5.6 equiv) in deoxygenated toluene (72 mL), water (72 mL), and EtOH (14 mL) was added 2-bromopyridine (1.8 mL, 19 mmol, 1 equiv). The reaction mixture was refluxed for 20 h before cooling to room temperature. Water was added and extracted with EtOAc. The organic layer was dried over $MgSO_4$, filtered, and concentrated in vacuo. The crude material was purified by flash column chromatography (petrol/EtOAc, 9:1, v/v) to yield a pale yellow liquid (2.84 g, 92%).

R_f 0.21 (petrol/EtOAc, 9:1, v/v); ^{1}H NMR (400 MHz, $CDCl_3$, δ) 8.70 (ddd, J = 5.0, 1.5, 1.5 Hz, 1H), 7.79−7.69 (m, 2H), 7.23 (ddd, J = 7.0, 5.0, 2.0 Hz, 1H); ^{13}C NMR (101 MHz, $CDCl_3$, δ): 157.6, 149.8, 139.3, 136.9, 128.5 (m, ^{2}H coupling), 126.6 (m, ^{2}H coupling), 122.2, 120.7; ESI-MS m/z (ion, %) 161 ([M + H]$^+$, 100); ESI-HRMS m/z 161.1119 [M + H]$^+$ (calcd for $C_{11}H_2D_3N$ 161.1122); IR (neat, ATR, cm^{-1}) 3052, 3012, 1595, 1569, 1470, 1433, 1382, 1332, 1300, 1246, 1153, 1098, 1055, 1015, 988, 908, 832, 820, 799, 750, 731, 642, 606, 552.

1-Deuterio(phenyl)acetylene ***2a−d***. Adapted from the literature procedure.[18] To a Schlenk tube under N_2 were added phenylacetylene (2.75 mL, 25 mmol, 1 equiv), K_2CO_3 (5.18 g, 37.5 mmol, 1.5 equiv), and dry deoxygenated MeCN (60 mL). The solution was stirred at room temperature for 30 min before D_2O (11.30 mL, 625 mmol, 25 equiv) was added and stirred for a further 1 h. The reaction mixture was diluted with CH_2Cl_2 (60 mL), and the organic layer was collected and dried over $MgSO_4$ and filtered followed by concentration in vacuo. The crude material was purified by distillation to yield a colorless liquid (1.14 g, 44%).

^{1}H NMR (400 MHz, $CDCl_3$, δ) 7.53−7.48 (m, 2H), 7.38−7.29 (m, 3H), 3.08 (s, 96% D incorporation); ^{13}C NMR (101 MHz, $CDCl_3$, δ) 132.3, 128.9, 128.4, 122.2, 83.3 (m, ^{2}H coupling), 77.03 (m, ^{2}H coupling); EI-GC-MS m/z (ion) 103 ([C_8H_5D]$^+$); EI-HRMS m/z: 103.0529 [C_8H_5D]$^+$ (calcd for C_8H_5D 103.0532); IR (neat, ATR, cm^{-1}) 3080, 3058, 2583, 1487, 1443, 1070, 1025, 917, 754, 689, 530, 483.

Manganese(I) (p-Tolylacetylide) Pentacarbonyl ***14***. Adapted from the literature procedure.[3] To a Schlenk tube under N_2 were added 1-ethynyl-4-methylbenzene (0.57 mL, 4.5 mmol, 1 equiv) and THF (30 mL). n-BuLi (1.80 mL, 2.5 M, 4.5 mmol, 1 equiv) was added dropwise to the solution at −78 °C and stirred for 30 min. A solution of $BrMn(CO)_5$ (1.24 g, 4.5 mmol, 1 equiv) in THF (60 mL) was added slowly via cannula and stirred at −78 °C for a further 1 h. The reaction mixture was warmed to room temperature, poured into water (45 mL), and extracted with CH_2Cl_2 (3 × 60 mL). The combined organic layers were dried over $MgSO_4$, filtered, and concentrated in vacuo. The crude material was purified by flash column chromatography (hexane/EtOAc, 99:1, v/v) to afford a yellow solid. The solid was dissolved in hexane and stirred over activated carbon for 10 min. Filtration through Celite and concentration in vacuo yielded a white crystalline solid (0.45 g, 32%).

^{1}H NMR (500 MHz, CD_2Cl_2, δ) 7.24−7.20 (m, 2H), 7.05 (d, J = 8.9 Hz, 1H), 2.31 (s, 3H); ^{13}C NMR (126 MHz, CD_2Cl_2, δ) 208.4, 207.6, 136.6, 131.6, 129.3, 124.7, 117.0, 89.2, 21.6; LIFDI-MS m/z (ion, %) 310 [M]$^+$; IR (CH_2Cl_2 solution, cm^{-1}) 3009, 2970, 2136, 2110, 2040, 2010, 1739, 1366, 1229, 1217.

■ ASSOCIATED CONTENT

Supporting Information

The Supporting Information is available free of charge on the ACS Publications website at DOI: 10.1021/jacs.8b09095.

Full experimental details, compound characterization data, Cartesian coordinates of all computed chemical structures (from DFT studies), including additional information as indicated in the main text within this manuscript; links to raw experimental data are also given for NMR spectra and in situ IR spectroscopic data (PDF) (CIF)

■ AUTHOR INFORMATION

Corresponding Authors

*jason.lynam@york.ac.uk

*ian.fairlamb@york.ac.uk

ORCID

Ian J. S. Fairlamb: 0000-0002-7555-2761

Notes

The authors declare no competing financial interest.

■ ACKNOWLEDGMENTS

We are grateful to Syngenta and the Engineering and Physical Sciences Research Council (EPSRC) (iCASE studentship to L.A.H. and for the computational equipment used in this study, ref EP/H011455/and EPSRC "ENERGY" grant, ref. EP/K031589/1) for funding. We thank Dr. Adrian C. Whitwood for the X-ray structure of compound **7b** and Professor Paul H. Walton for insightful comments on this work.

■ REFERENCES

(1) For selected reviews concerning earth abundant catalysis in general, see: (a) Su, B.; Cao, Z.-C.; Shi, Z.-J. Exploration of Earth-Abundant Transition Metals (Fe, Co, and Ni) as Catalysts in Unreactive Chemical Bond Activations. *Acc. Chem. Res.* **2015**, *48*, 886−896. (b) Bedford, R. B. How Low Does Iron Go? Chasing the Active Species in Fe-Catalyzed Cross-Coupling Reactions. *Acc. Chem. Res.* **2015**, *48*, 1485−1493. (c) Wang, D.; Astruc, D. The Recent Development of Efficient Earth-Abundant Transition-Metal Nanocatalysts. *Chem. Soc. Rev.* **2017**, *46*, 816−854. (d) Albrecht, M.; Bedford, R. B.; Plietker, B. Catalytic and Organometallic Chemistry of

DOI: 10.1021/jacs.8b09095
J. Am. Chem. Soc. 2019, 141, 2316−2328

Earth-Abundant Metals. *Organometallics* **2014**, *33*, 5619−5621. (e) Webster, R. L. *β*-Diketiminate Complexes of the First Row Transition Metals: Applications in Catalysis. *Dalton Trans* **2017**, *46*, 4483−4498. (f) Kitanosono, T.; Masuda, K.; Xu, P.; Kobayashi, S. Catalytic Organic Reactions in Water toward Sustainable Society. *Chem. Rev.* **2018**, *118*, 679−746.

(2) Bruce, M. I.; Goodall, B. L.; Iqbal, M. Z.; Stone, F. G. A.; Doedens, R. J.; Little, R. G. *ortho*-Metallation of Benzylideneaniline: Structure of $C_6H_5N{:}CH{\cdot}C_6H_4Mn(CO)_4$. *J. Chem. Soc. D* **1971**, *0*, 1595−1596.

(3) Zhou, B.; Chen, H.; Wang, C. Mn-Catalyzed Aromatic C−H Alkenylation with Terminal Alkynes. *J. Am. Chem. Soc.* **2013**, *135*, 1264−1267.

(4) (a) Wang, C. Manganese-Mediated C−C Bond Formation via C−H Activation: From Stoichiometry to Catalysis. *Synlett* **2013**, *24*, 1606−1613. (b) Liu, W.; Ackermann, L. Manganese-Catalyzed C−H Activation. *ACS Catal.* **2016**, *6*, 3743−3752. (c) Hu, Y.; Zhou, B.; Wang, C. Inert C−H Bond Transformations Enabled by Organometallic Manganese Catalysis. *Acc. Chem. Res.* **2018**, *51*, 816−827. (d) Cano, R.; Mackey, K.; McGlacken, G. P. Recent Advances in Manganese-Catalysed C−H Activation: Scope and Mechanism. *Catal. Sci. Technol.* **2018**, *8*, 1251−1266.

(5) (a) Zhou, B.; Ma, P.; Chen, H.; Wang, C. Amine-Accelerated Manganese-Catalyzed Aromatic C−H Conjugate Addition to *α,β*-Unsaturated Carbonyls. *Chem. Commun.* **2014**, *50*, 14558−14561. (b) Liu, W.; Zell, D.; John, M.; Ackermann, L. Manganese-Catalyzed Synthesis of *cis*-*β*-Amino Acid Esters through Organometallic C-H Activation of Ketimines. *Angew. Chem., Int. Ed.* **2015**, *54*, 4092−4096. (c) Liu, W.; Richter, S. C.; Zhang, Y.; Ackermann, L. Manganese(I)-Catalyzed Substitutive C−H Allylation. *Angew. Chem., Int. Ed.* **2016**, *55*, 7747−7750. (d) Hu, Y.; Wang, C. Manganese-Catalyzed Bicyclic Annulations of Imines and *α,β*-Unsaturated Esters via C−H Activation. *Sci. China: Chem.* **2016**, *59*, 1301−1305. (e) Lu, Q.; Klauck, F. J. R.; Glorius, F. Manganese-Catalyzed Allylation via Sequential C−H and C−C/C−Het Bond Activation. *Chem. Sci.* **2017**, *8*, 3379−3383. (f) Zell, D.; Dhawa, U.; Muller, V.; Bursch, M.; Grimme, S.; Ackermann, L. C−F/C−H Functionalization by Manganese(I) Catalysis: Expedient (Per)Fluoro-Allylations and Alkenylations. *ACS Catal.* **2017**, *7*, 4209−4213. (g) Ni, J.; Zhao, H.; Zhang, A. Manganese(I)-Catalyzed C−H 3,3-Difluoroallylation of Pyridones and Indoles. *Org. Lett.* **2017**, *19*, 3159−3162. (h) Wang, C.; Wang, A.; Rueping, M. Manganese-Catalyzed C−H Functionalizations: Hydroarylations and Alkenylations Involving an Unexpected Heteroaryl Shift. *Angew. Chem., Int. Ed.* **2017**, *56*, 9935−9938. (i) Cai, S.-H.; Ye, L.; Wang, D.-X.; Wang, Y.-Q.; Lai, L.-J.; Zhu, C.; Feng, C.; Loh, T.-P. Manganese-Catalyzed Synthesis of Monofluoroalkenes via C−H Activation and C−F Cleavage. *Chem. Commun.* **2017**, *53*, 8731−8734. (j) Liu, S.-L.; Li, Y.; Guo, J.-R.; Yang, G.-C.; Li, Z.-H.; Gong, J.-F.; Song, M.-P. An Approach to 3-(Indol-2-yl)succinimide Derivatives by Manganese-Catalyzed C−H Activation. *Org. Lett.* **2017**, *19*, 4042−4045. (k) Chen, S.-Y.; Li, Q.; Wang, H. Manganese(I)-Catalyzed Direct C−H Allylation of Arenes with Allenes. *J. Org. Chem.* **2017**, *82*, 11173−11181. (l) Zhu, C.; Schwarz, J. L.; Cembellin, S.; Greßies, S.; Glorius, F. Highly Selective Manganese(I)/Lewis Acid Cocatalyzed Direct C−H Propargylation Using Bromoallenes. *Angew. Chem., Int. Ed.* **2018**, *57*, 437−441. (m) Hu, Y.; Zhou, B.; Chen, H.; Wang, C. Manganese-Catalyzed Redox-Neutral C−H Olefination of Ketones with Unactivated Alkenes. *Angew. Chem., Int. Ed.* **2018**, *57*, 12071−12075.

(6) (a) He, R.; Huang, Z.-T.; Zheng, Q.-Y.; Wang, C. Manganese-Catalyzed Dehydrogenative [4 + 2] Annulation of N-H Imines and Alkynes by C-H/N-H Activation. *Angew. Chem.* **2014**, *126*, 5050−5053. (b) Shi, L.; Zhong, X.; She, H.; Lei, Z.; Li, F. Manganese Catalyzed C−H Functionalization of Indoles with Alkynes to Synthesize Bis/Trisubstituted Indolylalkenes and Carbazoles: the Acid is the Key to Control Selectivity. *Chem. Commun.* **2015**, *51*, 7136−7139. (c) Yang, X.; Jin, X.; Wang, C. Manganese-Catalyzed ortho-C−H Alkenylation of Aromatic N−H Imidates with Alkynes: Versatile Access to Mono-Alkenylated Aromatic Nitriles. *Adv. Synth. Catal.* **2016**, *358*, 2436−2442. (d) Lu, Q.; Greßies, S.; Klauck, F. J. R.; Glorius, F. Manganese(I)-Catalyzed Regioselective C−H Allenylation: Direct Access to 2-Allenylindoles. *Angew. Chem., Int. Ed.* **2017**, *56*, 6660−6664. (e) Lu, Q.; Greßies, S.; Cembellin, S.; Klauck, F. J. R.; Daniliuc, C. G.; Glorius, F. Redox-Neutral Manganese(I)-Catalyzed C−H Activation: Traceless Directing Group Enabled Regioselective Annulation. *Angew. Chem., Int. Ed.* **2017**, *56*, 12778−12782. (f) Wang, H.; Pesciaioli, F.; Oliveira, J. C. A.; Warratz, S.; Ackermann, L. Synergistic Manganese(I) C−H Activation Catalysis in Continuous Flow: Chemoselective Hydroarylation. *Angew. Chem., Int. Ed.* **2017**, *56*, 15063−15067. (g) Lu, Q.; Cembellín, S.; Greßies, S.; Singha, S.; Daniliuc, C. G.; Glorius, F. Manganese(I)-Catalyzed C-H (2-indolyl)methylation: Expedient Access to Diheteroarylmethanes. *Angew. Chem., Int. Ed.* **2018**, *57*, 1399−1403.

(7) (a) Zhou, B.; Hu, Y.; Wang, C. Manganese-Catalyzed Direct Nucleophilic C(sp^2)-H Addition to Aldehydes and Nitriles. *Angew. Chem., Int. Ed.* **2015**, *54*, 13659−13663. (b) Sueki, S.; Wang, Z.; Kuninobu, Y. Manganese- and Borane-Mediated Synthesis of Isobenzofuranones from Aromatic Esters and Oxiranes via C−H Bond Activation. *Org. Lett.* **2016**, *18*, 304−307. (c) Liang, Y.-F.; Massignan, L.; Liu, W.; Ackermann, L. Catalyst-Guided C = Het Hydroarylations by Manganese-Catalyzed Additive-Free C−H Activation. *Chem. - Eur. J.* **2016**, 22, 14856−14859.

(8) Liu, W.; Bang, J.; Zhang, Y.; Ackermann, L. Manganese(I)-Catalyzed C−H Aminocarbonylation of Heteroarenes. *Angew. Chem., Int. Ed.* **2015**, *54*, 14137−14140.

(9) Liu, W.; Richter, S. C.; Mei, R.; Feldt, M.; Ackermann, L. Synergistic Heterobimetallic Manifold for Expedient Manganese(I)-Catalyzed C-H Cyanation. *Chem. - Eur. J.* **2016**, 22, 17958−17961.

(10) Fairlamb, I. J. S. Pd-catalysed Cross-couplings for the Pharmaceutical Sector and a Move to Cutting-edge C−H Bond Functionalization: Is Palladium Simply Too Precious? In *Green and Sustainable Medicinal Chemistry*; Summerton, L., Sneddon, H. F., Jones, L. C., Clark, J. H., Eds.; RSC Publishing, 2016; Chapter 11, pp 129−139.

(11) (a) Liu, W.; Groves, J. T. Manganese Catalyzed C−H Halogenation. *Acc. Chem. Res.* **2015**, *48*, 1727−1735. (b) Yang, J.; Gabriele, B.; Belvedere, S.; Huang, Y.; Breslow, R. Catalytic Oxidations of Steroid Substrates by Artificial Cytochrome P-450 Enzymes. *J. Org. Chem.* **2002**, *67*, 5057−5067.

(12) Yahaya, N. P.; Appleby, K. M.; Teh, M.; Wagner, C.; Troschke, E.; Bray, J. T. W.; Duckett, S. B.; Hammarback, L. A.; Ward, J. S.; Milani, J.; Pridmore, N. E.; Whitwood, A. C.; Lynam, J. M.; Fairlamb, I. J. S. Manganese(I)-Catalyzed C−H Activation: The Key Role of a 7-Membered Manganacycle in H-Transfer and Reductive Elimination. *Angew. Chem., Int. Ed.* **2016**, *55*, 12455−12459.

(13) Hammarback, L. A.; Clark, I. P.; Sazanovich, I. V.; Towrie, M.; Robinson, A.; Clarke, F.; Meyer, S.; Fairlamb, I. J. S.; Lynam, J. M. Mapping Out the Key Carbon−Carbon Cond-Forming Steps in Mn-Catalysed C−H Functionalization. *Nat. Catal.* **2018**, *1*, 830−840.

(14) (a) Ward, J. S.; Lynam, J. M.; Moir, J. W. B.; Sanin, D. E.; Mountford, A. P.; Fairlamb, I. J. S. A Therapeutically Viable Photo-Activated Manganese-Based CO-Releasing Molecule (photo-CO-RM). *Dalton Trans* **2012**, *41*, 10514−10517. (b) Ward, J. S.; Bray, J. T. W.; Aucott, B. J.; Wagner, C.; Pridmore, N. E.; Whitwood, A. C.; Moir, J. W. B.; Lynam, J. M.; Fairlamb, I. J. S. Photoactivated Functionizable Tetracarbonyl(phenylpyridine)manganese(I) Complexes as CO-Releasing Molecules: A Direct Suzuki−Miyaura Cross-Coupling on a Thermally Stable CO-RM. *Eur. J. Inorg. Chem.* **2016**, *2016*, 5044−5051.

(15) Hydroxylated Mn(I) carbonyl clusters are reported in the literature; data correlates with the species indicated in the spectra in Figure 1a. The other related species (indicated by gold diamonds) are proposed to derive from related alkynylated Mn(I) carbonyl clusters. It ought to be noted that a mixture of different Mn(I) carbonyl clusters is likely present under the reactions, which is in keeping with observations recorded within the literature: For "$Mn(OH)(CO)_3$"-type clusters, see: (a) Clerk, M. D.; Zaworotko, M. J. High-Nuclearity Manganese Carbonyl Complexes: Structures of $[\{Mn(\mu^3{-}OH)(CO)_3\}_4]$ and $[Mn_7(\mu^3{-}OH)_8(CO)_{18}]$. *J. Chem. Soc., Chem. Commun.* **1991**, 1607−1608. For "$Mn(SR)(CO)_3$"-type clusters, see: (b) Gläser, S.; Mede, R.; Görls, H.; Seupel, S.; Bohlender, C.; Wyrwa, R.; Schirmer, S.; Dochow,

DOI: 10.1021/jacs.8b09095
J. Am. Chem. Soc. 2019, 141, 2316−2328

S.; Reddy, G. U.; Popp, J.; Westerhausen, M.; Schiller, A. Remote-Controlled Delivery of CO via Photoactive CO-Releasing Materials on a Fiber Optical Device. *Dalton Trans* **2016**, *45*, 13222−13233. For "Ru($\sigma\mu^2$-alkynyl)$(CO)_3$"-type clusters, see: (c) Bock, S.; Mackenzie, C. F.; Skelton, B. W.; Byrne, L. T.; Koutsantonis, G. A.; Low, P. J. Clusters as Ligands: Synthesis, Structure and Coordination Chemistry of Ruthenium Clusters Derived From 4- and 5-Ethynyl-2,2′-bipyridine. *J. Organomet. Chem.* **2016**, *812*, 190−196.

(16) We further recognize that a product-derived acetoxy-containing complex could be formed [κ^2-OAcMn$(CO)_3$(**3a**)].

(17) Perutz, R. N.; Sabo-Etienne, S. The σ-CAM Mechanism: σ Complexes as the Basis of σ-Bond Metathesis at Late-Transition-Metal Centers. *Angew. Chem., Int. Ed.* **2007**, *46*, 2578−2592.

(18) Jin, L.; Tolentino, D. R.; Melaimi, M.; Bertrand, G. Isolation of Bis(Copper) Key Intermediates in Cu-Catalyzed Azide-Alkyne "Click Reaction. *Sci. Adv.* **2015**, *1*, No. e1500304.

(19) Chinchilla, R.; Nájera, C. The Sonogashira Reaction: A Booming Methodology in Synthetic Organic Chemistry. *Chem. Rev.* **2007**, *107*, 874−922.

(20) Bruce, M. I.; Goodall, B. L.; Matsuda, I. Cyclometallation reactions. XIII. Reactions of Phenyl-Substituted Heterocyclic Nitrogen-Donor Ligands. *Aust. J. Chem.* **1975**, *28*, 1259−1264.

(21) Still, W. C.; Kahn, M.; Mitra, A. Rapid Chromatographic Technique for Preparative Separations with Moderate Resolution. *J. Org. Chem.* **1978**, *43*, 2923−2925.

(22) (a) Császár, P.; Pulay, P. Geometry Optimization by Direct Inversion in the Iterative Subspace. *J. Mol. Struct.* **1984**, *114*, 31−34. (b) Ahlrichs, R.; Bär, M.; Häser, M.; Horn, H.; Kölmel, C. Electronic Structure Calculations on Workstation Computers: The Program System Turbomole. *Chem. Phys. Lett.* **1989**, *162*, 165−169. (c) Deglmann, P.; Furche, F.; Ahlrichs, R. An Efficient Implementation of Second Analytical Derivatives for Density Functional Methods. *Chem. Phys. Lett.* **2002**, *362*, 511−518. (d) Deglmann, P.; May, K.; Furche, F.; Ahlrichs, R. Nuclear Second Analytical Derivative Calculations Using Auxiliary Basis Set Expansions. *Chem. Phys. Lett.* **2004**, *384*, 103−107. (e) Eichkorn, K.; Treutler, O.; Öhm, H.; Häser, M.; Ahlrichs, R. Auxiliary Basis Sets to Approximate Coulomb Potentials. *Chem. Phys. Lett.* **1995**, *240*, 283−290. (f) Eichkorn, K.; Weigend, F.; Treutler, O.; Ahlrichs, R. Auxiliary Basis Sets for Main Row Atoms and Transition Metals and Their Use to Approximate Coulomb Potentials. *Theor. Chem. Acc.* **1997**, *97*, 119−124. (g) Treutler, O.; Ahlrichs, R. Efficient Molecular Numerical Integration Schemes. *J. Chem. Phys.* **1995**, *102*, 346−354. (h) von Arnim, M.; Ahlrichs, R. Geometry Optimization in Generalized Natural Internal Coordinates. *J. Chem. Phys.* **1999**, *111*, 9183−9190.

(23) Klamt, A.; Schuurmann, G. COSMO: A New Approach to Dielectric Screening in Solvents with Explicit Expressions for the Screening Energy and its Gradient. *J. Chem. Soc., Perkin Trans. 2* **1993**, 799−805.

(24) (a) Grimme, S.; Antony, J.; Ehrlich, S.; Krieg, H. A Consistent and Accurate Ab Initio Parametrization of Density Functional Dispersion Correction (DFT-D) for the 94 Elements H-Pu. *J. Chem. Phys.* **2010**, *132*, 154104−154119. (b) Grimme, S.; Ehrlich, S.; Goerigk, L. Effect of the Damping Function in Dispersion Corrected Density Functional Theory. *J. Comput. Chem.* **2011**, *32*, 1456−1465.

DOI: 10.1021/jacs.8b09095
J. Am. Chem. Soc. 2019, 141, 2316−2328

ChemComm

COMMUNICATION

View Article Online
View Journal | View Issue

Cite this: *Chem. Commun.*, 2019, **55**, 3211

Received 10th January 2019,
Accepted 18th February 2019

DOI: 10.1039/c9cc00257j

rsc.li/chemcomm

Delineating the critical role of acid additives in Mn-catalysed C–H bond functionalisation processes†

L. Anders Hammarback,[a] Alan Robinson,[b] Jason M. Lynam *[a] and Ian J. S. Fairlamb *[a]

Addition of co-catalytic Cy_2NH to Mn-catalysed C–H bond activation reactions suggests that the conjugate acid, Cy_2NH_2X, influences catalysis. Here, acids are shown to positively influence C–H bond alkenylation catalysis involving alkynes. For certain types of alkynes an acid additive is critical to catalysis. In stark contrast, acids retard catalysis involving acrylates. $[Cy_2NH_2]X$ salts also play a key role in thwarting catalyst degradation to manganese clusters. Our findings enable unreactive substrates to be alkenylated.

The Earth abundant element, manganese, holds much promise in catalysis and applied chemical synthesis, as demonstrated by an eclectic array of recently discovered reactions.[1] Underpinning this rise to fame is a rich 40-year history[2] of stoichiometric organomanganese chemistry, particularly cyclomanganation and subsequent reactions of manganacycles. Catalytic C–H bond activation and functionalisation has grown from this base over the past 5 years, primarily inspired by Chen and Wang's[3] work reported in 2013, from which many important contributions have followed.[4] Mn^I-catalysed 'redox neutral' C–H bond functionalisation of, for example 2-phenylpyridine (**1**), by $BrMn(CO)_5$ (**2**), invoke $Mn(ppy)(CO)_4$ (**3**, ppy = 2-phenylpyridyl) formation. Reaction with an unsaturated 'acceptor' substrate (**4**), for example, alkenes, alkynes, carbonyls, isocyanates and cyanides, have been widely reported (Scheme 1).[5] Indeed, the synthetic methodologies developed far exceed detailed mechanistic studies, which have arguably lagged behind. However, recent mechanistic work[6,7] has shed light on the importance of CO liberation (from **3**), acceptor substrate (**4**) coordination (to give transient intermediate **I**) and migratory insertion leading to formation of 7-membered manganacycle (**II**), that can be characterised but only have a short relative lifetime.[6] Very little is known about the last step in the general catalytic scheme, namely protonation of **II** by substrate **1** (the 'acid'), to bring about liberation of product **5**.

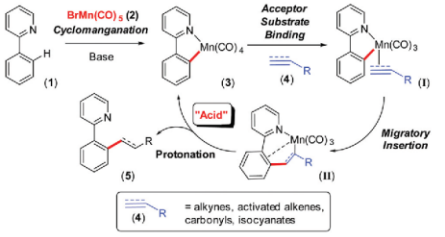

Scheme 1 Mechanistic picture for Mn^I-catalysed C–H bond activation and functionalisation, using a redox-neutral process.

The mechanistic picture detailed in Scheme 1 is not complete, as several reaction components can play the role of the acid,[8] from the donor C–H substrate, acceptor substrate, H_2O and the conjugate acid of the co-catalytic base, Cy_2NH, typically needed for catalysis.

In some reported methodologies, stronger carboxylic acid additives are required for productive catalysis,[9] or to increase the rate of protonation to avoid alternative reaction pathways.[7,10] It can also be envisaged that the conjugate acids of metal acetate type bases will have a similar effect in most reactions, when employed. The reason behind the effects of conjugate acids and acid additives in Mn^I-catalysed reaction have not been studied in detail, particularly in improving current promising synthetic methodologies.

To investigate the effect of additives in Mn^I-catalyzed C–H functionalisation reactions, $Mn(ppy)(CO)_4$ (**3**) was initially chosen as the entry point to probe subsequent steps, as no base additive nor 'Mn activation' is required. We have confirmed that **3** is a validated intermediate in the activation pathway for internal alkynes,[8] and a feasible entry point into the catalytic cycle for terminal alkynes. The reactions of 2-phenylpyridine **1** with unsaturated acceptor substrates (**4a–c**) mediated by **3**, in the presence of various additives, are collated in Fig. 1. Reaction of

[a] *Department of Chemistry, University of York, York, YO10 5DD, UK. E-mail: jason.lynam@york.ac.uk, ian.fairlamb@york.ac.uk*
[b] *Syngenta Crop Protection AG, Münchwilen, Breitenloh 5, 4333, Switzerland*

† Electronic supplementary information (ESI) available: Experimental procedures and compound characterisation. See DOI: 10.1039/c9cc00257j

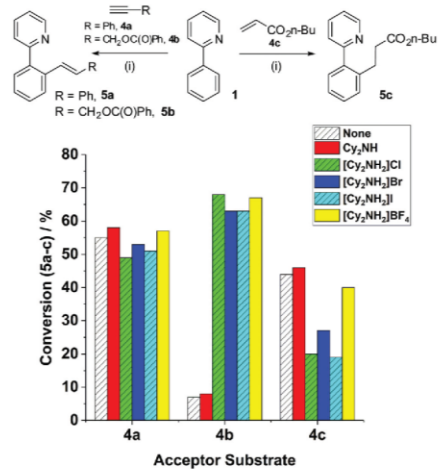

Fig. 1 The effect of base/conjugate acid additives in the reactions of **1** + **4a–c** → **5a–c**. Reaction conditions (i): $Mn(ppy)(CO)_4$ (**3**) (**2**, 10 mol%), **1** (2 equiv.), **4a–c** (1 equiv.), additive (20 mol%) – see figure legend key for details, *n*-Bu_2O, 100 °C, 3 h.

1 + **4a** → **5a** under standard conditions (at 100 °C, in *n*-Bu_2O, 3 h) Cy_2NH as the base, in the presence of $BrMn(CO)_5$ (10 mol%) as precatalyst, gave **5a** in 76% conversion (reported yield = 76%[3]). Employment of **3** as pre-catalyst gave a lower conversion to **5a** (55%). Addition of Cy_2NH did not noticeably affect the conversion to **5a** (58%), which is in line with previous proposals that the amine base is only required for activation of the Mn^I in the case of terminal alkynes.

Adding the conjugate acid of Cy_2NH, *i.e.* $[Cy_2NH_2]Br$, a side-product resulting from the initial C–H bond deprotonation in the reaction **1** + **4a** → **5a**, did not impact upon the conversion to **5a** (53%). The reaction is insensitive to changes in the anion, irrespective of the type of halide/pseudohalide (Fig. 1).

The employment of an alternative terminal alkyne, propargyl benzoate **4b** with **3** as the precatalyst, formed only a small amount of product **5b**, in the presence and absence of Cy_2NH {Conv. to **5b** 7% and 8% respectively (2.5×10^{-5} mol)}. The extent of product conversion appears to tally with the $[Mn_{TOTAL}]$ = 10 mol% (2.5×10^{-5} mol), indicating that there is limited turnover of the Mn catalyst. By contrast, the reaction mediated by $BrMn(CO)_5$ **2** and Cy_2NH gave **5b** with 54% conversion, in keeping with Chen and Wang's[3] observations using Et_2O solvent instead of *n*-Bu_2O (under equivalent reaction conditions obtaining 48% yield of **5b**). Limited catalyst turnover indicates an issue in either the protonation or recycling steps required for catalysis *vide supra*, leading to low product conversion and rapid catalyst degradation. The addition of $[Cy_2NH_2]Br$ had a profound and unexpected effect on product conversion to **5b**, increasing the conversion to 63%. The response was equally dramatic using $[Cy_2NH_2]Cl$, $[Cy_2NH_2]I$ or $[Cy_2NH_2]BF_4$ as acid additives.

In the original reaction of **1** + **4c** → **5c**, reported by Wang and co-workers,[11] it was suggested that $[Cy_2NH_2]Br$ acted as a proton source for the protonation step (not experimentally proven, but reasonably postulated within a reaction mechanism scheme). We thus assessed the impact of the base/conjugate acid additives in the reaction of **1** + **4c** → **5c**, employing **3** as the precatalyst (Fig. 1). When no additive was used in this reaction a lower conversion to **5c** (44%) was recorded than when $BrMn(CO)_5$ **2** and Cy_2NH were employed (79%). The lower product conversion can be rationalised as arising from no $[Cy_2NH_2]Br$ being present in the reaction mediated by **3**. Surprisingly, however, addition of $[Cy_2NH_2]Br$ was found to negatively affect conversion to product **5c** (27%). The negative influence of the conjugate acid is further compounded by altering the anion in $[Cy_2NH_2]X$ to chloride or iodide. Intriguingly, the less coordinating BF_4 counter-ion led to a product conversion similar to the reaction mediated by Cy_2NH (40% *versus* 46%, respectively).

In operando studies using infrared spectroscopic analysis: to gain insight into how $[Cy_2NH_2][X]$ (X = Br, Cl, I or BF_4) affects catalyst efficacy, the reactions of **1** + **4b–c** → **5b–c** were monitored *in operando* employing *in situ* IR spectroscopy, using a Mettler-Toledo ReactIR® instrument with Si-probe. This method allows for changes in metal carbonyl peaks to be monitored (qualitatively and quantitatively), being excellent spectroscopic handles for the observation of the dynamic processes occurring at the manganese centre. The reaction responding positively to acid, of **1** + **4b** → **5b**, mediated by precatalyst **3** (Fig. 2a) results in the initial appearance of two new species, with overlapping carbonyl bands, depicted by gold stars and closed red circles. After 30 minutes, a minor species with carbonyl bands at $\tilde{\nu}$1996 and 1944 cm^{-1} (black triangles) forms once catalysis is complete. We note the relative slow loss of **3** (trace quantities seen after *ca.* 5 minutes, depicted by closed blue circles), which is consistent with an independent mechanistic study examining the reaction of **1** + **4a** → **5a**.[3] The species depicted by gold stars is most likely a deactivation product, *i.e.* manganese hydroxyl-containing clusters previously proposed to be deactivation products for catalysis (see ESI†).[12] While the species depicted by closed red circles evolves and then rapidly depletes, suggesting its involvement as a transient intermediate.

However, when $[Cy_2NH_2][BF_4]$ was added to the reaction (Fig. 2b) the rate of formation of the previously observed deactivation species (gold stars) was greatly diminished. We note that another carbonyl-containing species is formed in this reaction (depicted by + symbols), which remains prominently after 30 minutes reaction time. Manganacycle **3** remains for the duration of the reaction (depleting to 30 minutes). The formation of manganese alkynyl-containing clusters is observed after 5 minutes reaction time (depicted by gold diamonds).

Monitoring the reaction of **1** + **4c** → **5c** without Cy_2NH (Fig. 2c) showed that two new significant overlapping carbonyl bands (depicted by closed gold circles) formed, *i.e.* similar bands to the manganese hydroxyl-containing clusters seen

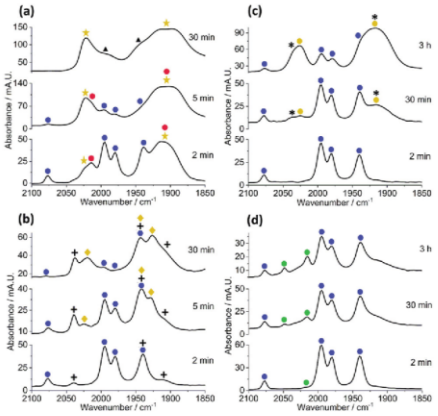

Fig. 2 Reaction monitoring using *in situ* IR monitoring using **3** as the pre-catalyst. (a) Reaction **1** + **4b** → **5b**, without Cy_2NH. (b) Reaction **1** + **4b** → **5b**, with $[Cy_2NH_2]BF_4$ (20 mol%). (c) Reaction **1** + **4c** → **5c**, without Cy_2NH. (d) Reaction **1** + **4c** → **5c** with $[Cy_2NH_2]$[Br] (20 mol%).

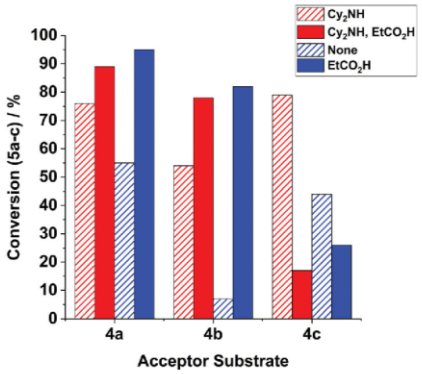

Fig. 3 The effect of additives in the reactions of **1** + **4a–c** → **5a–c** (see Fig. 1). General reaction conditions are detailed in Fig. 1, with the exception of the Mn precatalyst used: reactions mediated by $BrMn(CO)_5$ (10 mol%) are highlighted in red, and those mediated by manganacycle **3** (10 mol%) are highlighted in blue – see figure legend key for details of the additive.

when employing alkyne **4b** but not identical. Furthermore, manganacycle **3** persists throughout the reaction. Addition of $[Cy_2NH_2]Br$ to the reaction **1** + **4c** → **5c** (Fig. 2d), once again reduces the amount of manganese hydroxyl-containing clusters formed. Over longer reaction times $Mn_2(CO)_{10}$ is formed ($\tilde{\nu}$2048 and 2015 cm^{-1}, depicted by closed green circles), which is also known to be a competent precatalyst for this type of transformation. The formation of $Mn_2(CO)_{10}$ was not detected for the reaction conducted in the absence of $[Cy_2NH_2]Br$.

The take home messages from the *in operando* IR studies are:

• Addition of $[Cy_2NH_2]Br$ hinders the formation of manganese hydroxyl-containing clusters, and related clusters. In the case of the acrylate **4c** we note formation of $Mn_2(CO)_{10}$, after just 2 minutes, which becomes inactive as catalyst under these reaction conditions.

• $[Cy_2NH_2]Br$ increases the lifetime of manganacycle **3** in both reactions **1** + **4b–c** → **5b–c**, respectively.

Further studies on the acid additives – effect of pK_a: we extended our studies on the reaction of **1** + **4b** → **5b**, mediated by precatalyst **3** along with propionic acid (pK_a = 4.9 in H_2O[13]) as a co-catalyst (20 mol%), affording **5b** in 82% conversion – an enhancement of 75% when compared against the reaction without any additive (7%, *vide supra*, see Fig. 3). Switching to HCl (pK_a = −8 in H_2O) as the acid additive led to no enhancement in catalysis (5% conversion to **5b** recorded), while even stronger acids HBr (pK_a = −9 in H_2O[13]) and HI (pK_a = −10 in H_2O[13]) resulted in negligible product formation (≤1%). Interestingly, $HBF_4{\cdot}OEt_2$ (pK_a = −4.9 in H_2O[13]) enhanced product formation, affording **5b** in 62% conversion. This latter result possibly indicates that the relatively non-coordinating BF_4 can assist catalysis in some way, *i.e.* providing protons without catalyst degradation or by minimising halide coordination to Mn^I, consistent with the results presented in Fig. 1.

Examination of the reaction of **1** + **4b** → **5b** mediated by $BrMn(CO)_5$ **2**, with Cy_2NH (20 mol%) in the presence and absence of propionic acid (20 mol%), provided further evidence for an acid effect in enhancing the conversion of **5b** from 54% to 78% (Fig. 3).

The positive promoting effect of propionic acid in the reaction of **1** + **4b** → **5b** led us to examine the other acceptor substrates **4a** and **4c** (Fig. 3), for both $BrMn(CO)_5$ **2** and manganacycle **3** precatalysts. For phenyl acetylene **4a** we find that propionic acid enhances catalysis for both **2** and **3**, in the case of the latter, significantly (*i.e.* 95% conversion to **5a**, as compared to 55% in the absence of propionic acid). It is striking that the conjugate acids $[Cy_2NH_2]X$ do not positively influence catalysis under the same reaction conditions.

In the reaction of **1** + **4c** → **5c**, mediated by both $BrMn(CO)_5$ **2** and manganacycle **3** precatalysts, led to a significant reduction in product **5c** formation, which is consistent with the net negative effects of the conjugate acids $[Cy_2NH_2]X$ *vide supra*.

Promotion of substrates previously determined to be problematic for catalytic C–H bond alkenylation using Mn^I catalysis: we have previously determined that internal alkyne **6** strongly prefers reductive elimination pathways over protonation (in a reaction with 2-phenylpyridine **1**), thus rendering formation of alkenylated product **7** inaccessible.[8] Drawing on what had been learnt from this study we postulated that the protonation step could be assisted by $EtCO_2H$, bringing about the formation of alkenylated product **7**. Pleasingly, under the reaction conditions given in Scheme 2, **7** is formed in 20% yield (isolated product after chromatography), showcasing the ability of acid additives to form otherwise unachievable products for the Mn^I catalysis. The modest amount of **7** formed highlights the difficulty associated with the protonation step within the catalytic cycle, explaining why substrate sensitivity is sometimes observed.

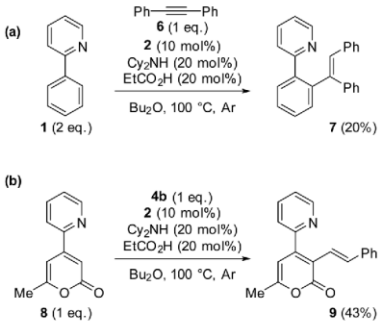

Scheme 2 (a) Effect of addition of $EtCO_2H$ to a reaction with diphenylacetylene **6**. (b) Effect of addition of $EtCO_2H$ to a reaction with **8**.

We next turned our attention to the reaction with substrate **8**, which had previously allowed us to characterise a key 7-membered manganacyclic intermediate, the anvil point to subsequent protonation or reductive elimination,[6] with the latter being preferred under typical catalytic reaction conditions (Scheme 2b). Quite remarkably we discovered that the reaction **8** + **4a** → **9** was made feasible by the addition of propionic acid affording **9** in 43% yield (isolated product after chromatography) (Scheme 2b). This result highlights the ability of acid additives to promote the protonation pathway, with concomitant formation of alkenylated products.

To summarise, we set out to understand the role of the conjugate acid, $[Cy_2NH_2]X$, formed by protonation of co-catalytic Cy_2NH base, in influencing C–H bond activation catalysis at Mn^I. We conclude that conjugate acids positively influence C–H bond alkenylation catalysis involving terminal and internal alkynes, which are found to be critical to productive catalysis. Importantly, the promotional effect of acid did enable unreactive substrates to be alkenylated involving both internal and terminal alkynes (Scheme 2). A dichotomy in behaviour is seen on switching from alkynes to an acrylate substrate, where catalysis is hindered by the presence of the conjugate acid containing a halide anion (*cf.* not a non-coordinating BF_4 anion). A secondary benefit of the $[Cy_2NH_2]X$ salts is to thwart Mn^I catalyst degradation to form inactive manganese clusters, which is an issue requiring attention in future catalyst design studies.[8]

We thank Syngenta and the Engineering and Physical Sciences Research Council (EPSRC) for iCASE funding for LAH, ref. EP/H011455.

Conflicts of interest

There are no conflicts to declare.

Notes and references

1 For selected reviews concerning manganese catalysis in general, see: (*a*) J. R. Carney, B. R. Dillon and S. P. Thomas, *Eur. J. Org. Chem.*, 2016, 3912–3929; (*b*) R. A. Baglia, J. P. T. Zaragoza and D. P. Goldberg, *Chem. Rev.*, 2017, **117**, 13320–13352; (*c*) F. Kallmeier and R. Kempe, *Angew. Chem., Int. Ed.*, 2018, **57**, 46–60; (*d*) M. Stanbury, J.-D. Compain and S. Chardon-Noblat, *Coord. Chem. Rev.*, 2018, **361**, 120–137.
2 M. I. Bruce, B. L. Goodall, M. Z. Iqbal, F. G. A. Stone, R. J. Doedens and R. G. Little, *J. Chem. Soc. D*, 1971, 1595–1596.
3 B. Zhou, H. Chen and C. Wang, *J. Am. Chem. Soc.*, 2013, **135**, 1264–1267.
4 Selected examples: (*a*) R. He, Z.-T. Huang, Q.-Y. Zheng and C. Wang, *Angew. Chem.*, 2014, **126**, 5050–5053; (*b*) W. Liu, D. Zell, M. John and L. Ackermann, *Angew. Chem., Int. Ed.*, 2015, **54**, 4092–4096; (*c*) B. Zhou, Y. Hu and C. Wang, *Angew. Chem., Int. Ed.*, 2015, **54**, 13659–13663; (*d*) W. Liu, J. Bang, Y. Zhang and L. Ackermann, *Angew. Chem., Int. Ed.*, 2015, **54**, 14137–14140; (*e*) C. Wang, A. Wang and M. Rueping, *Angew. Chem., Int. Ed.*, 2017, **56**, 9935–9938; (*f*) Q. Lu, S. Cembellín, S. Greßies, S. Singha, C. G. Daniliuc and F. Glorius, *Angew. Chem., Int. Ed.*, 2018, **57**, 1399–1403.
5 Y. Hu, B. Zhou and C. Wang, *Acc. Chem. Res.*, 2018, **51**, 816–827.
6 N. P. Yahaya, K. M. Appleby, M. Teh, C. Wagner, E. Troschke, J. T. W. Bray, S. B. Duckett, L. A. Hammarback, J. S. Ward, J. Milani, N. E. Pridmore, A. C. Whitwood, J. M. Lynam and I. J. S. Fairlamb, *Angew. Chem., Int. Ed.*, 2016, **55**, 12455–12459.
7 L. A. Hammarback, I. P. Clark, I. V. Sazanovich, M. Towrie, A. Robinson, F. Clarke, S. Meyer, I. J. S. Fairlamb and J. M. Lynam, *Nat. Catal.*, 2018, **1**, 830–840.
8 L. A. Hammarback, A. Robinson, J. M. Lynam and I. J. S. Fairlamb, *J. Am. Chem. Soc.*, 2019, **141**, 2316–2322.
9 H. Wang, F. Pesciaioli, J. C. A. Oliveira, S. Warratz and L. Ackermann, *Angew. Chem., Int. Ed.*, 2017, **56**, 15063–15067.
10 L. Shi, X. Zhong, H. She, Z. Lei and F. Li, *Chem. Commun.*, 2015, **51**, 7136–7139.
11 B. Zhou, P. Ma, H. Chen and C. Wang, *Chem. Commun.*, 2014, **50**, 14558–14561.
12 For '$Mn(OH)(CO)_3$' type clusters, see: (*a*) M. D. Clerk and M. J. Zaworotko, *J. Chem. Soc., Chem. Commun.*, 1991, 1607–1608; For 'Mn(SR)(CO)3' type clusters, see: (*b*) S. Gläser, R. Mede, H. Görls, S. Seupel, C. Bohlender, R. Wyrwa, S. Schirmer, S. Dochow, G. U. Reddy, J. Popp, M. Westerhausen and A. Schiller, *Dalton Trans.*, 2016, **45**, 13222–13233; For '$Ru(\sigma,\mu^2\text{-alkynyl})(CO)_3$' type clusters, see: (*c*) S. Bock, C. F. Mackenzie, B. W. Skelton, L. T. Byrne, G. A. Koutsantonis and P. J. Low, *J. Organomet. Chem.*, 2016, **812**, 190–196.
13 P. Y. Bruice, *Organic Chemistry*, 5th edn, Pearson, 2007.

Appendix 2: Monitoring Manganese Radicals using TRIR Spectroscopy

Appendix 2.1 Reaction With Photoredox Catalyst

$Mn_2(CO)_{10}$ **40** offer a good opportunity to probe additional manganese carbonyl-containing reaction systems to those discussed *vide supra*. The utilisation of this complex as a photo-initiator/catalyst in organic synthesis (in addition to being a thermal catalyst for C–H functionalisation), provide further incentive to understand and exploit its photochemical reactivity.[200, 201] As mentioned in Chapter 3.1.2, the initial photochemistry of **40** is well studied and radical **124** can be selectively generated using 400 nm light.[141] However, the understanding of the reactivity of **124** on ultra-fast timescales is limited and warrants further investigation.

A TRIR experiment using the LIFEtime experimental setup was conducted with 400 nm irradiation of **40** in MeCN ([**40**] = 1.33×10^{-3} mol dm^{-3}), to confirm the formation of the desired manganese radical (**Figure 73**). Initially, the bleaches corresponding to **40** and a broad band at 1984 cm^{-1} were observed, where the later compare well with the literature value for **124** (1984 cm^{-1}).[141] After 100 nanoseconds this complex depletes and was not present in the IR spectrum following 30–40 microseconds (k = $2.6 \pm 0.2 \times 10^5$ s^{-1} at room temperature). The newly formed species was assigned as being the cationic tri-carbonyl-tris-acetonitrile complex **270** and the IR bands (2053 and 1960 cm^{-1}) agree with those found in the literature (2057 and 1959 cm^{-1}).[202]

It has been proposed that it is the manganese radical **124** that is responsible for many of the photochemically initiated reactions with **40**.[201] Compounds who can interact with the manganese radical should increase the rate of consumption of **124**, regardless if it is forming the same end product (**270**) or another complex. The focus within this study is to explore new reactivities of **124**, rather than probing proposed reaction mechanisms. It has been found that many additives, such as alkenes, alkynes, and peroxides, does not react with **124**.[203]

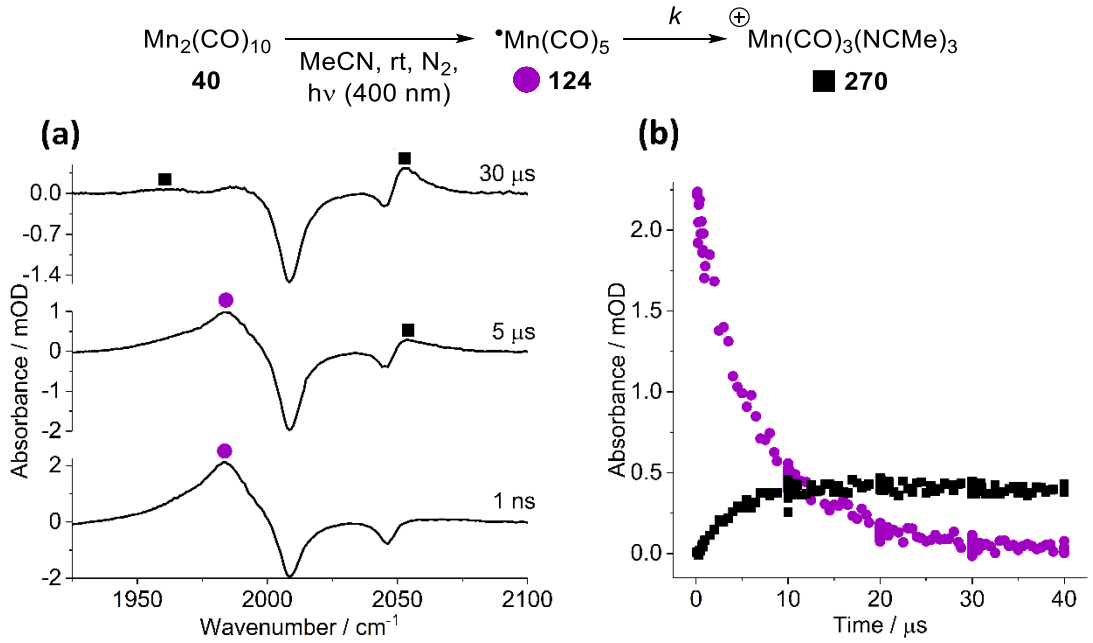

Figure 73. TRIR study of the photolysis of **40** in MeCN ([**40**] = 1.33 × 10^{-3} mol dm^{-3}). (a) IR spectra of the reaction showing the metal carbonyl region at various timepoints. Negative bleach bands corresponds to the loss of **40** after irradiation. (b) Kinetic plot of the formation of **270** (black squares, band at 2053 cm^{-1}) and depletion of **124** (purple circles, band at 1984 cm^{-1}), extracted from (a).

The emergence of photoredox-catalysis has allowed for extensive utilisation of ruthenium and iridium complexes in organic synthesis under photolysis conditions.[172] Their respective excited states are simultaneously very strong oxidants and reductants, leading to their wide-spread use. It was envisaged that the simultaneous irradiation of **40** and $[Ru(bpy)_3](PF_6)_2$ **271** should lead to the formation of **124** and an excited ruthenium complex. The ruthenium should be able to extract an electron from the manganese radical to promote further reactions. Therefore, an additional light source was fitted to the setup and the IR cell was continuously irradiated by 450 nm light, to excite the ruthenium. It was subsequently found that this setup was unnecessary, as the experiment proceeded identical with and without 450 nm irradiation, presumably due to the 400 nm pump beam exciting the tail of the UV-band for **271**.

Nevertheless, irradiating a 1.1:1 solution of **40** and **271** in MeCN ([**40**] = 1.37 × 10^{-3} mol dm^{-3} and [**271**] = 1.21 × 10^{-3} mol dm^{-3}), leads to the formation of **124** followed by **270** (**Figure 74**), the same as observed without ruthenium. The rate of formation of **270** is slightly slower at k = 1.54 ± 0.07 × 10^5 s^{-1} (k = 2.6 ± 0.2 × 10^5 s^{-1} at room temperature without Ru) but compare better with the loss of **124** (k_{dec} = 1.52 ± 0.03 × 10^5 s^{-1} at room temperature without ruthenium). Decreasing the amount of **271** added, lowers the rate of formation of **270** (for example; k = 0.29 ± 0.01 × 10^5 s^{-1} (at room temperature) at [**271**] = 0.30 × 10^{-3} mol dm^{-3}) and thereby increases the lifetime of the

radical. This means that the ruthenium can have a negative impact on the reaction and somehow hinders the radical from reacting to form **270**. It is unclear how this effect arises and requires further studies to be determined.

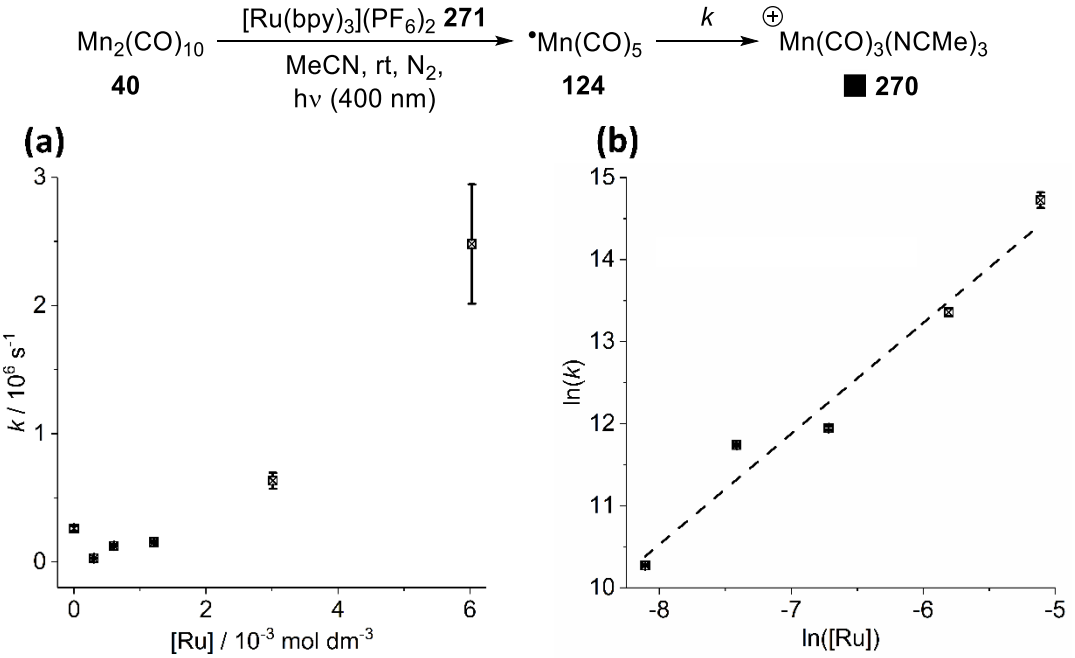

Figure 74. Impact of **271** on the rate of formation of cationic complex **270** from radical **124** ([**40**] = 1.37 × 10^{-3} mol dm^{-3} and [**271**] = 0–6.01 × 10^{-3} mol dm^{-3}). (a) Change in the rate of formation of **270** with increasing amounts of **271** added. (b) Reaction order determination for **271** where the slope of the linear regression was 1.35 ± 0.23 (R^2 = 0.92).

Increasing the quantity of ruthenium in the reaction above one equivalent, increased the rate of **270** formation (for example; k = 2.5 ± 0.5 × 10^6 s^{-1} (at room temperature) at [**271**] = 6.03 × 10^{-3} mol dm^{-3}). The reaction order in **271** was determined by varying the concentration of the ruthenium species in the experiment. The order was found to be 1.35 ± 0.23, which was not within error of being first order. However, there may be experimental errors, such as decreased light absorbance by the manganese with increasing ruthenium concentration, which skews the rate determination. Supplementary experiments determining the amount of manganese which is excited by the light in each of the reactions may give insight into the validity of the order determination. Radical recombination to regenerate **40**, is another process that may be taking place in these reactions and thereby inducing a competition with the reaction of the excited ruthenium species.

A final experiment using **271** was performed, where the concentration of **271** was kept constant and the manganese concentration was increased by a factor of 1.5 ([**40**] = 2.05 × 10^{-3} mol dm^{-3} and [**271**] = 6.01 × 10^{-3} mol dm^{-3}). The resulting rate of formation of

270 (k = 1.8 ± 0.3 × 10^6 s^{-1} at room temperature) was slightly lower, but within error of the corresponding reaction at the lower manganese concentration (k = 2.5 ± 0.5 × 10^6 s^{-1} at room temperature). This showed a zero order dependence in manganese, suggesting that the reaction mechanism does not involve any interaction between two manganese radicals. **271** on the other hand was most likely excited by the 400 nm light, after which it efficiently extracts the electron from **124**, giving rise to its dependence on the reaction rate.

Appendix 2.2 Reactions with Aryl Diazonium Salts

Aryl diazonium salts are highly reactive and have been successfully utilised in a wide-range of transition metal catalysed transformations.[204, 205] One manganese-mediated ($Cp'Mn(CO)_3$) protocol employing aryl diazonium salts has been reported, in which the diazonium salt was coupled to arenes via C–H bond functionalisation.[40] **40** was also found to be proficient as pre-catalyst under blue light irradiation, suggesting an initial formation of **124**. Therefore, it is not unlikely that the diazonium can interact with **124** to initiate that particular catalytic reaction.

An experiment was performed with 400 nm photolysis of a solution of **40** and $[PhN_2]BF_4$ **272** in MeCN ([**40**] = 1.33 × 10^{-3} mol dm^{-3} and [**272**] = 7.12 × 10^{-2} mol dm^{-3}), to probe the interaction between **124** and the diazonium salt (**Figure 75**). The tetrafluoroborate anion was employed for safety reasons, as it is significantly more stable than the halide derivates.[206] Initially, **124** was observed in the IR spectra and was replaced by a new Mn-carbonyl species (2080 cm^{-1}) over the first few microseconds (k = 8.6 ± 0.3 × 10^5 s^{-1} at room temperature). The band location of this species correlate well with literature values[207] for $[Mn(CO)_5(NCMe)]^+$ **273**, where the band around 2047 cm^{-1} could not be observed, due to overlapping with the bleach band. Lowering the amount of **272** used five times ([**272**] = 1.40 × 10^{-2} mol dm^{-3}), reduced the rate of formation for **273** (k = 1.8 ± 0.2 × 10^5 s^{-1} at room temperature) to become even slower than the formation of **270** without any additives (k = 2.6 ± 0.2 × 10^5 s^{-1} at room temperature).

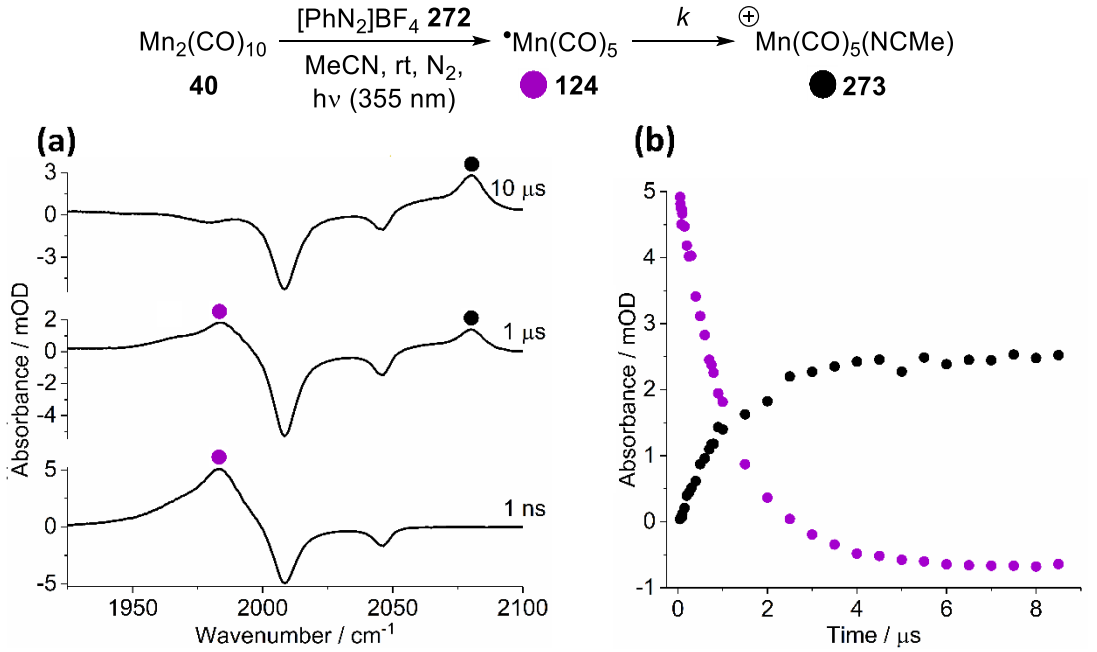

Figure 75. TRIR study of the photolysis of **40** and **272** in MeCN ([**40**] = 1.33 × 10^{-3} mol dm^{-3} and [**272**] = 7.12 × 10^{-2} mol dm^{-3}). (a) IR spectra of the reaction showing the metal carbonyl region at various timepoints. Negative bleach bands correspond to the loss of **40** after irradiation. (b) Kinetic plot of the formation of **273** (black circles, band at 2080 cm^{-1}) and depletion of **124** (purple circles, band at 1984 cm^{-1}), extracted from (a).

In a separate experiment **40** and **272** was irradiated at 400 nm in 2-minute intervals for an hour. **273** was isolated by crystallisation in CH_2Cl_2/pentane from the reaction mixture and a clean IR spectrum was recorded (2162, 2075 and 2050 cm^{-1}). This highlights that the manganese-complex is capable to activate aryl diazonium salts. The extra electron should most likely break the C–N_2 bond to generate N_2 and a benzene radical.

In an attempt to probe and utilise the formed aryl radical, B_2pin_2 was employed to quench the radical and generate the corresponding aryl-Bpin. It has been subsequently found that the borylated arene (Ph-Bpin) can be generated from a reaction between **272** (1 eq.) and B_2pin_2 (3 eq.) with **40** (4 mol%) in MeCN. The solution was irradiated with 450 nm light at room temperature and generate 96% yield of isolated product (reaction performed by Dr James D. Firth). This was an improvement on the current methodology[40] and further exploration of this chemistry is currently taking place.

Appendix 3: X-Ray Diffraction Data

Crystallographic data for compound 86

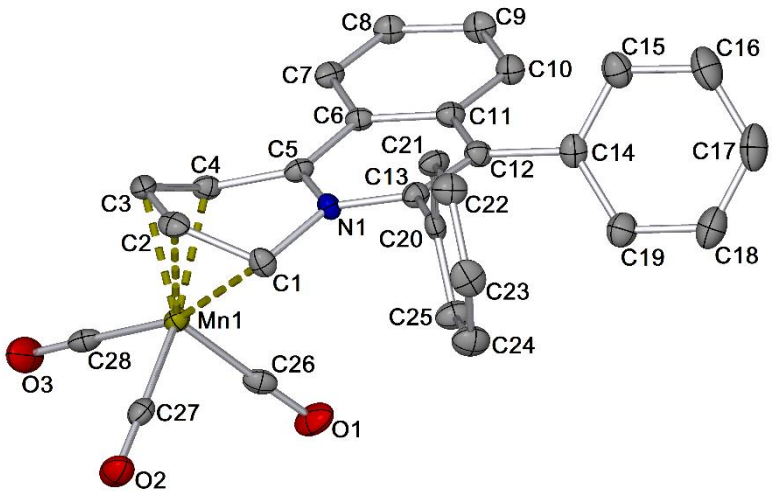

Figure 76. Single crystal X-ray diffraction structure of **86**. Thermal ellipsoids shown with 50% probability and hydrogen atoms removed for clarity. Selected bond lengths (Å): C1-C2: 1.446(4); C1-Mn1: 2.091(3); C1-N1: 1.476(3); C2-C3: 1.382(4); C2-Mn1: 2.095(3); C3-C4: 1.445(4); C3-Mn1: 2.083(3); C4-C5: 1.442(4); C4-Mn1: 2.162(3); C5-N1: 1.342(3); C12-C13: 1.372(4); C13-N1: 1.387(4); C26-Mn1: 1.804(3); C27-Mn1: 1.161(3); C28-Mn1: 1.798(3). Selected bond angles (°): C2-C1-N1: 115.7(2); C3-C2-C1: 113.1(3); N1-C5-C4: 155.5(2); C12-C13-N1: 119.7(2); O1-C26-Mn1: 178.5(3); C1-Mn1-C2: 40.41(11); C1-Mn1-C4: 74.07(11); C3-Mn1-C2: 38.63(11); C26-Mn1-C1: 97.38(13); C27-Mn1-C1: 96.86(12); C28-Mn1-C1: 163.33(13).

Table 22. Crystal data and structure refinement for compound **86**.

Identification code	ijsf1809
Empirical formula	$C_{28}H_{18}MnNO_3$
Formula weight	471.37
Temperature/K	109.95(10)
Crystal system	orthorhombic
Space group	Pbca
a/Å	19.1024(2)
b/Å	7.84458(12)
c/Å	32.2257(5)
α/°	90
β/°	90
γ/°	90
Volume/Å^3	4829.03(12)
Z	8

ρ_{calc}g/cm^3	1.297
μ/mm^{-1}	4.674
F(000)	1936.0
Crystal size/mm^3	0.275 × 0.226 × 0.02
Radiation	CuKα (λ = 1.54184)
2Θ range for data collection/°	7.178 to 134.13
Index ranges	-22 ≤ h ≤ 22, -6 ≤ k ≤ 9, -38 ≤ l ≤ 28
Reflections collected	9268
Independent reflections	4294 [R_{int} = 0.0312, R_{sigma} = 0.0438]
Data/restraints/parameters	4294/0/298
Goodness-of-fit on F^2	1.038
Final R indexes [I>=2σ (I)]	R_1 = 0.0457, wR_2 = 0.1022
Final R indexes [all data]	R_1 = 0.0637, wR_2 = 0.1095
Largest diff. peak/hole / e Å^{-3}	0.50/-0.38

[a] Refinement Special Details: The crystal contained disordered solvent for which a suitable discrete atom model could not be obtained therefore a solvent mask was used. There were 4 solvent voids per unit cell each with a volume of Ca 200 A^3 containing an estimated 51 electrons. This is consistent with there being approximately one DCM or pentane per void.

Crystallographic data for compound 255

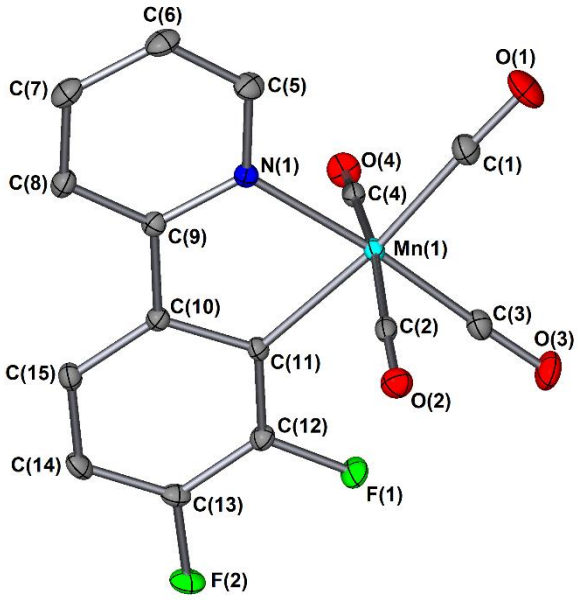

Figure 77. Single crystal X-ray diffraction structure of **255**. Thermal ellipsoids shown with 50% probability and hydrogen atoms removed for clarity. Selected bond lengths (Å): C1–Mn1: 1.8334(14); C2–Mn1: 1.8565(15); C3–Mn1: 1.8027(14); C11–Mn1: 2.0501(12); N1–Mn1: 2.0747(11). Selected bond angles (°): O2–C2–Mn1: 175.33(11); C1–Mn1–C11: 173.09(6); C3–Mn1–N1: 175.13(5); C11–Mn1–N1: 79.32(5).

Table 23. Crystal data and structure refinement for compound **255**.

Identification code	ijsf1706a
Empirical formula	$C_{15}H_6F_2MnNO_4$
Formula weight	357.15
Temperature/K	110.00(14)
Crystal system	monoclinic
Space group	$P2_1/c$
a/Å	10.96431(17)
b/Å	10.28440(11)
c/Å	12.84430(19)
α/°	90
β/°	112.5266(18)
γ/°	90
Volume/Å^3	1337.83(4)
Z	4
ρ_{calc}g/cm^3	1.773
μ/mm^{-1}	1.031
F(000)	712.0
Crystal size/mm^3	0.297 × 0.279 × 0.185
Radiation	MoKα (λ = 0.71073)
2Θ range for data collection/°	6.868 to 60.062
Index ranges	$-15 \leq h \leq 15$, $-14 \leq k \leq 14$, $-18 \leq l \leq 18$
Reflections collected	19351
Independent reflections	3911 [R_{int} = 0.0287, R_{sigma} = 0.0206]
Data/restraints/parameters	3911/0/208
Goodness-of-fit on F^2	0.979
Final R indexes [I>=2σ (I)]	R_1 = 0.0276, wR_2 = 0.1097
Final R indexes [all data]	R_1 = 0.0313, wR_2 = 0.1170
Largest diff. peak/hole / e Å^{-3}	0.35/-0.52

Crystallographic data for compound 258

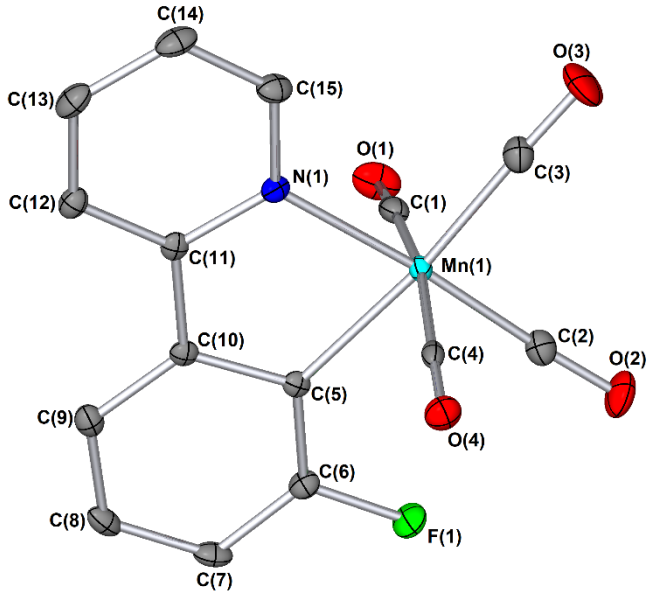

Figure 78. Single crystal X-ray diffraction structure of **258**. Thermal ellipsoids shown with 50% probability and hydrogen atoms removed for clarity. Selected bond lengths (Å): C1–Mn1: 1.855(2); C2–Mn1: 1.807(2); C3–Mn1: 1.832(2); C5–Mn1: 2.0557(18); N1–Mn1: 2.0749(16). Selected bond angles (°): O1–C1–Mn1: 175.39(17); C2–Mn1–N1: 175.81(8); C3–Mn1–C5: 173.60(8); C5–Mn1–N1: 79.39(7).

Table 24. Crystal data and structure refinement for compound **258**.

Identification code	ijsf1906
Empirical formula	$C_{15}H_7FMnNO_4$
Formula weight	339.16
Temperature/K	110.05(10)
Crystal system	monoclinic
Space group	$P2_1/c$
a/Å	10.8244(3)
b/Å	10.2702(3)
c/Å	12.9672(4)
α/°	90
β/°	111.698(4)
γ/°	90
Volume/Å^3	1339.39(7)
Z	4
ρ_{calc}g/cm^3	1.682

μ/mm^{-1}	8.314
F(000)	680.0
Crystal size/mm^3	0.179 × 0.139 × 0.102
Radiation	CuKα (λ = 1.54184)
2Θ range for data collection/°	8.792 to 134.156
Index ranges	-12 ≤ h ≤ 12, -12 ≤ k ≤ 12, -11 ≤ l ≤ 15
Reflections collected	4710
Independent reflections	2388 [R_{int} = 0.0215, R_{sigma} = 0.0301]
Data/restraints/parameters	2388/0/199
Goodness-of-fit on F^2	1.021
Final R indexes [I>=2σ (I)]	R_1 = 0.0262, wR_2 = 0.0628
Final R indexes [all data]	R_1 = 0.0311, wR_2 = 0.0654
Largest diff. peak/hole / e $Å^{-3}$	0.25/-0.26

Crystallographic data for compound 259

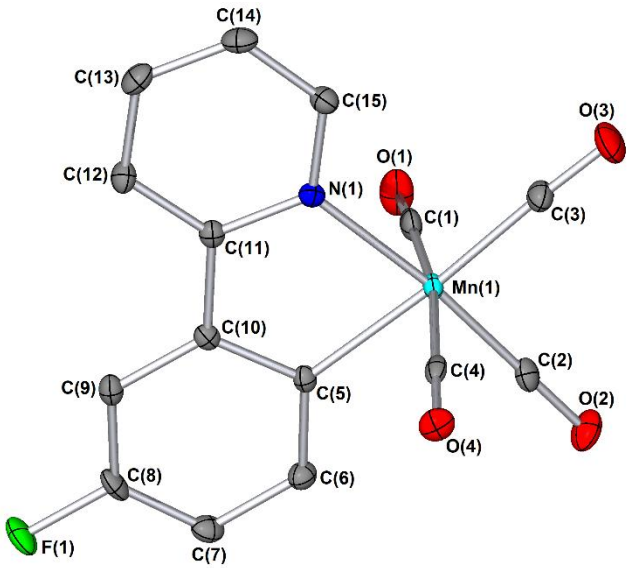

Figure 79. Single crystal X-ray diffraction structure of **259**. Thermal ellipsoids shown with 50% probability and hydrogen atoms removed for clarity. Selected bond lengths (Å): C1–Mn1: 1.8607(19); C2–Mn1: 1.8032(18); C3–Mn1: 1.8342(18); C5–Mn1: 2.0510(17); N1–Mn1: 2.0688(14). Selected bond angles (°): O1–C1–Mn1: 175.98(17); C2–Mn1–N1: 173.57(7); C3–Mn1–C5: 175.10(7); C5–Mn1–N1: 79.93(7).

Table 25. Crystal data and structure refinement for compound **259**.

Identification code	ijsf1907
Empirical formula	$C_{15}H_7FMnNO_4$
Formula weight	339.16
Temperature/K	110.00(14)
Crystal system	triclinic
Space group	P-1
a/Å	6.9560(3)
b/Å	10.2256(5)
c/Å	19.9590(8)
α/°	82.017(4)
β/°	87.388(4)
γ/°	72.478(4)
Volume/Å^3	1340.66(11)
Z	4
ρ_{calc}g/cm^3	1.680
μ/mm^{-1}	8.306
F(000)	680.0
Crystal size/mm^3	0.116 × 0.052 × 0.026
Radiation	CuKα (λ = 1.54184)
2Θ range for data collection/°	8.948 to 134.124
Index ranges	$-8 \leq h \leq 8$, $-12 \leq k \leq 10$, $-21 \leq l \leq 23$
Reflections collected	8464
Independent reflections	4798 [R_{int} = 0.0154, R_{sigma} = 0.0265]
Data/restraints/parameters	4798/0/397
Goodness-of-fit on F^2	1.057
Final R indexes [I>=2σ (I)]	R_1 = 0.0239, wR_2 = 0.0626
Final R indexes [all data]	R_1 = 0.0290, wR_2 = 0.0647
Largest diff. peak/hole / e Å^{-3}	0.29/-0.33

Appendix 4: NMR Spectra

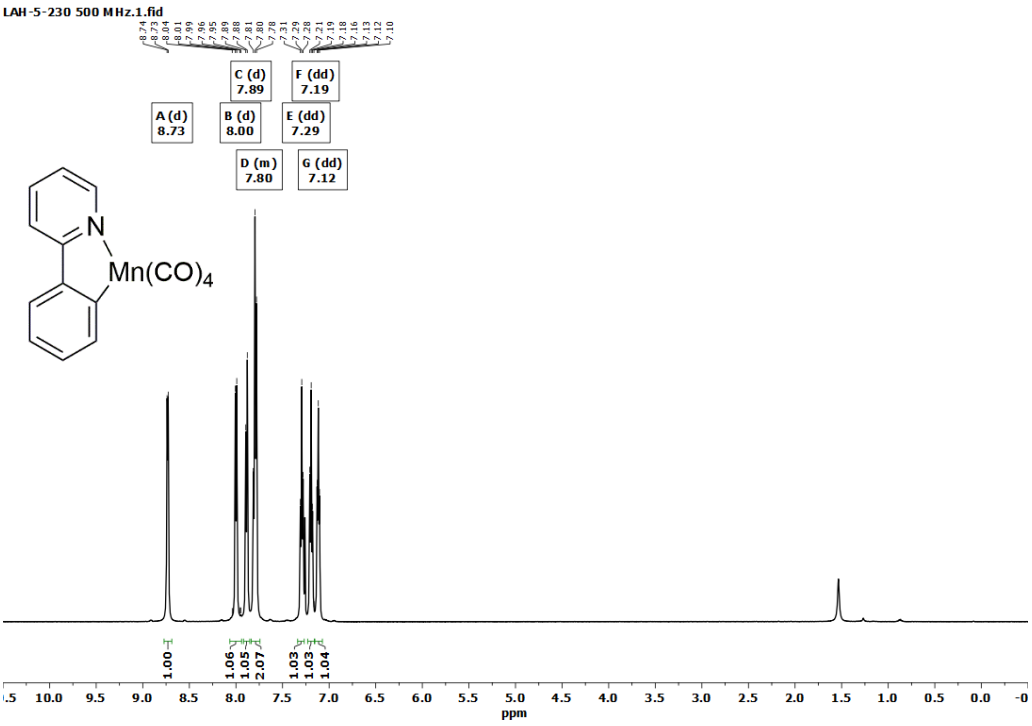

Figure 80. ^{1}H NMR spectrum of **10** (500 MHz, $CDCl_3$).

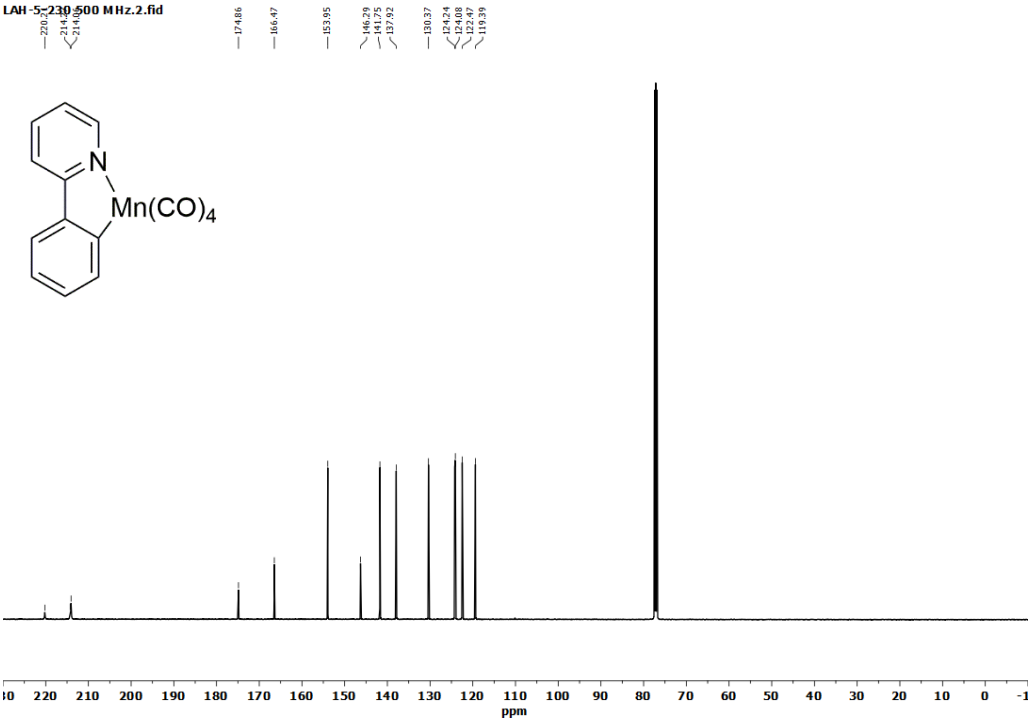

Figure 81. ^{13}C NMR spectrum of **10** (126 MHz, $CDCl_3$).

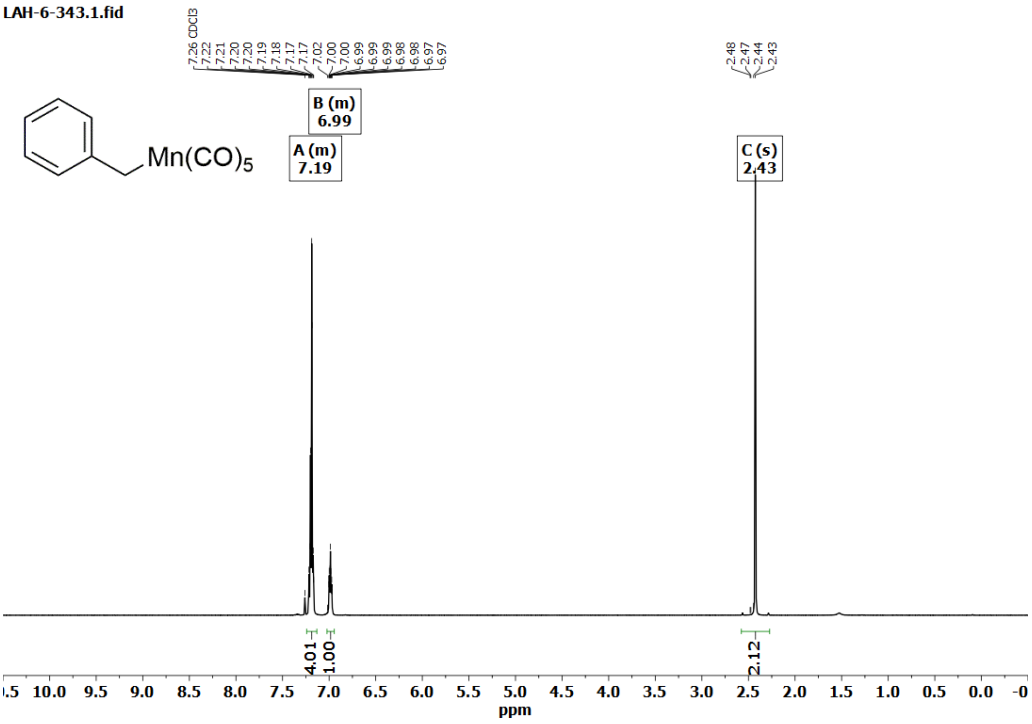

Figure 82. ^{1}H NMR spectrum of **19** (500 MHz, $CDCl_3$).

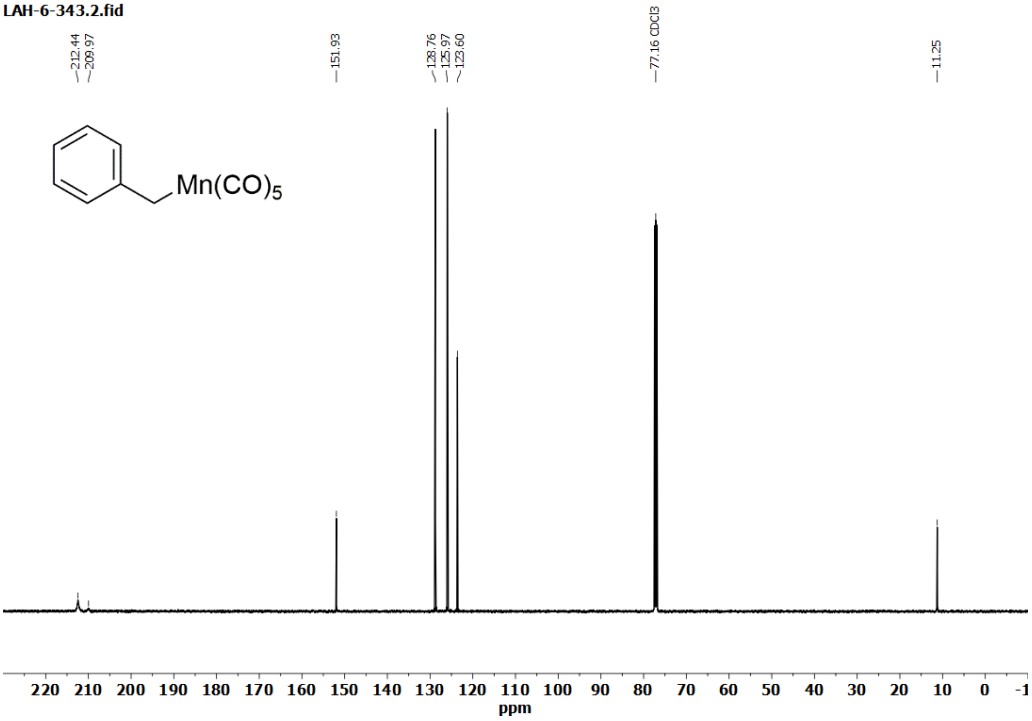

Figure 83. ^{13}C NMR spectrum of **19** (126 MHz, $CDCl_3$).

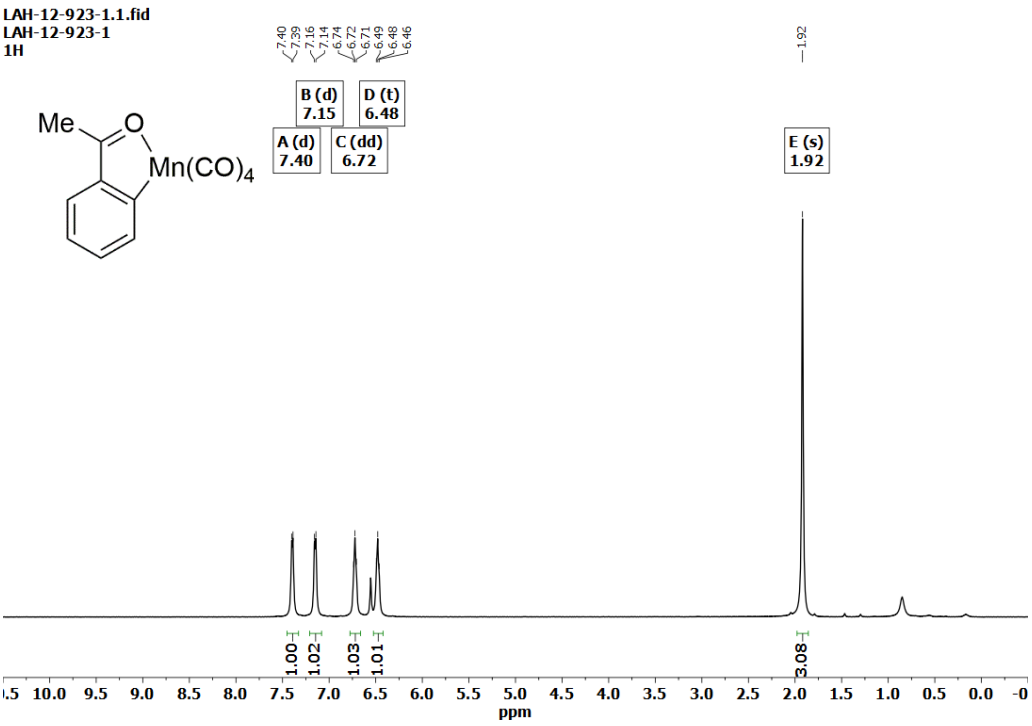

Figure 84. ^{1}H NMR spectrum of **20** (500 MHz, $CDCl_3$).

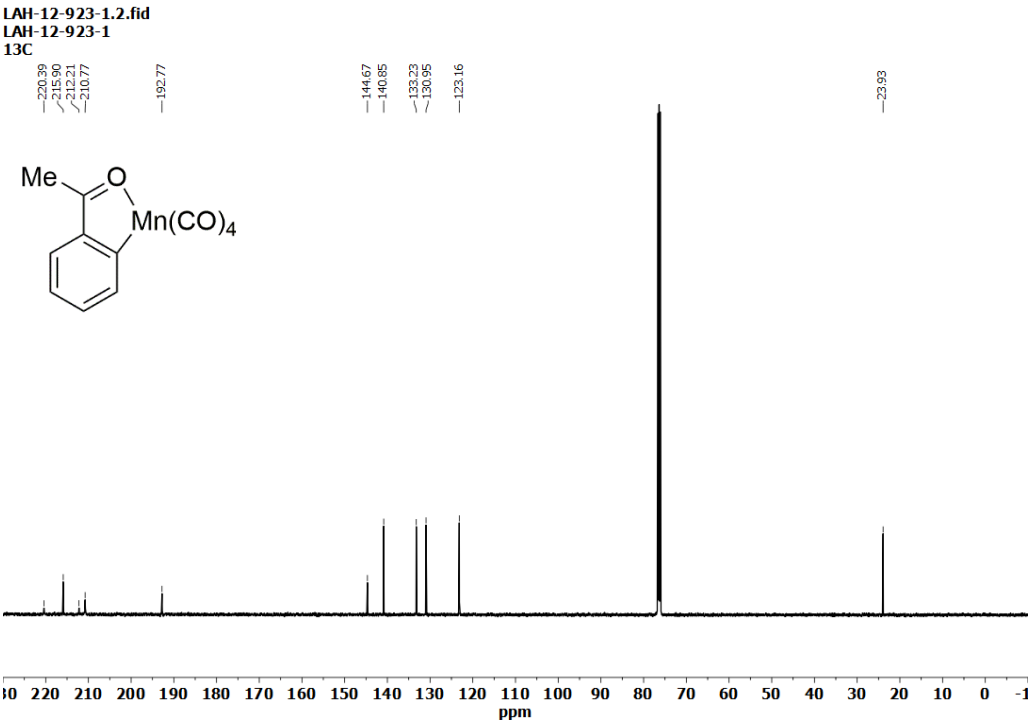

Figure 85. ^{13}C NMR spectrum of **20** (126 MHz, $CDCl_3$).

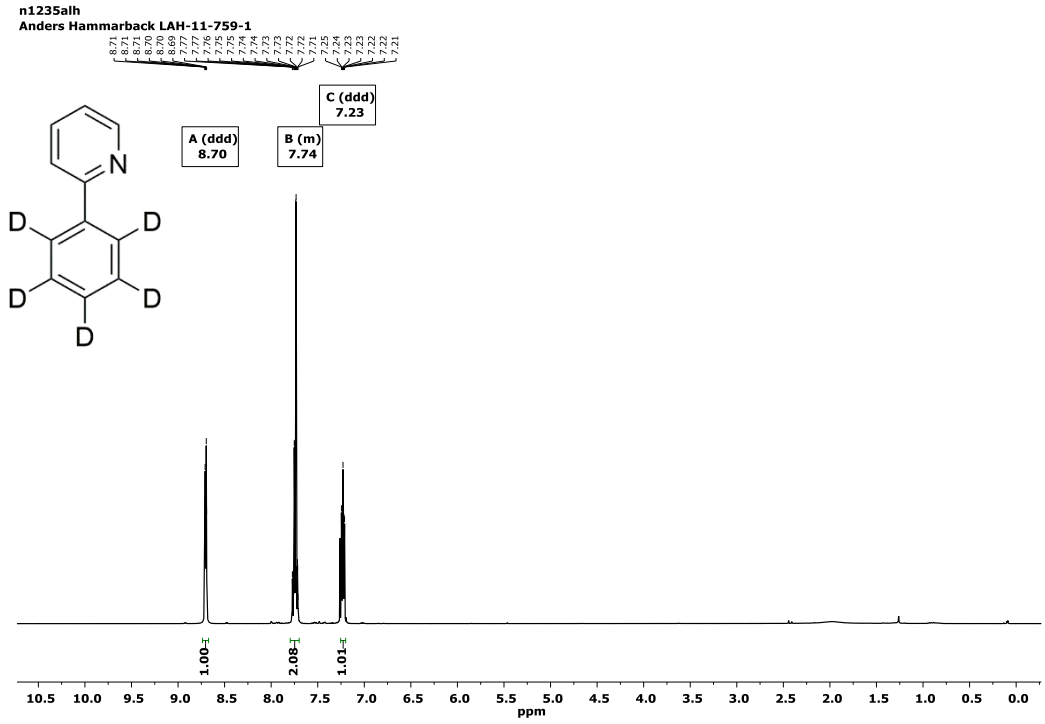

Figure 86. ^{1}H NMR spectrum of **33**-d_5 (400 MHz, $CDCl_3$).

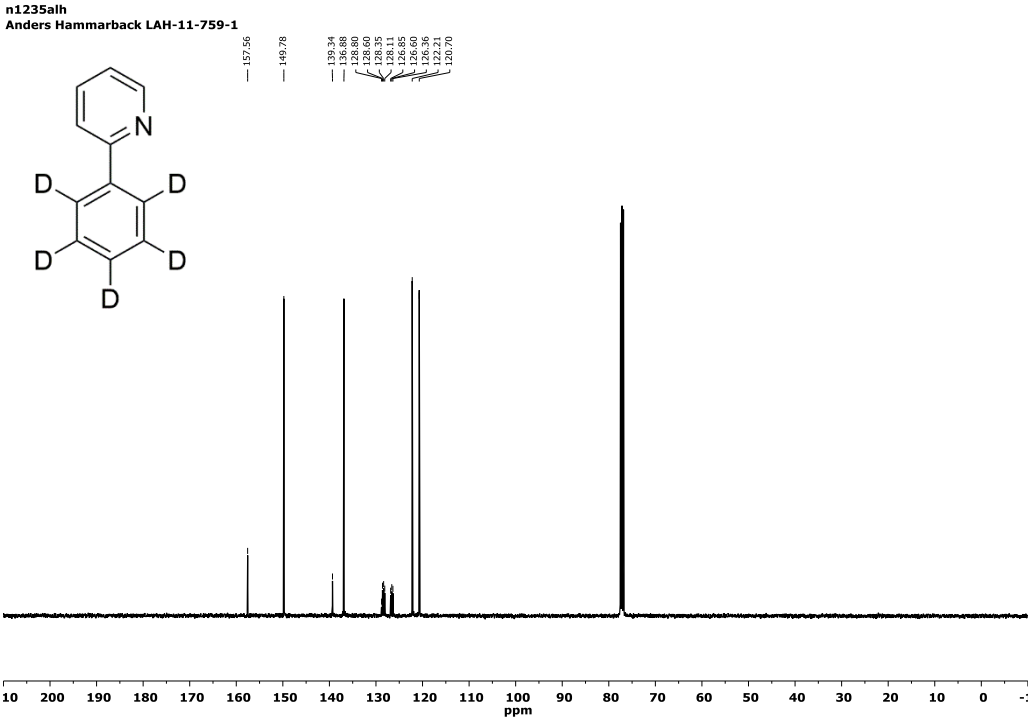

Figure 87. ^{13}C NMR spectrum of **33**-d_5 (101 MHz, $CDCl_3$).

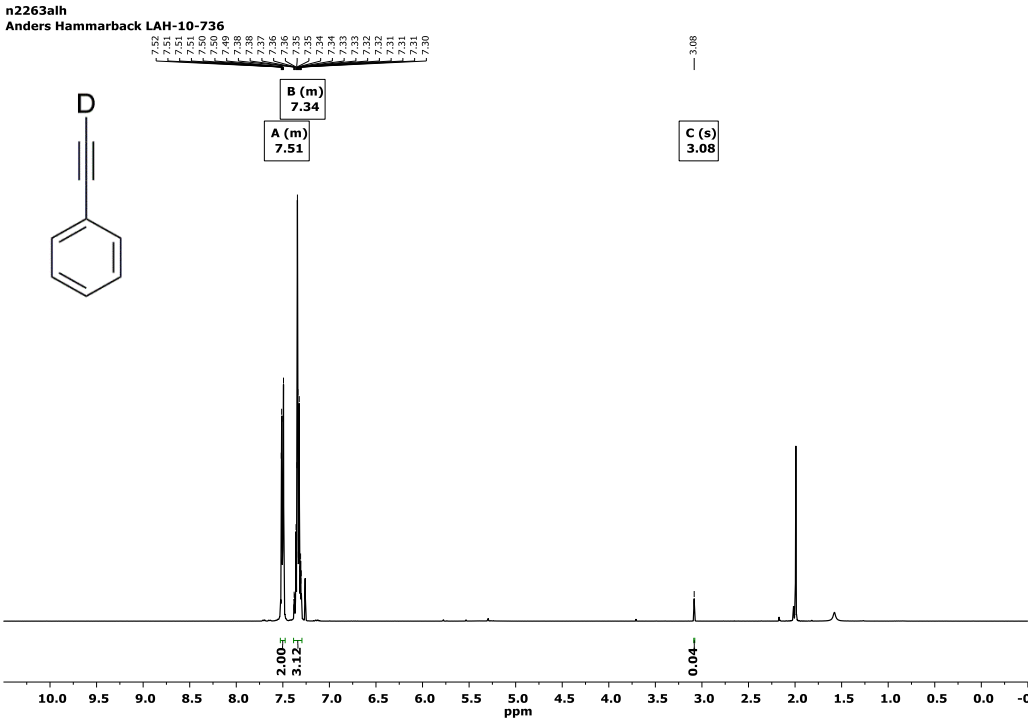

Figure 88. ^{1}H NMR spectrum of **34**-*d* (400 MHz, $CDCl_3$).

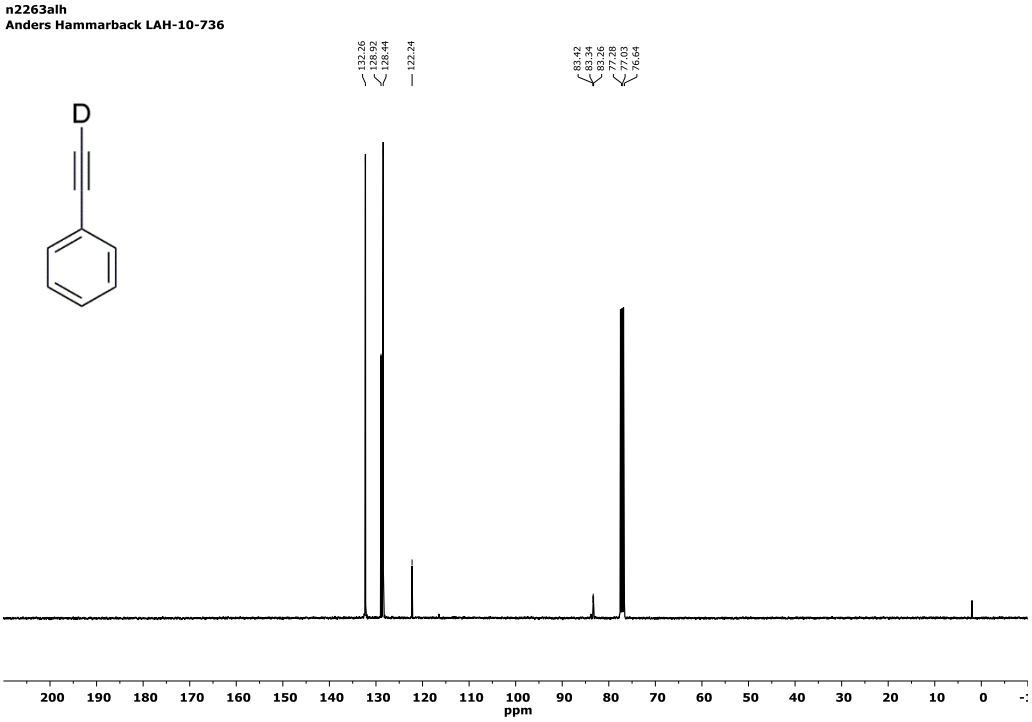

Figure 89. ^{13}C NMR spectrum of **34**-*d* (101 MHz, $CDCl_3$).

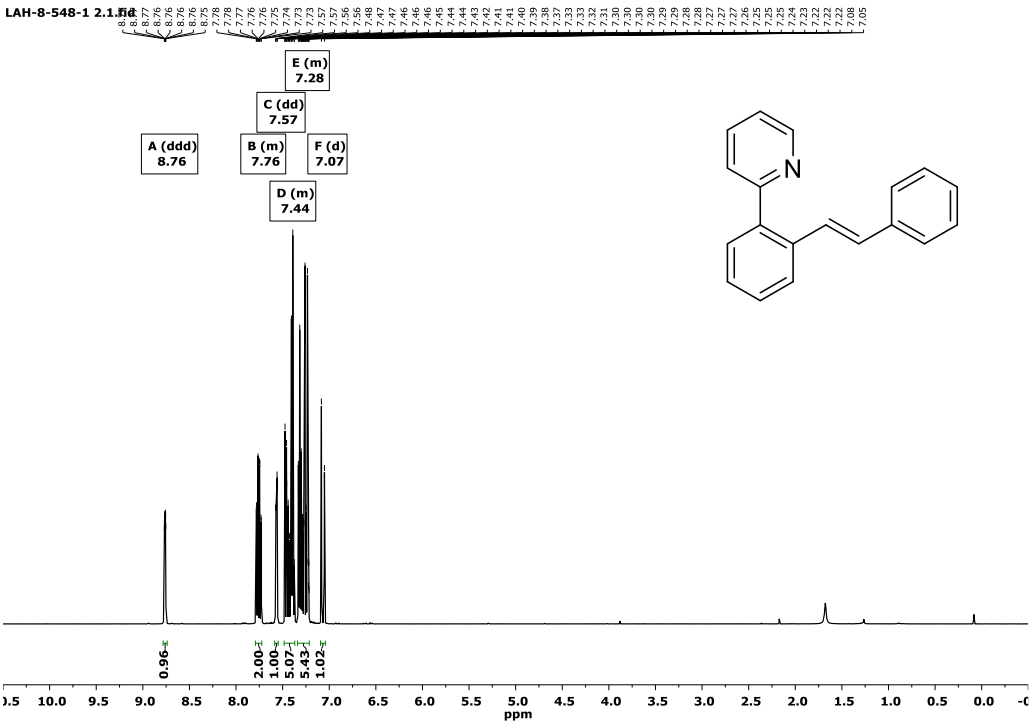

Figure 90. ^{1}H NMR spectrum of **35** (500 MHz, $CDCl_3$).

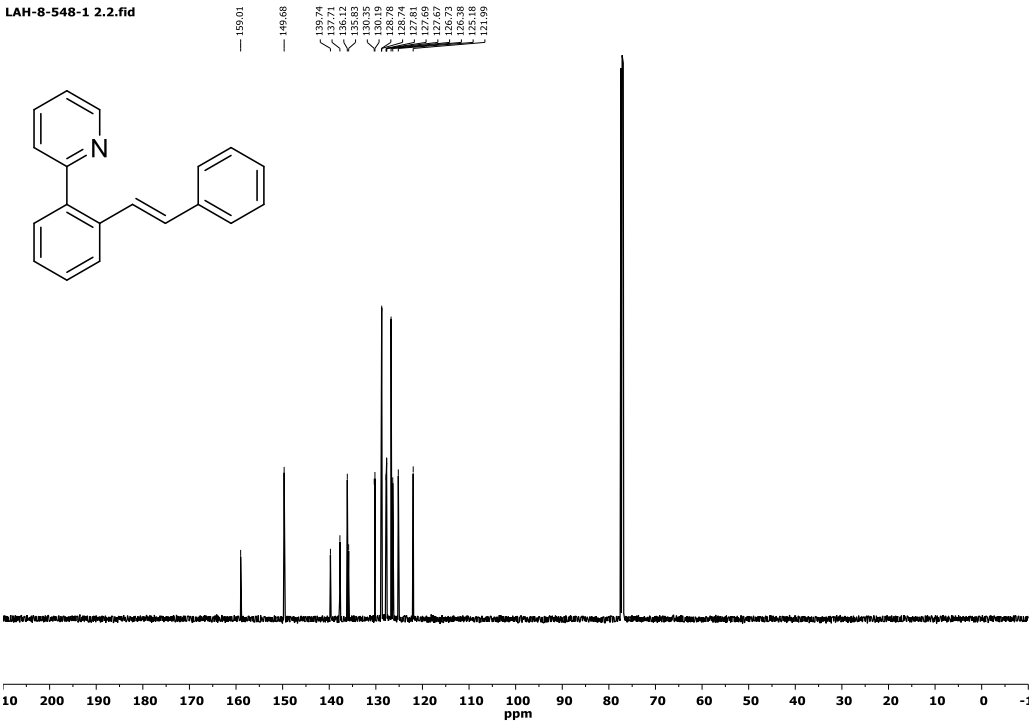

Figure 91. ^{13}C NMR spectrum of **35** (126 MHz, $CDCl_3$).

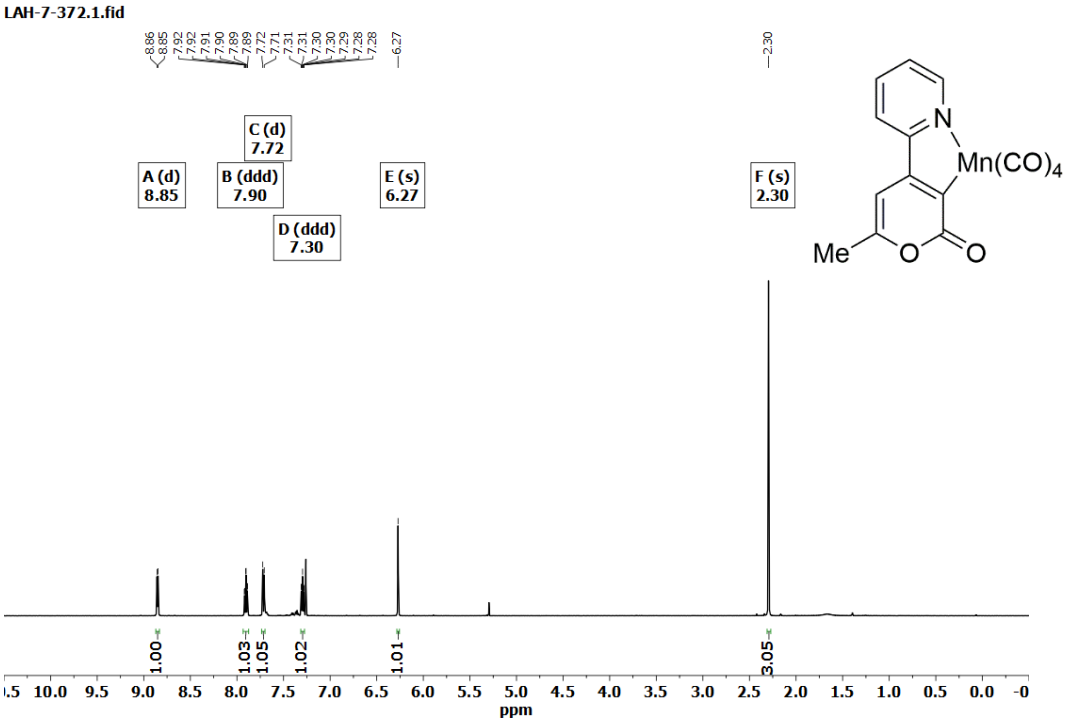

Figure 92. ^{1}H NMR spectrum of **50** (500 MHz, $CDCl_3$).

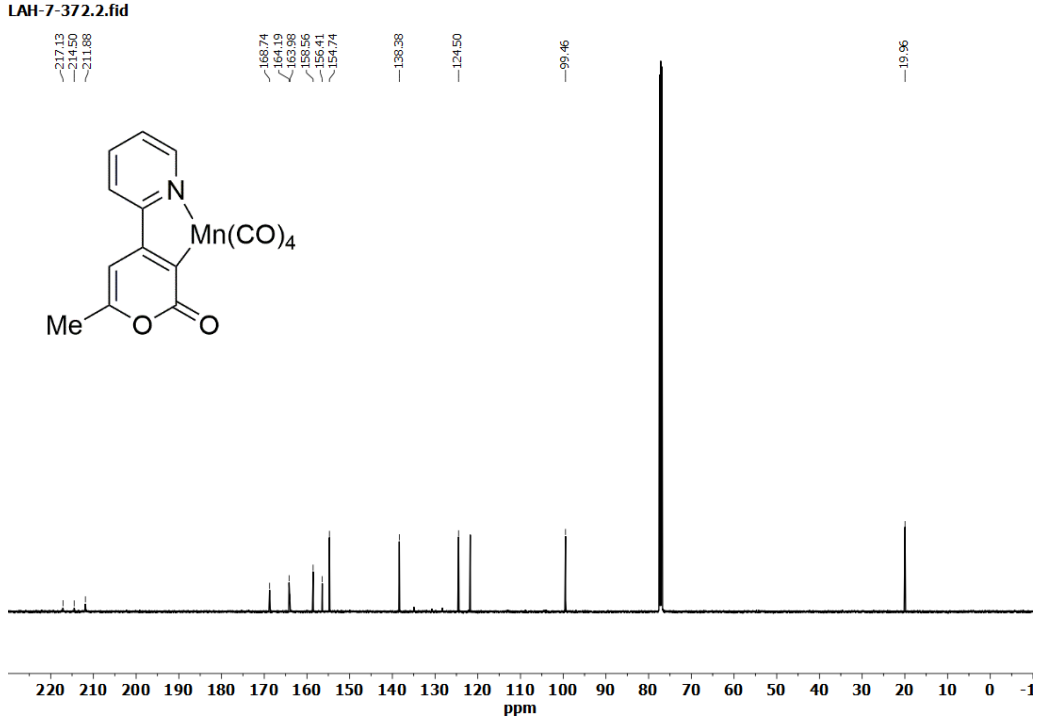

Figure 93. ^{13}C NMR spectrum of **50** (126 MHz, $CDCl_3$).

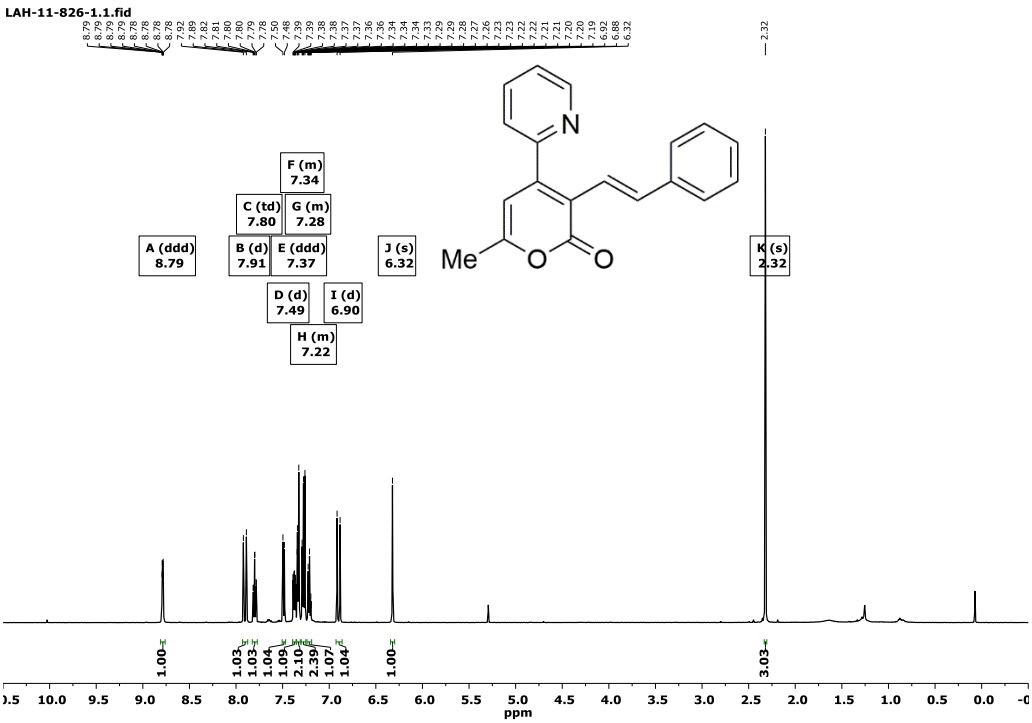

Figure 94. ^{1}H NMR spectrum of **52** (500 MHz, $CDCl_3$).

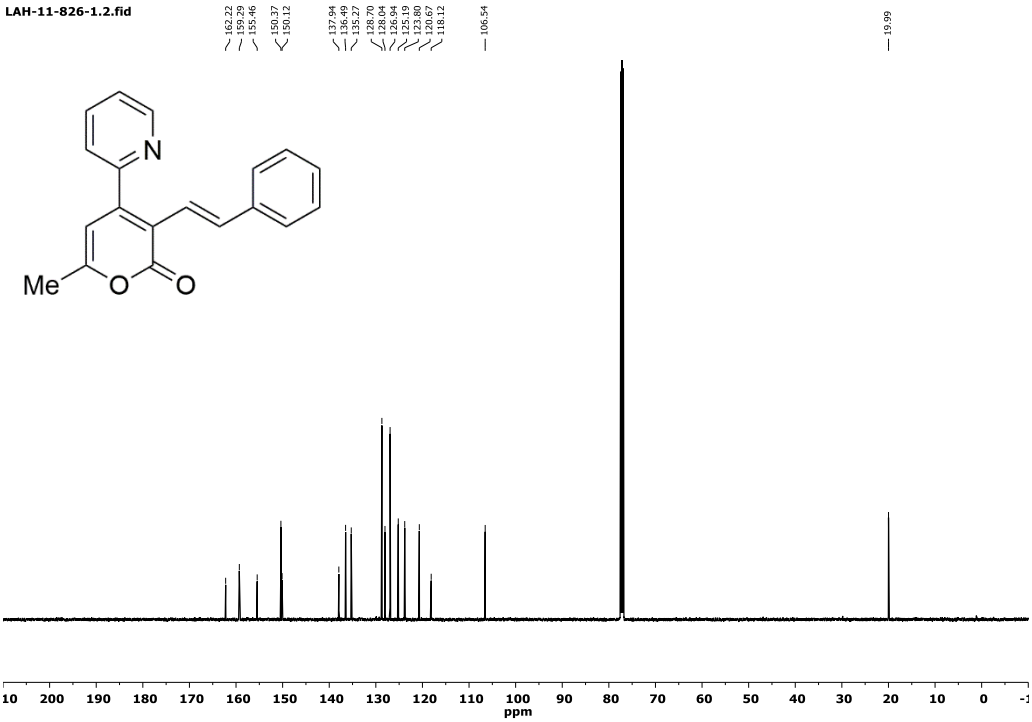

Figure 95. ^{13}C NMR spectrum of **52** (126 MHz, $CDCl_3$).

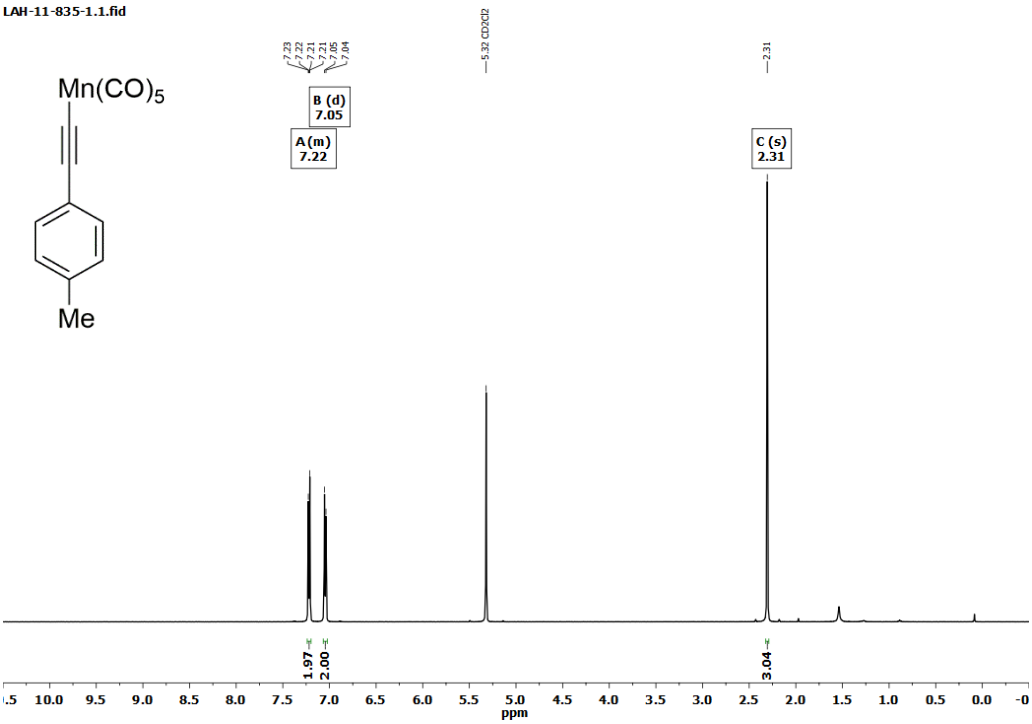

Figure 96. ^{1}H NMR spectrum of **60** (500 MHz, CD_2Cl_2).

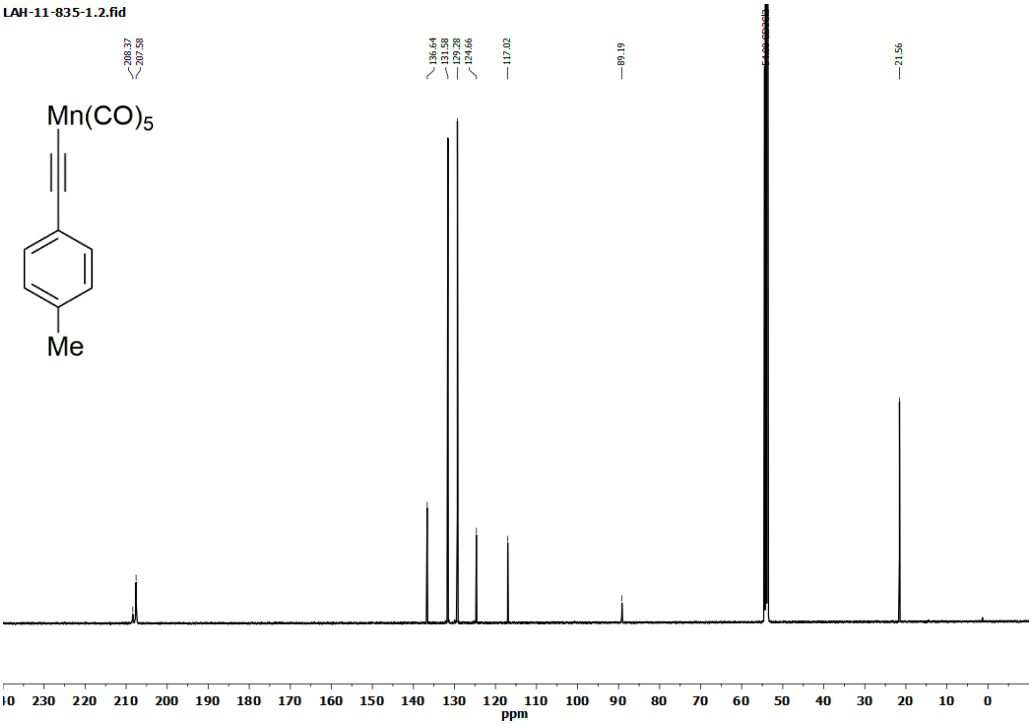

Figure 97. ^{13}C NMR spectrum of **60** (126 MHz, CD_2Cl_2).

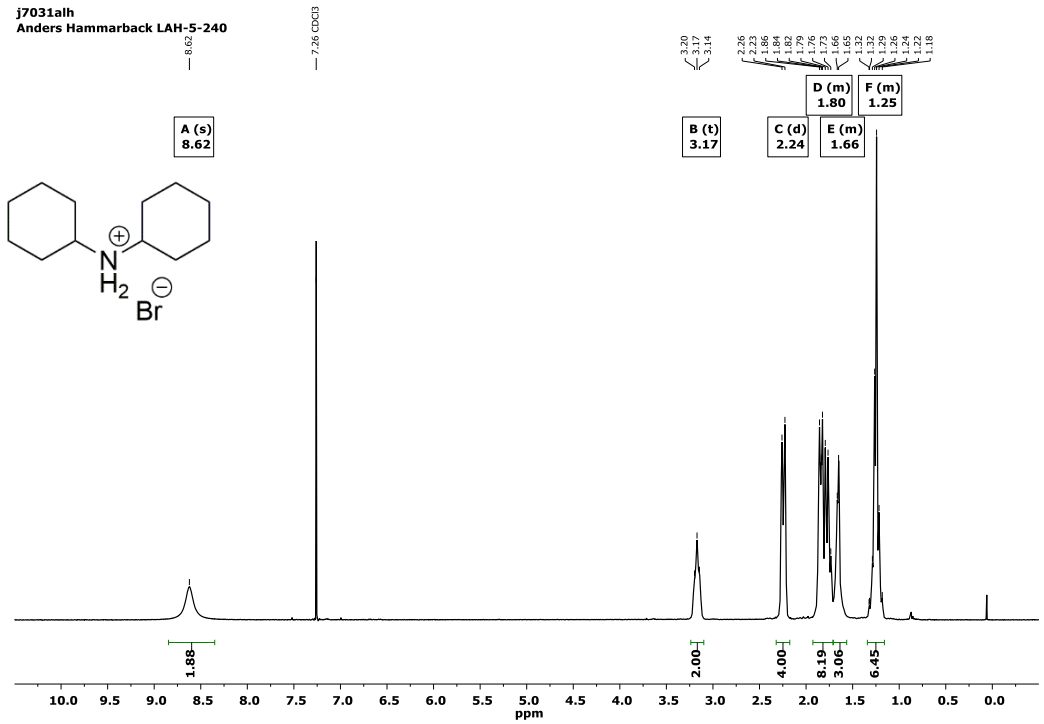

Figure 98. ^{1}H NMR spectrum of **62** (400 MHz, $CDCl_3$).

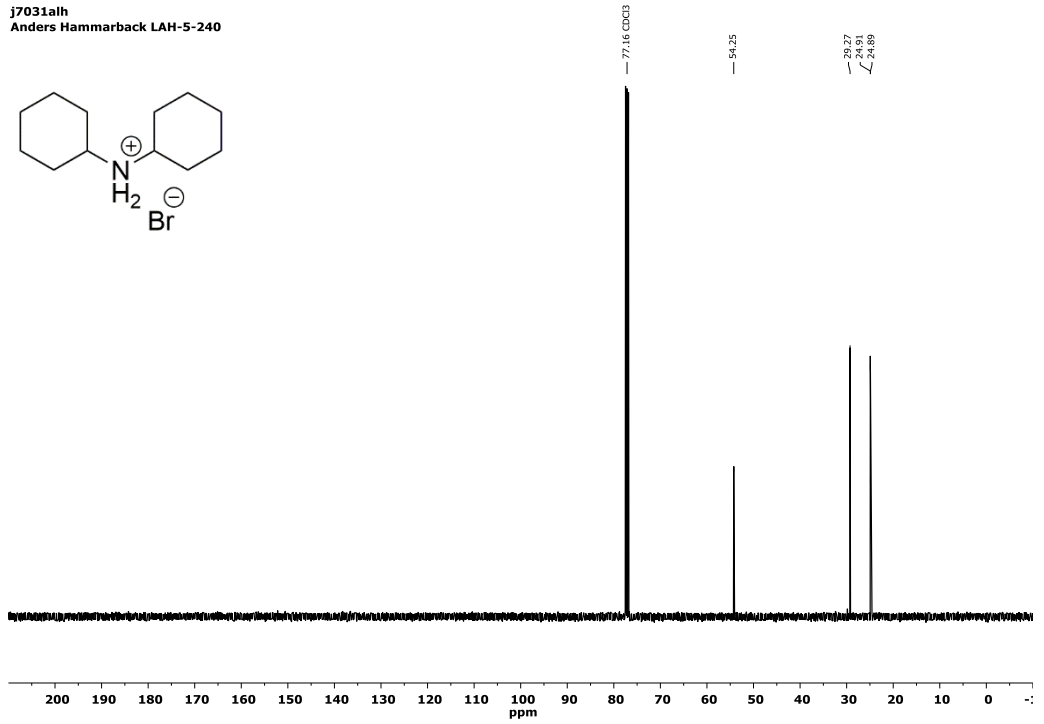

Figure 99. ^{13}C NMR spectrum of **62** (101 MHz, $CDCl_3$).

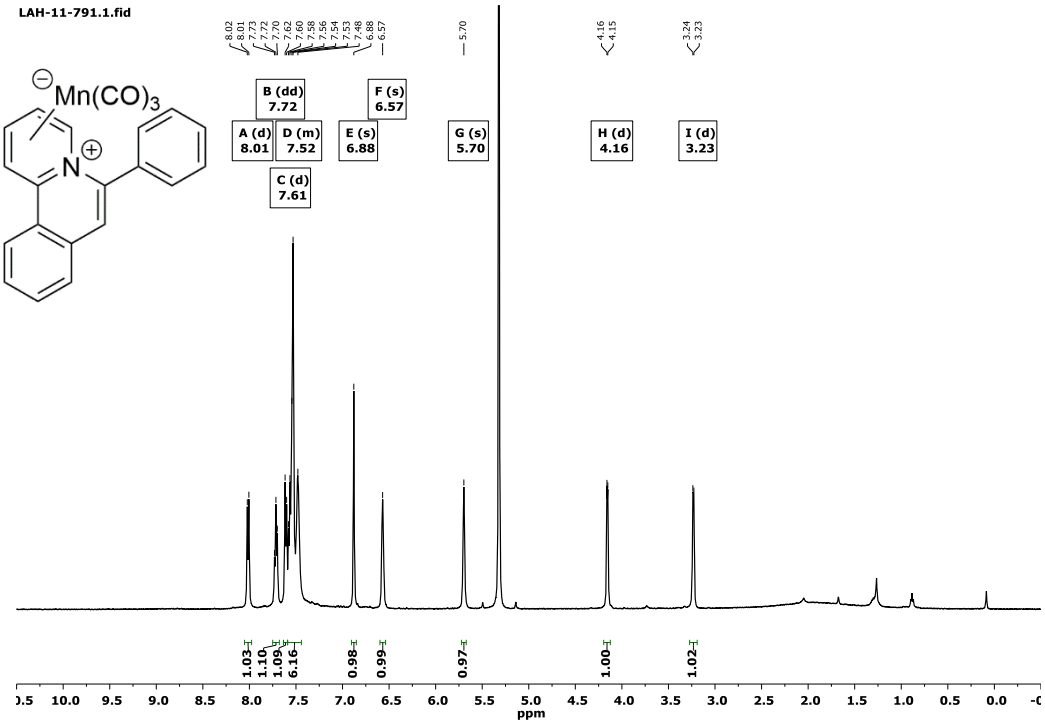

Figure 100. ^{1}H NMR spectrum of **75** (500 MHz, CD_2Cl_2).

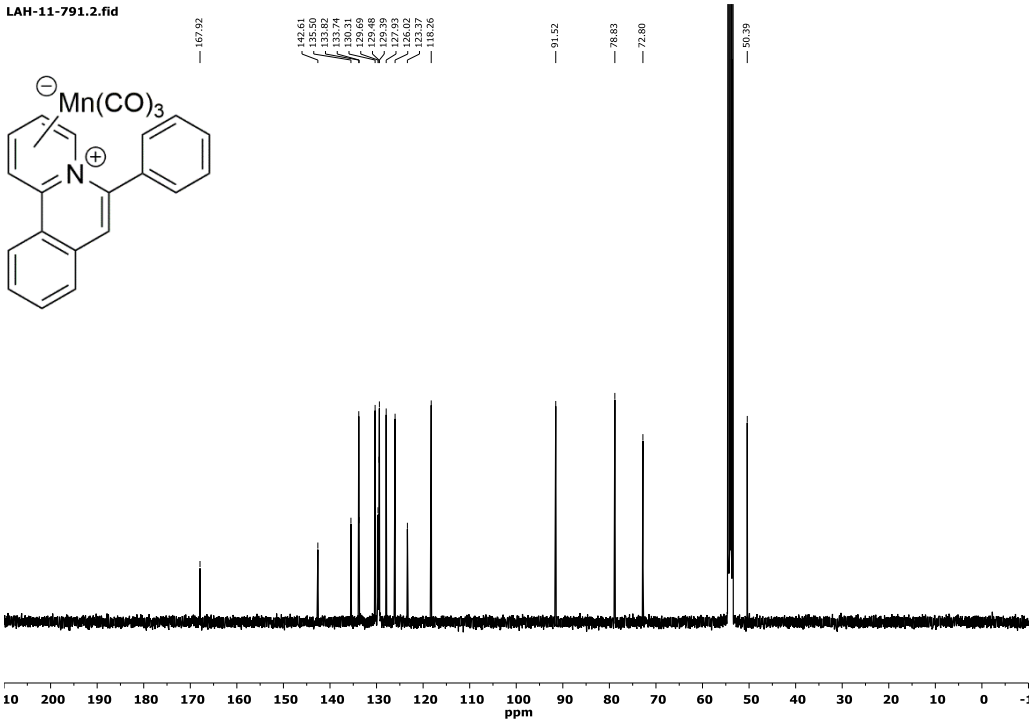

Figure 101. ^{13}C NMR spectrum of **75** (126 MHz, CD_2Cl_2).

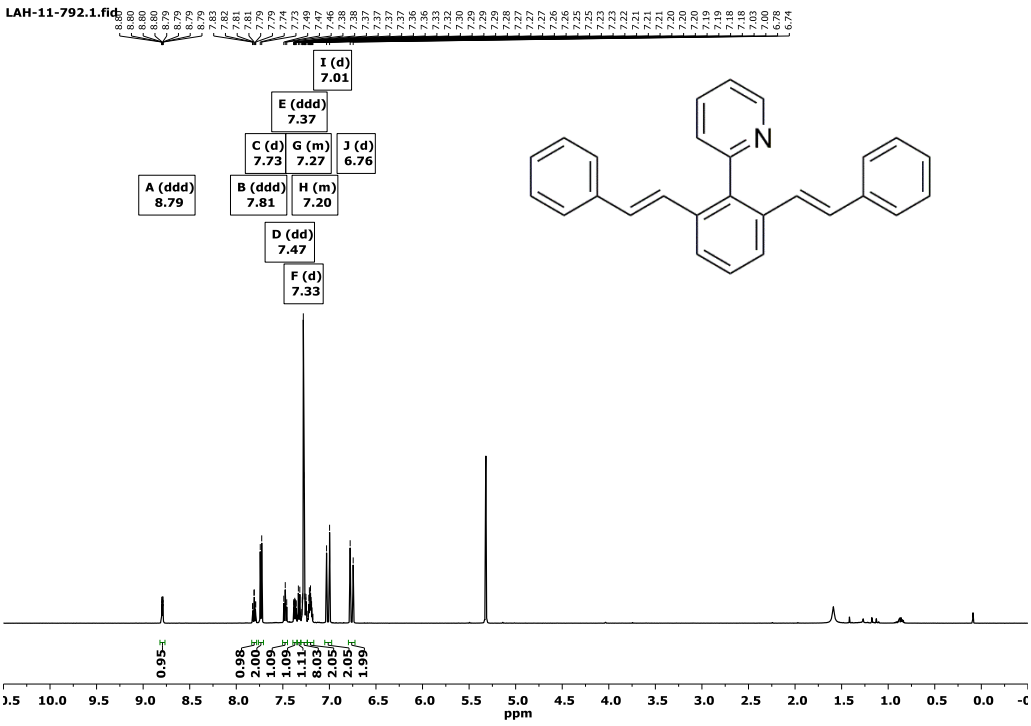

Figure 102. ^{1}H NMR spectrum of **76** (500 MHz, CD_2Cl_2).

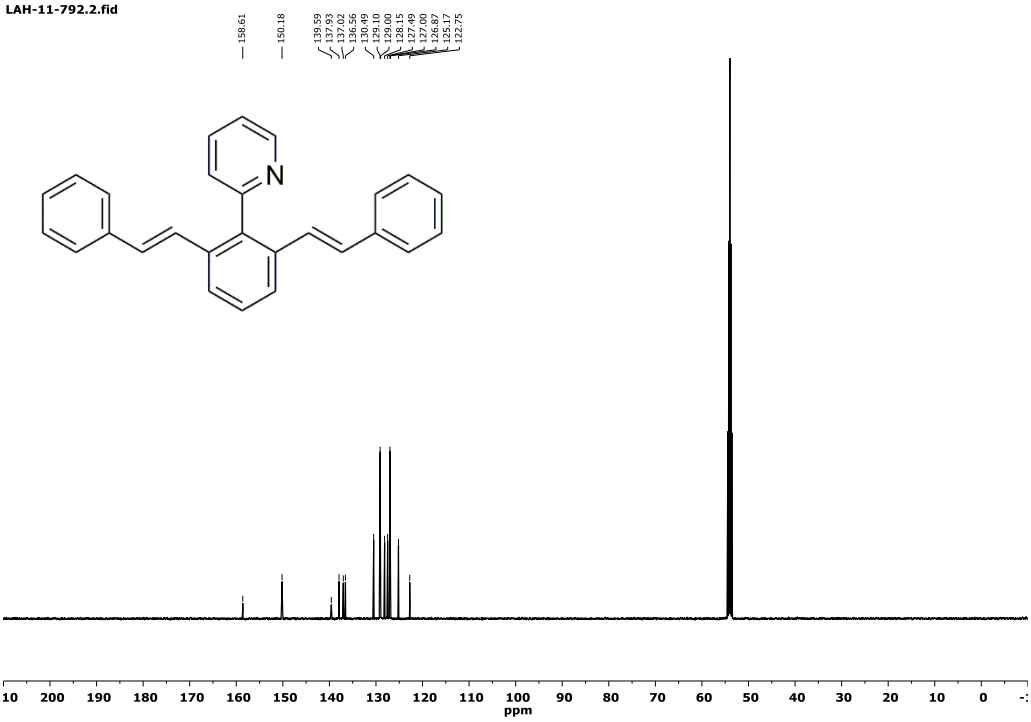

Figure 103. ^{13}C NMR spectrum of **76** (126 MHz, CD_2Cl_2).

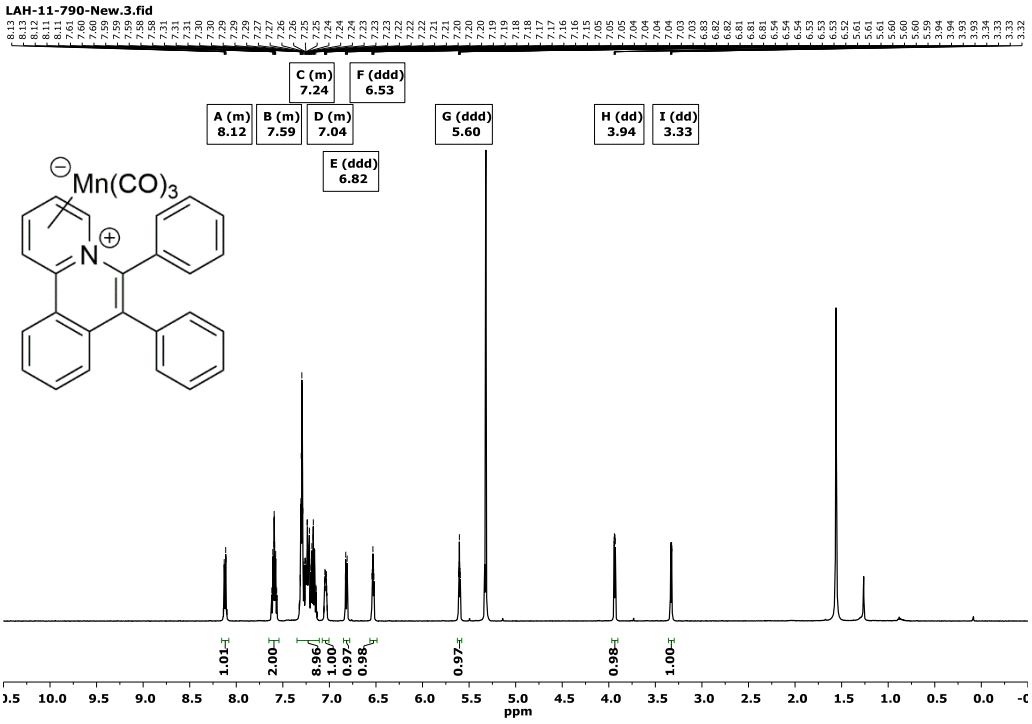

Figure 104. ^{1}H NMR spectrum of **86** (500 MHz, CD_2Cl_2).

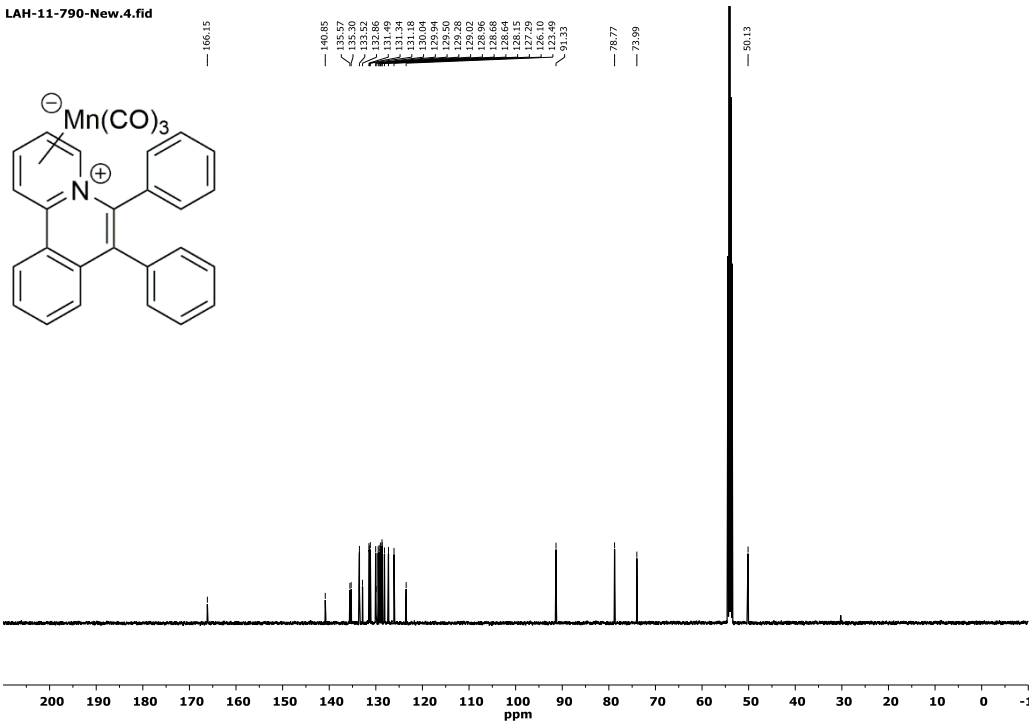

Figure 105. ^{13}C NMR spectrum of **86** (126 MHz, CD_2Cl_2).

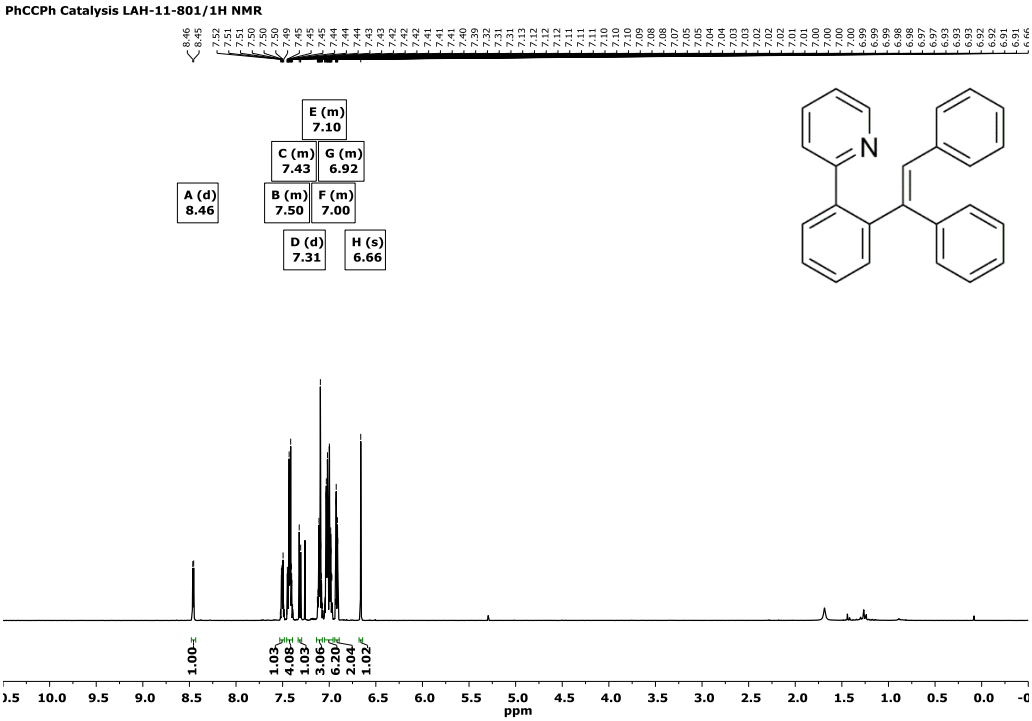

Figure 106. ^{1}H NMR spectrum of **89** (500 MHz, $CDCl_3$).

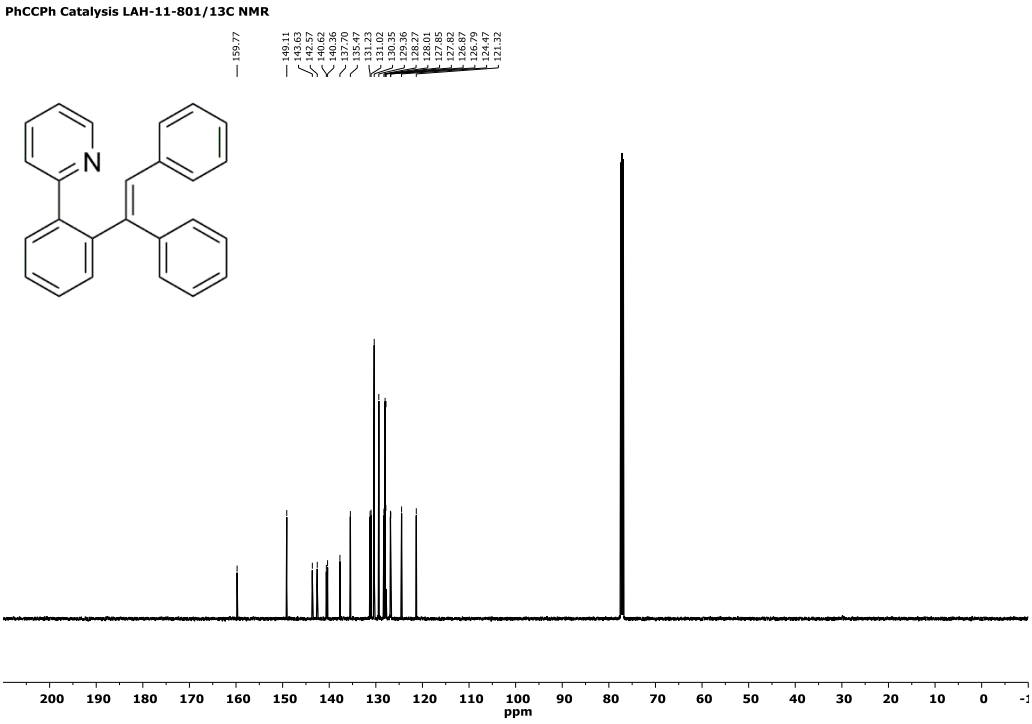

Figure 107. ^{13}C NMR spectrum of **89** (126 MHz, $CDCl_3$).

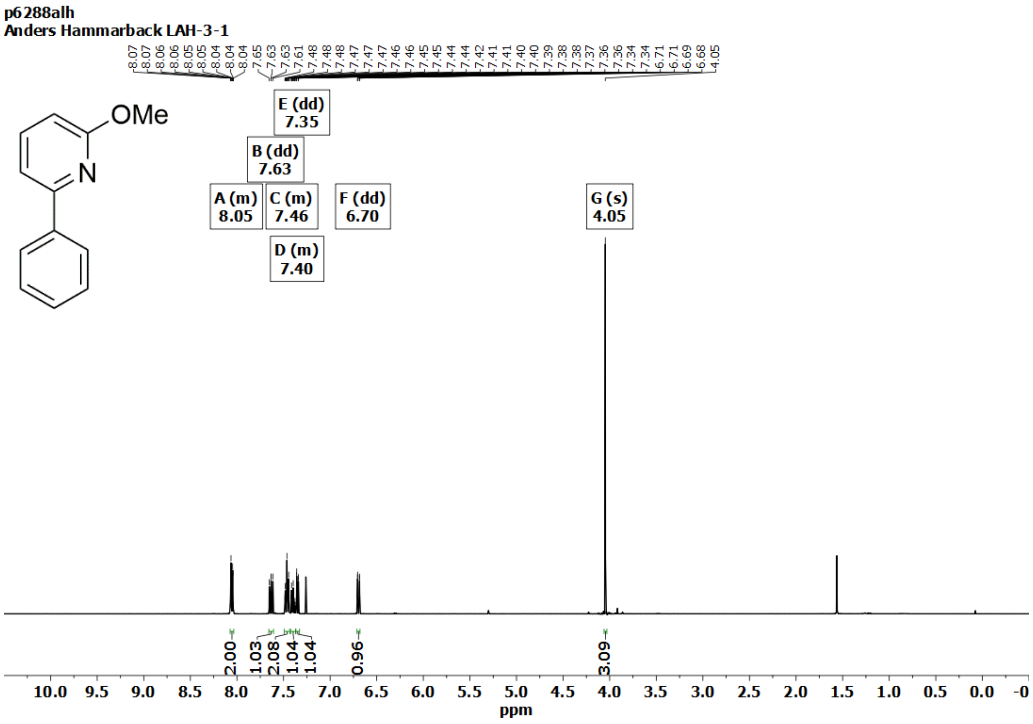

Figure 108. ^{1}H NMR spectrum of **131** (400 MHz, $CDCl_3$).

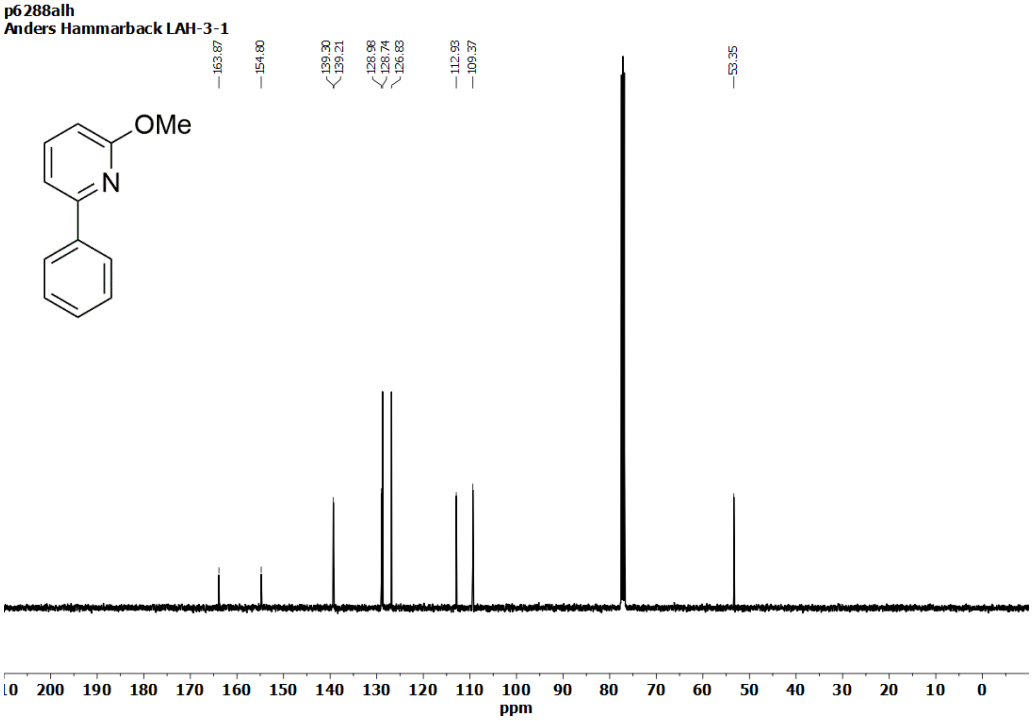

Figure 109. ^{13}C NMR spectrum of **131** (101 MHz, $CDCl_3$).

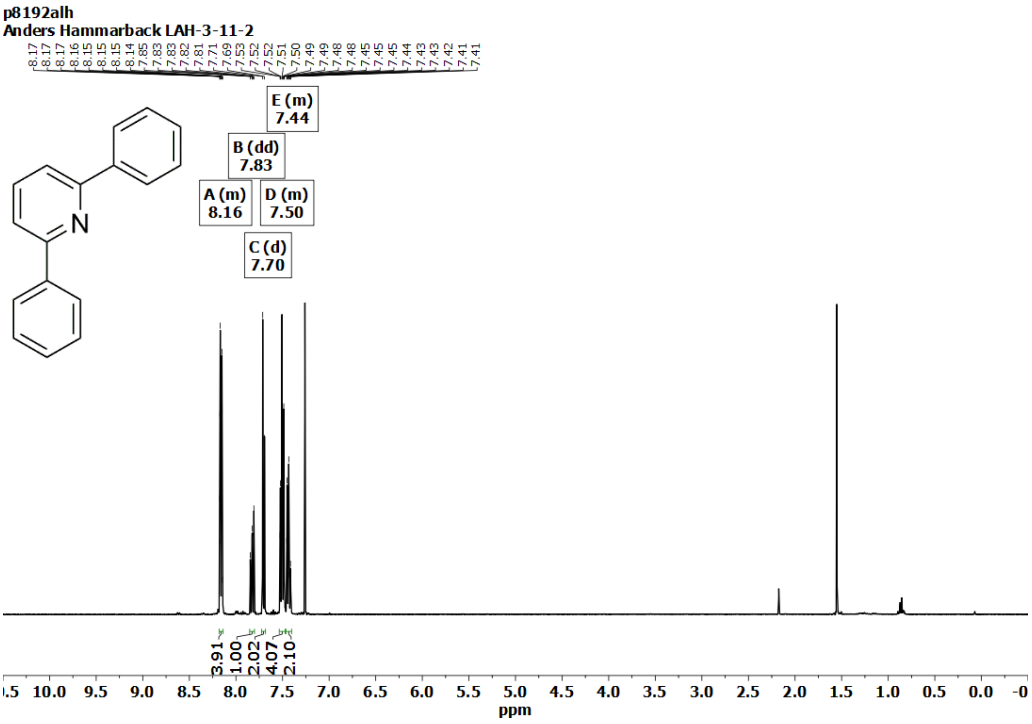

Figure 110. ^{1}H NMR spectrum of **132** (400 MHz, $CDCl_3$).

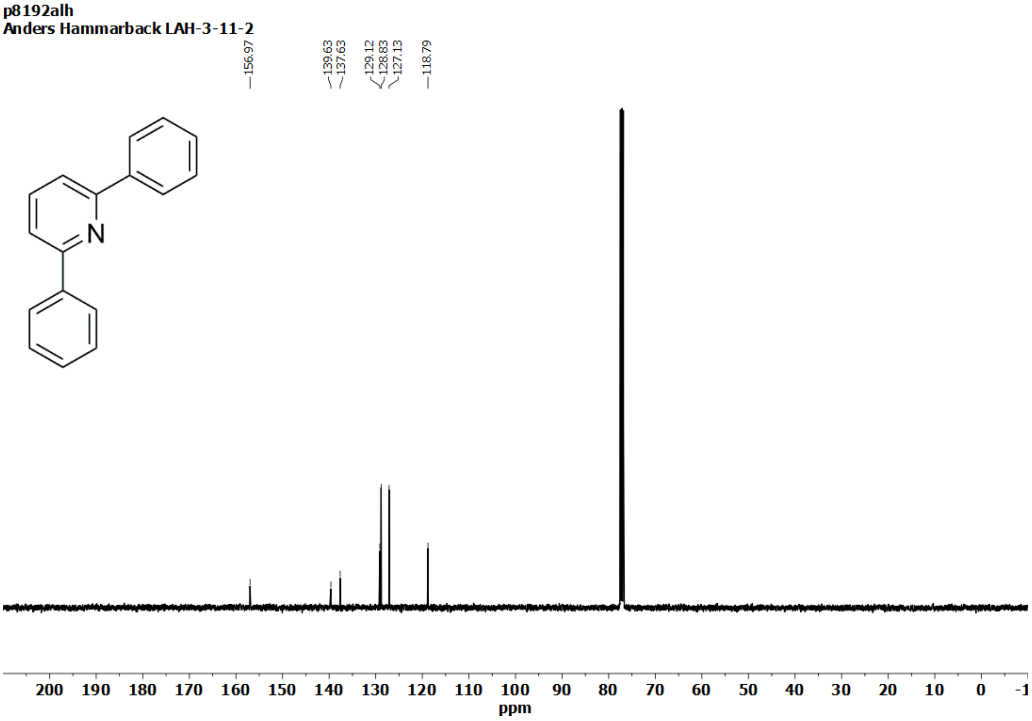

Figure 111. ^{13}C NMR spectrum of **132** (101 MHz, $CDCl_3$).

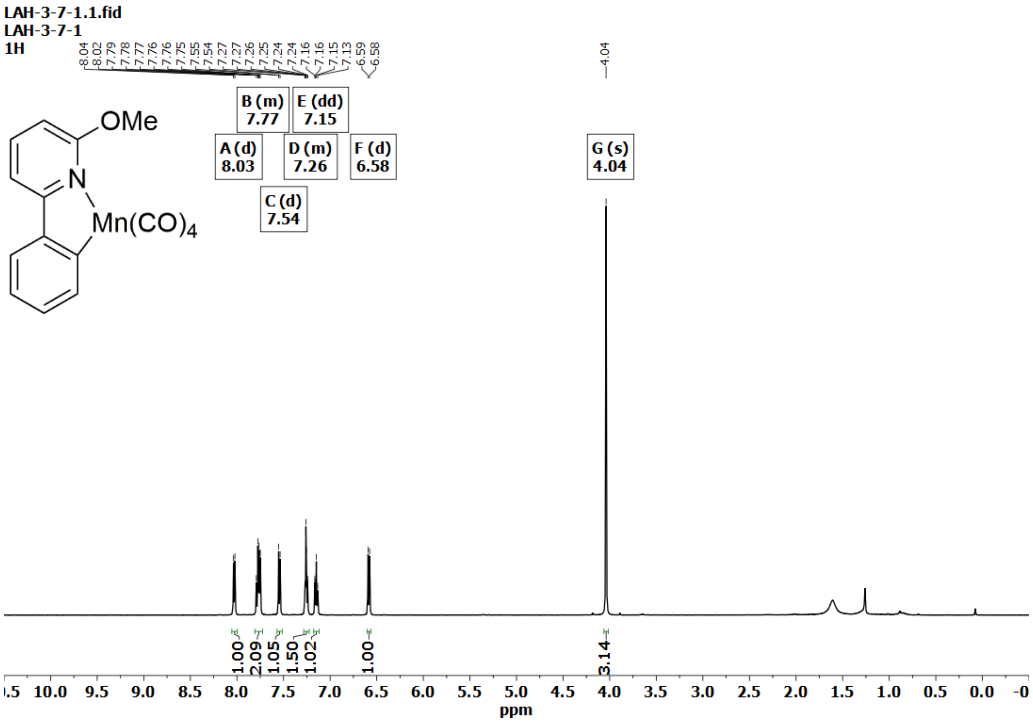

Figure 112. ^{1}H NMR spectrum of **133** (500 MHz, $CDCl_3$).

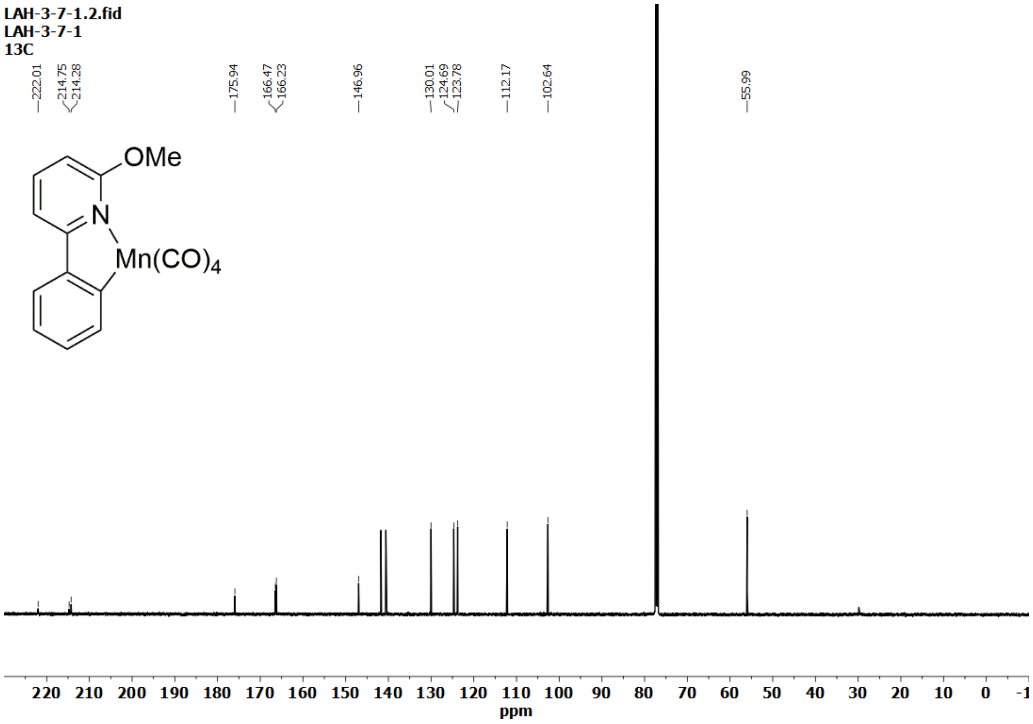

Figure 113. ^{13}C NMR spectrum of **133** (126 MHz, $CDCl_3$).

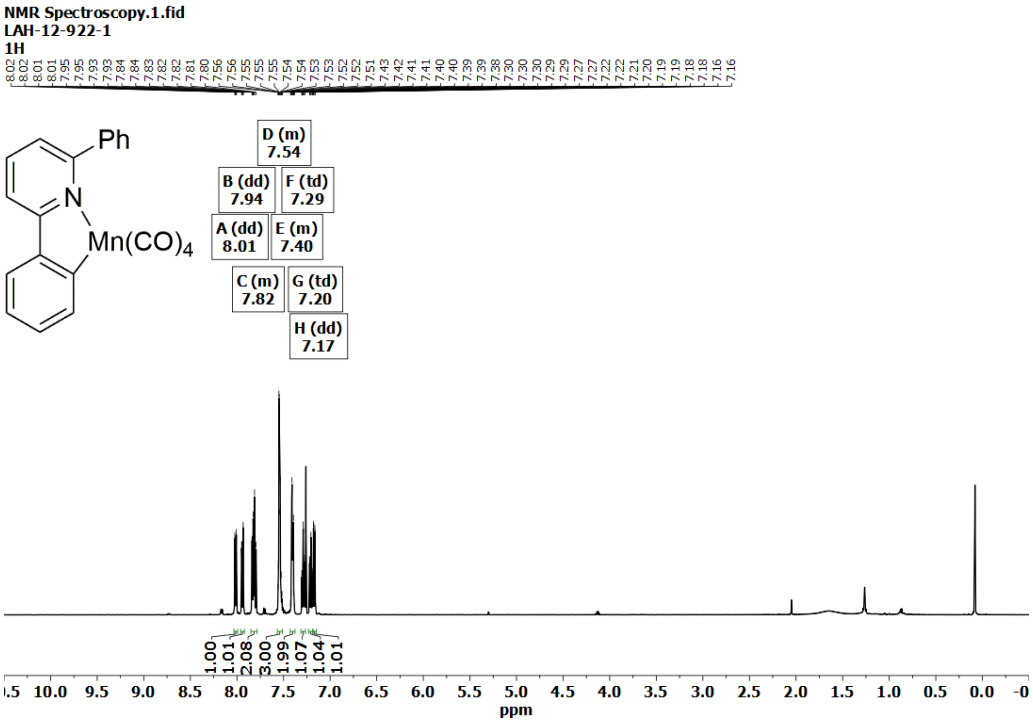

Figure 114. ^{1}H NMR spectrum of **134** (500 MHz, $CDCl_3$).

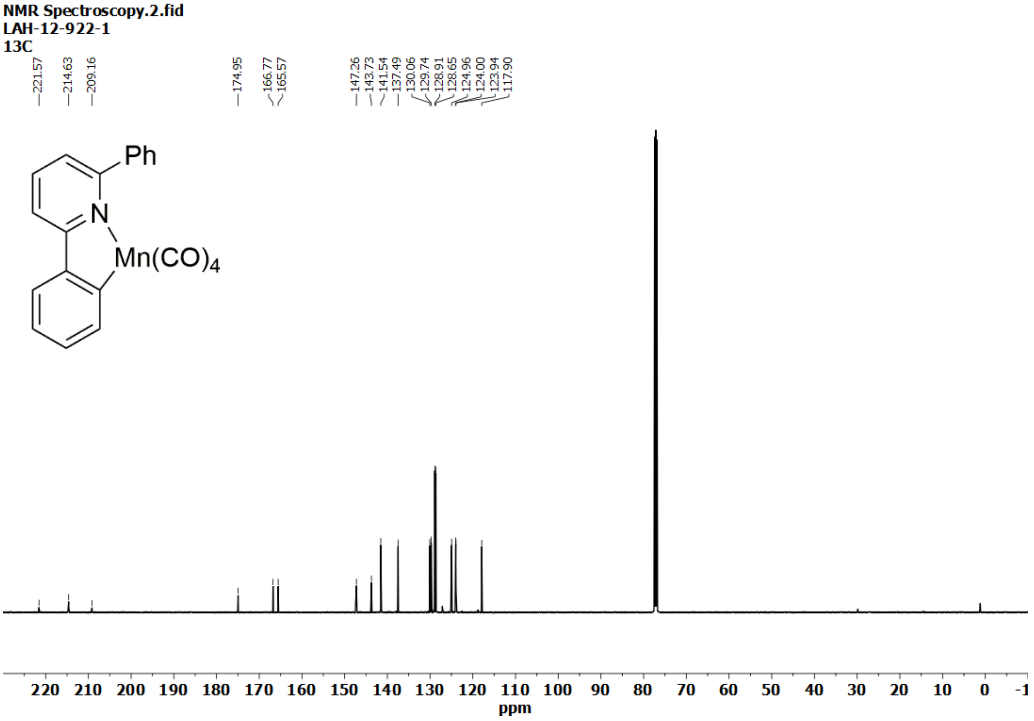

Figure 115. ^{13}C NMR spectrum of **134** (126 MHz, $CDCl_3$).

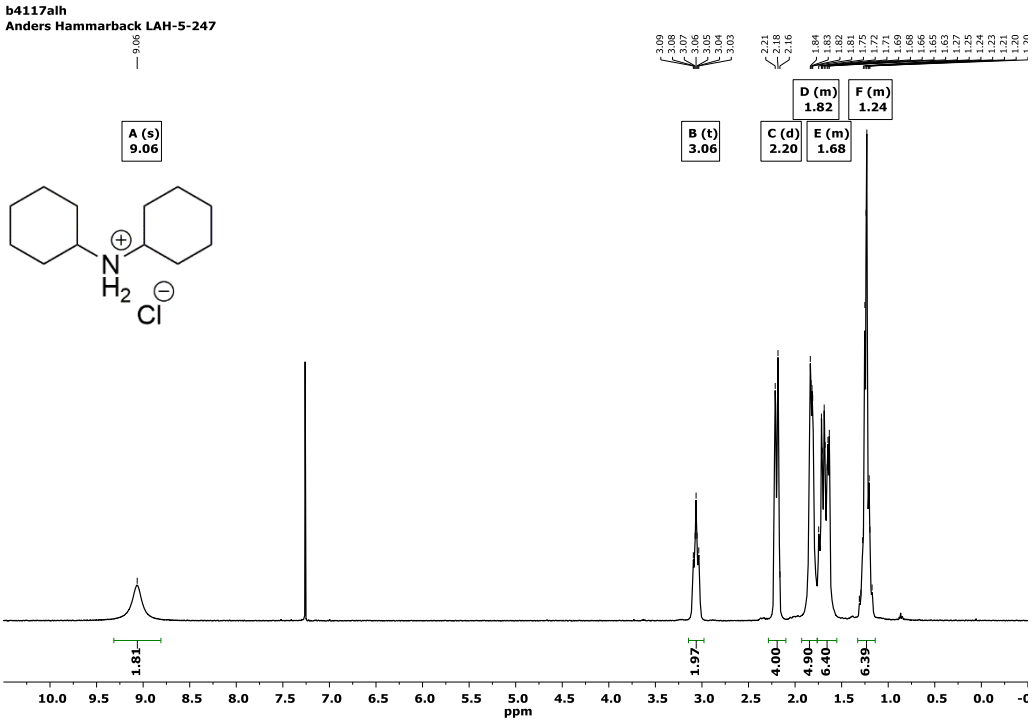

Figure 116. ^{1}H NMR spectrum of **171** (400 MHz, $CDCl_3$).

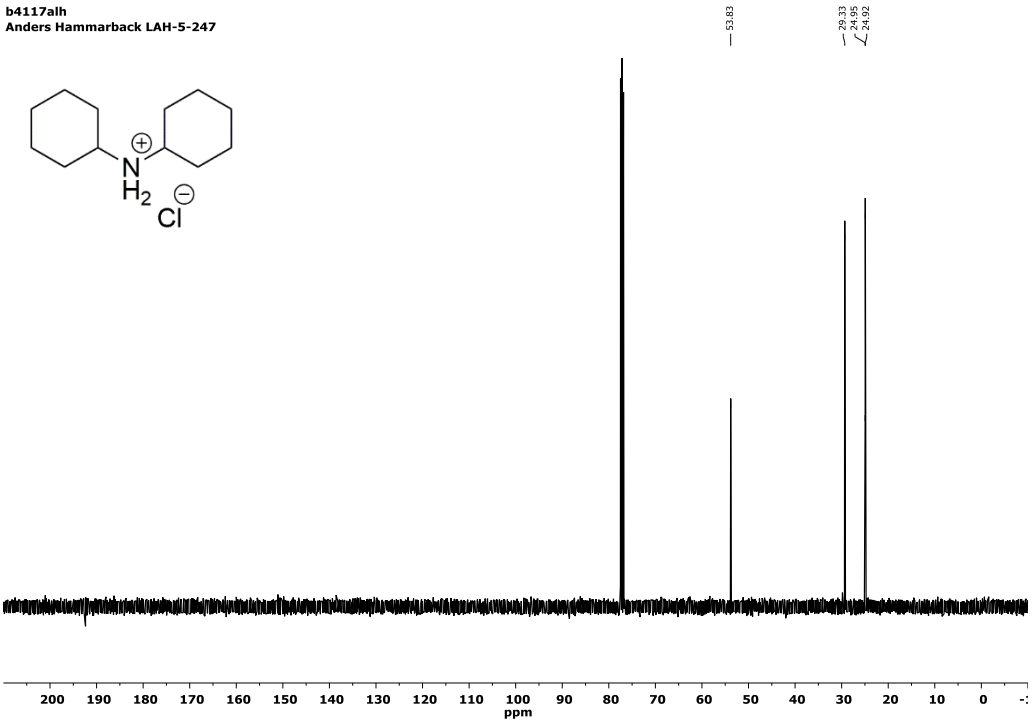

Figure 117. ^{13}C NMR spectrum of **171** (101 MHz, $CDCl_3$).

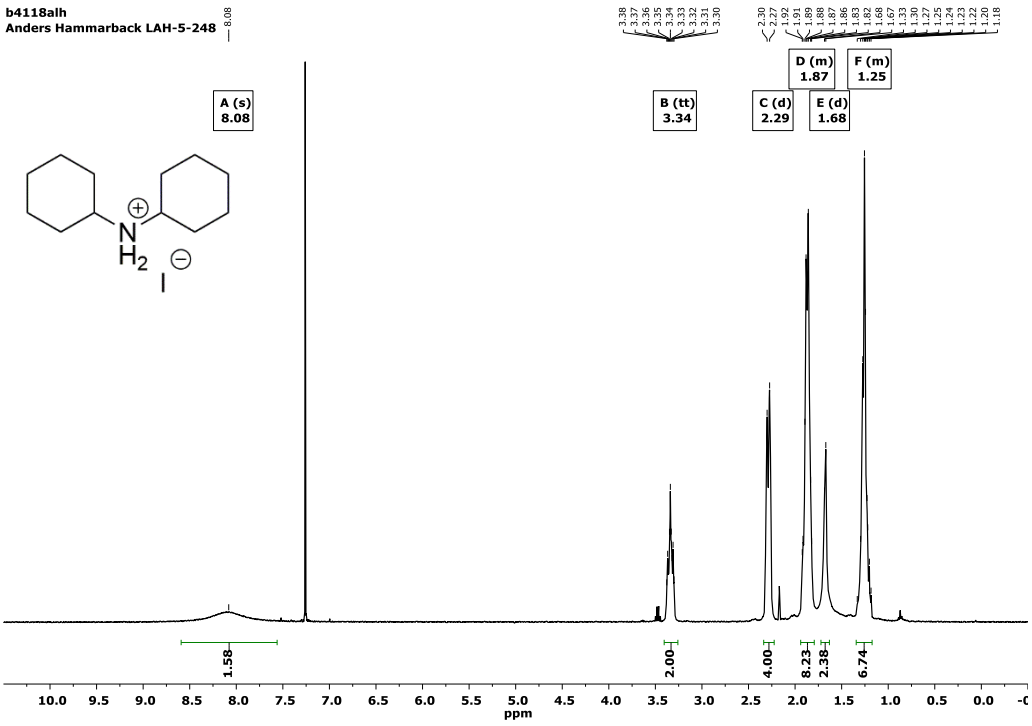

Figure 118. ^{1}H NMR spectrum of **172** (400 MHz, $CDCl_3$).

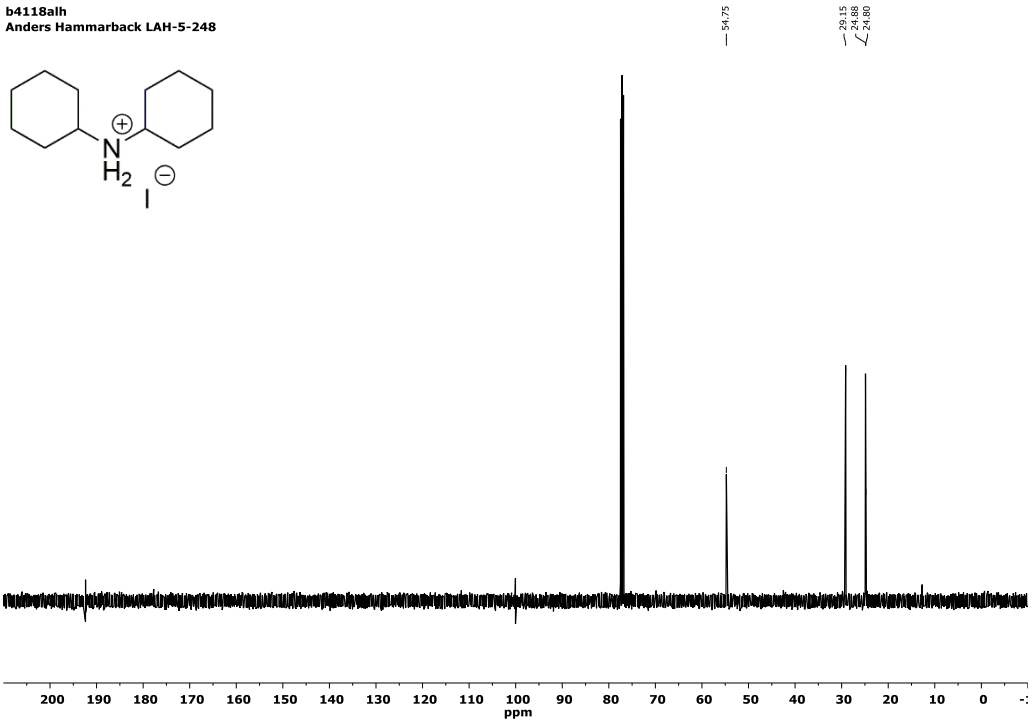

Figure 119. ^{13}C NMR spectrum of **172** (101 MHz, $CDCl_3$).

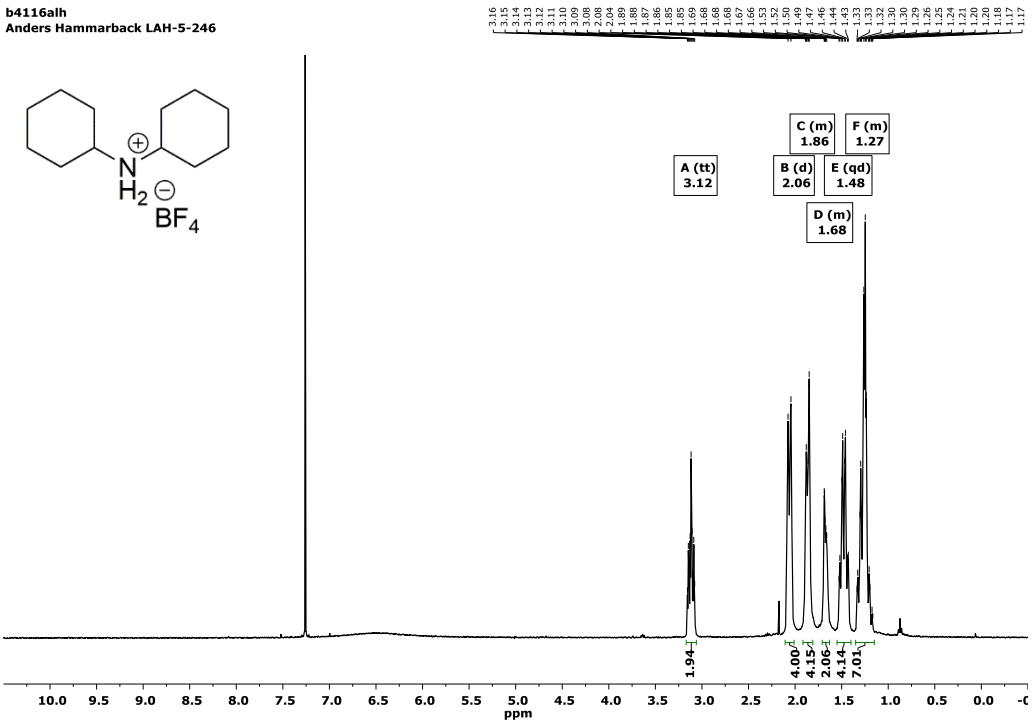

Figure 120. ^{1}H NMR spectrum of **173** (400 MHz, $CDCl_3$).

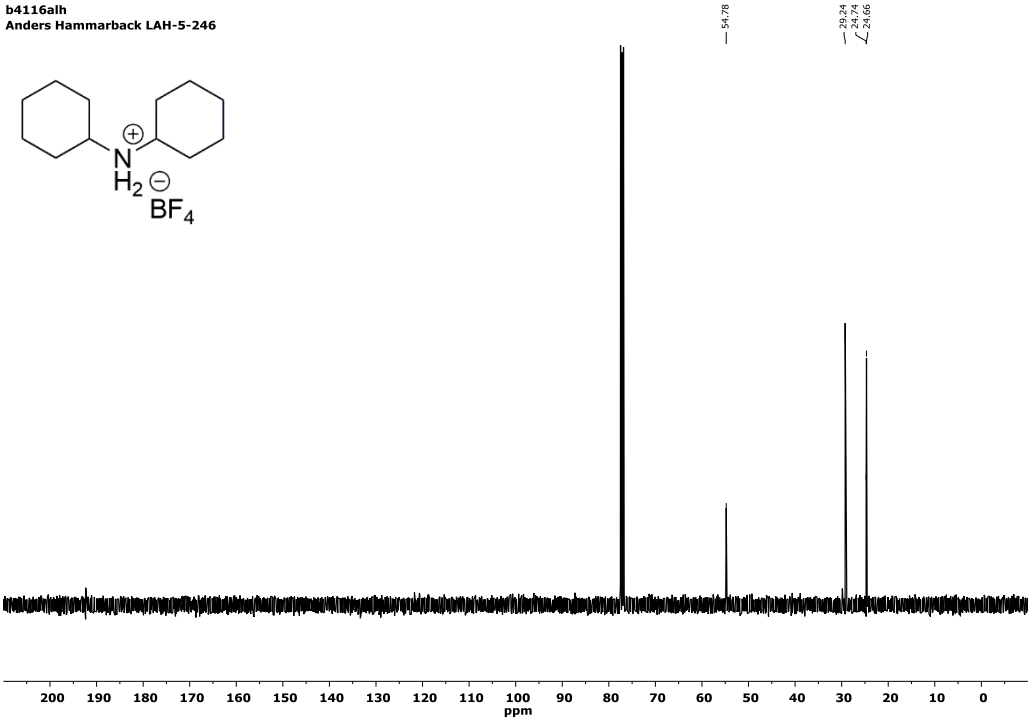

Figure 121. ^{13}C NMR spectrum of **173** (101 MHz, $CDCl_3$).

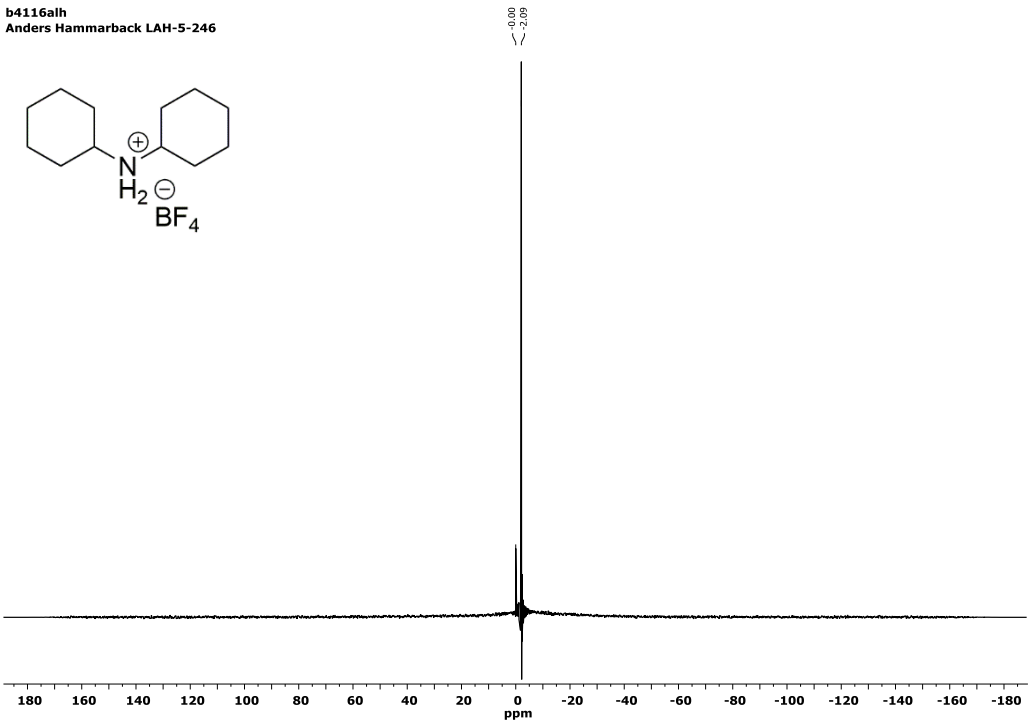

Figure 122. ^{11}B NMR spectrum of **173** (128 MHz, $CDCl_3$).

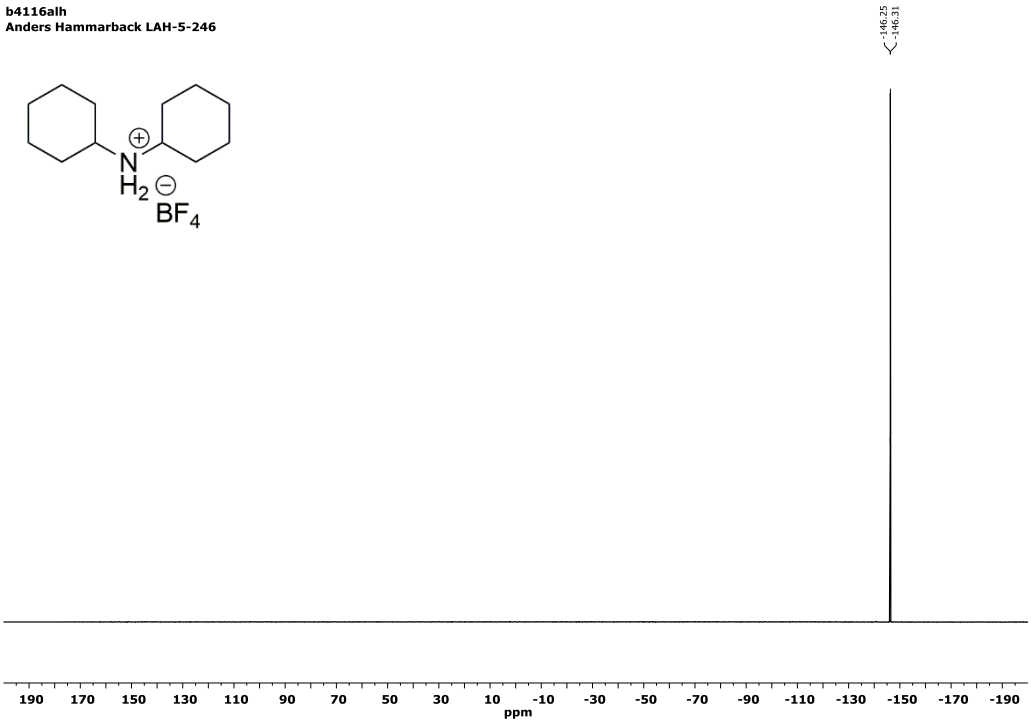

Figure 123. ^{19}F NMR spectrum of **173** (376 MHz, $CDCl_3$).

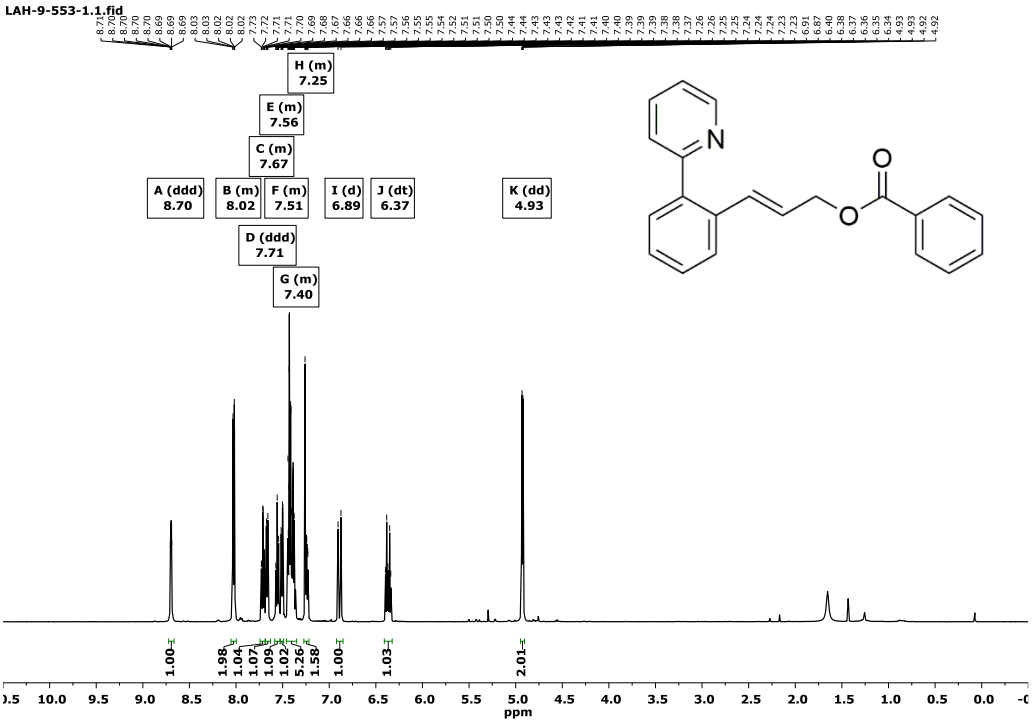

Figure 124. ^{1}H NMR spectrum of **174** (500 MHz, $CDCl_3$).

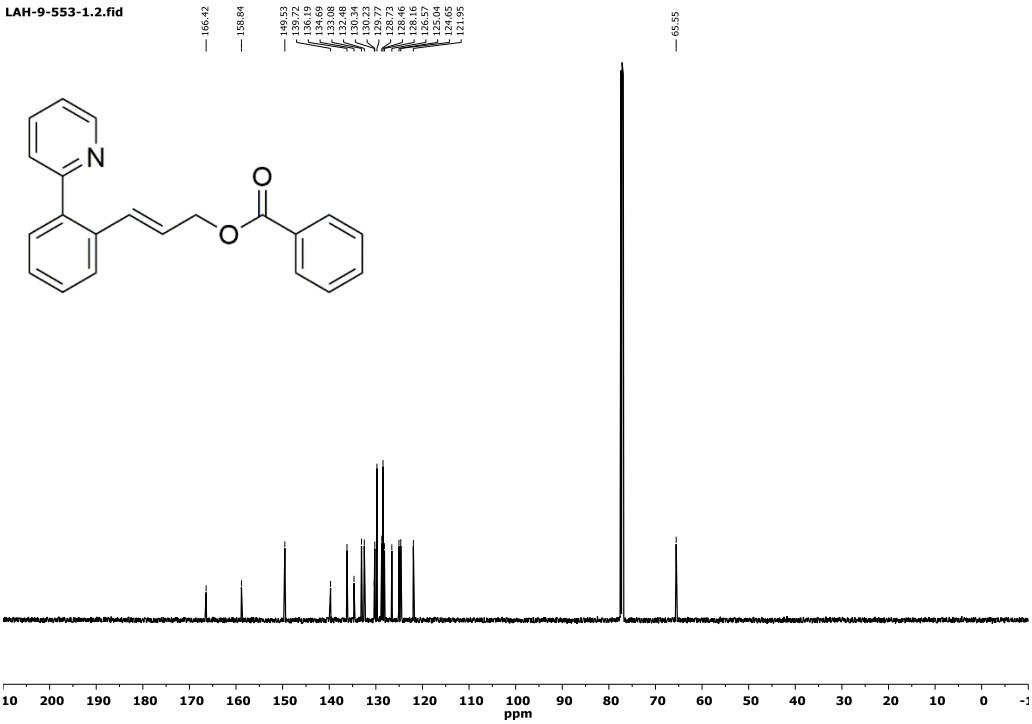

Figure 125. ^{13}C NMR spectrum of **174** (126 MHz, $CDCl_3$).

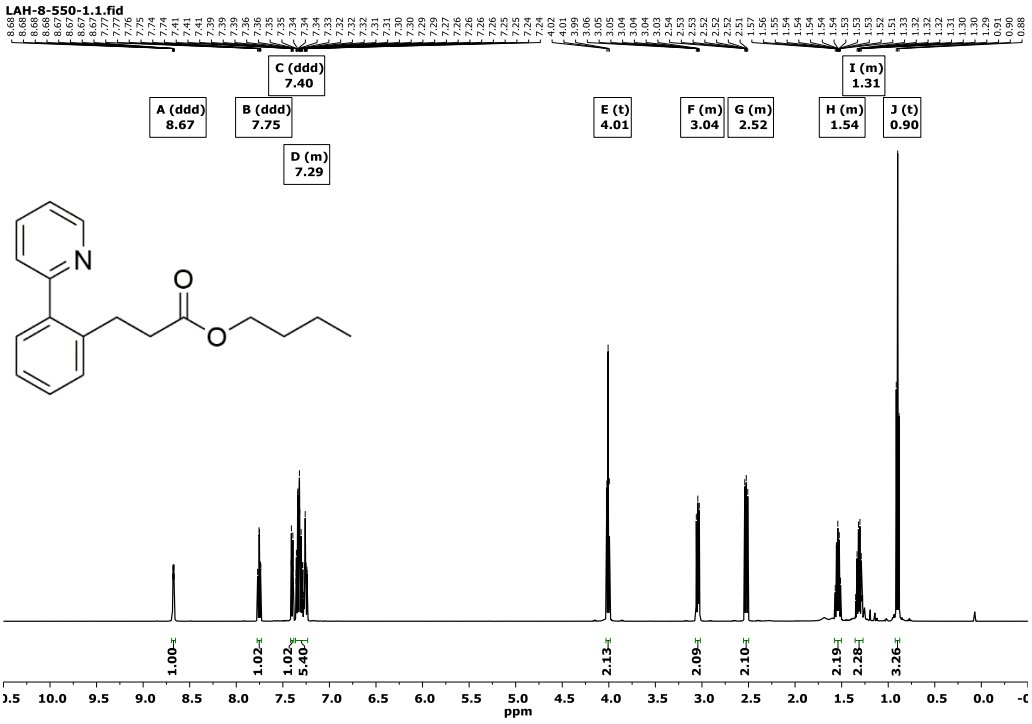

Figure 126. ^{1}H NMR spectrum of **175** (500 MHz, $CDCl_3$).

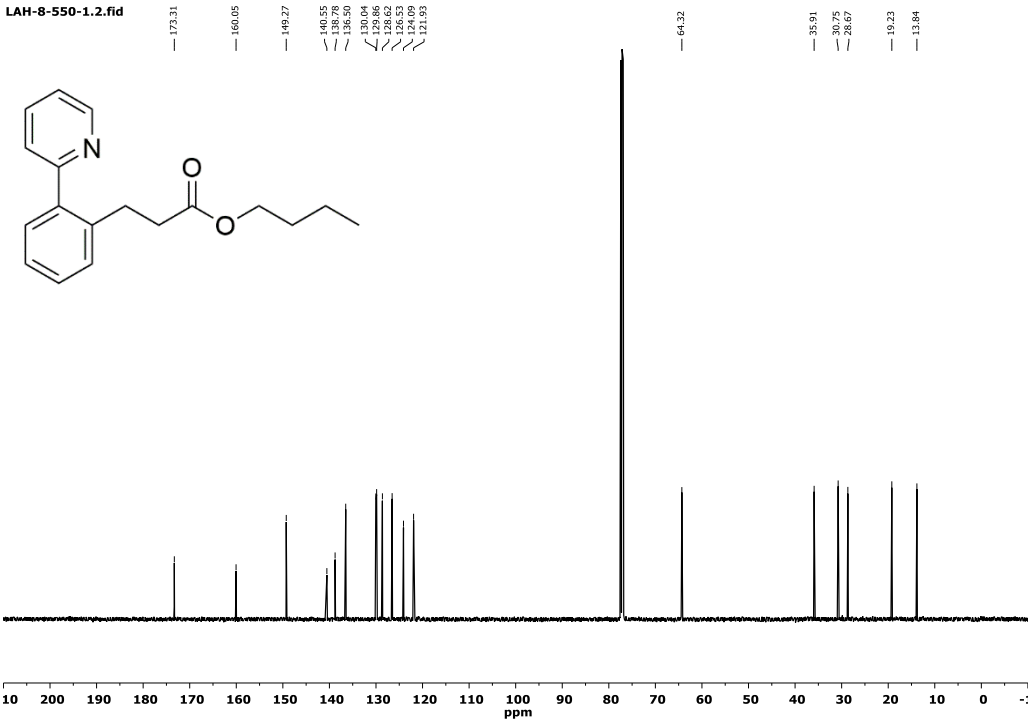

Figure 127. ^{13}C NMR spectrum of **175** (126 MHz, $CDCl_3$).

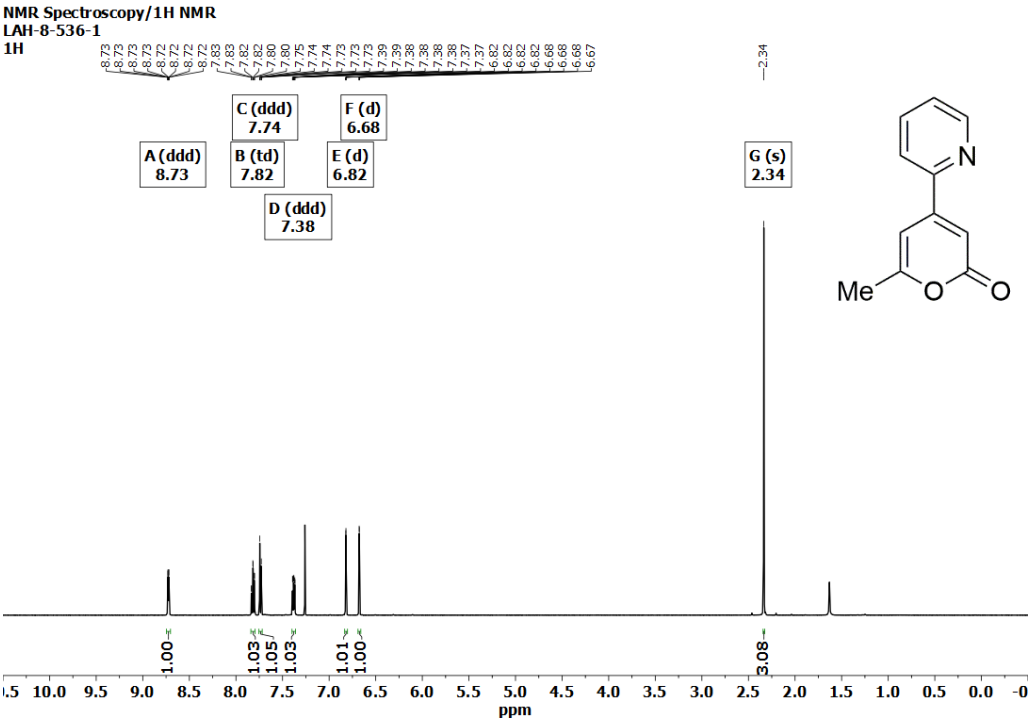

Figure 128. ^{1}H NMR spectrum of **176** (500 MHz, $CDCl_3$).

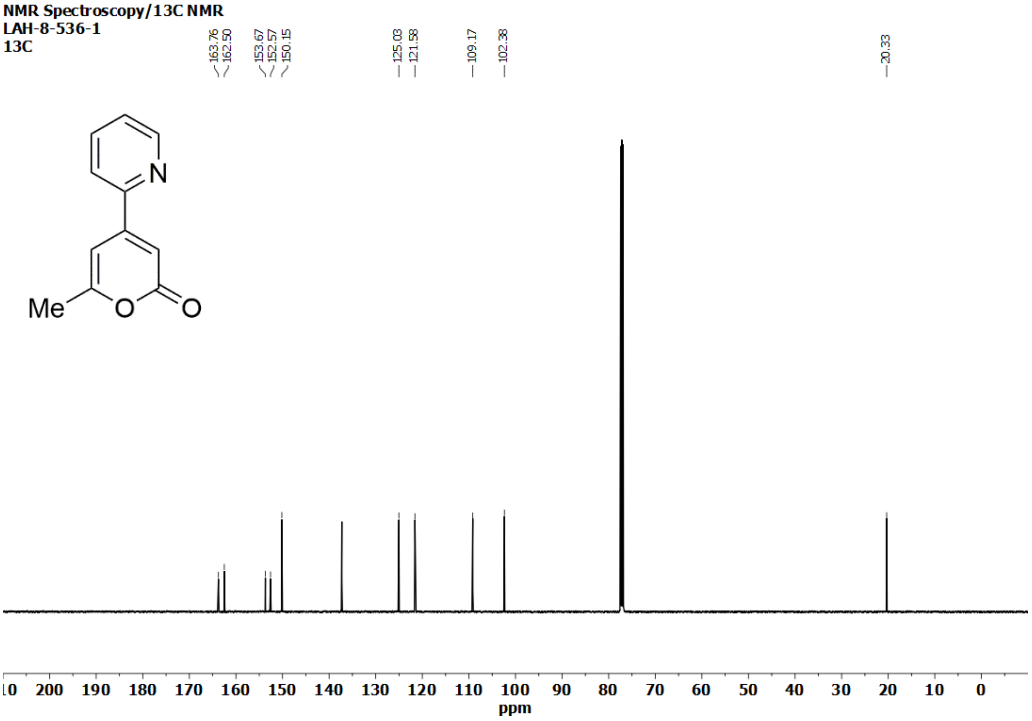

Figure 129. ^{13}C NMR spectrum of **176** (126 MHz, $CDCl_3$).

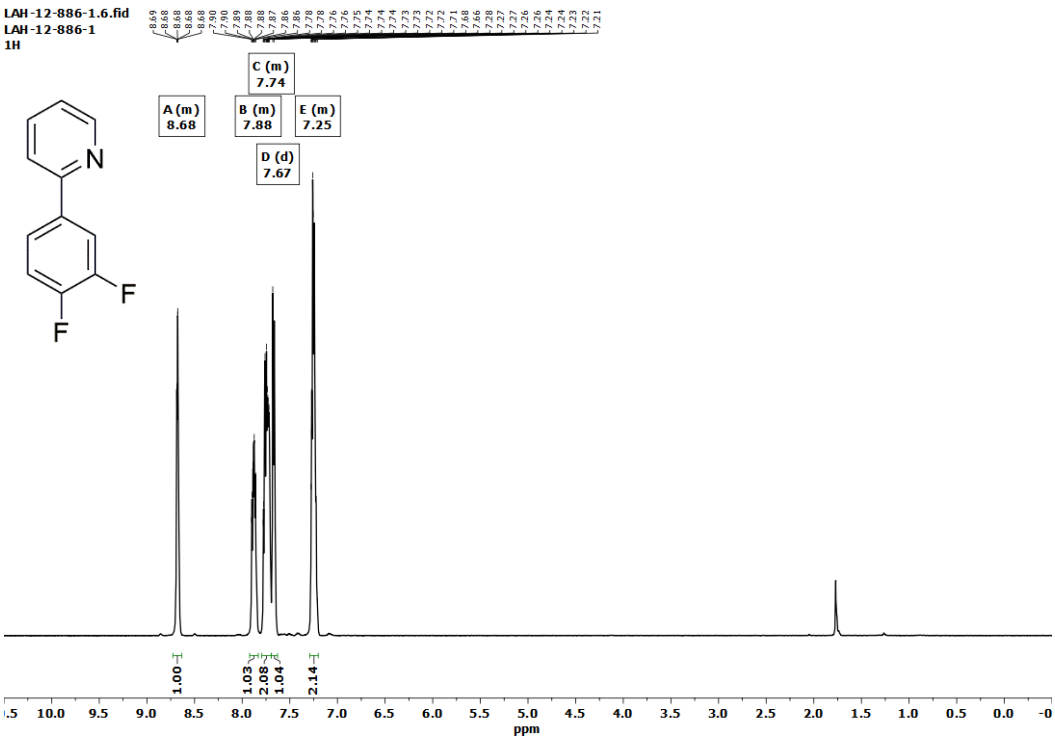

Figure 130. ^{1}H NMR spectrum of **254** (500 MHz, $CDCl_3$).

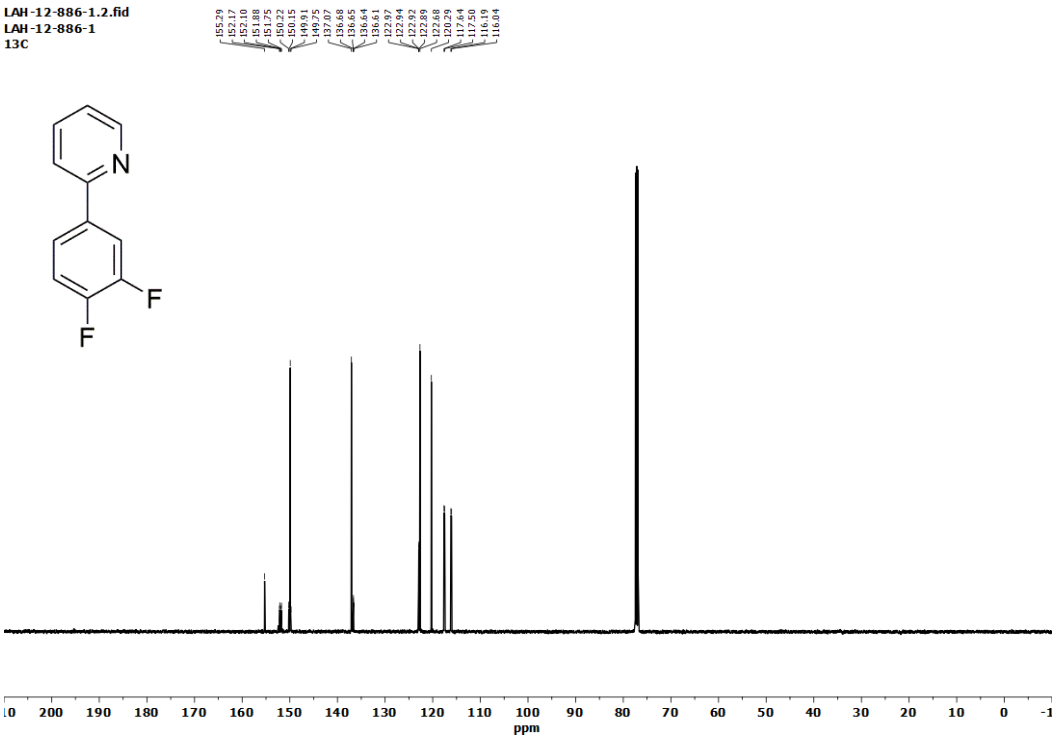

Figure 131. ^{13}C NMR spectrum of **254** (126 MHz, $CDCl_3$).

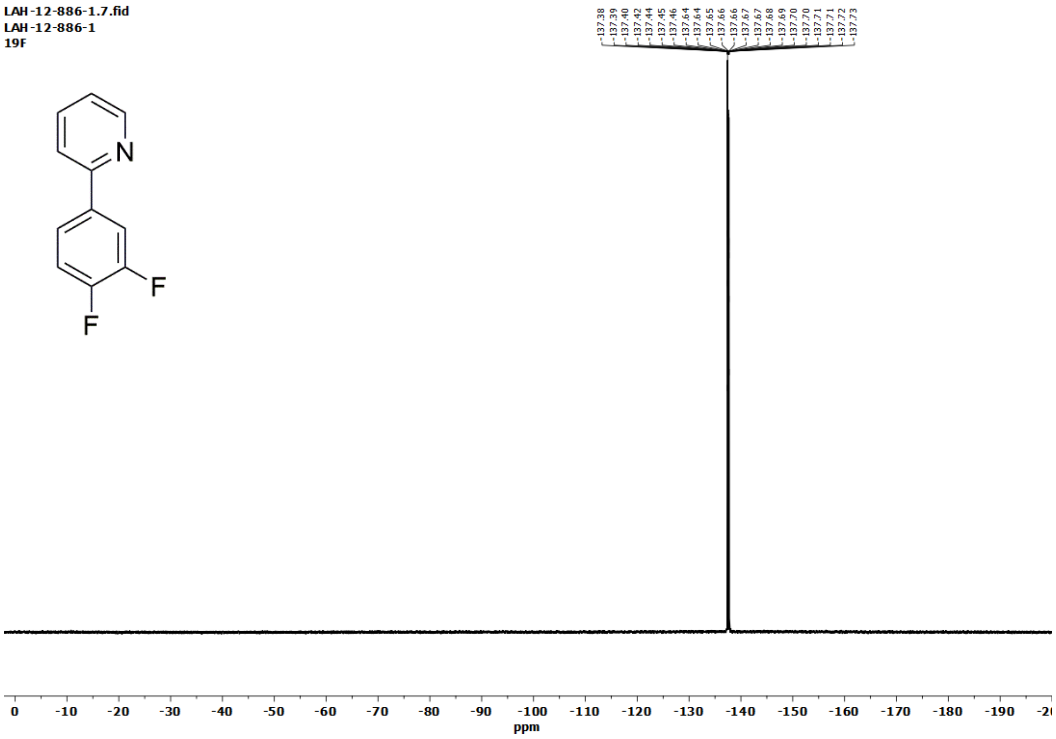

Figure 132. ^{19}F NMR spectrum of **254** (470 MHz, $CDCl_3$).

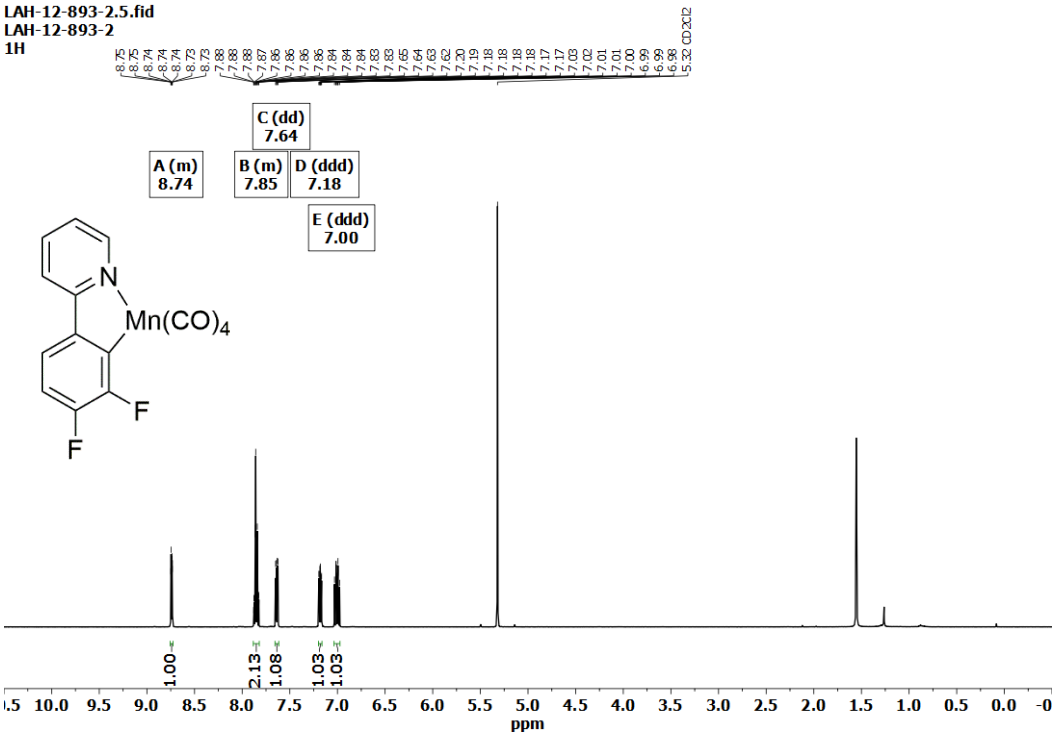

Figure 133. ^{1}H NMR spectrum of **255** (500 MHz, $CDCl_3$).

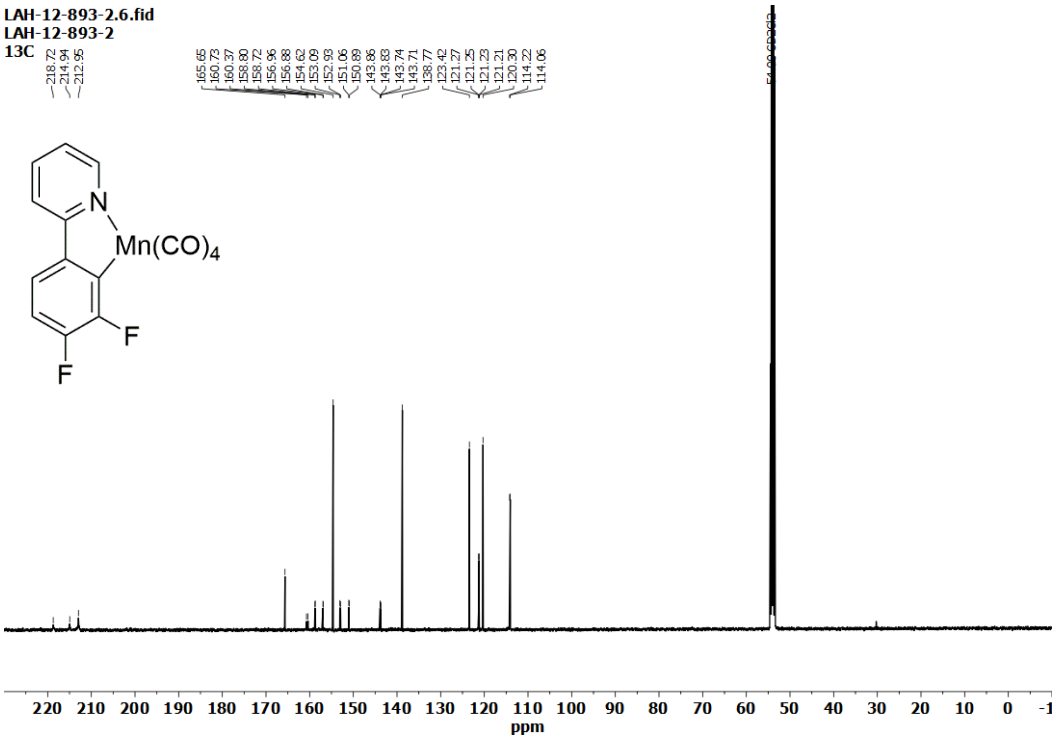

Figure 134. ^{13}C NMR spectrum of **255** (126 MHz, $CDCl_3$).

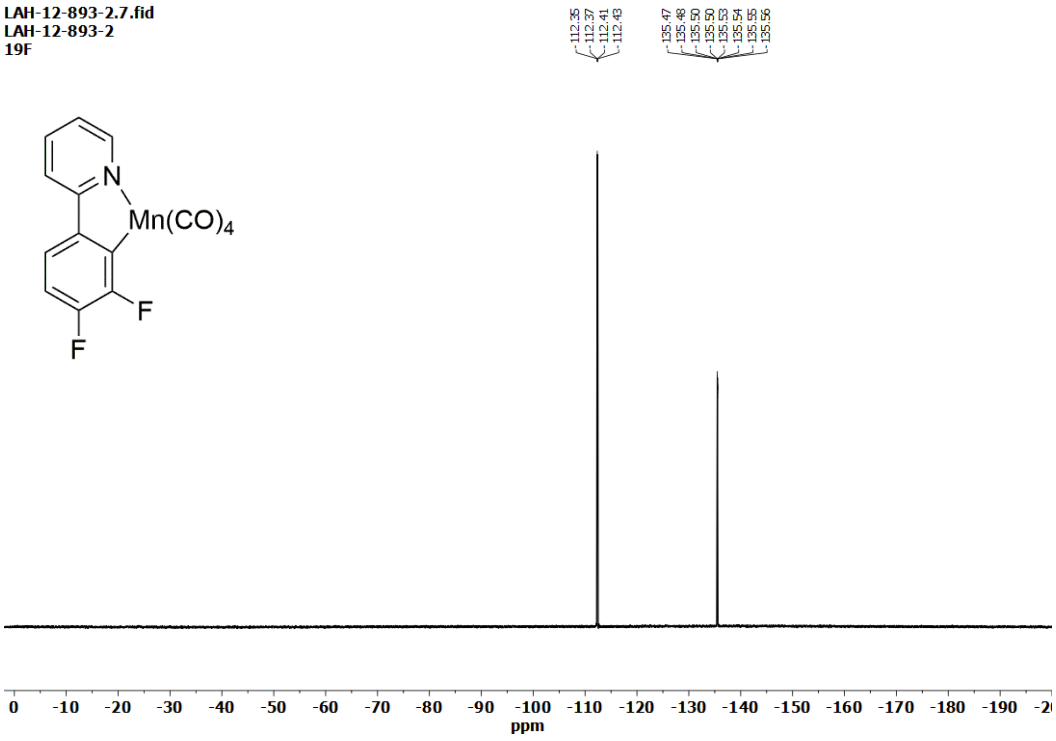

Figure 135. ^{19}F NMR spectrum of **255** (470 MHz, $CDCl_3$).

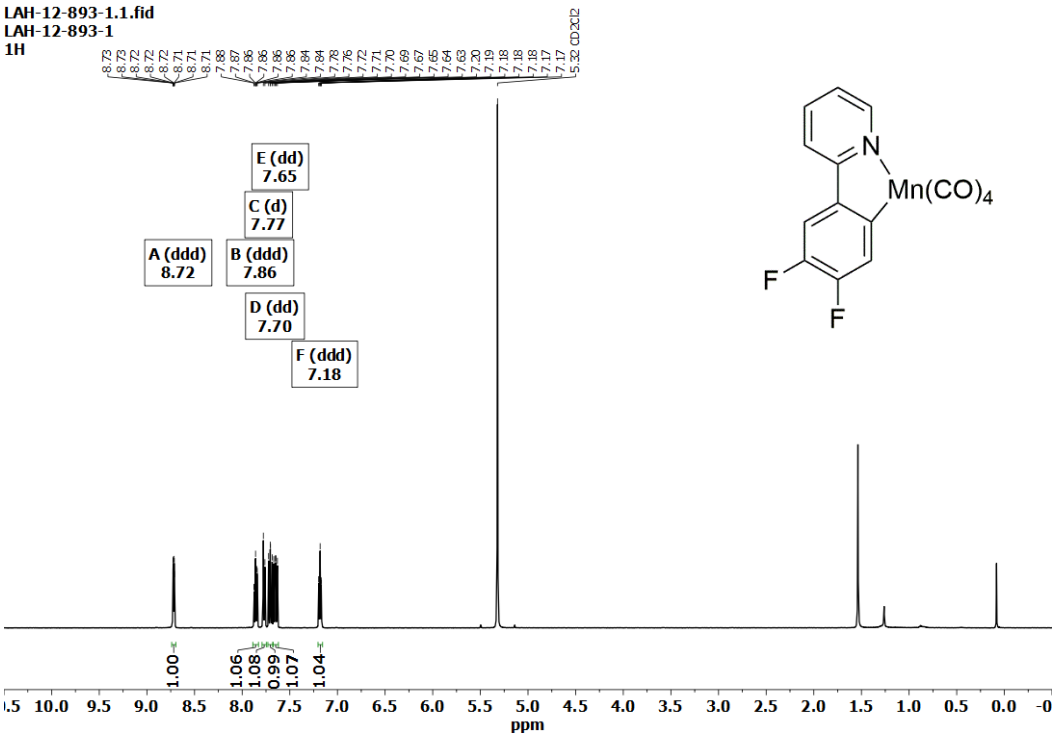

Figure 136. ^{1}H NMR spectrum of **256** (500 MHz, CD_2Cl_2).

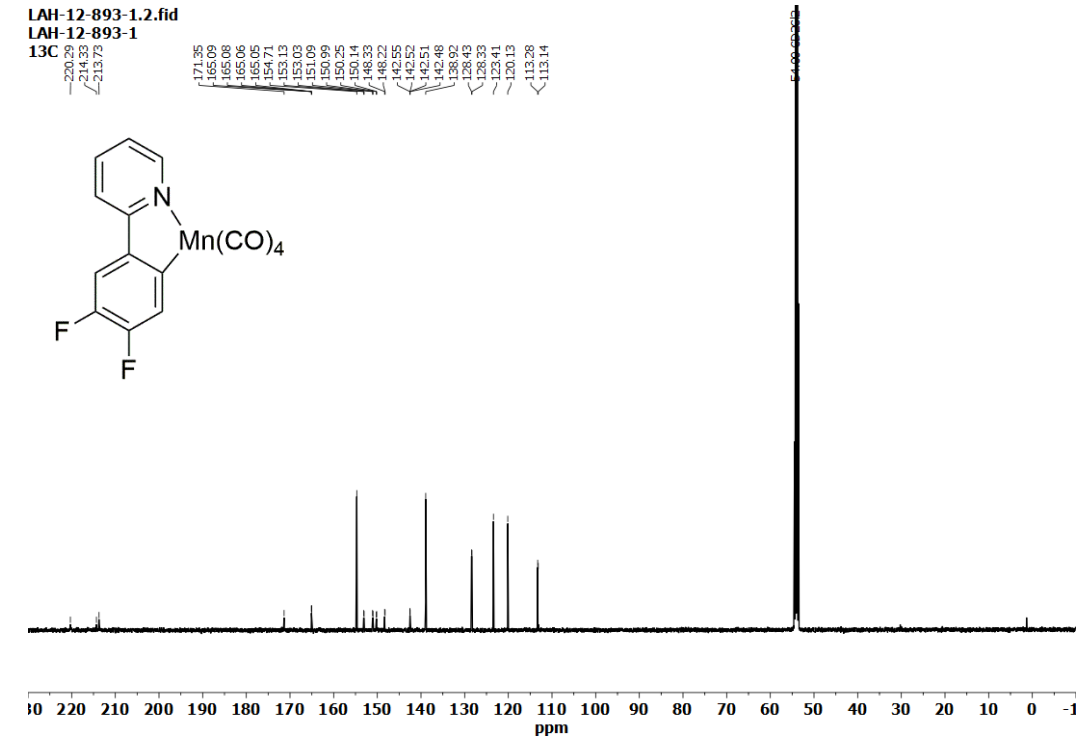

Figure 137. ^{13}C NMR spectrum of **256** (126 MHz, CD_2Cl_2).

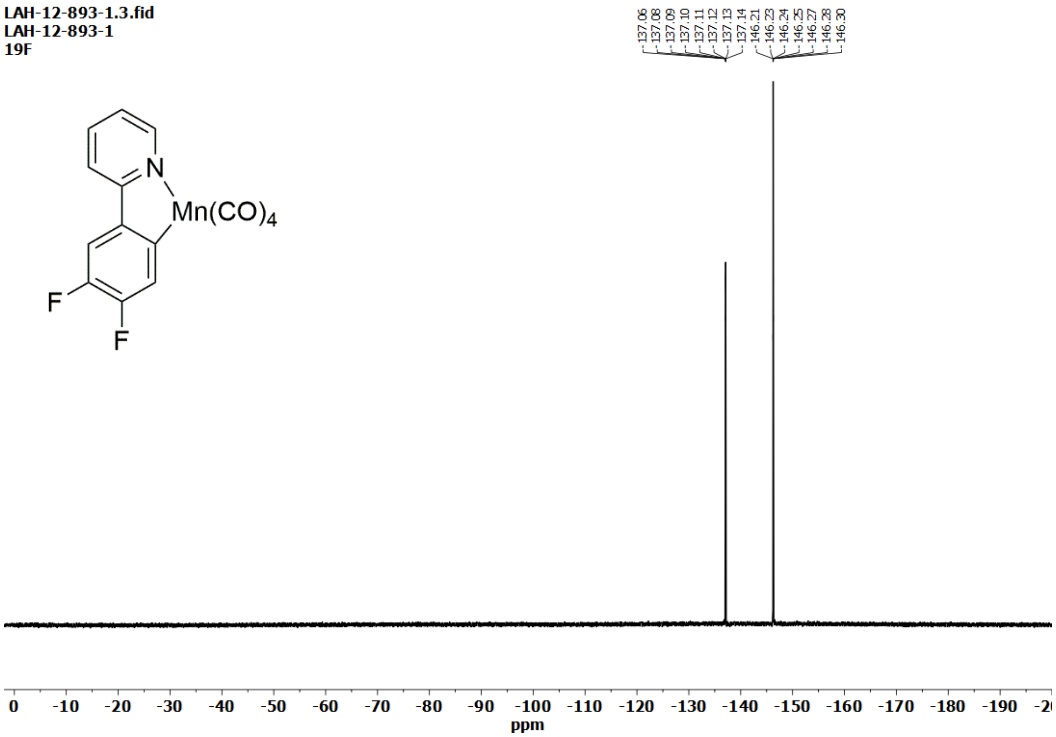

Figure 138. ^{19}F NMR spectrum of **256** (470 MHz, CD_2Cl_2).

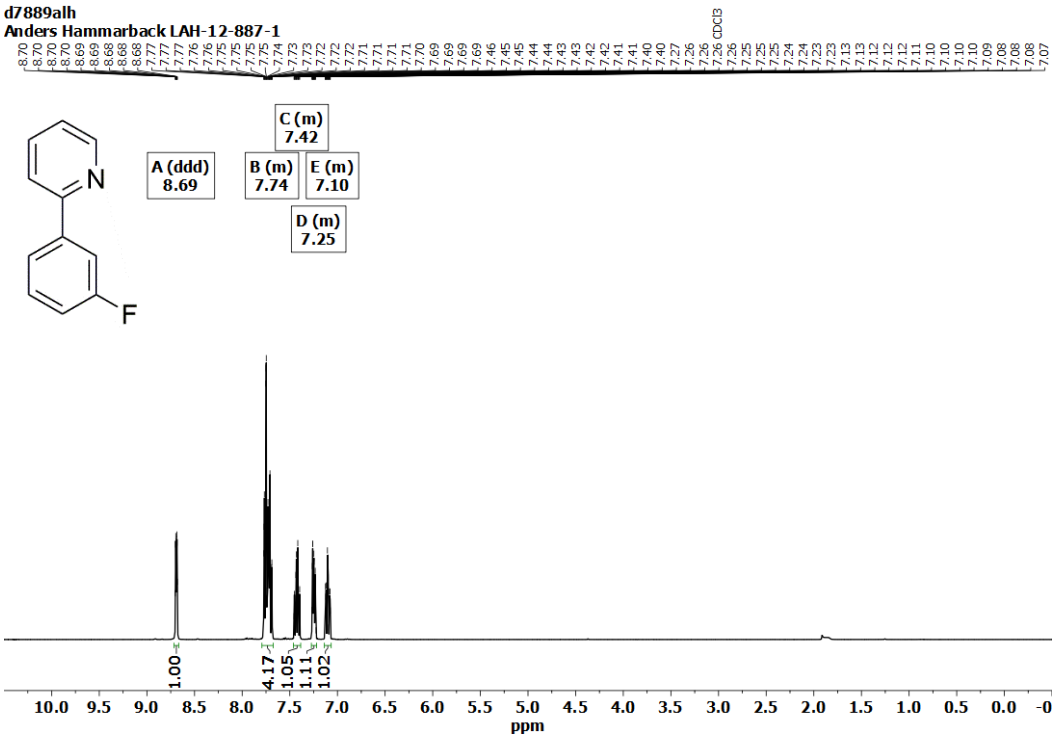

Figure 139. ^{1}H NMR spectrum of **257** (400 MHz, $CDCl_3$).

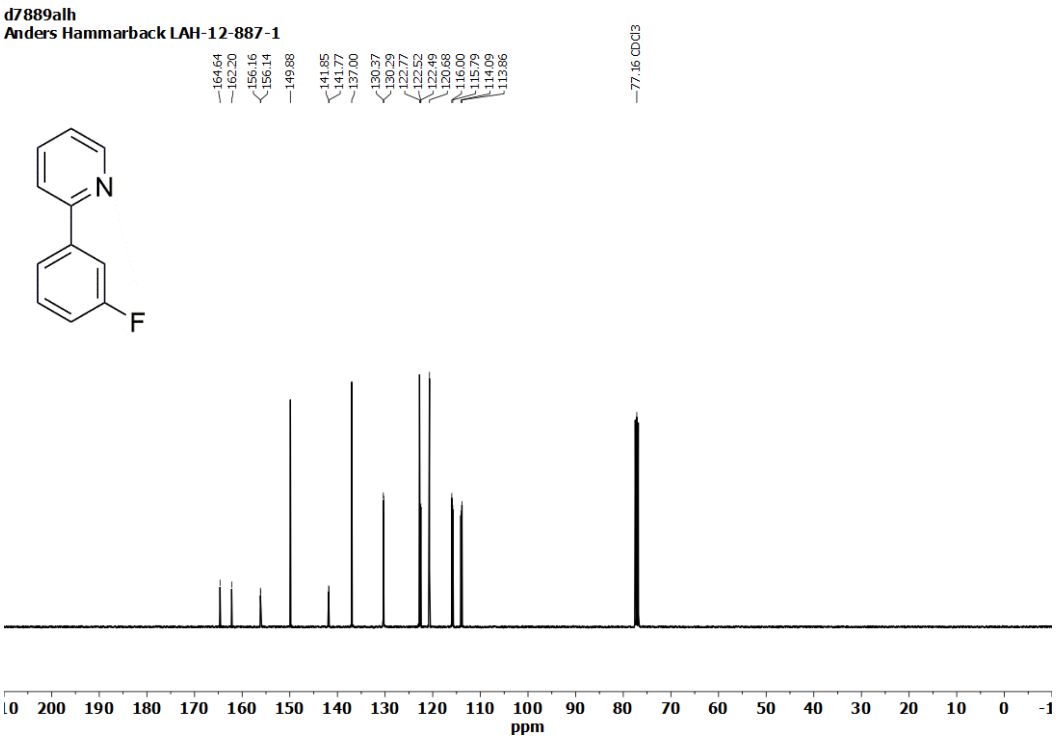

Figure 140. ^{13}C NMR spectrum of **257** (101 MHz, $CDCl_3$).

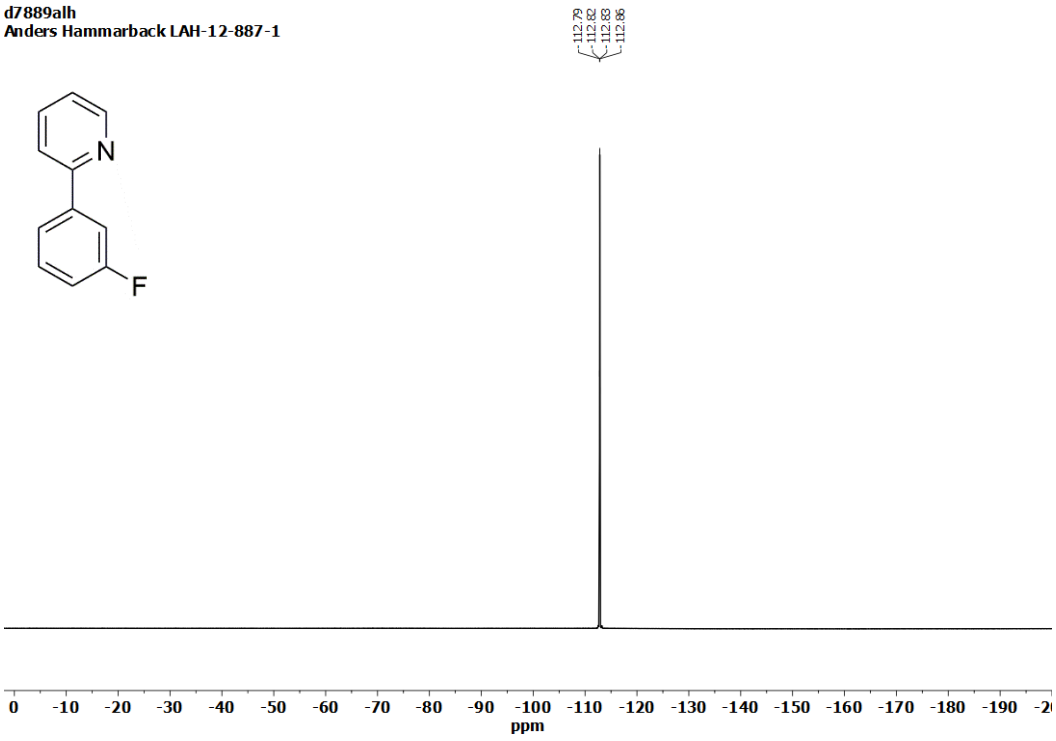

Figure 141. ^{19}F NMR spectrum of **257** (376 MHz, $CDCl_3$).

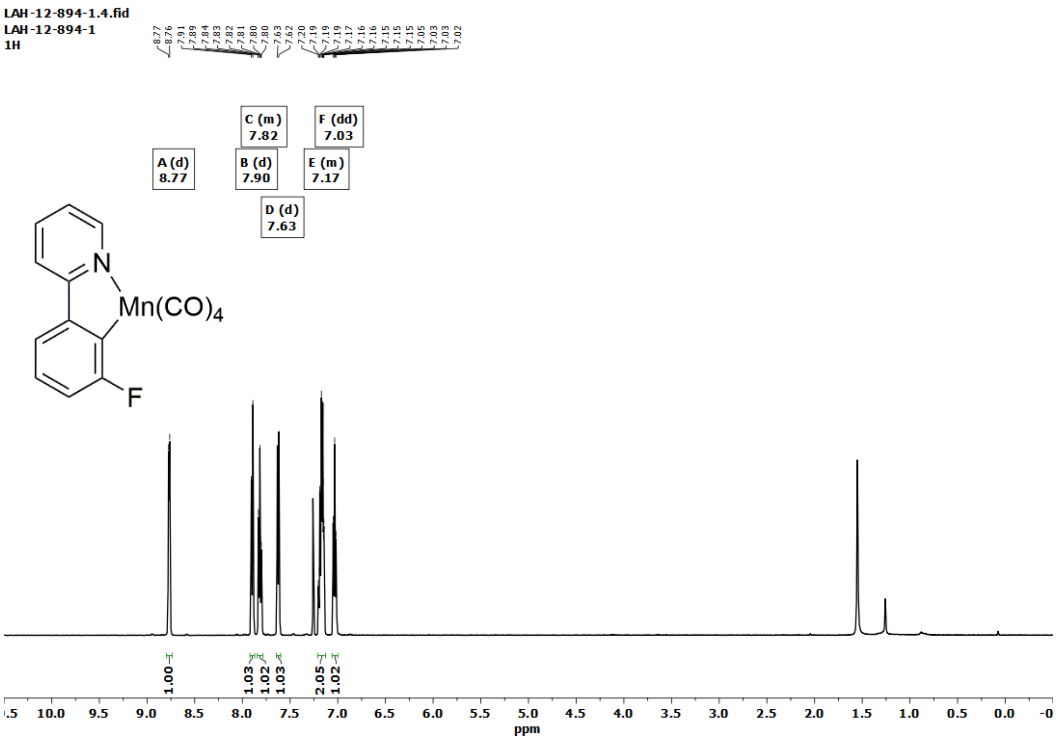

Figure 142. ^{1}H NMR spectrum of **258** (500 MHz, $CDCl_3$).

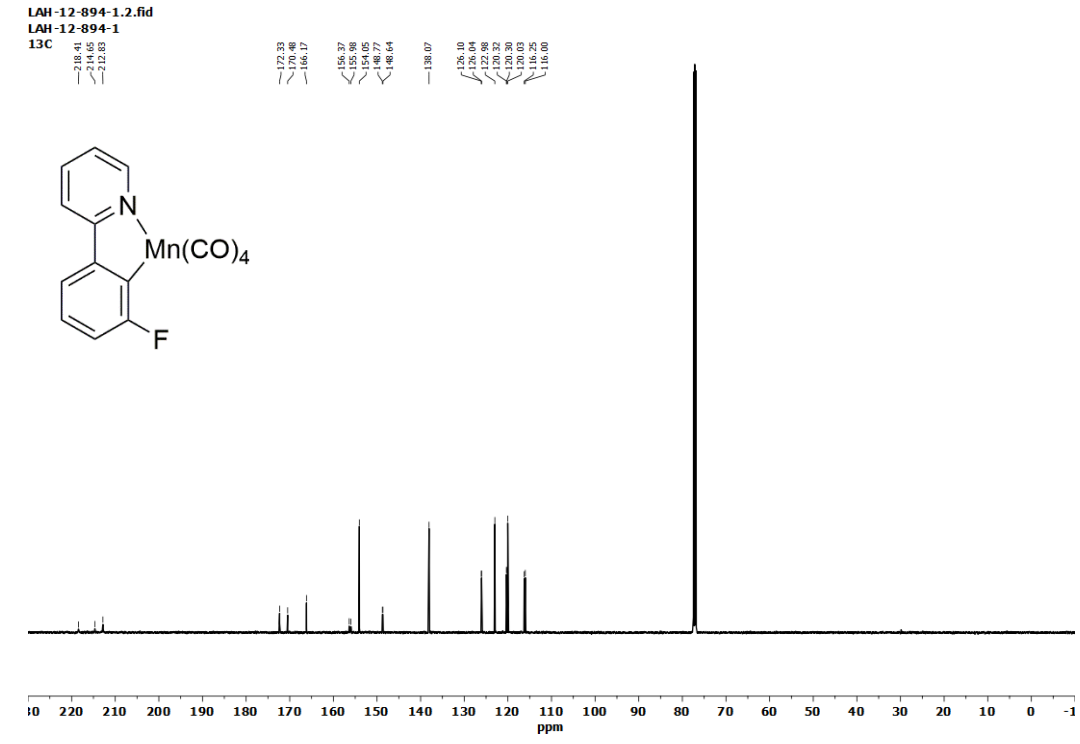

Figure 143. ^{13}C NMR spectrum of **258** (126 MHz, $CDCl_3$).

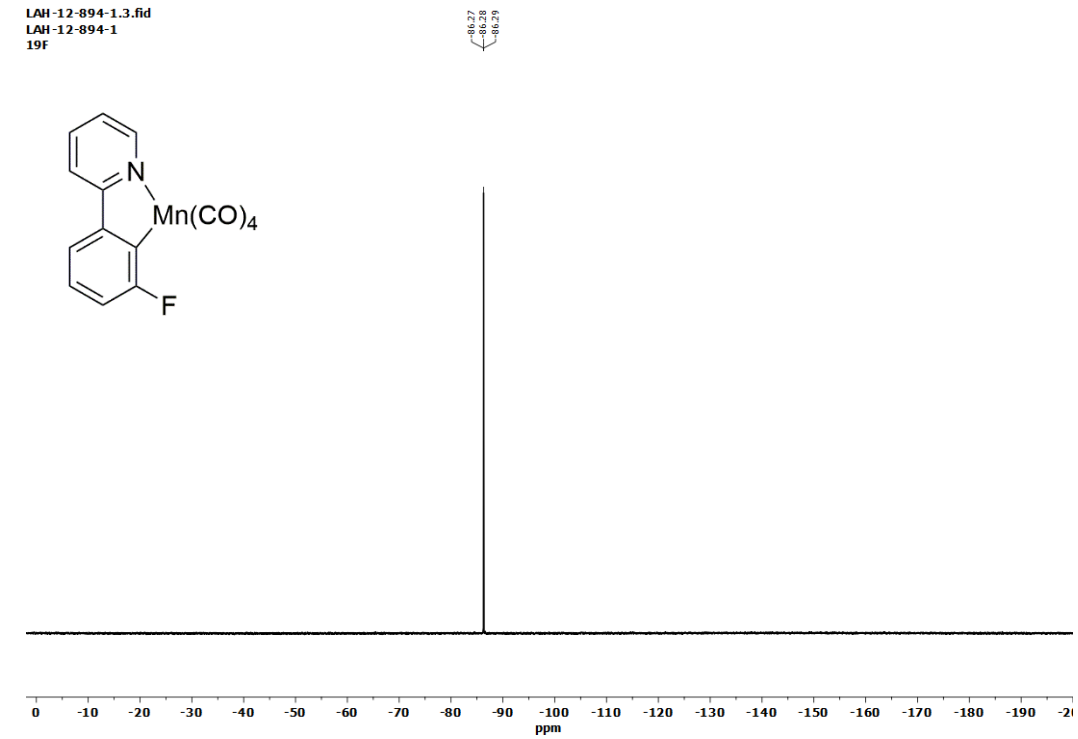

Figure 144. ^{19}F NMR spectrum of **258** (470 MHz, $CDCl_3$).

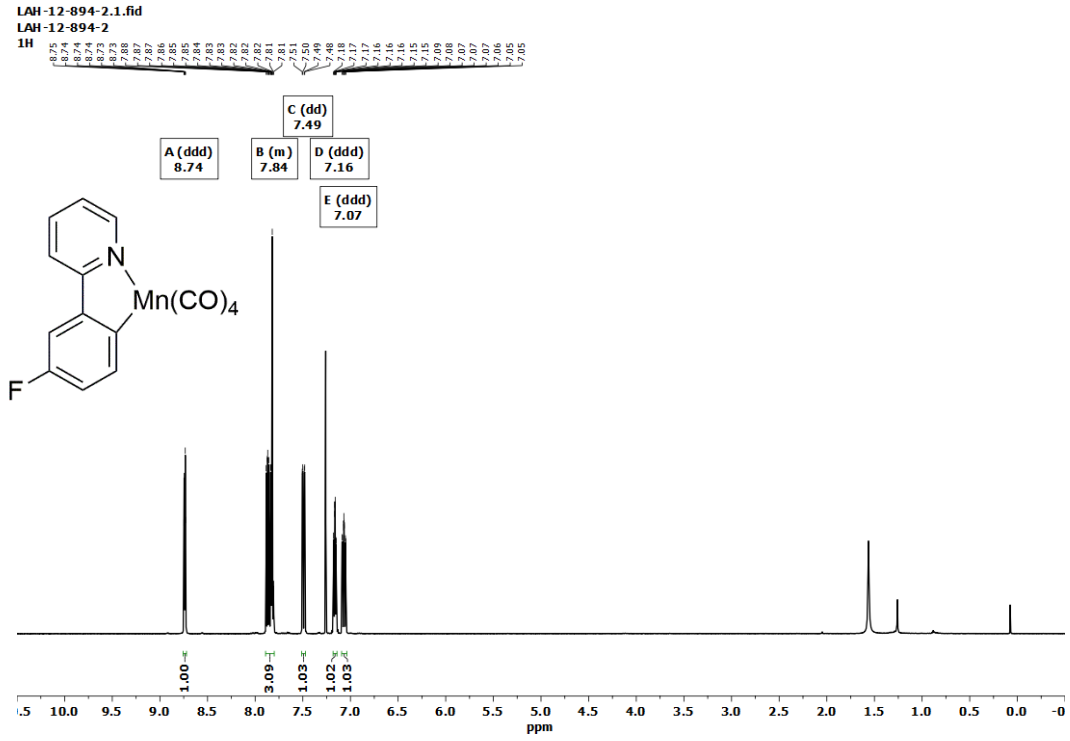

Figure 145. ^{1}H NMR spectrum of **259** (500 MHz, $CDCl_3$).

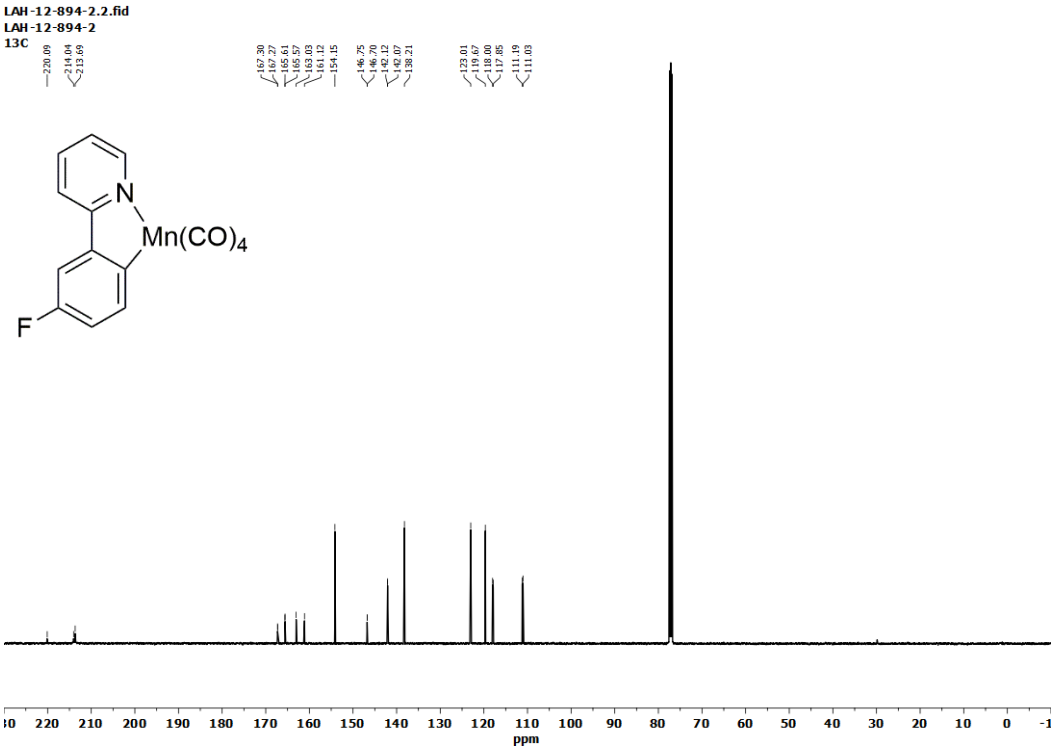

Figure 146. ^{13}C NMR spectrum of **259** (126 MHz, $CDCl_3$).

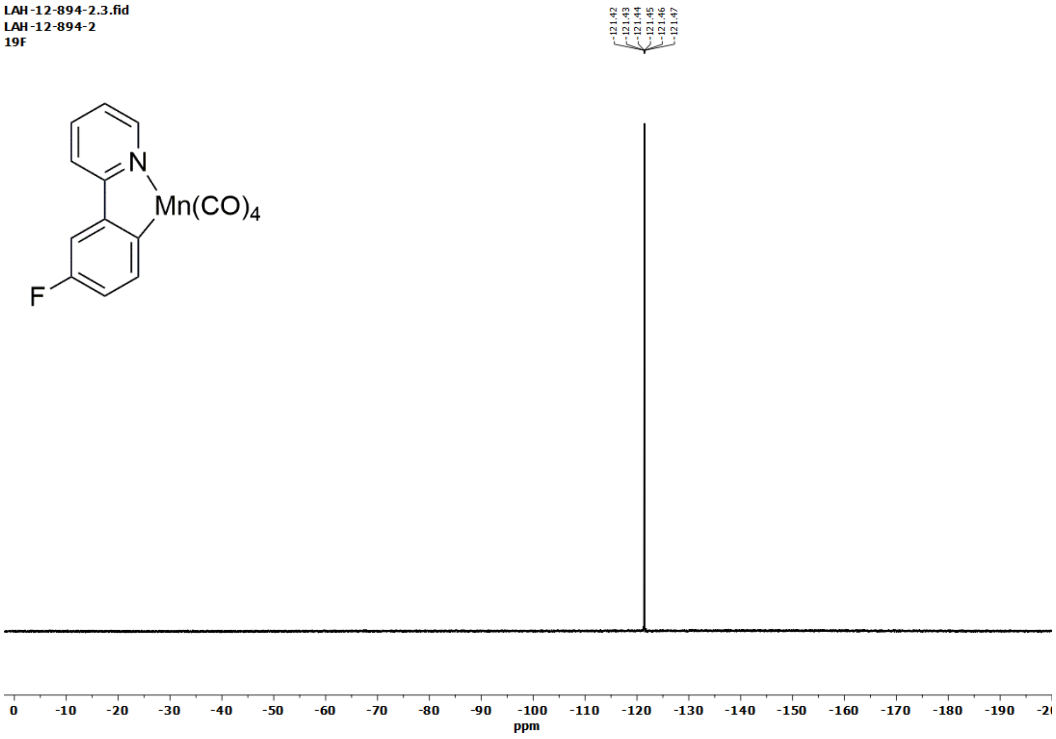

Figure 147. ^{19}F NMR spectrum of **259** (470 MHz, $CDCl_3$).

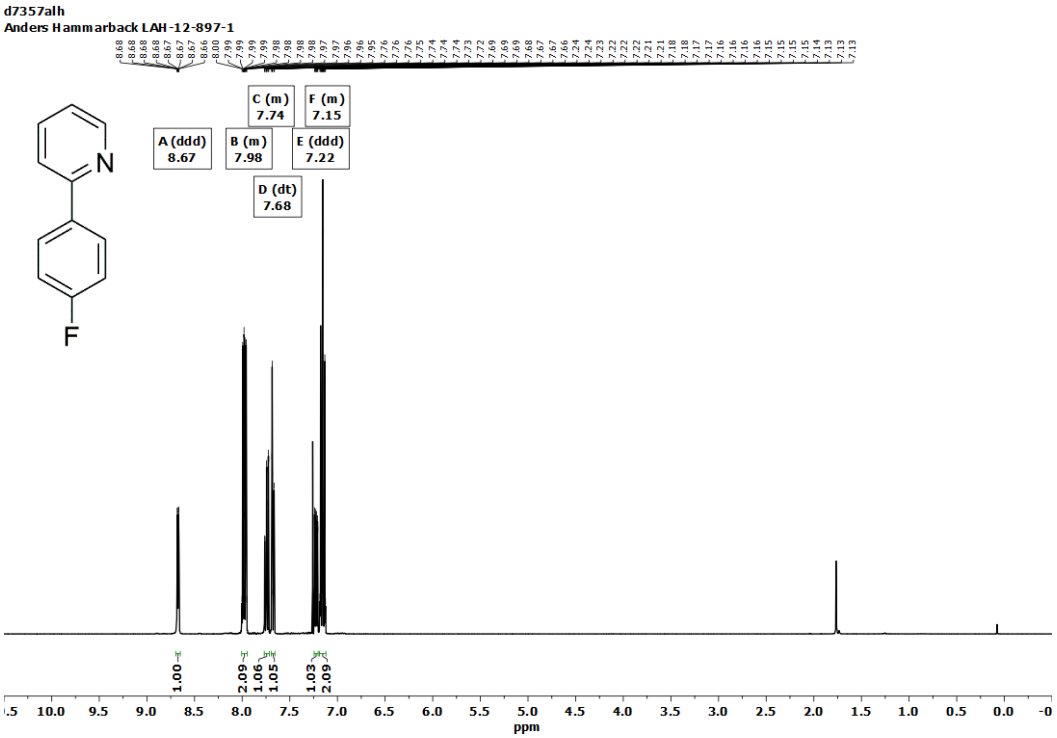

Figure 148. ^{1}H NMR spectrum of **260** (400 MHz, $CDCl_3$).

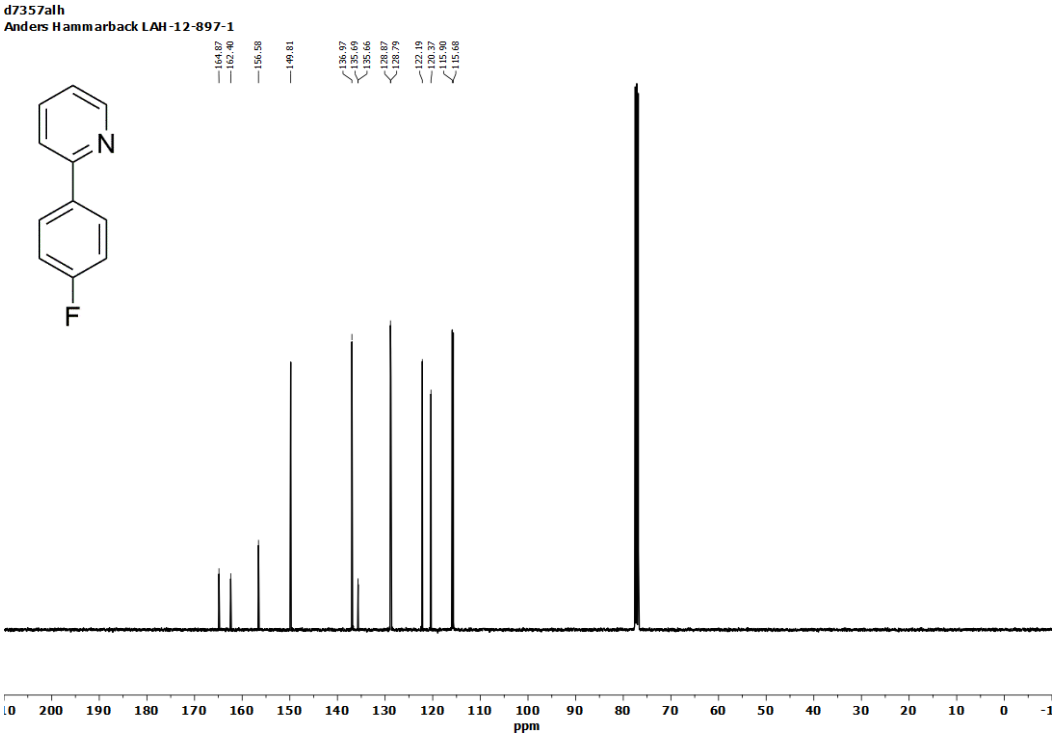

Figure 149. ^{13}C NMR spectrum of **260** (101 MHz, $CDCl_3$).

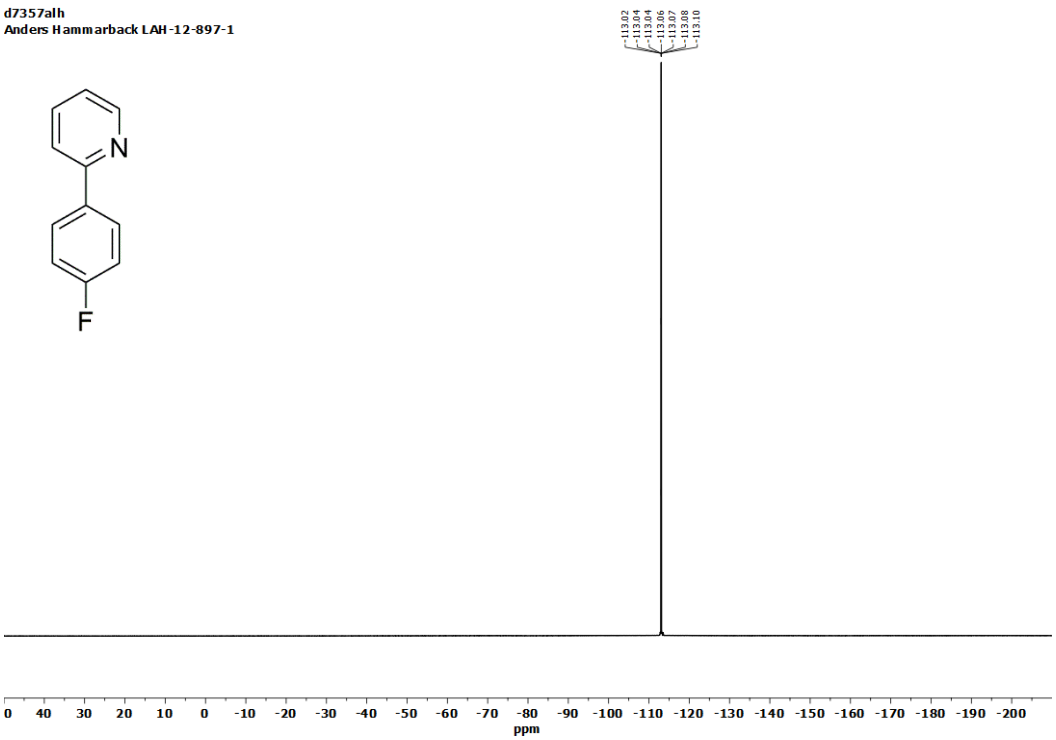

Figure 150. ^{19}F NMR spectrum of **260** (376 MHz, $CDCl_3$).

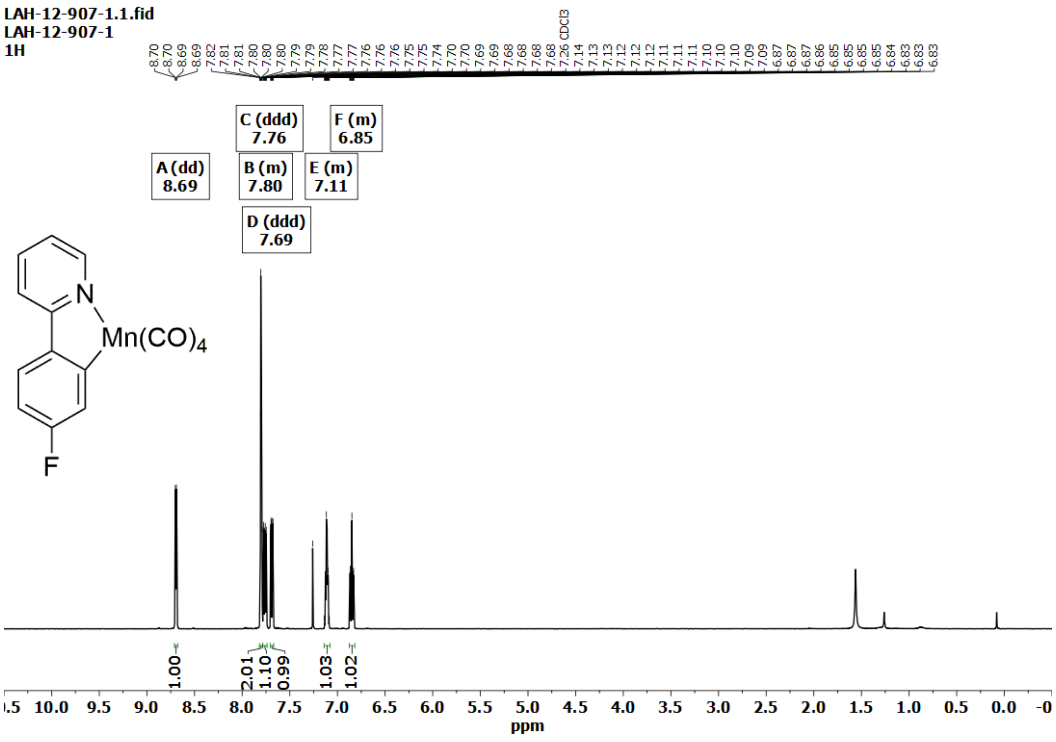

Figure 151. ^{1}H NMR spectrum of **261** (500 MHz, $CDCl_3$).

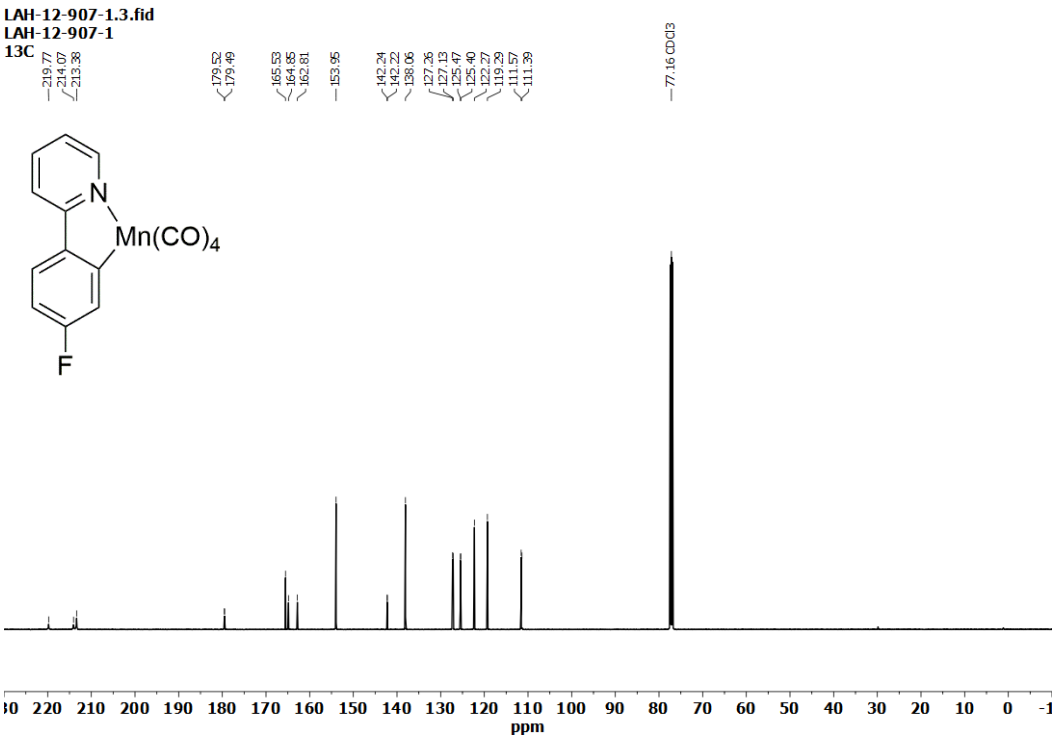

Figure 152. ^{13}C NMR spectrum of **261** (126 MHz, $CDCl_3$).

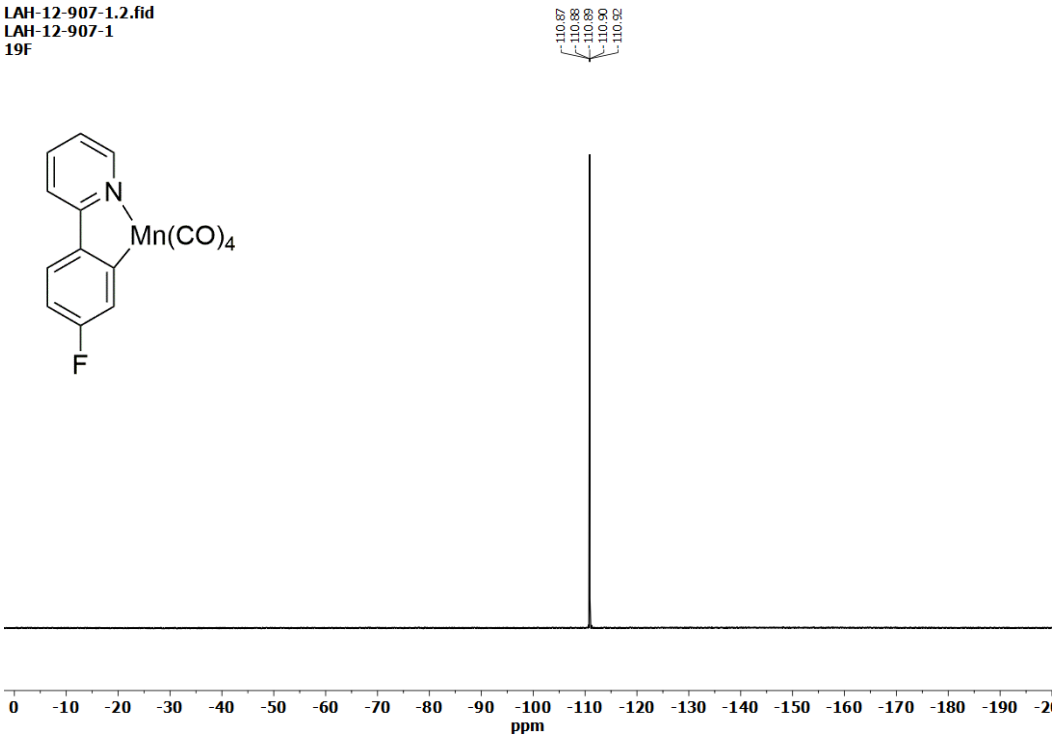

Figure 153. ^{19}F NMR spectrum of **261** (470 MHz, $CDCl_3$).

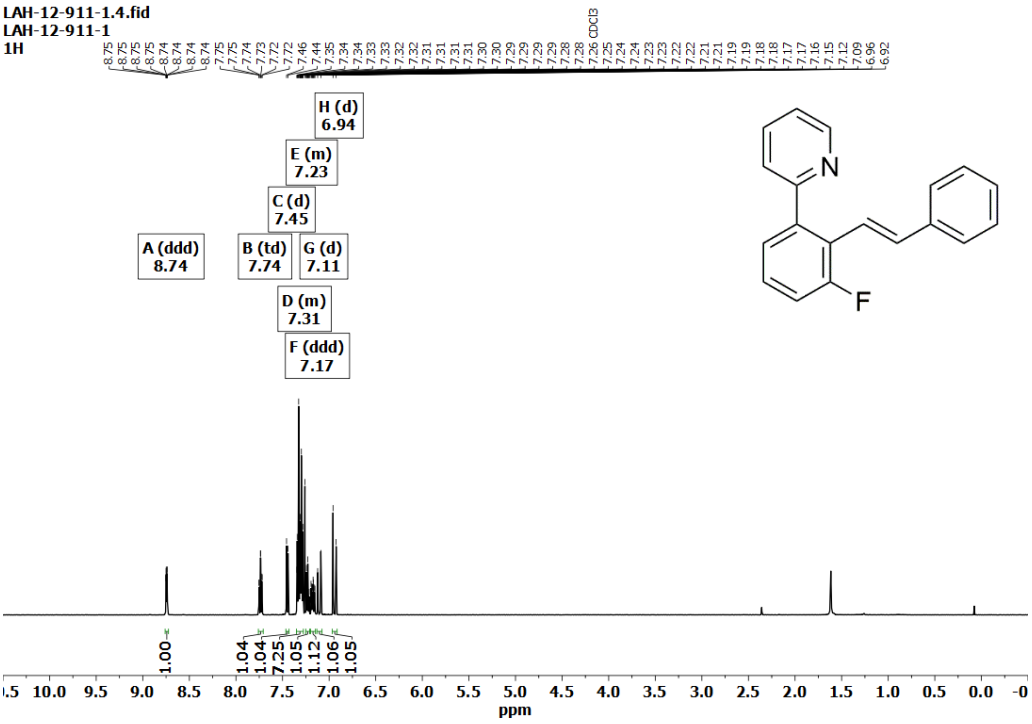

Figure 154. ^{1}H NMR spectrum of **262** (500 MHz, $CDCl_3$).

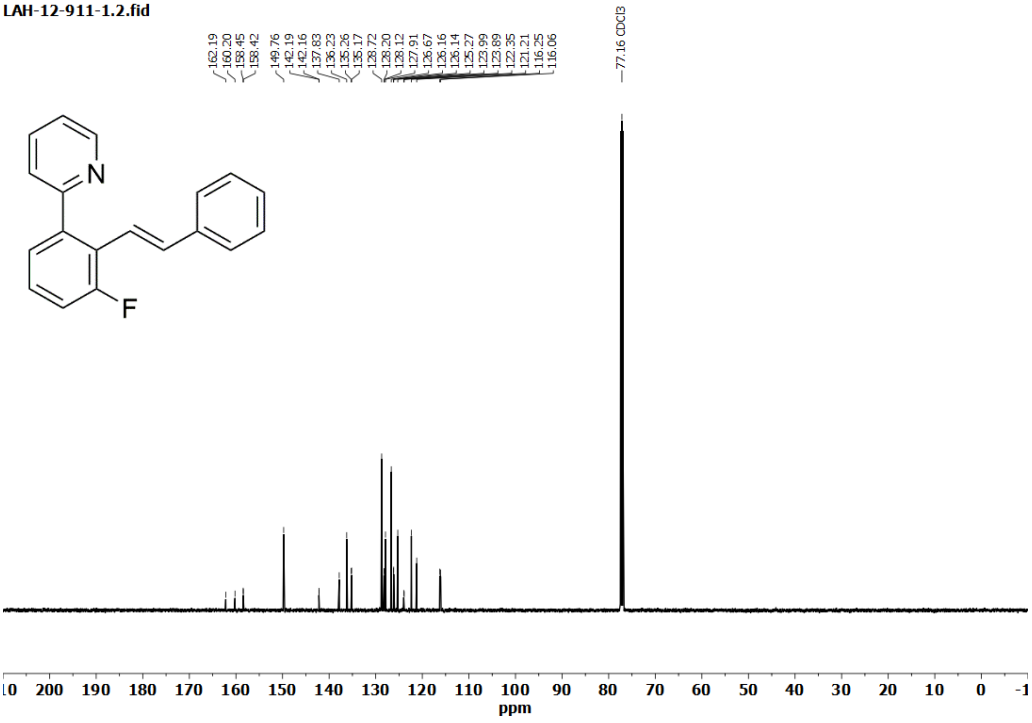

Figure 155. ^{13}C NMR spectrum of **262** (126 MHz, $CDCl_3$).

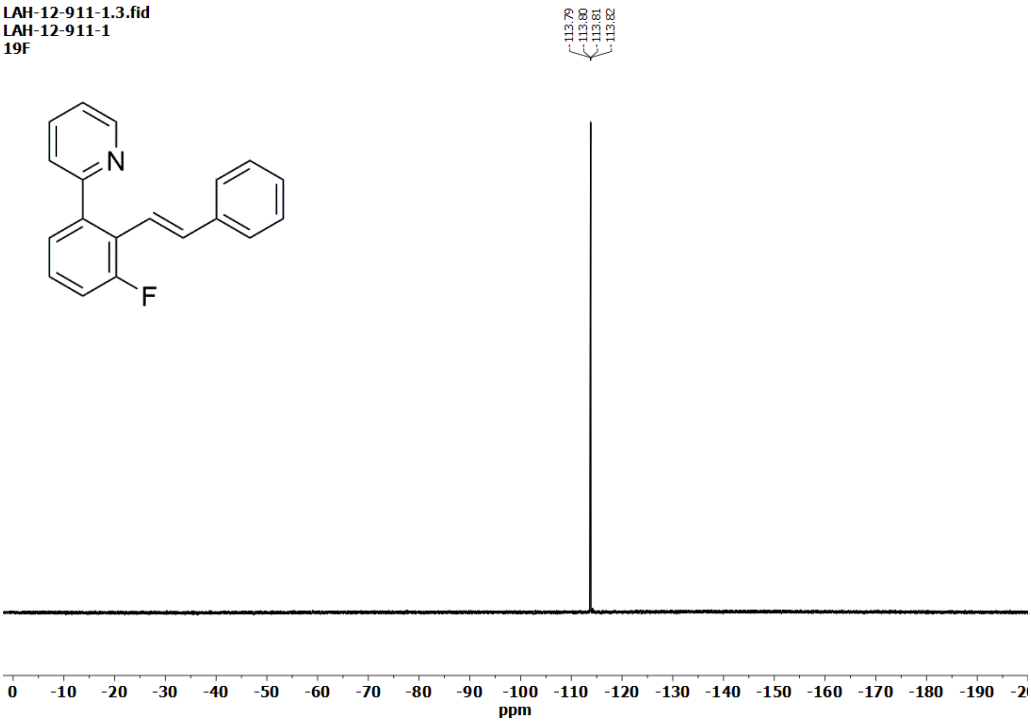

Figure 156. ^{19}F NMR spectrum of **262** (470 MHz, $CDCl_3$).

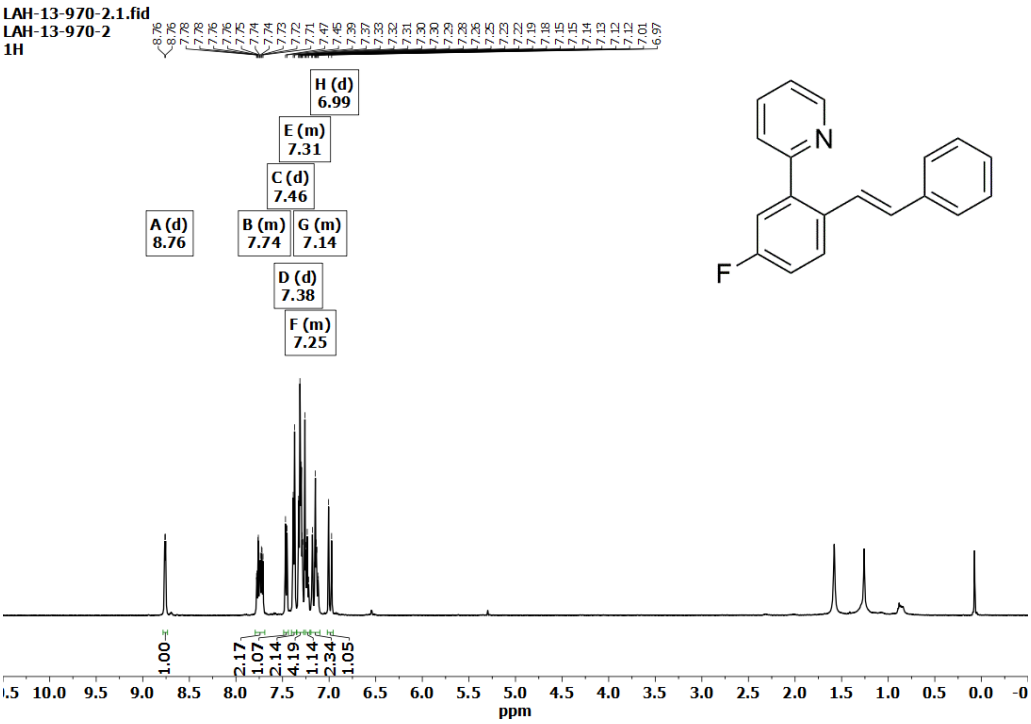

Figure 157. ^{1}H NMR spectrum of **263** (500 MHz, $CDCl_3$).

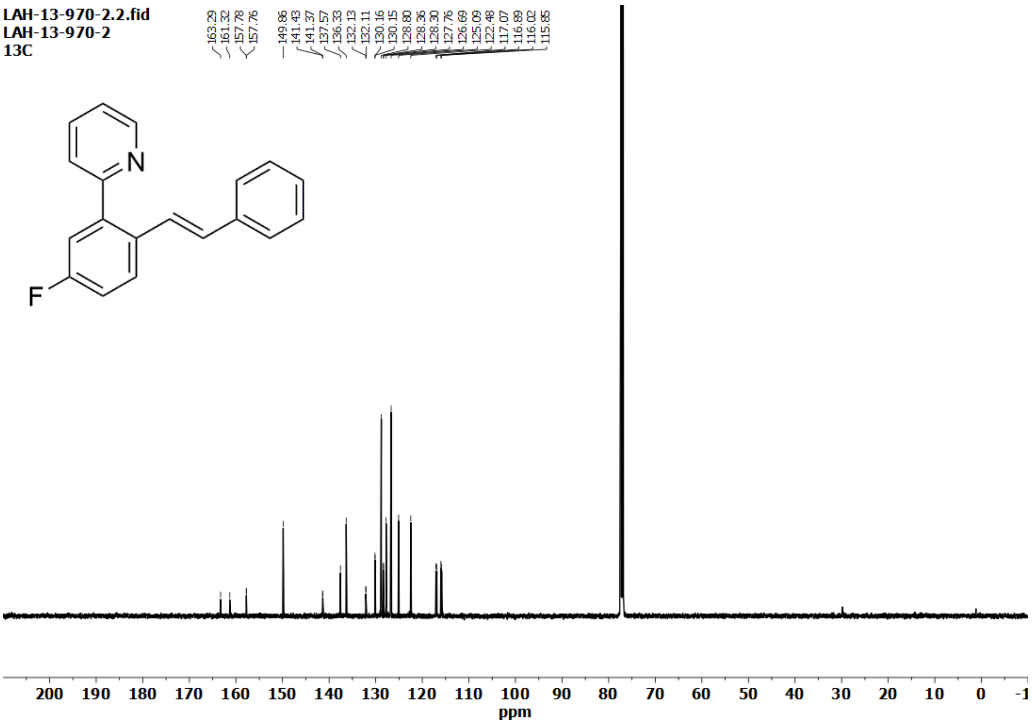

Figure 158. ^{13}C NMR spectrum of **263** (126 MHz, $CDCl_3$).

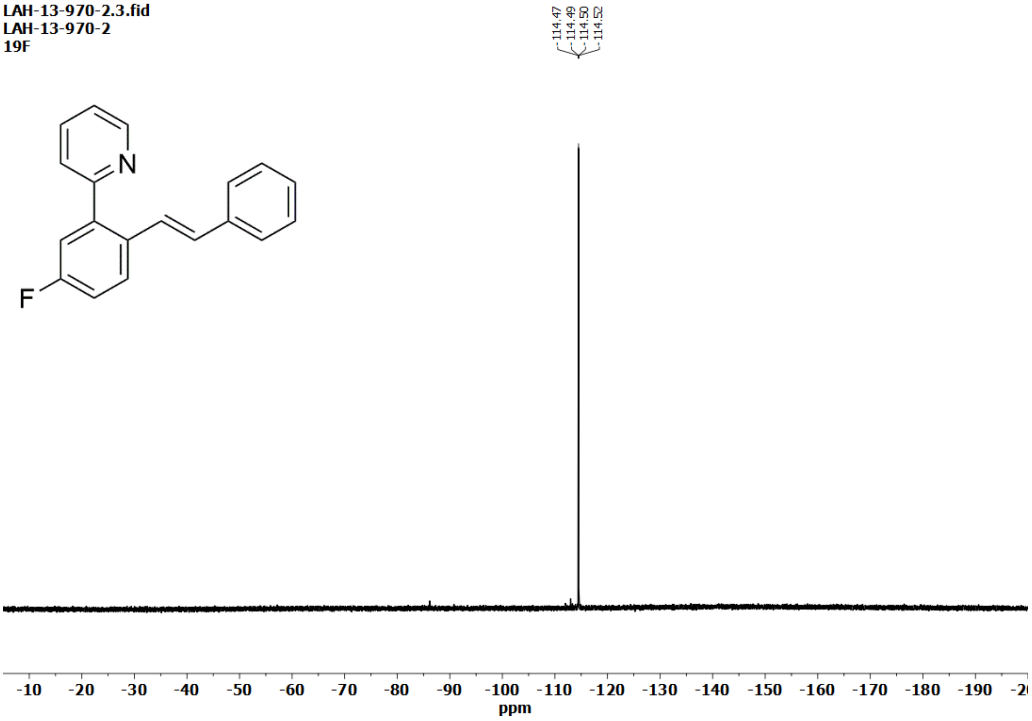

Figure 159. ^{19}F NMR spectrum of **263** (470 MHz, $CDCl_3$).

Appendix 5: TRIR Kinetics at Extended Times

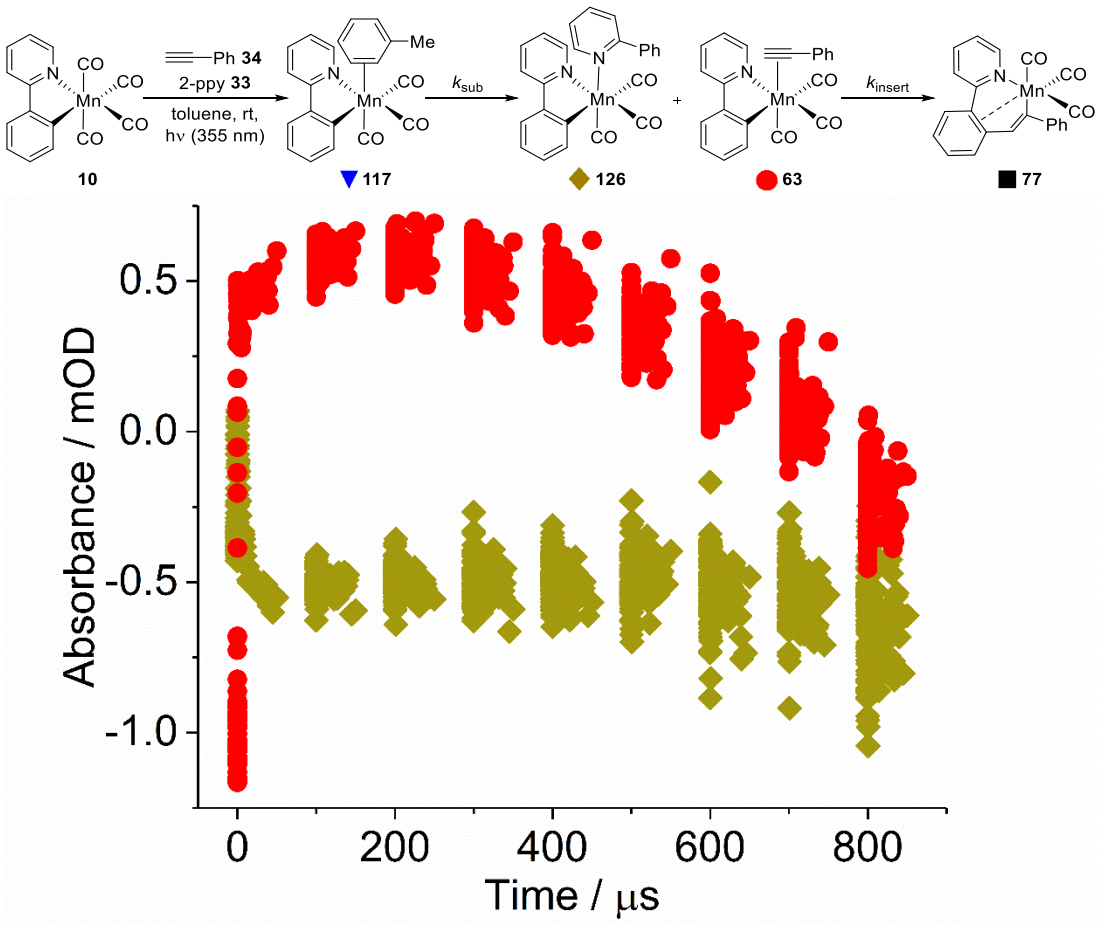

Figure 160. TRIR study of the photolysis of **10**, **34** and **33** in toluene ([**10**] = 1.94 × 10^{-3} mol dm^{-3}, [**34**] = 0.23 mol dm^{-3}), showing the extended kinetic traces (of **63** (red circles, band at 1943 cm^{-1}) and **126** (brown diamonds, band at 1996 cm^{-1})) of those shown in **Figure 33**. The data has been route mean square corrected and is smoothened by a 5-point smoothening function.

Appendix 6: List of Main Compound Structures

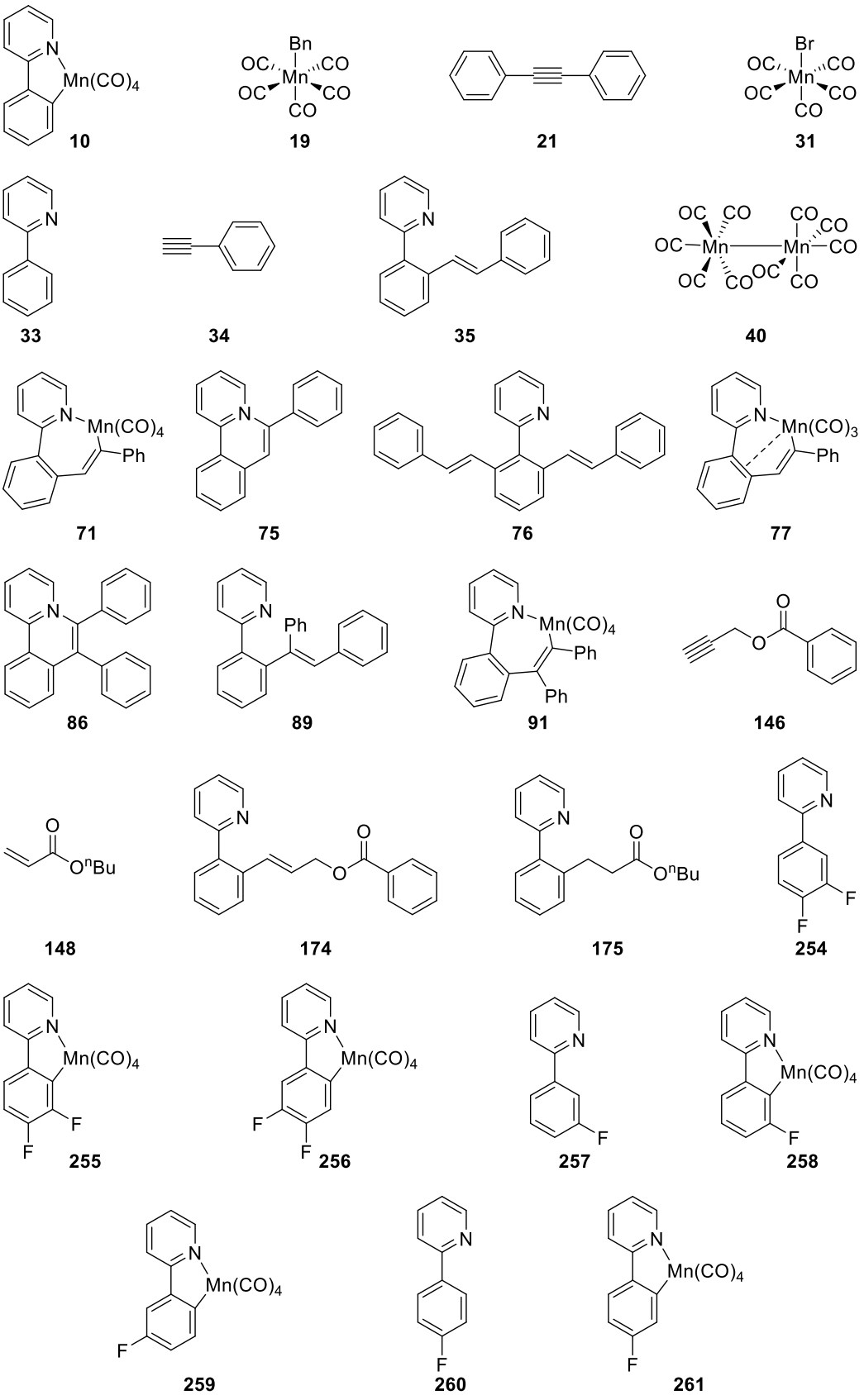

Figure 161. List of main compound structures.

Abbreviations

Ac	acetyl
AMLA	ambiphilic metal-ligand activation
aq.	aqueous
Ar	arene
ATR	attenuated total reflectance
Bn	benyl
Boc	*tert*-butoxycarbonyl
b.p.	boiling point
bpy	2,2’-bipyridine
br	broad
Bu	butyl
C	Celcius
ca.	*circa*
CLF	Central Laser Facility
CMD	concerted metalation deprotonation
CO-RM	carbon monoxide releasing molecule
Cy	cyclohexyl
Cp	cyclopentadienyl
Cp’	methylcyclopentadienyl
CV	coefficient of variation
DCE	1,2-dichloroethane
DCM	dichloromethane
dec.	decomposition

DFT	density functional theory
DMA	dimethylacetamide
DMSO	dimethylsulfoxide
EI	electron ionisation
ESI	electrospray ionisation
Et	ethyl
fac	facial
FT	Fourier transform
GC	gas chromatography
HR	high resolution
Hz	hertz
i-	*iso*-
IR	infrared
L	ligand
LIFDI	liquid introduced field desorption ionisation
lit.	literature
m-	*meta*-
M	mol dm^{-3} or metal
[M]	metal
Me	methyl
mer	meridional
MHz	megahertz
Mp	melting point
MS	mass spectrometry

Mw	molecular weight
N/A	not applicable
NBD	norbornadiene
NBN	norbornene
NMR	nuclear magnetic resonance
NTC	nortricyclene
o-	*ortho*-
OPA	optical parametric amplifier
p-	*para*-
Ph	phenyl
phen	phenanthroline
pin	pinacol ester
PMP	*para*-methoxyphenyl
ppm	parts per million
Pr	propyl
py	pyridine
ppy	2-phenylpyridyl
R_f	retention factor
rt	at ambient temperature
SM	starting material
t-	*tertiary*
TA	transient absorbance
TBAB	tetra butyl ammonium bromide
Tces	2,2,2-trichloroethoxysulfonyl

THF	tetrahydrofuran
TLC	thin layer chromatography
TOF	turnover frequency
TON	turnover number
Tol	tolyl
Tp*	tris(3,5-dimethyl-1-pyrazolyl)borate
TRIR	time-resolved infrared
$TR^{M}PS$	time-resolved multiple probe spectroscopy
TRO	time-resolved optical
UV	ultraviolet
Vis	visible
w.r.t.	with respect to

References

1. Wu, X.-F.; Anbarasan, P.; Neumann, H.; Beller, M., *Angew. Chem. Int. Ed.*, **2010,** *49*, 9047-9050.

2. Carney, J. R.; Dillon, B. R.; Thomas, S. P., *Eur. J. Org. Chem.*, **2016,** *2016*, 3912-3929.

3. Bauer, I.; Knölker, H.-J., *Chem. Rev.*, **2015,** *115*, 3170-3387.

4. Guo, X.-X.; Gu, D.-W.; Wu, Z.; Zhang, W., *Chem. Rev.*, **2015,** *115*, 1622-1651.

5. Ananikov, V. P., *ACS Catalysis*, **2015,** *5*, 1964-1971.

6. Cahiez, G.; Moyeux, A., *Chem. Rev.*, **2010,** *110*, 1435-1462.

7. Zhang, W.; Loebach, J. L.; Wilson, S. R.; Jacobsen, E. N., *J. Am. Chem. Soc.*, **1990,** *112*, 2801-2803.

8. Snider, B. B., *Chem. Rev.*, **1996,** *96*, 339-364.

9. Wang, D.; Loose, F.; Chirik, P. J.; Knowles, R. R., *J. Am. Chem. Soc.*, **2019,** *141*, 4795-4799.

10. Gensch, T.; Hopkinson, M. N.; Glorius, F.; Wencel-Delord, J., *Chem. Soc. Rev.*, **2016,** *45*, 2900-2936.

11. Clark, J. R.; Feng, K.; Sookezian, A.; White, M. C., *Nature Chem.*, **2018,** *10*, 583-591.

12. Anisimov, K. N.; Ioganson, A. A.; Kolobova, N. E., *Russ. Chem. Rev.*, **1968,** *37*, 184-197.

13. Bruce, M. I.; Iqbal, M. Z.; Stone, F. G. A., *J. Chem. Soc. A*, **1970**, 3204-3209.

14. Wang, C., *Synlett*, **2013,** *24*, 1606-1613.

15. Heck, R. F., *J. Am. Chem. Soc.*, **1968,** *90*, 313-317.

16. Grigsby, W. J.; Main, L.; Nicholson, B. K., *Organometallics*, **1993,** *12*, 397-407.

17. Pfeffer, M.; Urriolabeitia, E. P.; Fischer, J., *Inorg. Chem.*, **1995,** *34*, 643-650.

18. Bruce, M. I.; Goodall, B. L.; Iqbal, M. Z.; Stone, F. G. A.; Doedens, R. J.; Little, R. G., *J. Chem. Soc. D*, **1971**, 1595-1596.

19. Albert, J.; Cadena, J. M.; Granell, J.; Solans, X.; Font-Bardia, M., *J. Organomet. Chem.*, **2004,** *689*, 4889-4896.

20. Robinson, N. P.; Main, L.; Nicholson, B. K., *J. Organomet. Chem.*, **1988,** *349*, 209-218.

21. McKinney, R. J.; Firestein, G.; Kaesz, H. D., *Inorg. Chem.*, **1975,** *14*, 2057-2061.

22. Depree, G. J.; Main, L.; Nicholson, B. K.; Robinson, N. P.; Jameson, G. B., *J. Organomet. Chem.*, **2006,** *691*, 667-679.

23. Bruce, M.; Goodall, B.; Matsuda, I., *Aust. J. Chem.*, **1975,** *28*, 1259-1264.

24. Leeson, M. A.; Nicholson, B. K.; Olsen, M. R., *J. Organomet. Chem.*, **1999,** *579*, 243-251.

25. McKinney, R. J.; Kaesz, H. D., *J. Am. Chem. Soc.*, **1975,** *97*, 3066-3072.

26. Ressner, J. M.; Wernett, P. C.; Kraihanzel, C. S.; Rheingold, A. L., *Organometallics*, **1988,** *7*, 1661-1663.

27. Liebeskind, L. S.; Gasdaska, J. R.; McCallum, J. S.; Tremont, S. J., *J. Org. Chem.*, **1989,** *54*, 669-677.

28. Wilford, J. B. P.; Treichel, M.; Stone, F. G. A., *Proceedings of the Chemical Society*, **1963**, 218-219.

29. Depree, G. J.; Main, L.; Nicholson, B. K., *J. Organomet. Chem.*, **1998,** *551*, 281-291.

30. Tully, W.; Main, L.; Nicholson, B. K., *J. Organomet. Chem.*, **1995,** *503*, 75-92.

31. Suárez, A.; Faraldo, F.; Vila, J. M.; Adams, H.; Fernández, A.; López-Torres, M.; Fernández, J. J., *J. Organomet. Chem.*, **2002,** *656*, 270-273.

32. Liu, W.; Ackermann, L., *ACS Catalysis*, **2016,** *6*, 3743-3752.

33. Kuninobu, Y.; Nishina, Y.; Takeuchi, T.; Takai, K., *Angew. Chem.*, **2007,** *119*, 6638-6640.

34. Zhou, B.; Chen, H.; Wang, C., *J. Am. Chem. Soc.*, **2013,** *135*, 1264-1267.

35. Hu, Y.; Zhou, B.; Wang, C., *Acc. Chem. Res.*, **2018,** *51*, 816-827.

36. Zhou, B.; Ma, P.; Chen, H.; Wang, C., *Chem. Commun.*, **2014,** *50*, 14558-14561.

37. Liu, W.; Bang, J.; Zhang, Y.; Ackermann, L., *Angew. Chem. Int. Ed.*, **2015,** *54*, 14137-14140.

38. Cano, R.; Mackey, K.; McGlacken, G. P., *Catal. Sci.*, **2018,** *8*, 1251-1266.

39. DiBiase Cavanaugh, M.; Gregg, B. T.; Cutler, A. R., *Organometallics*, **1996,** *15*, 2764-2769.

40. Liang, Y.-F.; Steinbock, R.; Yang, L.; Ackermann, L., *Angew. Chem. Int. Ed.*, **2018,** *57*, 10625-10629.

41. Tsuji, H.; Yamagata, K.-i.; Fujimoto, T.; Nakamura, E., *J. Am. Chem. Soc.*, **2008,** *130*, 7792-7793.

42. Zhou, B.; Hu, Y.; Wang, C., *Angew. Chem. Int. Ed.*, **2015,** *54*, 13659-13663.

43. Liu, W.; Richter, S. C.; Zhang, Y.; Ackermann, L., *Angew. Chem. Int. Ed.*, **2016,** *55*, 7747-7750.

44. Yang, X.; Jin, X.; Wang, C., *Adv. Synth. Catal.*, **2016**, *358*, 2436-2442.

45. Zhou, B.; Hu, Y.; Liu, T.; Wang, C., *Nature Communications*, **2017,** *8*, 1169.

46. Liu, S.-L.; Li, Y.; Guo, J.-R.; Yang, G.-C.; Li, X.-H.; Gong, J.-F.; Song, M.-P., *Org. Lett.*, **2017,** *19*, 4042-4045.

47. Liu, W.; Zell, D.; John, M.; Ackermann, L., *Angew. Chem. Int. Ed.*, **2015,** *54*, 4092-4096.

48. Sueki, S.; Wang, Z.; Kuninobu, Y., *Org. Lett.*, **2016,** *18*, 304-307.

49. He, R.; Huang, Z.-T.; Zheng, Q.-Y.; Wang, C., *Angew. Chem.*, **2014,** *126*, 5050-5053.

50. Yahaya, N. P.; Appleby, K. M.; Teh, M.; Wagner, C.; Troschke, E.; Bray, J. T. W.; Duckett, S. B.; Hammarback, L. A.; Ward, J. S.; Milani, J.; Pridmore, N. E.; Whitwood, A. C.; Lynam, J. M.; Fairlamb, I. J. S., *Angew. Chem. Int. Ed.*, **2016,** *55*, 12455-12459.

51. Shi, L.; Zhong, X.; She, H.; Lei, Z.; Li, F., *Chem. Commun.*, **2015,** *51*, 7136-7139.

52. Kobayashi, K.; Sumitomo, H.; Ina, Y., *Polym. J.*, **1985,** *17*, 567-575.

53. Dong, Z.; Ren, Z.; Thompson, S. J.; Xu, Y.; Dong, G., *Chem. Rev.*, **2017,** *117*, 9333-9403.

54. Chen, B.; Dingerdissen, U.; Krauter, J. G. E.; Lansink Rotgerink, H. G. J.; Möbus, K.; Ostgard, D. J.; Panster, P.; Riermeier, T. H.; Seebald, S.; Tacke, T.; Trauthwein, H., *Appl. Catal. A-Gen.*, **2005,** *280*, 17-46.

55. Beletskaya, I. P.; Cheprakov, A. V., *Chem. Rev.*, **2000,** *100*, 3009-3066.

56. Peng, J.; Docherty, J. H.; Dominey, A. P.; Thomas, S. P., *Chem. Commun.*, **2017,** *53*, 4726-4729.

57. Leigh, J. K.; Rajput, J.; Richardson, D. E., *Inorg. Chem.*, **2014,** *53*, 6715-6727.

58. Sakuraba, H.; Ishizaki, H.; Tanaka, Y.; Shimizu, T., *J. Incl. Phenom.*, **1987,** *5*, 449-458.

59. Abonia, R.; Garay, A.; Castillo, J. C.; Insuasty, B.; Quiroga, J.; Nogueras, M.; Cobo, J.; Butassi, E.; Zacchino, S., *Molecules*, **2018,** *23*, 520.

60. Rotstein, B. H.; Hooker, J. M.; Woo, J.; Collier, T. L.; Brady, T. J.; Liang, S. H.; Vasdev, N., *ACS Med. Chem. Lett.*, **2014,** *5*, 668-672.

61. Vaughan, B. A.; Webster-Gardiner, M. S.; Cundari, T. R.; Gunnoe, T. B., *Science*, **2015,** *348*, 421-424.

62. Reetz, M. T.; de Vries, J. G., *Chem. Commun.*, **2004**, 1559-1563.

63. Boyarskiy, V. P.; Ryabukhin, D. S.; Bokach, N. A.; Vasilyev, A. V., *Chem. Rev.*, **2016,** *116*, 5894-5986.

64. Jia, C.; Lu, W.; Oyamada, J.; Kitamura, T.; Matsuda, K.; Irie, M.; Fujiwara, Y., *J. Am. Chem. Soc.*, **2000,** *122*, 7252-7263.

65. Otley, K. D.; Ellman, J. A., *Org. Lett.*, **2015,** *17*, 1332-1335.

66. Cheng, K.; Yao, B.; Zhao, J.; Zhang, Y., *Org. Lett.*, **2008,** *10*, 5309-5312.

67. Zhang, G.; Yang, L.; Wang, Y.; Xie, Y.; Huang, H., *J. Am. Chem. Soc.*, **2013,** *135*, 8850-8853.

68. Algarra, A. G.; Cross, W. B.; Davies, D. L.; Khamker, Q.; Macgregor, S. A.; McMullin, C. L.; Singh, K., *J. Org. Chem.*, **2014,** *79*, 1954-1970.

69. Zheng, L.; Hua, R., *J. Org. Chem.*, **2014,** *79*, 3930-3936.

70. Ma, W.; Graczyk, K.; Ackermann, L., *Org. Lett.*, **2012,** *14*, 6318-6321.

71. Davies, D. L.; Macgregor, S. A.; McMullin, C. L., *Chem. Rev.*, **2017,** *117*, 8649-8709.

72. Crabtree, R. H., *Angew. Chem. Int. Ed.*, **1993,** *32*, 789-805.

73. Atheaux, I.; Delpech, F.; Donnadieu, B.; Sabo-Etienne, S.; Chaudret, B.; Hussein, K.; Barthelat, J.-C.; Braun, T.; Duckett, S. B.; Perutz, R. N., *Organometallics*, **2002,** *21*, 5347-5357.

74. Perutz, R. N.; Sabo-Etienne, S., *Angew. Chem. Int. Ed.*, **2007,** *46*, 2578-2592.

75. Lafrance, M.; Rowley, C. N.; Woo, T. K.; Fagnou, K., *J. Am. Chem. Soc.*, **2006,** *128*, 8754-8756.

76. Davies, D. L.; Donald, S. M. A.; Macgregor, S. A., *J. Am. Chem. Soc.*, **2005,** *127*, 13754-13755.

77. David, L.; Keith, F., *Chem. Lett.*, **2010,** *39*, 1118-1126.

78. Ackermann, L., *Chem. Rev.*, **2011,** *111*, 1315-1345.

79. Kurzeev, S. A.; Kazankov, G. M.; Ryabov, A. D., *Inorg. Chim. Acta*, **2002,** *340*, 192-196.

80. Gorelsky, S. I.; Lapointe, D.; Fagnou, K., *J. Am. Chem. Soc.*, **2008,** *130*, 10848-10849.

81. Zaera, F., *Chem. Soc. Rev.*, **2014,** *43*, 7624-7663.

82. Greetham, G. M.; Sole, D.; Clark, I. P.; Parker, A. W.; Pollard, M. R.; Towrie, M., *Rev. Sci. Instrum.*, **2012,** *83*, 103107.

83. Blackmond, D. G., *Angew. Chem. Int. Ed.*, **2005,** *44*, 4302-4320.

84. Bray, J. T. W.; Ford, M. J.; Karadakov, P. B.; Whitwood, A. C.; Fairlamb, I. J. S., *React. Chem. Eng.*, **2019,** *4*, 122-130.

85. Barker, G.; McGrath, J. L.; Klapars, A.; Stead, D.; Zhou, G.; Campos, K. R.; O'Brien, P., *J. Org. Chem.*, **2011,** *76*, 5936-5953.

86. He, C.; Zhang, G.; Ke, J.; Zhang, H.; Miller, J. T.; Kropf, A. J.; Lei, A., *J. Am. Chem. Soc.*, **2013,** *135*, 488-493.

87. Cornils, B.; Herrmann, W. A.; Rasch, M., *Angew. Chem.*, **1994,** *106*, 2219-2238.

88. Whyman, R., *J. Organomet. Chem.*, **1974,** *66*, C23-C25.

89. Whyman, R., *J. Organomet. Chem.*, **1974,** *81*, 97-106.

90. Damoense, L.; Datt, M.; Green, M.; Steenkamp, C., *Coord. Chem. Rev.*, **2004,** *248*, 2393-2407.

91. Garland, M.; Bor, G., *Inorg. Chem.*, **1989,** *28*, 410-413.

92. Eischens, R. P.; Pliskin, W. A.; Francis, S. A., *J. Chem. Phys.*, **1954,** *22*, 1786-1787.

93. Tolman, C. A., *Chem. Rev.*, **1977,** *77*, 313-348.

94. Djukic, J.-P.; Maisse, A.; Pfeffer, M., *J. Organomet. Chem.*, **1998,** *567*, 65-74.

95. Clerk, M. D.; Zaworotko, M. J., *J. Chem. Soc., Chem. Commun.*, **1991**, 1607-1608.

96. Bock, S.; Mackenzie, C. F.; Skelton, B. W.; Byrne, L. T.; Koutsantonis, G. A.; Low, P. J., *J. Organomet. Chem.*, **2016,** *812*, 190-196.

97. Pan, X.; Philbin, C. E.; Castellani, M. P.; Tyler, D. R., *Inorg. Chem.*, **1988,** *27*, 671-676.

98. Schaller, C. P.; Cummins, C. C.; Wolczanski, P. T., *J. Am. Chem. Soc.*, **1996,** *118*, 591-611.

99. Gómez-Gallego, M.; Sierra, M. A., *Chem. Rev.*, **2011,** *111*, 4857-4963.

100. Towrie, M.; Gabrielsson, A.; Matousek, P.; Parker, A. W.; Rodriguez, A. M. B.; Vlček, A., *Appl. Spectrosc.*, **2005,** *59*, 467-473.

101. J C Owrutsky; D Raftery, a.; Hochstrasser, R. M., *Annu. Rev. Phys. Chem.*, **1994,** *45*, 519-555.

102. Moustakas, A.; Weitz, E., *J. Chem. Phys.*, **1993,** *98*, 6947-6957.

103. Heilweil, E. J.; Cavanagh, R. R.; Stephenson, J. C., *Chem. Phys. Lett.*, **1987,** *134*, 181-188.

104. Alharbi, A.; Boguslavskiy, A. E.; Austin, D.; Thiré, N.; Wood, D.; Hawkins, P.; McGrath, F.; Johnson, A. S.; Lopez-Quintas, I.; Schmidt, B.; Légaré, F.; Marangos, J. P.; Le, A.-T.; Bhardwaj, R., *Sci. Rep.*, **2018,** *8*, 3789.

105. Schmidhammer, U.; Roth, S.; Riedle, E.; Tishkov, A. A.; Mayr, H., *Rev. Sci. Instrum.*, **2005,** *76*, 093111.

106. Bloembergen, N., *Reviews of Modern Physics*, **1999,** *71*, S283-S287.

107. Johnson, C. K.; Bostick, J. M.; Mounter, S. A.; Ratzlaff, K. L.; Schloemer, D. E., *Rev. Sci. Instrum.*, **1988,** *59*, 2375-2379.

108. Bredenbeck, J.; Helbing, J.; Hamm, P., *Rev. Sci. Instrum.*, **2004,** *75*, 4462-4466.

109. Yu, A.; Ye, X.; Ionascu, D.; Cao, W.; Champion, P. M., *Rev. Sci. Instrum.*, **2005,** *76*, 114301.

110. Carroll, E. C.; Hill, M. P.; Madsen, D.; Malley, K. R.; Larsen, D. S., *Rev. Sci. Instrum.*, **2009,** *80*, 026102.

111. Greetham, G. M.; Donaldson, P. M.; Nation, C.; Sazanovich, I. V.; Clark, I. P.; Shaw, D. J.; Parker, A. W.; Towrie, M., *Appl. Spectrosc.*, **2016,** *70*, 645-653.

112. Fritzsch, R.; Greetham, G. M.; Clark, I. P.; Minnes, L.; Towrie, M.; Parker, A. W.; Hunt, N. T., *J. Phys. Chem. B*, **2019,** *123*, 6188-6199.

113. Keane, P. M.; Kelly, J. M., *Coord. Chem. Rev.*, **2018,** *364*, 137-154.

114. Brown, A. M.; McCusker, C. E.; Carey, M. C.; Blanco-Rodríguez, A. M.; Towrie, M.; Clark, I. P.; Vlček, A.; McCusker, J. K., *J. Phys. Chem. A*, **2018,** *122*, 7941-7953.

115. Childs, G. I.; Colley, C. S.; Dyer, J.; Grills, D. C.; Sun, X.-Z.; Yang, J.; George, M. W., *J. Chem. Soc., Dalton Trans.*, **2000**, 1901-1906.

116. Sun, X.-Z.; Grills, D. C.; Nikiforov, S. M.; Poliakoff, M.; George, M. W., *J. Am. Chem. Soc.*, **1997,** *119*, 7521-7525.

117. Cowan, A. J.; Portius, P.; Kawanami, H. K.; Jina, O. S.; Grills, D. C.; Sun, X.-Z.; McMaster, J.; George, M. W., *Proc. Natl. Acad. Sci.*, **2007,** *104*, 6933-6938.

118. Calladine, J. A.; Torres, O.; Anstey, M.; Ball, G. E.; Bergman, R. G.; Curley, J.; Duckett, S. B.; George, M. W.; Gilson, A. I.; Lawes, D. J.; Perutz, R. N.; Sun, X.-Z.; Vollhardt, K. P. C., *Chem. Sci.*, **2010,** *1*, 622-630.

119. Jackson, S. A.; Hodges, P. M.; Poliakoff, M.; Turner, J. J.; Grevels, F. W., *J. Am. Chem. Soc.*, **1990,** *112*, 1221-1233.

120. Hodges, P. M.; Jackson, S. A.; Jacke, J.; Poliakoff, M.; Turner, J. J.; Grevels, F. W., *J. Am. Chem. Soc.*, **1990,** *112*, 1234-1244.

121. Catellani, M.; Frignani, F.; Rangoni, A., *Angew. Chem. Int. Ed.*, **1997,** *36*, 119-122.

122. Guan, J.; Wriglesworth, A.; Sun, X. Z.; Brothers, E. N.; Zarić, S. D.; Evans, M. E.; Jones, W. D.; Towrie, M.; Hall, M. B.; George, M. W., *J. Am. Chem. Soc.*, **2018,** *140*, 1842-1854.

123. Farrell, I. R.; Matousek, P.; Towrie, M.; Parker, A. W.; Grills, D. C.; George, M. W.; Vlček, A., *Inorg. Chem.*, **2002,** *41*, 4318-4323.

124. Guillaumont, D.; Daniel, C.; Vlček, A., *Inorg. Chem.*, **1997,** *36*, 1684-1688.

125. Ma, F.; Jarenmark, M.; Hedström, S.; Persson, P.; Nordlander, E.; Yartsev, A., *RSC Adv.*, **2016,** *6*, 20507-20515.

126. Guillaumont, D.; Vlček, A.; Daniel, C., *J. Phys. Chem. A*, **2001,** *105*, 1107-1114.

127. Vlček, A. n., *Coord. Chem. Rev.*, **1998,** *177*, 219-256.

128. Balk, R. W.; Snoeck, T.; Stufkens, D. J.; Oskam, A., *Inorg. Chem.*, **1980,** *19*, 3015-3021.

129. Aucott, B. J., *PhD Thesis*. University of York, United Kingdom, **2019**.

130. Aucott, B. J.; Duhme-Klair, A.-K.; Moulton, B. E.; Clark, I. P.; Sazanovich, I. V.; Towrie, M.; Hammarback, L. A.; Fairlamb, I. J. S.; Lynam, J. M., *Organometallics*, **2019,** *38*, 2391-2401.

131. Moulton, B. E., *PhD Thesis*. University of York, United Kingdom, **2008**.

132. Boese, W. T.; Ford, P. C., *J. Am. Chem. Soc.*, **1995,** *117*, 8381-8391.

133. Hepp, A. F.; Wrighton, M. S., *J. Am. Chem. Soc.*, **1983,** *105*, 5934-5935.

134. Dunkin, I. R.; Haerter, P.; Shields, C. J., *J. Am. Chem. Soc.*, **1984,** *106*, 7248-7249.

135. Meyer, T. J.; Caspar, J. V., *Chem. Rev.*, **1985,** *85*, 187-218.

136. Zhang, J. Z.; Harris, C. B., *J. Chem. Phys.*, **1991,** *95*, 4024-4032.

137. Seder, T. A.; Church, S. P.; Weitz, E., *J. Am. Chem. Soc.*, **1986,** *108*, 7518-7524.

138. Waldman, A.; Ruhman, S.; Shaik, S.; Sastry, G. N., *Chem. Phys. Lett.*, **1994,** *230*, 110-116.

139. Yesaka, H.; Kobayashi, T.; Yasufuku, K.; Nagakura, S., *J. Am. Chem. Soc.*, **1983,** *105*, 6249-6252.

140. Kyu Kim, S.; Pedersen, S.; Zewail, A. H., *Chem. Phys. Lett.*, **1995,** *233*, 500-508.

141. Steinhurst, D. A.; Baronavski, A. P.; Owrutsky, J. C., *Chem. Phys. Lett.*, **2002,** *361*, 513-519.

142. Eastwood, J., *Unpublished Work*, University of York, United Kingdom, **2018**.

143. McCullen, S. B.; Brown, T. L., *Inorg. Chem.*, **1981,** *20*, 3528-3533.

144. Kobayashi, T.; Ohtani, H.; Noda, H.; Teratani, S.; Yamazaki, H.; Yasufuku, K., *Organometallics*, **1986,** *5*, 110-113.

145. Johnson, D., *Unpublished Work*, University of York, United Kingdom, **2018**.

146. Hammarback, L. A.; Clark, I. P.; Sazanovich, I. V.; Towrie, M.; Robinson, A.; Clarke, F.; Meyer, S.; Fairlamb, I. J. S.; Lynam, J. M., *Nat. Catal.*, **2018**.

147. Clarke, F., *MChem Project Report*, University of York, United Kingdom, **2017**.

148. Bruce, M. I., *Angewandte Chemie International Edition in English*, **1977,** *16*, 73-86.

149. Hu, Y.; Zhou, B.; Chen, H.; Wang, C., *Angew. Chem. Int. Ed.*, **2018,** *57*, 12071-12075.

150. Alharis, R. A.; McMullin, C. L.; Davies, D. L.; Singh, K.; Macgregor, S. A., *J. Am. Chem. Soc.*, **2019,** *141*, 8896-8906.

151. Zell, D.; Dhawa, U.; Müller, V.; Bursch, M.; Grimme, S.; Ackermann, L., *ACS Catalysis*, **2017,** *7*, 4209-4213.

152. Neville, A. G.; Brown, C. E.; Rayner, D. M.; Lusztyk, J.; Ingold, K. U., *J. Am. Chem. Soc.*, **1991,** *113*, 1869-1870.

153. Klamt, A.; Schüürmann, G., *J. Chem. Soc., Perkin Trans. 2*, **1993**, 799-805.

154. Cho, K.-B.; Kim, E. J.; Seo, M. S.; Shaik, S.; Nam, W., *Chem. Eur. J.*, **2012,** *18*, 10444-10453.

155. Wang, H.; Pesciaioli, F.; Oliveira, J. C. A.; Warratz, S.; Ackermann, L., *Angew. Chem. Int. Ed.*, **2017,** *56*, 15063-15067.

156. Ma, X.; Dang, Y., *J. Org. Chem.*, **2019,** *84*, 1916-1924.

157. Wang, C.; Wang, A.; Rueping, M., *Angew. Chem. Int. Ed.*, **2017,** *56*, 9935-9938.

158. Wang, C.; Maity, B.; Cavallo, L.; Rueping, M., *Org. Lett.*, **2018,** *20*, 3105-3108.

159. Flanagan, L.; Steen, R. R.; Saxby, K.; Klatter, M.; Aucott, B. J.; Winstanley, C.; Fairlamb, I. J. S.; Lynam, J. M.; Parkin, A.; Friman, V.-P., *Front. Microbiol.*, **2018,** *9*, 195.

160. Narayan, S.; Muldoon, J.; Finn, M. G.; Fokin, V. V.; Kolb, H. C.; Sharpless, K. B., *Angew. Chem. Int. Ed.*, **2005,** *44*, 3275-3279.

161. Clot, E.; Besora, M.; Maseras, F.; Megret, C.; Eisenstein, O.; Oelckers, B.; Perutz, R. N., *Chem. Commun.*, **2003**, 490-491.

162. Clot, E.; Oelckers, B.; Klahn, A. H.; Eisenstein, O.; Perutz, R. N., *Dalton Trans.*, **2003**, 4065-4074.

163. Clot, E.; Mégret, C.; Eisenstein, O.; Perutz, R. N., *J. Am. Chem. Soc.*, **2009,** *131*, 7817-7827.

164. Selmeczy, A. D.; Jones, W. D.; Partridge, M. G.; Perutz, R. N., *Organometallics*, **1994,** *13*, 522-532.

165. Guihaumé, J.; Clot, E.; Eisenstein, O.; Perutz, R. N., *Dalton Trans.*, **2010,** *39*, 10510-10519.

166. Bruce, M. I.; Goodall, B. L.; Stone, F. G. A., *J. Chem. Soc., Dalton Trans.*, **1978**, 687-694.

167. Morton, C.; Duncalf, D. J.; Rourke, J. P., *J. Organomet. Chem.*, **1997,** *530*, 19-25.

168. Bishop, A., *MChem Project Report*, University of York, United Kingdom, **2016**.

169. Jordan, C., *Unpublished Work*, University of York, United Kingdom, **2017**.

170. Milani, J.; Pridmore, N. E.; Whitwood, A. C.; Fairlamb, I. J. S.; Perutz, R. N., *Organometallics*, **2015,** *34*, 4376-4386.

171. El Seoud, O. A.; Baader, W. J.; Bastos, E. L., *Practical Chemical Kinetics in Solution. In Encyclopedia of Physical Organic Chemistry*, **2016**, 1-68.

172. Prier, C. K.; Rankic, D. A.; MacMillan, D. W. C., *Chem. Rev.*, **2013,** *113*, 5322-5363.

173. Koyama, D.; Dale, H. J. A.; Orr-Ewing, A. J., *J. Am. Chem. Soc.*, **2018,** *140*, 1285-1293.

174. Yan, T.; Feringa, B. L.; Barta, K., *ACS Catalysis*, **2016,** *6*, 381-388.

175. Neri, G.; Walsh, J. J.; Teobaldi, G.; Donaldson, P. M.; Cowan, A. J., *Nat. Catal.*, **2018,** *1*, 952-959.

176. de la Cruz Cruz, J. I.; Juárez-Saavedra, P.; Paz-Michel, B.; Leyva-Ramirez, M. A.; Rajapakshe, A.; Vannucci, A. K.; Lichtenberger, D. L.; Paz-Sandoval, M. A., *Organometallics*, **2014,** *33*, 278-288.

177. Pinto, M.; Friães, S.; Franco, F.; Lloret-Fillol, J.; Royo, B., *ChemCatChem*, **2018,** *10*, 2734-2740.

178. King, R. B.; Stokes, J. C.; Korenowski, T. F., *J. Organomet. Chem.*, **1968,** *11*, 641-643.

179. Hershberger, J. W.; Kochi, J. K., *Polyhedron*, **1983,** *2*, 929-934.

180. Still, W. C.; Kahn, M.; Mitra, A., *J. Org. Chem.*, **1978,** *43*, 2923-2925.

181. Ward, J. S.; Lynam, J. M.; Moir, J. W. B.; Sanin, D. E.; Mountford, A. P.; Fairlamb, I. J. S., *Dalton Trans.*, **2012,** *41*, 10514-10517.

182. Császár, P.; Pulay, P., *J. Mol. Struct.*, **1984,** *114*, 31-34.

183. Ahlrichs, R.; Bär, M.; Häser, M.; Horn, H.; Kölmel, C., *Chem. Phys. Lett.*, **1989,** *162*, 165-169.

184. Deglmann, P.; Furche, F.; Ahlrichs, R., *Chem. Phys. Lett.*, **2002,** *362*, 511-518.

185. Deglmann, P.; May, K.; Furche, F.; Ahlrichs, R., *Chem. Phys. Lett.*, **2004,** *384*, 103-107.

186. Eichkorn, K.; Treutler, O.; Öhm, H.; Häser, M.; Ahlrichs, R., *Chem. Phys. Lett.*, **1995,** *240*, 283-290.

187. Eichkorn, K.; Weigend, F.; Treutler, O.; Ahlrichs, R., *Theor. Chem. Acc.*, **1997,** *97*, 119-124.

188. Treutler, O.; Ahlrichs, R., *J. Chem. Phys.*, **1995,** *102*, 346-354.

189. Arnim, M. v.; Ahlrichs, R., *J. Chem. Phys.* **1999,** *111*, 9183-9190.

190. Grimme, S.; Ehrlich, S.; Goerigk, L., *J. Comput. Chem.*, **2011,** *32*, 1456-1465.

191. Grimme, S.; Antony, J.; Ehrlich, S.; Krieg, H., *J. Chem. Phys.*, **2010,** *132*, 154104.

192. Bew, S. P.; Hiatt-Gipson, G. D.; Lovell, J. A.; Poullain, C., *Org. Lett.*, **2012,** *14*, 456-459.

193. Zhang, H.; Yang, Z.; Ma, Q.; Liu, J.; Zheng, Y.; Guan, M.; Wu, Y., *Green Chem.*, **2018,** *20*, 3140-3146.

194. Gao, K.; Lee, P.-S.; Fujita, T.; Yoshikai, N., *J. Am. Chem. Soc.*, **2010,** *132*, 12249-12251.

195. Jin, J.; Wen, Q.; Lu, P.; Wang, Y., *Chem. Commun.*, **2012,** *48*, 9933-9935.

196. Xi, L.-Y.; Zhang, R.-Y.; Liang, S.; Chen, S.-Y.; Yu, X.-Q., *Org. Lett.*, **2014,** *16*, 5269-5271.

197. Fabry, D. C.; Ho, Y. A.; Zapf, R.; Tremel, W.; Panthöfer, M.; Rueping, M.; Rehm, T. H., *Green Chem.*, **2017,** *19*, 1911-1918.

198. Woo, H.; Cho, S.; Han, Y.; Chae, W.-S.; Ahn, D.-R.; You, Y.; Nam, W., *J. Am. Chem. Soc.*, **2013,** *135*, 4771-4787.

199. Li, H.; Li, Y.; Zhang, X.-S.; Chen, K.; Wang, X.; Shi, Z.-J., *J. Am. Chem. Soc.*, **2011,** *133*, 15244-15247.

200. Nuhant, P.; Oderinde, M. S.; Genovino, J.; Juneau, A.; Gagné, Y.; Allais, C.; Chinigo, G. M.; Choi, C.; Sach, N. W.; Bernier, L.; Fobian, Y. M.; Bundesmann, M. W.; Khunte, B.; Frenette, M.; Fadeyi, O. O., *Angew. Chem. Int. Ed.*, **2017,** *56*, 15309-15313.

201. Gilbert, B. C.; Kalz, W.; Lindsay, C. I.; McGrail, P. T.; Parsons, A. F.; Whittaker, D. T. E., *Tetrahedron Lett.*, **1999,** *40*, 6095-6098.

202. Chung, Y. K.; Williard, P. G.; Sweigart, D. A., *Organometallics*, **1982,** *1*, 1053-1056.

203. Eastwood, J., *Unpublished Work*, University of York, United Kingdom, **2019**.

204. Reay, A. J.; Hammarback, L. A.; Bray, J. T. W.; Sheridan, T.; Turnbull, D.; Whitwood, A. C.; Fairlamb, I. J. S., *ACS Catalysis*, **2017,** *7*, 5174-5179.

205. Mo, F.; Dong, G.; Zhang, Y.; Wang, J., *Org. Biomol. Chem.*, **2013,** *11*, 1582-1593.

206. Colleville, A. P.; Horan, R. A. J.; Tomkinson, N. C. O., *Org. Process Res. Dev.*, **2014,** *18*, 1128-1136.

207. Drew, D.; Darensbourg, D. J.; Darensbourg, M. Y., *Inorg. Chem.*, **1975,** *14*, 1579-1584.